UNIVERSITEIT GENT

Spatial and temporal petrological-geochemical variations in the volcanic rocks of the Saronic Gulf (West Aegean arc, Greece): influence of local geodynamic parameters on magma genesis.

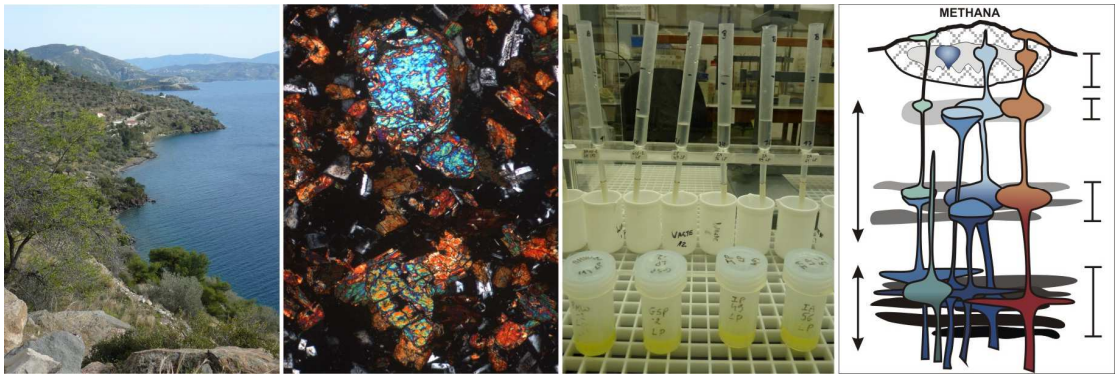

Ingrid Smet

Thesis submitted in partial fulfilment to achieve the degree of Doctor in Sciences, Geology

Academic year 2013-2014

Ghent University
Faculty of Sciences, Department of Geology and Soil Sciences
Research unit Mineralogy and Petrology
Krijgslaan 281, S8, WE13, B-9000 Ghent, Belgium

Supervisors: Prof. Dr. Marlina Elburg & Prof. Dr. Peter Van den haute

Members of the reading committee:

Prof. Dr. Marlina Elburg (University of Johannesburg, promotor)
Prof. Dr. Peter Van den haute (Ghent University, promotor)
Prof. Dr. Pieter Vroon (VU University Amsterdam)
Em. Prof. Dr. Jan Hertogen (KULeuven)

Other members of the examination committee:

Prof. Dr. Peter Finke (Ghent University, chair)
Prof. Dr. Frank Vanhaecke (Ghent University)
Prof. Dr. Johan De Grave (Ghent University)
Dr. Phlorias Mees (KMMA-Tervuren, Ghent University)

Public thesis defence:

Friday, 25th of April 2014 at 4.00pm, Auditorium Valere Billiet, S8, Krijgslaan 281, 9000 Ghent

To refer to this thesis:

Smet, I. 2014. Spatial and temporal petrological-geochemical variations in the volcanic rocks of the Saronic Gulf (West Aegean arc, Greece): Influence of local geodynamic parameters on magma genesis. PhD thesis, Ghent University, Belgium, 349p.

Table of Contents

Ithaca

Σὰ βγεῖς στὸν πηγαιμὸ γιὰ τὴν Ἰθάκη,
νὰ εὔχεσαι νά ῾ναι μακρὺς ὁ δρόμος,
γεμάτος περιπέτειες, γεμάτος γνώσεις.
Τοὺς Λαιστρυγόνας καὶ τοὺς Κύκλωπας,
τὸν θυμωμένο Ποσειδῶνα μὴ φοβᾶσαι,
τέτοια στὸν δρόμο σου ποτέ σου δὲν θὰ βρεῖς,
ἂν μέν᾽ ἡ σκέψις σου ὑψηλή, ἂν ἐκλεκτὴ
συγκίνησις τὸ πνεῦμα καὶ τὸ σῶμα σου ἀγγίζει.
Τοὺς Λαιστρυγόνας καὶ τοὺς Κύκλωπας,
τὸν ἄγριο Ποσειδῶνα δὲν θὰ συναντήσεις,
ἂν δὲν τοὺς κουβανεῖς μὲς στὴν ψυχή σου,
ἂν ἡ ψυχή σου δὲν τοὺς στήνει ἐμπρός σου.
Νὰ εὔχεσαι νά ῾ναι μακρὺς ὁ δρόμος.
Πολλὰ τὰ καλοκαιρινὰ πρωινὰ νὰ εἶναι
ποῦ μὲ τί εὐχαρίστηση, μὲ τί χαρὰ
θὰ μπαίνεις σὲ λιμένας πρωτοειδωμένους.
Νὰ σταματήσεις σ᾽ ἐμπορεῖα Φοινικικά,
καὶ τὲς καλὲς πραγμάτειες ν᾽ ἀποκτήσεις,
σεντέφια καὶ κοράλλια, κεχριμπάρια κ᾽ ἔβενους,
καὶ ἡδονικὰ μυρωδικὰ κάθε λογῆς,
ὅσο μπορεῖς πιὸ ἄφθονα ἡδονικὰ μυρωδικά.
Σὲ πόλεις Αἰγυπτιακὲς πολλὲς νὰ πᾷς,
νὰ μάθεις καὶ νὰ μάθεις ἀπ᾽ τοὺς
σπουδασμένους.
Πάντα στὸ νοῦ σου νά ῾χεις τὴν Ἰθάκη.
Τὸ φθάσιμον ἐκεῖ εἶν᾽ ὁ προορισμός σου.
Ἀλλὰ μὴ βιάζεις τὸ ταξίδι διόλου.
Καλλίτερα χρόνια πολλὰ νὰ διαρκέσει.
Καὶ γέρος πιὰ ν᾽ ἀράξεις στὸ νησί,
πλούσιος μὲ ὅσα κέρδισες στὸν δρόμο,
μὴ προσδοκώντας πλούτη νὰ σὲ δώσει ἡ Ἰθάκη.
Ἡ Ἰθάκη σ᾽ ἔδωσε τ᾽ ὡραῖο ταξίδι.
Χωρὶς αὐτὴν δὲν θά ῾βγαινες στὸν δρόμο.
Ἄλλα δὲν ἔχει νὰ σὲ δώσει πιά.
Κι ἂν πτωχικὴ τὴν βρεῖς, ἡ Ἰθάκη δὲν σὲ γέλασε.
Ἔτσι σοφὸς ποὺ ἔγινες, μὲ τόση πεῖρα,
ἤδη θὰ τὸ κατάλαβες οἱ Ἰθάκες τὶ σημαίνουν.

When you set sail for Ithaca,
wish for the road to be long,
full of adventures, full of knowledge.
The Lestrygonians and the Cyclopes,
an angry Poseidon — do not fear.
You will never find such on your path,
if your thoughts remain lofty, and your spirit
and body are touched by a fine emotion.
The Lestrygonians and the Cyclopes,
a savage Poseidon you will not encounter,
if you do not carry them within your spirit,
if your spirit does not place them before you.
Wish for the road to be long.
Many the summer mornings to be when
with what pleasure, what joy
you will enter ports seen for the first time.
Stop at Phoenician markets,
and purchase the fine goods,
nacre and coral, amber and ebony,
and exquisite perfumes of all sorts,
the most delicate fragrances you can find.
To many Egyptian cities you must go,
to learn and learn from the cultivated.
Always keep Ithaca in your mind.
To arrive there is your final destination.
But do not hurry the voyage at all.
It is better for it to last many years,
and when old to rest in the island,
rich with all you have gained on the way,
not expecting Ithaca to offer you wealth.
Ithaca has given you the beautiful journey.
Without her you would not have set out on the road.
Nothing more does she have to give you.
And if you find her poor, Ithaca has not deceived you.
Wise as you have become, with so much experience,
you must already have understood what Ithacas
mean.

Konstantinos Petrou Kavafis

Acknowledgements

Gent, Easter 2014

I remember being told by a fellow PhD student that a doctorate is not only studying for an academic degree or learning how to become an autonomous researcher – whether you like it or not, he said, it usually becomes a personal journey of self-discovery as well. I remember listening to my friend who was already in the 'thesis-zone' whereas I had just started my studies. And I remember not having a clue what he was going on about.

However, now that I finished my PhD thesis, I think I finally understand what he was trying to tell me. Forgive me if I sound too pompous, but I would dare describing the past 6.5 years as my personal odyssey. Although not involving a Trojan war, Cyclopes, Scylla or Charybdis, my road to Ithaka was an adventurous journey bringing both joy and sadness, triumph and frustration, questions and answers, happiness and pain, knowledge and ignorance, love and hate. I thereby ticked off the classic PhD hurdles of failed experiments, laptop crashes, lost data, relocation of one's supervisor, broken instruments, disagreements with colleagues or finding your own way as a scientist. But life outside the PhD also continues, of course, and with it the daily struggles and blessings. I lost loved ones, found new friends, saw relationships with those dearest to me change and was forced to look into the mirror and figure out who I am. Carrying out and completing this PhD was therefore a work of perseverance – as well as a hell of a ride that was worth every twist and turn.

Although I did it my way, I would be lying if I'd say I did it all by myself. Whether they were there from the day I was born or we met just the other day, the support of uncountable friends and colleagues, neighbours and family members, mentors and feline housemates, partners and sometimes even perfect strangers has been invaluable to me throughout this journey. So I will take some time now to express my thanks to as many of you as possible, in no particular order.

Trying to figure out when all of this started, I guess I have to go back to my toddler days when I started a rock/mineral collection with my brother and had my parents carrying all the pebbles I picked up during walks. Dearest mum, you taught me how to work hard, never give up, be thorough and do the best you can. Your support throughout my school years and academic career and your belief in your somewhat 'off the beaten track' daughter helped getting me to this day. If you can dream it, you can achieve it! Dearest dad, I have no doubt that I inherited my love for nature, interest in science and inclination towards discovery and adventure from you. Although geology is one of the very few topics that fails to raise your interest, you do come up to me with questions and thereby train me in communicating my knowledge to non-specialists – a skill I believe to be vital for any scientist. I hope we will soon embark on some more travelling adventures together! Dear brother, you have since long traded your fascination for minerals into a passion for astronomy – and I have always admired your dedication and professionalism for this hobby as well as your other interests. I furthermore appreciate that you provide me with the brand new challenge of becoming an aunt! As our family is rather small, the love, tasty food, good advice and cheering on of my four grandparents was even more important in becoming who I am. I will never forget any of you, whether or not you are still here or you recognise me when I come to visit.

I am also very grateful for the support from my academic family. My 'doktormutter' Marlina Elburg had the questionable honour to introduce me into hands-on geochemistry, subduction zone magmatism, thorough fieldwork and the fascinating world of petrography. Dear Marlina, thank you for sharing so much of your time and knowledge with me. We don't always agree on scientific matters but you did teach me to be critical to both my own work and that of others – besides educating me about red wine, oysters, animal names and opera. We had some great times together on fieldwork and

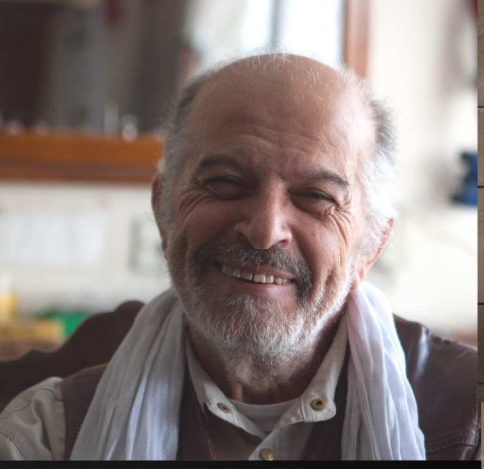













conferences which I sincerely hope to be continued! My second supervisor Peter Van den haute has been an invaluable help with all the practical issues that arise when one wants to submit and complete a PhD thesis. Dear Peter, I greatly appreciate the time you took to discuss with me your feedback on my manuscripts – your input from a different geological viewpoint was really interesting and refreshing. If your retirement-travels would ever steer you to an active volcano in Italy, Greece or elsewhere, please know that I will gladly help you organising such a trip!

My interest in igneous rocks was actually raised before I started my PhD research at Ghent University. As supervisor of my MSc dissertation at KU Leuven, Jan Hertogen gave me the chance to study the geochemistry and petrology of plutonic rocks from Norway. Dear Jan, I remember the slightly bewildered look on your face when we were discussing my first draft of the geochemistry interpretations, on the way back from the Harz & Eiffel excursion – I hope you enjoyed my doctoral dissertation more. I also vividly remember the feelings of excitement and accomplishment when I was interpreting the data of my MSc study into a petrogenetic model – it is this memory that eventually convinced me to continue this type of research in a PhD. Other academic family members include Richard Smeets and Roelaf Schuiling who first taught my supervisor Marlina Elburg the ins and outs of geochemical laboratory work and mentored her on her first volcanic fieldwork (on the Greek island of Santorini), respectively. Dear Richard, I greatly appreciate that you so willingly shared your knowledge of geochemical laboratory work and your clean lab with me. It really meant a lot that an expert (and very kind person) as yourself trusted my analytical chemistry skills and was always ready for advice or tea and a chat. Dear Olaf, it was great meeting you on the 2012 VOLSAM conference and having the pleasure of your positive, intelligent, open-minded and humoristic company on a number of occasions afterwards. A big thank you for the continuing stream of support-e-mails that pulled me through the stressful last 12 months!

Another person that I met on the VOLSAM conference and who became very important to me ever since is Tom Pfeiffer. Dearest Tom, you are one of the most warm-hearted, interesting, funny, daring and intelligent people I ever met and I am very grateful for all the things you taught me about volcanology during our adventures on Stromboli and Etna. Thank you also for trusting me to look after the loveliest 3-legged grey-beige tiger and for daily encouraging and supporting me with the PhD write-up. I hope we will undertake many more volcano expeditions together and I wish you the very best of luck with continuing to make your passion for travelling, volcanoes and photography your job!

Throughout the different conferences and seminars I attended, I got acquainted to many more colleagues who since became dear friends and form a circle of fellow PhD students cheering one another on during the different stages of the doctoral ordeal. The most important one is János Kodolányi who offered unwavering support and a strong believe in me from the start of my PhD up till my defence. Dearest János, our relationship went through many different phases over the past 5 years and I hope we can continue our friendship for many more yours to come. You were always ready to share your geochemical-petrological knowledge with me and to give advice and your opinion on my scientific writings and presentations. I furthermore spend some of the best times of my life with you doing hiking, cooking, laughing, talking, listening to music, travelling through France, watching movies and drinking some wine. You are one of the most beautiful, funny, caring, talented and kind people I ever met and I have learned so much from you on so many different levels.

Another ‘conference buddy’ dating back to those early PhD days is Dustin Trail – always a great pleasure to meet up with you and talk both serious science and total nonsense, you’re a star! More recently I had the pleasure to meet Angeliki Efstathiou – I thoroughly enjoy our discussions on Methana, volcanism and tectonics and look forward to do fieldwork together as well as to see you round up your PhD which I know will be fabulous, just as you are! Other wonderful fellow scientists I met during PhD work abroad and who have been an inspiration, a friend, a support and/or great fun to hang out with include Greg Van den Bleeken (keep up the gorgeous photography and green fingers!), Despina Kalispera, Jenny Rapp, Charlie Stamper, Cassian Pirard, Seann McKibbin, Beverley





THE NORTH FACE

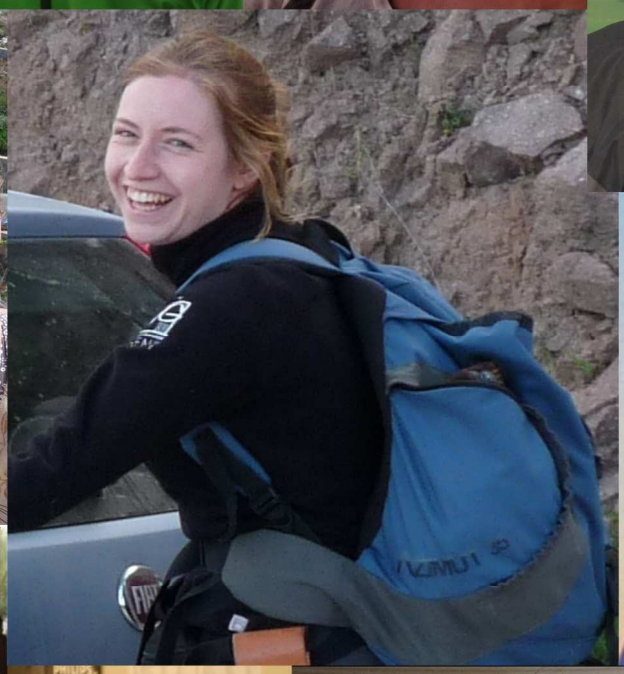






Coldwell, Kate Souders, Ananya Mallik, Jelle Van Sijl, Ineke Wijbrans, Marta Berkesi, Rui Leal Miranda, Joe Hiess, Sebastian Wiesmaier, Yi-Jen Lai, Vera Laurenz, Oliver Nebel, Kate Kiseeva, Evi Nomikou, Richard Arculus, Bruce Schaefer, Horst Marschall, Peter Ulmer, Tobi Rehder, Christian Kieslinger and Christian Kling.

Geochemical analyses at the VU University Amsterdam got me in touch with fellow PhD student Martijn Klaver who turned out to also be doing research in the South Aegean arc volcanoes. Martijn, thanks for sharing your office with me as well as your expertise in Hf isolation and taking apart a TIMS instrument. I thoroughly enjoyed us discussing our work, talking about travels, sampling Indonesian restaurants and comparing supervisors. I look forward to working together, seeing you graduate and showing you around the Saronic Gulf! Other friendly VU geology colleagues that help make my time there both more successful and agreeable include Lisette Kootker, Laura Font, Janne Koornneef, Bas van der Wagt, Pieter Vroon, Gareth Davies, Wim van Westrenen, Jan Wijbrans and Fenny Bosse. And let's not forget the hospitality of Floor Schuiling !

Working for 6.5 years at Ghent University of course also brought me in contact with a number of people which I hope to stay in touch with for a long time. I carried out my geochemical analyses at the Department of Analytical Chemistry where I met fellow PhD student Lana Van Heghe. Dear Lana, I am so glad that your first conference was at geological meeting and that we ended up going together! Through the years I have gotten to know you as a meticulous analytical chemist, great cook, lots of fun, caring friend, intelligent young woman and one of the funniest people I know. I wish you a long and happy future with Steven and look forward to more girls-night-and-sleep-overs in Athens! I am also grateful to Frank Vanhaecke for trusting a geologist with no analytical chemistry training to autonomously work in the clean lab and handle the OES and MS instruments! Friendly and helpful analytical chemistry colleagues furthermore include Bart Goossens, Veerle Devulder, Karen Van Hoecke, Steven Goderis, Lieve Balcaen, Chantal Hufkens and Karel Strijckmans. It was also a great pleasure to come across Bart Vekemans's enthusiasm and willingness to cooperate with researchers from very different fields.

In the corridors of the Department of Geology and Soil Sciences I met up with Willemijn Quaijtaal. Dear Willemijn, you are an intelligent and caring young woman, passionate about your science and with a weakness for plants and cats that is (not-so-)vaguely familiar to me. I enjoy your wicked sense of humour and our coffee breaks and pep-up-talks. Soon, you too will be rounding up your thesis and I wish you the very best of luck in your pursuit of an academic career! Fellow corridor-man Dimitri Vandenberghe was always ready to listen to my little tragedies, both work-related and of more private nature, and give his thoughtful advice. Dear Dimi, I simply cannot imagine to have carried out my PhD without the pleasure of your friendship and company. You are one of those people that helped me along the personal discovery part of the PhD journey whilst at the same time sharing your experiences in academic matters and scientific writing. I hope you will be able to continue your outstanding research and I promise to (try to) always have some Duvel in the fridge in Athens! Significantly boosting the positive atmosphere of our group, Gilles Velghe was a great colleague to have around when I started to work at the Mineralogy and Petrology group. Dear Gilles, trying to make me trip and stealing my frituur-meat aside, I am so happy to have you amongst my friends. You are one of the most positive people I know, with a great sense of humour and a big heart – please never change. Karen Fontijn undertook her PhD in volcanology with Marlina as her co-supervisor – which sort of makes her my doctorsister? Dear Karen, you are slightly quieter than most people and so it took me a bit of extra time to get to know you, but it was so worth it. In you, I found a true friend, good scientist, intelligent young woman and warm-hearted person with a passion for Africa and the safety for people living near volcanoes. I honestly think the world can never have enough Karens and I look forward to working together and trying to unravel that Plinian eruption of the Saronic Gulf!

Rindert Janssens was one of the students on the first Santorini-Naxos field trip that I was assisting in. Dear Rindert, I don't know anyone else who combines a big heart with a wicked sense of humour











move the cat





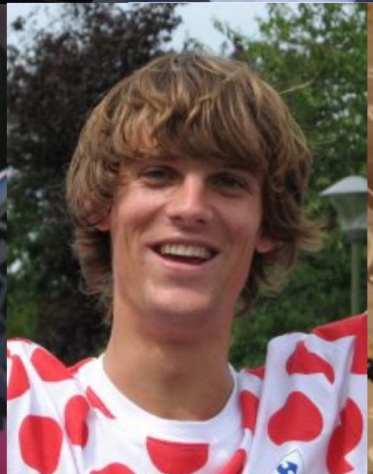

and a courageous attitude to life as you do. You have been a great support to me at the emotionally most difficult times and a great friend throughout – I wish you many more travels to mythical places as Ladak or Iran and hope we will stay in touch no matter what! Elien De Pelsmaeker showed interest in a geochemical-petrological master thesis and so we undertook fieldwork on Methana together. Dear Elien, I had the pleasure to see you evolve from a bright and keen master student into a hard-working, intelligent and determined fellow PhD student. At the same time, you became a kind a caring friend, always ready to share a laugh as well as to offer your shoulder. You're a great person and I can't wait to return the favour and cheer you on in the final stages of your PhD! My other female MinPet PhD colleague and doctorsister on Peter's side was Cilia Derese. Dear Cilia, our initial friendship got some dents early on along the way, but your courage to want to work them out got us closer again and am very grateful to count a dynamic, thoughtful, kind and interesting person as yourself amongst my friends. I wish you the best of luck with the move to Mainz and hope to stay in touch and meet up every once in a while! Other UGent geology colleagues more than worth mentioning for their fun company, cheering in my final PhD marathon and/or technical support include: Vera Marcelino, Mathijs Dumon, Thomas Vandorpe, Jasper Van Nieuland, Tim De Kock, Emmanuel Opolot, Ann-Eline De Beer, Jan Jurceka, David Van Rooij, Koen De Rycker, Daniëlle Schram, Mary-Ann del Marmol, Pieter Gurdebeke, Stanislas Delivet, Katharine Maussen, Gerald Ernst, Paul De Paepe, Johan De Grave, Georges Stoops, Phlorias Mees, Wim Lievens, Marc Faure and Kurt Blom.

Working in Gent eventually led to living in Gent – and what an extremely good thing it did, because my neighbours have been so supportive and downright wonderful that I would almost say 'With neighbours like these, who needs friends?'. Dear Syf, Tom, Son, Pat and Sam, some of the best moments of these past years were spend talking, eating, laughing or gardening with you! Thank you so much for the looking after my cats and plants and your seemingly unlimited support during the final weeks of the PhD in the form of bringing me food to stay alive, getting me a coffee to stay awake and keeping me company to stay human. I will miss you all and am considering renting neighbouring flats for you in Athens. As for my soft, fluffy and conveniently very quiet house mates Casper, Neko, Juul and Schnappi – you kept me sane and helped me more than you'll ever (care to) know!

Apart from friends, colleagues and neighbours that I met throughout the past years at Ghent University I also had the ongoing friendship, trust and support from friends made in the past. Dearest Evelien, we have been living in the same cities for a number of years now so that whenever I go next, my love will always stay with you although I do hope to keep in touch on a regular base. As my best and 'oldest' friend you know me very well and I do hope that also means you know that whatever the future brings I want to be there for you. After striking up great friendships during our master studies at Cardiff University we kept in touch despite moving around the world and each continuing their very own personal journey of life. Dear Pooja, Maria and Chris, your support and believe in me even if we were quite far apart meant the world to me and I praise myself lucky to have met such wonderful people like you. This also goes for you, dearest auntie Janet! Whether it was a hearty meal, a long talk, birthday celebrations, a stroll around town, a gardening day out or having a comforting mug of tea in the conservatory: both you and Marion have been wonderful friends, cheering me on during the PhD, enjoying time an some laughs together, giving me support and good advice whenever I needed it – you are stars!

Finally, there are also new friends for the future. Dear Christo, thanks for sharing your Athens with me, for all the nice food, laughter and talks so far and for coming all the way to Belgium to prepare Greek dishes for my PhD reception! Voula, Jörg and Kiki: we only started out our friendships and already you have shown me so much kindness and support and did we share much laughter, secrets, beautiful evenings and wine – the best is yet to come?

To everyone mentioned above and to all of you whom I forgot but will be banging my head against the wall for as they spring to mind when the thesis is already printed: thank you ever so much and all the best of luck in the future!

List of abbreviations used in this work

all	allanite
Am / am	amphibole
and	andesite
ap	apatite
bas	basalt
BCS	British Chemical Standard
BSE	Bulk Silicate Earth
Bt / bt	biotite
c-gr	coarse-grained
Cpx / cpx	clinopyroxene
CRM	Certified Reference Material
CrS	Cr-spinel
dac	dacite
(A)FC	(Assimilation and) Fractional Crystallisation
EC	Equilibrium Crystallisation
f-gr	fine-grained
Fe_2O_3* (or FeO*)	all iron reported as Fe_2O_3 (or as FeO)
FTO	Fe-Ti-oxides
gm	groundmass
grt	garnet
GSJ	Geological Survey of Japan
hbl	hornblende
HFSE	High Field Strength Elements
HP	High Pressure
HREE	Heavy REE
ICP	Inductively Coupled Plasma
ICP-OES	ICP -Optical Emission Spectrometry
ICP-Q-MS	ICP-Quadrupole-MS
LA	Laser Ablation
KF(Z)	Kefalonian Fault (zone)
LILE	Large Ion Lithophile Elements
LOI	Loss On Ignition
LP	Low Pressure
LREE	Light REE
MC-ICP-MS	Multi Collector ICP-MS

MOR(B)	Mid Ocean Ridge (Basalt)
MREE	Middle REE
MS	Mass Spectrometry
NA	Not Analysed
NAFZ	North Anatolian fault zone
Ol / ol	olivine
op	opacite
Opx / opx	orthopyroxene
ox	Fe-Ti-oxides
PDC	Pyroclastic Density Current
Pl / pl	plagioclase
ppl	under plane polarised light
ppm	parts per million
ps	pseudomorph
Px / px	pyroxene
Qtz / qtz	quartz
REE	Rare Earth Elements
SAAVA	South Aegean active volcanic arc
sed	sedimentary
SE	Standard Error
StDev / SD	Standard Deviation
USGS	United States Geological Survey
V (or ves)	vesicle
wt%	weight percent
WR	Whole Rock
xpl	under crossed polars
Zr / zrc	zircon

Chapter 1: Introduction

The current study on subduction-related volcanic rocks from Greece is situated within the broader geological context of plate tectonics and arc magma genesis. The general social, economic and scientific relevance of subduction zone studies is outlined and the specific research opportunities of the South Aegean arc are highlighted. A short overview on the history of geological research in the Saronic Gulf presents the context and relevance of the here presented geochemical-petrological study on Aegina, Methana and Poros.

1.1. Plate tectonics and subduction

The 'discovery' of plate tectonics in the late 1960s – early 1970s was a milestone for the understanding of geological processes that shaped our planet since its birth: for the first time it was possible to unify observations on seafloor spreading, continental drift and the formation of continental mountain ranges (Dickinson, 1970; Turcotte & Schubert, 2002; Schmincke, 2006; Spandler & Pirard, 2013). Plate tectonics explain how mantle convection leads to adiabatic upwelling of the asthenospheric mantle which, in turn, can undergo decompression melting (Fig. 1.1A). The resulting basaltic magmas may erupt at the earth's surface, breaking up tectonic plates in the process and forming new oceanic crust. Sustained upwelling of mantle melts will progressively push apart the pieces of torn-up plate (divergent plate margins) as the newly formed oceanic crust continuous to spread along its Mid Ocean Ridge (MOR) (Fig. 1.1A). With time, the young oceanic lithosphere (crust and underlying rigid lithospheric mantle) is hydrated by seawater and covered by continent-derived pelagic sediments, making it gradually cooler and increasingly thick and dense. As this oceanic lithosphere is pushed away from its MOR, 'drifting' on its underlying asthenospheric mantle, it will eventually come into contact with the boundary of another drifting piece of lithosphere (Fig. 1.1A). If this other plate with which it converges is a younger oceanic crust or a continental plate, the cooler and denser oceanic crust will be tectonically forced below it, leading to the formation of a subduction zone (Fig. 1.1A). Consumption of oceanic lithosphere in subduction zones at 'convergent plate margins' thus represents the necessary counterpart of formation of oceanic crust in MOR at divergent plate boundaries (Fig. 1.1A) (Turcotte & Schubert, 2002; Schmincke, 2006).

Subduction is one of the most fundamental processes on earth as it causes many present-day natural phenomena that have a daily impact on human life around the world (earthquakes, volcanic eruptions, ore deposits of precious metals and of trace elements indispensable for modern technology, …) (Schmincke, 2006; Chiaradia et al., 2012). The fact that subduction-related magmas represent only 10% of all annually erupted lavas is no measure for the importance of arc volcanic studies for hazard assessment: more than 80% of historically reported volcanic eruptions took place in arc settings (Schmincke, 2006). Subduction is also the driving force of mountain building which, together with arc volcanism, is thought to have led to the formation of the continental crust on which we live and to the redistribution of chemical elements between the earth's mantle and crust (Dickinson, 1971; Rudnick, 1995).

1.2. Genesis of arc magmas

Growing awareness of plate tectonics and the importance of subduction zones resulted in increasing research efforts in the field of subduction-related magmatism (see Spandler & Pirard, 2013, and references therein). This rapidly led to a general understanding of the chemical-physical processes that trigger arc volcanism above a subducted plate (Gill, 1981). The package of seawater-altered oceanic crust, its underlying lithospheric mantle and its overlying sediments that is pushed below the neighbouring plate is generally referred to as the 'subducted slab' (Fig. 1.1B). As this subducted slab is sinking into the mantle below the overriding plate, it is submitted to increasing temperatures and pressures which lead to a series of chemical-mineralogical reactions. At shallow depths and low temperatures (ca. 50km depth and 50-300°C), dehydration of the subducted slab will release interstitial and more loosely bound water from subducted sediments and hydrated oceanic crust (Fig. 1.1B). These hydrous fluids can subsequently ascent and give rise to fore-arc hydrothermal phenomena (Spandler & Pirard, 2013). As temperature and pressure continue to increase deeper into the mantle, most of the water initially present in the subducted sediments and altered oceanic crust is thought to have been released before the downgoing slab reaches sub-arc depths of ca. 90-160 km (Fig. 1.1B). Water is however also stored in hydrated mantle lithologies (serpentinite) of the oceanic lithosphere and of the mantle wedge above the subducted slab (Fig. 1.1B). At fore-arc depth and temperatures, this water is largely retained in the serpentine minerals. At sub-arc depths and 650-800°C, however, these serpentine minerals will gradually breakdown and also release their water contents (Fig. 1.1B) (Spandler & Pirard, 2013). As this water migrates upwards into the overlying (and

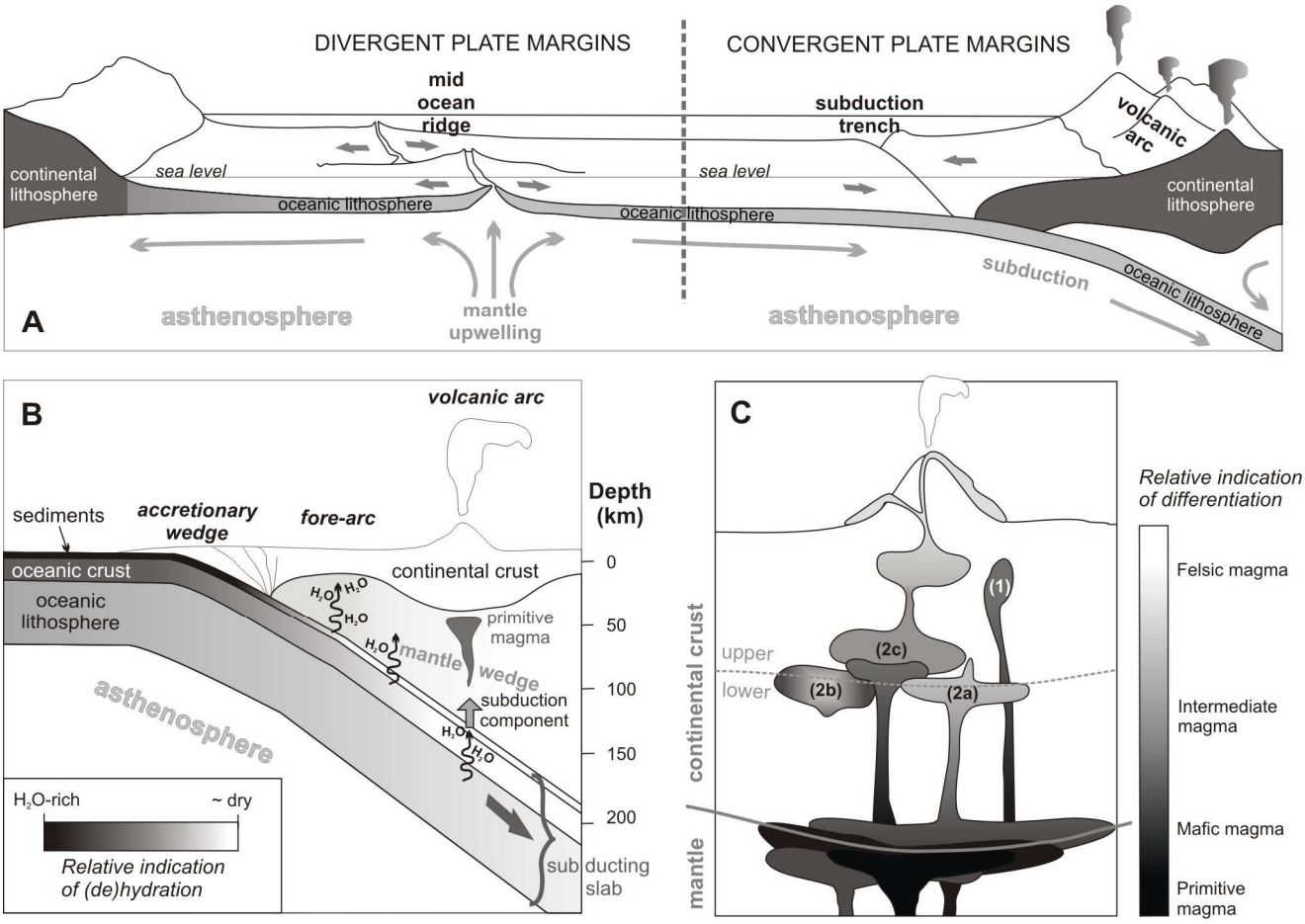

Figure 1.1. *Geological context of this petrological-geochemical study volcanic rocks from the South Aegean arc*. (A) Arc volcanism and subduction zones in relation to plate tectonics. (B) Profile through an ocean-continent subduction zone with indication of the main water-bearing lithologies, their gradual dehydration and formation of primitive arc magmas. (C) Crustal differentiation of primitive magmas through crystal fractionation as they cross the crust-mantle boundary and continue their ascent to the earth's surface (for (1) to (2c), see text).

hotter) altered oceanic crust and subducted sediments, it will react with these lithologies (as aqueous fluid and/or as hydrous melt) and partially inherit their geochemical signature. The combination of serpentine-derived aqueous fluids and material from the overlying oceanic crust and subducted sediments is referred to as the 'subduction component' (Fig. 1.1B). Addition of this slab-derived hydrous fluid into the overlying mantle wedge will locally lower the mantle's solidus temperature and hence induce partial melting. If such partial melts can be efficiently segregated from the solid residue of the meta-somatised mantle wedge, they rise as primitive arc magmas towards the mantle-crust boundary (Fig. 1.1B). Due to the density contrast between mantle and (lower) crust lithologies, hydrous basaltic magmas are likely to stall at the base of the crust (a process called 'underplating') where they slowly start to cool and crystallise mafic minerals (Fig. 1.1C). The presence of water in these primitive magmas enhances the stability of ferromagnesian minerals such as olivine, hornblende, clinopyroxene and garnet relative to plagioclase and orthopyroxene (Dessimoz et al., 2012 and references therein). As these Mg-Fe-rich, silica-poor minerals are denser than the initial melt, their crystallisation causes a decrease in Mg-Fe content and density of the remaining melt. Continuing differentiation of the (relatively) silica-enriched residual melt according to this process of crystal fractionation might render its density smaller than that of the lower crustal country rocks in which it is stalled. If this evolved magma can effectively segregate from the crystallised minerals, it will then continue its ascent through the crust (Fig. 1.1C). The resulting mafic-intermediate magma can either (1) complete its journey towards the earth surface without further delay and erupt in an arc volcano or (2) stall once again at a more shallow crustal level (see Fig. 1.1C). In the latter case, the stalled magma will slowly cool down and (2a) fractionate until the residual melt is once again able to ascent, or (2b) completely solidify into a subvolcanic pluton, or (2c) 'trap' another, more mafic ascending magma upon which interaction between the two magmas can trigger remobilisation of the older, more evolved magma (see Fig. 1.1C).

1.3. Subduction zone magmatism: remaining issues

The above described processes of magma generation through hydrous mantle melting and differentiation of the resulting mafic melts towards more felsic compositions en-route to the surface are broadly accepted by the scientific community. But despite these and other important discoveries, many issues regarding arc-related volcanism and the petrogenesis of subduction zone magmas remain unanswered. Some of the important questions that require clarification are: What lithology of the subducted slab is the main source for the geochemical signature of the subduction component that metasomatises the mantle wedge – the serpentinised lithosphere, the altered oceanic crust or the subducted sediments (Spandler & Pirard, 2013)? And is this subducted slab-derived component an aqueous fluid, a supercritical liquid or a hydrous melt? (Kessel et al., 2005)? What are the relative contributions of the different sources (subducted slab, mantle wedge, overlying crust) to the geochemical composition of arc lavas (Kersting et al., 1996)? How do differentiation processes in the overlying crust affect the geochemistry of traversing arc magmas, thereby filtering certain elements which could eventually be recycled into the mantle (Davidson et al., 2007)? And which mechanisms are responsible for the accumulation of industrially relevant trace elements in specific types of arc-derived continental crust (for example porphyry Cu deposits frequently associated with high Sr/Y magmas - Chiaradia et al., 2012)? Exactly how does physical-chemical interaction between two compositionally distinct magmas (mingling and mixing) take place (Wilcox, 1999)? How do mafic replenishments trigger rejuvenation of stalled crystal mushes and their subsequent volcanic eruption (Huber et al., 2011)? What is the effect of the composition, thickness and tectonic regime of the overlying crust on the geochemistry of the magmas and the location, timing and style of volcanic eruptions (Wallace & Carmichael, 1999)? To what extent are present-day subduction zone processes representative of similar mechanisms thought to be responsible for the formation of the continental crust early on in the earth's history (Elburg et al., 2013)? A range of scientific disciplines is currently applied to resolve these remaining issues from different angles (e.g. geochemical /petrological studies of serpentinites/ ophiolite complexes/ exhumed portions of arc lithosphere/ arc volcanic rocks, experimental studies on magma chamber dynamics/ crystallisation/ partial melting; geophysical/

structural/ volcanological studies of arc volcanoes; numerical modelling of geochemical compositions / volcanic eruptions / subduction zone physics,… - see literature list at the end of this work). Whilst such studies render breakthroughs in the understanding of individual aspects of subduction, they become increasingly diversified. The growing demand for (a return to) more integrated subduction studies reflects awareness of the risk to lose focus and expresses the need for a multi-disciplinary approach of volcanological and petrological systems through the combination of research efforts from different sub-disciplines (see for example the description of sessions GMPV19, TS7.3/GMPV22, GD5.4/GMPV23/ SM6.9/TS7.11, GD5.7/GMPV26/SM6.10/TS7.13, GMPV32/NH2.6 and GMPV35 programmed for the EGU 2014 General Assembly; the summary of sessions 06e, 07b, 07d and 08a organised for the Goldschmidt 2014 conference or the scope of the 2014 IAVCEI co-organised 1st International Workshop on Volcano Geology).

1.4. Why study the South Aegean arc?

The study area of this PhD research is the westernmost part of the South Aegean active volcanic arc (Saronic Gulf, Greece) which is the result of prolonged subduction of the African plate beneath the Eurasian continent. As the entire Aegean area has been targeted by many geophysical and structural geological investigations, the geodynamic evolution and present-day geometry of this subduction zone are well constrained (see Chapter 2) – making it an excellent 'natural laboratory' to study the influence of local tectonics on arc magmatism. The complex geodynamic setting of the Aegean micro-plate, wedged between Africa, Eurasia and the Anatolian plate, furthermore resulted in along-arc variations in the thickness of the overriding continental crust as well as in the convection dynamics of the respective sub arc mantle. Combination of this interesting tectonic setting and explosive volcanism in historic times rendered central and eastern parts of the South Aegean arc the focus of intensive geochemical, petrological and volcanological research throughout the past 4 decades (see for example Di Paola, 1974; Pichler & Schiering, 1977; Sparks, 1985; Fytikas et al., 1986; Mitropoulos & Tarney, 1992; Druitt et al., 1999; Zellmer et al., 2000; Rinaldi & Venuti, 2003; Mortazavi & Sparks, 2004; Anastasakis & Piper, 2005; Buettner et al., 2005; Holness et al., 2005; Martin et al., 2006a; Bachmann et al., 2007; Francalanci et al., 2007; Zellmer & Turner, 2007; Pe-Piper & Moulton, 2008; Bailey et al., 2009; Gertisser et al., 2009; Vaggelli et al., 2009; Braschi et al.; 2012; Spandler et al., 2012; Cantner et al., 2014;…). Older papers thereby usually present a general geochemical-volcanological-petrological interpretation of the main magmatic regions, whereas more recent publications on the individual volcanic centres of Kos, Yali, Nisyros, Santorini, Kolumbo and Milos are mainly studies on distinct volcanic phases or from the viewpoint of a specific sub-discipline. Compilation of knowledge from the large number of specialised publications on these islands generates a good understanding of the general petrology and the influence of local tectonics on the spatial and temporal evolution of magma genesis.

In comparison to this large amount of research on the central and eastern parts of the South Aegean arc, the volcanic deposits of the western part have been virtually overlooked during the past 40 years: only a handful of publications discusses the petrology, geochemistry or volcanology of the volcanic deposits on Aegina, Methana and Poros (Fytikas et al., 1987; Dietrich et al., 1988; St. Seymour, K., 1996 ;Pe-Piper & Piper, 2013). The few publications on geochemical, petrological and volcanological variations along the South Aegean arc (e.g. Innocenti et al., 1981; Fytikas et al., 1984; Mitropoulos et al., 1987; Pe-Piper & Piper, 2002; Francalanci et al., 2005; Pe-Piper & Piper, 2005) thereby based their interpretation of the Saronic Gulf volcanism on older information which represents a rather small and incomplete dataset compared to the large amount of detailed and up-to-date information available for the other South Aegean arc volcanoes.

1.5. After a century of research, what is there left to study?

Late 19th century geologist Henry Stephen Washington (famous as the 'W' in the CIPW calculations) wrote: "Aegina and … Methana, which are plainly seen from the Acropolis of Athens, had always presented themselves as a promising field for petrographical investigations" (Washington, 1894). According to him, the volcanic origin of Methana was first recognised in 1819 by Dodwell who suggested it for investigation to future geologists. Despite this recommendation, the region only received some scientific interest when a group of physical geographers returned from Stromboli where they had observed the 1866 effusive volcanic eruption on Nea Kameni (Reiss et al., 1867). The volcanic rocks of Aegina, Methana and Poros were therefore not subjected to proper geological research until Washington's 1894-1895 trilogy on the Saronic Gulf (Washington, 1894, 1895 & 1895b). Washington's detailed field observations led to the conclusion that all volcanic deposits on Aegina, Methana and Poros were formed during 'dome type' eruptions. His petrographic description of the textures of the Aegina-Methana-Poros volcanic rocks and the varying mineralogical contents of these lavas and their 'endogenous enclosures' is relevant and accurate to this day, and the 16 major element analyses he published on representative rock samples were some of the first and most complete geochemical data sets in his time (Washington 1894, 1895 & 1895b).

Geological interest in the magmatic centres of the Saronic Gulf renewed around the mid-20th century when von Leyden (1940) studied the deposits from a volcanological point of view, accompanying thorough descriptions of individual volcanic outcrops with detailed sketches (Fig. 1.2). His acknowledgements include Prof. Dr. V. M. Goldschmidt (father of modern-day geochemistry) for the preparation of thin sections of his Aegina-Methana-Poros rock samples (von Leyden, 1940). These samples and thin sections were subsequently used in the PhD study of Davis (1957). The merit of her petrographic and geochemical research is confirmation of and further addition to Washington's microscopic observations, illustration of the region's petrography with detailed drawings (Fig. 1.3) and microphotographs, a significant addition of the Saronic Gulf's major element geochemical database and compilation of the very first geological maps of Aegina and Methana (Davis, 1957).

The development of micro-probe analysis allowed determination of the geochemical composition of individual mineral grains, a technique which was applied to the volcanic rocks of the Saronic Gulf as part of the PhD thesis of Pe (1971). In the papers based on her PhD research, Pe published geochemical compositions of the minerals that are dominant in the lavas from Aegina, Methana and Poros, as well as whole rock geochemical data on all major element oxides and some trace elements. Within the framework of the (then newly introduced) model of plate tectonics, Pe presented some first insights into the crystallisation sequences and petrogenesis of the Saronic Gulf magmas (Pe, 1972, 1973 & 1974), and obtained the area's first radiogenic isotope ratios ($^{87}Sr/^{86}Sr$ – Pe, 1975). So from the 1890's up until 1975, the volcanic rocks of Aegina, Methana and Poros were subjected to petrological studies that applied innovative research methods and resulted in the most complete geochemical and petro-graphical databases of volcanic regions in those days.

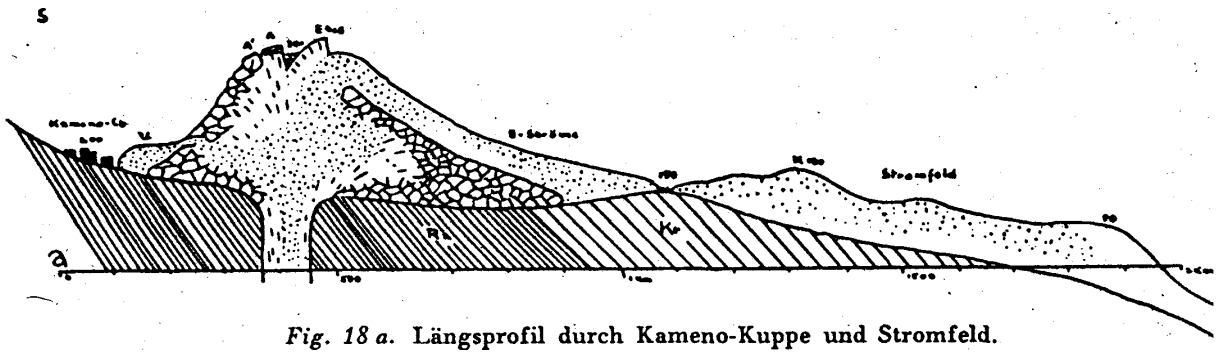

Figure 1.2. *Sketch of a length profile through the Kammeno dome and lava stream* - von Leyden, 1940. These effusive deposits were formed during Methana's 220 BC eruption and are nowadays known as the Phase H Mavri Petra volcanic complex.

Over the last 40 years, however, the Saronic Gulf lost this 'pole position' to the central and eastern parts of the South Aegean arc: despite important developments in (analytical) geochemistry and petrology, no such research has been recently carried out on the arc's westernmost centres apart from the few earlier mentioned studies. The limited amount of geochemical-petrological-volcanological data avail-able in literature, however, suggests that the volcanic rocks of Aegina, Methana and Poros are significantly different with respect to their geochemical composition, age, mineral contents and eruption style. The geological context of the volcanic deposits of the Saronic Gulf is furthermore very well-known as most geological research carried out on Aegina, Methana and Poros since the late 1970s focussed on geophysics (e.g. Pe-Piper et al., 1983; Volti, 1999; Makris et al., 2004; van Hinsbergen et al., 2004; Efstathiou et al., 2012), the hydrothermal systems on and around Methana (e.g. Hübner et al., 2004; D'Alessandro et al., 2008; Dotsika et al., 2010), sub-marine volcanic deposits (e.g. Clift & Blusztajn, 1999; Nomikou et al., 2013), geological mapping (e.g. Gaitanakis, 1984; Dietrich et al., 1993a&b; Gaitanakis & Dietrich, 1995), structural geology and the influence of tectonics on volcanism (e.g. Gülen, 1990; Schwandner, 1998; Pe-Piper & Piper, 2005; Pe-Piper & Piper, 2013), geochronology (e.g. Fytikas et al., 1976; Pe-Piper et al., 1983; Matsuda et al., 1999) and geo-archaeology (e.g. Dorais & Shriner, 2002).

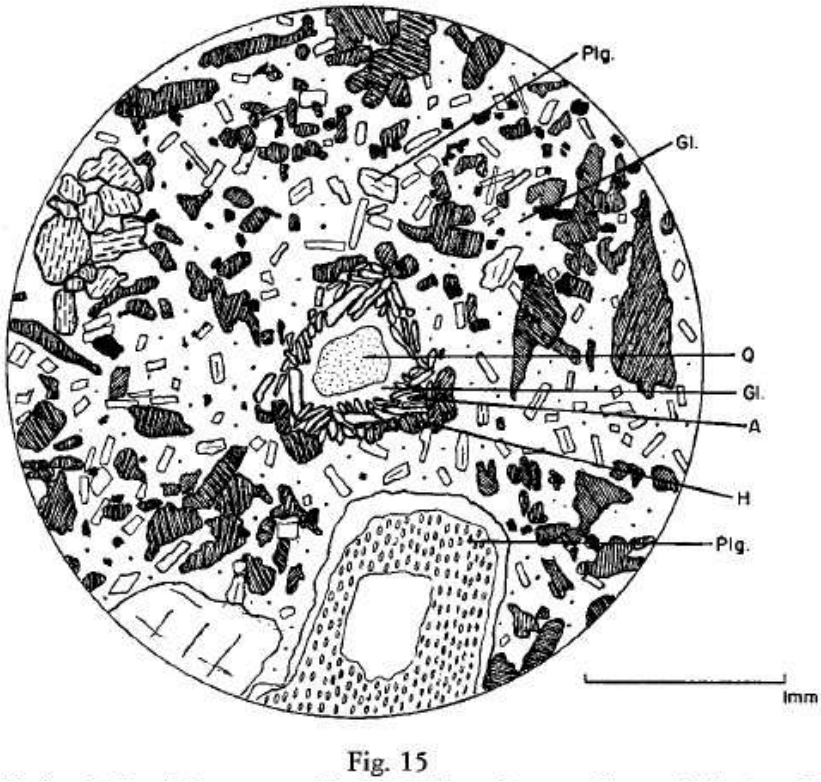

Figure 1.3. *Sketch of the microscopic texture and mineral composition of one of Aegina's lavas* – Davis, 1957. In the centre a quartz xenocryst (Q) with a reaction rim of glass (Gl.), augite (A) and hornblende (H) (often referred to as a 'quartz ocellus'); below it a large plagioclase crystal (Plg.) with a broad zone of parallel oriented melt inclusions.

The unknown petrogenesis of most deposits and shortage of qualitative geochemical data in combination with a thorough knowledge of the local geodynamics thus render the volcanic centres of the Saronic Gulf once again interesting study areas for detailed geochemical and petrological research with application of modern analytical methods.

1.6. Objectives of this PhD research

The **main goals** of the PhD research presented in this doctoral dissertation are:

- Generation of a complete and representative set of whole rock geochemical data for all volcanic deposits on the magmatic centres of Aegina, Methana and Poros
- Identifying genetically different volcanic deposits and interpreting their petrogenesis
- Investigating the spatial and temporal evolution of magma genesis in the Saronic Gulf

- Assessment of the influence of regional tectonics on the timing and localisation of the area's volcanism and on the eruption dynamics

- Improvement of the general understanding of magma genesis and subsequent crustal differentiation of subduction-related volcanic rocks

The following **work** was **undertaken** in order to try achieve these goals:

- A large number of representative samples was collected during a series of detailed and adequately documented field trips

- Thorough petrographic study was carried out for several samples of each volcanic unit

- Representative samples underwent whole rock analyses of their major and trace element concentrations and Sr-Nd-Hf-Pb isotopic composition

- All information from fieldwork, petrography and geochemistry was combined to clarify the petrogenesis of the different volcanic units

- Geochemical modelling was used to test and further refine these hypotheses

- Literature information on the geology of the Saronic Gulf was integrated as much as possible into the resulting petrogenetic models

1.7. Short overview of this doctoral dissertation

Chapter 2 starts with a general outline of the geodynamic evolution of the South Aegean arc and the present-day geometry of its subduction zone. The literature-based geology is subsequently presented for each of the three volcanic islands, omitting detailed geochemical-petrological information as this will be introduced later on in discussion sections of relevant chapters.

Chapter 3 reports in detail the methodology that was adopted during fieldwork, petrography, sample preparation, rock powder dissolution, Sr-Nd-Hf-Pb isolation and subsequent chemical analyses.

Chapter 4 presents the detailed petrographic and geochemical study of a single volcanic unit (the 'Delta 2 unit' on Methana) in order to constrain the mineralogical and geochemical variability that typically occurs within an individual eruption event.

Chapter 5 subsequently discusses all other volcanic units on Methana, comparing their petrography and geochemistry to one another and to the Delta 2 unit.

Chapter 6 contains all information on the geochemistry and petrology of the volcanic deposits on Aegina and of the 1 km² volcanic peninsula on Poros.

Chapter 7 compares the different petrogeneses inferred for the three magmatic centres in order to constrain the spatial-temporal evolution of the Saronic Gulf volcanism.

Chapter 2: Geological setting

Located in the Saronic Gulf south of Athens, the islands of Aegina, Methana and Poros represent the western part of the present-day active South Aegean arc (Fig. 2.1). This chapter describes the larger geodynamic context of the Saronic Gulf volcanic deposits which are known from literature to show a subduction signature in their geochemistry. An initial discussion of the temporal and spatial evolution of subduction in the Aegean area facilitates the subsequent explanation of the present-day geometry of the subduction zone. The three volcanic centres which are the subject of this PhD research are introduced with a brief summary on their geology, tectonic structure and geothermal activity. These aspects, as well as a presentation of the literature-based information on their geochemistry and petrology, will be discussed in more detail in the relevant sections of subsequent chapters. Only a minimum of information on the geochemistry, petrology and volcanology of the other South Aegean arc centres is provided as an along-arc comparison falls outside the scope of this work. For more information on the central and eastern volcanic deposits of the South Aegean arc, the reader is referred to the references in section 1.4.

2.1 Tectonic development of the Hellenic subduction zone

Evidence for ca. 1.25 Ga subduction is found in primitive ultra-potassic rocks from the SE Aegean area (Samos and Bodrum) whose geochemical signature is (partially) derived from an enriched mantle that could be widely distributed throughout the Mediterranean domain (Robert et al., 1992). The Pb

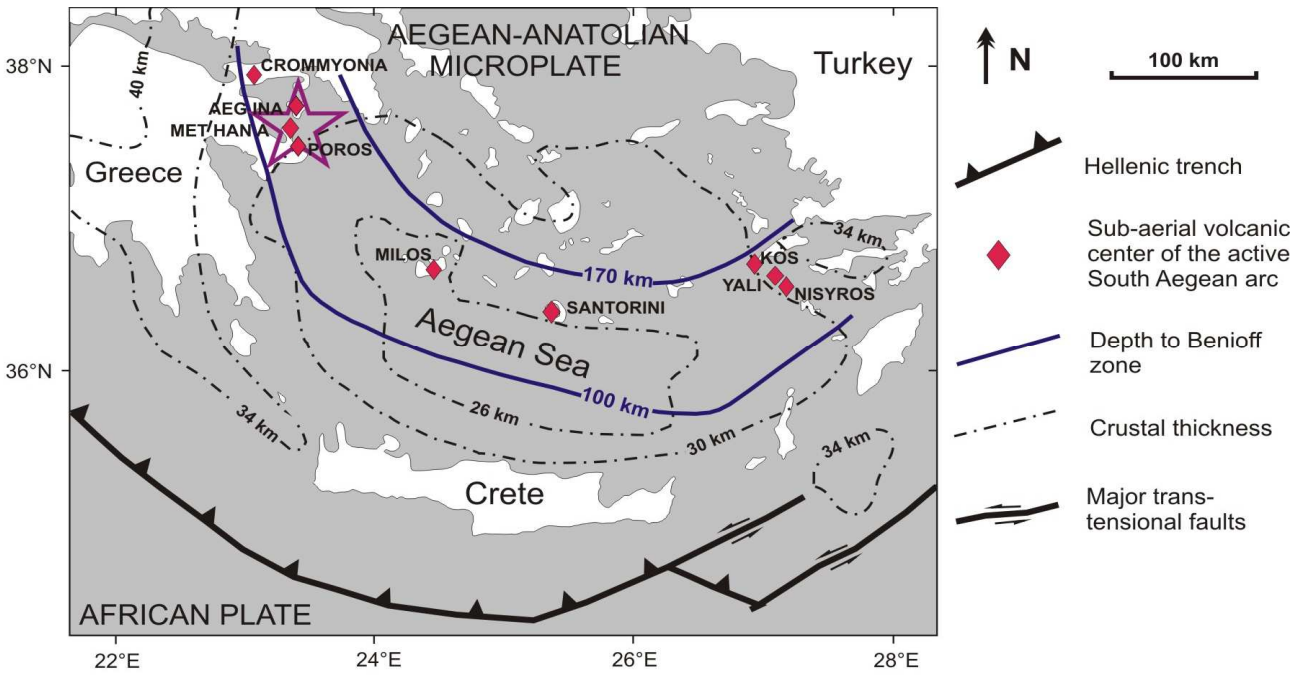

Figure 2.1. *Geodynamic setting of the volcanic centres of the active South Aegean arc*, after Bailey et al (2009) and references therein. The study area of this PhD research comprises the islands of Aegina and Poros and Methana peninsula, all located in the Saronic Gulf south of Athens (indicated with a purple star). Green dotted rectangle represents the outline of Fig. 2.8A.

isotopic signature of mafic volcanics from the Neogene Aegean back-arc also infers an enrichment event older than 1 Ga (Pe-Piper, 1994). The resulting U, Th and LILE enriched mantle is proposed to also play a role in the magma genesis of the South Aegean arc (Pe-Piper & Piper, 2001). There is however no known Proterozoic crust nor geophysical information that can confirm this inferred subduction event.

This is in contrast to the area's Mesozoic subduction history which is well understood from both structural tectonic studies and seismic imaging of the slab(s). Van Hinsbergen et al. (2005) reconstructed the convergence history the Aegean region from a particular nappe stack in western Greece where the Hellenides (mountain belt created by the collision between Africa and Eurasia) have been little affected by late-orogenic extension (Fig. 2.2A). The different nappes are thereby interpreted as upper crustal segments (5-10 km thick) that were decoupled from their underlying (and further subducted) oceanic or continental lithosphere and tectonically stacked below one another (Fig. 2.2B) (van Hinsbergen et al., 2005, and references therein). The oldest nappe is an ophiolite complex which represents the upper lithospheric part of the Late Triassic to Early Jurassic Vardar ocean (Fig. 2.2C). Intra-oceanic north-eastward subduction of this basin occurred throughout the Jurassic, creating a magmatic arc along the southern margin of the Eurasian plate(Fig. 2.2C) (Roberston et al., 2012). The 700 km long subducted slab of the southern part of the Vardar ocean eventually detached by the end of the Jurassic and has been sinking into the mantle ever since (Fig. 2.2C) (van Hinsbergen et al., 2005).

Convergence between Africa and Eurasia also continued after this slab break-off and a new zone of northward subduction was formed by the Early cretaceous (Fig. 2.2C). This second subduction zone was shifted ca. 1000 km to the north of the subducted western Vardar ocean and consumed a number of both oceanic and continental units before the remaining 300 km of the Vardar basin were also

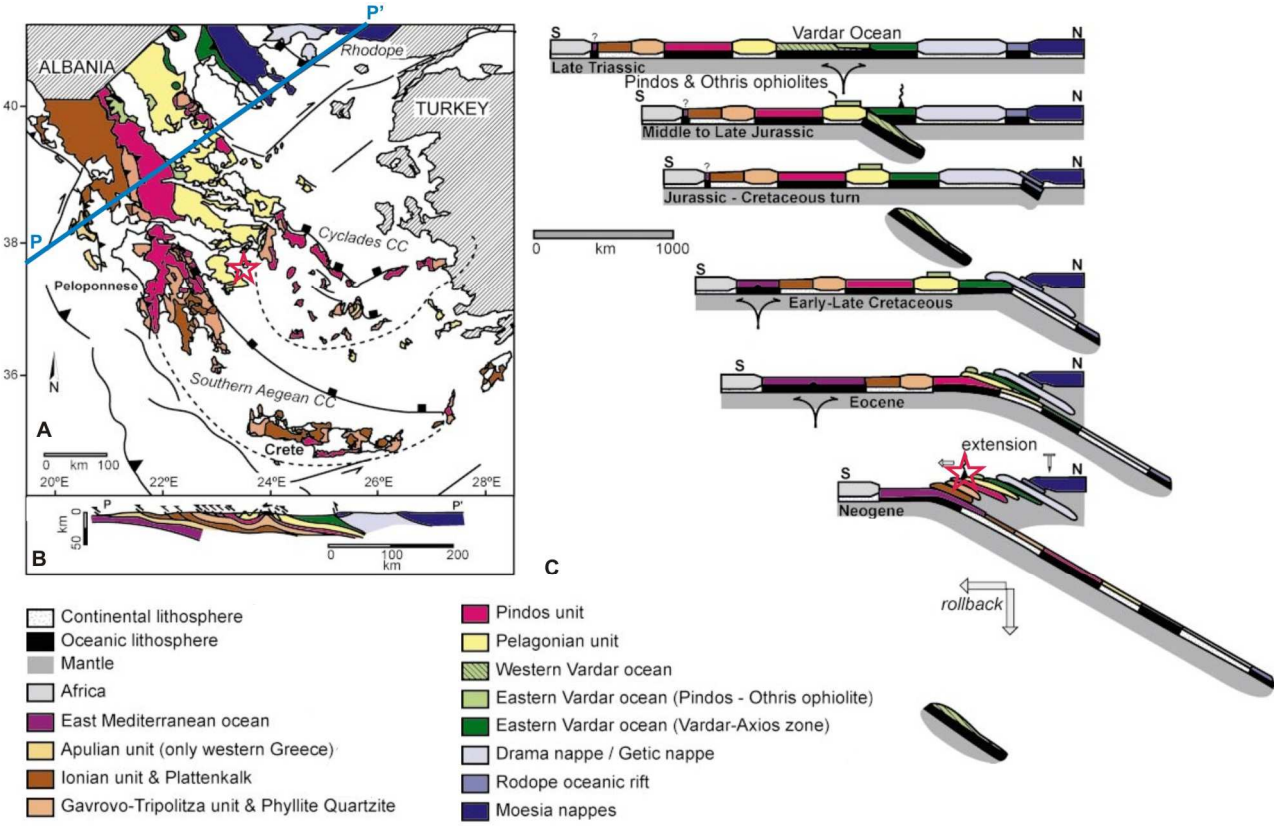

Figure 2.2. *Tectonic development of the Hellenic area,* from van Hinsbergen et al. (2005). (A) Simplified geological map of Greece. CC = core complex, blue line P-P' indicates the location of the profile in (B) Schematic cross-section of the Aegean nappe stack. (C) Overview of the development subduction, delamination and nappe stacking during the Alpine orogeny in Greece. Red star = location of the Saronic Gulf.

subducted by the end of the Cretaceous (Fig. 2.2C). During this subduction of the eastern Vardar oceanic crust, the upper lithologies decoupled from their down-going lithosphere and underthrusted the earlier subducted Rhodope nappe stack (Fig. 2.2C). Throughout the Cenozoic, subduction continued in much the same way with de-lamination between subducted upper and lower crust and successive underthrusting of different upper crustal units of both oceanic (Pindos, Eastern Mediterranean) and continental (Pelagonian, Ionian, Apulian, …) origin (Fig. 2.2C).

This process of continuous subduction has been going on since the early Cretaceous and resulted in the subduction of ca. 1500 km of lithosphere (Fig. 2.3). As up to 900 km of this subducted slab consists of continental terrains whose density is smaller than that of the mantle, tension between the buoyant continental terrains and the gravity-pulled oceanic basins could have triggered tearing and breaking off the slab. However, no slab break-off occurred so far as the subducted continental units are relatively small (ca. 100 km) and separated from one another by oceanic basins (van Hinsbergen et al., 2005; Jolivet & Brun, 2010). The 1500 km long Aegean subducted slab thus sunk across the 660 km mantle discontinuity and is now anchored in the lower mantle. Its 300 km long horizontally positioned part at the upper-lower mantle boundary (Fig. 2.3) reflects ca. 300 km of slab rollback since the initiation of north-south extension in the Aegean sea. The individual segment of subducted slab imaged in the middle mantle (Fig. 2.3) is commonly interpreted as the broken off slab of the western Vardar ocean that was consumed in the first subduction zone (van Hinsbergen et al, 2005).

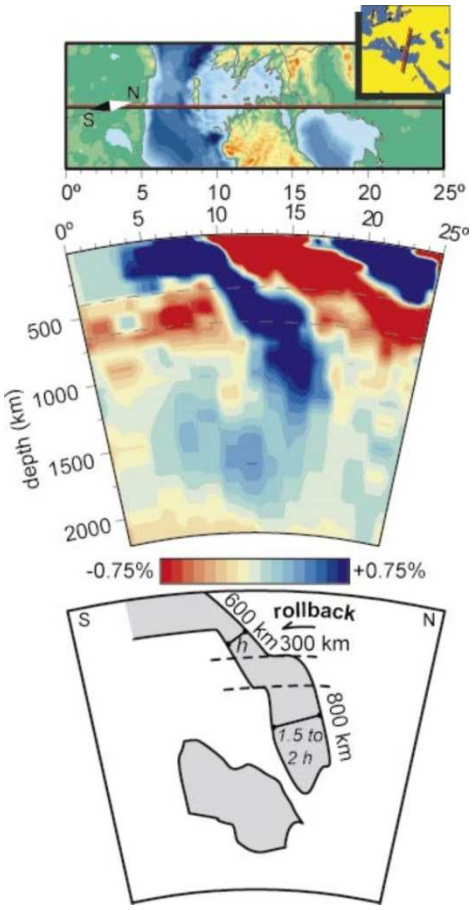

Figure 2.3. *Seismic tomography model and interpretation of a cross-section of the subducted slab in the central Aegean* (van Hinsbergen et al., 2005, and references therein).

2.2 Cenozoic geodynamic evolution of the Aegean region

Throughout the above described evolution of Hellenic subduction, volcanism migrated from a Cretaceous magmatic arc in the Balkan to the Rhodope massif where large amounts of granitoids were emplaced during the Early Eocene (Fig. 2.4A) (Pe-Piper & Piper, 2006; Jolivet & Brun, 2010). Around 66 Ma, however, obduction in the eastern Mediterranean region nearly stopped the up till then relatively fast convergence of between Africa and Eurasia. The Aegean slab started to retreat with respect to the overlying Aegean microplate as it sunk solely due to its own weight (Jolivet & Brun, 2010). By 50 Ma, the convergence rate increased again and reinstalled the Balkans' compressional regime with southward propagation of thrusting and nappe understacking. For reasons still unknown, the more southerly located Rhodope massif experienced an extensional regime in this period (Fig. 2.4A).

From 35-30 Ma onwards, the earlier initiated slab roll-back continued at higher speed due to the decrease in Africa's absolute northward motion. This increased slab roll-back led to further development of an extensional tectonic regime in the back-arc and thus coincided with the onset of widespread volcanism in northern Greece (Fig. 2.4B). Between 24 and 15 ma, the slab roll-back driven retreat of the African plate relative to Eurasia once again increased and triggered the southward migration of the volcanic arc at an average rate of ~2 cm/year as well as widespread north-south extension in the Aegean Sea (Fig. 2.4B).

From 17 Ma onwards the Aegean domain experienced fundamental changes in tectonic style which seemed to have divided the area in two more or less rigid blocks on either side of a postulated, but to date not ascertained, Mid-Cycladic lineament (Fig. 2.4C). Whereas western Greece rotated 40-50° clockwise between 15 and 8 Ma, the eastern Aegean-Anatolian block experienced slower counter-clockwise rotation (Fig. 2.4C) (Pe-Piper & Piper, 2006; Jolivet & Brun, 2010).

Meanwhile, Arabia had detached from the African plate and was moving faster northwards along the Dead Sea fracture zone (Fig. 2.5). Convergence of Arabia with Anatolia resulted in the formation of the North Anatolian fault zone (NAFZ - Fig. 2.5) which propagated westward and reached the Aegean Sea around 5 Ma (fig. 2.4D).

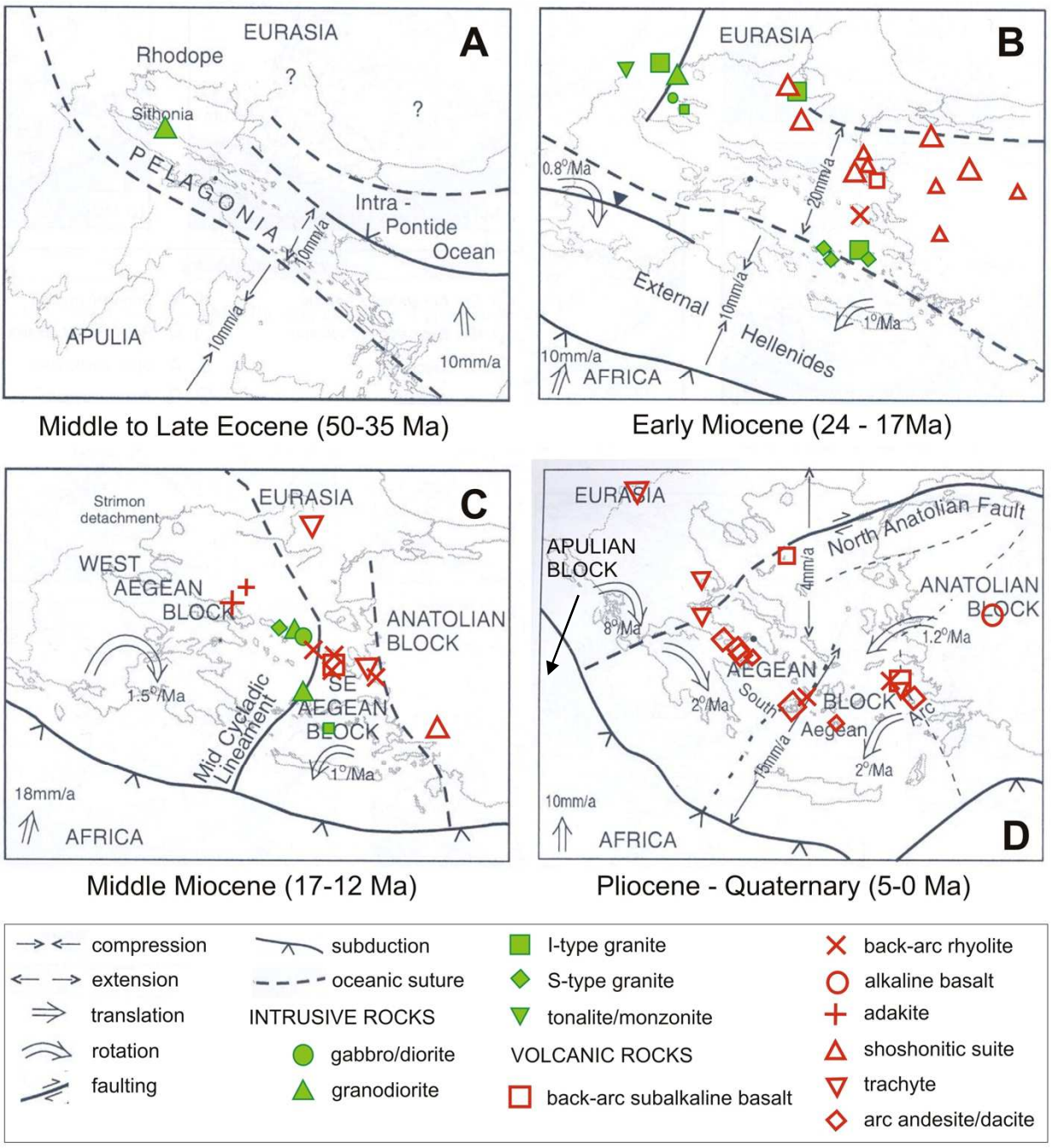

Figure 2.4. *Paleogeographic reconstruction of important periods in the Cenozoic tectonic evolution of the Aegean region*, after Pe-Piper & Piper (2006). Solid lines indicate block boundaries, dashed lines inferred boundaries. Locations and types of magmatic activity that occurred during these periods are indicated with symbols, the size of which correlates with the volume of the igneous bodies.

Counter-clockwise rotation of the eastern Aegean area followed at an increased rate due to collision with the westward escaping Anatolian block. At the same time, the western Aegean region continued to rotate clockwise due to pressure from its collision with the Apulian continental block (10°-15° over the last 5 Ma) (Fig. 2.4D). This collision changed the boundary between the African (Apulia) and Eurasian (Aegean-Anatolian) plates in the westernmost part of the subduction zone into a continent-continent type interaction along the Kefalonian Fault (KF - Fig. 2.5) (Papazachos et al., 2000). The easternmost part of the subduction zone remained a continental-oceanic type interaction where the east Mediterranean ocean floor is still subducting below the Aegean-Anatolian microplate (Cyprus trench, Fig. 2.5).

The Pliocene clockwise and anti-clockwise rotations of the western and eastern Aegean blocks, respectively, also contributed the present-day fast (~2 cm/year) south-westward motion of the Aegean-Anatolian microplate which overrides the African oceanic (Mediterranean) lithosphere. The volcanic arc which formed 35-30Ma ago in the North Aegean thereby migrated about 600 km southward to its present-day position in the South Aegean (Fig. 2.4B-D) (Pe-Piper & Piper, 2006; Jolivet & Brun, 2010).

2.3 Present-day geometry of the Aegean subduction zone

The Wadati-Benioff zone below the South Aegean volcanic centres is located at a depth of 120-140 km in the Saronic Gulf (Methana-Aegina respectively), 150 km in the central (Milos, Santorini) and 150-160 km in the easternmost part of the arc (Nisyros-Kos) (Papazachos et al., 2000). The present-day geometry of the subducted slab resembles that of an amphitheatre, with the large NW-SE oriented

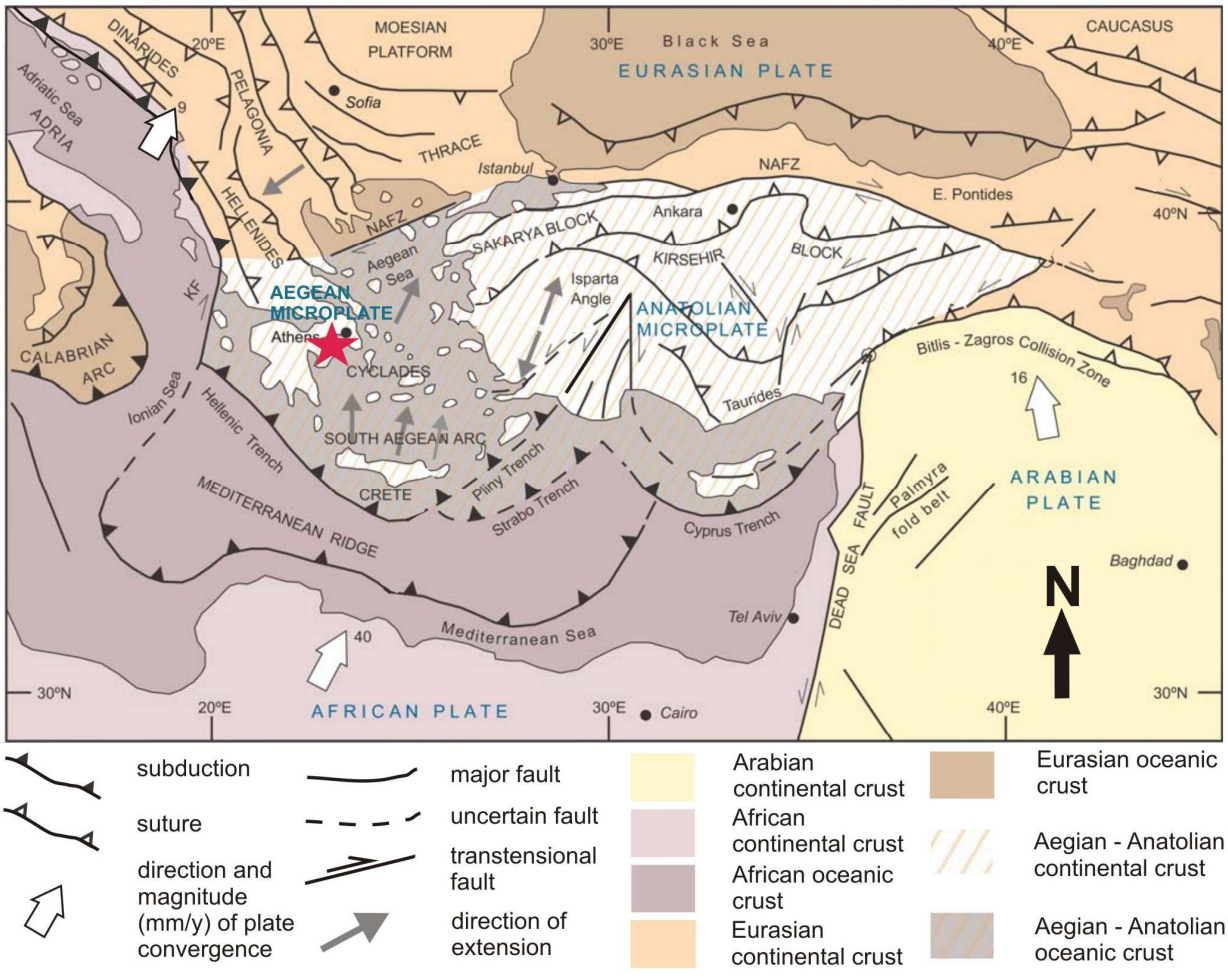

Figure 2.5. *Tectonic map of the Aegean and eastern Mediterranean region*, showing the plate boundaries, main suture zones, (in)active subduction zones and major fault systems, after Dilek & Altunkaynak (2009). Red star indicates location of the Saronic Gulf.

western part more or less at a right angle to the smaller eastern section (Fig. 2.5) (Papazachos & Nolet, 1997). From west to east along the arc there is an increase in the dip angle of the upper part of the subducted plate: the western segment of the African slab dips at ~25° whereas the eastern segment dips at ~35°. The smaller dip of the western part is thereby thought to reflect flattening due to south-westward overriding of this subducted African slab by the Aegean-Anatolian microplate (Papazachos et al., 1995; Papazachos & Nolet, 1997; Kassaras et al., 2005; Sodoudi et al, 2006). Tomographic studies furthermore reveal the presence of a kink in the subducted plate at about 80-100 km depth where its initial ~25-35° dip steepens to a ~45° dip (Papazachos & Nolet, 1997; van Hinsbergen et al., 2005; Sodoudi et al, 2006; Jolivet & Brun, 2010). This change in slab dip angle is thought to represent the transition from coupling between subducted African crust and overriding Eurasian crust to decoupling of these two plates and a freely dipping African lithosphere at depths greater than 100 km (Papazachos et al., 2000).

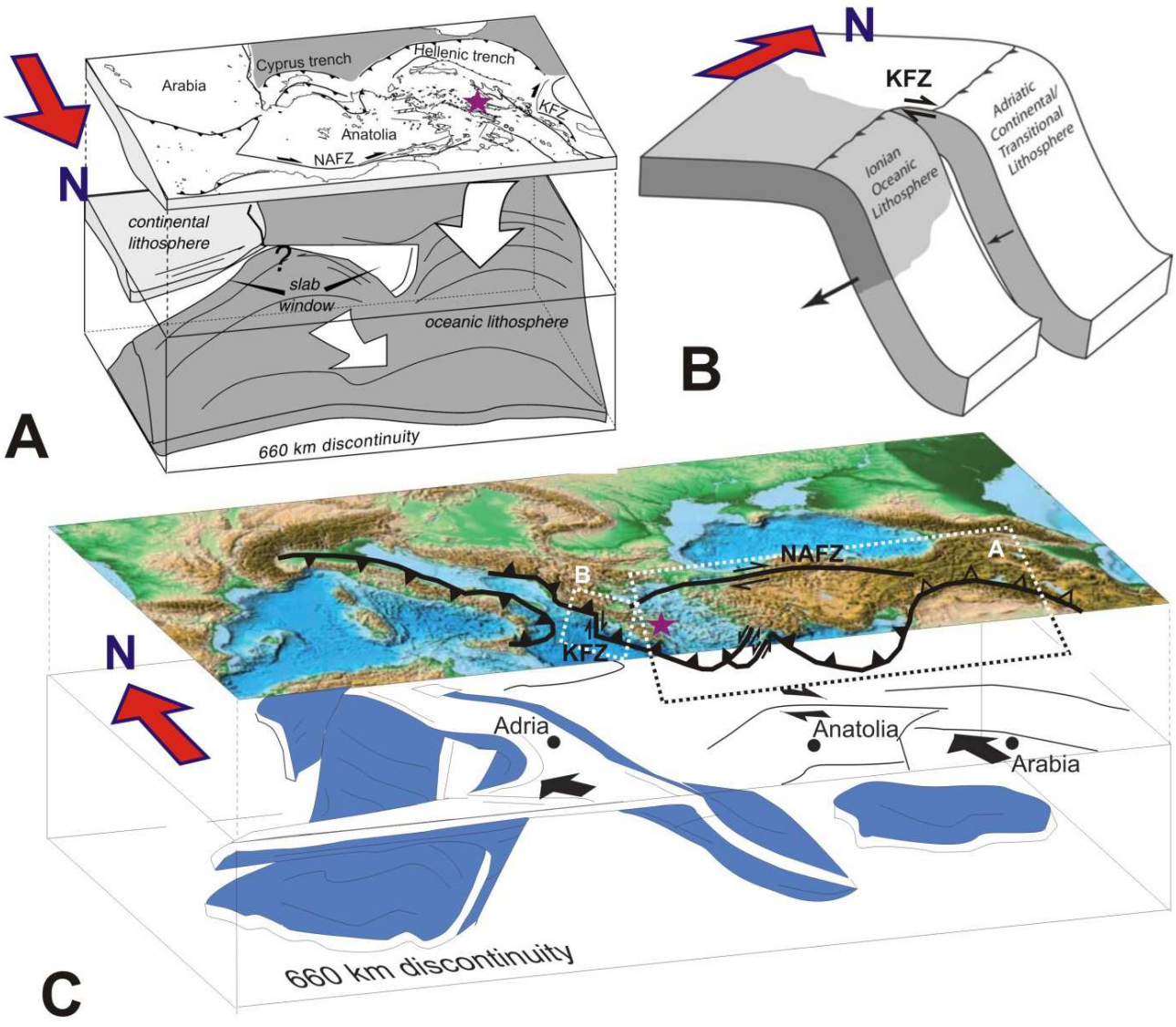

Figure 2.6. *Schematic diagram of the 3D structure of the subducted lithosphere in and around the Hellenic subduction zone.* (A) Slab detachment below the Arabian plate propagated westwards towards the easternmost part of the Aegean Arc, resulting in a slab window below Nisyros, after Facenna et al. (2006). (B) Slab tear below the KFZ in the westernmost part of the Aegean arc, after Suckale et al. (2009). Approximate extent of denser oceanic lithosphere indicated in grey, arrows highlight the relative roll-back velocity in the two segments. (C) Overview of the architecture of the subduction zones in the Mediterranean region, after Faccenna & Becker (2010). Dotted frames represent the approximate locations of figures (A) and (B), purple star indicates the Saronic Gulf.

In the easternmost part of the south Aegean arc, close to western Turkey and below the volcanic centre of Nisyros, a tomographically imaged slab discontinuity between 70 and 100 km depth (Papazachos & Nolet, 1997) coincides with an earthquake-free zone (Papazachos et al., 2000). This area is also characterised by lower seismic mantle velocities which represent the presence of hotter (asthenospheric?) mantle and are therefore interpreted to reflect a vertical tear within the subducted slab (de Boorder et al., 1998; Govers & Wortel, 2005). Faccenna et al. (2006) propose that this 'slab window' below the easternmost part of the Aegean arc is the westward propagation of the slab break-off that occurred around the Middle Miocene in the Bitlis collision zone, where Arabia subducted below Eurasia (see Fig. 2.5). They suggest that there is a single subducting oceanic slab which extends continuously from the Hellenic trench over the Cyprus trench to the Bitlis suture and which remains intact below most of the Aegean arc, but was broken below eastern Anatolia due to subduction of the buoyant Arabian continent (Fig. 2.6A). This slab detachment below eastern Anatolia thought to have propagated westwards as a horizontal tear below Cyprus and the Nisyros-Yali-Kos volcanic field (Fig. 2.6A).

Slab break-off below the Bitlis suture is also proposed as the ultimate cause for the Late Miocene-Pliocene plate re-organisation of the area, with formation and westward propagation of the North Anatolian Fault zone and the westward movement of the Anatolian block which subsequently assisted the south-westwards overriding of the Mediterranean ridge by the Aegean microplate (Fig. 2.4 & 2.5) (Faccenna et al., 2006).

The westernmost edge of the Aegean's subducted oceanic lithosphere is represented by the transtensional Kefalonia Fault (KF) (Fig. 2.5). The Kefalonian Fault zone thereby accommodates the 100 km dextral offset which formed between the subducted slab's northern and southern segments as a result of their different slab roll-back rates (Fig. 2.6B). The cause of these different roll-back rates can be traced back to the start of subduction of the Ionian oceanic lithosphere 8-4 Ma ago: roll-back of this dense mafic slab would have been faster than slab roll-back of the more buoyant, continental Adriatic lithosphere to its north (Suckale et al, 2009). Govers & Wortel (2005) argue that ongoing subduction and roll-back caused extensional stress between the Ionian and Adriatic segments of the subducted slab and eventually resulted in a vertical tear between them (Fig. 2.6B).

2.4 Volcanism in the South Aegean arc

The South Aegean active volcanic arc (SAAVA) stretches from the Kos-Yali-Nisyros volcanic field in the east, over the volcanic island groups of Milos and Santorini in the central part, to the volcanic centres of the Saronic Gulf (Aegina, Methana and Poros) and Crommyonia in the west (Fig. 2.1).

The continental crust below the Saronic Gulf represents the transition between the 40 km thick continental plate of the Hellenides and the extensional Aegean back-arc basin and is thought to be about 32 km thick (average from a range of values from Papazachos et al., 1995; Tirel et al., 2004; Kassaras et al., 2005, Karagianni et al., 2005 and Sachpazi et al., 2007). The Aegean microplate has been undergoing north-south extension since the Late Eocene and this led to a thinned continental crust of about 24-25km in the central part of the South Aegean arc (below Santorini). Western Turkey's continental crust is thought to be up to 35 km thick, but estimates for the crustal thickness below the Kos-Nisyros volcanic region are not unanimous: Tirel et al. (2004) and Kassaras et al. (2005) suggest a crust of about 24-25 km thick, similar to Santorini; but Papazachos et al. (1995), and Sodoudi et al. (2006) infer a crust of 27 – 30 km, intermediate between Santorini and the Saronic Gulf.

A continuous low-velocity anomaly, located directly below and parallel to the South Aegean volcanic arc at a depth between 60 and 90 km, probably reflects the primary magma source (Papazachos et al., 2005). Similar low velocities measured nearer the surface (at 30-40km depth) are thought to also reflect the presence of partial melts related to the area's active magmatism (Karagianni

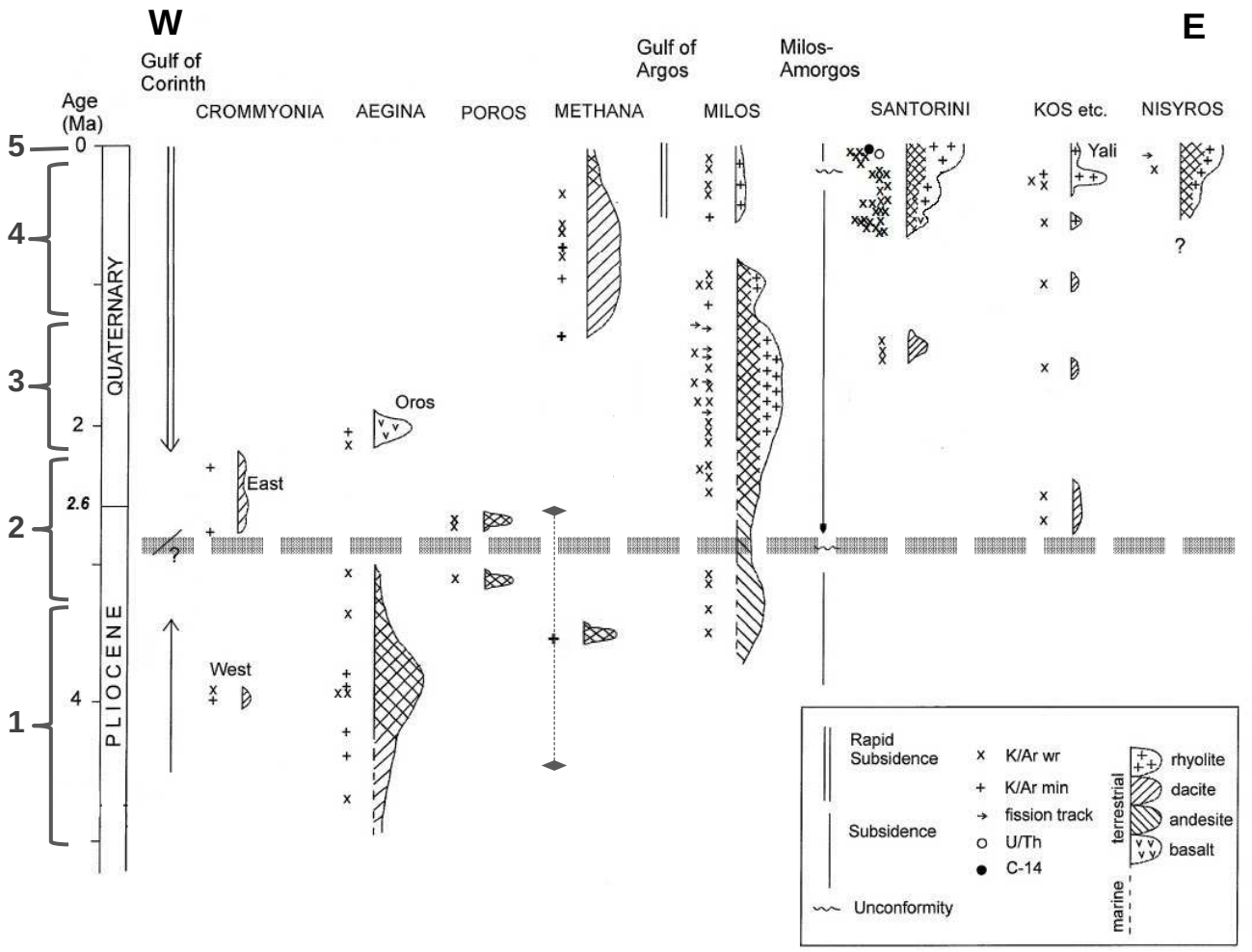

Figure 2.7 *Summary of the volcanic stratigraphy of all volcanic centres of the South Aegean active volcanic arc,* drawn after Pe-Piper & Piper (2002) with indication of the analytical uncertainty on the new K/Ar date for Methana's oldest deposits (3.5±0.9Ma). Pliocene-Quaternary boundary and division of the Quarternary into the Pleistocene (main part) and the Holocene (last 10000 years) taken from the Geological Society of America (2012). Thick grey dashed line indicates the pause between the two phases of basin subsidence which broadly correlate with two main periods of volcanic activity. The 5 time intervals (numbered) to the left of the timescale refer to the relative ages of the five volcanic litho-stratigraphic units defined in Fig. 2.8.

et al., 2002). Volcanic activity in the South Aegean arc can be broadly divided into two main periods which also correlate with evidence for two major phases of basin subsidence in the area of the arc (Pe-Piper & Piper, 2002). The first period of volcanic activity took place in the western half of the arc (Aegina, Crommyonia, Methana, Poros and Milos) during the early to mid-Pliocene (Fig. 2.7). This first period of volcanic activity was followed by a period of volcanic quiescence renewal of activity occurred around the Pliocene-Quaternary boundary. The start of this second period of volcanic activity also represents the initiation of volcanism in the central and eastern parts of the area (Santorini, Kos, Yali, Nisyros) (Fig. 2.7). So whereas initiation of all volcanic centres of the western SAAVA occurred during the first period of volcanic activity, the eastern half of the arc was mainly active from the Mid-Pleistocene onward. Initiation of volcanic activity thus seems to have shifted with time from west to east along the arc (Fig. 2.7).

This eastward advancement of volcanism seems to be linked to the geodynamic evolution of the eastern Mediterranean domain: spatial-temporal correlation between extension of the Aegean microplate and initiation or renewal of volcanic activity indicates a strong influence of the region's large-scale tectonics on the dynamics of volcanic eruptions (Francalanci et al., 2005 and references

therein; Pe-Piper & Piper, 2005). So whereas subduction is the primary cause for formation of the SAAVA magmas, timing and location of their eruption seems to be controlled by the network of extensional faults in the overlying Aegean microplate (Fytikas et al., 1984; Papazachos & Panagiotopoulos, 1993; Piper & Perissoratis, 2003; van Hinsbergen et al., 2004; Pe-Piper & Piper, 2006; Nomikou et al., 2013; Pe-Piper & Piper, 2013). This influence of the area's main tectonic lineaments on the eruption dynamics is also reflected in the elliptical shape of the different volcanic fields as these are always developed with the longest axes perpendicular to the subduction trench (Francalanci et al., 2005).

Besides the E-W varying thickness of the Aegean micro-plate and the eastwards shift in activation of SAAVA volcanism, there are also distinct along-arc variatons in the eruption style, mineralogy and geochemical composition of the volcanic deposits (Innocenti et al., 1981; Fytikas et al., 1984; Mitropoulos et al., 1987; Mitropoulos & Tarney, 1992; Francalanci et al., 2005; Pe-Piper & Piper, 2005; Shimizu et al., 2005; Dotsika et al., 2009; Elburg et al., 2013). The most striking along arc difference is that whereas the volcanic deposits of the western part of the arc consist almost exclusively of effusive lava domes and flowes, the central and eastern SAAVA centres also contain significant volumes of explosively deposited pyroclastic rocks. As there are many literature studies on the volcanic deposits of the central and eastern parts of the South Aegean arc (see references in section 1.4), the volcanology of Nisyros, Yali, Kos, Santorini and Milos is not further discussed here.

2.5 Western part of South Aegean arc: The Saronic Gulf

The volcanic centres of the Saronic Gulf are located on top of ca. 32 km of continental. The 40 km thick Hellenides which override the westernmost part of the Hellenic subduction zone are shown to have a sharp discontinuity at about 23 km depth, interpreted as a mid-crustal contact between upper crustal sedimentary units and a mid-to-lower crust crystalline basement (Suckale et al., 2009). High-resolution seismic imaging of this westernmost part of the subduction zone suggests that the subducted oceanic slab is ca. 20 km thick and approximately 200 My old (Suckale et al. 2009). The same study also indicates that the bulk of fluid transfer from subducted slab into overlying mantle occurs more than 90 km below the Saronic Gulf.

The Pliocene to recent subaerial volcanic deposits of the Saronic Gulf are distributed over four different locations (see Fig. 2.1): 1) the Crommyonia area along the east coast of Greece; 2) the southern and north-western parts of Aegina island; 3) the centre and northern part of Methana peninsula and 4) the small peninsula of Sferia on the southern coastline of Poros island. This western part of the South Aegean arc lacks composite volcanic structures with a large caldera such as the ones present in the eastern (Nisyros) and central (Santorini) parts. Instead, it is characterised by smaller, often monogenetic, eruptive centres which extruded their magmas from vents or from fissures. These enclave-bearing lava domes and flows have a mainly andesitic - dacitic composition, but minor basaltic andesites and rhyodacites are also present. Rare pyroclastic rocks are limited to some small scoria and pumice deposits on Methana and minor tuffs on Aegina and around Crommyonia. This lack of pyroclastic deposits is commonly interpreted as proof that the Saronic Gulf was not the scene of highly explosive eruptions such as the ones known to have occurred throughout the rest of the arc. Equivalents to the large volumes of rhyolitic magmas that erupted during the later volcanic stages on Milos, Santorini, Kos and Nisyros (Fig. 2.7) are also absent in the western part of the arc where all volcanic rocks have a silica content equal to or below 70 wt%. The start of volcanic activity on Aegina in the Lower Pliocene (ca. 4.7 Ma) represents the initiation of magmatism in the entire South Aegean arc. Methana is regarded as a present-day active volcano with hydrothermal vents and a last historic eruption dating back 2230 years. The Saronic Gulf thus represents the longest active volcanic region of the entire South Aegean (Fig. 2.7) (Pe-Piper & Piper, 2002).

The volcanic area of **Crommyonia** (also known as Sousaki volcano) is located along the coastline of the Saronic Gulf (Fig. 2.1). It consists of less than 1km² of scattered small (rhyo-)dacitic lava domes

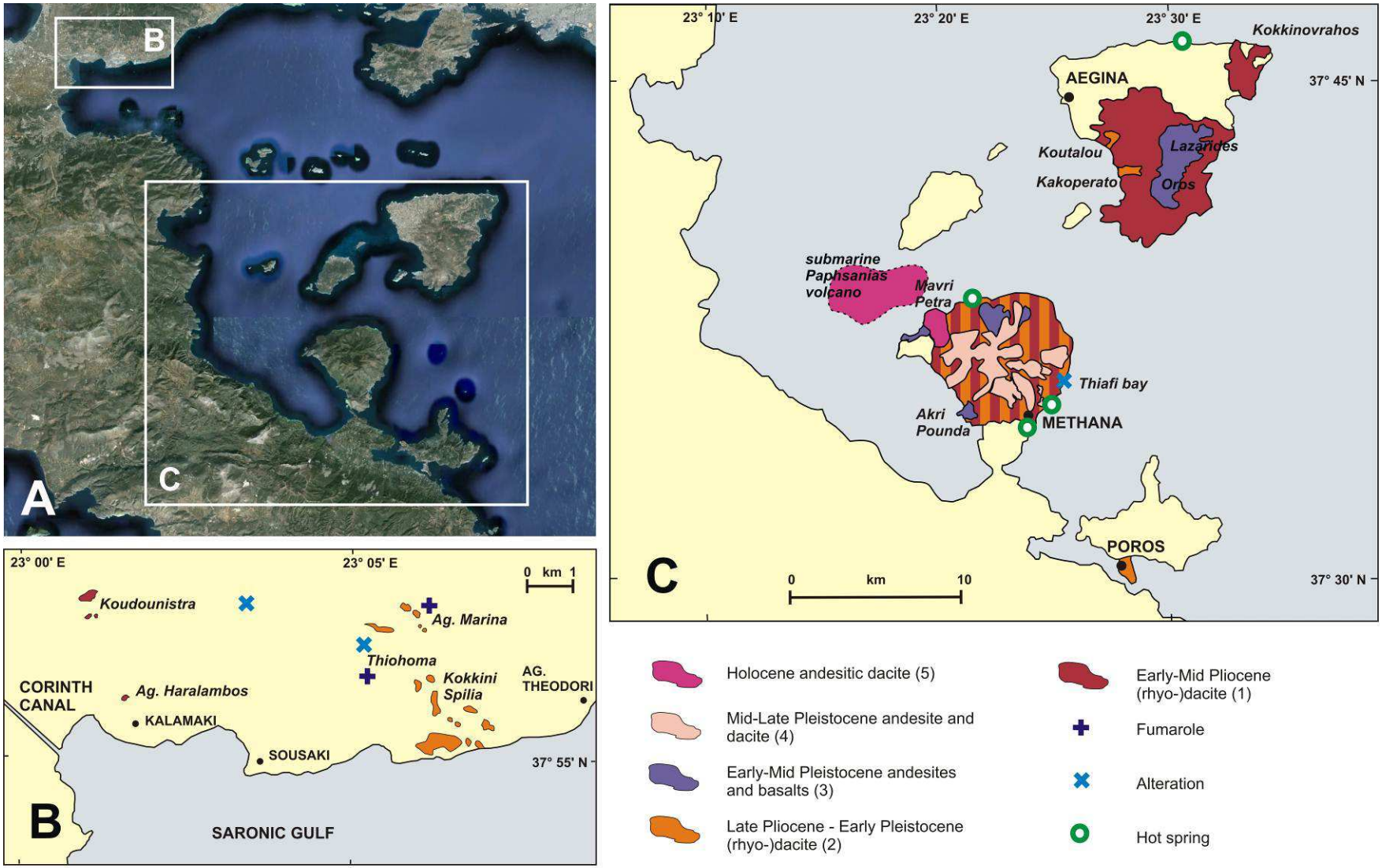

Figure 2.8. *Overview of the geographic location and volcanic stratigraphy of the magmatic centres of the western part of the South Aegean active volcanic arc.* (A).Enlarged satellite image of the Saronic Gulf area. (Google Earth, 2013) (B) Enlarged geological map of the Crommyonia volcanic area (Pe-Piper & Piper, 2002). (C) Enlarged geological map of volcanic deposits on Aegina, Methana and Poros (drawn after Pe-Piper & Piper (2002) with implementation of recent stratigraphic information from Pe-Piper & Piper (2013) and Nomikou et al. (2013)). The (bracketed) numbers behind the 5 litho-stratigraphic units correspond to the 5 time intervals indicated on Fig. 2.7.

and flow that were erupted during the first and at the start of the second volcanic phase and which show intense hydrothermal alteration (Fig. 2.7 & 2.8B) (Pe, 1972; Pe-Piper & Hatzipanagiotou, 1997). Despite the fact that this minor volcanic area with present-day active fumaroles (Fig. 2.8B) is traditionally regarded as part of the Saronic Gulf volcanism (Washington 1894, 1895 & 1895b; Davis, 1957; Pe, 1972; Pe-Piper & Hatzipanagiotou, 1997, Pe-Piper & Piper, 2005), its mineralogy and geochemistry differ significantly from that of the other Saronic Golf volcanic deposits. The present work does not include any new data for the Crommyonia area as it focusses on the three main magmatic centres of the western part of the South Aegean arc, located in the Saronic Gulf.

The peninsula of **Methana** is regarded as an active volcanic centre due to its present-day geothermal springs and 230BC effusive eruption which was described by Strabo (Fig. 2.8C). As pointed out before, it is the centre with the longest history of volcanic activity within both the Saronic Gulf and the entire South Aegean arc (Fig. 2.7). The volcanic rocks on Methana are small andesitic to dacitc flows and domes that radiate outward from the central part of the peninsula, thereby overlying older volcanics and the Mesozoic sedimentary basement (Fig. 2.8C) (Pe-Piper & Piper, 2005). A recent study of Pe-Piper & Piper (2013) introduces a new volcanic stratigraphy for Methana as well as a detailed study of the evolution of volcanism on this peninsula, which is shown to be strongly linked to the active tectonic regime of the Saronic Gulf area (Fig. 2.9).

During early to mid-Pliocene times, a first large volcanic edifice is inferred to have formed along N-S normal faults (Phase A on Fig. 2.9). Subsequently, these volcanic deposits were eroded and reworked into a volcaniclastic apron as there was a pause in volcanic activity around the Pliocene-Pleistocene boundary (Phase B on Fig. 2.9). A change in the region's tectonic regime with the onset of NE-SW strike-slip faulting is thought to have initiated the second period of volcanic activity by triggering a caldera-forming explosive eruption, the testimony of which are small number of pyroclastic deposits (Phase C on Fig. 2.9). Volcanism then resumed its effusive eruption style and has been building up the present-day volcanic edifice of Methana peninsula ever since. Dacites and andesites were deposited along NE-SW faults that were active during the early to mid-Pleistocene (Phase D to E in fig. 2.9). Another change in tectonic regime during the late-Pleistocene caused the onset of E-W normal faulting systems which are still active today and seem to have formed important pathways for the magmas of the more recent volcanic deposits (Phase F to H on Fig. 2.9).

The volcanic centre of Methana furthermore comprises submarine volcanic deposits which are located in the Epidavros basin about 2 km NW of Methana peninsula (Fig. 2.8C & 2.10). This submarine volcano was discovered in 1987 and named after the Greek writer Pausanias that described the sub-aerial and offshore volcanic phenomena of the most eruption that had occurred ca. 2230 years ago (Pavlakis et al., 1990). The Pausanius volcano is located within a neotectonic graben that is bounded by E-W trending faults (Fig. 2.10A & C). Based on seismic reflections, late Pleistocene (and possibly Holocene) sediments had been deposited in this graben prior to emplacement of the submarine volcanic rocks which themselves lack a sedimentary cover (Fig. 2.10B) (Nomikou et al., 2013). This suggests that the submarine Pausanius eruption products are the result of relatively recent, Holocene volcanic activity (Fig. 2.8C).

Aegina is the second largest volcanic centre of the Saronic Gulf after Methana. Volcanism began in the early Pliocene with minor phreatic eruptions and deposition of rhyodacitic tuffs and pumice (Pe-Piper & Piper, 2005). Most of the present-day volcanic edifice was subsequently formed by effusive dacitic-andesitic volcanic activity which lasted throughout the region's first phase of volcanism (Fig. 2.7 & 2.8C). Minor lava flows of more mafic composition which erupted around the Plio-Pleistocene boundary represent the island's short-lived second phase of volcanic activity (Fig. 2.7 & 2.8C). The fact that this last episode of volcanic activity followed a phase of considerable faulting and uplift and erupted from two sets of fissures suggests that the spatial-temporal evolution of Aegina's volcanism is also linked to the area's tectonic regime (Pe-Piper & Piper, 2005). More indications for an important influence of the extensional regime on local magmatism is the hydrothermal activity along NNE-SSW faults in the northern part of the island (Fig. 2.8C) and the many hundred meters of subsidence that occurred prior to any volcanic activity (van Hinsbergen et al., 2004). The volcanic stratigraphy of

Aegina is less well understood than the volcanic evolution of Methana and is discussed, together with the geological map of Aegina, in Chapter 6 (Fig. 6.1).

The third volcanic centre of the Saronic Gulf is represented by the 1 km² of andesitic-dacitic lavas that are exposed along the southern coastline of the island of **Poros** (Fig. 2.8C). These effusive rocks erupted from WNW-ESE oriented fissures around the start of the SAAVA's second period of volcanic activity (Fig. 2.7). The geological map of Poros' volcanic peninsula of Sferia is presented in Chapter 6 (Fig. 6.6)

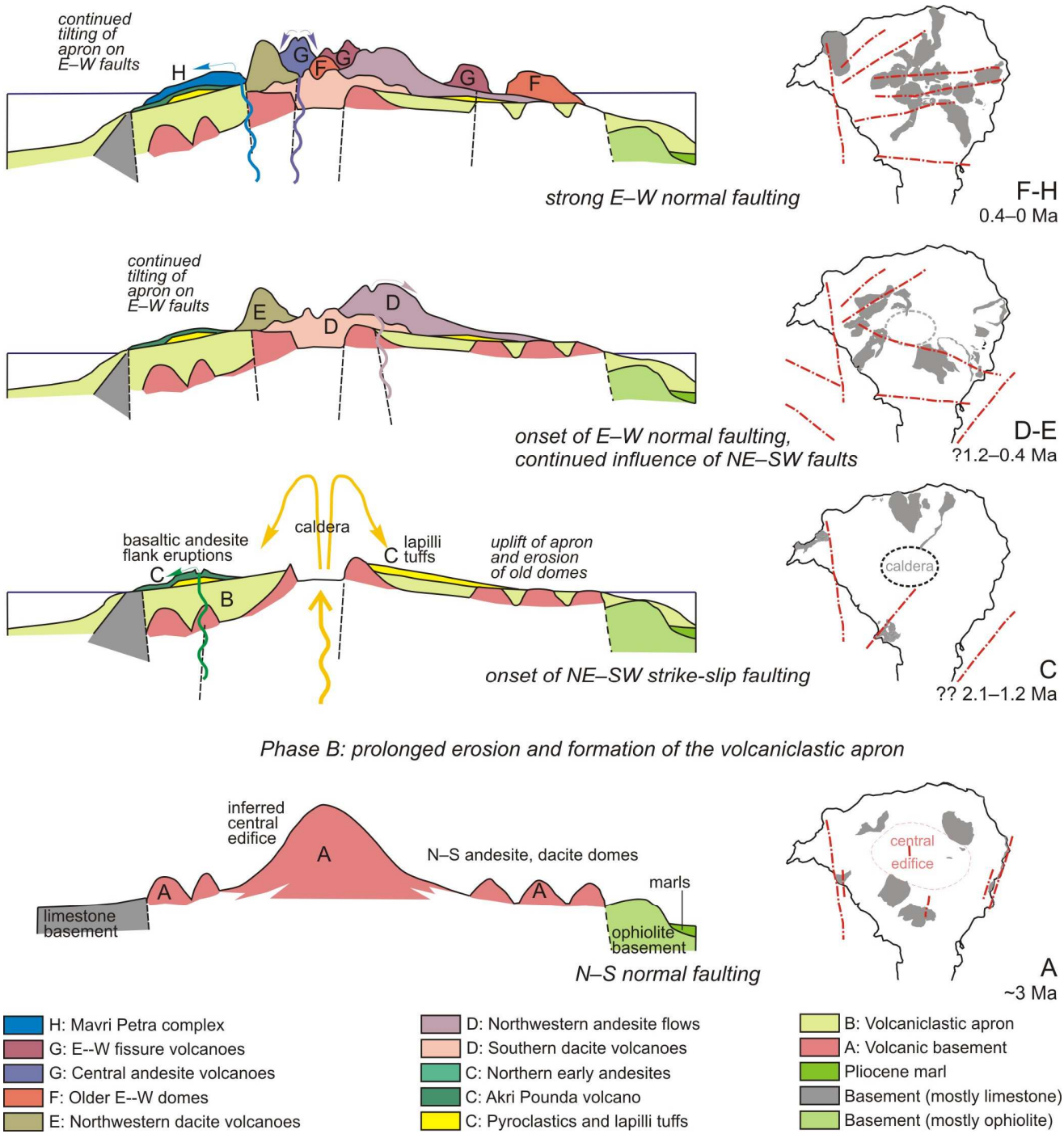

Figure 2.9. *Temporal-spatial evolution of volcanism on Methana* is correlated with major changes in the tectonic regime of the Saronic Gulf (Pe-Piper & Piper, 2013). See also the volcanological map of Methana (Fig. 5.1).

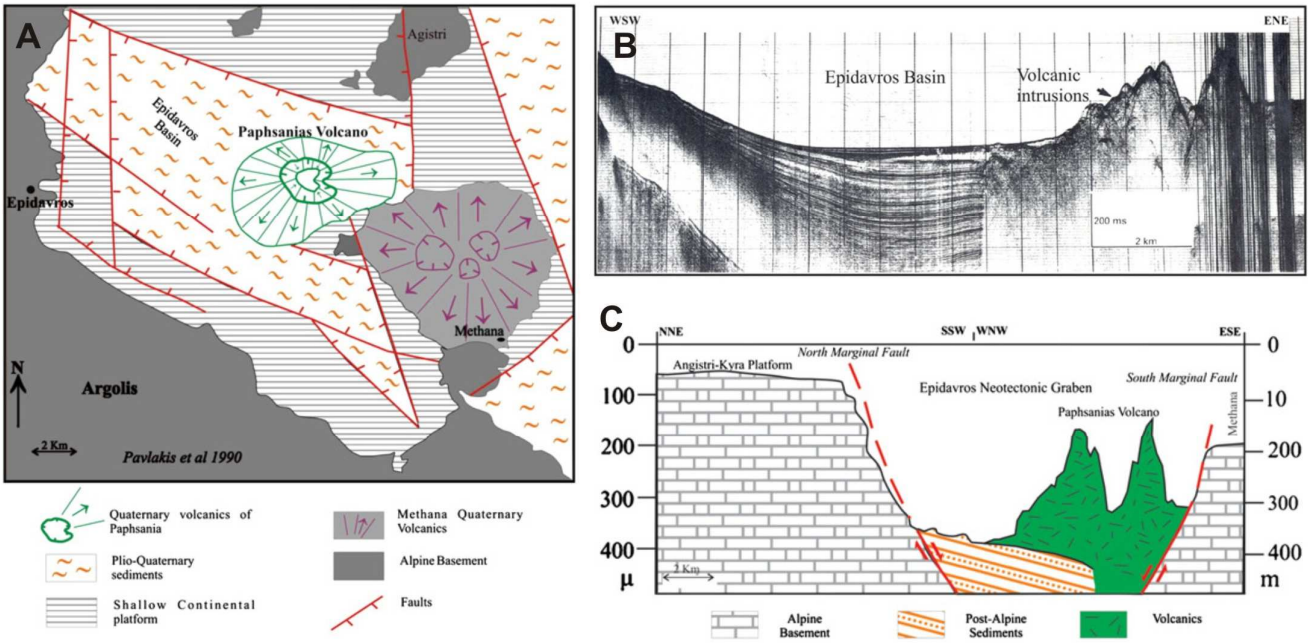

Figure 2.10. *The submarine Pausanius volcano* (Nomikou et al., 2013). (A) Tectonic sketch map of the SW Saronic Gulf, showing the submarine Pausanias volcano within the Plio-Quarternary tectonic graben of the Epidavros basin. (B) Seismic profile across the Pausanias submarine volcano. (C) Geological interpretation of seismic profile in B, showing the cone structure of the volcano within the neotectonic graben.

Chapter 3: Methodology

This chapter contains all information on the geochemical analyses (different sample digestion & preparation methods, Sr-Nd-Hf-Pb separation, measurement sequences, calibration, standardisation, instrument settings and data reduction) to allow verification of the obtained accuracy and precision of the geochemical data presented in this study. Samples brought back from fieldwork were subjected to a petrographical study on the basis of which the least weathered rocks were selected for major element analyses. Major element contents were then used to identify the samples that seemed the most interesting for further trace element analysis. The resulting trace element geochemistry was, in turn, studied to select the most appropriate rock samples for Sr-Nd-Hf-Pb isotopic analyses.

3.1 Fieldwork & sampling

The most recent geological maps of Aegina (Dietrich et al., 1993a), Methana (Gaitanakis & Dietrich, 1995) and Poros (Schwandner, 1998) formed the basis for all fieldwork and sampling carried out during this study. As many different volcanic units as possible were sampled in order to construct a picture of the overall variation in mineralogy, petrography and geochemistry. The geographical location of each sampling locality was determined by GPS in UTM coordinates (grid zone 34S WGS84) and can be found in Appendix A. Each volcanic outcrop was studied in detail (type of deposit, fresh or altered outcrop, presence of enclaves, estimation of enclave vol%, shape and grain size of enclaves, …), described in field notes and documented with photographs (Fig. 3.1A). Some of the resulting field photographs are presented in the field work sections of Chapters 4 to 6, together with descriptions of the sampled outcrops. A number of samples was retrieved from each volcanic lithology (host rock, enclave, pyroclastic deposit, …) and compared to one another to determine the most representative (and least weathered) one(s) to retain for further research (Fig. 3.1B,C). The volume of the individual host rock samples thereby varied between ~750 and 1500 cm^3, depending on the size and distribution of larger phenocrysts: coarse-grained rocks require larger sample volumes to represent the average composition of the outcrop than fine-grained lithologies do. Whenever their size and abundance allowed to do so, the same approach was used when sampling enclaves. Once selected for further research, each rock sample was given a unique ID, written several times on the sampling bag as well as on a piece of paper stored together with the sample in a thoroughly sealed plastic bag (Fig. 3.1D).

3.2 Microscopic study

The majority of samples was selected for petrographic study and thin sections of these rocks were made by Mr Jan Jurceka in the thin section workshop of the Laboratory of Mineralogy and Petrology at the Department of Geology and Soil Science of Ghent University. Using a water-cooled diamond saw, any weathering or alteration surfaces present on the rock samples were removed. A slice of approximately 1 cm thick was cut from each sample on which a representative section of the lithology (about 2 cm x 4 cm) was indicated. If there was host rock material attached to the outer rim of enclave samples, or when small enclaves were discovered within host rock samples, care was taken to include the contact zone between both rock types in the thin section. Fragile rock types such as pumice, scoria or weakly cemented sedimentary basement rocks and xenoliths were embedded in a

transparent epoxy resin to facilitate cutting and further processing. Finished thin sections contain a slice of rock sample with a final thickness of approximately 30µm.

All thin sections of igneous rock samples were studied with an Olympus BH-2 BHTP polarising microscope. This petrographic study allows to: 1) select the least altered samples for geochemical analyses; 2) identify the mineralogy of the different samples; and 3) study the different mineral and rock textures. Whereas the first purpose aims at ensuring that subsequent geochemical analyses reflect initial rock geochemistry and not secondary weathering, the last two purposes are vital for the interpretation of geochemical data and contribute to the overall understanding of the petrogenesis of the volcanic rocks. To document different textures and mineral assemblages, a ColorViewIII camera (Soft Imaging System GmbH) was used to photograph areas of the thin sections which were magnified 25, 40, 100 or 200 times. Some of the resulting photomicrographs are presented in the petrographic sections of Chapters 4 to 6, together with descriptions of the mineralogy and textures observed during the microscopic study. Text books primarily used during petrography for the identification of minerals and microstructures of igneous rocks are Nesse (2004) and Vernon (2004), respectively.

Figure 3.1. *Fieldwork and sampling on the volcanic centres of Aegina, Methana and Poros*. (A) Each outcrop is thoroughly observed and described before (B) a number of samples are collected. (C) Different samples taken from each volcanic lithology are carefully studied with a hand lens to determine their mineralogy, check for signs of weathering and select the most representative for further research. (D) Each rock sample is stored with its ID in a thoroughly sealed plastic sampling bag before it is mailed to Belgium.

3.3 Sample preparation for whole rock geochemical analysis

Rock samples were cut with a water-cooled diamond saw in order to 1) get rid of altered or weathered parts; 2) remove small enclaves from the host rock samples and host rock material from the enclave samples; and 3) reduce the large samples to smaller blocks of about 4 cm x 4 cm x 2cm which fit the jaw crusher. Some rock material was always retained for future reference, but most of the cleaned up sample blocks were further processed for whole rock geochemical analyses. Selected sample blocks were rinsed with deionised (Milli-Q) water (vesicular samples such as pumice and scoria were first cleaned in an ultrasonic Milli-Q water bath) and dried at 110° C in a laboratory drying oven. The dried sample blocks were then crushed in a stainless steel jaw crusher until all pieces were smaller than 6mm (Fig. 3.2A). In case of large sample volumes, a representative split was taken (Fig. 3.2D). The crushed samples were subsequently pulverised in an agate mill (Retsch planetary ball mill PM100 or Fritsch pulverisette 6) until the resulting powder was so fine that no more grains could be felt when the sample was rubbed between one's fingertips (approximately smaller than 2 µm) (Fig. 3.2B-D).

Pulverisation with an agate mill takes longer than with a tungsten-carbide mill, but it assures that contamination of trace elements necessary for qualitative trace element and Pb isotopic measurements is negligible. Throughout the preparation of rock samples for whole rock (WR) geochemistry, special care was taken to avoid cross-contamination between samples by thorough cleaning of the jaw crusher, sample splitter and utensils with a vacuum cleaner, compressed air and ethanol. In between milling different samples, agate mills and utensils were thoroughly cleaned with a dry toothbrush and ethanol. In some cases it was also necessary to pulverise quartz sand for 15 min to get rid of all material from the previous sample and/or to 'pre-contaminate' by pulverising and subsequently discarding a small amount of the next sample. The risk of sample cross-contamination was furthermore minimised by having only one sample container open at any given time as well as by physically separating finished samples or samples that await crushing/pulverising, from those samples that are being processed.

Figure 3.2. *Preparation of selected rock samples for whole rock geochemical analysis*. (A) The stainless steel jaw crusher used to crush the rock samples to particles smaller than 6mm. (B) Container of the agate Retsch planetary ball mill PM100 and the set of six smaller agate balls used to pulverise the samples to particles smaller than 2µm. (C) Sample ready to be pulverised to a fine-grained powder in the Fritsch pulverisette 6 agate ball mill. (D) Sample IM310 processed for whole rock geochemical analysis: the plastic tube in the top right corner contains the split of sample powder for WR geochemical analysis - the plastic bag contains the split of excess crushed sample.

3.4 ICP-OES analysis: major element and Sc, V, Cr, Ni, Cu, Zn, Sr, Y, Zr & Ba contents

Sample digestion for major element analysis with ICP-OES is done by flux-melting in order to retain all silica in the resulting solutions (acid digestion with HF leads to loss of silica as SiF_4, Walsh et al., 1997). Some trace elements can also be measured from these solutions and the Zr concentrations used in this work for geochemical interpretations are those analysed by ICP-OES since flux-melting ensures complete digestion of the otherwise resistant zircon mineral (see section 3.5.3).

3.4.1 Flux melting

About 4-5 g of sample powder is weighed into a ceramic crucible and heated for at least 2 hours in a laboratory drying oven at 110°C. The content of adhered water (H_2O wt%) of each sample is then defined as the weight loss observed, measured after cooling to room temperature in an desiccator. In a next step, the samples are heated up to 950°C for 8 hours in a furnace, subsequently cooled to room temperature and weighed to determine the samples' loss on ignition (LOI) which represents the loss of volatiles (e.g. structural H_2O, N_2, SO_2, CO_2, …) as well as oxidation of Fe^{2+} to Fe^{3+} (FeO to Fe_2O_3). The 4-5 g of sample that underwent these heating steps are recovered and stored in a desiccator.

About 0.15 g of this devolatilised sample powder is homogenised with ~0.6 g of mixed lithium meta-/tetraborate flux (65:35, Breitländer Specflux A1222), quantitatively transferred into a graphite crucible and fused in a furnace at 1050°C for 18-20 minutes. The resulting melt is then quenched and shattered in 90 ml 2% HNO_3 (+ 2ppm Pt to allow correction for instrumental drift, see below). The glass fragments usually dissolved within half an hour. The final sample dilution obtained in this way (~600 times) reduces major element concentrations to the range that can be optimally analysed with ICP-OES and prevents damage of the instrument's plasma torch that might otherwise occur due to high Li and B-salt contents (Walsh, 1997). The following day, about 30 ml of the final solutions is pipetted into (pre-cleaned) 50 ml centrifuge tubes in order to minimise the amount of carbon particles introduced into the ICP-OES instrument. Major element analyses are carried out within 5 days of the flux-melting procedure to avoid silica loss by precipitation, which can occur after this time span.

A set of rock reference materials, bracketing the expected major element compositions of the samples, is digested and diluted together with the samples and used as calibration standards (also known as primary or internal standards). These certified reference materials are United States Geological Survey (USGS) standards DTS-2b (dunite), BHVO-2 (basalt), AGV-2 (andesite), GSP-2 (granodiorite) and QLO-1 (quartz latite) as well as Geological Survey of Japan (GSJ) standards JG-2 (granite) and JSy-1 (syenite). British Chemical Standard (BCS) certified reference materials CRM393 or CRM513 (both limestone) and CRM 512 (dolomite) are used as extra calibration standards for the geochemical analysis of calcareous basement and xenolith samples. A procedural blank (0.6 g flux taken through the entire flux-melting digestion procedure together with samples and standards) represents the origin of the calibration lines. There are furthermore 1 to 3 sample duplicates (a rock powder from which two times 0.15 g was weighed for analysis) taken along in any one measurement series to assess the reproducibility of the entire sample preparation and ICP-OES analysis (representing the analytical uncertainty). Overall accuracy of the ICP-OES analyses is evaluated through measurement of secondary or external standards as unknowns: BCR-2 (USGS, basalt), JB-2 (JGS, basalt) and, depending on which one of these two standards was already used for calibration, either BCS-CRM393 or BCS-CRM513 (limestone).

3.4.2 ICP-OES measurements

Inductively Coupled Plasma Optical Emission Spectrometry (ICP-OES) is an analytical technique in which an aqueous sample solution is nebulised and injected into an inductively coupled argon plasma (Fig. 3.3). Due to the high plasma temperature (7000-8000 K), atoms ionise and/or take up energy, which lifts them to an excited state before they fall back to their ground state by sending out

electromagnetic radiation. The different wavelengths within this radiation are characteristic of the elements present in the sample and the intensity measured for each wavelength-signal correlates with the concentration of a certain element.

In this study, concentrations of major elements Si, Al, Mg, Ca, Ti, Fe, Mn, Na, K and P, and trace elements Ba, Sr, Zr, Y, V, Cr, Ni, Sc, Cu and Zn were measured by performing manual sample uptake and subsequent analysis with a Spectro Arcos ICP-OES instrument (Fig. 3.3A). This specific ICP-OES instrument is set up in such a way that the radiation sent out from excited atoms and ions is radially observed (Fig. 3.3D). The different wavelengths are registered simultaneously by 32 linear CCD detectors arranged in a Paschen-Runge setup. The Smart Analyzer Vision (SAV) software that

Figure 3.3. *Major element analysis by ICP-OES.* (A) The Spectro Arcos ICP-OES used in this study. (B) Sample introduction involves pump-assisted uptake of an aqueous sample solution. (C) The sample is nebulised and taken through the spray chamber where only the finest drops are transmitted towards the plasma – coarser drops are drained away as waste. (D). The IC plasma, with 1) end of the quartz glass torch; 2) the RF coil securing high voltage to maintain the plasma; 3) the ICP flame and 4) radial viewing of the ICP.

accompanies this instrument allows selection of specific wavelengths for each element of interest - the wavelengths used in this study are presented in Table 3.1. Since different elements can send out very similar wavelengths, it is important to choose for each element of interest wavelengths that are free from spectral interference from other elements.

Major element	*Wavelentgh (nm)*	*Trace element*	*Wavelentgh (nm)*
$Si_{(1)}$	251.612	Ba	455.404
$Si_{(2)}$	288.158	Sr	407.771
Al	176.641	$Zr_{(1)}$	339.198
$Mg_{(1)}$	202.647	$Zr_{(2)}$	343.823
$Mg_{(2)}$	285.213	Y	371.030
$Ca_{(1)}$	317.933	V	292.464
$Ca_{(2)}$	422.673	Cr	205.618
$Ti_{(1)}$	334.187	Ni	231.604
$Ti_{(2)}$	334.941	Sc	361.384
Fe	259.941	$Cu_{(1)}$	324.754
$Mn_{(1)}$	257.611	$Cu_{(2)}$	327.396
$Mn_{(2)}$	260.569	Zn	213.856
$Na_{(1)}$	588.995		
$Na_{(2)}$	589.592		
K	766.491		
P	177.495		

Table 3.1. The specific wavelengths analysed in this study for the determination of the rock samples' major and (some) trace element composition.

Each time the ICP-OES instrument is started up, its settings (gas flows, RF power, position of the plasma torch relative to radial observation point, …) need to be tuned to ensure optimal measurement conditions for the subsequent analytical session. Table 3.2 presents the main (ranges of) instrument settings typically applied on the Spectro Arcos ICP-OES during the different analytical sessions throughout this project. After optimisation of the measurement settings and stabilisation of the plasma, the calibration standards and procedural blank are measured. For each selected wavelength, the signal intensity peaks obtained from these calibration standard measurements are then used to ensure correct settings for on-peak measurement as well as adequate identification of the background signal subtracted from the intensity peak. Combination of the element-specific signal intensities measured for the calibration standards with their internationally accepted element concentration within the final dilutions renders the calibration lines used to calculate element concentrations of the unknowns. The GeoRem database (http://georem.mpch-mainz.gwdg.de/) was thereby consulted for the internationally accepted whole rock composition of the used rock reference materials.

Every ICP-OES sample analysis (unknown or standard) is composed of 5 individual measurements, which are checked for repeatability. After every sample analysis the instrument is rinsed for 2 to 3 minutes with a 2% HNO_3 solution to avoid any memory effects which might reflect the composition of a previous sample on the analysis of the next one. Because the plasma's temperature is not completely stable throughout a measurement day (8 to 12 hours), the radiation intensity detected for a certain concentration will slightly vary when analysed at different moments of the day. This is known as instrumental drift. The internal Pt standard added in exactly the same amount to all samples and standards allows a first, sample-specific, correction for the sensitivity fluctuation of the ICP-OES. A second, element-specific, drift correction was carried out via sample-standard bracketing:

the same solutions of two calibration standards (BHVO-2 and QLO-1) were analysed before and after every measurement set of 6 samples (unknowns and/or secondary standards) and the observed instrumental drift interpolated over the 6 ICP-OES analyses in between.

Instrument accessories	
Type of nebuliser	Cross-flow nebuliser
Type of spray chamber	Scott-type double pass spray chamber
Instrument settings *	
Sample uptake rate	1500 µL min^{-1}
RF power	1375-1475 W
Coolant gas flow rate	11-14 L min^{-1}
Auxiliary gas flow rate	0.8-1.15 L min^{-1}
Nebuliser gas flow rate	0.8-0.95 L min^{-1}
Data acquisition parameters	
Sample preflush time	45 s
Detected wavelengths	Entire spectral range between 130 and 770 nm
Measurement time	24 s
Number of measurements	5

Table 3.2. Specific instrument accessories, typical instrument settings and data acquisition parameters used on the Spectro Arcos instrument during the different ICP-OES analytical sessions carried out for this study between 11 February 2009 and 29 September 2012. * = optimised daily for (i) maximum sensitivity and (ii) minimal levels of detector background noise for Mn (257.610 nm), Pb (186.215 nm), Pb (220.351 nm) and As (189.042 nm).

The element concentrations automatically calculated for each sample by the SAV software (in mg/l) were transferred to a MS Excel spread sheet for further data reduction. Drift correction was carried out based on the internal Pt standard and the BHVO-2 and QLO-1 bracketing standards. Using the exact dilution of each sample and standard, their whole rock composition was calculated and the major elements conventionally expressed as oxide wt%. A first quality check of the ICP-OES geochemical data is provided by the sum of all major element oxide concentrations: only those analyses for which the total lies between 98.5 and 101.5% are accepted. The relative standard deviation of different analyses of the same sample or standard solution is used as a measure for the precision and is <1% for the major elements, <5% for Ba, Sr, Zr, Y, V and Sc and <10% for Cr, Ni, Cu and Zn. The accuracy of the geochemical data obtained within one ICP-OES measurement series is assessed by the concentrations calculated for the rock reference materials that were analysed as 'unknowns' (secondary standards). Table 3.3 compares the reference compositions of the secondary rock standards with the average values of their composition obtained over all ICP-OES analyses carried out in this study. For igneous and siliciclastic samples, the difference between measured and preferred concentrations is better than 2% relative for the major elements and trace elements Ba, Sr, Zr and V; better than 5% relative for Sc, Co, Y and Zn; and around 10% relative for for Ni and Cr concentrations over 30 ppm. The geochemical composition measured in this study for the secondary limestone standards indicates that the ICP-OES obtained concentrations for calcareous samples are in agreement within 5% relative for Fe_2O_3* (all iron expressed as Fe_2O_3), CaO, Ba, Sr and Zn and within 10% relative for SiO_2, Al_2O_3, MgO, MnO, Y and Cr. The geochemical compositions of Saronic Gulf samples determined in this study with ICP-OES are presented in Appendix B (igneous rocks) and in Appendix F (sedimentary basements and xenoliths).

	BCR-2			JB-2			CRM393			CRM513	
wt% *ppm*	Aver. (n=24)	1 SD (n=24)	Litera-ture	Aver. (n=16)	1 SD (n=16)	Litera-ture	Aver. (n=2)	1 SD (n=2)	Litera-ture	n=1	Litera-ture
SiO_2	53.90	0.41	54.10	53.42	0.37	53.50	1.09	0.00	1.24	0.41	0.40
TiO_2	2.27	0.04	2.26	1.17	0.02	1.19	0.01	0.00	0.02		
Al_2O_3	13.39	0.09	13.50	14.69	0.11	14.70	0.18	0.00	0.21	0.19	0.19
Fe_2O_3*	13.74	0.18	13.80	14.23	0.18	14.25	0.08	0.00	0.08	0.05	0.05
MnO	0.20	0.03	0.20	0.22	0.00	0.22	0.02	0.00	0.02	0.02	0.02
MgO	3.56	0.09	3.59	4.62	0.05	4.62	0.30	0.00	0.27	0.35	0.32
CaO	7.09	0.12	7.12	9.82	0.18	9.82	98.59	1.29	97.88	96.88	98.58
Na_2O	3.12	0.03	3.16	2.03	0.02	2.04					
K_2O	1.79	0.02	1.79	0.42	0.00	0.42	0.01	0.00	0.04	0.02	0.03
P_2O_5	0.35	0.00	0.35	0.10	0.00	0.10	0.01	0.00	0.01		
Ba	682.3	11.5	677.0	224.8	7.5	222.0	99.4	0.04	95.0	177.0	
Sr	338.3	2.7	340.0	180.5	2.1	178.0	282.7	1.5	282.7	237.8	264.2
Zr	186.1	4.3	184.0	51.1	2.5	51.0	21.3	0.2		15.02	
Y	36.3	0.6	37.0	24.0	0.4	23.750	5.4	0.0	5.8	7.36	6.92
V	408.6	9.7	416.0	559.7	19.2	575.0	7.0	0.4		4.61	
Cr	14.1	1.5	15.0	24.0	2.4	25.40	5.5	3.0		13.01	14.54
Ni	15.0	5.8	14.5	13.4	8.4	14.0	1.3	0.1		79.28	
Sc	34.4	4.0	33.0	56.5	6.9	54.0	0.7	0.2		0.11	
Zn	133.5	9.1	127.0	110.8	3.6	110.0	16.1	0.3		25.27	24.83
Cu	14.1	0.8	19.0	223.2	6.2	225.0	8.2	0.5		13.70	

Table 3.3. Compilation of major and some trace element compositions of secondary rock standards obtained during different ICP-OES analytical sessions between 11 February 2009 and 29 September 2012. The preferred (literature) geochemical composition of these standards is taken from the GeoReM website (http://georem.mpch-mainz.gwdg.de/, downloaded on October 5th, 2013). n = total number of analyses for respective standard; Aver. = average over n analyses; 1 SD = 1 standard deviation over n analyses; Fe_2O_3* = all iron expressed as Fe_2O_3. Concentration of major element oxides in weight percent (wt%) and of trace elements in parts per million (ppm).

3.5 ICP-Q-MS analysis: trace element concentrations

Whereas the solutions for major element analysis were prepared in a laboratory equipped with conventional extraction hoods, most sample digestions for trace element ICP-MS analysis were carried out in class 10 laminar flow hoods in the PicoTrace clean lab of the Department of Analytical Chemistry, since splits from some of these solutions were further used for isotope geochemistry. It is mainly the high contamination risk of Pb isotopic analyses that requires sample preparation with the utmost care, using ultra-pure acids and applying elaborate cleaning procedures for each container the samples come into contact with during sample preparation and MC-ICP-MS analyses. Detailed information on the different cleaning steps and required purity of the used acids can be found in Smet et al. (2010). Some laboratory equipment used for trace element and isotope ratio analysis is thereby made of PTFE (polytetrafluoroethylene) or PFA (a perfluoroalkoxy copolymer) which are relatively high temperature resistant and hydrophobic materials also known under the brand name 'Teflon'.

3.5.1 Low pressure acid digestion

Approximately 100 mg of powdered rock sample (not the aliquot that underwent LOI) is weighed into a 15 ml flat bottom Teflon (PFA) screw cap vial. One ml of 16M HNO_3 and 2 ml of 22M HF are added, the vials tightly closed and put for at least 24 h on a hotplate at 110-120°C. This first step with

HF is necessary to break down the silicates by converting them to fluorides (Walsh et al., 1997). After subsequent evaporation to dryness, 1 ml of 16M HNO_3 and 3 ml of 11M HCl are added, the vials again firmly closed and left for 24 h on the hotplate – this time only at 100°C to avoid overpressure within the formed *aqua regia* solution. This second step is necessary to break down the fluoride precipitates formed in the first step. After dry-down, 1 ml of 16M HNO_3 is added, the vial is closed and gently swirled and then straight away opened and placed on a hotplate at 110-130°C to evaporate to dryness. Repetition of this third step forms the fourth and final step of the low pressure HF/HNO_3/HCl sample digestion. It should be noted that this procedure is inadequate to dissolve resistant minerals such as zircon and that it results in the loss of silica (as volatile SiF_4) and B. Approximately 6 ml of 7M HNO_3 is added to the dried sample and the closed Teflon vials placed overnight on a hotplate at 110-130°C. After cooling the sample to room temperature, clarity of the solution is carefully studied against the light to check whether all sample residue seems re-dissolved. If this is the case, a split of approximately 1 ml of this solution is transferred to a second (thoroughly cleaned) 15 ml Teflon vial for trace element analysis. This 1/6 split, as well as the 5/6 share of the sample kept aside for radiogenic isotope geochemistry, is then evaporated to dryness. The trace element split is transferred to the geochemistry lab, where it is re-dissolved in 12 ml of 2% HNO_3 (+ 5ppb In and 10 ppb B & Tl). The same 2% HNO3 (with In, B & Tl) is also used to prepare the final dilutions (approximately 5000 times) in pre-cleaned 45 ml centrifuge tubes.

An empty Teflon vial taken through the entire low pressure (LP) acid digestion, splitting and final dilution procedure represents the full procedural blank used as origin for the calibration lines. Different amounts of primary (calibration) standards BHVO-2 (0.05 g, 0.10 g and 0.15g) and AGV-2 (0.10 g and 0.15 g) are digested and diluted together with the other samples and used for calibration of the trace element analysis. Secondary standards JB-2 and BCR-2 are also prepared together with each new trace element measurement series, as well as 2 to 3 duplicates of representative samples. The 5 ppb In, 10 ppb B and 10 ppb Tl added to all unknown samples, blanks and standards act as internal standards for drift correction. Instrumental drift is additionally corrected for by standard bracketing which is done with a ~5000 times diluted solution of BHVO-2.

For each set of trace element analyses a second ~5000x dilution of a representative sample is spiked with two different multi-element standards to allow quantification of the amount of interference of light/middle rare earth element (LREE/MREE) oxides on the middle/heavy rare earth elements (MREE/HREE). Multi-element standard 'spike 1' contains the elements Ho, Tb, La and Ba of which the isotopes ^{165}Ho, ^{159}Tb, ^{139}La and ^{135,137}Ba can form oxides (^{16}O) that interfere with the measurement of ^{181}Ta, ^{175}Lu, ^{155}Gd and ^{151,153}Eu, respectively. Formation in the ICP of the $^{138}Ba^{2+}$ ion will furthermore cause interference with the analysis of the $^{69}Ga^{+}$ ion, and if the La-hydroxide $^{139}La^{16}O^{1}H$ is formed it will interfere with ^{156}Gd. The second multi-element standard 'spike 2' contains Pr and Eu in order to monitor the interference of ^{141}Pr and ^{151,153}Eu oxides on ^{157}Gd and ^{167}Er, ^{169}Tm, respectively. The extra dilution of the representative sample is split in five ways: 1 split is not spiked and serves as the origin for the two calibration lines which result from spiking two splits with different concentrations of 'spike 1' and spiking the remaining two splits with varying amounts of 'spike 2'. Knowledge of the calibration lines for interference during an analytical session is combined with measurement of the ThO concentration in each individual analysis to carry out a sample-specific interference correction during off-line data reduction (see later). Despite the fact that (hydr)oxides of minor element titanium can interfere with the analysis of trace elements Cu and Zn ($^{49}Ti^{16}O$ on ^{65}Cu and $^{49}Ti^{16}O^{1}H$ on ^{66}Zn), no such interferences seem to have occurred during the ICP-Q-MS analyses carried out in this study.

3.5.2 ICP-Q-MS measurements

The sample introduction system is the same as that of ICP-OES: an aqueous, slightly acid sample solution is transformed into a mist and injected into the plasma where the prevailing high temperatures cause atoms of most elements to ionise, mainly into a singly charged positive ion. The ionised sample is then extracted by sampling cones and led via a series of lenses to the mass spectrometer where they are separated on the basis of their mass-to-charge (m/q) ratio. Those ions with a specific m/q

ratio that passed through the mass spectrometer are eventually counted by detectors and the resulting signal intensity is proportional to the element concentration within the sample.

For the trace element analysis carried out in this study, two different inductively coupled quadrupole mass spectrometer instruments (ICP-Q-MS) were used: first a PerkinElmer SCIEX Elan 5000 and later on a Thermo Scientific™ XSeries2 (see Fig. 3.4). Sampling was done manually during measurements with the Elan 5000 but automatically (using a Cetac ASX-520 AutoSampler) on the XSeriesII (Fig. 3.4A). Both instruments contain a quadrupole filter: four parallel, cylindrical rods are electronically connected as pairs forming two oscillating electrical fields at right angles with one another. By changing the voltage over the rods, varying ions with a certain mass-to-charge ratio will

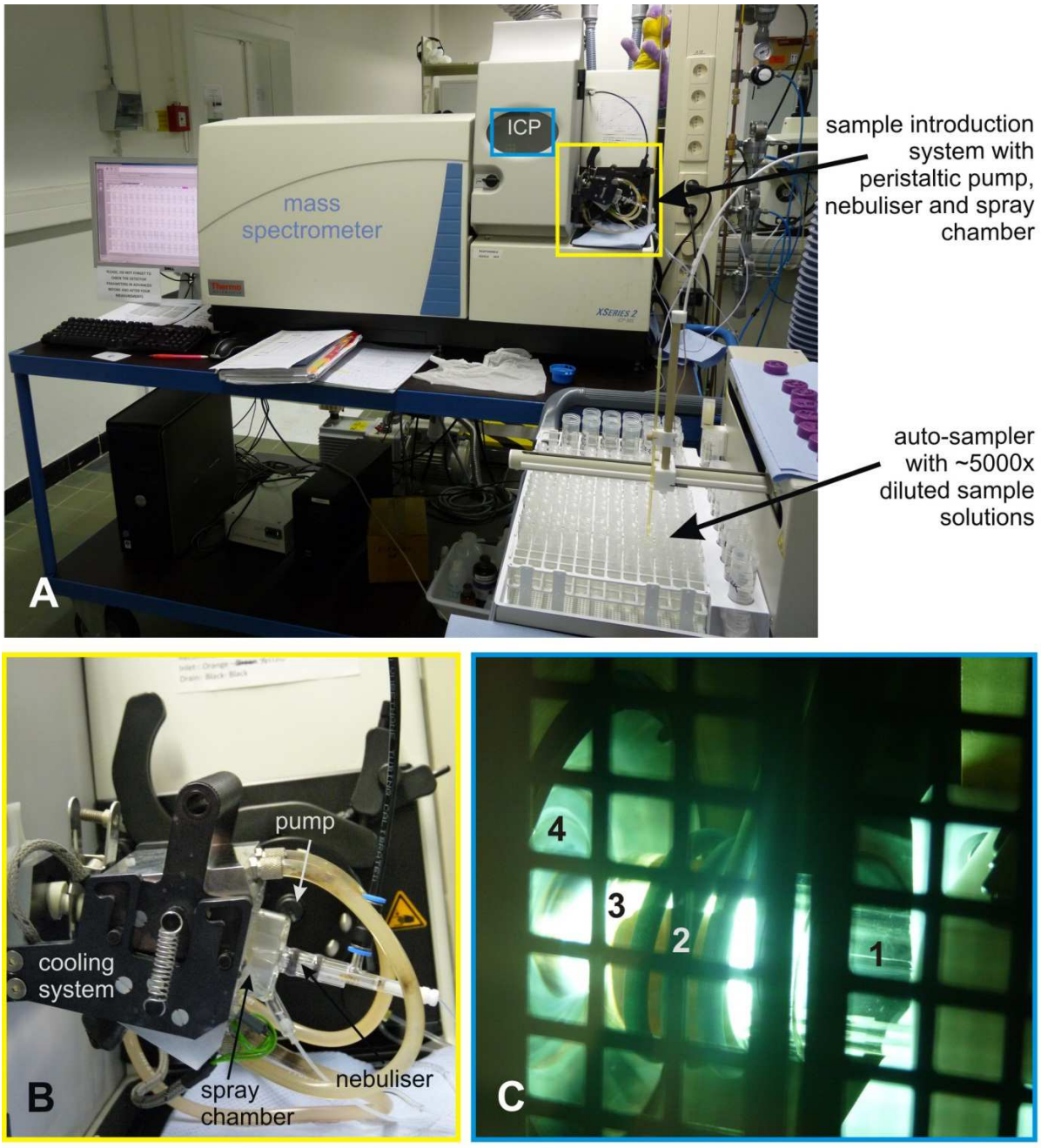

Figure 3.4. *Trace element analysis by ICP-Q-MS.* (A) The ThermoScientific XSeriesII used in this study, with the Cetac ASX-520 AutoSampler, the sample introduction system, the area where the ICP is generated and the quadrupole-based mass spectrometer. (B) The sample is taken up with the assistance of a peristaltic pump, taken through a nebuliser and the resulting sample mist has to pass through a cooled spray chamber before it is transported into the plasma. (C). The IC plasma, with 1) end of the quartz glass torch; 2) the RF coil securing high voltage to maintain the plasma; 3) the ICP flame and 4) the sampling cone which extracts the ionised elements.

have a stable trajectory through the quadrupole mass spectrometer and be able to reach the detectors. The detection system of the Elan 5000 was a channeltron continuous dynode electron multiplier (De Muynck, 2008, and references therein), the XSeries II is equipped with an electron multiplier with discrete dynodes (Van Heghe, 2013, and references therein).

As with the ICP-OES analyses, care needed to be taken to avoid interferences from elements other than the one of interest. Isobaric interference, for example, is due to the fact that isotopes of different elements can have very similar masses: the ^{58}Ni isotope has the highest relative abundance of this element (68%) but ^{58}Fe represents 0.28% of all iron, which is a major element in the studied rocks - ^{60}Ni (26%) is thus monitored instead of ^{58}Ni. Doubly charged ions can also interfere with singly charged ions of half their atomic mass ($^{138}Ba^{2+}$ has a m/q that can not be resolved from $^{69}Ga^{+}$ using ICP-Q-MS). Polyatomic interference results from interaction between H_2O from the aqueous solution and Ar plasma gas with the analyte elements, forming oxide, hydroxide, nitride and argonide ions (for example $^{141}Pr^{16}O$ interferes with ^{157}Gd, $^{159}Tb^{16}O$ with ^{175}Lu, $^{182}W^{40}$Ar with ^{202}Hg,...). The atomic masses used to determine the samples' trace element composition are presented in Table 3.5; mass 248 (ThO) was also monitored to use the specific ThO^{+}/Th^{+} ratio of each sample for oxide interference corrections. Data reduction is carried out off-line, using the 'raw' data (intensities in counts per second (cps) monitored for every analysed mass) in a MS Excel spread sheet (M. Elburg, personal communication).

Every sample analysis consists of 4 to 5 individual measurements, which are checked for internal repeatability and from which the average value is used for further data reduction (see data acquisition parameters in Table 3.4). In between two sample analyses, either the ICP-Q-MS is rinsed for 2-3

PerkinElmer SCIEX ELAN 5000		**ThermoScientific™ XSeriesII**
	Instrument accessories	
GemTip cross-flow nebulizer	Type of nebuliser	Concentric nebuliser
PerkinElmer Type II spray chamber	Type of spray chamber	Impact bead spray chamber
Ni, aperture diameter 1.0 mm	Sampling cone	Ni, aperture diameter 1.1 mm
Ni, aperture diameter 1.0 mm	Skimmer	Ni, aperture diameter 0.75 mm
	Instrument settings *	
1000 µL min^{-1}	Sample uptake rate	500 µL min^{-1}
1000-1100 W	RF power	1270-1400 W
15 L min^{-1}	Plasma gas flow rate	13 L min^{-1}
0.8 L min^{-1}	Auxiliary gas flow rate	0.7-0.8 L min^{-1}
0.8-1.0 L min^{-1} *	Nebuliser gas flow rate	0.7-1.0 L min^{-1} *
	Data acquisition parameters	
60 s	Sample preflush time	50 s
Peak hopping	Scanning mode	Peak hopping
1	Number of acquisition points per spectral peak	1
50 ms	Dwell time	10-20 ms
20	Number of sweeps	100
3	Number of readings	NA
4	Number of replicates	5

Table 3.4. Instrument accessories, instrument settings and data acquisition parameters typically applied on the two quadrupole-based ICP-mass spectrometers used for the WR trace element analyses carried out for this PhD study between 4 February 2009 and 28 September 2012. NA = Not applicable; * = optimised daily for (i) maximum sensitivity for $^{9}Be^{+}$, $^{59}Co^{+}$, $^{103}Rh^{+}$, $^{115}In^{+}$, $^{208}Pb^{+}$ and (ii) minimal formation of oxides (checking that $^{232}Th^{16}O^{+}/^{232}Th^{+}$ < 5-6%).

	BCR-2 (n=25)				JB-2 (n=17)			
	Average (ppm)	1 StDev (ppm)	Literature (ppm)	*Deviation from recommended value (%relative)*	**Average (ppm)**	1 StDev (ppm)	Literature (ppm)	*Deviation from recommended value (%relative)*
^{7}Li	**9.74**	0.46	9.00	*8.2*	**7.64**	0.85	8.00	*4.5*
^{9}Be	**2.27**	0.23	2.35	*3.4*	**0.16**	0.05	0.23	*32.6*
^{45}Sc	**33.8**	0.7	33.0	*2.3*	**54.7**	1.9	54.0	*1.2*
^{49}Ti	**13585**	480	13500	*0.6*	**6867**	317	7074	*2.9*
^{51}V	**419.8**	9.8	416.0	*0.9*	**578.4**	15.30	575.0	*0.6*
^{53}Cr	**16.0**	1.2	15.0	*6.3*	**25.1**	1.6	25.40	*1.2*
^{59}Co	**37.8**	0.8	37.0	*2.2*	**36.7**	1.4	38.0	*3.5*
^{60}Ni	**13.3**	0.6	14.5	*8.1*	**15.0**	0.8	14.0	*7.0*
^{65}Cu	**19.5**	5.8	19.0	*2.8*	**221.5**	10.3	225.0	*1.6*
^{66}Zn	**132.5**	4.3	127.0	*4.4*	**105.8**	4.2	110.0	*3.9*
^{69}Ga	**23.5**	2.9	23.0	*2.2*	**18.8**	3.4	18.00	*4.7*
^{85}Rb	**46.0**	0.9	46.9	*1.9*	**6.16**	0.20	6.30	*2.2*
^{88}Sr	**344.2**	4.5	340.0	*1.2*	**180.2**	15.6	178.0	*1.2*
^{89}Y	**35.5**	0.6	37.0	*4.0*	**23.2**	0.8	23.75	*2.5*
^{90}Zr	**185.7**	3.5	184.0	*0.9*	**49.1**	4.5	51.0	*3.7*
^{93}Nb	**12.5**	0.3	12.6	*0.6*	**0.65**	0.23	0.55	*18.9*
^{95}Mo	**242.0**	31.5	250.0	*3.2*	**1.12**	0.22	1.19	*5.7*
^{133}Cs	**1.21**	0.05	1.21	*0.1*	**0.82**	0.03	0.82	*0.5*
^{137}Ba	**674.6**	7.6	677.0	*0.4*	**218.6**	7.1	222.0	*1.5*
^{139}La	**25.1**	0.2	24.9	*0.7*	**2.36**	0.33	2.25	*4.7*
^{140}Ce	**52.5**	0.5	52.9	*0.7*	**6.97**	0.77	6.70	*4.0*
^{141}Pr	**6.65**	0.09	6.70	*0.7*	**1.23**	0.12	1.15	*6.9*
^{146}Nd	**28.7**	0.30	29.7	*3.5*	**6.43**	0.43	6.30	*2.0*
^{147}Sm	**6.57**	0.12	6.58	*0.2*	**2.26**	0.12	2.25	*0.3*
^{151}Eu	**1.98**	0.04	1.96	*0.9*	**0.83**	0.04	0.84	*0.9*
^{157}Gd	**6.66**	0.18	6.75	*1.3*	**3.03**	0.16	3.10	*2.3*
^{159}Tb	**1.04**	0.02	1.07	*2.7*	**0.56**	0.02	0.58	*2.7*
^{163}Dy	**6.41**	0.15	6.41	*0.1*	**3.92**	0.15	3.90	*0.6*
^{165}Ho	**1.29**	0.02	1.28	*0.68*	**0.85**	0.03	0.88	*3.7*
^{167}Er	**3.68**	0.10	3.66	*0.5*	**2.54**	0.10	2.55	*0.3*
^{169}Tm	**0.53**	0.01	0.54	*2.4*	**0.38**	0.01	0.37	*2.3*
^{173}Yb	**3.38**	0.08	3.38	*0.1*	**2.51**	0.09	2.50	*0.4*
^{175}Lu	**0.50**	0.01	0.50	*0.4*	**0.38**	0.01	0.39	*2.4*
^{178}Hf	**4.78**	0.08	4.90	*2.5*	**1.50**	0.12	1.45	*3.4*
^{181}Ta	**0.76**	0.04	0.74	*3.4*	**0.05**	0.02	0.04	*27.9*
^{208}Pb	**10.4**	0.54	11.0	*5.6*	**5.00**	0.34	5.10	*1.9*
^{232}Th	**5.86**	0.08	5.70	*2.8*	**0.28**	0.03	0.27	*3.3*
^{238}U	**1.64**	0.04	1.58	*3.9*	**0.15**	0.01	0.16	*8.7*

Table 3.5. Compilation of the trace element composition (with indication of the specific isotope measured for each trace element) of secondary standards BCR-2 and JB-2 obtained in this study throughout different ICP-Q-MS analyses between 4 February 2009 and 28 September 2012. The recommended (literature) geochemical composition of these standards is taken from the GeoReM website (http://georem.mpch-mainz.gwdg.de/ , downloaded on October 5th, 2013); n = total number of analyses for respective standard; 1 StDev = 1 standard deviation over n analyses. All concentrations in ppm.

minutes with ~2% HNO_3 (Elan 5000) or an instrument blank (~3-4% HNO_3) is measured after a 5 s rinse with ~2% HNO_3 (XSeriesII). Every four sample analyses are bracketed with a measurement of BHVO-2. The REE spiked solutions and calibration standards are ideally measured both at the start and the end of every analytical session. Both on the Elan 5000 and the XSeriesII Th and ThO+ are analysed to assess the amount of oxide formation for each sample individually. For measurements on the XSeriesII, values for CeO^+/Ce^+ and Ba^{2+}/Ba^+ are additionally determined after tuning and stabilisation of the ICP-Q-MS instrument.

Off-line data reduction starts with subtracting the sample-specific instrumental blank (3-4% HNO_3 analysed prior to every standard or unknown) from the subsequent sample analysis. The next step involves correction of the LREE/MREE oxide interference on the intensities measured for the MREE/HREE. This correction combines the oxide interference calibration lines calculated from the analyses of the spiked solutions with the CeO^+/Ce^+ ratio determined at the start of each trace element measurement sequence and with the ThO^+/Th^+ ratio monitored in all sample analyses. Fluctuations in the sensitivity of the ICP-Q-MS throughout an analytical session (= instrumental drift) are corrected for in first instance using the intensities analysed for internal standards B, In and Tl. These three standards were hereby chosen to represent the entire mass range of trace elements of interest, with the lighter elements (Li, Be) mainly drift corrected by B, the heavier elements by Tl and the majority of elements by In. This approach is preferred to drift correction with only one internal standard (for example In) because the matrix effects that influence instrumental drift are variably active across the analysed mass range. Further drift correction is carried out through sample-standard bracketing (interpolation of element-specific intensities measured in the BHVO-2 bracketing standards which were analysed before and after every 4 sample analyses). The resulting intensities of the monitored masses are then converted to element concentrations using the calibration lines calculated from the full procedural blank and primary standards BHVO-2 and AGV-2. The whole rock trace element composition of unknowns and secondary standards is eventually calculated taking into account their final dilutions. The relative standard deviation obtained from ICP-Q-MS analysis of duplicate samples (different sample solutions of one rock powder) represents the precision of the analysed trace element concentrations and is better than or equal to 5%.

Table 3.5 presents the average trace element compositions obtained for BCR-2 and JB-in this study, as well as their recommended values listed on the GEOREM website (http://georem.mpch-mainz.gdwg.de). Trace element concentrations obtained for secondary standards BCR-2 and JB-2 are representative of the accuracy of the trace element measurement procedure and is shown to be mostly 1-6% relative; apart from Li and Ni (<8.5% relative) and up to 33% relative in case of very low concentrations of Be, Nb and Ta (see Table 3.5).

3.5.3 Zircon non-dissolution

The trace element compositions obtained for igneous and sedimentary rocks from the Saronic Gulf are presented in Appendix C and F, respectively. Comparison of the zirconium concentrations analysed with ICP-OES with those from ICP-Q-MS analysis indicates large discrepancies between the two methods for approximately 50% of the samples. When both analytical techniques are comparably accurate there should, however, be a positive correlation of approximately 1:1 between the samples' ICP-Q-MS and ICP-OES Zr contents.

Figure 3.5A shows that whereas ca. 50% of the Saronic Gulf samples does define such a linear trend of similar ICP-OES and ICP-Q-MS obtained Zr concentrations (grey dotted line), the other half plots above this correlation in a cloud of significantly higher ICP-OES zirconium contents at given ICP-Q-MS Zr concentrations. The zirconium concentrations obtained for secondary rock reference materials BCR-2 and JB-2 via ICP-OES are however very similar those analysed with ICP-Q-MS, and both are well within 5% of the recommended literature values (see Table 3.3 and 3.5). This suggests that the discrepancy in ICP-OES and ICP-Q-MS obtained zirconium concentrations is not caused by inaccurate determination via either analytical method.

Plotting the ratio of the ICP-Q-MS over the ICP-OES obtained zirconium concentrations against the silica contents (Fig. 3.5B) results in a negative correlation for the host rock samples (black dotted arrow) and a bimodal distribution for the enclave compositions. Petrographic study of the samples with significantly lower $Zr_{(ICP\text{-}Q\text{-}MS)}/Zr_{(ICP\text{-}OES)}$ values furthermore reveals that these rocks commonly contain zircon. The flux-melting digestion procedure for major element analysis on the ICP-OES is capable of fully dissolving this mineral, but zircon is known to be resistant to commonly used low pressure acid digestion procedures such as the one applied in this study prior to trace element ICP-Q-MS analysis. The discrepancy between the ICP-OES and ICP-Q-MS zirconium concentrations is therefore thought to reflect non-dissolution of zircon: when a rock sample does not contain zircon, most zirconium is residing in more easily dissolvable groundmass which renders similar ICP-Q-MS and ICP-OES determined Zr contents; but when zircon crystals are present they will not be dissolved by the low pressure (LP) digestion procedure and thus cause erroneously low ICP-Q-MS whole rock Zr concentrations.

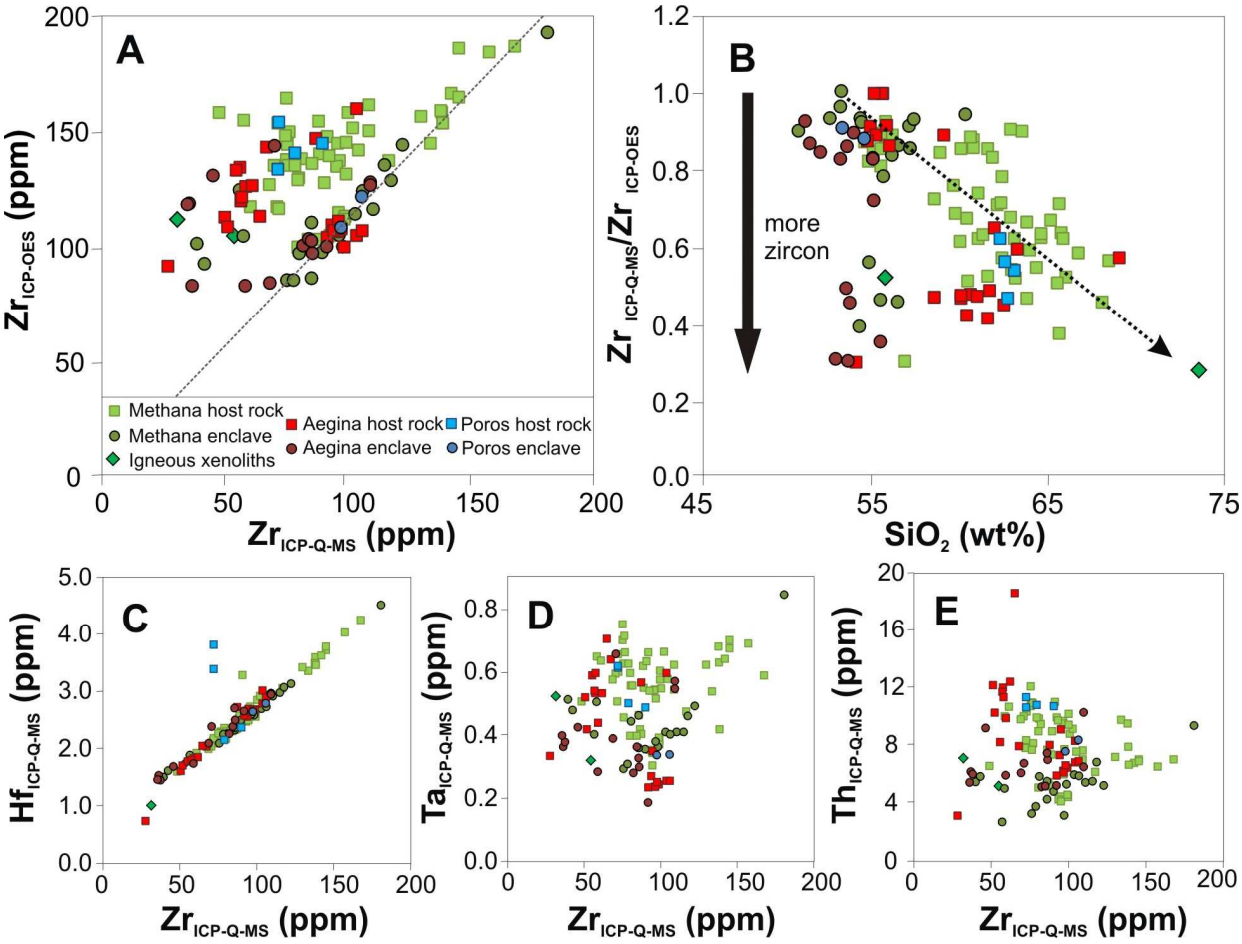

Figure 3.5. *Comparison of the Zr concentrations obtained by ICP-OES and by ICP-Q-MS* suggests non-dissolution of zircon for the samples analysed by ICP-Q-MS. The Saronic Gulf samples are grouped as enclaves, host rocks or igneous xenoliths based on field work and petrography. See text for discussion.

The positive correlation between the Zr concentration discrepancy and silica contents could thereby reflect the increasing stability of zircon in more evolved magmas, leading to only ~50% Zr recovery for the LP acid digestion procedure. One third of the enclaves also have ICP-OES Zr concentrations two times higher than ICP-Q-MS Zr contents – suggesting that some of the more mafic enclaves also contain zircon. Due to these discrepancies between the ICP-OES and ICP-Q-MS obtained zirconium concentrations, only the Zr contents obtained via flux-melting and subsequent ICP-OES are used for further interpretation. Zirconium is however not the only element hosted by zircon -

Hf is known to substitute for Zr in this mineral. Figure 3.5C indeed shows a nearly perfect correlation between the Zr and Hf concentrations obtained via ICP-Q-MS analysis. As the Zr concentrations from the ICP-Q-MS data are discarded due to zircon non-dissolution, the Hf concentrations measured from the LP acid digestion solutions are also not further discussed in this work. The Zr contents measured in the flux-melting solutions are instead used as a proxy for Hf in the discussion of $^{176}Hf/^{177}Hf$ isotope ratios. Besides Zr and Hf, the other high field strength elements (HFSE) Nb, Ta, U and Th are known to be present in small amounts in zircon. To check whether these trace element concentrations are also biased by the presence of zircon and its incomplete digestion in the ICP-Q-MS sample preparation method, these elements were plotted against the Zr contents obtained via ICP-Q-MS (Fig. 3.5D-E). In comparison to the clear correlation observed for Hf (Fig3.5C), these elements do not show any trend, indicating that their concentrations are not influenced by the presence of zircon and that they are an accurate estimation of the whole rock trace element composition.

3.6 MC-ICP-MS analysis: Sr-Nd-Hf-Pb isotopic composition

For those samples selected for isotopic analysis, the 5/6th splits retained after the LP acid digestion are further processed: first by sequential isolation of both Sr and Pb on Sr resin (50-100 µm, Eichrom Technologies, LLC) and then by separation of Nd via combined use of TRU and Ln resin (both 50-100 µm, Eichrom Technologies, LLC). Based on the Sr, Nd and Pb isotopic compositions a further sample selection was carried out for whole rock Hf isotopic analysis. For these final geochemical analyses, new sample solutions were prepared applying the LP acid digestion method for presumably zircon free samples but a HP acid digestion procedure for those rocks that showed large discrepancies between their Zr contents obtained via ICP-OES and ICP-Q-MS. Separations of Sr, Nd, Hf and Pb were carried out in series of up to 21 samples at one time, always including one full procedural blank and (at least) one secondary standard to allow accuracy assessment of each individual separation series. All element isolations and subsequent sample preparation for MC-ICP-MS analyses were undertaken in a clean lab.

3.6.1 Sr & Pb isolation

Smet et al. (2010) combined and simplified the methods of De Muynck et al (2009) and Deniel and Pin (2001) into a fit-for-purpose Sr-Pb isotopic analysis procedure for volcanic rocks. Since lead is a common environmental contaminant, the utmost care needs to be taken to prevent Pb contamination of the samples. A rigorous cleaning procedure of Teflon vials, pipet tips, centrifuge tubes, acid containers, auto-sampler vials,… was therefore developed and is discussed in detail in Smet et al. (2010). The reasoning behind it is to pre-clean every piece of lab equipment with the same acid, and (at least) the same acid concentration, as the one it will come in contact with during sample preparation. Only Milli-Q water and ultrapure nitric, hydrochloric and fluoric acid are used for sample digestion and element separation.

One day prior to Sr and Pb separation, the 5/6th sample parts of the LP acid digestion are re-dissolved in 1.3 ml 7N HNO_3 and placed overnight on a hotplate at 110°C. The next morning, upon cooling to room temperature, these 1.3 ml sample solutions are quantitatively transferred to (pre-cleaned!) 1.5 ml centrifuge tubes and centrifuged for approximately 2 min at 6000 rotations per minute (rpm). Bio-Rad Micro Bio-Spin™ columns (6 mm internal diameter and ca. 3 cm high, see Fig. 3.6) are filled with approximately 300 µl new Sr resin after which the resin beds are consecutively cleaned with 6 ml 6N HCl, 4 ml 8N HCl and 3 ml Milli-Q water (Fig. 3.6). The resin beds are conditioned with 1 ml 7N HNO_3 and the Teflon vials originally used for the samples' digestions are placed below the columns in order to collect the elute which contains all elements except Sr and Pb, which are retained on the Sr resin. The upper 1.1 ml of sample solution is then carefully pipetted from its centrifuge tube onto the column. About 0.2 ml of sample solution is left in the centrifuge tube because it possibly contains solid residues which can clog the isolation column. The excellent accuracy of secondary standards shows that analysis of only 85% of the isolated Sr and Pb fractions (1.1 ml of 1.3 ml

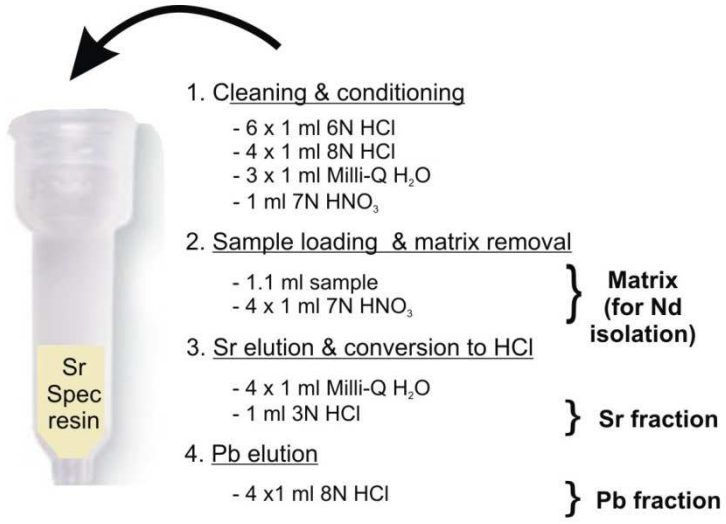

Figure 3.6. *Schematic overview of the combined Sr and Pb isolation with Sr Spec resin.* See text for further details.

solution) does not cause isotopic fractionation. The sample's matrix elements are eluted from the column with 4 ml 7N HNO_3 (Fig. 3.6). This eluent contains the sample's Nd fraction and is therefore dried down and stored for subsequent Nd isolation and isotopic measurements. Only the sample's Sr and Pb are now retained within the Sr resin. The Sr fraction is released from this resin with 4 ml Milli-Q water, whereas the Pb content can be collected in 4 ml 8N HCl (Fig. 3.6). The Sr and Pb fractions, collected in 7 ml spherical bottom Teflon vials, are evaporated to dryness at 110°C after which a couple of 15N HNO_3 drops are added to break down any organic material originating from the resin. These droplets of nitric acid are subsequently dried down on a hotplate at 110°C after which this nitration step is repeated once more. The dry Sr and Pb fractions are then carefully stored in the clean lab until the analysis of their isotopic composition. The Sr resin is washed on the columns with Milli-Q water and subsequentially recovered for future Sr isolations. It is important to note that during this study Sr resin has never been recycled for Pb isolation due to the high risk of sample cross contamination.

3.6.2 Nd isolation

The two-column sequential separation of light rare earth elements (LREE) presented by Pin & Zalduegui (1997) was adapted into a fit-for-purpose Nd separation scheme for geological silicate samples by Míkóva & Denkóva (2007). The latter extraction chromatographic procedure was largely followed for the Nd separations carried out in this study. In a first step, the REE are separated from their matrix on TRU resin, after which the LREE are eluted directly onto Ln resin. This Ln releases the LREE sequentially according to their increasing atomic mass, so that for any Ln resin-filled column the exact moment of Nd elution can be identified through determining its specific elution profile. To allow accurate analysis of the $^{143}Nd/^{144}Nd$ ratio, special attention needs to be paid to the complete separation of Sm from the Nd fraction.

One day prior to Nd isolation, the sample matrices recycled from the Sr and Pb separation are re-dissolved in 1.3 ml 2N HNO_3 and placed overnight on a hotplate at 110°C. The next morning, upon cooling to room temperature, these 1.3 ml sample solutions are quantitatively transferred to 1.5 ml centrifuge tubes and centrifuged. Large Bio-Rad chromatography columns (6 mm internal diameter and ca. 9 cm high, see fig. 3.7) are filled with ~1.5 ml Ln resin (resulting in a resin bed of 4.5 cm high), successively cleaned with 8 ml 6N HCl, 8 ml 0.25N HCl, 8 ml 0.75N HCl and 4 ml Milli-Q water and then finally pre-conditioned with 4 ml 0.05N HNO_3 (Fig. 3.7). Due to the height and volume of the Ln resin bed this preparation takes up to 3 hours, during which the TRU columns are prepared and the first step of extraction chromatography is carried out. Small Bio-Rad Micro Bio-Spin™ columns (6 mm internal diameter and ca. 3 cm high, see Fig. 3.7) are filled with approximately 300 µl TRU resin after which the resin beds are cleaned with 1 ml 2N HNO_3, 1 ml 0.05N HNO_3 and 1 ml Milli-Q water. These three cleaning steps are repeated after which the TRU resin beds are pre-conditioned with 1 ml 2N HNO_3 (Fig. 3.7). Approximately 1.1 ml of the centrifuged 1.3 ml sample solution are pipetted onto the TRU resin bed and whilst this resin retains the sample's REE, its matrix is removed with 4 ml 2N HNO_3

(Fig. 3.7). Once the preparation of the Ln columns is ready, the smaller TRU columns are placed on top of them and the LREE are eluted from the TRU resin straight onto the Ln resin with 4 ml 0.05N HNO_3 (Fig. 3.7). The LREE are successively eluted from the Ln resin with 0.25N HCl. The first 6 ml 0.25N HCl elutes La, Ce and Pr from the Ln resin and is discarded, and the next 6 ml 0.25N HCl is collected in a 7 ml spherical bottom Teflon vial as it contains most of the Nd fraction (Fig. 3.7). Samarium is only efficiently eluted from the Ln resin with somewhat stronger hydro-chloric acid, and so 3 ml 0.75N HCl is brought onto the columns to elute any remaining Nd as well as the Sm fraction. The Nd fractions are evaporated to dryness on a hotplate at 110°C, nitrated twice and eventually stored until their isotopic analysis. Both resins can be re-used for Nd separations. The TRU resin is washed whilst in the columns with the same cleaning steps carried out prior to sample loading (Fig. 3.7) and then recycled into a clean container. Upon cleaning with 4 ml 6N HCl and 4 ml Milli-Q water, the Ln resin is not recycled but instead remains in the columns, which are stored in Milli-Q water until the next Nd isolation.

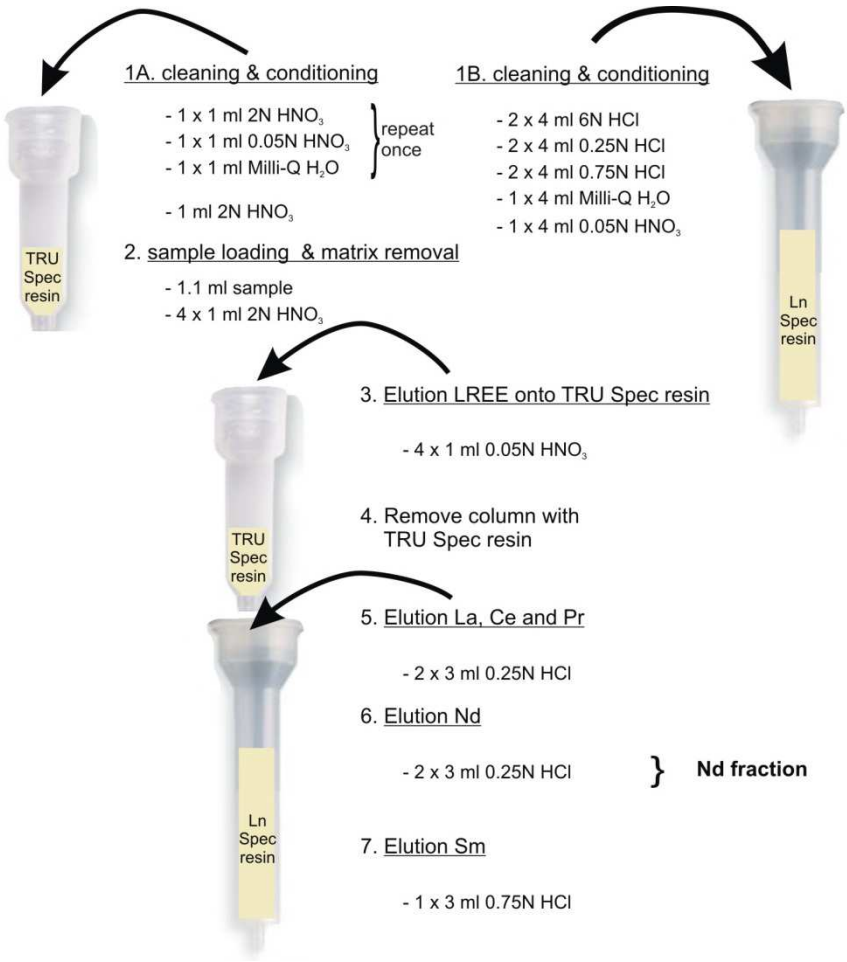

Figure 3.7. *Schematic overview of the Nd isolation successively on TRU Spec and Ln Spec resin.* See text for further details.

3.6.3 High pressure acid digestion in Parr™ bombs

Based on the discrepancy between their ICP-Q-MS and ICP-OES analysed Zr contents (see section 3.5.3), the samples selected for whole rock Hf isotopic analyses were divided into samples which seem to contain zircon and zircon-free samples. Of the latter group, sample dissolutions were made using the low pressure acid digestion procedure with HF, HNO_3 and *aqua regia* discussed in section 3.5.1 (Fig. 3.8A). To achieve digestion of the zircon crystals present in the second group of samples, an equivalent acid digestion procedure at higher pressure (HP) was carried out in 4 Parr™ bombs (volume = 23 ml; max T = 250°C; max P = 1800 psig; Parr Instrument Company, Moline, Illinois, USA). These Parr™ bombs consist of an inner PTFE vial which contains the sample powder and digestion acids, and which becomes a sealed pressure vessel upon wedging into its outer stainless steel jacket and placement in an oven at 185°C (Fig. 3.8B, C). Sample digestion in such HP vessels requires special care concerning the volumes and strengths of the acids submitted to higher temperatures and pressures in order to avoid explosion of the HP 'bombs'. The particular design used in this study was equipped with a safety rupture disc that would release in case of overpressure. The elevated temperatures and pressures used to digest silicate samples in these Parr™ bombs can lead

to migration of acid vapours outwards through the PTFE inner vessel and corrosion of the stainless steel outer jacket. In turn, there is a possibility that material from the outer metal jacket enters the PTFE vial and thus contaminates the sample it contains. A thorough cleaning procedure of the PTFE vials has been developed and tested to assess the Hf blanks potentially resulting from cross-contamination by the previously HP digested sample. These tests showed that the cleaning procedures for the PTFE vessels reduced the Hf blanks derived from the HP digestion to a maximum 10 pg of Hf for each individual sample. These maximum 10 pg blanks are negligible in comparison to a minimum Hf content of 50 ng in each of the analysed samples. For lead isotopic analysis, however, the Parr^{TM} bomb HP acid digestion would add too much Pb to our samples (up to 3.1 ng) in comparison to the LP acid digestion procedure carried out in the clean lab (which has maximum dissolution blanks of 20 pg).

The total procedure of cleaning the 4 Parr^{TM} bombs and subsequently carrying out HP acid digestions takes 10 working days. The PTFE vials and their caps are rinsed with Milli-Q water and dirt on their outer sides is cleaned of with a paper tissue. The PTFE vessels are then filled with Milli-Q water, closed and placed into a large glass beaker in which 6N HCl is poured until it nearly reaches the base of their cap. This set-up is left boiling for about 2-3 hours on a hotplate at 250°C and is necessary to further remove the PTFE vessels' outer dirt derived from corrosion of the steel jacket. This first step is then repeated a second time with a different, cleaner 6N HCl solution and a third time with 7N HNO_3. After every cleaning step the PTFE vials and caps are rinsed with Milli-Q water. The inner PTFE vials and caps are then completely submersed into a (yet cleaner) 7N HNO_3 solution and left boiling for a couple of hours at 300°C to clean the inside of the vessels. This step is repeated once with relatively clean 6N HCl after which the vials and caps are rinsed with Milli-Q water. Each vial is then individually filled for two thirds with 7N HNO_3, closed and left on a hotplate at 130°C for 2-3 hours. The final cleaning step involves filling the inner PTFE vials with ~1.8 ml 7N HNO_3 and ~ 3.8 ml HF, enclosing them in their respective stainless steel jackets (which were cleaned with either dry tissues or water and a sponge) and placing the assembled bombs for about 24 hours in an oven at 185°C (Fig. 3.8C). This last cleaning step mimics the circumstances under which the samples undergo their first HP acid digestion step: 0.1 g of rock powder is weighed into a glass vial and quantitatively transferred to a pre-cleaned PTFE vial. After ~1.8 ml ultrapure 7N HNO_3 and ~ 3.8 ml ultrapure HF are added, the PTFE vial is closed and placed into its stainless steel vessel. The bombs are then re-assembled and placed for 4 days in an oven at 185°C. After approximately 96 hours, the bombs are taken out of the oven and cooled to room temperature. They are disassembled and the PTFE vessels are taken out, opened and put on a hotplate at 110-130°C until the sample solution is evaporated to dryness. In the second digestion step ~1.8 ml ultrapure 7N HNO_3 and ~3.8 ml 6N HCl are added to the sample. The reassembled bombs are subsequently

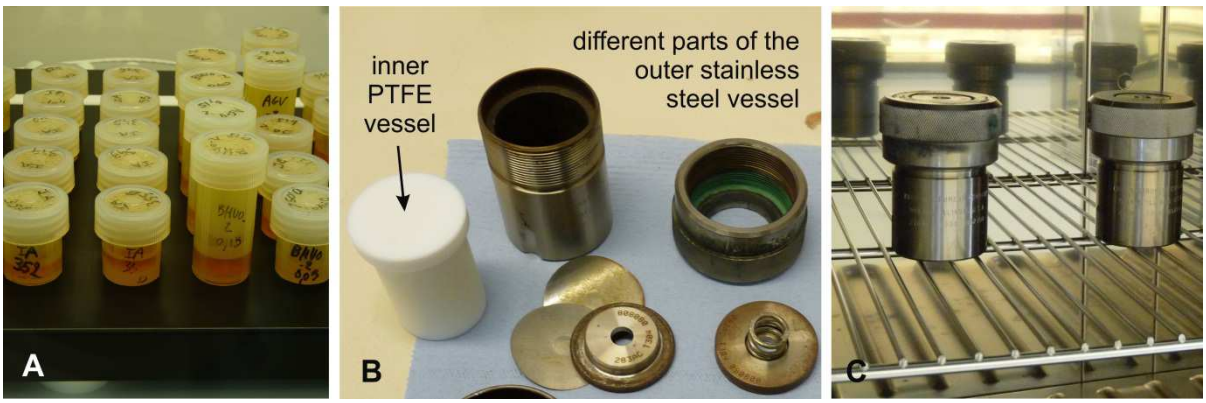

Figure 3.8. *Acid digestion procedures used to dissolve the silicate rock samples in this study.* (A) Second step of the low pressure (LP) acid digestion: samples are dissolving with *aqua regia* on a hotplate at 100°C. (B) Different parts of a Parr^{TM} bomb used for high pressure (HP) acid digestion of zircon-containing samples prior to Hf isolation. (C) Two assembled Parr^{TM} bombs undergoing the final cleaning step with HF/HNO_3 in a drying oven at 185°C. See text for further details.

placed in an oven at 185° C for about 48 hours. After this last Parr^{TM} bomb acid digestion step the sample solutions are quantitatively transferred to (pre-cleaned) flat bottom 15 ml PTFE vials and dried down on a hotplate at only 100°C to avoid boiling. Meanwhile, the PTFE vessels of the Parr^{TM} bombs are again thoroughly cleaned for the next 4 sample digestions. After evaporation to dryness, the digested samples are nitrated twice and stored for later Hf isolation at the VU University Amsterdam. In total 31 unknowns, 1 duplicate, 3 secondary standards and 3 full procedural blanks were prepared using this HP acid digestion procedure. Eleven HP acid digested samples that clearly contain zircon were also prepared for Hf isolation according to the LP acid digestion procedure. This was done in order to assess the difference in $^{176}Hf/^{177}Hf$ isotopic composition that could potentially result from analysing only groundmass Hf (LP acid digestion) or groundmass as well as zircon Hf (HP acid digestion).

3.6.4 Hf isolation

Hafnium isolation and MC-ICP-MS isotopic measurements at the VU University Amsterdam were funded by the European Union under the Seventh Framework Programme as TransNational Access project 079-TNA3 of the European Research Infrastructure for Planetary Science (EuroPlanet). Final sample preparation and Hf isolation was carried out in the clean laboratory of the Department of Deep Earth and Planetary Sciences under guidance of the head of the clean room, Richard Smeets. The applied Hf separation procedure is based on the method of Münker et al. (2001), set-up by Nebel et al. (2009) and further refined by Eric Fulmer, Thomas Kruijer and Martijn Klaver. Four series of Hf separation, each consisting of 21 samples, were carried out on Ln resin columns, made from shrink PTFE. These Hf columns have a 40 mm long bottom reservoir with an inner diameter of ~5.6 mm that is half filled with 1 ml Ln resin (100-150µm, Eichrom Technologies, LLC) and a wider (~12mm inner diameter) top reservoir with a volume of approximately 15 ml (Fig. 3.9). Due to the height and volume of the Ln resin bed, the aqueous solutions used for Hf isolation drip through very slowly. Each series (consisting of 21 samples) of Hf isolations is therefore carried out over two successive days.

The first day involves re-dissolution of the digested rock samples in 4 ml 2-3N HCl and overnight heating on a hotplate at 110°C. The Hf columns are successively cleaned with 15 ml 2N HF, 15 ml 6-7N HCl, 15 ml 2N HF and 15 ml 6-7N HCl (Fig. 3.9). After these pre-cleaning steps, the Hf columns are placed in centrifuge tubes containing 0.1N HCl and covered with parafilm.

On the second day, the Hf columns undergo two final cleaning steps of 15 ml 2N HF and 15 ml 6-7N HCl after which they are pre-conditioned with 2 times 8 ml 3N HCl. Meanwhile, the samples are taken from the hotplate and placed for 10 minutes in an ultrasonic bath in order to improve their dissolution and homogenisation. Sample solutions are then checked against the light to assure there are no visible precipitates left. The resulting clear solutions have a yellow

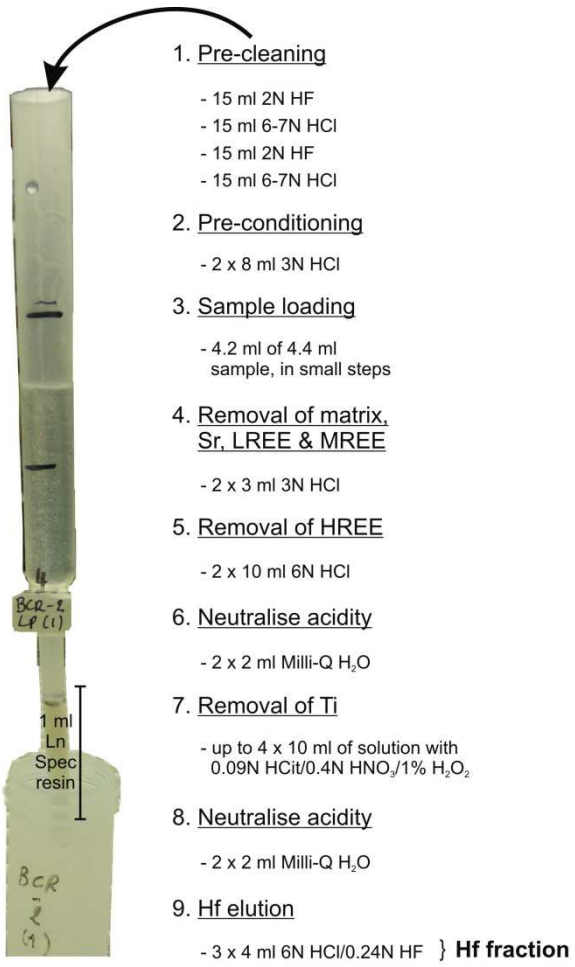

Figure 3.9. *Schematic overview of the Hf isolation on shrink Teflon columns with Ln Spec resin.* See text for further details.

colour due to the presence of iron as Fe^{3+}. Since this ion takes up too much active space on the Ln resin, it is transformed to the Fe^{2+} ion that passes much faster and easier through the Hf column. This iron reduction is done by adding 1.0N ascorbic acid (HAsc) to the samples until the yellow solutions are colourless and a final ascorbic acid concentration of ~0.1N is obtained (about 400 µl of 1.0N HAsc was added to all samples). The resulting ~4.4 ml sample solutions (2-3N HCl and 0.1N HAsc) are transferred to 10 ml (pre-cleaned) centrifuge tubes and centrifuged for 4 minutes at 4000 rpm. Meanwhile, the PTFE vials in which the samples were re-dissolved are rinsed with Milli-Q water and cleaned with a weak acid solution of 0.56N HNO_3 and 0.24N HF on a hotplate at 110°C. After centrifuging, 4.2 ml of the 4.4 ml sample solutions is loaded onto the pre-cleaned and conditioned Hf columns – special care is taken not to disturb the bottom layer, which potentially contains microscopic precipitates that can clog the Ln resin. Another 6 ml of 3N HCl is added to remove the remaining matrix as well as Sr, LREE and MREE (Fig. 3.9). Removal of the HREE is carried out by adding 20 ml 6N HCl, after which the columns are rinsed with Milli-Q water to neutralise the strong acidity (Fig. 3.9). At this point of the Hf separation procedure, the samples colour the Ln resins in different shades of yellow/orange depending on their Ti contents. To remove the Ti fraction (as TiO_2-H_2O_2 complex), the columns are rinsed with a mixture of 0.09N citric acid (HCit)/0.4N HNO_3/1% H_2O_2 until the resin beds are white again (Fig. 3.9; 20-30 ml of the HCit/HNO_3/H_2O_2 solution sufficed for the majority of samples apart from the most mafic rocks such as BHVO-2 or mafic enclaves which required up to 40 ml to remove all Ti). After the removal of Ti only the HFSE remain on the Ln resin beds and the columns are rinsed with 4 ml Milli-Q water. The cleaned PTFE vials of the original sample solutions are now placed underneath the respective Hf columns and the Hf fractions are finally collected in 12 ml 6N HCl/0.24N HF (Fig. 3.9). The first few ml of this elute mainly contain Zr because the Zr and Hf elution peaks partially overlap. The presence of Zr in the matrix of the Hf fraction does however not affect the $^{176}Hf/^{177}Hf$ isotopic analysis (Martijn Klaver, personal communication). The Hf fractions are finally dried down on a hotplate at 120°C and stored for Hf isotopic analysis. The Ln resin is rinsed with Milli-Q water after which the Hf columns are placed in 0.1N HCl and stored until the next Hf separation.

3.6.5 Isotopic analyses: MC-ICP-MS instruments and mass discrimination

Prior to isotopic analysis, Sr, Nd, Hf and Pb fractions were re-dissolved in 1 ml of the weak acid in which they would be analysed with the multi-collector inductively coupled plasma mass spectrometer (MC-ICP-MS). In order to define the concentrations of these element fractions and allow preparation of final dilutions that are optimal for the isotopic measurements, ~5% of these 1 ml Sr, Nd, Pb and Hf fractions was quantitatively analysed by quadrupole-based ICP-mass spectrometry.

In general, a MC-ICP-MS has the same ionisation source as the other analytical instruments used in this study (inductively coupled plasma) and a sample extraction interface similar to the one of the ICP-Q-MS instruments used for trace element analysis (sampling cone, skimmer and lens system). The mass spectrometer and detector system are, however, different from the previously discussed ICP-instruments. In order to minimise spectral interference on the isotopes of interest, the MC-ICP-MS instruments used in this study are equipped with a double focussing mass spectrometer, which consists of an electric field that is followed by a magnetic field (known as a 'Nier-Johnson geometry sector field mass spectrometer'). After extraction from the plasma, the different ions are first guided through the electrostatic sector, which reduces the distribution of their kinetic energy so that all ions have the same velocity when they subsequently enter the magnetic sector. This uniform velocity of the ions improves the resolving power of the magnetic sector, which spatially separates the different ions on the basis of their mass-to-charge ratio (m/q). Finally, up to nine different mass-to-charge ratios can be simultaneously monitored by the 9 Faraday cups of the detector. It is this aspect of a multi-collector detector that allows the precise measurements of isotope ratios required for this study.

Apart from potential spectral interferences, observed isotopic ratios also need to be corrected for mass discrimination, which is caused by the fact that the efficiency with which ions are extracted and transmitted from the ICP to the detector is greater for the heavier than for the lighter isotopes of one

element. There are two main methods of mass discrimination correction based on different isotope ratios observed within one analysis: internal and external normalisation (De Muynck, 2008). Internal normalisation involves correction of the measured isotope ratio to an invariant isotope ratio of the same element (for example variable $^{87}Sr/^{86}Sr$ corrected for with invariant $^{86}Sr/^{88}Sr$ ratio). When the element of interest has no invariant isotope ratio, only external normalisation with the invariant isotope ratio of an element of similar mass range can be applied (for example normalisation of the $^{85}Rb/^{87}Rb$ to the invariant $^{86}Sr/^{88}Sr$ ratio, or of the $^{206}Pb/^{204}Pb$ ratio to the invariant $^{205}Tl/^{203}Tl$ ratio). A mass discrimination correction alternative to external normalisation is external standardisation: the observed isotope ratios of a sample are referenced to the observed isotope ratios of a known standard which was measured before and after the sample analysis (sample-standard bracketing).The specific mass discrimination corrections used for the analysis of each isotopic system are presented below.

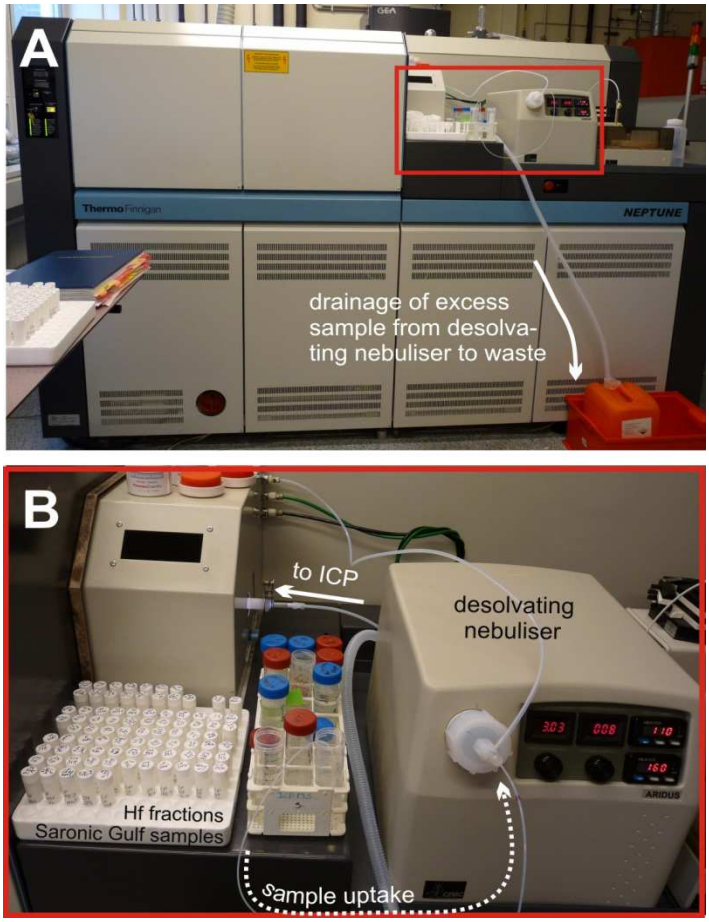

Figure 3.10. *MC-ICP-MS instrument and sample introduction system used during the WR Hf isotopic analyses carried out at the VU University Amsterdam*. See text for further details.

During each MC-ICP-MS analytical session, instrumental blanks are measured for background correction purposes (if necessary) and full procedural blanks are analysed to assure that no contamination occurred throughout sample processing. The internal precision of the different isotopic compositions is assessed by the specific standard error (SE) of individual analyses. The standard deviation (SD) of multiple analyses of the same sample or standard represents the external reproducibility. The accuracy of the isotopic analyses is reflected by the isotope ratios obtained for certified reference materials.

The multi-collector ICP-MS instrument used in this study was a Thermo Scientific Neptune (Fig. 3.10A), either at the Department of Analytical Geochemistry in Ghent University (Sr-Nd-Pb) or at the Department of Deep Earth and Planetary Sciences at VU University Amsterdam (Hf). For the Sr, Nd and Pb isotopic analyses, sample uptake was done using a Cetac ASX-100 Micro Auto-sampler in combination with a peristaltic pump and a 50 µl micro-concentric PFA nebuliser. For the Hf isotopic measurements, sample uptake was carried out manually in combination with a 50 µl/min desolvating nebulising system (Cetac Aridus; Fig. 3.10B). The latter system creates a dry plasma (less interference from oxide and hydroxide ions) and improves sample transport efficiency, which leads to increased sensitivity and thus precise analysis of smaller concentrations. Both Neptune MC-ICP-MS instruments were operated in low-resolution mode during all isotopic analyses.

3.6.6 Sr isotopic analysis

The purified Sr fractions and a solution of certified isotope reference material NIST SRM987 (strontium carbonate; National Institute for Standards and Technology, USA) were all diluted with

~0.28N HNO_3 to a concentration which varied from 200 to 400 ppb depending on the sensitivity of the MC-ICP-MS during a particular analytical session. The same ~0.28N HNO_3 dilution acid was used to measure instrumental blanks at the start of each measurement series as well as after every 5-6 samples. Since the signals from these instrumental blanks were always negligible in comparison to the signal intensity obtained for the (diluted) Sr fractions (<0.06%), no blank corrections were carried out. Procedural blanks (undiluted) were also negligible for every Sr isotopic measurement series carried out in this study (<1ng, which represents 0.05% of the minimal 20µg sample originally weighed in). Each sample analysis consisted of 50 individual measurements (see Table 3.6). In order to minimise memory effects, the MC-ICP-MS was rinsed for 200 to 250 s with ~0.28N HNO_3 before each sample analysis (or instrumental blank).

The specific cup configuration chosen for the Sr isotopic measurements during this study is presented in Table 3.6. $^{83}Kr^+$ is monitored to assess potential isobaric interferences from $^{84}Kr^+$ and $^{86}Kr^+$ on $^{84}Sr^+$ and $^{86}Sr^+$, respectively. Throughout the analytical sessions of this study, however, $^{83}Kr^+$ signal intensities never exceeded the levels of background noise associated with the detectors, so that no correction for krypton interference was necessary. Rubidium is monitored at m/q 85 to allow correction for isobaric interference of $^{87}Rb^+$ on $^{87}Sr^+$. Most Rb is removed during the Sr isolation

Instrument accessories						
Type of nebuliser	Micro-concentric nebuliser					
Type of spray chamber	Combined cyclonic/double-pass spray chamber made of quartz glass					
Sampling cone	Ni, aperture diameter 1.1 mm					
Skimmer	Ni, aperture diameter 0.8 mm					
Instrument settings *						
Sample uptake rate	50-100 µL min^{-1}					
RF power	1200-1300 W					
Plasma gas flow rate	15 L min^{-1}					
Auxiliary gas flow rate	0.7-0.8 L min^{-1}					
Nebuliser gas flow rate	0.85-1.05 L min^{-1}					
Data acquisition parameters						
Scanning mode	Static, multi-collection					
Integration time	4.2 s					
Number of cycles	10 per block					
Number of blocks	5					
Measurement time per sample	~ 210 s					
Sr cup configuration						
Faraday cup	L3	L2	L1	C	H1	H2
Ion of interest (relative abundance)	$^{83}Kr^+$ (11.49)	$^{84}Sr^+$ (0.56)	$^{85}Rb^+$ (72.17)	$^{86}Sr^+$ (9.86)	$^{87}Sr^+$ (7.00)	$^{88}Sr^+$ (82.58)
Isobaric interference (relative abundance)		*$^{84}Kr^+$ (57.00)*		*$^{86}Kr^+$ (17.30)*	*$^{87}Rb^+$ (27.83)*	
Amplifier (Ohm)	10^{11}	10^{11}	10^{11}	10^{11}	10^{11}	10^{11}

Table 3.6 Instrument accessories & settings, data acquisition parameters and cup configuration used during the Sr isotopic analyses for this PhD study. Relative abundances of different isotopes of an element are from Rosman & Taylor (1998). * = optimised daily for maximum $^{88}Sr^+$ intensity.

procedure but sometimes minor traces of it remained in the Sr fraction, resulting in a <0.2% contribution of Rb at m/q 87. This interference was corrected for using a $^{85}Rb/^{87}Rb$ ratio of 2.59265 and assuming that Rb and Sr have the same mass discrimination behaviour. Mass discrimination correction of the observed $^{87}Sr/^{86}Sr$ ratio was carried out via internal normalisation to a $^{86}Sr/^{88}Sr$ ratio of 0.1194, applying the mass dependent Russell equation (exponential law):

$$R_{true}/R_{observed} = (m_1/m_2)^{\beta}$$

with β the mass discrimination factor, R_{true} the corrected isotope ratio, $R_{observed}$ the experimentally measured isotope ratio, and m_1 and m_2 the masses of the isotopes in the ratio R (Russell et al., 1978). Both Rb interference and mass discrimination corrections were carried out on-line with the software of the Neptune MC-ICP-MS.

All $^{87}Sr/^{86}Sr$ isotope ratios obtained for this study have a 1SD <0.000075, resulting in a 1SE <0.000011. Figure 3.11 presents the Sr isotopic compositions (with their specific 2SE) obtained for certified reference materials during MC-ICP-MS analyses between May 2009 and October 2012. Their

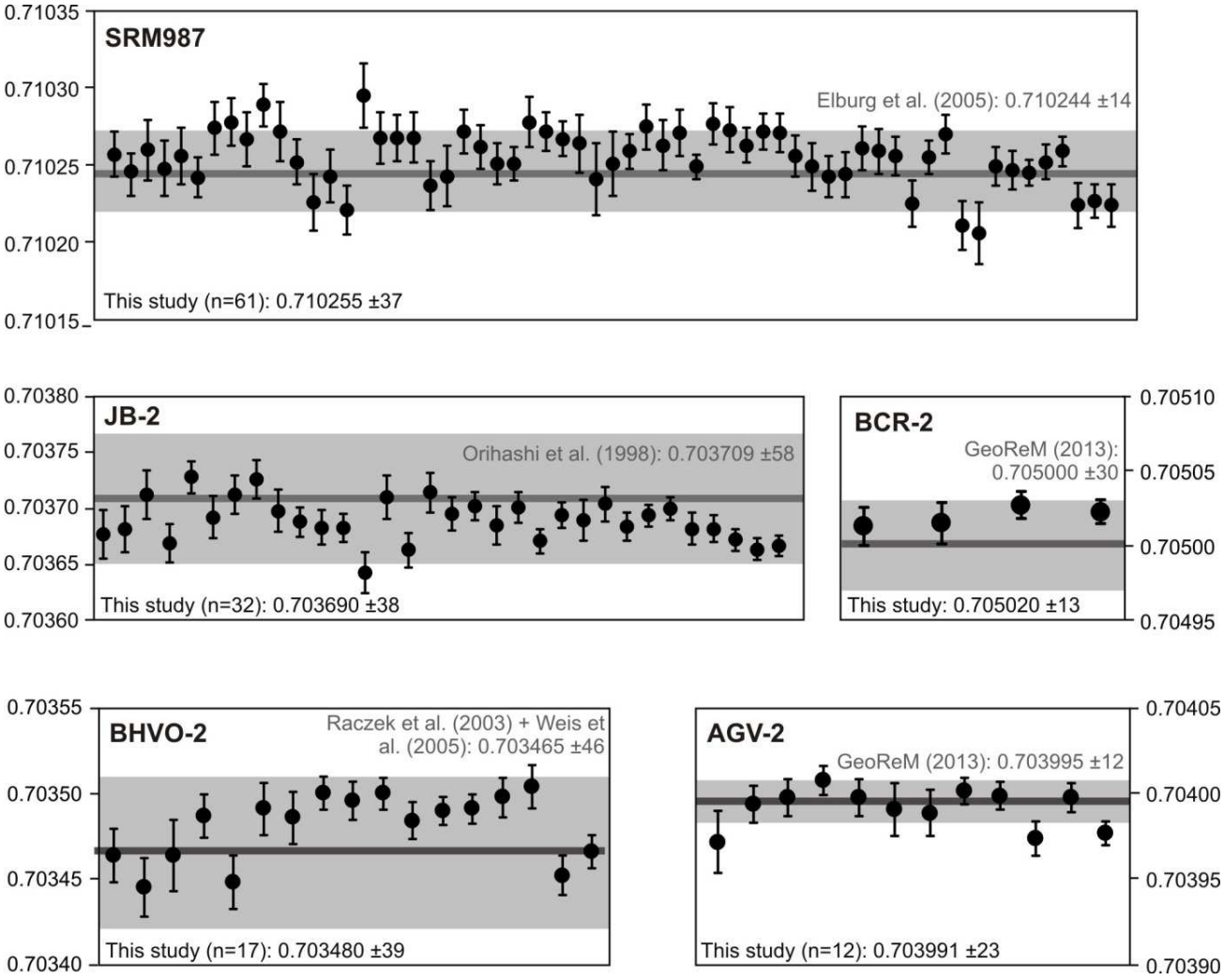

Figure 3.11. $^{87}Sr/^{86}Sr$ *isotopic compositions obtained for certified reference materials during the analytical sessions of this PhD study.* Error bars of individual analyses represent 2SE; the average value obtained in this study is given together with its 2SD uncertainty (for example: 0.703480 ±39 = $^{87}Sr/^{86}Sr$ ratio of 0.703480 with 2SD of 0.000039). Dark grey line represents the literature value provided; light grey bar represents 2SD uncertainty of this literature value. Literature data 'GeoReM (2013)' are taken from the GeoReM website (http://georem.mpch-mainz.gwdg.de/, downloaded on October 5th, 2013) See text for further details on instrument settings and data reduction.

average values (and 2SD) are: 0.705020±13 for BCR-2 (n=4); 0.703690±38 for JB-2 (n=32); 0.703480±39 for BHVO-2 (n=17): 0.703991±23 for AGV-2 (n=12) and 0.710255±37 for SRM987 (n=61). These average values are within analytical uncertainty equal to the respective literature $^{87}Sr/^{86}Sr$ isotopic ratios (Fig. 3.11), indicating good accuracy for the Sr isotopic compositions of the Saronic Gulf samples presented in Appendix D (igneous rocks) and Appendix F (sedimentary basement samples and xenoliths).

3.6.7 Nd isotopic analysis

The purified Nd fractions and a solution of certified isotope reference material JNdi-1 (neodymium oxide; Geological Survey of Japan) were diluted with ~0.28N HNO_3 to a concentration which varied from 100 to 500 ppb depending on the sensitivity of the MC-ICP-MS during a particular analytical session. The same ~0.28N HNO_3 dilution acid was used to measure instrumental blanks at the start of each measurement series as well as after every 5-6 samples. These instrumental blanks were usually not distinguishable from the background noise of the detectors (max 7.5 ppt whereas final dilutions of Nd fractions were min 100ppb). Therefore, blank corrections were not carried out. Procedural blanks

Instrument accessories	
Type of nebuliser	Micro-concentric nebuliser
Type of spray chamber	Combined cyclonic/double-pass spray chamber made of quartz glass
Sampling cone	Ni, aperture diameter 1.1 mm
Skimmer	Ni, aperture diameter 0.8 mm

Instrument settings *	
Sample uptake rate	50-100 µL min^{-1}
RF power	1200-1300 W
Plasma gas flow rate	13 L min^{-1}
Auxiliary gas flow rate	0.7-0.85 L min^{-1}
Nebulizer gas flow rate	0.85-1.05 L min^{-1}

Data acquisition parameters	
Scanning mode	Static, multi-collection
Integration time	4.2 s
Number of cycles	10 per block
Number of blocks	5
Measurement time per sample	~ 210 s

Nd cup configuration

Faraday cup	L4	L3	L2	L1	C	H1	H2	H3	H4
Ion of interest (relative abundance)	$^{142}Nd^+$ (27.2)	$^{143}Nd^+$ (12.2)	$^{144}Nd^+$ (23.80)	$^{145}Nd^+$ (8.30)	$^{146}Nd^+$ (17.20)	$^{147}Sm^+$ (14.99)	$^{148}Nd^+$ (5.70)	$^{149}Sm^+$ (13.82)	$^{150}Nd^+$ (5.60)
Isobaric interference (relative abundance)	*$^{142}Ce^+$ (11.11)*		*$^{144}Sm^+$ (3.07)*				*$^{148}Sm^+$ (11.24)*		*$^{150}Sm^+$ (7.38)*
Amplifier (Ohm)	10^{10}	10^{11}	10^{11}	10^{11}	10^{11}	10^{12}	10^{11}	10^{12}	10^{11}

Table 3.7 Instrument accessories & settings, data acquisition parameters and cup configuration used during the Nd isotopic analyses for this PhD study. Relative abundances of different isotopes of an element are from Rosman & Taylor (1998); isotopes indicated in grey are not used for further data reduction. * = optimised daily for maximum $^{144}Nd^+$ intensity.

(undiluted) were also negligible for every Nd isotopic measurement series (<0.1ng, which represents 0.01% of the minimal 0.7µg sample originally weighed in). Each analysis consisted of 50 individual measurements (see Table 3.7) and in order to minimise memory effects, the MC-ICP-MS was rinsed in between every two sample analyses for 200-250 s with ~0.28N HNO_3.

The Neptune MC-ICP-MS cup configuration chosen for the Nd isotopic measurements is presented in Table 3.7. The Nd isotopic ratio of interest in this study, $^{143}Nd/^{144}Nd$, needs to be corrected for the isobaric interference of $^{144}Sm^+$ on $^{144}Nd^+$. In contrast to the Sr isotopic data reduction where interfering element Rb has only two isotopes and so its mass discrimination is assumed the same as that of Sr (external normalisation), Sm has 7 isotopes of which ^{147}Sm and ^{149}Sm are free of isobaric interferences and have a known $^{147}Sm/^{149}Sm$ ratio of 1.0846599 - allowing mass discrimination correction via internal normalisation. The Sm specific mass discrimination factor β can thus be calculated via the Russell equation (exponential law) and entering both this β value and the recommended$^{144}Sm/^{147}Sm$ ratio of 0.204803 into the Russell equation allows calculation of the $^{144}Sm/^{147}Sm$. Since the signal intensity observed for $^{147}Sm^+$ is also known, the signal intensity

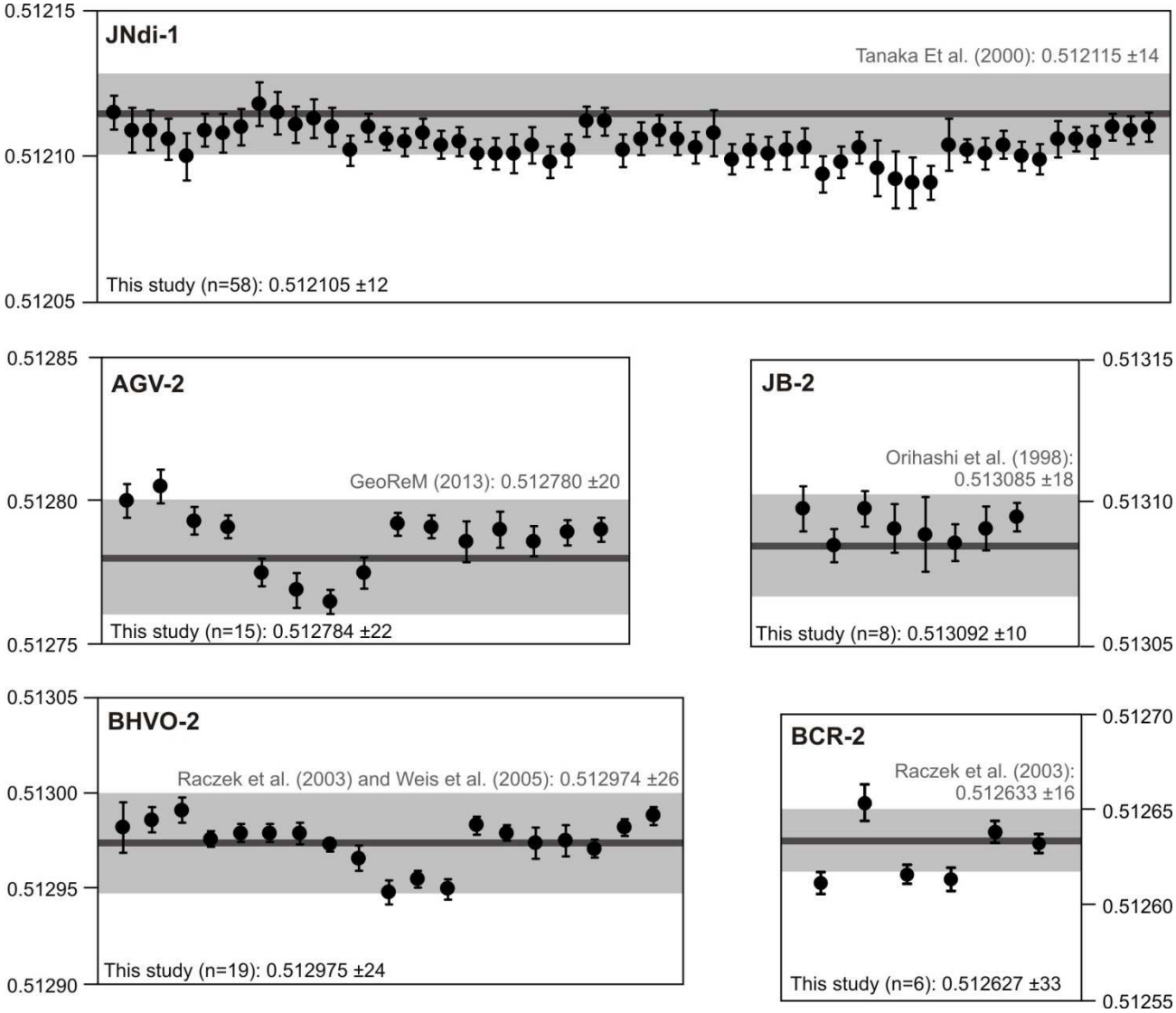

Figure 3.12. *$^{143}Nd/^{144}Nd$ isotopic compositions obtained for certified reference materials during the analytical sessions of this study.* Error bars of individual analyses represent 2SE; the average value obtained in this study is given together with its 2SD uncertainty (for example: 0.512784 ±22 = $^{143}Nd/^{144}Nd$ ratio of 0.512784 with 2SD of 0.000022). Dark grey line represents the literature value provided; light grey bar represents 2SD uncertainty of this literature value. Literature data 'GeoReM (2013)' are taken from the GeoReM website (http://georem.mpch-mainz.gwdg.de/, downloaded on October 5th, 2013) See text for further details on instrument settings and data reduction.

observed for $^{144}Sm^{+}$ can be calculated. Interference correction for $^{144}Sm^{+}$ on $^{144}Nd^{+}$ is then easily carried out as subtraction of the $^{144}Sm^{+}$ signal intensity from the total intensity monitored for mass 144. The observed $^{143}Nd/^{144}Nd$ ratio is then recalculated to the true $^{143}Nd/^{144}Nd$ ratio through mass discrimination correction with the Russell equation in which the Nd β factor is derived using the known $^{144}Nd/^{146}Nd$ ratio of 1.385233. Data reduction of the raw signal intensities into interference- and mass discrimination-corrected $^{143}Nd/^{144}Nd$ ratios is carried out on-line with the software of the Neptune MC-ICP-MS.

The internal precision of the final $^{143}Nd/^{144}Nd$ ratios obtained in this study is ≤0.000007 (1SE) whereas the overall external reproducibility of the Nd isotopic compositions presented in this study is ≤0.000017 (1SD). Figure 3.12 presents all Nd isotopic ratios (with their respective 2SE) for secondary standards analysed in the period between July 2010 and October 2012. Average values (and their 2SD) of these certified reference materials are: 0.512627±33 for BCR-2 (n=6); 0.513092±10 for JB-2 (n=8); 0.512975±24 for BHVO-2 (n=19): 0.512784±22 for AGV-2 (n=15) and 0.0.512105±12 for JNdi-1 (n=58). Figure 3.12 thereby indicates that whereas the $^{143}Nd/^{144}Nd$ ratios obtained in this study for rock reference materials AGV-2, JB-2, BHVO-2 and BCR-2 plot randomly around their recommended values, those for JNdi-1 are systematically lower than the literature value of Tanaka et al. (2000). This discrepancy between JNdi-1's recommended Nd isotopic composition and its $^{143}Nd/^{144}Nd$ ratios obtained in this study probably reflects that the currently recommended $^{143}Nd/^{144}Nd$ composition of this certified reference material is slightly too high. Contamination of the JNDi-1 solution analysed in this study or an overall inhomogeneity of this certified reference material are less likely causes of this discrepancy given the rare occurrence of Nd and the careful preparation of the JNdi-1 neodymium oxide, respectively. The Nd isotopic compositions of the Saronic Gulf samples presented in Appendix D (igneous rocks) and Appendix F (sedimentary basement samples and xenoliths) are regarded accurate since for each standard material the average Nd composition obtained in this study is within error of its recommended $^{143}Nd/^{144}Nd$ ratio (Fig. 3.12).

3.6.8 Pb isotopic analysis

All purified Pb fractions and a solution of certified reference material NIST SRM 981 (common lead isotopic standard; National Institute for Standards and Technology, USA) were diluted with ~0.28N HNO_3 to a concentration which varied from 100 to 400 ppb depending on the sensitivity of the MC-ICP-MS during a particular analytical session. This ~0.28N HNO_3 dilution acid was also used for the measurement of an instrumental blank before each Pb isotopic analysis. The signal intensity of these blanks was always distinctly higher than the detectors' background noise, representing about 0.05 to 0.5% of the intensity observed for samples and standards. Blank correction was therefore necessary to obtain accurate Pb isotopic ratios, and carried out by subtracting the signal intensity of the blank from the intensities observed in the subsequent sample or standard analysis. Procedural blanks (undiluted) were found to be negligible for each Pb isotopic measurement series carried out during this study (<0.4 ng, which represents 0.08% of the minimal 0.5 µg sample originally weighed in). Each sample analysis consisted of 50 individual measurements (see Table 3.8). Memory effects are a more significant issue for Pb isotopic analysis because this element has the tendency to 'stick' to the parts of the MC-ICP-MS that come in contact with the sample (mainly introduction system, sampling cone and skimmer). In order to reduce this memory effect, the MC-ICP-MS instrument was rinsed after every sample analysis for up to 500 s with ~0.5N HNO_3.

The Neptune cup configuration chosen for the Pb isotopic measurements is presented in Table 3.8. The Pb isotopic ratios conventionally used in geochemical studies need to be corrected for potential isobaric interference of $^{204}Hg^{+}$ on $^{204}Pb^{+}$. This correction is usually carried out assuming an invariant $^{204}Hg/^{202}Hg$ ratio of 0.230 and using the observed intensity of $^{202}Hg^{+}$ to calculate the contribution of $^{204}Hg^{+}$ to the signal intensity detected for mass 204. The intensities observed for $^{202}Hg^{+}$ were however generally negligible and equal to background noise after blank correction, so that mercury interference corrections were not necessary. Since the lead isotopic system does not contain an invariant Pb

isotope ratio, mass discrimination correction has to be carried out either by Tl correction (external normalisation) or sample-standard bracketing (external standardisation). External normalisation involved addition of Tl isotope reference material NIST SRM 997 to each sample and standard and using the mass discrimination factor obtained for Tl to approximate the β value for Pb (see Smet et al., 2010). Tl normalisation was carried out only in the first two Pb isotopic measurement series of this study, and simultaneously with sample-standard bracketing which is done by interpolation of the Pb isotope ratios obtained for the NIST SRM 981 standard measured before and after each sample. This external standardisation correction was carried out applying the NIST SRM 981 values of 36.7258, 15.499, and 16.9416 for $^{208}Pb/^{204}Pb$, $^{207}Pb/^{204}Pb$ and $^{206}Pb/^{204}Pb$, respectively, (Baker et al., 2004) and the error propagation formula of Elburg et al. (2005). These two methods of mass discrimination correction yielded isotopic compositions identical to one another within analytical uncertainty (Smet et al., 2010), and the sample-standard bracketing procedure according to Elburg et al. (2005) was used for the data reduction of all Pb isotope ratios presented in this study. Measurement of the Pb isotopic composition of a single sample thus involved the analysis of blank 1 – NIST SRM 981 – blank 2 – sample – blank 3 – NIST SRM 981 (about 40 minutes per sample). Blank corrections and correction for the mass discrimination between the different Pb isotopes was carried out off-line in an MS Excel spreadsheet.

Instrument accessories	
Type of nebuliser	Micro-concentric nebuliser
Type of spray chamber	Combined cyclonic/double-pass spray chamber made of quartz glass
Sampling cone	Ni, aperture diameter 1.1 mm
Skimmer	Ni, aperture diameter 0.8 mm

Instrument settings *	
Sample uptake rate	50 µL min-1
RF power	1200-1300 W
Plasma gas flow rate	13-14 L min-1
Auxiliary gas flow rate	0.7-0.9 L min-1
Nebulizer gas flow rate	0.8-1.0 L min-1

Data acquisition parameters	
Scanning mode	Static, multi-collection
Integration time	4.2 s
Number of cycles	10 per block
Number of blocks	5
Measurement time per sample	~ 210 s

Pb cup configuration

Faraday cup	L3	L2	L1	C	H1	H2	H3
Ion of interest (relative abundance)	$^{202}Hg^+$ (29.86)	$^{203}Tl^+$ (29.52)	$^{204}Pb^+$ (1.40)	$^{205}Tl^+$ (70.48)	$^{206}Pb^+$ (24.10)	$^{207}Pb^+$ (22.10)	$^{208}Pb^+$ (52.40)
Isobaric interference (relative abundance)			*$^{204}Hg^+$ (6.87)*				
Amplifier (Ohm)	10^{11}	10^{11}	10^{11}	10^{11}	10^{11}	10^{11}	10^{11}

Table 3.8 Instrument accessories & settings, data acquisition parameters and cup configuration used during the Pb isotopic analyses for this PhD study. Relative abundances of different isotopes of an element are from Rosman & Taylor (1998); * = optimised daily for maximum $^{208}Pb^+$ intensity.

The internal precision (1SE) of the final $^{206}Pb/^{204}Pb$, $^{207}Pb/^{204}Pb$ and $^{208}Pb/^{204}Pb$ ratios obtained in this study is generally ≤0.001, ≤0.001 and ≤0.002, respectively. The external reproducibility (1SD) of individually analysed Pb isotopic compositions is usually ≤0.006, ≤0.005 and ≤0.012 for the $^{206}Pb/^{204}Pb$, $^{207}Pb/^{204}Pb$ and $^{208}Pb/^{204}Pb$ ratios, respectively. The $^{206}Pb/^{204}Pb$, $^{207}Pb/^{204}Pb$ and $^{208}Pb/^{204}Pb$ ratios (with 2SD error bars) of each individual analysis carried out on secondary standards between June 2009 and October 2012 are shown in figures 3.13, 3.14 and 3.15, respectively. The average values obtained for isotopic reference materials JB-2, BHVO-2, BCR-2 and AGV-2 during this period of time are presented in Table 3.9, together with their Pb isotopic composition found in literature. These average values agree within error with the respective literature isotopic ratios (Table 3.9), suggesting that the Pb isotopic compositions of the Saronic Gulf samples presented in Appendix D (volcanic rocks) and Appendix F (sedimentary basement samples and xenoliths) are accurate.

	$^{206}Pb/^{204}Pb$	2 SD	$^{207}Pb/^{204}Pb$	2SD	$^{208}Pb/^{204}Pb$	2 SD
JB-2 (n=30-32)	18.3446	0.0106	15.5640	0.0096	38.2869	0.0245
Baker et al. (2004)	*18.3435*	*0.0017*	*15.5619*	*0.0016*	*38.2784*	*0.0050*
BHVO-2 (n=13-15)	18.6609	0.0443	15.5434	0.0218	38.2541	0.0697
GeoReM (2013)	*18.6600*	*0.0480*	*15.5430*	*0.0200*	*38.2510*	*0.0640*
BCR-2 (n=5-7)	18.7632	0.0085	15.6296	0.0008	38.7500	0.0370
GeoReM (2013)	*18.7610*	*0.0140*	*15.6220*	*0.0100*	*38.7300*	*0.0400*
AGV-2 (n=11-12)	18.8760	0.0140	15.6223	0.0033	38.5564	0.0169
GeoReM (2013)	*18.8730*	*0.0120*	*15.6260*	*0.0080*	*38.5400*	*0.0400*
LB43 this study (n=9)	18.7101	0.0165	15.5914	0.0176	38.8058	0.0556
Elburg et al. (2007) -MC-ICP-MS	18.7250	0.0080	15.5900	0.0060	38.8200	0.0160
M. Elburg, pers. com. - TIMS	18.7103	0.0020	15.5747	0.0020	38.7647	0.0064

Table 3.9 $^{206}Pb/^{204}Pb$, $^{207}Pb/^{204}Pb$ and $^{208}Pb/^{204}Pb$ ratios obtained for international rock reference materials JB-2, BHVO-2, BCR-2 and AGV-2, as well as for in-house standard LB43, and comparison to their respective literature values. Analytical uncertainty is represented as 2SD over (multiple measurements of) the different aliquots that were dissolved for the different Pb isotopic measurement series – indicated as n = x. See text for further discussion.

The statistical variation of these average values is however larger than expected from the 2SD uncertainty generally found for a single sample analysis (see above). For all 4 international standard materials, the average values of the three Pb isotopic ratios are furthermore calculated from a varying number of individual analyses (see Table 3.9; n = x to y). The reason for this is shown in figures 3.13 to 3.15: each of the four reference materials has outliers to the overall average composition for at least one of its three Pb isotope ratios. These aberrant Pb isotopic compositions are consequently measured for the solution of one particular standard digestion (aliquot) – indicating that they are not resulting from instrumental imprecision or inaccuracy, but from inhomogeneity of the powders of the reference material themselves. The varying degree of Pb isotopic heterogeneity between different rock reference materials, and sometimes even between different splits from the same standard powder, is a well-known issue within Pb isotope geochemistry (Woodhead & Hergt, 2000; Baker et al., 2004; Elburg et al., 2005; Weis et al., 2005). The absence of a truly homogenous rock powder reference materials as Pb isotopic standard due to apparent nugget contamination of the available rock reference materials can be partially accommodated by the analysis of 1) multiple international rock standards within each measurement series; and 2) an internal lab standard with known isotopic composition gathered via different high-precision isotopic analyses (Smet et al., 2010). The volume of rock powder of such an 'in-house' standard is smaller than the amounts prepared for international rock standards and therefore likely to be more homogenous. The in-house standard used in this study is Ca-rich

island arc basalt LB43, which was previously characterised for its isotopic composition via both TIMS (Adelaide, Australia) and MC-ICP-MS (Amsterdam, the Netherlands). Figures 3.13 to 3.15 indeed show that none of the different Pb isotopic analyses of LB43 can be considered as outliers. The

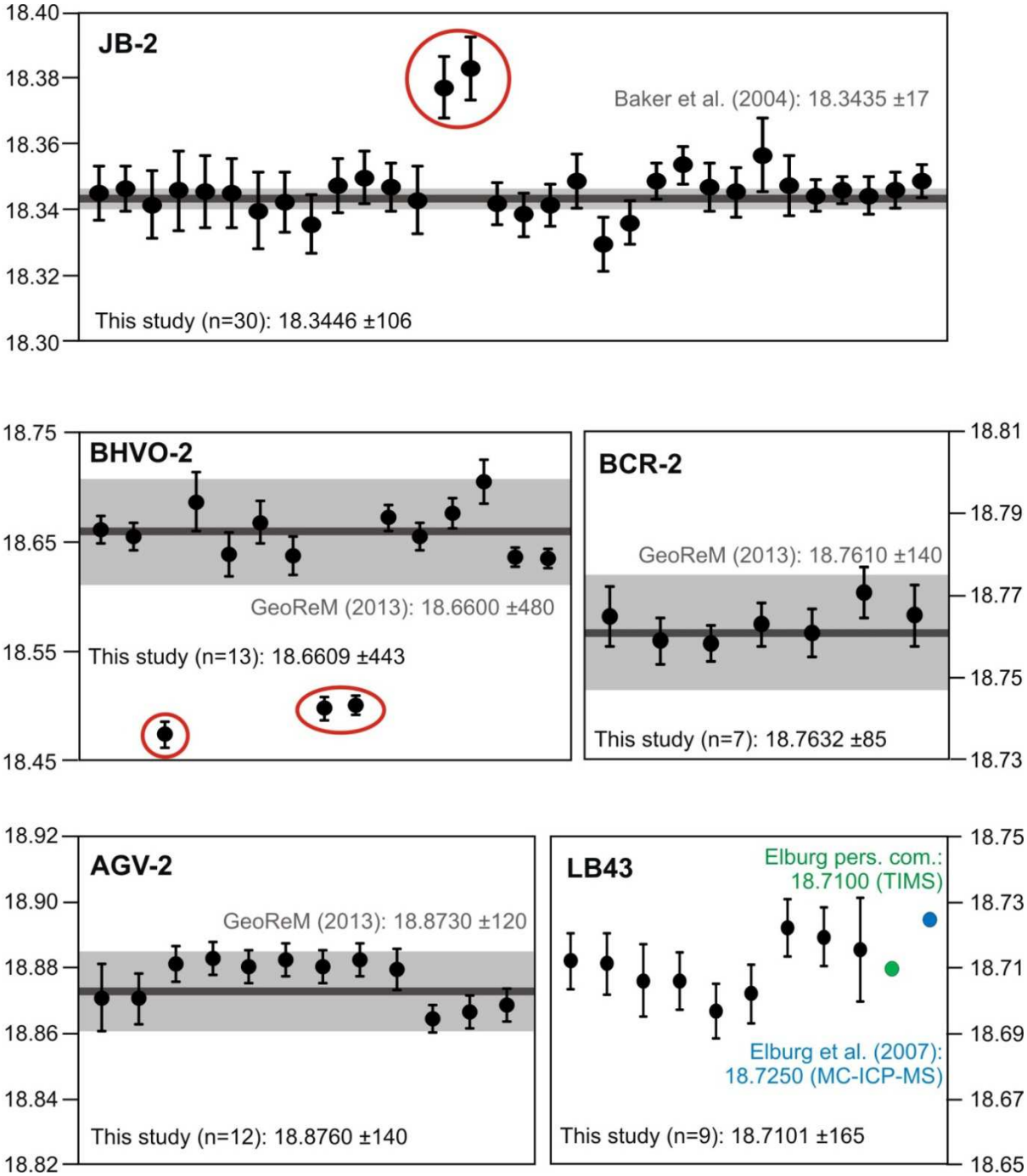

Figure 3.13. *$^{206}Pb/^{204}Pb$ isotopic compositions obtained for certified reference materials and in-house standard LB43 during the analytical sessions of this study.* Error bars of individual analyses represent 2SD (2SE error bars are smaller than the symbol size). Individual analyses circled in red represent al outliers. The average value obtained in this study is given together with its 2SD uncertainty (for example: 18.8760 ±140 = $^{206}Pb/^{204}Pb$ ratio of 18.8760 with 2SD of 0.0140. Dark grey line represents the literature value written in dark grey; light grey bar represents 2SD uncertainty of this literature value. Literature data 'GeoReM (2013)' are taken from the GeoReM website (http://georem.mpch-mainz.gwdg.de/, downloaded on October 5th, 2013). Previously determined Pb isotopic composition of in-house standard LB43 given in green and blue. See text for further details on instrument settings and data reduction.

analytical precision of this in-house standard is furthermore similar to uncertainty obtained for the international rock reference materials (see Table 3.9).

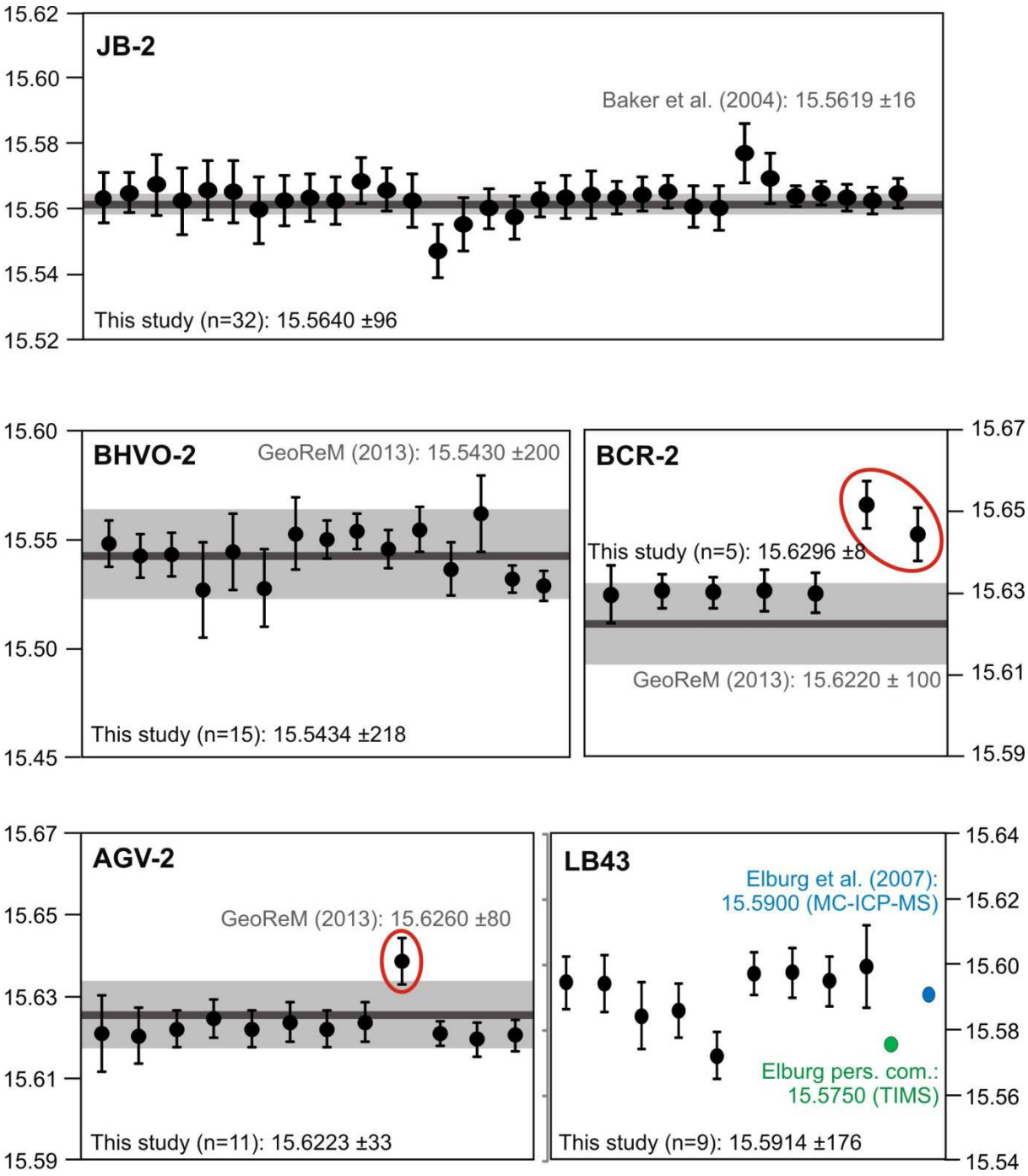

Figure 3.14. *$^{207}Pb/^{204}Pb$ isotopic compositions obtained for certified reference materials and in-house standard LB43 during the analytical sessions of this study.* Error bars of individual analyses represent 2SD (2SE error bars are smaller than the symbol size). Individual analyses circled in red represent outliers. The average value obtained in this study is given together with its 2SD uncertainty (for example: 15.5914 ±176 = $^{207}Pb/^{204}Pb$ ratio of 15.5914 with 2SD of 0.0176. Dark grey line represents the literature value written in dark grey; light grey bar represents 2SD uncertainty of this literature value. Literature data 'GeoReM (2013)' are taken from the GeoReM website (http://georem.mpch-mainz.gwdg.de/, downloaded on October 5th, 2013). Previously determined Pb isotopic composition of in-house standard LB43 given in green and blue. See text for further details on instrument settings and data reduction.

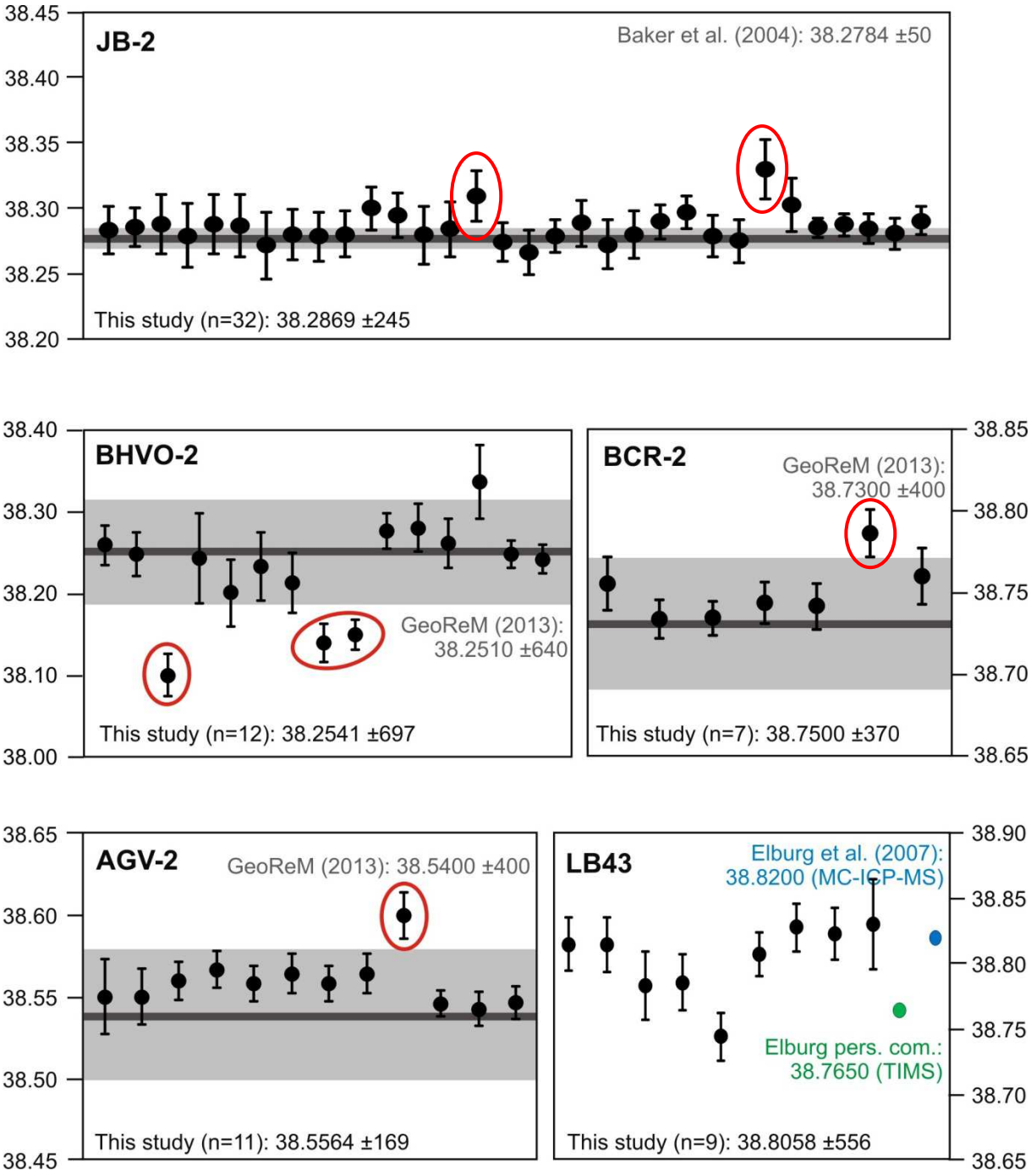

Figure 3.15. *$^{208}Pb/^{204}Pb$ isotopic compositions obtained for certified reference materials and in-house standard LB43 during the analytical sessions of this study.* Error bars of individual analyses represent 2SD (2SE error bars are smaller than the symbol size). Individual analyses circled in red represent outliers. The average value obtained in this study is given together with its 2SD uncertainty (for example: 38.5564 ±169 = $^{208}Pb/^{204}Pb$ ratio of 38.5564 with 2SD of 0.0169. Dark grey line represents the literature value written in dark grey; light grey bar represents 2SD uncertainty of this literature value. Literature data 'GeoReM (2013)' are taken from the GeoReM website (http://georem.mpch-mainz.gwdg.de/ , downloaded on October 5th, 2013). Previously determined Pb isotopic composition of in-house standard LB43 given in green and blue. See text for further details on instrument settings and data reduction.

3.6.9 Hf isotopic analysis

The purified Hf fractions and a solution of certified isotope reference material JMC 475 (Johnson Matthey synthetic Hf standard) were diluted with a weak acid solution of ~0.56N HNO_3 and ~0.24N HF to a concentration 50 ppb. The same ~0.56N HNO_3/0.24N HF dilution acid was used to measure an instrumental blank at the start of each analytical session. This blank was never distinguishable from the background noise of the detectors (< 0.05 mV intensity for $^{180}Hf^+$ compared to a 3350 mV $^{180}Hf^+$ signal for 50 ppb Hf) so that no blank corrections were carried out. Procedural blanks (undiluted) were

Instrument accessories	
Type of nebuliser	Desolvating nebuliser, Cetac Aridus
Sampling cone	Ni, aperture diameter 1.1 mm
Skimmer	Ni, aperture diameter 0.8 mm
Instrument settings	
Sample uptake rate (Aridus)	50 µL min^{-1}
Sample Ar gas flow rate *	0.8-0.9 L min^{-1}
Sweep Ar gas flow (Aridus) *	2.76-3.03 L min^{-1}
Nitrogen gas flow (Aridus) *	7-11 mL min^{-1}
RF power	1200 W
Plasma Ar gas flow rate	16 L min^{-1}
Auxiliary Ar gas flow rate	0.9 L min^{-1}
Data acquisition parameters	
Scanning mode	Static, multi-collection
Idle time	1.0 s
Integration time	2.0 s
Number of cycles	30 per block
Number of blocks	3
Measurement time per sample	~270 s
Baseline detection prior to each analysis	25 s

Nd cup configuration

Faraday cup	L4	L3	L2	L1	C	H1	H2	H3	H4
Ion of interest (relative abundance)	$^{171}Yb+$ (14.28)	$^{173}Yb+$ (16.13)	$^{175}Lu+$ (97.41)	$^{176}Hf+$ (5.26)	$^{177}Hf+$ (18.60)	$^{178}Hf+$ (27.28)	$^{179}Hf+$ (13.62)	$^{180}Hf+$ (35.08)	$^{182}W+$ (26.50)
Isobaric interference (relative abundance)				$^{176}Yb+$ (12.76)				$^{180}W+$ (0.12)	
Isobaric interference (relative abundance)				$^{176}Lu+$ (2.59)					
Amplifier (Ohm)	10^{11}	10^{11}	10^{11}	10^{11}	10^{11}	10^{11}	10^{11}	10^{11}	10^{11}

Table 3.10 Instrument accessories & settings, data acquisition parameters and cup configuration used during the Hf isotopic analyses for this PhD study. Relative abundances of different isotopes of an element are from Rosman & Taylor (1998); isotopes indicated in grey are not used for further data reduction. * = optimised daily for maximum $^{180}Hf^+$ intensity.

negligible for both the LP and HP digestion series (< 40 pg Hf, which represents < 0.035% of the minimal 120 ng sample originally weighed in). Each sample analysis consisted of 90 individual measurements (see Table 3.10) and in order to minimise memory effects, the MC-ICP-MS was rinsed in between every two sample analyses with ~0.56N HNO_3/0.24N HF until the $^{180}Hf^+$ signal was reduced to initial background levels (usually for 200 to 250 s). Sampling was carried out manually using a desolvating nebulising system (Cetac Aridus).

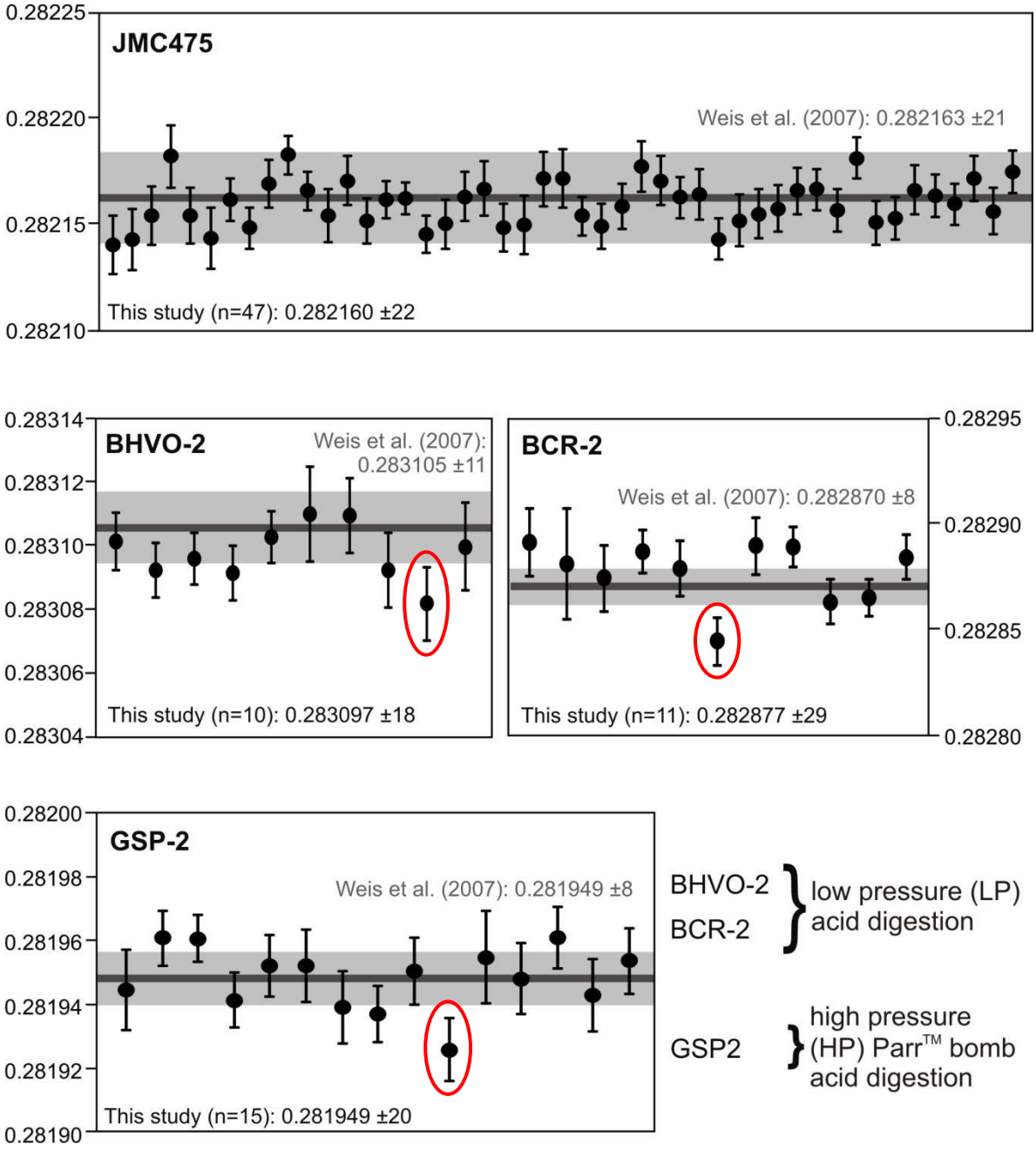

Figure 3.16. *$^{176}Hf/^{177}Hf$ isotopic compositions obtained for certified reference materials in this study.* Error bars of individual analyses represent 2SE; the average value obtained in this study is given together with its 2SD uncertainty (for example: 0.281949±20 = $^{176}Hf/^{177}Hf$ ratio of 0.281949 with 2SD of 0.000020). Dark grey line represents the literature value written in dark grey; light grey bar represents 2SD uncertainty of this literature value. Literature data 'GeoReM (2013)' are taken from the GeoReM website (http://georem.mpch-mainz.gwdg.de/, downloaded on October 5th, 2013) See text for further details on instrument settings and data reduction.

The Neptune MC-ICP-MS cup configuration chosen for the Hf isotopic measurements is presented in Table 3.10. The Hf isotopic ratio of interest in this PhD study, $^{176}Hf/^{177}Hf$, needs to be corrected for the isobaric interferences of both $^{176}Lu^+$ and $^{176}Yb^+$ on $^{176}Hf^+$. This was done in a similar manner as the correction for interference of $^{144}Sm^+$on $^{144}Nd^+$ (see section 3.6.7), assuming a similar mass discrimination factor for Hf, Yb and Lu; applying true values for $^{176}Yb/^{173}Yb$ and $^{176}Lu/^{175}Lu$ of 0.79631 and 0.02655, respectively; and using the calculated β^{Hf} (see below) and observed $^{173}Yb^+$ and $^{175}Lu^+$ intensities to obtain the true contribution of $^{176}Lu^+$ and $^{176}Yb^+$ to the signal intensity observed at mass 176 (Nebel et al., 2009). These interference corrections were not strictly necessary for the measurements of Hf isotopic standard JMC-475 as the Lu and Hf signal intensity observed in this solution was as low as the detector background noise ($1.0*10^{-6}$ V). For all rock reference materials and samples, however, there was typically 10 to 1000 times more Yb and Lu present. As these significantly elevated signal intensities for ^{171}Yb, ^{173}Yb and ^{175}Lu ($1.0*10^{-5}$ to $1.5*10^{-3}$ V) could thereby be only 300 times smaller than the signal intensity of ^{176}Hf ($1.0\text{-}5.0*10^{-1}$ V), correction for the interference of $^{176}Lu^+$ and $^{176}Yb^+$ on $^{176}Hf^+$ was required and thus carried out for all Hf isotopic analyses. The observed $^{176}Hf/^{177}Hf$ ratio is finally recalculated to the true $^{176}Hf/^{177}Hf$ ratio through mass discrimination correction with the Russell equation in which the Hf β factor is derived using the known $^{179}Hf/^{177}Hf$ ratio of 0.7325. Data reduction of the raw signal intensities into interference and mass discrimination corrected $^{176}Hf/^{177}Hf$ ratios was carried out on-line with the software of the Neptune MC-ICP-MS.

The internal precision of the final $^{176}Hf/^{177}Hf$ ratios obtained in this study is ≤0.000008 (1SE) whereas the overall external reproducibility of the Hf isotopic compositions presented here is ≤0.000070 (1SD). Figure 3.16 shows all Hf isotopic ratios (with their respective 2SE) analysed for secondary standards in the period of 18 to 21 February 2013. Average values (and their 2SD) of these certified reference materials are: 0.282877±28 for BCR-2 (n=11); 0.281949±20 for GSP-2 (n=15); 0.283097±18 for BHVO-2 (n=10); and 0.282160±22 for JMC 475 (n=47). The average values obtained for these standards are within error of the respective literature $^{176}Hf/^{177}Hf$ isotopic ratios (Fig. 3.16), suggesting good accuracy for the Hf isotopic compositions of the Saronic Gulf rock samples, all presented in Appendix E.

3.6.10 Hf isotopic composition of both LP and HP digested samples

As mentioned above, sample preparation for whole rock Hf isotopic analysis involved either HP or LP acid digestion depending on the fact whether the sample (was likely to) contained zircon, or not. The international rock reference materials chosen to assess the accuracy of our Hf isotopic data were also prepared according to this line of thought: mafic standards BCR-2 and BHVO-2 underwent LP acid dissolution (2 aliquots of each), whereas felsic standard GSP-2 was digested in Parr™ bombs (3 aliquots). The Hf isotopic composition obtained for these different standard solutions are in agreement with literature values (see Fig. 3.16). For 11 Saronic Gulf samples that clearly contained zircon, a second aliquot was prepared together with the other LP digestions to investigate whether different Hf isotopic compositions would be revealed by the two dissolution procedures. Therefore, two standards were also prepared according to the alternative digestion method: one aliquot of GSP-2 underwent LP acid dissolution and one aliquot of BHVO-2 was dissolved under HP in a Parr™ bomb.

For each of these two differently digested standard solutions, the four analyses are within error of one another and define an average $^{176}Hf/^{177}Hf$ ratio with relatively small 2SD values (see Fig. 3.17A-B). The $^{176}Hf/^{177}Hf$ ratio obtained in this study for a LP acid digested aliquot of GSP-2 is however significantly higher than the literature Hf composition (Fig. 3.17A). This probably reflects non-dissolution of zircon crystals in the LP sample solution (see 3.5.3): due to their very low Lu/Hf ratio, zircons preserve lower $^{176}Hf/^{177}Hf$ ratios as they are not affected by the in-growth of ^{176}Hf resulting from the decay of ^{176}Lu. The significant age of the Silver Plume granodiorite from which rock reference material GSP-2 is produced (ca. 1425 Ma, pers. comm. Marlina Elburg) therefore explains the very radiogenic Hf isotopic composition of the groundmass (LP dissolution) in comparison to the non-radiogenic, initial $^{176}Hf/^{177}Hf$ contents of the granodiorite's zircon crystals (reflected in the less

radiogenic $^{176}Hf/^{177}Hf$ ratio of the HP solution which is a mixture of the groundmass and zircon Hf isotopic compositions). Although no zircon is expected in BHVO-2, the HP dissolution of this standard also yields a $^{176}Hf/^{177}Hf$ ratio that is significantly lower than the Hf composition recommended in the literature (Fig. 3.17B). The difference in Hf isotopic composition between the LP and HP digested solution of BHVO-2 might reflect the presence of resistant accessory minerals that contain Hf. The difference in $^{176}Hf/^{177}Hf$ ratio between the LP and HP digested solutions is twice as large for GSP-2 (~0.000140) as for BHVO-2 (~0.000070). For both standards, however, the $^{176}Hf/^{177}Hf$ ratio is lower for the HP than for the LP dissolution (Fig. 3.17A-B).

Compared to the significantly different Hf isotopic composition for the LP and HP dissolutions of GSP-2, there is little to no difference between the $^{176}Hf/^{177}Hf$ ratios of LP and HP dissolutions obtained for zircon-bearing volcanic rocks from the Saronic Gulf (Fig. 3.17C). The Hf isotopic analysis of the LP and HP dissolutions are equal within analytical uncertainty for samples IP49, IA59, IA61, IM313, DPM28 and IA338 (Fig. 3.17C). For samples IA56, IA97, IM29, IM36, the two digestion methods result in slightly different $^{176}Hf/^{177}Hf$ ratios (difference of 0.000025 to 0.00000035) of which the HP digestion renders the higher Hf isotope ratio (Fig. 3.17C). Only for sample DPM42 does the difference in $^{176}Hf/^{177}Hf$ ratio between the LP and HP digestion follow the trend of standards BHVO-2 and GSP-2 with a lower Hf isotope ratio for the HP than for the LP solution (Fig. 3.17).

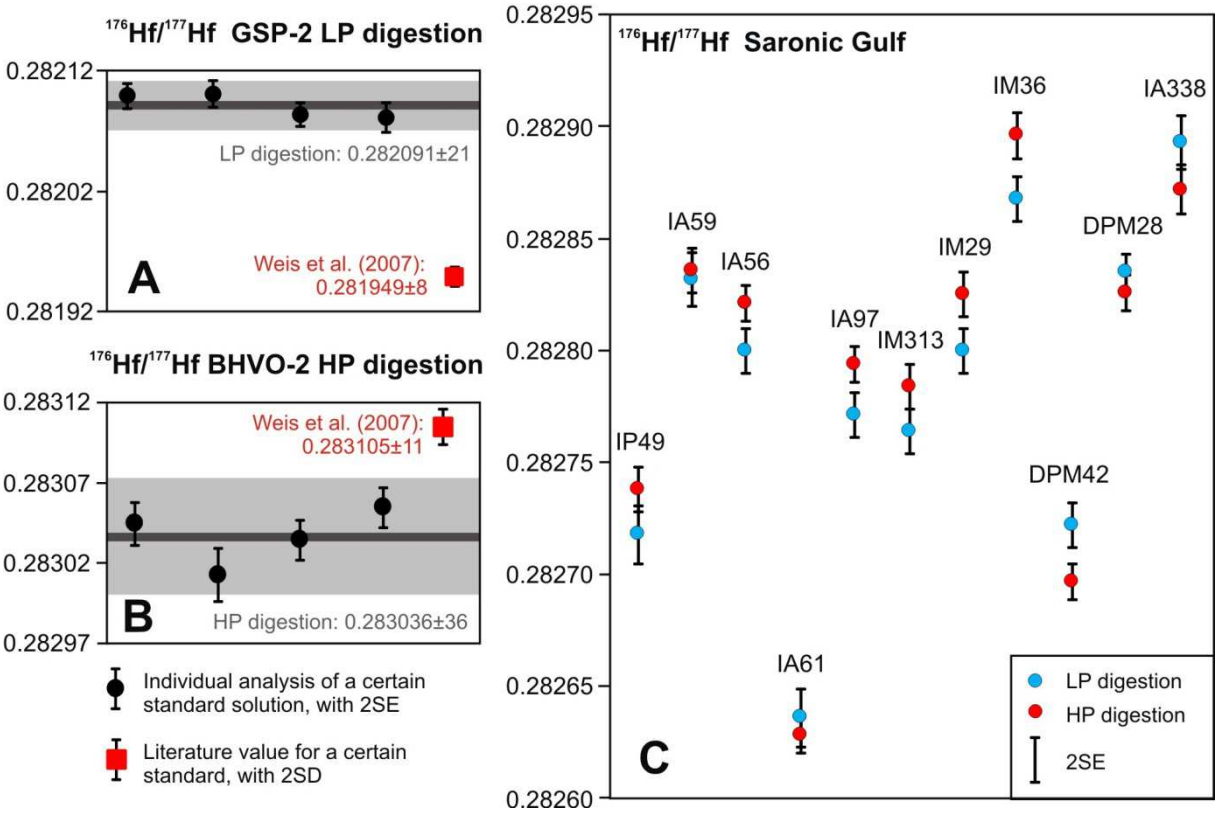

Figure 3.17. *$^{176}Hf/^{177}Hf$ isotopic compositions obtained for GSP-2, BHVO-2 and 11 Saronic Gulf samples for a LP, a HP and both LP and HP dissolutions, respectively.* (A-B) Average values obtained in this study and found in literature are given together with their 2SD uncertainty (for example: 0.283105±11 = $^{176}Hf/^{177}Hf$ ratio of 0.283105 with 2SD of 0.000011). Dark grey line represents the average value obtained in this study, written also in dark grey; light grey box represents 2SD uncertainty of this average value. See text for discussion.

Chapter 4: Detailed petrographic and geochemical study of the Delta 2 volcanic unit on Methana

Petrological studies of volcanic provinces are commonly based on a limited number of samples for each individual unit due to the effort and cost involved with geochemical analyses. This chapter, however, discusses the mineralogy, microscopic texture and geochemical composition of 48 samples that were all collected from just one volcanic unit on Methana. The aim of this study is to gain an understanding of the mineralogical, textural and compositional range within a single volcanic unit, prior to comparing Methana's different volcanic units with one another. The significance of geochemical variations between different volcanic units can thus be judged relative to the compositional heterogeneity within the more thoroughly characterised unit. The outcrops indicated as the 'Delta 2' unit on the geological map of that Gaitanakis and Dietrich (1995) are selected for this detailed study. According to Gaitanakis and Dietrich (1995), they consist of 'dacite and rhyodacite' that was erupted around 0.5-0.9 Ma by 'southern fissure volcanoes'. The enclave-bearing Delta 2 unit is furthermore representative of the dacitic-andesitic lava flows and domes that are the dominant volcanic deposits on Methana. Its detailed petrographic and geochemical information is therefore also used to obtain an insight into the complex processes that most of Methana's volcanic rocks underwent in the subvolcanic magma plumbing system.

4.1 Fieldwork and macroscopic observations

4.1.1 Aerial extent of the Delta 2 unit and physical occurrence of its outcrops

During a one-week field campaign in April 2010, 67 Delta 2 samples were collected from which 28 host rocks and 20 enclaves were selected for further research (details on the sampling locations can be found in Appendix A1). A selection of these samples was also used for the MSc thesis of De Pelsmaeker (2011).

Rocks of the Delta 2 unit are exposed at three different areas, situated in the south-eastern part of Methana. The locality with the largest surface area of this unit occurs at Loutses, just north-west of the main town Methana. It comprises a series of different lava flows in its southern part, and a volcanic dome (Chionessa – highest point of the Delta 2 unit at 684 m above sea level) and ridge in the northern part (Fig. 4.1). All but one of the flows have been sampled, as well as the base of the volcanic ridge and Chionessa dome. This ridge and dome are grouped as the Loutses 'NW section', whereas the different flows will be further referred to as E flow, SE flow, S flow and SW flow (see Fig. 4.1). The second largest area underlain by Delta 2 rocks is situated at the Tsonaka locality, NW of the town of Methana, and comprises 6 smaller outcrops overlying older volcanic deposits. The geographical pattern of these outcrops suggests that this could have been one continuous lava flow that was 'dismembered' by erosion (Fig. 4.1). The third and smallest area occurs east of the Kossona hill (Kossona Vouno) and represents a single lava flow (Fig. 4.1).

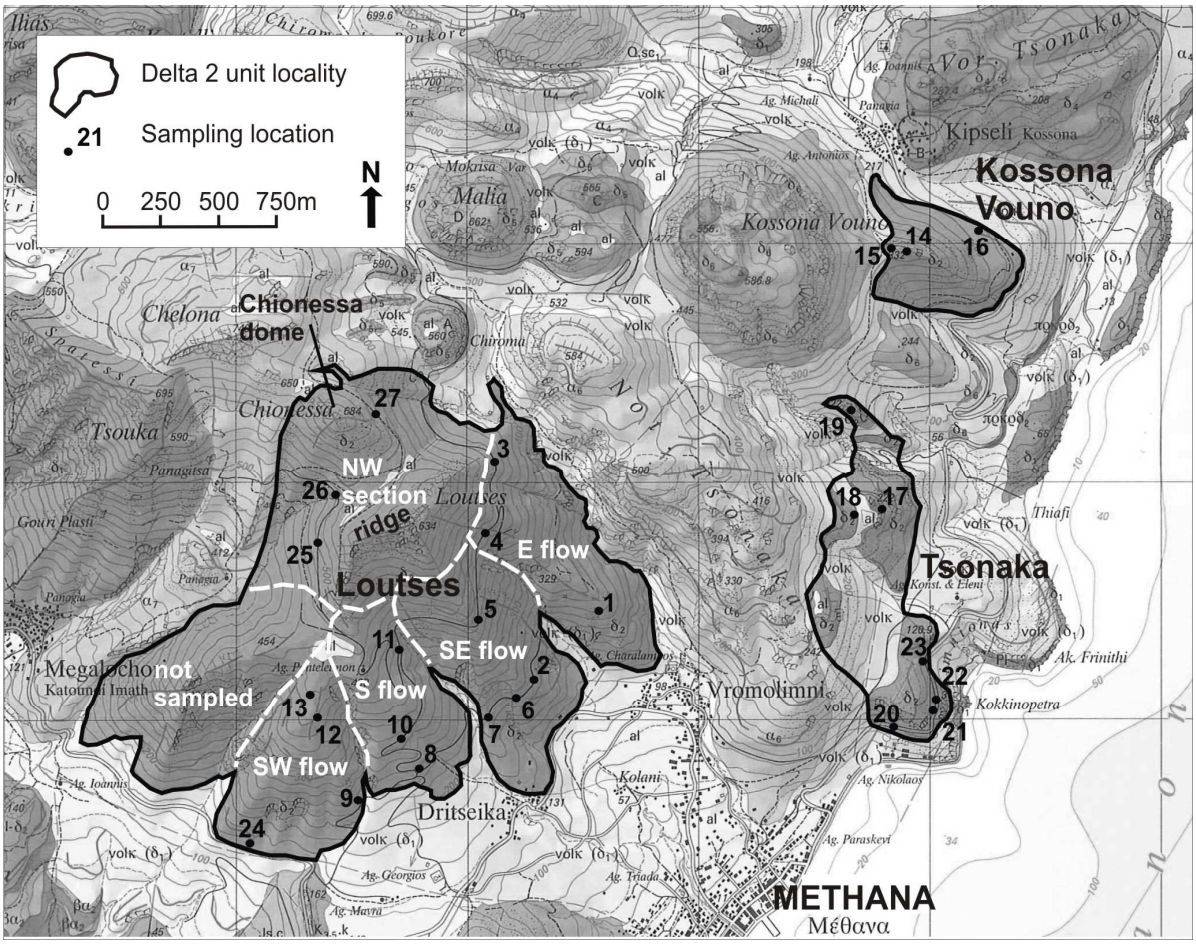

Figure 4.1 *Fieldwork map for the Delta 2 volcanic unit.* The southeast corner of the geological map of Methana (Gaitanakis & Dietrich, 1995) shows the three areas where rocks of the Delta 2 volcanic unit are exposed, the subdivision of the largest area (Loutses) and the sampling locations (numbered).

The study area is largely covered by vegetation and many slopes are transformed into agricultural terraces with walls made from volcanic rocks (Fig. 4.2A). The best outcrops are therefore found along roads or tracks and in river valleys or creek beds. The deposits of the Delta 2 unit occur as lavas with cooling joints (sometimes with basal and/or capping breccias), as lava breccia and as poorly sorted block (-and-ash) flow deposits. Overlying volcanic deposits sometimes have an erosive base into underlying volcaniclastic deposits (Fig. 4.2B). Without exception, every outcrop of the Delta 2 volcanic unit revealed a very crystal-rich lava (further referred to as 'host rock') containing rounded pieces of a more vesicular lithology (further referred to as 'enclaves'). Sampling mainly targeted the more massive lavas and lava breccia, but in the absence of suitable outcrops samples were collected from individual lava blocks which likely originated from uphill in-situ Delta 2 flows (locations 13 and 21). The poorly sorted block-and-ash flow deposits occasionally contain very large, rounded lava blocks which have a red coloured outer surface (interpreted to reflect oxidation) (Fig. 4.2C) and a grey-coloured core. Such blocks exhibit radial joints (Fig. 4.2D) and sometimes alignment of feldspar grains or elongated enclaves parallel to the outer margin of the lava block. These blocks are interpreted as large fragments of solidifying lava that broke off from flows or small domes and were transported downhill within a block-and-ash flow. As these blocks consist of fresher rock material than the oxidised smaller lava blocks surrounding them, they were preferentially sampled (locations 2, 6, 8 and 23).

4.1.2 Macroscopic characteristics of host rocks and enclaves

The macroscopically distinguishable crystals that make up the bulk of a sample's mineralogy are referred to as *phenocrysts.* Both host rocks and enclaves contain besides such relatively small phenocrysts also macroscopically identifiable *macro-phenocrysts.* The more fine-grained material between these macro-phenocrysts and phenocrysts seems homogeneous even when studied with a hand lens and is referred to as *groundmass*.

About half of the Delta 2 host rocks' volume is groundmass, usually homogeneously grey or brown-red in colour. Several outcrops, however, show heterogeneously distributed grey patches within a mostly brown-red coloured rock, or vice versa. At some sample locations the lavas show alternating grey and red bands oriented more or less parallel to one another and deflected around enclaves (Fig. 4.3A), interpreted as flow banding. The porphyritic host rocks contain 15-30 vol% of macro-phenocrysts (up to 6mm long) that show limited grain size variability between different outcrops. These macro-phenocrysts are mostly feldspar and amphibole, but sometimes also biotite and/or quartz (Fig. 4.3B). Phenocrysts of green clinopyroxene were only observed in the SW flow of the Loutses area.

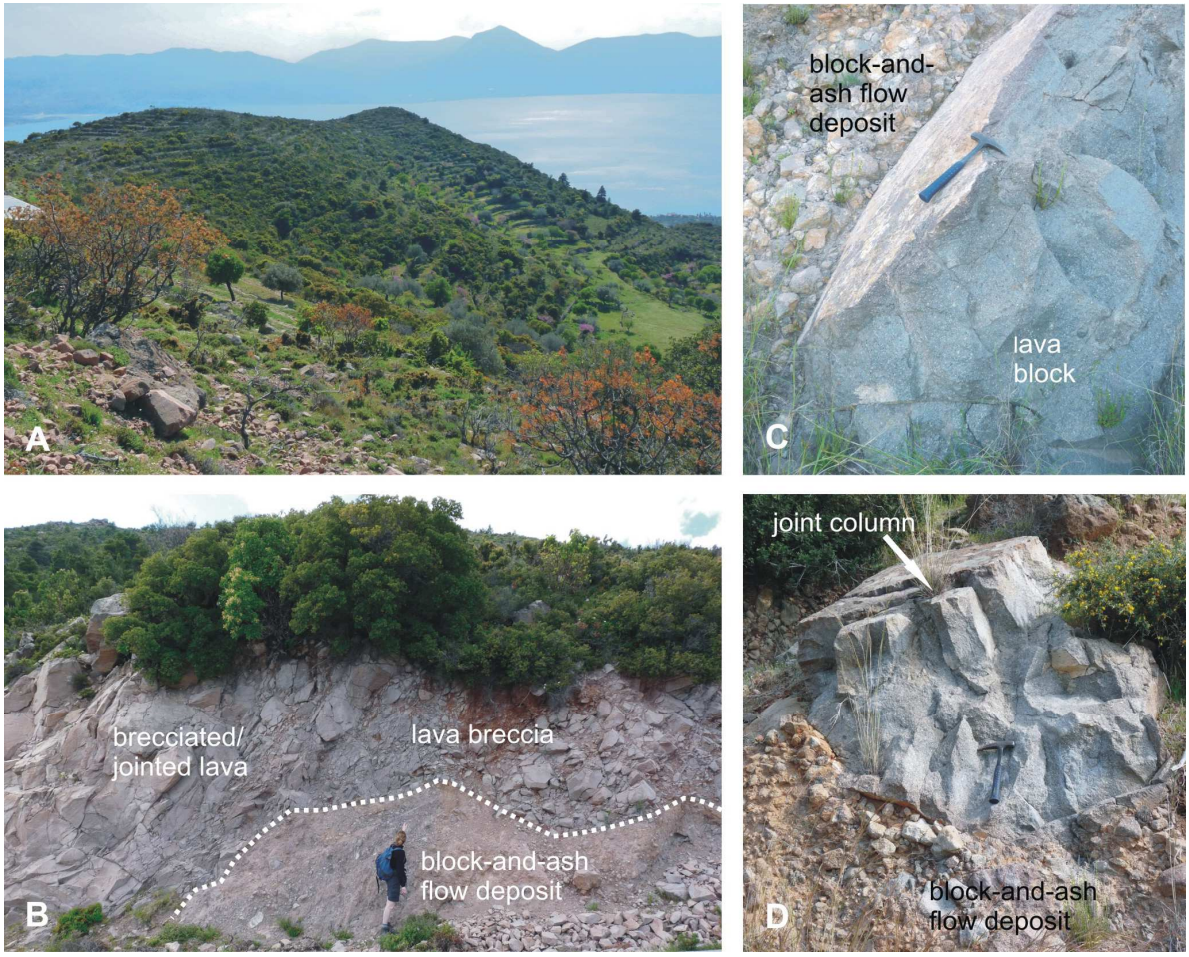

Figure 4.2 *Volcanic outcrops on Methana.* (A) View from sampling location 22 (see Fig. 4.1) towards the SSW. Most volcanic outcrops on Methana are covered with vegetation and hills are often transformed into terraces with walls constructed from volcanic rock. (B) Road cut at sampling location 4. On the right, a lava breccia overlies and cuts into the black-and-ash flow deposit below (white dotted line indicates boundary between these two deposits). From right to left this lava breccia gradually changes into a more massive, brecciated and jointed lava. (C). At sampling location 2 a large lava block is present within a block-and-ash flow deposit. Note the slightly darker colour (red) of the outer rim of the block, where the hammer rests, compared to its lighter colour (grey) in its interior. (D) Sampling location 6 consists of a large lava block within a poorly sorted volcaniclastic flow. The radial cooling joints form a polygonal network when viewed from the top (hammer for scale).

Phenocrysts represent 10-20 vol% of the host rocks but could not be unambiguously identified in the field.

Enclaves are characterised by a dense granular mass of phenocrysts, with only little groundmass, no more than 10 vol.% of macro-phenocrysts and a higher vesicularity than the lavas. So whereas host rocks consist dominantly of groundmass and macro-phenocrysts, enclaves mainly contain phenocrysts, which vary from one enclave to the next between coarse-grained (most crystals about 4 mm; Fig. 4.3C) and fine-grained (most crystals ≤ 1 mm; Fig. 4.3D). Only one or two enclaves display a gradual change from a more fine-grained to a more coarse-grained texture; chilled or crenulated margins were not observed. The mineralogy of the enclaves is less variable than that of the host rocks (mainly feldspar and amphibole), but the volume percentage of mafic minerals is larger than in the host rocks. Primary biotite or quartz are a rare occurrence in the enclaves, but if quartz is present, it is always mantled by a reaction rim of fine-grained, dark green crystals (Fig. 4.3D).

Within a single outcrop, as well as between different outcrops, the size of the enclaves ranges from 0.5 to 70 cm (Fig. 4.3 A, E-G). Enclaves also show a variable phenocryst grain size which does not correlate with their maximum dimension. They are mostly rounded to ellipsoidal (both in 2D in the rock face and in 3D, as observed when chiselled or weathered out) (Fig. 4.3 A, E-G). Sometimes they appear to be flattened, with a maximum length to width ratio of 5:1; angular enclaves are rare. Distribution and orientation of enclaves within a single outcrop is random, and only in some cases (for example large lava blocks) they are oriented parallel to the aligned texture defined by feldspar crystals, interpreted as a flow texture. Fine-grained enclaves are sometimes found in clusters of up to 15 (Fig. 4.3G). For each Delta 2 sampling location the volume percentage of enclaves, their grain-size and maximum dimension was estimated in the field. Despite the general lack of correlation between enclave dimension and grain size or density, their occurrence varies across 5 topographic areas. Table 4.1 shows that for each of these 5 localities, all outcrops show similar amounts and types of enclaves that are distinctly different from the other four areas (Table 4.1).

Locality	**Vol% outcrop**	**Most abundant**	**Maximum size**	**Least abundant**	**Maximum size**
Loutses, E & SE flows	2-4%	Fine grained	30 cm	Coarse grained	5 cm
Loutses, S & SW flows	1-2%	Coarse grained	15 cm	Fine grained	5 cm
Loutses, NW section	Up to 10%	Fine grained	50 cm	Coarse grained	10 cm
Tsonaka	1-2%	Coarse grained	5 cm	Fine grained	15 cm
Kossona Vouno	Up to 10%	Coarse grained	70 cm	Fine grained	30 cm

Table 4.1 Estimated volume percentage and characteristics of enclaves in lavas from the five areas with distinctly different enclave composition.

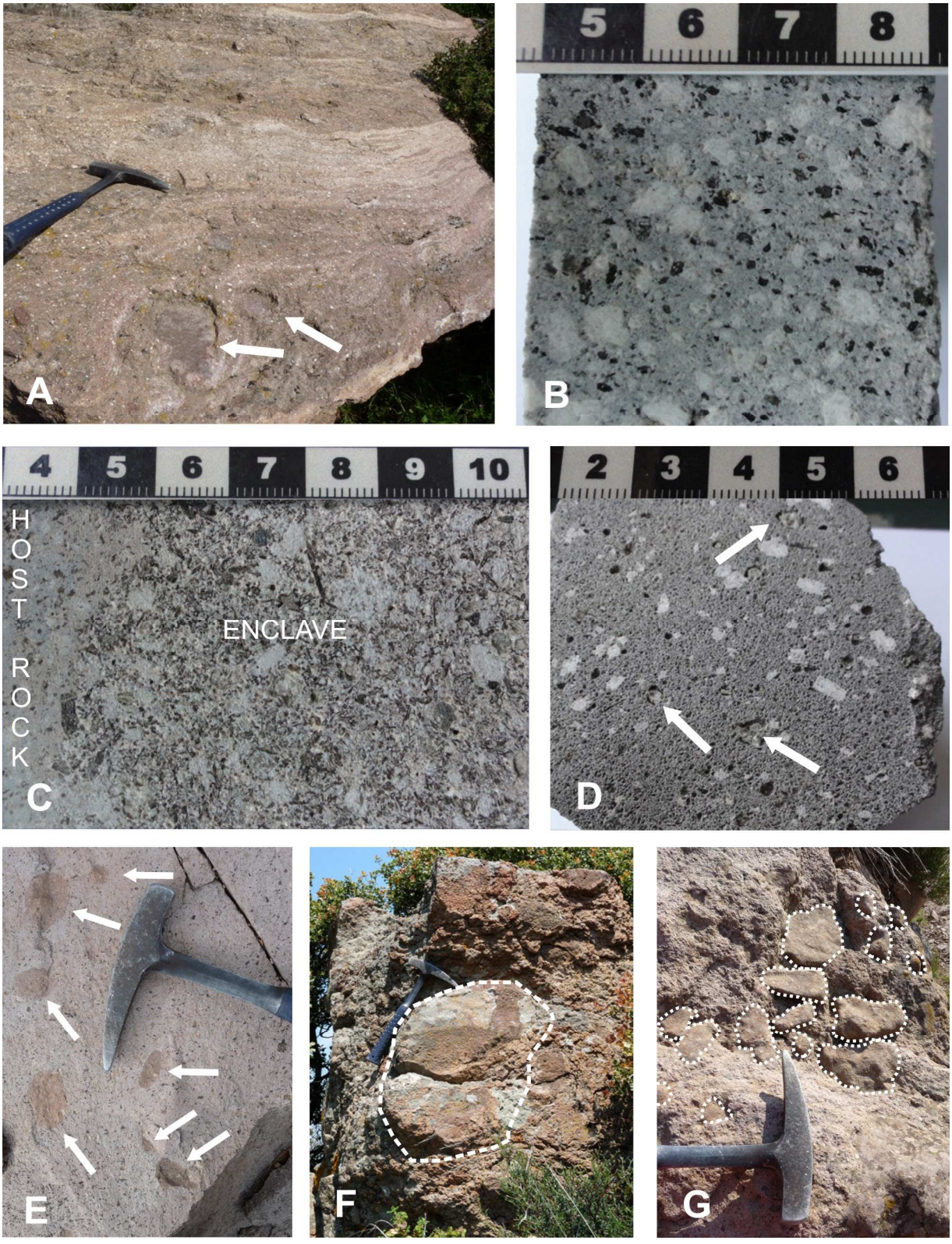

Figure 4.3 *Macroscopic features of the Delta 2 volcanic rocks.* Scale bar in cm, white crystals = plagioclase, black crystals = amphibole (A) Flow banding in the lava of sampling location 24; white arrows indicate enclaves. (B) Porphyritic texture of host rock DPM50. (C) Texture of coarser-grained enclave DPM36 and the contact with its host rock. (D) Texture of finer-grained enclave DPM64, white arrows indicating quartz ocelli. (E) Host rock enclosing rounded enclaves (indicated with white arrows) at sampling location 4. (F) Large enclave in lava flow at sampling location 12; note the basal and top breccia below and above (hammer for scale). (G) A group of finer-grained enclaves (see white-dashed lines) within the lava flow at sampling location 22.

4.2 Petrography

In host rocks or enclaves with a macroscopically brown-reddish groundmass (as opposed to the grey appearance of most outcrops and samples), the majority of hydroxyl-bearing minerals are pseudomorphically replaced by aggregates of smaller opaque crystals (Fig. 4.6C). These aggregates are often interpreted as pseudomoprhs after amphibole since they commonly show euhedral outlines typical of amphibole crystals. The red-coloured groundmass of such samples is thought to reflect oxidation during, or shortly after, eruption and deposition. Rock samples with a grey-coloured groundmass usually show significantly less alteration of their water-rich minerals and are therefore interpreted to be 'fresher' than their red-oxidised counterparts. The petrographic study (and subsequent geochemical analysis) is therefore mainly focused on rock samples with a grey-coloured groundmass.

4.2.1 Mineralogy and texture of the host rocks

The macroscopically adopted crystal-size categories of *macro-phenocrysts* (1-6mm) and *phenocrysts* (0.2-1mm) are further used throughout the petrographic description of the host rocks with the addition of *microlites*, which are small crystals (< 0.2mm) that, together with *glass*, make up the *groundmass* (Williams et al., 1954).

All host rocks contain plagioclase (30-70%, mostly euhedral, tabular) and amphibole (10-40%, mostly euhedral, prismatic to acicular) as major mineral phases. Both minerals are present as macro-phenocrysts and as phenocrysts, and define a seriate texture (Fig. 4.4A-C). All host rocks also contain euhedral, columnar clinopyroxene (0.5-7%) (Fig. 4.4D) and rounded quartz (0.5-5 %) (Fig. 4.4B) as macro-phenocrysts and/or as phenocrysts. Biotite (0-10%) is often present as eu- to anhedral, tabular to prismatic macro-phenocrysts and/or phenocrysts (Fig. 4.4A, C). Phenocrysts of euhedral, columnar orthopyroxene are rather uncommon (0-1%), except for the host rock samples from the Tsonaka area which all contain minor amounts (1-5%) of orthopyroxene (Fig. 4.4B). Tsonaka is also the only locality where orthopyroxene is more abundant than clinopyroxene. Despite the presence of quartz, some host rocks contain up to 1 vol% of subhedral olivine macro-phenocrysts which usually contain inclusions of brown Cr-spinel octahedra (Fig. 4.4E). Euhedral, prismatic zircon grains (30-150 µm) were found as inclusions in large crystals of plagioclase, amphibole, biotite or quartz in ca. one third of the host rock thin sections (Fig. 4.4F). Apatite is a common accessory mineral occurring as acicular crystals in plagioclase, as phenocrysts or as microlites. Groundmass microlites are dominantly (needle-shaped) plagioclase, in addition to opaque minerals (probably Fe-Ti oxides, 1-5%, eu- to anhedral, equidimensional), some (acicular) amphibole and rare (prismatic) pyroxene.

Macro-phenocrysts are responsible for the host rocks' porphyritic texture and represent between 15 and 40 volume%. The difference in grain size between these large crystals and the more subhedral microlites in the groundmass is pronounced, but the dimensions of the phenocrysts cover the entire size range between these two end members. Tabular and prismatic phenocrysts of plagioclase, amphibole and pyroxene are always lined up and deflected around the macro-phenocrysts, defining a flow texture that is present in all host rocks (Fig. 4.4A, B, D). All host rocks furthermore contain up to 5 vol% of irregularly shaped vesicles which are usually about 1mm large.

4.2.2 Mineralogy and texture of the enclaves

Most of the minerals identified in the host rocks are also observed in the enclaves, but mafic minerals are more abundant. Plagioclase (10-60%) and amphibole (15-45%) are present in each enclave as macro-phenocrysts, phenocrysts and microlites (Fig. 4.5A, B). Opaque minerals (probably Fe-Ti-oxides, 3-10%) occur as both phenocrysts and microlites. Clinopyroxene is not uncommon as macro-phenocrysts and/or as phenocrysts, but it only occurs in about 50% of the enclaves, some of which contain higher amounts of this mineral than any host rock (up to 10%) (Fig. 4.5A). For the

enclaves, orthopyroxene is not restricted to the Tsonaka locality, but also found in some enclaves from Kossona Vouno. This mineral only occurs as phenocrysts, and in somewhat higher amounts in fine-grained (up to 20% in DPM12) than in coarse-grained enclaves (Fig. 4.5B). Biotite (0-7%) is mainly present as macro-phenocrysts but in smaller amounts than in the host rocks (Fig. 4.5C), and it was not observed in the Kossona Vouno enclaves. Large quartz crystals (0-1%), of similar size and shape as those in the host rocks but mantled by prismatic pyroxene, only occur in up to 30% of the enclaves whereas all host rocks contain this mineral. Olivine is slightly more common in enclaves than in host rocks and again occurs as subhedral (macro-)phenocrysts containing Cr-spinel (Fig. 4.5D). Apatite is less conspicuous in the enclaves and contrary to the host rocks, no zircon was observed in any of the enclaves.

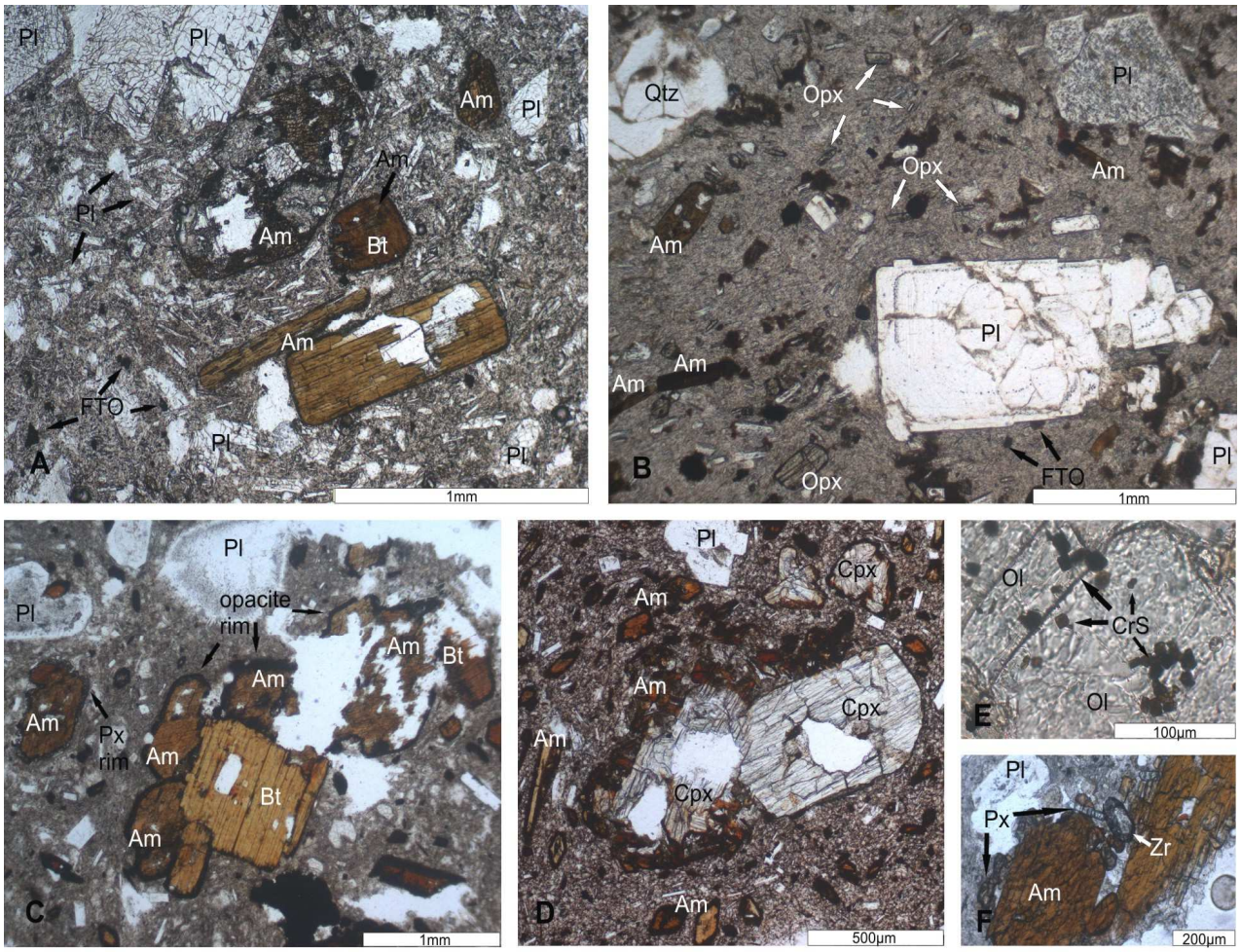

Figure 4.4 *Photomicrographs of host rocks under plane polarised light (ppl).* Pl = plagioclase, Am = amphibole, Bt = biotite, FTO = Fe-Ti-oxides, Qtz = quartz, Opx = orthopyroxene, Cpx = clinopyroxene, Ol = olivine, CrS = Chrome-spinel, Px = pyroxene, Zr = zircon. (A) DPM8, Loutses SE flow. Porphyritic rock with macro-phenocrysts of plagioclase and amphibole, a biotite crystal and phenocrysts of plagioclase and opaque minerals. The prismatic plagioclase microlites define a flow texture around the large crystals. (B) DPM55, Tsonaka. Macro-phenocryst of anhedral quartz and of both a sieve-textured, subhedral and an unsieved euhedral plagioclase grain. Phenocrysts of orthopyroxene, amphibole and plagioclase in fine-grained groundmass define a flow texture. (C) DPM39, Kossona Vouno. Macro-phenocryst of biotite partially rimmed by smaller amphibole crystals, with both hydrous phases showing an opaque reaction rim. The isolated amphibole macro-phenocryst to the left is mantled by fine-grained pyroxene. Note the two subhedral plagioclase crystals at the top, one with a sieve-textured core and one with a sieve-textured rim. (D) DPM57, Loutses SW flow. Two clustered euhedral clinopyroxene phenocrysts partially mantled by smaller amphibole crystals. Two smaller subhedral clinopyroxene phenocrysts at the top right also show a brown-red coloured rim. Small amphibole and plagioclase phenocrysts and microlites define a flow texture around the cluster. (E) DPM46, Tsonaka. Octahedral, brown Cr-spinel inclusions in a large olivine crystal. (F) DPM45, Tsonaka. Small, euhedral zircon within a large amphibole phenocryst that is partially overgrown and replaced by fine-grained pyroxene.

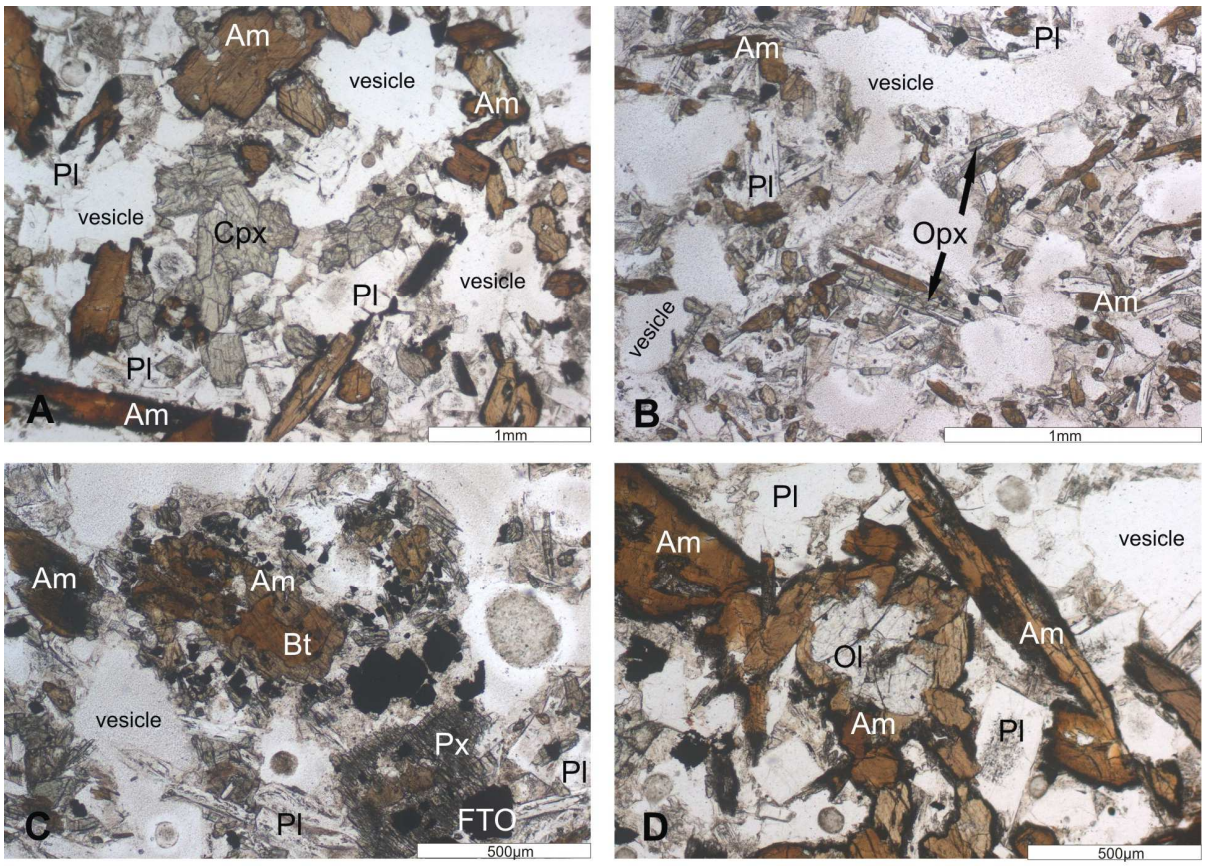

Figure 4.5 *Photomicrographs of enclaves under plane polarised light (ppl),* mineral acronyms as in Fig. 4.4. (A) Coarse-grained enclave DPM35A, Kossona Vouno. Typical enclave consisting of an equigranular network of randomly oriented amphibole, (clino)pyroxene and plagioclase phenocrysts and irregular, rounded vesicles. Note that clinopyroxene has a tendency to cluster, whereas amphibole grains are more often single individuals (B) Fine-grained enclave DPM64, Loutses NW section. Phenocrysts of mainly orthopyroxene, amphibole and plagioclase in a groundmass of glass and some microlites. Note the higher vesicularity compared to coarse grained enclave DPM35A. (C) DPM64, Loutses NW section. Sub- to anhedral biotite overgrown by amphibole. Also note the remnant of an amphibole grain in the bottom right corner, largely replaced by fine grained pyroxene (D) DPM35A, Kossona Vouno. Amphibole is usually present as individual crystals which only cluster when overgrowing another mineral. In this image amphibole grains cluster around an olivine crystal with Cr-spinel inclusions. Note the opaque reaction rims of the euhedral amphibole grains.

The macro-phenocrysts observed in enclaves are somewhat smaller than those in host rocks (0.5 – 5 mm), and present in significantly lower amounts. Fine-grained enclaves hereby tend to have more of these large crystals than the more coarse-grained enclaves. Enclave phenocrysts are also somewhat smaller in size (0.1-0.5mm) but so numerous (up to 50 vol%) that they define a crystal framework. For all enclaves this framework mainly consists of prismatic to tabular plagioclase and amphibole crystals. Only enclaves DPM56A and DPM56B form an exception as they lack amphibole phenocrysts but have large amounts of orthopyroxene instead. In contrast to the host rocks' flow texture, prismatic phenocrysts in enclaves are always randomly oriented (Fig. 4.5A, B). Phenocryst dimensions are usually uniform within a single enclave but do vary between enclaves. The difference between 'fine-grained' and 'coarse-grained' enclaves observed during fieldwork thus translates to the size of their phenocrysts, which define an equigranular texture of randomly oriented prismatic crystals. There are two end members: 'coarse-grained' enclaves contain 70-85 vol% phenocrysts (length to width ratio around 3:1), 5 to 15 vol% vesicles and small amounts of microlites and glass (Fig. 4.5A), whilst 'fine-grained' enclaves are usually made up of 60-80 vol% phenocrysts (aspect ratio 5:1), between 10 and 25 vol% vesicles and larger amounts of groundmass (Fig. 4.5B). Whereas groundmass represents up to half of the host rocks' volume, it is less important in enclaves where it displays a higher proportion of glass to microlites (<0.1mm). Enclaves have an overall significantly higher vesicularity than host rocks,

due to 5-25 vol% vesicles with a diameter of up to 2.5mm (Fig. 4.5A-D). These vesicles are usually in part delineated by mineral grains but have an overall rounded shape due to their curved contact-surface with interstitial glass. None of the studied enclaves have a dictytaxitic texture (with irregularly shaped vesicles representing cavities in between crystals).

4.2.3 Mineral-specific textures and mineral intergrowths

Unless stated otherwise, the following observations were made in thin sections of host rocks and enclaves alike and mainly describe the macro-phenocrysts and larger phenocrysts. Smaller phenocrysts and microlites tend to be homogeneous crystals without much internal texture.

Plagioclase shows both simple and polysynthetic twinning, sometimes with clear oscillatory zoning either throughout the whole crystal or restricted to certain zones (Fig. 4.6A). Zoning can be either continuous or discontinuous. Some plagioclase macro-phenocrysts display a sieve texture, across the whole crystal or restricted to certain areas, and coexist with plagioclase grains of similar dimension but without sieve texture (Fig. 4.4B, C). Anhedral mineral inclusions of Fe-Ti-oxides or amphibole can occur, either distributed randomly throughout a plagioclase crystal or localised in certain zones (Fig. 4.6A). Euhedral zircon inclusions have also been observed. Some host rocks from the Loutses area (E & SE flow and NW section) contain a few plagioclase macro-phenocrysts with an extensive sieve-textured core and an unsieved rim containing subhedral grains of olivine and/or clinopyroxene (Fig. 4.6B). Plagioclase crystals sometimes occur as glomerocrysts. Macro-phenocrysts with sharp polysynthetic twinning were selected to estimate the plagioclase composition using the Michel-Lévy method (Nesse, 2004). Maximum extinction angles varied from one host rock to the next between 30° and 36° - suggesting an anorthite content of 45-60%. Plagioclase crystals with polysynthetic twins, mostly found in host rocks, are thus andesine to labradorite.

Amphibole can form simple twins and is often continuously or discontinuously zoned - with sometimes both types of zoning present within one thin section. Opaque reaction rims of varying thickness are commonly present, and smaller crystals are sometimes completely altered to an opaque, fine-grained aggregate (Fig. 4.4C, 4.6C). Heterogeneously distributed mineral inclusions are mainly plagioclase and Fe-Ti-oxides, but inclusions of zircon or biotite are also observed. In host rocks, but even more so in enclaves, large amphibole crystals are partially or totally replaced by a fine-grained aggregate of ortho- and/or clinopyroxene (sometimes with plagioclase and Fe-Ti-oxides; Fig. 4.5C). This type of aggregate can occur both in the centre of the crystal or at the rim, usually following the amphibole outline (Fig. 4.4A). All prismatic pyroxene grains of such aggregates are optically continuous, suggestive of epitaxial replacements (Fig. 4.5C, 4.6D). A new amphibole rim or a mantle of new, smaller amphibole crystals often grows around such pseudomorph aggregates - especially so in enclaves. Fine-grained pyroxene-rich zones can also be overgrown by a new, more coarse-grained pyroxene rim (Fig. 4.6D). Amphibole grains with this type of replacement occur together with amphibole crystals of similar size and shape that only have a (thin) opaque reaction rim (Fig. 4.4A). Amphibole crystals tend to mainly cluster together when overgrowing other minerals. Nearly all olivine found in enclaves and host rocks is mantled by amphibole (Fig. 4.5D), and amphibole was also found to nucleate on clinopyroxene (Fig. 4.4D). Amphibole grains usually show orange-brown to dark red-brown pleochroism, yellow to olive-green pleochroism is less common. Extinction is mainly oblique with an extinction angle between 10° and 30°. Highest interference colour is second order yellow-green (birefringence up to 0.030) and interference figures are biaxially negative. These optical properties suggest that the Delta 2 amphibole crystals have a hornblende composition (Nesse, 2004).

Biotite is mainly eu- to subhedral and occasionally has inclusions of zircon, plagioclase, amphibole or oxides. Fine-grained aggregates of mainly plagioclase, pyroxenes, and oxides are found to replace the rim of a biotite grain (Fig. 4.6E). This replacement texture was found in both host rocks and enclaves, disrupting the euhedral form of the biotite itself but with the overall shape of the aggregate still mimicking the euhedral biotite crystal. This is therefore likely to be a dehydration replacement of

the biotite rather than nucleation and growth of these anhydrous minerals on the otherwise euhedral biotite crystals. Whereas amphibole is replaced by epitaxially grown clino- and/or orthopyroxene (Fig. 4.6D), the fine-grained pyroxene, plagioclase and Fe-Ti-oxide grains replacing biotite crystals are randomly oriented (Fig. 4.6E). Within one sample anhedral biotite grains with such replacement aggregates can occur together with euhedral biotite crystals showing only a (thin) opaque reaction rim. Sometimes biotite phenocrysts are mantled by amphibole (Fig. 4.5C). Biotite found in the Delta 2 samples shows an olive green/light brown to dark brown/dark red-brown pleochroism.

Quartz always occurs as anhedral, rounded, and internally fractured grains. Within enclaves, they are rimmed by fine-grained, radially oriented, prismatic clinopyroxene crystals – also referred to as 'quartz ocelli' (Fig. 4.6F). Quartz is however more abundant in host rocks, where it usually lacks such a reaction rim (Fig. 4.4B). A quartz crystal with a prismatic, euhedral zircon inclusion was observed in one host rock sample.

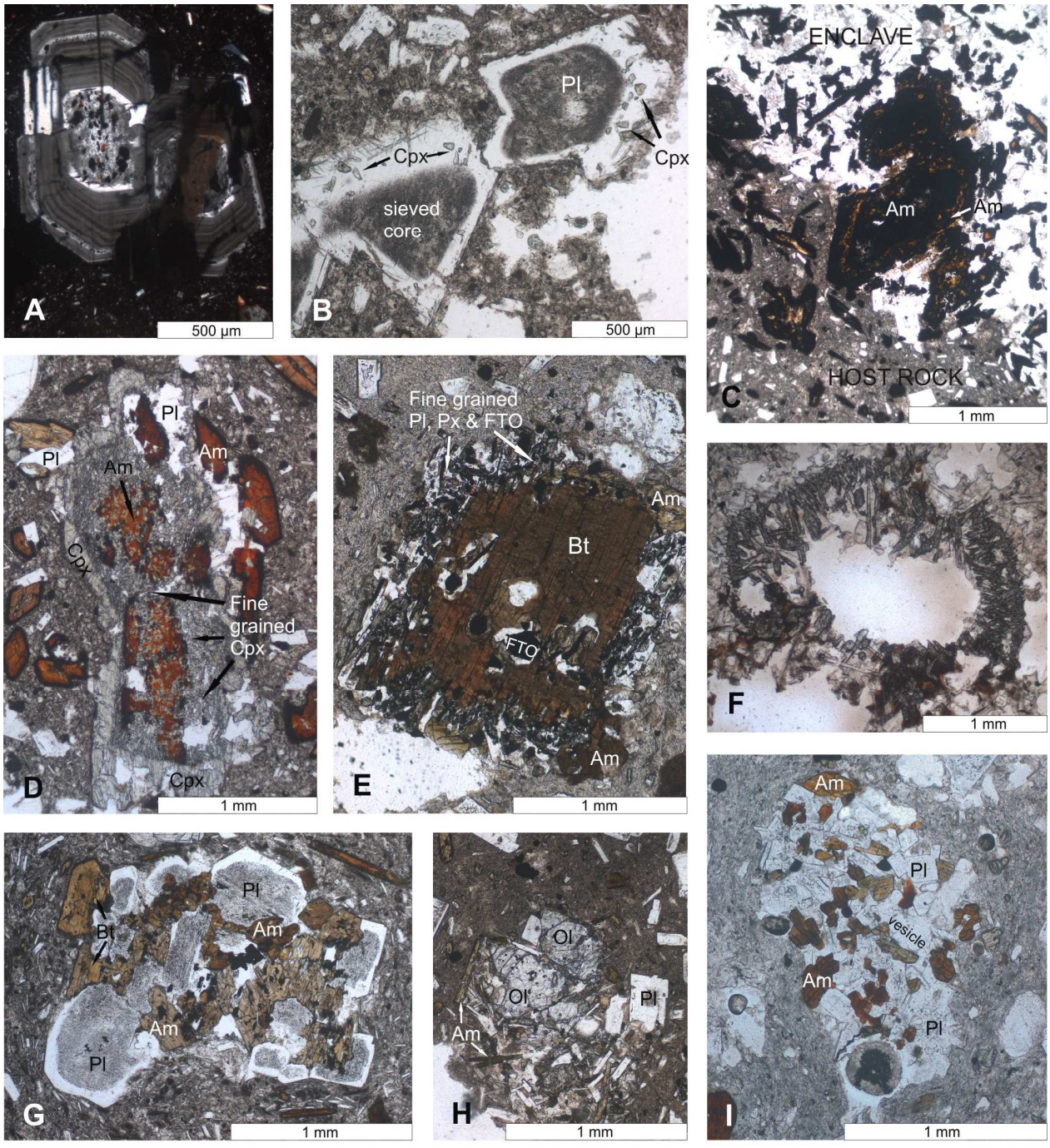

Both clino**pyroxene** and orthopyroxene mainly occur as euhedral, short prismatic crystals. They are heterogeneously distributed throughout the rock samples both as individual grains and as glomeroporphyritic clusters.(Fig. 4.4A & 4.4D). Both pyroxenes furthermore occur as fine-grained, subhedral crystal aggregates replacing amphibole or biotite (Fig. 4.6D, E). In certain samples clinopyroxene was found to have red brown rims of varying thickness or it was mantled by subhedral amphibole grains (Fig. 4.4D). **Clinopyroxene** crystals show continuous as well as discontinuous zoning, and sometimes single twins. Delta 2 clinopyroxene crystals have a high positive relief, are usually colourless but sometimes light green to light grey, in which case they are also (weakly) pleochroic. Elongated clinopyroxene crystals show inclined extinction (15° to 50°) and some basal sections revealed a biaxially positive interference figure. The clinopyroxene in the Delta 2 volcanic rocks is probably augite (Nesse, 2004). In contrast to clinopyroxene, **orthopyroxene** crystals never show twining and they are not overgrown or replaced by other minerals. The faintly grey-green, high relief orthopyroxene grains commonly show typical green-red pleochroism and a biaxially negative interference figure. They usually have low interference colours, but some orthopyroxene grains display up to first order orange-red (birefringence of 0.015).

Olivine crystals are rare in host rocks and enclaves alike. When present, they occur with red-brown iddingsitised cracks and outer rims and they are grouped in clusters. They usually contain inclusions of brown, octahedral Cr-spinel and are often overgrown by an amphibole rim (Fig. 4.5D) or by prismatic pyroxene crystals. Since all host rocks contain quartz, olivine found in host rocks always co-exists with quartz. The olivine crystals encountered in Delta 2 rocks are colourless and not pleochroic. They have a high positive relief, show no clear cleavage but do have distinctive irregular fractures which can be coloured red-brown due to local oxidation and alteration. Delta 2 olivine grains have intermediate interference colours, only up to second order purple (birefringence of 0.037), suggesting a Mg-rich composition (Nesse, 2004) which is in agreement with the brown-red Cr-spinel octahedra it often includes.

Apatite is usually present as small, prismatic to acicular crystals within plagioclase or as groundmass microlites. A few larger grains are however also identified as host rock phenocrysts.

Figure 4.6 *Photomicrographs of mineral-specific textures and mineral intergrowths*. (B) to (I) under plane polarised light (ppl), (A) under crossed polars (xpl), mineral acronyms as in Fig. 4.4. (A) Host rock DPM33, Loutses SW flow. Two large, euhedral plagioclase crystals show a complex combination of textures: anhedral, sieved core with anhedral inclusions of oxides and amphibole, mantled by an euhedral inclusion-free rim, which is in turn overgrown by a broad rim of oscillatory zoned plagioclase. This is followed by an inclusion-rich rim similar to the core, and finally another oscillatory zoned rim. (B) Host rock DPM20, Loutses SE flow. Two plagioclase crystals with sieved, anhedral core and euhedral rim with subhedral clinopyroxene inclusions. (C) Contact between enclave DPM29B and its host rock, Loutses S flow. Both rock types show opaque reaction rims around their brown-coloured hydrous minerals, and the smaller prismatic amphibole phenocrysts are totally altered to an opaque aggregate. This is typical for samples with a macroscopic brown-reddish groundmass. Note the 2 large amphibole crystals with a dark core but overgrown by a newer amphibole rim. The largest of these crystals straddles the contact between host rock and enclave. (D) Host rock DPM34, Kossona Vouno, showing a common amphibole texture. One or two large amphibole crystals in the centre are partially replaced by fine-grained clinopyroxene. Around this epitaxial replacement is a fine-grained rim of clinopyroxene, in turn overgrown by coarser grained clinopyroxene. The right side of this mineral aggregate is partially mantled by plagioclase, in turn overgrown by euhedral amphibole grains which are similar to the amphibole phenocrysts left of the aggregate. (E) Host rock DPM50, Tsonaka. Whereas disequilibrium replacement or overgrowth of amphibole occurs in an epitaxial manner, this is not so for biotite. Replacement or overgrowth of this hydrous mineral always involves an equigranular aggregate of different water-free minerals that are randomly oriented. The large biotite crystal in this picture has an anhedral form, with an aggregate rim of pyroxene, plagioclase and opaque oxides, showing a euhedral outer boundary, but an anhedral contact with the remainder of the biotite. (F) Enclave DPM56B, Tsonaka. Mantle of prismatic, radially orientated clinopyroxene crystals that represent the mafic reaction rim of a ‘quartz ocellus’ (quartz grain itself is however lost during thin section preparation). (G) Host rock DPM58, Loutses SW flow. Holocrystalline cumulophyric cluster of plagioclase, (biotite mantled by) amphibole and Fe-Ti-oxides. Note that the plagioclase crystals all have sieve-textured cores, similar to commonly found large individual plagioclase crystals. (H) Host rock DPM46, Tsonaka. Cumulophyric cluster of two olivine crystals (with Cr-spinel) with acicular amphibole and prismatic plagioclase, possibly representing a ‘micro-enclave’. (I) Host rock DPM45, Tsonaka. This cluster of granular, randomly oriented plagioclase and amphibole with a few vesicles is interpreted as a micro-enclave.

Zircon only occurs as prismatic, euhedral inclusions in large crystals of plagioclase, amphibole or biotite which usually show disequilibrium textures. These zircon crystals are thereby always observed in host rocks, never in enclaves.

Besides glomeroporphyritic **clusters** consisting exclusively of clinopyroxene or plagioclase (sometimes also of orthopyroxene or olivine), cumulophyric clusters of plagioclase, amphibole, oxides ± biotite ± pyroxene also occur in host rocks, and sometimes even in enclaves. The crystals in such clusters are usually eu-to subhedral, with internal (disequilibrium) textures similar to those of individual large crystals (Fig. 4.6G). Clusters of subhedral olivine (with Cr-spinel) and prismatic amphibole, pyroxene and plagioclase are sporadically present in host rocks (Fig. 4.6H). In some host rocks up to 5mm large equigranular, porphyritic clusters of plagioclase, amphibole, Fe-Ti-oxides ± pyroxene show a texture very similar to the enclaves and are therefore seen as **micro-enclaves** that were not macroscopically identified in the field (Fig. 4.6I).

Enclaves sometimes show a strongly heterogeneous distribution of minerals, vesicles, hyaline areas or phenocryst size within a single thin section. Contacts between host rocks and enclaves are always sharp, with no chilled margins nor any indications of specific reactions not observed elsewhere in the sample. In some cases large crystals of plagioclase or amphibole are found across enclave-host rock boundaries, halfway into the enclave and halfway into the host rock (Fig. 4.6C).

4.3 Geochemical data

All major and trace element concentrations and Sr, Nd and Pb isotopic compositions analysed for host rocks and enclaves from the Delta 2 unit can be found in Appendices B1, C1 and D1, respectively. Since volcanic rocks on Methana are all younger than 5 Ma (Pe-Piper & Piper, 2013), no age corrections have been carried out for the isotopic ratios.

4.3.1 Major element geochemistry

The Delta 2 samples define one continuous medium-K trend, as defined by Gill (1981) (Fig. 4.7A). According to the total alkali versus silica (TAS) diagram of Le Maitre et al. (2002) host rocks are andesites to dacites (SiO_2 = 59-68 wt%), the highest silica content belonging to DPM42 (Fig. 4.7B). Enclaves are more mafic (SiO_2 = 50-62 wt%) and generally have an andesitic to basaltic-andesitic composition. Only the two Kossona Vouno enclaves DPM36 and DPM41B are basalts. MgO concentrations vary between 6.5 wt% (enclave DPM41B) and 1.7 wt% (host rock DPM42). Compared to other host rocks with similar silica contents, the seven samples from the Loutses SW and S flows show distinctly higher MgO concentrations (Fig. 4.7C). Magnesium numbers (Mg# = molar $Mg/(Mg+Fe_{tot})$) range from 62 to 47, with the higher values belonging to enclaves and the lower ones to host rocks (Appendix B1). Only Tsonaka enclaves DPM56A and DPM56B (sampled close to one another) lie below the Mg# trend defined by all other Delta 2 samples at a value of 42.5. Despite varying degrees of scatter in the Harker variation diagrams, CaO (4.5 to 12 wt%), Fe_2O_3* (3.8 to 8 wt%) and TiO_2 (0.4 to 0.9 wt%) concentrations clearly show decreasing trends with decreasing magnesium content (Fig. 4.7D-F). Enclaves DPM56A and DPM56B show somewhat higher TiO_2 (and Fe_2O_3*) contents than other Delta 2 samples with similar amounts of MgO. Trends in Harker variation diagrams for Na_2O (not shown), MnO, Al_2O_3 and P_2O_5 (not shown) are less well-defined, due to scatter which tends to be highest amongst the enclaves (Fig. 4.7G-H).

Figure 4.7 also shows that the large compositional range of the Delta 2 unit is more or less present within each of the three different study areas, and it is not the result of three smaller, locality-specific ranges that complement one another. Despite the fact that samples from the Loutses, Tsonaka and Kossona Vouno locality overlap, there is a geochemical difference between enclaves and host rocks, with the former being overall more mafic than the latter. There is however no distinct compositional gap between host rocks and enclaves at the Loutses or Tsonaka localities - together they define a single trend. Only the enclaves and host rocks sampled near Kossona Vouno display a distinct

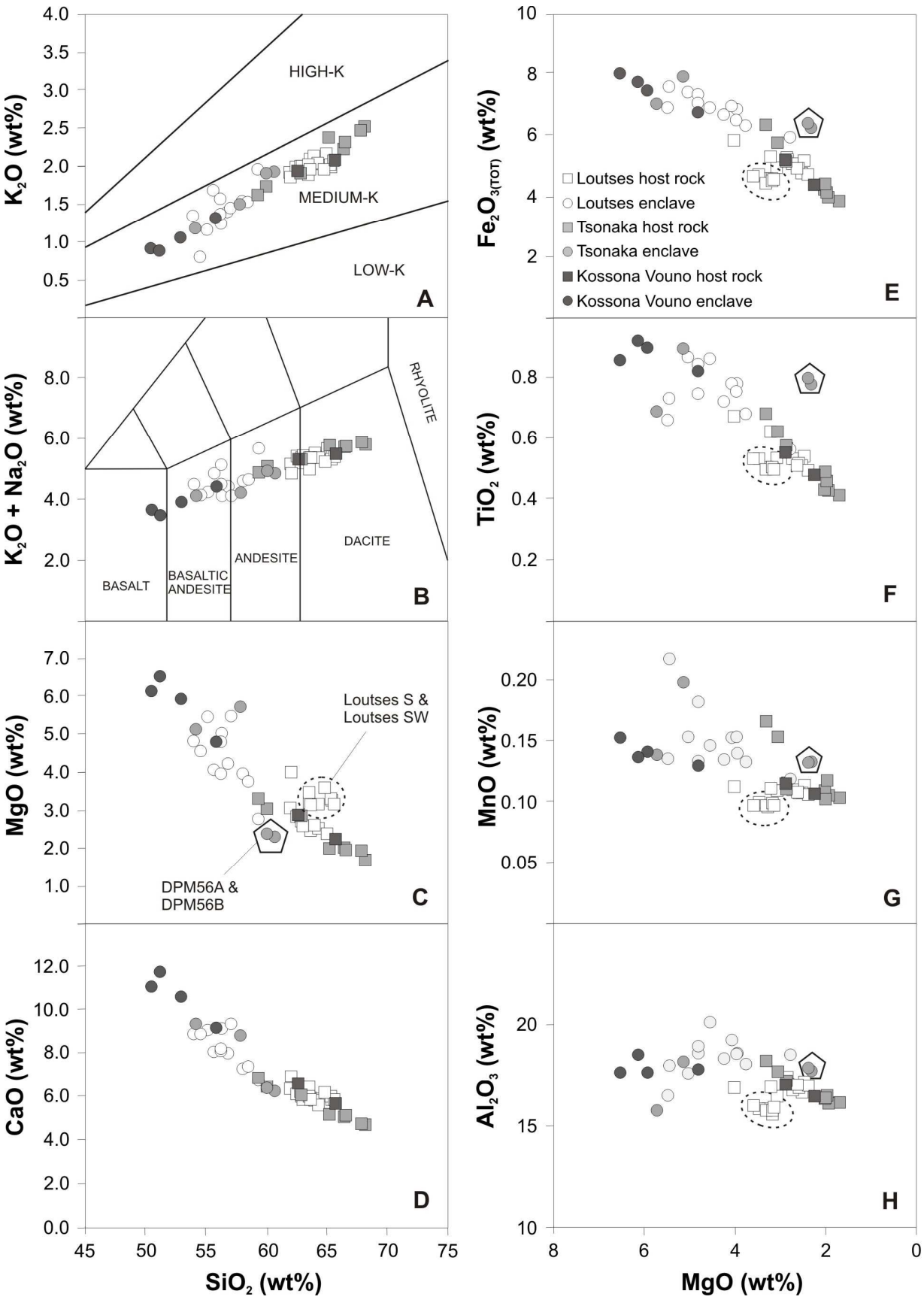

Figure 4.7 *Whole rock major element variation diagrams for host rocks and enclaves of the Delta 2 volcanic unit*, grouped according to sampling localities (note that Al_2O_3 concentrations start at 10 wt% in diagram 4.7H).

geochemical gap between them. It is however not clear whether this really is a geochemical signature or rather the result of less dense sampling of the smaller Kossona Vouno locality.

Exceptions to some of the above discussed major element trends are the 7 host rock samples collected from the Loutses S and SW flows and enclaves DPM56A and DPM56B. Based on their major element composition, the Loutses samples will be further subdivided into Loutses South (S and SW flow) and Loutses North (E & SE flow and N section). Since the composition of DPM56A and DPM56B is distinctly different from the other Delta 2 enclaves, they will also be separately indicated in the following diagrams.

4.3.2 Trace element geochemistry

Trace elements plotted against SiO_2 or MgO often define scattered patterns. Yttrium concentrations, for example, range from 15 to 32 ppm, irrespective of MgO content but with enclaves generally at values higher than 20 ppm, and host rocks mostly lower than 20 ppm (Fig. 4.8A). Scandium, V, Cr and Co show overall decreasing trends with decreasing magnesium contents, with the highest concentrations belonging to either one of the basaltic enclaves (DPM41B or DPM36), and the lowest values to the host rock with the highest silica contents (DPM42). Scandium concentrations thereby range between 10 – 40 ppm (Fig. 4.8B), V varies from 65 to 265 ppm and Co from 8 to 30 ppm. Chromium is usually lower than 100 ppm, with the exception of the very high Cr contents of enclaves DPM41B and DPM49 (130 and 160 ppm respectively) on the one hand, and the very low Cr concentrations of enclaves DPM56A and DPM56B on the other hand (<10 ppm). Nickel values are generally lower than 40 ppm (enclaves DPM56A and DPM56B have the lowest Ni contents, < 5 ppm), except for the Loutses South host rocks whose Ni contents range from 44 to 52 ppm (Fig 4.8C). These samples are also enriched in Cr, but not in Sc, V or Co. High field strength elements (HFSE) Zr (80 – 205 ppm), Hf (1.5 – 4.5 ppm), Nb (4 – 14 ppm) and Ta (0.3 – 0.85 ppm) show broadly negative correlations with MgO content (Fig 4.8D). The highest HFSE concentrations are always found in enclaves DPM56A and DPM56B. Concentrations of incompatible trace elements Th (3 – 12 ppm), U (0.8 – 2.8 ppm) and Pb (5 – 13.5 ppm) increase systematically with decreasing magnesium contents in a single smooth trend for all Delta 2 samples, including Loutses South host rocks and enclaves DPM56A and DPM56B (Fig. 4.8E).The large ion lithophile elements (LILE) Ba (170 – 520 ppm), Rb (15 – 80 ppm) and Cs (0.5 – 4 ppm) also increase with decreasing MgO contents (Fig. 4.8F). Despite scatter, Sr concentrations decrease with declining magnesium contents. All Delta 2 rocks contain less than 400 ppm Sr, except for the Loutses South host rocks which contain between 460 and 560 ppm Sr (Fig. 4.8G). Rare earth element (REE) concentrations increase with decreasing magnesium contents, with enclave DPM56B showing the highest values relative to its silica content. Loutses South host rocks form a cluster above the main trend for light REE (LREE), and below it for heavy REE (HREE). Despite larger scatter on individual REE variation diagrams, all Delta 2 volcanic samples plot on a single well defined La/Lu versus MgO trend, apart from the Loutses South host rocks and enclave DPM56B (Fig. 4.8H).

Chondrite-normalised REE patterns of representative host rocks (SiO_2 64-68 wt%) and enclaves (SiO_2 50-60 wt%) from the different sampling localities, including most primitive enclave DPM36, most felsic host rock DPM42 and the geochemically distinct Loutses South host rocks and enclave DPM56B are presented in Fig. 4.9. All Delta 2 samples show LREE enrichment and a slightly concave HREE pattern. The four different host rocks plot closely together, including the Loutses South sample with its higher La/Lu ratio (Fig. 4.8H). The four enclaves are spread across a much larger range of values and show a somewhat lower gradient in their REE pattern than the host rocks. All patterns show a negative Eu anomaly which is usually smaller for enclaves than for host rocks. However, the most pronounced Eu anomaly is found in enclave DPM56B – the sample with the overall highest REE concentrations.

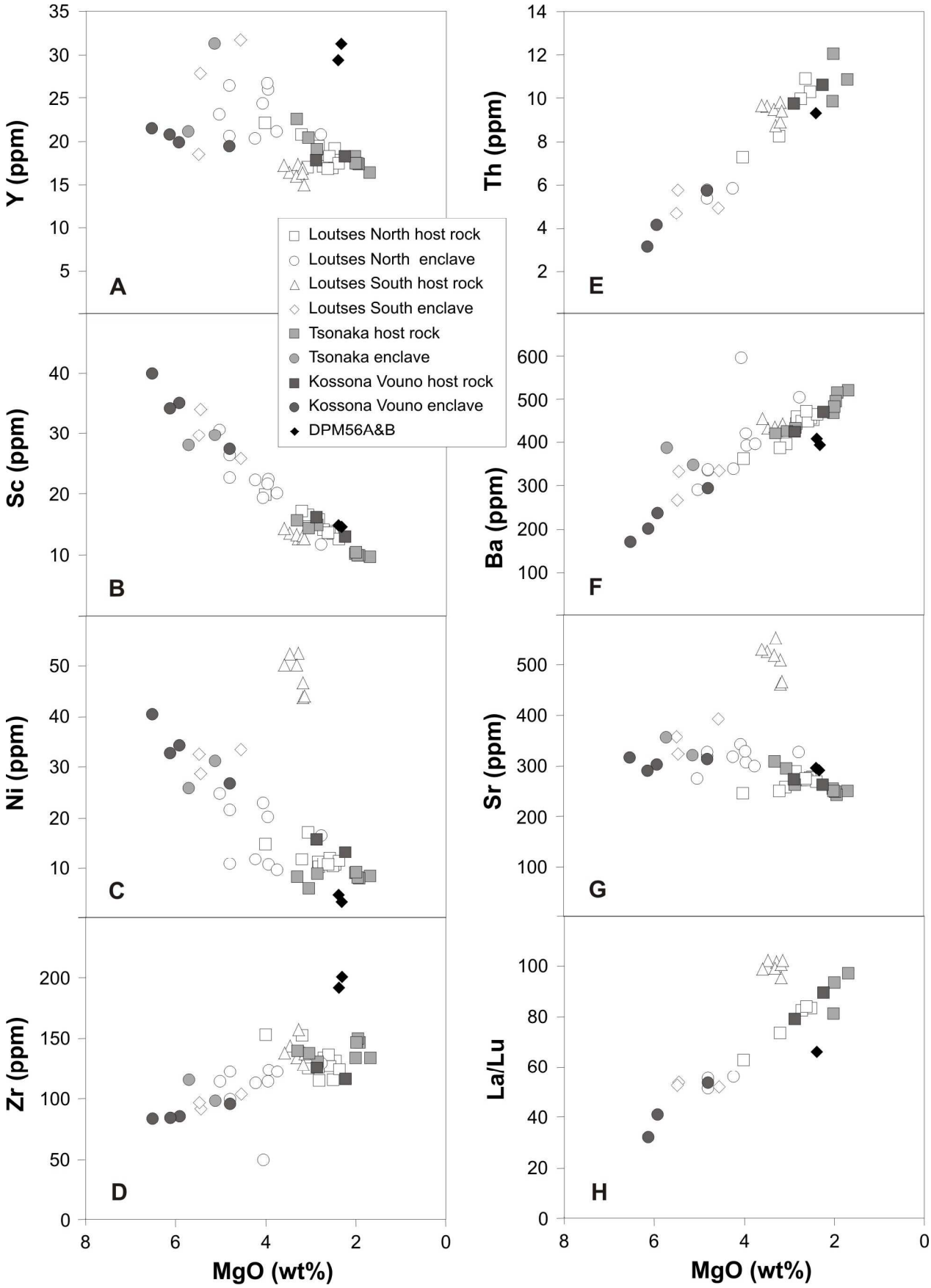

Figure 4.8 *Whole rock trace element variation diagrams for all host rocks and enclaves of the Delta 2 unit*.

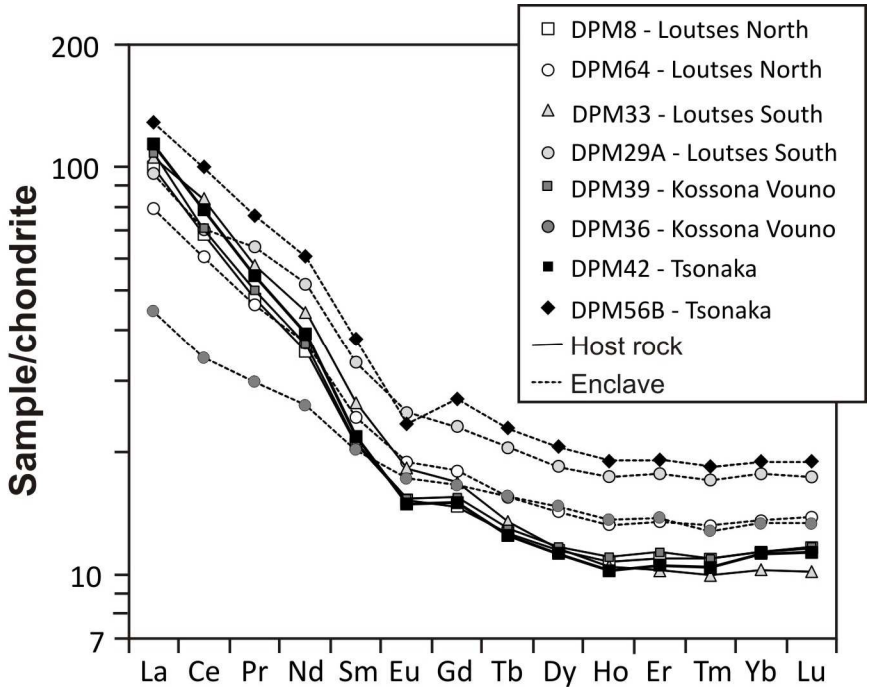

Figure 4.9 *Chondrite-normalised REE patterns for representative host rocks and enclaves of the Delta 2 unit* sampled at the different localities. Normalisation factors from McDonough and Sun (1995).

MORB-normalised trace element abundance patterns of the same representative samples as in Fig. 4.9 show positive K and Pb anomalies and negative Nb, Ta, P and Ti anomalies (Fig. 4.10). Together with enrichments in the LILE (Cs, Rb, Ba, K and Sr) and enrichment of LREE over HREE, these are all characteristics of arc volcanics (Gill, 1981). The more restricted geochemical variability of host rocks compared to enclaves is again visible in Fig. 4.10. Loutses South host rocks are distinct from the other host rock samples due to their high Sr contents and enclave DPM56B due to its overall highest HFSE and REE contents. Enclave DPM36 defines the most mafic sample of the Delta 2 unit, with the lowest concentrations of LILE and HFSE and rather low REE contents.

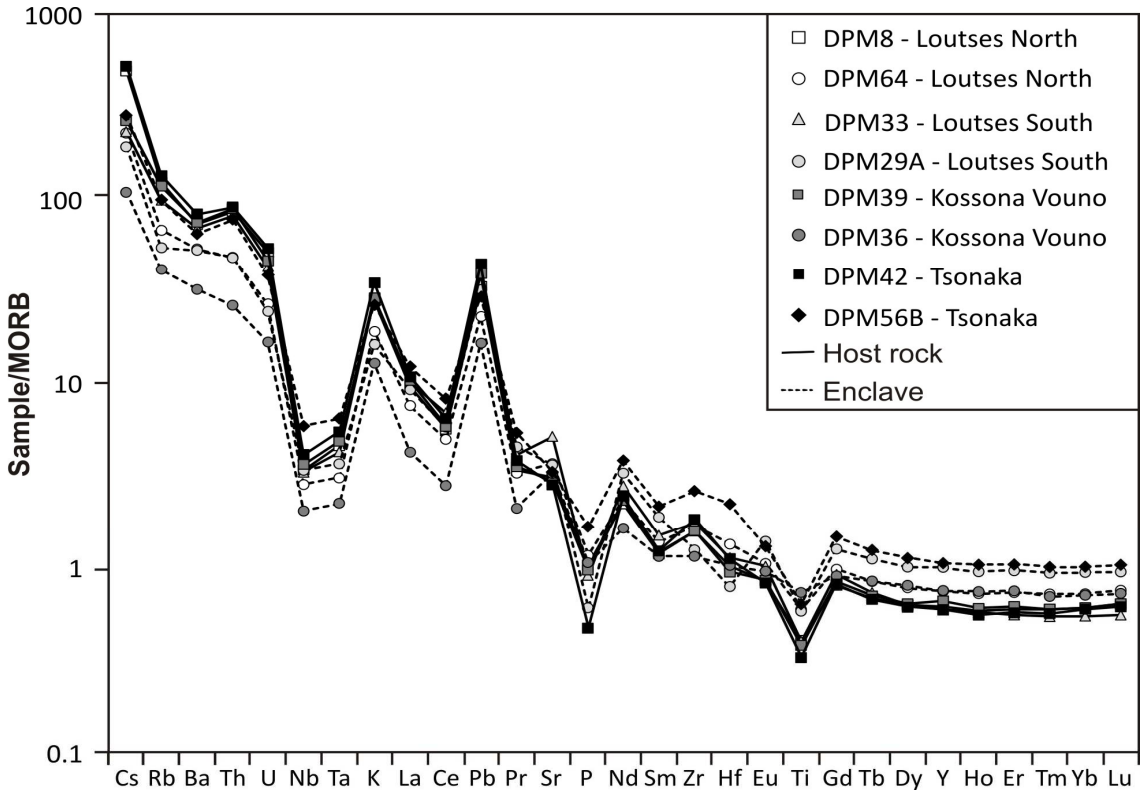

Figure 4.10 *MORB-normalised trace element abundance patterns for representative host rocks and enclaves of the Delta 2 unit*, sampled at the different localities. Normalisation factors from Sun & McDonough (1989).

Fig. 4.11 shows Ni and Zr contents for enclave-host rock pairs that were collected from 14 Delta 2 sampling locations. Based on the positive correlation between silica contents and zirconium concentrations, Zr is interpreted as an incompatible element and higher Zr concentrations reflect further differentiated magmas. The diagram shows that for nearly all enclave-host rock pairs the enclaves are less evolved than their respective hosts, but the contrast in zirconium content between enclaves and host rocks is very variable. Despite their lower silica and higher magnesium contents compared to their host rock, enclaves DPM56A and DPM56B contain significantly more Zr than their host. Nickel concentrations are usually higher in enclaves than in their respective host rocks. Exceptions to this are enclaves DPM56A and DPM56B (low Ni), and the Loutses South lavas which display the highest nickel contents of the entire Delta 2 unit. When two enclaves are sampled from a single outcrop, they are sometimes geochemically very similar and sometimes surprisingly different (see Fig. 4.11)

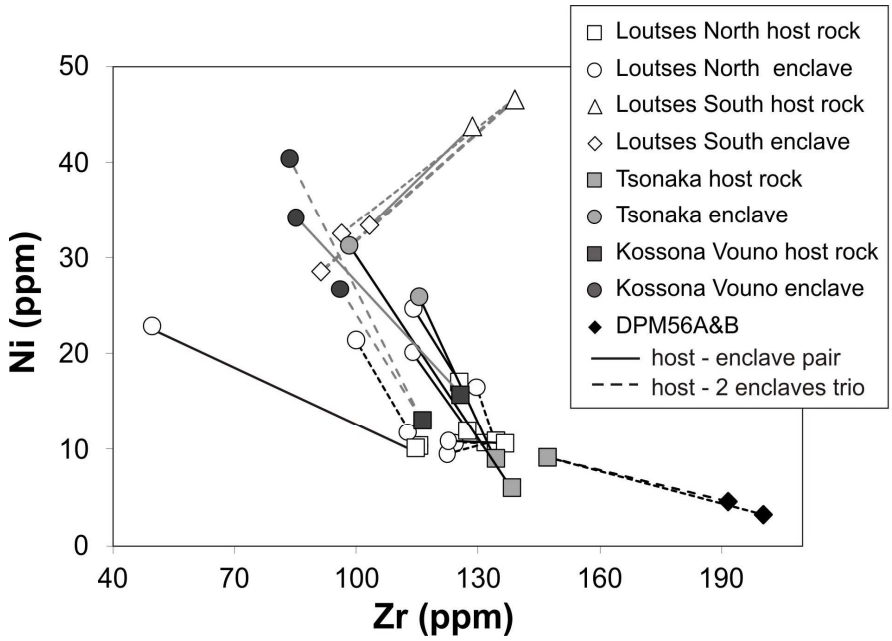

Figure 4.11 *Diagram showing the Zr and Ni concentrations of host rocks and their respective enclaves,* sampled together at a certain location (indicated with tie-line).

4.3.3 Isotope geochemistry

The $^{87}Sr/^{86}Sr$ and $^{143}Nd/^{144}Nd$ ratios for the Delta 2 samples range from 0.7049 to 0.7079 and from 0.5127 to 0.5123, respectively (Fig. 4.12A). Most volcanic rocks plot in the field that is enriched relative to Bulk Silicate Earth (BSE), but enrichment is generally less pronounced in the enclaves than in the host rocks. The most mafic enclave, DPM36, has the highest $^{143}Nd/^{144}Nd$ value and the second lowest $^{87}Sr/^{86}Sr$ ratio (after Loutses South host rock DPM26). Compared to the other enclaves, DPM56B has much higher Sr and lower Nd isotope ratios, in keeping with its aberrant major and trace element geochemistry. The Delta 2 sample with the highest $^{87}Sr/^{86}Sr$ value and lowest $^{143}Nd/^{144}Nd$ composition is not most felsic host rock DPM42, but host rock DPM66. The expected negative correlation between Sr and Nd isotopes is well defined, with only minor scatter for rocks with $^{143}Nd/^{144}Nd$ values around 0.51255. However, the Sr-rich host rocks from Loutses South plot significantly below this trend, due to their low $^{87}Sr/^{86}Sr$ values (Fig. 4.12B). Despite the scatter, Fig. 4.12C shows a broad negative correlation between $^{143}Nd/^{144}Nd$ ratios and silica contents. Strontium isotopic compositions increase with increasing silica content, except for the Loutses South host rocks which combine the lowest $^{87}Sr/^{86}Sr$ ratios with rather high silica contents (Fig. 4.12D). With regards to

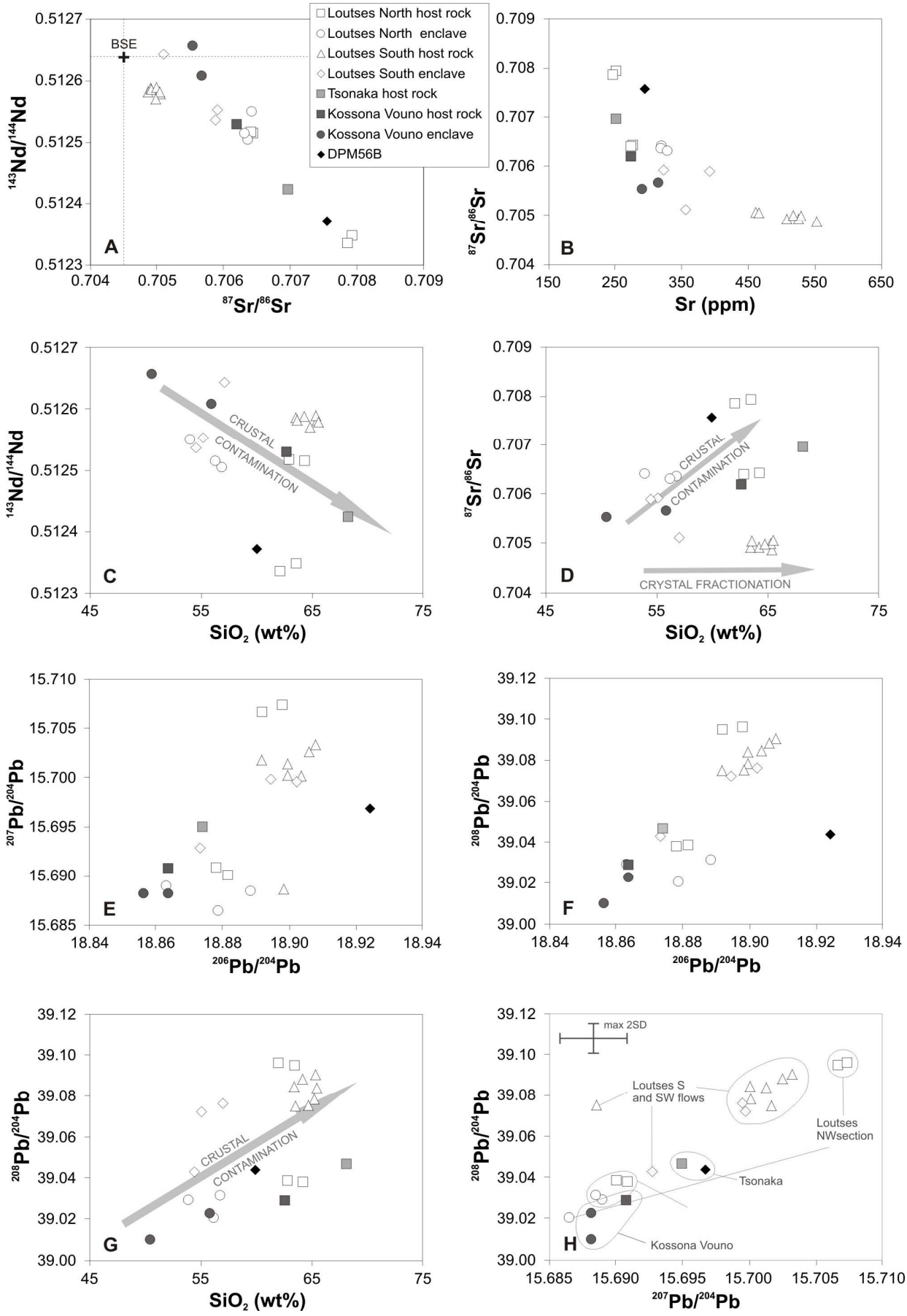

Figure 4.12 *Whole rock Sr, Nd and Pb isotope diagrams for the Delta 2 volcanic rocks*. BSE = bulk silicate earth (Workman & Hart, 2005).

the Pb isotopic compositions, $^{206}Pb/^{204}Pb$, $^{207}Pb/^{204}Pb$ and $^{208}Pb/^{204}Pb$ ratios range between 18.85 to 18.93, 15.68 to 15.71 and 39.01 to 39.10 respectively (Fig. 4.12E-F). All Delta 2 volcanic rocks thereby plot well above the Northern Hemisphere Reference Line (Hart, 1984), which plots beneath the diagrams in Fig. 4.12 E-F. Despite scatter, there is a positive correlation between Pb isotopic ratios and increasing silica contents (Fig. 4.12G).

Whereas the enclaves' Sr-Nd isotopic signature can be more or less grouped and distinguished from that of the host rocks (Fig. 4.12A), the range of Pb isotopic compositions represented by the enclaves overlaps the Pb isotopic variety of the host rocks (Fig. 4.12E, F). The systematics of less differentiated enclaves and more evolved host rocks, observed in the major and trace element as well as in the Sr and Nd isotope ratios, is therefore not reflected in the Pb isotopic compositions. Instead, the samples seem to be grouped according to their geographical location: enclaves and host rocks from a certain locality often show similar Pb isotope ratios (Fig. 4.12H). Only the Loutses NW section shows a distinctly different Pb isotopic composition for enclaves and host rocks, the latter being more enriched in radiogenic lead. All samples lie on a single $^{208}Pb/^{204}Pb$ versus $^{207}Pb/^{204}Pb$ trend, and the distinction in Pb isotopic composition between the Kossona Vouna, Tsonaka and Loutses S flow localities is outside of analytical error. The Pb isotopic composition of the Loutses SE flow overlaps with that of the Kossona Vouno rocks, as do the Pb isotopic ratios of the Loutses S flow with the Loutses SW flow (Fig. 4.12H). Different locations define smaller, individual ranges of Pb isotopic compositions which together constitute the total variety of Pb isotope ratios in the Delta 2 volcanic unit. The Pb isotopic system therefore seems decoupled from the Sr-Nd isotopic systems which are in line with the major and trace element geochemistry of the volcanic rocks of the Delta 2 unit.

4.4 Discussion of field observations and petrography

4.4.1 Origin of the more mafic enclaves

Enclaves more mafic than their host rock were first studied in granodiorites and monzogranites from all over the world (Didier, 1973, and references therein). Similar mafic enclaves were subsequently recognised in associated sub-volcanic rocks (Didier, 1973) and eventually in different volcanic deposits around the globe (Didier and Barbarin, 1991). Scientific interest in these enclaves and their host rocks continued to increase and they remain an important research topic in both plutonic and volcanic environments (see for example Elburg, 1996; Zellmer and Turner, 2007; Davi et al., 2010; Kocak et al., 2011). Enclaves often have specific macroscopic and petrographic characteristics that reveal whether they were incorporated by their host rocks as a solid rock or as a crystallising magma (Didier and Barbarin, 1991).

When originating from a solid rock, enclaves can represent either xenoliths or restites. Xenoliths are fragments of wall rock, incorporated into the host magma during differentiation at depth or upward migration, and are typically angular in shape. Enclaves in the Delta 2 unit are however mostly rounded and lack evidence of contact metamorphism (Fig. 4.3). Restites are remnants of the source rock, for example sub-volcanic plutons, cumulates (accumulated products of fractional crystallisation), metasediments, … which partially melted to produce the host magma (Chappell and White, 1991). The enclaves' texture (presence of vesicles and glass, no orientation of the prismatic crystals,…) does however not agree with a metamorphic, sedimentary or plutonic origin. In fact, the petrography of these enclaves is unlike any of the petrographic characteristics of the effusive and explosive volcanic deposits or sedimentary basement and xenoliths studied in this PhD research. This strongly suggests that the mafic enclaves of the Delta 2 unit were not incorporated into their host deposits as (completely) solidified rocks.

When formed from a crystallising magma, enclaves can represent fragments of cumulate rocks with interlocking, equigranular, euhedral crystals and little or no interstitial glass or groundmass. The enclaves of the Delta 2 unit, however, have elongated crystals with sometimes larger aspect (length-

to-width) ratios than crystals of the same mineral in their host rocks. They furthermore have higher glass contents and vesicularity than their host rocks (Fig. 4.5) - eliminating a cumulate origin and suggesting quicker cooling of the enclave magma than its host rock. These quick cooling rates are thought to be lower than expected from quenching due to contact of hot magma with cool wall rock which would have caused the formation of chilled margins. Other indications that the Delta 2 enclaves do not represent such outer margins of the magma chamber are their high vesicularity and the fact that they contain at least three crystal populations (macro-phenocrysts; framework phenocrysts, groundmass microlites Fig. 4.5 & 4.6) which suggests more stages of cooling than expected for chilled margins.

The coexistence of olivine and quartz in a single host rock sample clearly points to interaction of (at least) two chemically and mineralogically different magmas. The enclaves are thereby interpreted to represent a more mafic magma that physically mingled with the more felsic host rock magma that was crystallising in a magma chamber. The contacts between Delta 2 enclaves and the hosts are sharp but never quenched, and sometimes with large crystals straddling the boundary (Fig. 4.6C). This indicates that they represent blobs of a magma that was at least still partially liquid when mingled with the host magma.

4.4.2 Mechanism of enclave formation

The mechanism(s) by which magma mingling results in post-eruption identifiable host rock and enclaves is still under debate. Coombs et al. (2002) and Martin et al. (2006a) describe two models for mingling between a mafic and a more felsic magma. One end-member scenario involves a vigorously convecting felsic magma chamber that disrupts a basal layer of more mafic magma; or forceful intrusion of mafic magma as a fountain into felsic magma. Such processes would form individual mafic droplets within the more felsic host magma. Crystallisation of the more mafic magma, due to thermal equilibration with the cooler felsic magma, starts at the exterior of the mafic droplets and gradually shifts to their interior. The phenocryst dimensions of such enclaves should therefore be a function of their size, with smaller enclaves being more finely crystalline than larger enclaves which could exhibit an inwards increase in grain size. Enclaves of the Delta 2 unit, however, neither show a correlation between diameter and grain size (Fig. 4.13), nor an increase in grain size towards their centre. Chilled margins were also not observed. These observations argue against formation of the enclaves' plagioclase-amphibole crystal framework during cooling of the enclave magma *after*

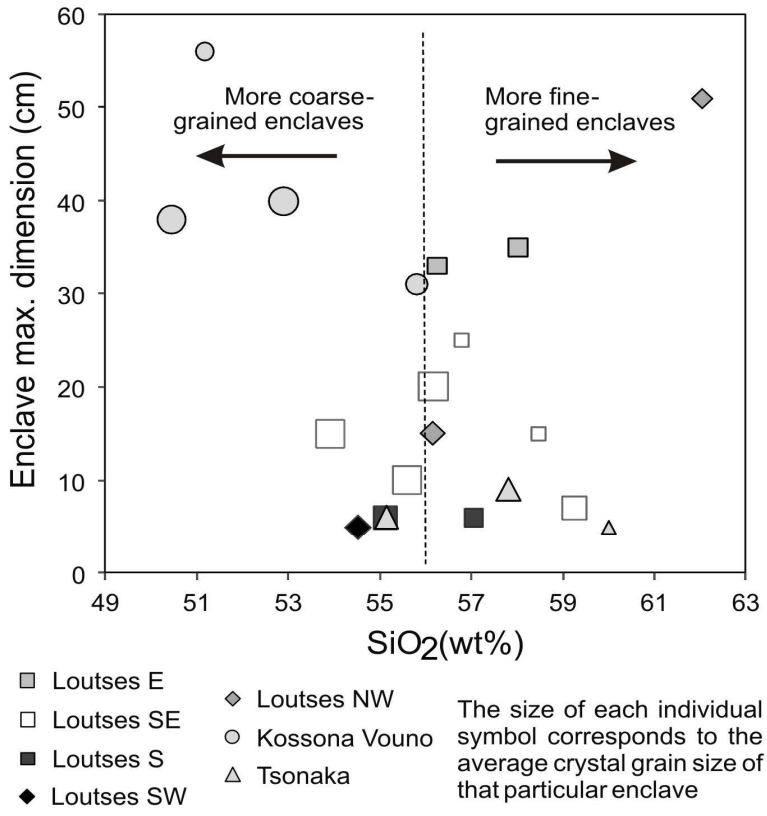

Figure 4.13 *Diagram showing the lack of correlation between the enclaves' locality* (symbols), *their dimension* (Y-axis) *and their average grain size* (individual size of the symbols). However, there seems to be a negative correlation between the silica content of the Delta 2 enclaves and their average grain size.

it has been distributed throughout the host magma as mafic droplets.

Most Delta 2 enclaves have a homogeneous grain size, favouring the other end-member model which envisages a less forceful replenishment of mafic magma that stagnates at the bottom of the felsic magma chamber. Thermal equilibration then forces the mafic magma to crystallise, with the resulting crystal size being a function of depth beneath the cooler, more felsic magma. As crystallisation continues, the residual mafic magma becomes increasingly saturated in volatile phases and crystallisation-induced vesiculation can subsequently decrease the density of the mafic magma. When the mafic magma's density thereby becomes lower than that of the overlying felsic magma, the (by now partially crystallised) mafic magma rises and physically disperses within the host magma. In this context, finely crystalline enclaves are formed close to the interface of the two magma bodies where contrast in temperature and composition is largest, whereas coarsely crystalline enclaves are formed deeper in the mafic magma body (inter alia Coombs et al., 2002; Martin et al., 2006a). Enclave dimensions are hereby unrelated to their grain size as the partially crystallised 'mafic foam layer' only starts to break up during ascent and dispersion into the felsic magma.

The Delta 2 unit has some large clusters of enclaves with identical grain size but varying shapes and dimensions ('monogenetic swarms' following the nomenclature of Didier and Barbarin, 1991) - Fig. 4.3G). These enclave clusters are therefore interpreted as remnants of the disaggregation process of mafic magma into smaller enclaves during ascent and eruption of the felsic host magma, equivalent to similar enclave groups found in the young Santorini lavas (Martin et al., 2006b).The plagioclase-amphibole phenocryst framework typical of the Delta 2 enclaves is therefore thought to have crystallised whilst the mafic enclave magma ponded beneath the felsic magma. Large crystals across host-enclave boundaries, and the presence of glass, microlites and rounded vesicles in all enclaves, indicate that the mafic magma was still above its solidus at the start of post-crystallisation disaggregation in the felsic host rock magma.

The enclave formation of the Delta 2 unit is thus intermediate to the two end-member models described above: a mafic magma injection that starts to crystallise at the bottom of a more felsic magma chamber, but which is dispersed throughout the latter when it is still partially liquid. Coombs et al. (2002) showed that in comparable arc settings only 35 volume % of incoming andesitic magma needs to crystallise to trigger a density inversion relative to the dacitic host magma. Martin et al. (2006b) found that in similar Santorini enclaves plagioclase crystallinities greater than ~30 vol.% resulted in a touching plagioclase framework, coherent and viscous enough to withstand volatile exsolution and enclave transport. Their experiments showed that frameworks composed of high-aspect ratio crystals (crystallising closer to felsic magma) are weaker so that they break up more easily in response to vesicle expansion. Enclave magma with low-aspect ratio crystals (formed lower in the mafic magma layer) turned out to be stronger and therefore more easily preserved as vesicular, partially-crystalline mafic enclaves. Delta 2 enclaves that are coarse-grained have fewer vesicles, lower crystal aspect ratios, more framework-phenocrysts and less groundmass than fine-grained enclaves – in agreement with Martin et al. (2006b). Fine-grained Delta 2 enclaves, on the other hand, tend to be more silica-rich (Fig. 4.13) and contain more macro-phenocrysts with disequilibrium textures than the coarse-grained enclaves. This can be ascribed to their initial crystallisation location: fine-grained enclaves crystallised closer to the mafic-felsic boundary, where they are more exposed to physical interaction with the overlying host magma (and its crystals) than in the lower regions of the mafic magma layer. It is however unclear how much of the mafic magma's phenocryst framework was already developed prior to disaggregation into the felsic magma as mafic enclaves. Large crystals with disequilibrium features petrographically indistinguishable from host rock macro-phenocrysts commonly occur in enclaves and sometimes even straddle the boundary between both lithologies (Fig. 4.4-4.5-4.6). Such macro-phenocrysts probably originate from the felsic magma and have been incorporated into the mafic enclave magma when the latter 1) forcefully intruded the magma chamber, 2) crystallised near the boundary with the overlying felsic magma, and 3) physically interacted with the felsic host rock magma as it was disaggregated into enclaves. So whereas the enclaves' lack of chilled margins or inward increasing grain size contradicts formation of the enclaves as almost completely

liquid magma pockets in a crystal-bearing felsic host magma, their crystal framework can not have been completely rigid prior to their disaggregation into their host magma as they seem have exchanged (macro-)phenocrysts with the latter upon their incorporation. The enclaves phenocryst framework is thereby interpreted to have been partially formed whilst the mafic magma differentiated at the bazse of the magma chamber and to have then been further developed after incorporation into the overlying host rock magma.

4.4.3 Magma mingling and mixing

Interpretation of field observations and petrographic data revealed that enclaves and host rock represent a mafic and a more felsic magma, respectively, which interacted with one another both before and whilst the mafic enclaves were dispersed throughout the felsic host. Chappell (1996) defines mingling as 'the combination of two components in a way that they remain individually identifiable'. In the Delta 2 volcanic unit, mingling is thus represented by the presence of enclaves in host lavas (Fig. 4.3) and magmatic flow banding (Fig. 4.3A). It is however unlikely that this exclusively involved physical dispersion, without any chemical interaction between the mingling magmas. Complete combination of two components into one homogenous hybrid magma, on the other hand, was originally defined as 'mixing' (Chappell, 1996). The term 'mixing' is however often used to describe any process between purely mechanical mingling of two magmas and their complete geochemical homogenisation – partially due to the difficulty of confidently discriminating between these 2 processes. Mixing will therefore refer throughout this work to the process by which two magmas are physically *and* chemically combined.

Mineral textures of resorption, replacement by a different mineral assemblage, and growth of new rims around a crystal (of the same mineral or of (a) different mineral(s)) are widespread in both enclaves and host rocks (Fig. 4.4, 4.5 and 4.6) and indicate disequilibrium between a mineral phase and its surroundings. Caution must be taken, however, when interpreting such chemico-physical disequilibria between single minerals and their host liquid as they do not only result from mixing of different magmas but can also reflect degassing or changes in temperature/ pressure within the closed system of a single magma. The presence of both quartz and Mg-rich olivine, observed in the same Delta 2 samples which furthermore lack any clues to incorporation of quartz- and/or olivine-rich xenoliths, is a strong indication of mixing between two mineralogically different magmas.

4.4.4 Other processes involved in the petrogenesis of the Delta 2 volcanic unit

Couch et al. (2001) showed that ponding of a hotter magma at the base of a magma chamber will result in a thermal boundary layer in the overlying felsic magma which can become unstable in as little as tens of days. This heated felsic magma, with resorption and disequilibrium textures in its phenocrysts due to the increased temperature, will form plumes into the above cooler felsic magma and induce **convective self-mixing** – resulting in subtle geochemical differences within different parts of the magma chamber. Some of the petrographic textures frequently observed in Delta 2 samples (juxtaposition of fully sieve-textured subhedral and unsieved euhedral plagioclase crystals; of normally and inversely zoned minerals or of euhedral amphibole and partially resorbed, or completely replaced amphibole crystals, ...) are also described by Couch et al. (2001), supporting a potential role for convective self-mixing in the petrogenesis of the Delta 2 rocks.

Delta 2 host rocks have large amounts of (macro-)phenocrysts and their enclaves mainly consist of a crystal framework of randomly oriented plagioclase and amphibole. The high degree of crystallinity of both rock types, together with the presence of newly crystallised rims on plagioclase and amphibole (interpreted to have formed after the mafic injection) suggest that **crystallisation** was also an important process for both host rock and enclave magma. Crystallisation in a low viscosity, crystal-poor mafic melt is likely to happen as *fractional (or Rayleigh) crystallisation*, where the crystallised minerals are progressively removed from the cooling magma. Within more viscous, felsic magmas the

presence of other crystals can however hinder the gravitational settling of newly formed minerals, which then remain in contact with the crystallising melt. The process by which there is a complete chemical equilibrium between this remaining melt and all crystallising phases is referred to as *equilibrium (or batch) crystallisation* (Albarède, 1995; Sha, 2012). A combination of fractional and equilibrium crystallisation is common since neither pure fractional crystallisation, nor equilibrium crystallisation alone, are likely to occur in natural igneous rocks. Whether it is thereby rather fractional than equilibrium crystallisation that dominates the concentration evolution of a certain element in a magmatic system depends on diffusion rates, crystal growth rates, crystal sizes and crystal magmatic residence times for the minerals in which the element is compatible (Sha, 2012).

As crystallisation of a magma usually happens whilst it resides in the lithosphere, this process is often accompanied by **assimilation** of wall rock (DePaolo, 1981). Magma rising from the source area in the mantle wedge is thought to stop either at the base of the crust or somewhere within the lower or upper crust. The combination of assimilation and crystallisation is therefore reflected in a more crustally-enriched isotopic signature with increasing differentiation. Despite the absence of crustal xenoliths in the Delta 2 rocks, isotope geochemistry reveasl that crustal assimilation also did play a role in the differentiation of the Delta 2 magmas (see Fig. 4.12).

The presence of zircon as inclusions in macro-phenocrysts of the Delta 2 host lavas is somewhat unusual in a volcanic setting (Fig. 4.4F). These zircons are euhedral and show clear oscillatory zoning (Fig. 4.14) which suggests an igneous origin of undisturbed crystallisation from core to rim – rather than a xenocrystic origin through wall rock assimilation. Applying the zircon saturation thermometry equations of Hanchar and Watson (2003) to the whole rock major element and Zr concentrations of the Delta 2 host rocks results in zircon crystallisation temperatures below the solidus of felsic magmas (725-760°C). So by the time Delta 2 host rock magmas were crystallising these zircons, they would have been too viscous to be able to erupt (Pistone et al., 2013). This contradiction between the presence of zircons in Delta 2 lavas and the immobility of their host magma inferred from its chemical composition therefore suggests the presence, at some stage, of a more evolved magma – or involvement of a sub-volcanic pluton. As none of the Delta 2 rocks contain K-feldspar, the more crystal-rich protolith from which the zircon-containing macro-phenocrysts are derived is thought to be a felsic crystal mush rather than a sub-volcanic plutonic rock. Furthermore, the macro-pheno-crysts hosting euhedral zircons usually show intense disequilibrium features and all quartz grains observed in the Delta 2 rocks are embayed crystals. The igneous zircon crystals can therefore be explained by **partial melting** of an inferred crystal-rich host magma from which these zircons originally crystallised. Whether it was rather *equilibrium (batch*) *melting* or *fractional (Rayleigh) melting* can not be easily deter-mined, but the high crystallinity inferred for this zircon-containing crystal mush renders effective removal of melt fractions unlikely, thus favouring equilibrium melting.

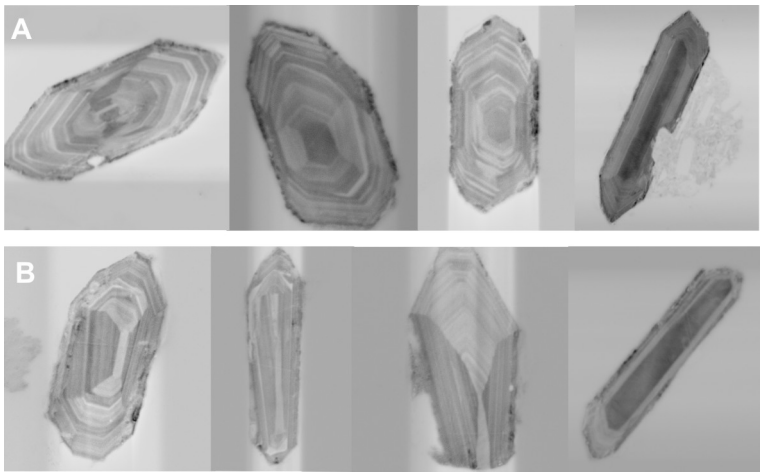

Figure 4.14.*Cathodeluminiscence pictures of typical zircons* separated from (A) Loutses S flow host rock DPM28, and from (B) Tsonaka host rock DPM42. Crystals are approximately 30 to 100 µm wide, and 100 to 200 µm long.

Other mechanisms could also have contributed to the petrogenesis of the Delta 2 enclaves and their host rocks besides the differentiation processes already discussed above. Sisson and Bacon (1999) propose that rapidly crystallising mafic magmas injected between a more evolved, cooler

magma and its cumulates could undergo second boiling (= gas exsolution resulting from oversaturation in volatile phases due to crystallisation of non-hydrous minerals). This could in turn lead to overpressure within the mafic magma and eventual segregation of remaining mafic liquid into the overlying magma body. Such **filter pressing** – either gas-driven as a result from second boiling or due to gravitational collapse of a crystal framework – is another mechanism separating melt from crystals during crystallisation and differentiation of a magma. Partially crystallised, undercooled inclusions produced in magma mingling events are considered as one of the environments where gas-driven filter pressing could effectively lead to expulsion of fractionated liquids (Sisson and Bacon, 1999). The fact that the more silica-rich, finer grained enclaves have more vesicles than the more mafic, coarser grained ones might indicate a role for second boiling in the enclaves' petrogenesis – and hence minor involvement of gas-driven filter pressing.

Diffusion should also be mentioned as a process that potentially influenced the chemical composition of the Delta 2 rocks, since both trace element and isotopic equilibration between host rocks and their enclaves have been reported in igneous units elsewhere (i.e. Elburg, 1996; Feeley et al., 2008). The importance of trace element diffusion between liquids, solids or a liquid and a solid is still under debate, as well as the effectiveness of *thermally-driven diffusion (Soret effect)* relative to *chemical diffusion* and the exact physical mechanisms of diffusion between enclaves and their host rocks (see for example Grasset and Albarède, 1994; Perugini et al., 2003; Dominguez et al, 2011; Perugini and Poli, 2012). Due to the present-day limited understanding of this differentiation process, diffusion will not be further discussed in relation to the petrogenesis of the Saronic Gulf volcanic deposits.

4.4.5 Petrogenesis deduced from macro- and microscopic observations

Based on the microscopic observations that phenocrysts and microlites from both host rocks and enclaves are usually euhedral and show little to no overgrowth or replacement, they are inferred to have mainly formed in equilibrium with the final melt (now groundmass). Macro-phenocrysts commonly have a more subhedral habitus and often show complex disequilibrium textures (see section 4.2.3). They are therefore interpreted as 'antecrysts': crystals that did not crystallise from the magma in which they are now hosted but which do originate from the same magmatic system (Charlier et al., 2005; Jerram & Martin, 2008; Larrea et al., 2013). These antecrysts are thereby derived from a different magma that is either more primitive (e.g. Mg-rich olivine crystals now in intermediate-felsic Delta 2 host rocks) or more evolved (e.g. embayed quartz with a clinopyroxene reaction rim now in Delta 2 enclaves), or from the same magma batch but during crystallisation events that preceded the final stages of differentiation (e.g. euhedral zircon inclusions as relic from earlier crystallisation of the more felsic crystal mush). The overall petrogenetic history of the volcanic rocks of the Delta 2 unit is envisaged as follows (see figure 4.15):

A mafic magma (proto-magma of enclaves) replenishes the chamber of a relatively cold and felsic, largely crystallised magma (proto-magma of the host rocks) (Fig. 4.15A-B). The mafic magma is thereby hot and not very crystal rich in comparison to the felsic crystal mush. As it settles at the bottom of the magma chamber, the mafic magma will start to cool against the overlying crystal mush. The onset of this thermal equilibration between the two magmas will initiate crystallisation in the mafic magma and as silica-poor melts are generally of low viscosity, these crystallising minerals are easily removed by gravitational settling. As crystallisation and cooling continue, the mafic magma's viscosity will increase and later formed crystals can be isolated from the remaining melt either through complete overgrowth by a chemically different zone or by inclusion in other crystals. With further cooling, the mafic magma's viscosity keeps increasing and equilibrium crystallisation will gradually gain importance over fractional crystallisation. Host rocks often preserve clusters of large plagioclase, amphibole and biotite crystals, which are resorbed and/or replaced to varying extent and sometimes contain euhedral zircons. This suggests that (parts of) the more felsic, crystal-rich magma was originally more solidified but that it undergoes partial melting due to injection of the hotter, more mafic magma (Fig. 4.15A-B).

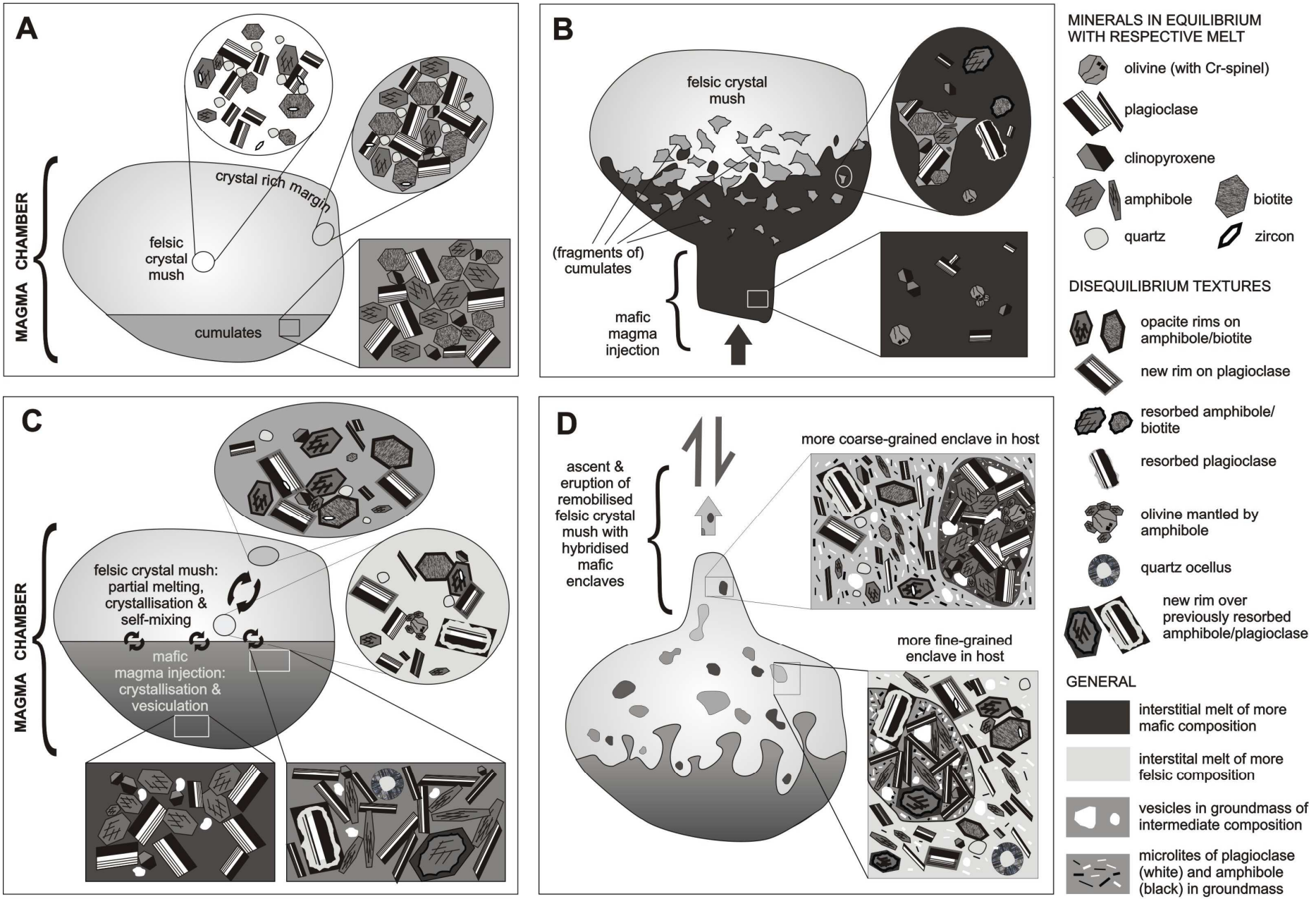

Figure 4.15. P*etrogenesis of the Delta 2 lavas and their enclaves*., deduced mainly from field observations and petrography.

While the felsic crystal mush experiences partial melting, its viscosity will decrease. Thermal equilibration between both magma bodies will thus also diminish the difference between their viscosities so that it will gradually become easier for the mafic enclave magma and felsic host rock magma to mingle. Subsequent mixing and mingling between the different products of the crystallising mafic magma and the partially melting felsic crystal mush can account for all macro- and microscopic observations.

Host rock *macro-phenocrysts* with complex zoning, replacement, resorption and/or dehydration textures are derived from the crystal mush that resided in the magma chamber prior to the mafic injection. Especially embayed quartz, macro-phenocrysts with euhedral zircon inclusions and holocrystalline micro-aggregates of eu- to subhedral macro-phenocrysts are thought to have such a 'restitic' origin due to partial melting of the initial crystal mush (Fig. 4.15B). Olivine crystals in the host rocks are thought to originate from the mafic magma because they are mantled by more intermediate mineral phases (amphibole, plagioclase, pyroxene) which probably formed upon incorporation of olivine antecrysts in the felsic magma. Some of the host rocks' *phenocrysts* also show severe disequilibrium features and are therefore inferred to have formed within the residual melt of the initial crystal mush shortly before the mafic injection. Most of the phenocrysts, however, are interpreted to have crystallised from the host rock magma's interstitial melt (mixture of residual and newly formed by partial melting) throughout the later phases of interaction between mafic magma and felsic mush. This crystallisation of the host rocks' phenocryst population probably occurred prior to eruption, when partial melting of the host crystal mush had ceased, as well as during the early stages of magma ascent to the surface. The host rock's *groundmass* is composed of glass and microlites and solidified during magma ascent and upon eruption. Vesicles also formed within the host rock during these final petrogenetic steps.

Enclaves are characterised by (a framework of) prismatic, randomly orientated *phenocrysts* which mainly formed whilst the mafic magma ponded below the felsic crystal mush. Fine-grained enclaves contain elongated phenocrysts with large crystal aspect ratios and reflect relatively fast cooling due to their proximity to the colder felsic crystal mush (Fig. 4.15C). In comparison, coarser grained enclaves have distinctly more tabular framework crystals with smaller crystal aspect ratios which reflect cooling and crystallising at a slower rate, further away from the boundary between the two magmas (Fig. 4.15C). The few *macro-phenocrysts* that are present in enclaves always show severe disequilibrium features and seem derived from the more felsic crystal mush. Such quartz, plagioclase, amphibole and biotite crystals could have been present at the bottom of the felsic magma chamber as (loose) cumulates when the mafic magma entered the chamber and engulfed them (Fig. 4.15B). Exchange of (macro-)phenocrysts between the two magmas probably also occurred at later stages when the partially crystallised enclaves were mingled with their host magma. Exsolution of volatile phases from the mafic magma could have started during this first phase of crystallisation at the bottom of the magma chamber and initiated, or at least promoted, this mingling of the enclave magma with the host magma. Upon dispersion throughout the felsic host magma, the enclave melt reacted with newly incorporated antecrysts of the felsic crystal mush and continued crystallisation of phenocrysts and construction of a randomly oriented crystal framework (Fig. 4.15D). The rounded vesicles and glassy *groundmass* however indicate that there was at least some interstitial melt left when the enclaves completely solidified upon ascent and eruption of their host rock magma.

4.5 Geochemical modelling

Field observations and petrography attest to intensive magma mingling and mixing in the petrogenesis of the Delta 2 lavas and their enclaves. Scatter in geochemical data however precludes simple mixing between a felsic magma and an injected more mafic magma. The geochemistry of the Delta 2 samples furthermore suggests involvement of crystal fractionation in the rocks' petrogenesis (Sc very compatible in the enclave suite - Fig. 4.8B, Zr less incompatible in the host rocks - Fig. 4.8D, Eu-anomaly more pronounced in the host rocks - Fig.4.9, …).

To better constrain the identity of crystallising minerals as well as the relative importance of the different processes on the host rocks' and enclaves' evolution, the geochemical variation of the Delta 2 unit was modelled as closely as possible using the RockWare IgPet software (2012 version; https://sites.google.com/site/igpethome/home). This software uses mathematical expressions for fractional crystallisation (FC) (Neumann et al., 1954), equilibrium crystallisation (EC) (Shaw, 1970) and binary mixing (Langmuir et al., 1978) as well as assimilation combined with fractional crystallisation (AFC – DePaolo, 1981). The outcome of such geochemical modelling is often non-unique and therefore most useful as a tool to disproof a certain hypothesis when the observed data can not be mathematically reproduced. If modelling a geochemical dataset is successful, it provides merely support for a hypothesis, never proof.

It seems that multiple differentiation processes were involved in the Delta 2 petrogenesis over a prolonged time, as well as (at least) two geochemically distinct magmas which exchanged crystals with one another. The main goal of modelling the Delta 2 geochemistry is to reconstruct the crustal differentiation processes that occurred in the magmas through testing the petrogenesis inferred from field observations and petrography (section 4.4.5). Identification and characterisation of potential mantle sources, subducted slab components and crustal contaminants will be further discussed with the geochemistry of the entire Methana peninsula in Chapter 5.

4.5.1 Major elements

Calculations applying the least squares regression of the major elements (after Bryan et al., 1969) are used to test the plausibility of crystal fractionation, partial melting and magma mixing, as well as to characterise the mineral assemblage(s) involved in crystallisation and/or melting. The mineral chemistry necessary for these calculations is presented in Table 4.2 and was preferentially taken from literature data of crystals from Methana's volcanic rocks (olivine, Fe-Ti-oxides, ortho- and clinopyroxene, plagioclase and amphibole; Mitropoulos and Tarney, 1992). In the absence of such compositional data for minerals from Methana, apatite (Gertisser et al., 2009) and Cr-spinel (Vagelli et al., 2009) from Santorini and biotite from Kos (Bachmann et al., 2010) were selected as most suitable alternatives (see Table 4.2). Whenever different geochemical data are available for minerals from Methana (Mitropoulos and Tarney, 1992), the most mafic mineral composition is used to model the enclaves' evolution and the most felsic mineral for the host rock calculations. When the IgPet software finds a mathematical solution to reproduce a certain rock composition, it also automatically calculates the rock's expected trace element composition by applying a fixed set of distribution coefficients (see Table 4.3). These trace element calculations are however not further discusses since they were only used as an extra check for the plausibility of a certain major element model solution but not for further geochemical modelling calculations.

Throughout all geochemical modelling attempts to reproduce the major element compositions of the **Delta 2 enclaves**, both orthopyroxene and Cr-spinel were rejected as crystallising mineral phases. Minor amounts of olivine crystallisation (< 3%) were only modelled as long as amphibole did not take part in the crystal fractionation process – which is very unlikely given the vast amount of amphibole phenocrysts in the enclaves' crystal framework. Fractional crystallisation of plagioclase, amphibole, clinopyroxene, Fe-Ti-oxides and apatite from an initial melt similar to most mafic enclave DPM36 can reasonably reproduce the major element composition of most felsic enclave DPM23 (see Table 4.4). This crystallising mineral assemblage agrees very well with the observed mineralogy of the enclaves and is therefore realistic under the Delta 2 magma chamber conditions. However, the model also shows that as much as 65.2% of DPM36 needs to be crystallised *and* removed, with only 34.8% of interstitial melt remaining to form DPM23 (Table 4.4). This means that the incompatible element contents should approximately triple from the most mafic to the most felsic enclave. Zirconium, Th and U contents in the most evolved Delta 2 enclaves are however only up to twice the amounts present in DPM36, indicating that no more than 50% of crystal fractionation occurred if all enclaves were derived

from most mafic enclave DPM36. It therefore seems that the more evolved enclaves could not have been derived directly from the most mafic ones through fractional crystallisation.

Mineral/**Oxide**	SiO_2	TiO_2	Al_2O_3	FeO	MnO	MgO	CaO	Na_2O	K_2O	P_2O_5	Cr_2O_3
Fe-Ti-oxide-1	2.98	10.72	2.36	80.7	0.68	1.75	0.81	0	0	0	0
Fe-Ti-oxide-2	0.47	6.34	2.4	88.92	0.46	1.41	0	0	0	0	0
Plag-An90-1	59.26	0	30.17	0	0	0	9.96	0.61	0	0	0
Plag-An50-2	60.46	0	30.78	0	0	0	5.64	3.12	0	0	0
ClinoPX-1	50.18	0.92	4.19	8.37	0	16.51	19.39	0.44	0	0	0
ClinoPX-2	49.95	0.88	4.02	8.17	0.2	13.79	22.45	0.52	0	0	0
Olivine-Fo87-1	40.35	0	0	12.55	0	47.1	0	0	0	0	0
Olivine-Fo75-2	38.4	0	0	22.96	0	38.64	0	0	0	0	0
Amph-1	43.65	1.9	13.36	10	0	16.4	11.92	2.77	0	0	0
Amph-2	47.71	1.14	8.51	14.39	0.45	14.43	11.72	1.67	0	0	0
OrthoPX	52.14	0	1.61	20.75	1.25	22.48	1.03	0.74	0	0	0
Cr-Spinel	0	0.49	21.47	23.03	0.21	13.49	0	0	0	0	41.32
Biotite	39.73	4.36	14.95	15.54	0.16	15.36	0	0.81	9.1	0	0
Apatite	0.23	0	0.01	0.43	0.18	0.09	55.7	0.09	0.03	43.23	0
Quartz	100	0	0	0	0	0	0	0	0	0	0

Table 4.2. Geochemical composition of the minerals used in the least squares regression calculations for the major element modelling. 1 = most mafic composition, used for enclave calculations; 2 = most felsic composition, used for host rock calculations; Plag = plagioclase; PX = pyroxene; Amph = amphibole. Data for Fe-Ti-oxides, plagioclase, pyroxenes, olivine and amphiboles from Mitropoulos and Tarney (1992); Cr-spinel from Vagelli et al. (2009); apatite from Gertisser et al. (2009); biotite from Bachmann et al. (2010).

The large range of major element composition represented by the enclaves was thus subdivided into the smaller groups previously identified from field observations, petrography and/or major and trace element geochemistry. The composition of the Loutses North enclaves ranges from DPM5 to DPM23, and can be explained by 24.2% of fractional crystallisation of the former to reproduce the latter (Table. 4.4). The optimal mineral assemblage of this crystallisation model is again the one observed in the samples themselves: plagioclase, amphibole, clinopyroxene, Fe-Ti-oxides and apatite (see Table 4.4). The Kossona Vouno enclaves represent the most mafic compositions amongst all Delta 2 samples, are the only enclaves which geochemically do not overlap with their host rocks and define an independent trend for MnO, Y, REE, … (see Fig. 4.7G, 4.8A). Attempts to model the Kossona Vouno enclaves' major element geochemistry exclusively through fractional crystallisation were not successful: about half of the most mafic magma (DPM36) would need to crystallise and fractionate in order for the remaining melt to have a composition similar to that of the least mafic enclave (DPM41A) (Table 4.4) - but Zr, Th, U, Nb and Ta show only a 1.5 times increase over the entire Kossona Vouno enclave range. The geochemical composition of the Kossona Vouno enclaves often defines a straight trend on the extension of which also many Delta 2 host rocks are located (Fig. 4.8C, G & Fig. 4.9A, C). A second modelling attempt therefore involved simple mixing between DPM36 and most felsic host rock DPM42. This resulted in a good match between the calculated and observed geochemistry of least mafic Kossona Vouno enclave DPM41A (SSR=0.071, Table 4.4) when 70% of DPM36 is mixed with 30% of DPM42 – inferring that binary mixing between a more mafic magma and a more felsic crystal mush was the main differentiation process involved in the petrogenesis of the enclaves of the Kossona Vouno area. Modelling the geochemical composition of

the Tsonaka enclaves by fractional crystallisation yielded an acceptable amount of crystallisation (31.8%, Table 4.4), but the calculated major element concentrations did not match the observed ones as well as for the Loutses North enclaves (SSR = 0.740 instead of 0.128, see table 4.4). Attempts to reproduce the composition of the Tsonaka enclaves by simple mixing also failed (Table 4.4). Eventually, a combination of both 19% of fractional crystallisation as well as mixing yielded an excellent reproduction of Tsonaka's least mafic enclave DPM49 (Table 4.4). The crystallising mineral assemblage in this AFC model is again amphibole, plagioclase, clinopyroxene, Fe-Ti-oxides and apatite.

Mineral/ **Element**	*Plagioclase*	*Olivine*	*ClinoPX*	*OrthoPX*	*Amph*	*Fe-Ti-oxide*
K	0.11	0.01	0.02	0.01	0.33	0.01
Rb	0.07	0.01	0.03	0.02	0.05	0.01
Ba	0.16	0.01	0.02	0.02	0.22	0.01
Sr	1.8	0.01	0.12	0.02	0.19	0.01
V	0	0	1.1	1.1	6	30
Cr	0.01	0.1	10	13	4.2	16
Ni	0.01	15	3.5	8	8	10
Zr	0.01	0.1	0.2	0.08	0.1	0.4
Sc	0	0	3	3	12.5	2
Cu	0	0	0	0	0	2
La	0.2	0.001	0.1	0.003	0.17	0.001
Ce	0.18	0.001	0.15	0.006	0.44	0.001
Nd	0.14	0.001	0.2	0.01	0.76	0.001
Sm	0.11	0.001	0.25	0.012	1.2	0.001
Eu	0.1	0.001	0.27	0.015	1.4	0.001
Gd	0.09	0.001	0.29	0.017	1.7	0.001
Dy	0.07	0.001	0.31	0.025	2.1	0.001
Er	0.05	0.001	0.33	0.035	2	0.001
Yb	0.03	0.001	0.35	0.05	2	0.001
Y	0.05	0.001	0.33	0.025	2.1	0.001

Table 4.3. Mineral/melt distribution coefficients (of the main minerals) used for the trace element calculations that are automatically carried out in IgPet based on the model solution provided by the major elements. These trace element concentrations are not further discussed in this work as they were only used as a secondary check to see how realistic a major element solution was. Abbreviations as in Table 4.2.

Based on field observations and petrography, the **Delta 2 host rocks** are inferred to have formed by partial melting of a crystal mush. This hypothesis was modelled with the IgPet software as inverted crystallisation: instead of reproducing the decrease in silica content that an interstitial melt would experience upon partial melting of a crystal mush, it was modelled as crystallising, from the least evolved host, those minerals interpreted to have undergone melting. The mathematical equivalent for the 'inverted partial melting model' presented here would be equilibrium crystallisation rather than fractional crystallisation. In IgPet, the difference between FC and EC depends on whether the mineral compositions change or stay constant throughout the differentiation interval, respectively. Since the mineral compositions used for these host rock calculations (the more felsic compositions, see Table 4.2) were kept constant throughout the crystallisation calculations, modelling of the Delta 2 host rocks indeed represents equilibrium crystallisation.

ENCLAVES	FC	Fe-Ti-oxide-1	Plag-An90-1	Clino-PX-1	Amph-Hbl-1	Apatite	F	SSR	EV
	Mixing	MafEM	%	FelEM	%	Hybrid			
DPM36 to DPM23 (ALL)	FC	2.6%	29.6%	8.7%	22.5%	1.6%	0.348	1.677	X
DPM5 to DPM23 (Loutses North)	FC	1.4%	9.0%	8.4%	4.9%	0.4%	0.758	0.128	V
Crystallisation Loutses North		*6%*	*37%*	*35%*	*20%*	*2%*	*Recalculated to 100%*		
DPM36 to DPM41A (Kossona Vouno)	FC	2.4%	21.3%	13.8%	12.6%	1.2%	0.492	0.997	X
DPM36 to DPM41A (Kossona Vouno)	Mixing	DPM 36	69.9%	DPM 42	30.1%	DPM 41A	NA	0.071	V
DPM53 to DPM49 (Tsonaka)	FC	2.6%	20.5%	/	8.2%	0.5%	0.682	0.740	X
DPM53 to DPM49 (Tsonaka)	Mixing	DPM 53	83.7%	DPM 42	16.3%	DPM 49	NA	2.898	X
DPM53 to DPM49 (Tsonaka)	FC & mixing	0.4%	1.1%	9.7%	7.4%	0.2%	0.812	0.022	V
		DPM 53	43.9%	DPM 42	37.4%	DPM 49			
Crystallisation Tsonaka		*2%*	*6%*	*52%*	*39%*	*1%*	*Recalculated to 100%*		
HOST ROCKS	***FC***	***Fe-Ti-oxide-2***	***Plag-An50-2***	***Clino-PX-2***	***Amph-Hbl-2***	***Apatite***	**F**	**SSR**	**EV**
	Mixing	***MafEM***	***%***	***FelEM***	***%***	***Hybrid***			
DPM4 to DPM42 (ALL)	*FC*	*0.5%*	*14.4%*	*4.4%*	*9.2%*	*0.4%*	0.711	0.220	V
Crystallisation all host rocks		*2%*	*50%*	*15%*	*32%*	*1%*	*Recalculated to 100%*		
DPM4 to DPM42 (ALL)	*Mixing*	*DPM 36*	*28.6%*	*DPM 42*	*71.4%*	*DPM 4*	NA	0.080	V

Table 4.4. Results of the attempt to model the Delta 2 unit's major element geochemistry using the IgPet software. FC : fractional crystallisation; MafEM = mafic end member; FelEM = felsic end member; hybrid = hybride magma resulting from mixing between MafEM and FelEM; F = fraction of remaining melt; SSR = sum of squared residuals (calculated using a weighting factor of 0.4 for SiO_2; 0.5 for Al_2O_3 and 1 for all other major element oxides); EV = evaluation, indicating the models interpreted to be less realistic with a red cross, and the ones that are plausible with a green V. For all host rocks, the Loutses North enclaves and the Tsonaka enclaves geochemical modelling indicated crystal fractionation as an important petrogenetic process. The mineral assemblages resulting from these models are recalculated to 100 wt% in order to allow comparison between one another and to use these crystallising mineral assemblages in the trace element geochemical modelling.

Resulting models indicate that quartz was probably not involved in the host rock's melting process. Biotite is only accepted in the models as long as there is no amphibole; but the Y contents and amphibole phenocrysts of the host rocks clearly indicate that the latter mineral also played a role in host rock differentiation after magma chamber replenishment. The mineral assemblage that likely crystallised from the least evolved host rock, DPM4, to form a residual melt that resembles the WR major element contents of most evolved host rock, DPM42, turns out to be the same as the enclaves' crystallising mineral assemblage: plagioclase, amphibole, clinopyroxene, Fe-Ti-oxides and apatite –

but with geochemically more evolved mineral compositions (see Table 4.2). These are also the main minerals observed in the host rocks' thin sections. The IgPet model further suggests that it is mainly plagioclase and amphibole (50% and 32%, respectively) that undergo partial melting, which agrees with the petrographic observation that most macro-phenocrysts with disequilibrium features are plagioclase and amphibole. Incorporation of 29% melt, generated by partial melting of the crystal cargo of the initial host magma, into DPM42 can successfully reproduce the major element contents of least felsic host DPM4 – approximated by an inversed model of fraction crystallisation (see Table 4.4).

The importance of mixing for the host rocks' composition was also investigated. Mixing of about 71% of the most felsic crystal mush (host rock DPM42) with 29% of the most mafic magma (enclave DPM36) thereby replicates the geochemistry of least felsic host DPM4 extremely well (see Table 4.4). The large differences in initial chemistry, temperature and viscosity expected for these magmas, however, imply a process of assimilation rather than true mixing since both magmas would need to reach a thermal equilibrium (and thus similar viscosity) before they can be efficiently mixed with one another. The excellent agreement of the geochemical mixing model with the observed compositions nevertheless indicates that assimilation played a role in the petrogenesis of more mafic host rocks.

4.5.2 Trace elements

Magma mixing and crystal mingling indicate that the petrogenesis of the Delta 2 magmas did not happen in a closed system and that whole rock data are unlikely to represent liquid compositions. An excellent reproduction of the Delta 2 trace element compositions through geochemical modelling is thus probably not obtainable. Instead, trace element modelling is used to further refine the Delta 2 petrogenesis inferred from the major element modelling: one differentiation process for all host rocks involving partial melting and mixing/assimilation; and up to three differentiation paths for the enclave magma. The mineral assemblages of plagioclase, amphibole, clinopyroxene, Fe-Ti-oxide and apatite that were identified from the enclave major element modelling are now used for further geochemical calculations involving the trace elements. Relative amounts of these 5 minerals within the crystallising assemblage are calculated from the two 'accepted' major element models for the Loutses North and Tsonaka enclaves. Recalculation of these mineral modes to 100% resulted in two different mineral assemblage compositions (see Table 4.4). These two mineral assemblages are further used in order to assess the plausibility of the bulk distributions coefficients chosen for the trace element geochemical models (see Table 4.5 and discussion below). Information on an element's compatibility in certain minerals given throughout the remainder of this section is based on distribution coefficient data from the GERM distribution coefficient database (http://earthref.org/KDD/). Amongst the most incompatible elements, Ba shows a kink in the overall Delta 2 trend - suggesting it is slightly less incompatible in the host rocks than in the enclaves (Fig. 4.10F). Cesium and Rb show a straight trend for the entire Delta 2 unit, but they also display scatter that is possibly related to the presence of biotite. Thorium is therefore chosen as variable on the X-axis to represent increasing differentiation: its concentration quadruples from the most mafic to the most felsic Delta 2 sample and it shows the least scatter (Fig. 4.8E).

The two different enclave trends observed in the Harker variation diagram for MnO (and to a lesser extent Al_2O_3) (Fig. 4.7G, H) re-emerge in an **Y versus Th diagram** (Fig. 4.16A). The Kossona Vouno series describe a rather flat trend that can be reproduced by simple mixing between the most mafic enclave and the most felsic host rock. The most evolved enclaves hereby represent about 70% of mafic magma and 30% of felsic crystal mush, in agreement with the major element modelling (Table 4.4). However, 10% of fractional crystallisation of the most mafic enclave concurrently with assimilation of the most evolved host (AFC; with an assimilation to fractional crystallisation ratio (=A/FC) of 0.7), also reproduces the Kossona Vouno enclave trend (Fig. 4.16A). As discussed above, a model involving assimilation is preferred to one of true mixing to obtain the major element compositions of less evolved lavas. The trace element calculations also indicate that the process of AFC requires a smaller amount of the felsic end member to be taken up by the mafic end member

than in case of simple mixing. Crystal fractionation is furthermore expected to occur when the mafic magma cools during mixing/mingling with the felsic crystal mush. The process of AFC is therefore more probable for the Kossona Vouno enclave series than simple mixing. The two mineral assemblages modelled in section 4.5.1 to fractionate from enclave magmas are i) the *plagioclase rich assemblage* with 37% plagioclase, 6% Fe-Ti-oxides, 35% clinopyroxene, 20% amphibole and 2% apatite; and ii) the *plagioclase poor assemblage* with 6% plagioclase, 2% Fe-Ti-oxides, 52% clinopyroxene, 39% amphibole and 1% apatite (Table 4.4). Yttrium is highly compatible in apatite, compatible in clinopyroxene as well as in amphibole, rather incompatible in Fe-Ti-oxides and very incompatible in plagioclase. With the IgPet modelled $D_{bulk}(Y)$ of 1.3 (= bulk distribution-coefficient of Y within the entire crystallising mineral assemblage; obtained via trial and error modelling calculations) and the D(Y) of plagioclase ($D_{plg}(Y)$) and Fe-Ti-oxides ($D_{FeTi-ox}(Y)$) taken as zero, we can calculate the $D_{(CMA)}(Y)$ (= the bulk distribution coefficient of Y in the compatible mineral assemblage) based on

$$D_{bulk}(Y) = 0.37*D_{plg}(Y) + 0.06*D_{FeTi-ox}(Y) + 0.57*D_{(CMA)}(Y) \quad \textit{(for the plagioclase rich assemblage)}$$

$$D_{bulk}(Y) = 0.06*D_{plg}(Y) + 0.02*D_{FeTi-ox}(Y) + 0.92*D_{(CMA)}(Y) \quad \textit{(for the plagioclase poor assemblage)}$$

These distribution coefficients for the mineral assemblages in which Y is compatible ($D_{(CMA)}(Y)$) are 2.3 and 1.4 for the plagioclase rich and the plagioclase poor mineral assemblage, respectively (Table 4.5). A $D_{(CMA)}^{max}(Y)$ can also be calculated from maximum D(Y) values found in literature (Table 4.5) and recalculation to 100% of the compatible minerals in the respective crystallising assemblages:

$$D_{(CMA)}^{max}(Y) = 0.35*D_{amph}^{max}(Y) + 0.61*D_{clinopx}^{max}(Y) + 0.04*D_{apatite}^{max}(Y) \quad \textit{(plagioclase rich)}$$

$$D_{(CMA)}^{max}(Y) = 0.42*D_{amph}^{max}(Y) + 0.57*D_{clinopx}^{max}(Y) + 0.01*D_{apatite}^{max}(Y) \quad \textit{(plagioclase poor)}$$

This GERM-derived $D_{(CMA)}^{max}(Y)$ is 2.2 for the plagioclase rich assemblage, and 1.8 for the plagioclase poor assemblage (Table 4.5). Comparison of the IgPet derived $D_{(CMA)}(Y)$ with the GERM calculated $D_{(CMA)}^{max}(Y)$ as well as with the maximum D(Y) values found in literature suggest that the Kossona Vouno enclave series probably fractionated a plagioclase rich mineral assemblage (similar to one modelled for the Loutses North enclaves) rather than a plagioclase poor assemblage (Table 4.5).

All enclaves outside the Kossona Vouno series group into a different trend, starting with higher Y contents at lower SiO_2 content which then decrease rapidly in a non-linear way with increasing silica, pointing towards crystal fractionation as the dominant differentiation mechanism (Fig. 4.8A). Trace element modelling shows that about 25% of FC suffices to reproduce this second main enclave series of Y compatibility (Fig. 4.16A). This result is similar to the major element calculations where 19-24% of FC reproduces the Tsonaka and Loutses North enclaves, respectively (Table 4.4). The above outlined calculations for the Kossona Vouno series were also carried out for the main enclave series. An IgPet modelled $D_{bulk}(Y)$ of 2.6 thereby translates into IgPet derived $D_{(CMA)}(Y)$ values of 2.8 and 4.6, for the plagioclase-poor and the plagioclase-rich mineral assemblage respectively (Table 4.5). A value of 4.6 is towards the high side of the range found in literature (Table 4.5) as well as higher than 2.4, the $D_{(CMA)}^{max}(Y)$ calculated for the plagioclase-rich assemblage (Table 4.5). The $D_{(CMA)}^{max}(Y)$ calculated for the compatible minerals of the plagioclase poor assemblage is however lower, namely 2.2. This value is closer to both the IgPet derived $D_{(CMA)}$ of 2.8 for the plagioclase poor mineral assemblage as well as the maximum GERM D values for the minerals in which Y is compatible (Table 4.5). It therefore seems more likely that the main enclave series fractionated mostly clinopyroxene and amphibole, in a plagioclase poor mineral assemblage (Table 4.4). That 25% of FC of exactly the plagioclase poor mineral assemblage calculated for the Tsonaka enclaves (Table 4.4) produces the Y differentiation

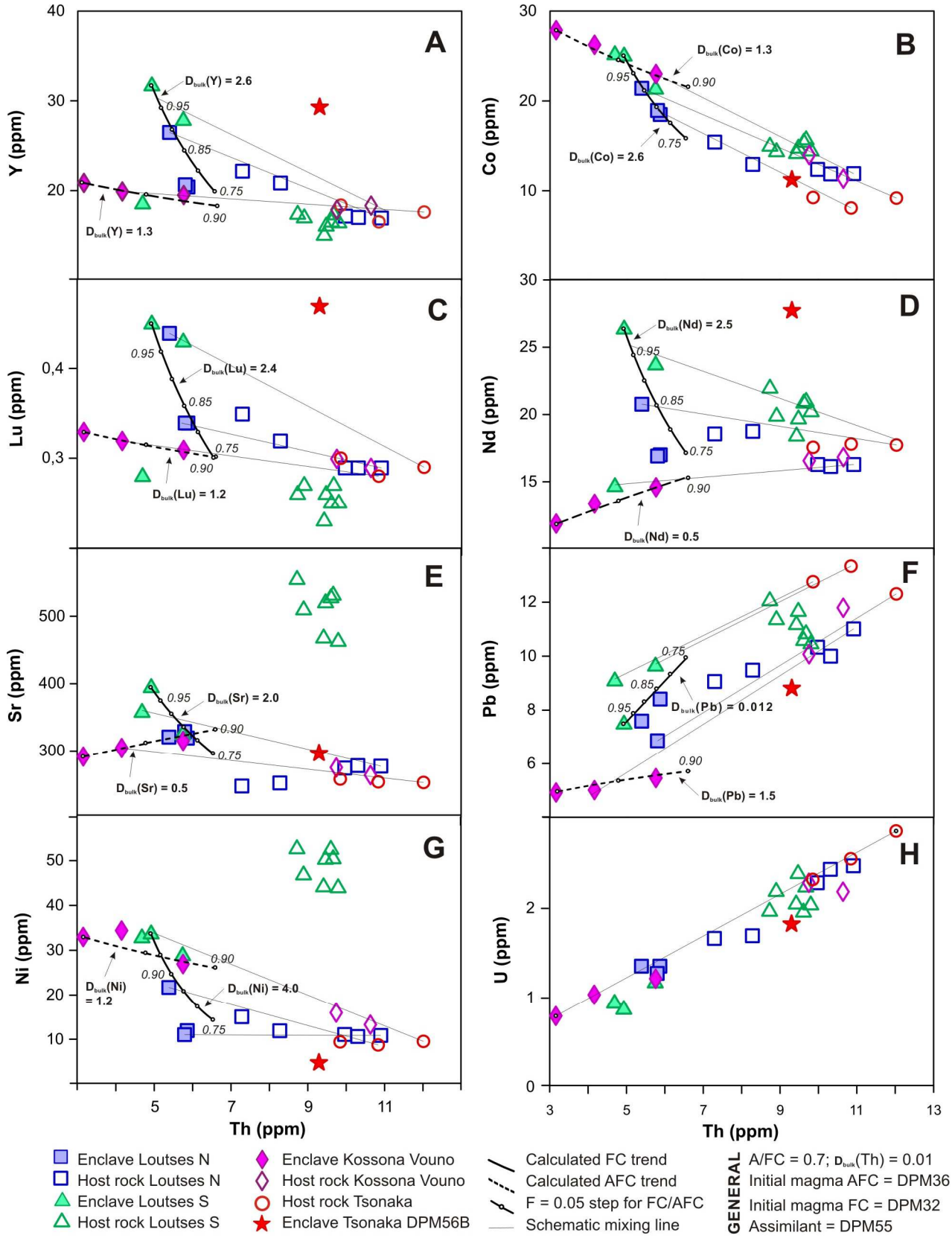

Figure 4.16. *Trace element modelling of the Delta 2 host rock and enclave compositions* using the RockWare IgPet software (2012 version; https://sites.google.com/site/igpethome/home). See text for discussion.

trend of the main enclave series is however unlikely, as it is impossible to get a bulk D of 2.8 for an assemblage that mainly consists of clinopyroxene (D<2.4) and amphibole (D<1.5) and only small amounts of apatite (D<20). If AFC is used to model the main enclave series, only A/FC ratios of about 0.1 can reproduce this trend – or unrealistically high D_{bulk}(Y) values. Fractional crystallisation therefore remains most appropriate to model the petrogenesis of the main enclave trend.

Subsequent mixing between the more evolved host rocks and a less mafic enclave from either the Kossona Vouno or main enclave series reproduces most of the host rock samples and more intermediate enclaves. Only some of the Loutses South host rocks seem to plot slightly below these mixing trends whereas enclave DPM56B plots well above the mixing lines (Fig. 4.16A).

In comparison to Y, Co is more compatible in clinopyroxene and amphibole, similarly incompatible in plagioclase but compatible in Fe-Ti-oxides and incompatible in apatite. The **Co versus Th variation diagram** seems to reflect a single decreasing trend with increasing differentiation for the Delta 2 unit, but individual modelling of the Kossona Vouno and the main enclave trend (with the same parameters as the ones used for Y calculations) surprisingly reproduces all enclaves' compositions (Fig. 4.16B). The more felsic enclaves of either trend are hereby obtained at F values (=fraction of remaining melt) similar to the ones found for the Y modelling (Fig. 4.16A, B). Figure 4.16B also reflects higher compatibility of Co within the crystallising assemblage of the main enclave trend than in the Kossona Vouno trend. Taking into account the minerals in which Co is compatible as well as the IgPet modelled $D_{(bulk)}$ for the main enclave series (2.6, Table 4.5), calculations similar to the ones carried out for the Y trace element model render a $D_{(CMA)}$(Co) value of 2.8 and 4.3 for the plagioclase poor and rich assemblage, respectively. Since both $D_{(CMA)}$(Co) fall within the range of values found in literature but the $D_{(CMA)}$(Y) calculated from the plagioclase rich assemblage was found to be unrealistic for the main enclaves series, the 2.8 value of the plagioclase poor assemblage is preferred for Co. The IgPet derived D_{bulk}(Co) of 1.3 for the Kossona Vouno trend translates into a $D_{(CMA)}$(Co) value of 1.4 and 2.1 for the plagioclase poor and rich assemblage respectively (Table 4.5). The plagioclase rich mineral assemblage is however preferred for the 10% AFC of the Kossona Vouno series, as this value agrees best with its relatively high amounts of Fe-Ti-oxides (10%) and clinopyroxene (57%) and the high compatibility of Co in these minerals. So as for the Y geochemical model, a plagioclase and clinopyroxene rich mineral assemblage suits the 10% AFC differentiation trend of the Kossona Vouno series best, whereas the plagioclase poor mineral assemblage results in more realistic distribution coefficients for the 25% FC differentiation of the main enclave series. Simple mixing of more intermediate enclaves with felsic end-member host rocks replicates the rest of the Delta 2 Co contents – including the Loutses South host rocks and enclave DPM56B (Fig. 4.16B).

The contrasting petrogenetic models observed in the Y versus Th diagram for the two enclave series (Fig. 4.16 A) can be extrapolated to the MREE (Y is geochemically equivalent to Ho) and appear to be also present in the HREE and LREE (see Fig. 4.16C and D for **Lu and Nd**, respectively). Both Lu and Nd trends of the main enclave series and the Kossona Vouno series can be modelled with the same parameters as before: 10% of AFC for the Kossona Vouno enclaves; 25% of FC for the main enclaves - but they render different values for $D_{(bulk)}$. The bulk distribution coefficient deduced for the Kossona Vouno series remains smaller than the one of the main enclave trend – around or below 1, reflecting an overall incompatibility of the REE in the crystallising mineral assemblage as expected from literature D(REE) values. The IgPet derived $D_{(CMA)}$(Lu) and $D_{(CMA)}$(Nd) of the different mineral assemblages are compared to the equivalent literature derived $D_{(CMA)}^{max}$(Lu) and $D_{(CMA)}^{max}$(Nd) (Table 4.5). This shows that the most probable distribution coefficients for the Kossona Vouno series are usually near the upper limit of the literature values – which was also the case for Y. The REE distribution coefficients most suitable for the main enclave series are however always well above the literature derived maximum values (Table 4.5), suggesting that for these elements the 25% FC model with the plagioclase poor assemblage is not entirely correct. Simple mixing between more mafic enclaves and more felsic hosts seems to reproduce most other Delta 2 samples - except for Tsonaka enclave DPM56B (and the Loutses South hosts for Lu) (Fig. 4.16C, D).

		IgPet[1] modelled D values				GERM[2] derived max (average) D values				
Y	*CMA*	*$D_{(bulk)}$*		*$D_{(CMA)}$*		*Melt*	*Amph*	*Clinopx*	*Apatite*	*$D_{(CMA)}^{max}$*
	Amph + Clinopx + Apatite	*Kossona Vouno*	1.3	**37% plg**	**2.3**	Basaltic	0.6 (0.35)	2.4 (0.65)	13.3	**2.2**
				6% plg	1.4					1.8
		Main enclave	2.6	37% plg	4.6	Andesitic	1.5 (1.1)	2.4 (1.0)	20	2.4
				6% plg	**2.8**					**2.2**
Co	*CMA*	*$D_{(bulk)}$*		*$D_{(CMA)}$*		*Melt*	*Amph*	*Clinopx*	*FeTi-ox*	*$D_{(CMA)}^{max}$*
	Amph + Clinopx + FeTi-ox	*Kossona Vouno*	1.3	**37% plg**	**2.1**	Basaltic	2	2 (1.3)	3.4 (2.2)	**2.1**
				6% plg	1.4					2.0
		Main enclave	2.6	37% plg	4.3	Andesitic	6.1 (4.0)	5.5	6.0 (4.0)	5.7
				6% plg	**2.8**					**5.8**
Lu	*CMA*	*$D_{(bulk)}$*		*$D_{(CMA)}$*		*Melt*	*Amph*	*Clinopx*	*Apatite*	*$D_{(CMA)}^{max}$*
	Amph + Clinopx + Apatite	*Kossona Vouno*	1.2	37% plg	2.1	Basaltic	1.0 (0.7)	1.12 (0.9)	3.7 (2.0)	1.2
				6% plg	**1.3**					**1**
		Main enclave	2.4	37% plg	4.2	Andesitic	2.1 (1.3)	2.0 (1.2)	13.8 (8.0)	2.5
				6% plg	**2.6**					**2.2**
Nd	*CMA*	*$D_{(bulk)}$*		*$D_{(CMA)}$*		*Melt*	*Amph*	*Clinopx*	*Apatite*	*$D_{(CMA)}^{max}$*
	Amph + Clinopx + Apatite	*Kossona Vouno*	0.5	**37% plg**	**0.9**	Basaltic	0.7 (0.4)	0.69 (0.3)	14	**1.2**
				6% plg	0.5					0.8
		Main enclave	2.5	37% plg	4.4	Andesitic	1.2 (0.7)	0.86 (0.7)	32.8	2.3
				6% plg	**2.7**					**1.3**
Sr	*CMA*	*$D_{(bulk)}$*		*$D_{(CMA)}$*		*Melt*	*Plagioclase*		*Apatite*	*$D_{(CMA)}^{max}$*
	Plagioclase + Apatite	*Kossona Vouno*	0.5	**37% plg**	**1.3**	Basaltic	3.7 (1.8)		1.3 (1.1)	**3.6**
				6% plg	7.1					3.4
		Main enclave	2.0	**37% plg**	**5.1**	Andesitic	5.3 (2.1)		1.4 (1.3)	**5.1**
				6% plg	28.6					4.8
Pb	*CMA*	*$D_{(bulk)}$*		*$D_{(CMA)}$*		*Melt*	*Plagioclase*			*$D_{(CMA)}^{max}$*
	Plagioclase	*Kossona Vouno*	1.5	**37% plg**	**4.1**	Basaltic	2.7 (0.9)			**2.7**
				6% plg	25,0					2.7
		Main enclave	0.012	37% plg	0.03	Andesitic	1.1 (0.61)			1.1
				6% plg	**0.2**					**1.1**
Ni	*CMA*	*$D_{(bulk)}$*		*$D_{(CMA)}$*		*Melt*	*Amph*	*Clinopx*	*FeTi-ox*	*$D_{(CMA)}^{max}$*
	Amph + Clinopx + FeTi-ox	*Kossona Vouno*	1.2	**37% plg**	**2.0**	Basaltic	9	10 (5.6)	6.5	**9.3**
				6% plg	1.3					9.5
		Main enclave	4.0	37% plg	6.6	Andesitic	6.8	9.0 (4.6)	5.5	6.2
				6% plg	**4.3**					**8**

[1] RockWare IgPet software (2012 version; https://sites.google.com/site/igpethome/home);
[2] GERM distribution coefficient database (http://earthref.org/KDD/);
CMA = compatible mineral assemblage - the minerals in which a certain trace element is compatible; Amph = amphibole; Clinopx = clinopyroxene, FeTi-ox = Fe-Ti-oxides;
$D_{(bulk)}$ = bulk distribution coefficient of trace element within the entire crystallising mineral assemblage; $D_{(CMA)}$ = average distribution coefficient of trace element for the part of the mineral assemblage in which it is compatible; $D_{(CMA)}^{max}$ = maximum $D_{(CMA)}$ calculated from the highest D values found in literature;
37% plg & 6% plg = the mineral assemblages modelled to crystallise in order to replicate the major element geochemistry of the Loutses North and Tsonaka enclaves, respectively, recalculated to 100% (see Table 4.4)
Black and bold indicates the mineral assemblage who's IgPet derived $D_{(CMA)}$ is most probable, taking into account the $D_{(CMA)}$ of the other mineral assemblage and the maximum (and average) GERM D values, the GERM-derived $D_{(CMA)}^{max}$ and relative amounts of compatible minerals it presents.
Green and bold indicates those most probable mineral assemblages for which the IgPet derived $D_{(CMA)}$ is lower than or equal to the equivalent literature derived $D_{(CMA)}^{max}$ – indicating that the specific trace element model produces realistic distribution coefficients.

Table 4.5. Results of IgPet geochemical modelling in an attempt to reproduce the Delta 2 unit's trace element geochemistry: comparison of distribution coefficients derived from geochemical modelling with those calculated from literature. See text for discussion.

In the **Sr versus Th variation diagram** the modelled trends of 10% AFC for the Kossona Vouno enclaves and about 25% of FC for the main enclave series are less obvious than in the previous diagrams (Fig. 4.16 E). Strontium, a LILE compatible mainly in plagioclase and apatite, shows an increasing differentiation trend for the Kossona Vouno series, with an overall incompatible $D_{(bulk)}(Sr)$ = 0.5 (Table 4.5). Comparison of the IgPet derived $D_{(CMA)}(Sr)$ and literature derived $D_{(CMA)}^{max}(Sr)$ values for the plagioclase rich and poor assemblage shows that only the former mineral assemblage renders a realistic $D_{(CMA)}(Sr)$ value of 1.3 (Table 4.5). Despite the fact that up to now trace element modelling of the main enclave series always favoured the plagioclase poor mineral assemblage, this assemblage renders unrealistic high values for Sr compatibility. It is the plagioclase rich assemblage that results in the more plausible distribution coefficient for Sr in the compatible mineral assemblage ($D_{(CMA)}(Sr)$ = 5.1; Table 4.5). Simple mixing between the most felsic host rocks and more evolved enclaves can explain the Sr contents of most Delta 2 samples – apart from the Loutses South host rocks with their distinctively high Sr concentrations (Fig. 4.15E).

The **Pb versus Th diagrams** show that geochemical modelling of the Pb concentrations seems to further support a more plagioclase and clinopyroxene rich mineral assemblage for the Kossona Vouno differentiation and a more amphibole rich mineral assemblage for the main enclave petrogenesis (Fig. 4.16F). But the lack of correlation between data and model, both on the graph and in calculated $D_{(CMA)}(Pb)$ values, also indicates that these models are not entirely correct (Table 4.5). Perhaps an accessory mineral phase, not identified in the major element models, also played a role in the Pb geochemistry of the Delta 2 rocks.

For **nickel**, another element compatible in clinopyroxene, amphibole and Fe-Ti-oxides, the modelled $D_{(CMA)}(Ni)$ values agree well with the literature-derived data (Fig. 4.16G and table 4.5). Mixing between further differentiated enclaves and most evolved host rocks then reproduces the Ni composition of most intermediate volcanic rocks (Fig. 4.16G). Only the geochemistry of the Ni-rich Loutses South host rocks remains unexplained since they plot well above any possible mixing trend between enclaves and host rocks.

Based on Fig. 4.16A-G and Table 4.5, trace element modelling reflects only two different enclave petrogeneses. The Kossona Vouno series seems to have undergone about 10% of AFC, with assimilation of the most felsic host rock and crystallisation of a mineral assemblage similar to 37% plagioclase, 6% Fe-Ti-oxides, 35% clinopyroxene, 20% amphibole and 2% apatite. Trace element modelling for the main enclave series was less successful for Y, Lu and Nd, but overall suggests that differentiation involved up to 25% of FC of a mineral assemblage with less plagioclase, Fe-Ti-oxides and apatite but more amphibole and clinopyroxene than the mineral assemblage involved in the petrogenesis of the Kossona Vouno enclaves. Simple mixing between intermediate enclaves and felsic host rocks can account for most other Delta 2 samples, apart from the Loutses South host rocks and enclave DPM56B. For trace elements equally incompatible as Th, the entire Delta 2 geochemical data range falls nicely along one straight trend. In the case of **U** for example (Fig. 4.16H) this could reflect simple mixing between the most primitive and most evolved sample (which is however precluded from major and trace element modelling) or constant and similar chemical affinities for U in all crystallising and partial melting systems.

4.5.3 Radiogenic isotopes

Since the radiogenic isotope composition of a magma remains unchanged during fractional and/or equilibrium crystallisation, variation of isotopic composition can only be due to mixing processes involving different sources that participated in the rocks' petrogenesis. In the next paragraphs Sr, Nd and Pb isotope ratios will be used to further constrain the sources that contributed to the genesis of the Delta 2 magmas, as well as to test the hypotheses that emerged from major and trace element modelling above: (1) the spread in host rock geochemistry (apart from the Loutses South samples) is mainly explained by partial melting of the most felsic host rock and mixing with (more evolved)

enclaves; (2) there is no single model that can account for the geochemical composition of all enclaves; (3) the Kossona Vouno enclaves (and Loutses South enclave DPM29B) represent the most primitive Delta 2 samples having undergone about 10% of AFC in the felsic magma chamber; (4) all other enclaves are more evolved to start with and seem to have undergone about 25% of fractional crystallisation whilst ponding in the felsic magma chamber.

Most of the Sr and Nd isotopic spread of the Delta 2 unit can be explained by simple mixing between two end members: the most mafic enclave DPM36 and the most 'crustal' host rock DPM66 (Fig. 4.17A). This binary mixing reproduces the Sr and Nd isotopic composition of all host rocks except for the ones sampled from the Loutses South area. The Loutses South host rocks plot significantly to the left of the main mixing trend, defining a third geochemical end member with lower $^{87}Sr/^{86}Sr$ ratios for their $^{143}Nd/^{144}Nd$ composition (Fig. 4.17A). Enclave compositions also plot along the binary mixing line, but with increased scatter for the three Loutses South enclaves which also plot to the left of the mixing trend, towards the composition of their hosts (Fig. 4.17A). Loutses North enclave DPM9 is also offset from the main mixing curve, towards a higher $^{87}Sr/^{86}Sr$ ratio (Fig. 4.17A). Incorporation of macro-phenocrysts from the surrounding host magma might explain the scatter in the Sr-Nd isotope geochemistry of these enclaves (see section 4.6.1).

Further discussion of the isotopic composition of the Delta 2 rocks is based on plots where both axes have the same denominator, making it easier to recognise mixing trends as this process is known to produce straight lines in such plots (Langmuir et al., 1978). The same modelling parameters used in Fig. 4.16D for the Kossona Vouno and main enclave series are applied in a $^{143}Nd/^{144}Nd$ versus 1/Nd plot. Due to their previously discussed difference in REE contents, the two enclave series also represent distinct trends on this graph (Fig. 4.17B). These two enclave trends in Nd geochemistry can once again be modelled by 10% of AFC (Kossona Vouno) and 25% of FC (main enclaves). Mixing between more evolved enclaves and the isotopically more crustally enriched host rocks explains all other samples (apart from DPM56B and the Loutses South hosts, Fig. 4.17B).

Only these mixing lines between intermediate enclaves and most evolved host rocks, however, can be recognised in the $^{87}Sr/^{86}Sr$ versus 1/Sr graph (Fig. 4.17C). The enclaves do not show their binary character in this plot, and, as was also the case for trace element modelling of Sr, can not be convincingly reproduced by the AFC and FC model that seems to explain the REE, more compatible trace elements and the $^{143}Nd/^{144}Nd$ composition. It is unclear whether this should be interpreted as inadequacy of the binary AFC and FC enclave hypothesis or as the effect of incorporation of Sr-rich antecrysts. Strontium and Nd isotopic compositions reflect the involvement of three sources in the Delta 2 petrogenesis: the overall most primitive end-member is represented by enclave DPM36, host rock DPM66 is the second and most crustally contaminated isotopic end-member and the Loutses South host rocks represent a third component with a distinct combination of lowest $^{87}Sr/^{86}Sr$ and intermediate $^{143}Nd/^{144}Nd$ ratios.

In the $^{87}Sr/^{86}Sr$ versus $^{143}Nd/^{144}Nd$ diagram host rocks overall tend to have a more crustal signature whereas all enclaves are positioned closer to bulk silicate earth (Fig. 4.12A). The Pb isotopic systematics of the Delta 2 samples, however, rather group host rocks and enclaves together according to their sampling locality – suggesting that their Pb isotope signature is decoupled from their Sr-Nd isotopic system (Fig. 4.12A). Indeed, where the Sr and Nd isotope ratios are in good agreement with the trace element models of two distinct enclave differentiation trends, followed by mixing of the resulting enclaves and the most evolved host rocks, these trends can not be recognised in the Pb (isotopic) system (Fig. 4.17D-F). The processes of mixing and assimilation, inferred from major, trace and Sr-Nd isotopic geochemical modelling, are inferred to represent the final stages of differentiation within an upper crustal magma chamber. The fact that the Pb isotopic composition of the Delta 2 samples does not reflect these final differentiation processes suggests that their Pb isotopic signature is either inherited from earlier or later events, or derived through altogether different processes. Since the Pb concentrations in subducted sediment are thought to be up to 100 times larger than lead

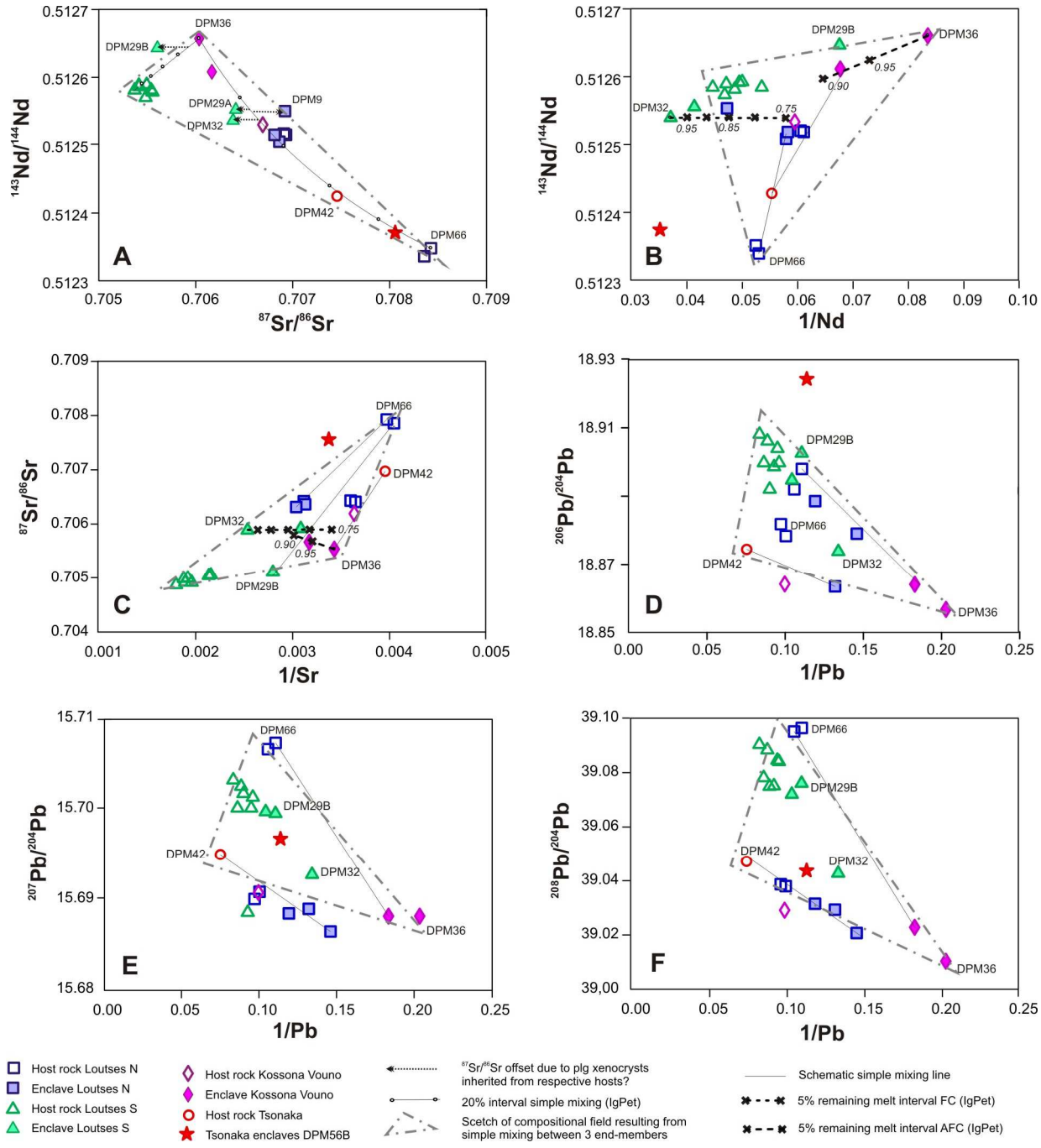

Figure 4.16. *Testing the trace element models on the Sr-Nd-Pb isotope ratios of the Delta 2 unit* and identifying different sources that contributed to the rocks' petrogenesis.

contents in the mantle (GERM database; http://earthref.org/GERMRD/), the rather crustal Pb isotopic composition of even the more primitive Delta 2 samples might reflect contamination of the mantle wedge by lead from subducted sediments. The two host rock end-members defined by Sr-Nd isotope ratios are so similar in their Pb contents and isotopic signature that they can be reduced to one 'crustal' Pb isotopic end-member (Fig. 4.17D-F). Basaltic enclave DPM36 also remains the most primitive end-member in Pb isotopic systematics. But whereas simple mixing between this enclave and the more radiogenic hosts might seem to reproduce most of the Delta 2 samples' Pb geochemistry (Fig. 4.12 E, F & H), the graphs showing both Pb content and isotopic composition suggest involvement of a third end-member with a Pb geochemistry similar to Tsonaka host rock

DPM42 which was, based on its major and trace element contents, the most evolved host rock (Fig. 4.17D-F). This third Pb isotopic end-member can however only be identified in diagrams involving both lead concentrations and Pb isotopic compositions (compare Fig. 4.17D,E & F with Fig. 4.12 E,F & H). This suggests that it is standing out as a potential end-member merely due to its highest Pb concentration (it's Pb isotopic composition is within the mixing array between most mafic enclave DPM36 and the most crustally contaminated host rock) – which is by definition only influenced by crystal fractionation processes. Tsonaka host rock DPM42 therefore remains the most evolved sample within major and trace element geochemical modelling, but does not represent an isotopically distinct end-member.

4.6 Linking geochemistry and petrography: discussion

4.6.1 Scatter in geochemical data

Petrographic observations and major element modelling suggest that macro-phenocrysts of olivine (and hence their Cr-spinel inclusions), quartz, zircon and large subhedral biotite grains with extensive disequilibrium features are antecrysts (see 4.4.5). Euhedral biotite phenocrysts are however inferred to have crystallised in the magma chamber after mafic replenishment, despite the fact that this mineral was not identified as a crystallising phase in the geochemical modelling. This ubiquitous presence of antecrystic macro-phenocrysts with disequilibrium features clearly indicates that whole rock geochemical data of both host rocks and enclaves do not represent liquid compositions. Exchange of crystals between enclave magma and host felsic mush, or within different regions of either one of them, could have easily shifted the whole rock composition (liquid + phenocrysts + antecrysts) away from mixing trends or crystallisation curves. The effect of this crystal exchange on geochemical scatter can be tested with a trace element that is compatible within specific minerals that also bare indications of disequilibrium.

Chromium is a major constituent in Cr-spinel, which was identified as inclusions in olivine crystals, themselves overgrown by amphibole. Chromium is furthermore highly compatible in clinopyroxene from mafic to intermediate rocks (GERM partition coefficient database; http://earthref.org/KDD/). Clinopyroxene is present throughout the Delta 2 unit either as minor phenocryst or groundmass phase, but some Delta 2 samples have significantly larger amounts of clinopyroxene in the form of glomeroporphyritic clusters overgrown by amphibole. Figure 4.18 shows the Cr contents with increasing differentiation of the Delta 2 volcanic rocks, grouped as enclaves or host rocks with either 1) olivine hosted Cr-spinel and clinopyroxene clusters; 2) significant amounts of clinopyroxene clusters or 3) no Cr-spinel or clinopyroxene clusters. If one can assume that the amphibole overgrowths on the olivine and clinopyroxene clusters indicate that these minerals are not in equilibrium with their surrounding groundmass, this diagram shows the scatter that can result from incorporation of antecrysts due to magma mingling. The samples represented in Fig. 4.18 by round blue symbols lack Cr-bearing minerals with disequilibrium features, and they show two rather well-defined trends: decreasing concentrations for the enclaves from which clinopyroxene could have been crystallised – and a shallower trend for the host rocks reflecting a less important role for Cr–bearing minerals in their differentiation (blue arrows in Fig. 4.18). Glomeroporphyritic clinopyroxene-bearing enclaves tend to show elevated Cr contents up to 100ppm but still reflect a trend of overall decreasing Cr content. This is also the case for two of the Cr-spinel bearing enclaves, but enclaves DPM41B and DPM49 plot significantly higher at 130 and 160 ppm respectively. These two enclaves may well be outliers exactly because of the Cr-spinel present within out-of-equilibrium olivine crystals. The host rocks have an overall lower Cr content up to 40 ppm, except for those that have significant amounts of hornblende-mantled clinopyroxene: they show Cr contents up to 100ppm. Amongst these host rocks with glomeroporphyritic clinopyroxene are the 7 Loutses South host rock samples which also display the highest Ni contents. Mingling between a more felsic crystal mush and a more primitive magma with Cr/Ni-rich minerals could explain both their elevated Cr and Ni contents. Figure 4.18 thus illustrates how the presence of antecrystic clinopyroxene and/or olivine with Cr-spinel inclusions can increase the

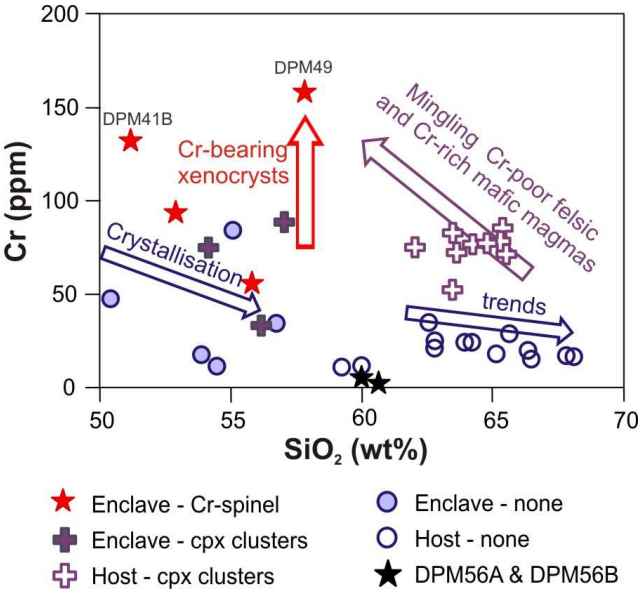

Figure 4.18. *Harker variation diagram of Cr contents illustrates how Cr-rich antecrysts play a role in the amount of scatter observed in whole rock chromium concentrations.* Delta 2 host rocks and enclaves are grouped into samples that do have Cr-bearing minerals with disequilibrium features and those that do not. See text for discussion.

scatter in whole rock chromium concentrations. Scatter in certain minor and trace element diagrams might therefore partially result from the exchange of crystals between (different zones of) a more felsic crystal mush and a more mafic replenishment, as well as from mixing of geochemically very distinct magmas. Incorporation of antecrystic minerals is also shown to strongly affect the bulk composition of volcanic rocks from the Azores (Larrea et al., 2013) and to control variations in the whole rock composition of a lamprophyre sill (Ubide et al., 2012).

But it is not only in the trace element geochemistry that relatively well defined trends are obliterated by scatter. The $^{143}Nd/^{144}Nd$ versus $^{87}Sr/^{86}Sr$ graph, for example, clearly defines one mixing trend and one individual cluster – except for the Loutses South enclaves and DPM9 which are scattered around the mixing line (Fig. 4.17A). Fine-grained enclave DPM29B thereby contains many large crystals with disequilibrium features similar to the ones found in its host rock. As Sr is more compatible in plagioclase than Nd is in amphibole, exchange of these two minerals between host and enclave magma will mainly result in a shift in the enclave's $^{87}Sr/^{86}Sr$ ratio towards its host rock's isotopic composition. More coarse-grained enclaves DPM29A and DPM32 contain fewer of such host-derived antecrysts, which could explain their smaller offset from the mixing curve (Fig. 4.17A). Loutses North enclave DPM9 is another sample that plots outside the main mixing trend, but towards the Sr isotopic composition of the most 'crustally enriched' Loutses host rock (Fig. 4.17A). This fine grained enclave contains many large plagioclase crystals with disequilibrium features – its offset is therefore interpreted as the result of incorporation of Sr rich plagioclase antecrysts from the host rock. The scatter in the overall well-defined $^{87}Sr/^{86}Sr$ - $^{143}Nd/^{144}Nd$ trend could thus reflect crystal mingling in the enclaves closer to the mafic - felsic boundary, similar to the scatter observed in trace elements such as Cr (see Fig. 4.18). Plagioclase antecrysts whose Sr isotopic composition is not in equilibrium with that of the surrounding groundmass are also found in volcanic deposits on Stromboli (Francalanci et al., 2012). A similar influence of antecrysts on the bulk isotopic composition of their host magmas is furthermore observed for the Icelandic rift zone basalts whose large scatter in $^{87}Sr/^{86}Sr$ isotopic compositions is shown to reflect incorporation of different plagioclase populations of uncertain origin (phenocrysts, antecrysts, xenocrysts?) (Gronvold et al., 2007).

The fact that scatter in geochemical data is more pronounced for enclaves than for host rocks (see sections 4.3) could be linked to the initial differences in temperature and geochemistry of these two magmas, as well as their relative volumes. Upon injection in the magma chamber, the hotter, less viscous mafic magma incorporates some of the more felsic crystal mush as cumulate clusters (and/or chilled margins). This more felsic, solid material is then partially melted and incorporated in the hotter mafic melt, adding to the increase in silica content of the more mafic magma. The larger crystals are however mantled or only incompletely resorbed/replaced, so that they remain within the mafic magma as anhedral crystals with an antecrystic composition within the relatively small enclaves that were eventually sampled for whole rock (WR) analysis. Just a few of such antecrysts will therefore have a large impact on the enclave's WR content of elements that are compatible in those specific minerals. The initial crystal mush is cooler and more viscous than the injected more mafic magma, reducing its

uptake of mafic magma to small amounts of melt and some (olivine) crystals near the felsic-mafic boundary. The mafic melt is then locally homogenised with interstitial and newly formed partial melts of the felsic crystal mush, shifting its overall WR composition towards lower silica contents. So whereas host rocks have more macro-phenocrysts with disequilibrium textures than the enclaves, only few of these antecrysts originate from the mafic replenishment. All others are from the initial silica-rich crystal mush and therefore less geochemically different from the hosts rock's phenocrysts.

4.6.2 Major element modelling

Using literature data of mineral compositions from Methana, geochemical modelling of the Delta 2 samples' major elements suggests that differentiation in the magma chamber (after mafic replenishment) mainly concerned those minerals that are major components in the rocks: plagioclase, amphibole, clinopyroxene, Fe-Ti-oxides and apatite. Based on these modelling calculations, quartz and biotite seem not to have been involved in the host rocks' differentiation after mafic replenishment. As already discussed in section 4.4.5, quartz and biotite macro-phenocrysts in both in host rocks and enclaves are therefore interpreted as antecrysts from the more solidified felsic crystal mush that resided in the magma chamber prior to the mafic injection. Zircon inclusions in large amphibole, biotite or plagioclase grains indicate that their host crystals are also such antecrysts, since inferred zircon crystallisation temperatures are near the more felsic crystal mush's solidus – making it impossible for the host rock magmas to erupt (see 4.4.4). The absence of olivine in any of the modelled crystallising mineral assemblages suggerst that olivine crystals with Cr-spinel inclusions are inherited from the mafic magma's differentiation prior to the moment it entered the more felsic magma chamber. Olivine is therefore also interpreted as an antecryst in both enclaves and host rocks. Petrography revealed the presence of euhedral orthopyroxene phenocrysts, lacking any disequilibrium features, in some enclaves and host rocks. The petrographic characteristics of these orthopyroxene phenocrysts suggests that their crystallisation mainly occurred after mafic replenishment, whereas none of the modelling calculations involve orthopyroxene in the crystallising mineral assemblage. This discrepancy between information gathered from petrography and from modelling calculations illustrates the limitation of geochemical models to fully reproduce all magma chamber processes that played a role in the petrogenesis of the Delta 2 volcanic rocks. A minor role for orthopyroxene as crystallising phase in the initial felsic crystal mush is possible, but euhedral olivine suggests that the initial mafic magma was silica under-saturated and thus less likely to crystallise this mineral. Orthopyroxene is therefore interpreted to have mainly crystallised as prismatic, euhedral grains within hybrid enclave and host rock magmas that resulted from partial melting, crystal fractionation, mixing and mingling of the above two initial magma compositions.

The host rocks' major element range can be entirely reproduced by resorption of previously crystallised minerals into the more felsic host magma – but mixing of intermediate host rock magma with intermediate enclave magma did probably also play a role. The compositional range of the enclave data can however not be modelled by a single liquid line of descent from the most mafic enclave but instead three enclave groups, each with a slightly different petrogenesis, could be identified. The enclaves from Loutses North could have evolved from their most mafic sample by fractional crystallisation. This is however not the case for the Kossona Vouno enclaves: these overall more 'primitive' enclaves favour differentiation mainly by mixing of magma represented by the most mafic enclave DPM36 with magma represented by the most felsic host rock DPM42. The enclaves from the Tsonaka locality are best reproduced by a combination of both mixing and fractional crystallisation.

4.6.3 Trace element modelling

In contrast to the three different evolutionary models needed to reproduce the major element contents of the enclaves, most trace element calculations only reflect two distinct enclave series. Both thereby involve crystallisation of the same mineral assemblage as the one inferred from major element modelling: plagioclase, apatite, Fe-Ti-oxides, amphibole and clinopyroxene. Trace element geochemistry of the 'Kossona Vouno enclave series' (including one Loutses South sample) can be reproduced by up to 10% of AFC, with a constant A/FC ratio of 0.7, using mafic composition DPM36 as a starting point whilst assimilating most felsic host rock DPM42. The mineral assemblage of the Kossona Vouno enclave series is thought to be similar to the relative amounts of crystallising minerals calculated from the major element model of the Loutses North enclaves: up to 6% Fe-Ti oxides, about equal amounts of plagioclase and clinopyroxene but less amphibole. The second trace element trend is the 'main enclave series' (= the two other Loutses South enclaves, and all Loutses North and Tsonaka enclaves except for DPM56B). This series is best modelled by up to 25% of fractional crystallisation, starting from the least evolved composition (DPM32). The largely ferromagnesian composition of the crystallising mineral assemblage of the Tsonaka enclaves (calculated in the major element modelling, only up to 6% plagioclase) seems appropriate to explain the geochemistry of the main enclave series. Simple mixing between the different enclaves and more evolved host rocks explains the compositions of more intermediate host rocks – apart from the Loutses South samples which sometimes form an individual cluster. The contribution from partial melting of the initial felsic crystal mush to the host rocks' chemical composition is thus less obvious from trace element modelling.

Table 4.5 presents the average distribution coefficient for the minerals in which the different elements of Fig. 4.16 are compatible. These values are overall comparable with available literature data – except for Sr and Pb in the main enclave series. These estimated mineral-melt distribution coefficients are systematically lower for the Kossona Vouno series than the main enclave trend – in agreement with the GERM database (http://earthref.org/KDD/) which shows that compatibility is generally lower in a more primitive magma than in a further evolved magma. The most primitive (basaltic) enclaves were indeed found in the Kossona Vouno flow whilst all other enclaves are basaltic-andesitic to andesitic in composition. The overall good agreement between trace element modelling-derived distribution coefficients and the literature values for these coefficients is therefore interpreted as support for an enclave magma genesis involving two distinct differentiation paths.

4.6.4 Radiogenic isotopes

Strontium and Nd isotope systematics of the Delta 2 unit support the petrogenesis derived from major and trace element modelling. They furthermore identify three main sources that contributed to the magma genesis: a primitive magma represented by most mafic Kossona Vouno enclave DPM36, and two very distinct crustal end-member compositions (most crustally imprinted Loutses North host rock DPM66 and Loutses South host rock DPM26). The Pb isotopic geochemistry, however, seems to be disconnected from all other geochemical parameters. With respect to Pb isotope ratios, Kossona Vouno enclave DPM36 remains the most primitive sample but the two crystal mush end-members defined by the Sr-Nd isotopes fall together as one host rock end-member. The impression that less crustally enriched Tsonaka host rock DPM42 is a second crustal source in Fig. 4.17 D, E & F is doubtful as it seems to result from it being a concentration end-member.

The Sr-Nd-Pb isotope ratios of the Delta 2 samples were compared to literature values for subducted sediments, MORB, depleted mantle and (upper) continental crust (GERM database; http://earthref.org/GERMRD/). This revealed that the Delta 2 unit's Sr-Nd isotope ratios are broadly intermediate between global compositions of MORB/mantle and subducted sediments, with only the most primitive Delta 2 enclaves resembling continental or island arc andesite compositions (Kelemen et al., 2003). The Pb isotopic composition of even the most primitive Delta 2 enclaves is however

towards the more enriched side of the range of values found for sediments in subduction trenches from around the world (Plank & Langmuir, 1998) or continental and island arc andesites. Both the radiogenic lead geochemistry of the more mafic enclaves and the correlation between the volcanic rocks' Pb isotope ratios and their sampling locality will be further discussed in Chapter 5.

As mentioned above, the most primitive Sr and Nd isotopic signature found in the Delta 2 unit is a mixture between crustal and mantle values. This more depleted Sr-Nd isotope signature seems to have been significantly enriched by assimilation during further differentiation in the crust (Fig. 4.12C & D, Fig. 4.17A). For the Nd isotopic contamination there only seems to be one crustal end-member, approximated by most enriched Loutses North host DPM66 (Fig. 4.12D, 4.17B). On a silica versus $^{87}Sr/^{86}Sr$ diagram, assimilation-induced changes of the Sr isotopic signature of the Delta 2 samples seem governed by two different crustal end-members represented on the one hand by most crustal host DPM66 and on the other hand by Loutses South host rock sample DPM26 which actually has the overall lowest $^{87}Sr/^{86}Sr$ ratio (Fig. 4.17C). This could, however, be induced by the Loutses South host rocks' high Sr contents (Fig. 4.12B): if they would have started out as a melt with Sr isotopic compositions similar to primitive melts of for example the Kossona Vouno host rocks, their higher Sr contents would have (partially) buffered this $^{87}Sr/^{86}Sr$ value, diluting the more radiogenic Sr composition acquired by further crustal differentiation through assimilation.

4.6.5 Genesis of the two different enclave magma series

Whereas major and trace element geochemistry requires just one felsic crystal mush composition for the petrogenesis of all host rocks through partial melting and mixing, the radiogenic isotopes infer the involvement of two different crustal sources. Major and trace element geochemistry of the enclaves can only be satisfactorily modelled by respectively three and two different initial mafic compositions and subsequent differentiation trends, but the Sr-Nd-Pb isotopic compositions point towards one common 'primitive' magma source (see Table 4.6). Assuming that both enclave series are indeed derived from the same primary source, how could this primitive magma have evolved into a two different enclave suites? And can the geochemical composition of the Loutses and Tsonaka enclaves be derived from the most primitive Kossona Vouno enclave?

Looking at the chondrite-normalised REE diagram (Fig. 4.19A), most mafic Kossona Vouno enclave DPM36 and least evolved Loutses South enclave DPM32 show very similar patterns more or less parallel to one another but with the latter at higher concentrations than the former. Crystal fractionation of minerals that do not host REE could cause such an upward shift for the remaining, fractionated melt. A small negative Eu anomaly in the pattern of DPM32 is absent in the pattern of DPM36 and might indicate that plagioclase fractionated from the primitive magma (DPM36) as it differentiated into DPM32 (Fig. 4.19A). Fig 4.16A shows that Y is enriched in the more evolved DPM32, suggesting that no significant amphibole or clinopyroxene crystallised if this enclave's

End member	Representative sample	# Mg	$^{87}Sr/^{86}Sr$	$^{143}Nd/^{144}Nd$	Pb isotopic ratios
Mafic magma	DPM36 (KV enclave)	highest	2nd lowest	highest	overall lowest
Felsic crystal mush 1	DPM66 (Loutses N host)	interm	highest	lowest	Highest $^{207}Pb/^{204}Pb$, $^{208}Pb/^{204}Pb$
Felsic crystal mush 2	DPM26 (Loutses S host)	interm	lowest	2nd highest	Highest $^{206}Pb/^{204}Pb$

Table 4.6. *Three different end-members can be identified, based on the geochemistry of the Delta 2 volcanic rocks.* Differentiation of these three end-member composition by different stages of crystal fractionation, partial melting, mixing and mingling can reproduce all Delta 2 geochemical compositions (apart from Tsonaka enclaves DPM56A & DPM56B). See text for discussion. KV = Kossona Vouno; interm = intermediair.

composition was derived from DPM36 by means of crystal fractionation. Cobalt and Ni contents of DPM32 are similar or slightly lower than the concentrations of DPM36, despite DPM32's more evolved character (Fig. 4.16B & G). Perhaps this is the signature of minor amounts of olivine that fractionated from DPM36 to drive the remaining melt towards DPM32's composition. A primitive mantle-normalised diagram of the two enclaves shows that incompatible elements such as Ta, Nb, Ta and Ba show elevated contents in the more evolved Loutses South enclave compared to the more primitive Kossona Vouno sample (Fig. 4.19B). So if the former evolved from the latter, crystal fractionation would have increased these very incompatible element contents. Vanadium contents of DPM32 are less than half the amount present in DPM36 (not shown), whereas Ti contents are the same for both enclave compositions (Fig. 4.19B). In line with the reasoning for similar Ni and Co contents that indicate (minor) olivine fractionation, these could be indications that Fe-Ti-oxides were also involved in the differentiation of starting composition DPM36 into DPM32. Accordingly, the equally low amounts of P suggest apatite fractionation (Fig. 4.19B). Uranium and incompatible LILE Cs, Rb and K, however, show somewhat higher concentrations in DPM36 than in DPM32. This can not be explained by crystallisation of any mineral that could fractionate simultaneously with the above inferred minerals. It could perhaps be a signature inherited from the surrounding wall rock of the magma chamber where mafic magma similar to DPM36 differentiated into DPM32's composition – as long as the wall rock of this differentiation location has a Sr and Nd isotopic composition that is not too different from the initial mafic magma.

So if both enclave series are derived from the same primitive magma, the most mafic Kossona Vouno enclave is regarded as representative of this initial enclave magma. Stalling and AFC differentiation of this basaltic magma near the mantle-crust boundary would have little effect on its isotopic composition. Fractional crystallisation of plagioclase, olivine, Fe-Ti-oxides and apatite could drive the residual melt towards a composition similar to enclave DPM32, which represents the starting composition of the 'main enclave series' differentiation trend. As this (similar to DPM32) residual melt is mobilised and on its way to the earth's surface, it encounters and replenishes the magma chamber of a more felsic crystal mush. Geochemical modelling suggests that further differentiation of this basaltic-andesitic DPM32 magma in the felsic magma chamber would involve crystallisation of mainly amphibole and clinopyroxene (see footnote Table 4.5). All Loutses N and Tsonaka enclaves seem to have undergone such a dual-stage differentiation process, together with Loutses South enclaves DPM32 and DPM29A. The other Loutses South enclave, DPM29B, seems to have gone through the one-stage enclave magma genesis represented by the Kossona Vouno enclaves. They seem to have travelled from the mantle source to the felsic crystal mush without having undergone much fractionation. Geochemical modelling suggests that subsequent AFC differentiation of this Kossona Vouno primitive magma involved fractionation of more plagioclase, Fe-Ti oxides and apatite (footnote

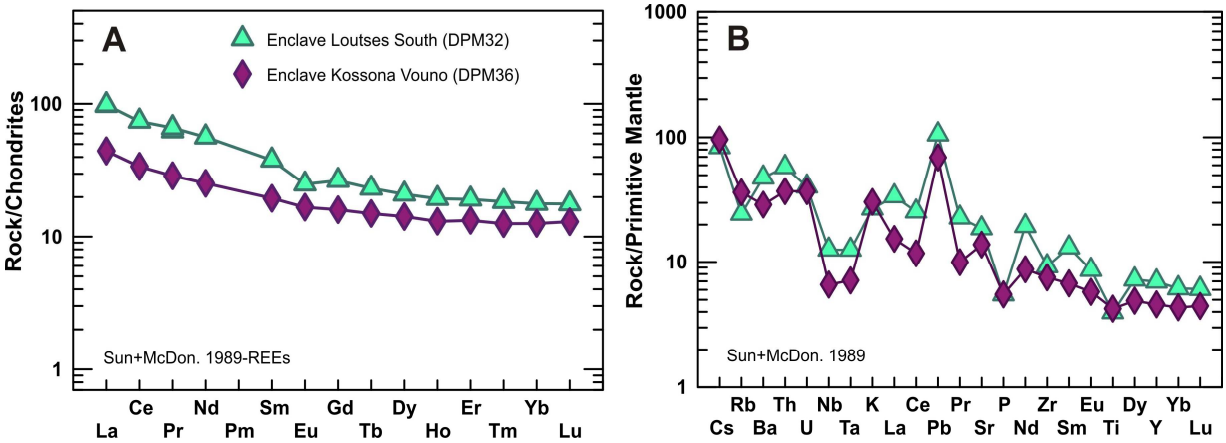

Figure 4.19. *Normalised trace element abundance diagrams for the most mafic samples of the two different enclave series*: DPM36 for the Kossona Vouno series and DPM32 for the main enclave series. Normalisation factors from Sun & McDonough (1989), see text for discussion.

Table 4.5) than the two-stage enclave series – supporting the assumption that it skipped an earlier AFC stage involving these minerals.

Only the two geochemically and mineralogically aberrant Tsonaka enclaves DPM56A & DPM56B remain unexplained by the above discussed two-stage enclave petrogenesis. Their highly differentiated major and trace element geochemistry and unique petrography with orthopyroxene instead of amphibole framework crystals suggests an origin as remaining melt fraction after crystallisation or the involvement of filter-pressing in their specific petrogenesis.

4.6.6 Comparison of the Delta 2 unit to similar South Aegean arc volcanic deposits

Mixing between a replenishing mafic melt and a more evolved magma is also recognised in the petrogenesis of effusive volcanic deposits in the central and eastern parts of the South Aegean arc. The oldest volcanic rocks on **Santorini** are the **Akrotiri** rhyolitic to rhyodacitic lavas which hold about 4% of mafic inclusions (Mortazavi & Sparks, 2004). The main minerals in both host rock and enclaves are plagioclase and amphibole, with the former showing complex textures of oscillatory, normally and inversely zoning and the latter often having opaque reaction rims. The host rocks furthermore show a seriate texture for both plagioclase and amphibole - all characteristics they have in common with the Delta 2 rocks. An important difference, however, is that the Akrotiri enclaves have crenulated and chilled margins which are believed to be the result from rapid quenching of the mafic magma upon mingling with the rhyolitic one (Mortazavi & Sparks, 2004).

The youngest volcanic deposits on **Santorini**, the dacitic lava flows of the **Kameni Islands**, also contain more mafic enclaves. These lavas are different from the Delta 2 rocks as they do not contain any hydrous mineral phases, but similar in the fact that their enclaves have no chilled margins and partially crystallised prior to their dispersal in the dacitic magma. Martin et al. (2006a) also recognise a range between fine grained and coarse grained enclaves, with phenocryst aspect ratios for the end members nearly identical to the ones observed in the Delta 2 unit. A relatively thin layer of mafic magma cooling and crystallising between the base of the felsic magma and the wall rock would result into a more uniform grain size, suggesting that the range in enclave grain size reflects the presence of a relatively large volume of replenishing magma (Martin et al., 2006a).

The rhyodacitic post-caldera domes of **Nisyros** contain enclaves which are usually smaller when fine-grained and larger when coarse-grained (Braschi et al., 2012) – a correlation absent in the Delta 2 rocks. They further differ from the Delta 2 enclaves due to their crenulated and chilled margins, but have macro-phenocrysts across the host – enclave contact in common with them.

On **Kos**, the Vigla dacite stocks contain andesitic enclaves mainly consisting of plagioclase, amphibole and biotite. Again, these enclaves are often characterised by chilled margins indicative of quenching against the more felsic host magma (Pe-Piper & Moulton, 2008). Large plagioclase crystals within these enclaves show complex zoning and sieve textures similar to plagioclase in the dacitic host. Andesite clasts (and andesitic enclaves within rhyolite clasts) from the Kos Plateau Tuff also show mineral textures that were interpreted as indicative of widespread magma mixing: plagioclase with embayed cores, complex zoning and sieve textures; ovoid quartz with a mantle of clinopyroxene; and both hornblende and biotite pseudomorphically replaced by a fine-grained mass of opaques, pyroxenes and quartz (Pe-Piper & Moulton, 2008).

The disequilibrium features described abive for enclave-bearing arc lavas from Santorini, Nisyros and Kos are interpreted as the result of magma mixing and crystal mingling. The same mineral textures occur throughout the Delta 2 volcanic rocks – mainly in host rocks but also in some enclave-hosted macro-phenocrysts. Delta 2 rocks thereby contain more disequilibrium textures indicative of prolonged interaction between two geochemically contrasting magmas than any other South Aegean arc deposit. Disequilibrium features commonly observed in the Delta 2 rocks include (1) complete dehydration of hydrous minerals (replacement of biotite by plagioclase, Fe-Ti-oxides and pyroxene (Fig. 4.6E); replacement of amphibole by pyroxene (Fig. 4.6D)); (2) mantling of antecrysts (quartz mantled by pyroxene (Fig. 4.6F); olivine mantled by amphibole (Fig. 4.5D);…); and (3) nucleation and

growth of a mineral that was (temporarily) unstable before (new amphibole rim around amphibole crystal with thick opaque reaction rim (Fig. 4.6C); fresh amphibole crystals mantling a larger amphibole that is (partially) replaced by pyroxene (Fig. 4.6D);…). Some of these textures can only be explained by different phases of amphibole (in)stability; prolonged periods of mineral replacement or transport of individual crystals from the felsic magma into the mafic magma and vice versa Together with the lack of chilled margins, sometimes observed for enclaves from Santorini or Nisyros, this indicates that the two contrasting magmas of the Delta 2 unit were in physical contact with one another for a longer period of time than any of the volcanic deposits described above. In accordance with the argumentation of Martin et al (2006b), the large range of Delta 2 enclave grain sizes is interpreted to result from a relatively large volume of replenishing mafic magma which seems to have remobilised the initial felsic crystal mush that eventually erupted as the Delta 2 host rocks.

Magmatic zircons are not uncommonly encountered in the Delta 2 host rocks (Fig. 4.14), but apart from the Kos Platea Tuff (Bachmann et al., 2007) rarely described for any other South Aegean arc volcanic deposit. This suggests that the crystal mush below Methana was initially more evolved, further crystallised and thus less eruptible than the ones that were remobilised below Santorini and Nisyros-Kos. A more viscous, immobile crystal mush clearly needs more heat to be remobilised – and thus a larger mafic replenishment. Partial melting of this further evolved crystal mush would also require more time – adding to the magnitude and ubiquitous occurrence of disequilibrium features. A final argument for unusually long interaction between the more mafic magma and more felsic crystal mush prior to eruption, is the absence of a geochemical gap between Delta 2 enclaves and host rocks. The contrast between the 3 wt% SiO_2 *overlap* of Delta 2 enclaves and host rocks (see section 4.3.1) and the 7 to 12 wt% SiO_2 geochemical *gap* observed in similar South Aegean arc deposits is a significant difference (see Table 4.7). The Delta 2 unit's continuous variation in geochemical composition results from both higher silica contents in its enclaves and lower SiO_2 concentrations in its host rocks. Such increased 'homogenisation' of the geochemistry of its lavas and enclaves in comparison to the other South Aegean arc volcanics could be achieved by chemical interaction between both magmas (mixing) over a long period of time – possibly at higher temperatures resulting from relatively large mafic replenishments.

South Aegean arc volcanic centre	Volcanic unit	Enclave SiO_2	Host rock SiO_2	Reference
Methana	Delta 2 unit	50-62 wt%	59-68 wt%	This work
Santorini	Akrotiri rhyodacitic to rhyolitic lavas	51-56 wt%	68-72 wt%	Mortazavi & Sparks (2004)
Santorini	Kameni dacites	51-58 wt%	65 wt%	Martin et al. (2006a)
Nisyros	Post-caldera rhyodacites	54-59 wt%	66-72 wt%	Braschi et al. (2012)
Kos	Vigla dacite & Kos Platea Tuff	56-58 wt%	64-70 wt%	Pe-Piper & Moulton (2008)

Table 4.7. Comparison of the silica content range of Delta 2 enclaves and host rocks with the SiO_2 compositions encountered in similar host rocks and enclaves from the central and eastern parts of the South Aegean active volcanic arc.

4.6.7 Delta 2 volcanic deposits: a single unit?

The initial aim for this detailed petrographic and geochemical study of Methana's Delta 2 rocks was to assess the mineralogical and compositional variety that can be expected within one single volcanic unit. But do all observations, data and interpretations discussed above support the initial assumption

that all Loutses, Tsonaka and Kossona Vouno lavas belong to the same volcanic unit? What actually defines a 'single volcanic unit'?

On the geological map of Gaitanakis & Dietrich (1995), the volcanic deposits of the three Delta 2 areas are identified as 'dacite and rhyodacite δ2' belonging to the 'southern fissure volcanoes' that were dated ca. 0.9-0.5 Ma. and described as domes and flows that erupted from 120-145° oriented fissures which intersect NNE-NE oriented faults. This suggests that the fieldwork prior to geological mapping of the Methana peninsula indicated all Delta 2 volcanic rocks to have been deposited during a relatively short period of time and that their eruption was linked to tectonic activity along specifically oriented fissures and faults. This conceptual bridge between volcanic activity on one hand and the lithology and geographical occurence of the volcanic deposits on the other hand is also expressed in the definition of an 'eruption unit' (Fisher & Schmincke, 1984). Groppelli & Viereck-Goette (2010) apply the same approach of using the lithostratigraphic units initially observed/inferred during fieldwork as a basis for the definition of volcanic units on the final map. This is especially useful during the initial survey of a volcanic area, when lithological properties and stratigraphic relationships of the volcanic deposits are the only characteristics that can be easily distinguished. Subsequent petrographic and geochemical analysis should however be used to obtain a more comprehensive definition of an already identified litho-stratigraphic unit (Groppelli & Viereck-Goette, 2010).

Based on the different petrogenesis inferred for the **Kossona Vouno** enclaves and the geochemical gap that only occurs between host rocks and enclaves from this area, it might be interpreted as an individual volcanic unit. Field observations furthermore identified it as the only locality where up to 10% of large coarse-grained enclaves are dominant. The enclaves from Tsonaka and Loutses North seem to have a similar petrogenesis, but whereas most **Tsonaka** enclaves are coarse-grained, all Loutses North enclaves are dominantly fine-grained. Host rocks from the **Tsonaka** locality are furthermore the only ones that always contain orthopyroxene, sometimes even in higher amounts than clinopyroxene. The **Loutses North** host rocks are the only ones where complexly sieved and zoned large plagioclase crystals were found with an unsieved outer rim full of subhedral pyroxene inclusions. All these subtle macroscopic, petrographic and geochemical differences can either reflect that they are in fact different volcanic units, but can also result from tapping different parts of a single magma chamber throughout the Delta 2 eruption. The **Loutses South** host rocks, however, differ significantly from any other Delta 2 rock due to their very distinct Sr, Ni, Y, La/Lu and $^{87}Sr/^{86}Sr$ composition. This is in agreement with a recent paper on the revised volcanic stratigraphy of Methana (Pe-Piper & Piper, 2013), where the Loutses South lava flows are classified in a different, much older unit on the basis of their subdued morphology and considerable faulting and alteration. The geochemical data presented in this work thus support the fieldwork-derived interpretation of Pe-Piper & Piper (2013).

4.6.8 Role of local tectonics on eruption of the Delta 2 magmas

When the Loutses South host rocks are not taken into account, all volcanic deposits of the Delta 2 unit can be derived from just two geochemical end-members (Table 4.6) – even enclaves from the two different petrogenetic series can be isotopically traced back to one more primitive end-member. Was it then this pulse of mantle wedge melting and subsequent ascent of mafic magma that gave rise to the eruption of the Delta 2 deposits? Most of the enclave magma seems to have undergone a first stage of crystal fractionation of anhydrous minerals prior to replenishing the more felsic magma chamber. Unusually long interaction between the more mafic magma and the more felsic crystal mush is reflected in the overall absence of a geochemical gap between enclaves and host rocks. Mafic injections in a felsic magma chamber are often identified as the trigger of volcanic eruptions (amongst others Sparks et al., 1977; Sparks, 1997; Eichelberger, 1995; Eichelberger et al., 2000), but literature on such mafic replenishments commonly describes a geochemical gap and/or inferred short time of interaction between both magmas. This renders the initiation of a 'Delta 2' effusive eruption solely by mafic replenishment doubtful – there is no obvious reason why the very crystal rich Delta 2 magmas

would not have remained within the thick continental crust of Methana as sub-volcanic igneous bodies. Fault (re-)activation within the extensional tectonic regime of the South Aegean arc could however have facilitated ascent of the Delta 2 magmas and influenced the timing and location of their eruption from linear volcanic vents (fissures). Significant influence of the active tectonic regime in the South Aegean arc on the time and place of its volcanic activity has also been suggested by Pe-Piper & Piper (2002), and proven for volcanic deposits on Aegina and Milos by van Hinsbergen et al. (2004). The presence of the submarine Pausanias Volcano along a normal fault on the edge of a graben (Fig. 2.10) (Nomikou et al., 2013)clearly supports a role for local tectonics in the emplacement of lavas in the Methana volcanic area. Methana volcanic peninsula was even the study area for research on the influence of changes in regional fault patterns on eruption style and on erupted volumes of volcanic products (Pe-Piper & Piper, 2013). The eruption of the Delta 2 arc magmas that seem to have been previously stalled within the thick continental crust below Methana is therefore interpreted as the result of the active extensional regime in the Saronic Gulf.

4.7 Petrogenesis of the Delta 2 volcanic unit

Except for the Loutses South flows, all Delta 2 lavas were probably erupted within the same phase of volcanic activity. Whereas timing and location of the Delta 2 eruption was largely conditioned by the area's tectonic regime, magmatism below Methana is caused by subduction and the upwelling of a primitive melt from the mantle wedge source area. One portion of this primitive magma underwent assimilation and fractional crystallisation of mainly plagioclase, olivine, Fe-Ti oxides and apatite at a depth where amphibole was not stable and the surrounding wall rock does not show a great isotopic contrast to the magmas (perhaps close to the mantle-crust boundary?). Another part of this primitive magma continued its ascent towards higher located crustal magma chambers without this first stage of differentiation. Prior to mafic replenishment, these crustal magma chambers hosted more felsic crystal mushes under temperature, pressure and geochemical conditions that favour amphibole stability and allow zircon crystallisation. These magma chambers are thus inferred to have a basal layer of plagioclase, amphibole and clinopyroxene cumulates; crystal rich margins with higher amounts of felsic minerals and an interior crystal mush of even more felsic composition (Fig. 4.15A). Injection of a relatively large amount of olivine-bearing mafic magma disrupted the basal cumulates – fragmenting them and pushing other cumulate parts towards the centre of the magma chamber (Fig. 4.15B). The mafic magma then stagnated at the bottom of the magma chamber for a relatively long time prior to its dispersion as enclaves into the overlying host magma. The more mafic magma thereby underwent differentiation by fractional crystallisation whilst ponding below the more felsic crystal mush. This involved crystallisation of phenocrysts, formation of a plagioclase-amphibole crystal framework and disequilibrium reactions with antecrysts derived from the crystal mush's cumulates or chilled margins. The large volume of mafic magma was hereby somewhat stratified, with crystallisation of more fine grained, prismatic phenocrysts closer to the overlying crystal mush and formation of larger, more tabular crystals closer to the bottom of the magma chamber (Fig. 4.15C). Meanwhile, the overlying felsic crystal mush underwent partial melting as well as self-mixing (Fig. 4.15C). While both magmas were still partially liquid, the basal mafic magma became unstable, broke up and was dispersed through the (more liquid parts) of the overlying felsic magma. This process is reflected in the randomly oriented crystal framework that characterises the enclaves (Fig. 4.15D). Subsequently, (parts of) this mixture of felsic magma and mafic enclaves was remobilised and erupted as the Delta 2 volcanic unit - probably due to activation of extensional faults. Groundmass and vesicles present in enclvaes and host rocks, as well as the host rocks' flow texture were formed during this process of ascent and eruption (Fig. 4.15D). Most host rocks and enclaves can thus be explained by tapping different parts of a single magma chamber, which was the scene of prolonged interaction between a more mafic magma and a more felsic crystal mush prior to the Delta 2 eruption (Fig. 4.15D). Only the Loutses South host rocks are so geochemically distinct that they are inferred to be derived from a different felsic magma chamber.

Whereas the Delta 2 rocks show many similarities with equivalent enclave-bearing lavas from other parts of the South Aegean arc, they are distinct with regard to: 1) the magnitude and diversity of disequilibrium textures of their minerals, reflected in the lack of correlation between the rocks' mineralogy and their geochemical composition; 2) the absence of any chilled margins and quench or dictyataxitic textures in the enclaves; and 3) the lack of a geochemical gap between host rock and enclave compositions. This makes the Delta 2 volcanic unit unique amongst the South Aegean arc volcanic deposits and is interpreted as the result of prolonged interaction of a relatively large batch of mafic magma with an overlying more felsic crystal mush. The prolonged interaction inferred to have happened between the mafic and felsic magma suggests that Delta 2 unit could have further evolved at depth into a pluton. The active extensional tectonic regime of the Saronic Gulf, however, initiated further ascent through the 32 km thick crust below Methana, leading to eruption of the Delta 2 magmas.

Chapter 5: Volcanic activity on Methana peninsula:

Sources, processes and evolution

The detailed study of the 'Delta 2' volcanic unit in the previous chapter illustrates the complex processes that may occur in magmas residing in a crustal magma chamber prior to eruption. The geochemical data presented in Chapter 4 furthermore support the new stratigraphy of Pe-Piper & Piper (2013) according to which the Delta 2 lava flows south of Loutses belong to a different volcanic phase. This chapter discusses the other volcanic deposits of Methana. Besides andesitic to (rhyo-) dacitic lava flows and domes with abundant enclaves similar to the Delta 2 unit, these also include a few rhyodacitic and basaltic-andesitic pyroclastic deposits (Fig. 5.1, phase C). The microscopic and geo-chemical characteristics of all these volcanic deposits are compared to one another in order to 1) obtain insight into the magma plumbing system below Methana; 2) determine whether differentiation processes, other than the ones identified in Chapter 4, were involved in the magma genesis; 3) investigate if there is a time-dependent trend in the geochemical composition of Methana's volcanic rocks; and 4) further constrain the identity of the different sources that contributed to the formation Methana's volcanis rocks. For the latter objective, geochemical data of sedimentary basement rocks as well as of non-volcanic xenoliths found in the pyroclastic deposits are investigated as potential crustal contaminants. Geochemical data of Methana's volcanic deposits reported in literature are included to help clarify the main differentiation trends of Methana's volcanic rocks.

5.1 Fieldwork observations

All volcanic rocks were sampled on the basis of the geological map of Gaitanakis & Dietrich (1995). For the purpose of discussing their geochemistry and petrology, however, they have been re-classified according to the new volcanic stratigraphy of Pe-Piper & Piper (2013) (see Fig. 5.1). The exact location from where each sample was taken is presented in Appendix A2, together with a short description of the relevant outcrop. The rocks that represent the first phase of volcanism on Methana, the volcanic basement (Phase A) and the volcaniclastic apron (Phase B), were sampled along the western margin and in the central part of Methana peninsula (Fig. 5.1). Due to their older age, these rocks are eroded and partially covered by the younger volcanic deposits of the second period of volcanic activity (Phase C to H). This hinders differentiation between individual volcanic phases of Methana's first volcanic deposits, which could have been extruded over a long period of time, involving a variety of rock types similar to those in units C to H (personal communication Prof. Dr. Georgia Pe-Piper). Most of the volcanic rocks on Methana are enclave-bearing lava flows and domes, similar to the Delta 2 unit. Phase C however also contains the pyroclastic deposits from explosive eruptions (with rare sedimentary xenoliths), thought to mark the renewal of volcanic activity after a period of volcanic quiescence (Fig. 5.1) (Pe-Piper & Piper, 2013).

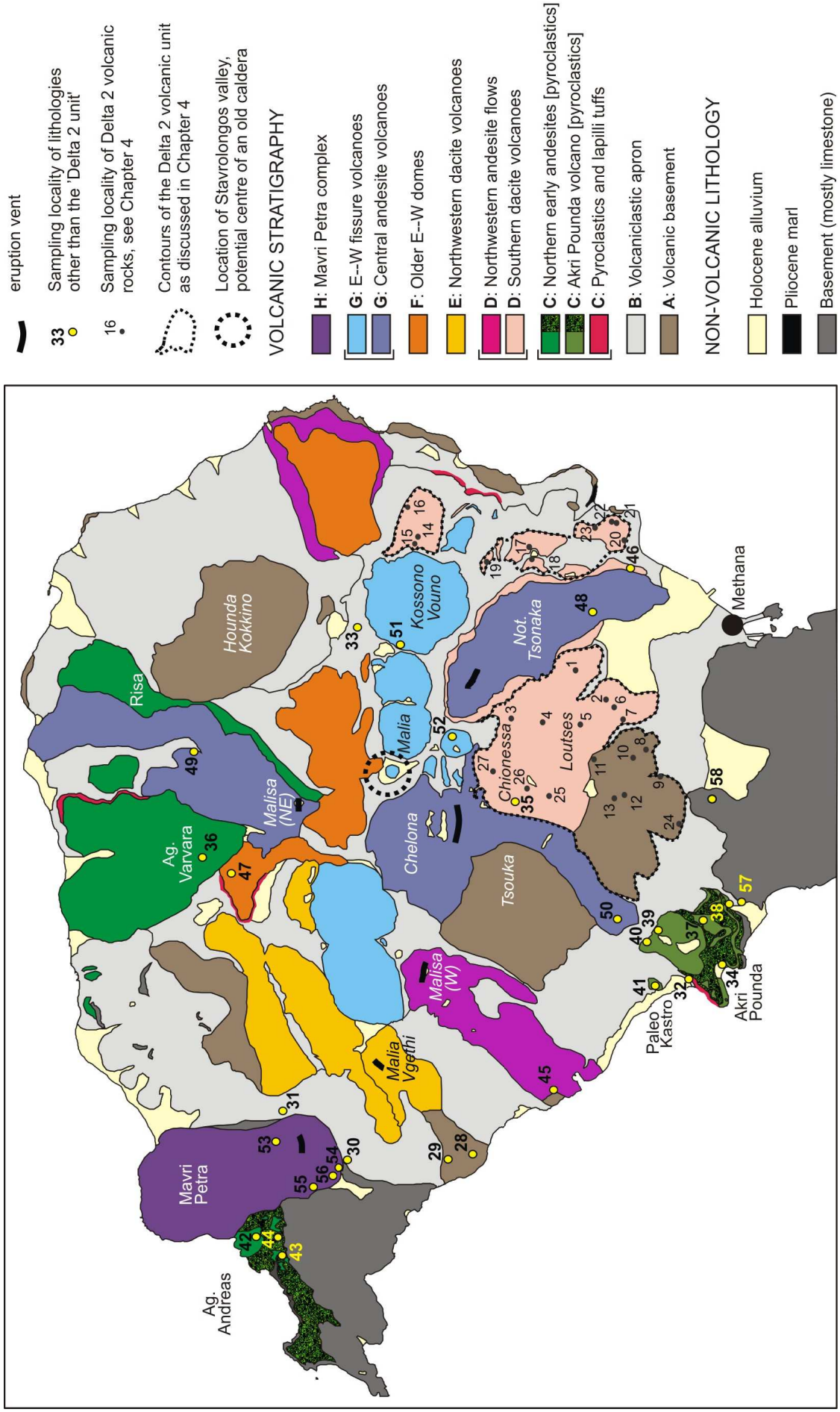

Figure 5.1 *Geological map of Methana peninsula*, after Pe-Piper & Piper (2013), showing the locations from where all petrographically and geochemically studied rocks were sampled (see also Appendix A2).

Volcanic outcrops at the sampling localities indicated on Fig. 5.1 were thoroughly studied during fieldwork and on the basis of their physical appearance interpreted to represent three types of deposits: effusive lava domes and flows rich in enclaves, pyroclastic fallout deposits and pyroclastic density current (PDC) deposits. The field observations described in the next paragraphs are grouped according to these three types of deposits: a geochronological overview of the effusive volcanics is followed by the characteristics of the phase C fallout deposits and overlying PDC deposits.

5.1.1 Lava domes and flows, rich in enclaves (Phase A-H)

The majority of volcanic rocks cropping out on Methana occur as andesitic to (rhyo-) dacitic lava domes and flows containing enclaves that are more mafic than their hosts - equivalent to the volcanic rocks of the Delta 2 unit described in Chapter 4. The younger lavas and domes are less weathered than the underlying, older effusive volcanic deposits of which mainly the more distal parts can be observed. These 'downslope' effusive lavas are intensely auto-brecciated and thus more prone to weathering than their more massive counterparts closer to the vent. In case of a viscous lava, gravitationally induced dome collapse or disintegration of the front of a lava flow generates *block-and-ash flow deposits*: poorly sorted deposits of ash and somewhat rounded, dense to poorly vesicular, lava blocks (Rose et al., 1977). Such 'gravitational' block-and-ash flows usually form small-volume deposits of andesitic to dacitic composition, with meter-sized blocks of lava that often show radial jointing (Schmincke, 2006). Where the outcrops were merely such weathered, poorly sorted block-and-ash flow deposits, samples were taken from the large, generally less weathered dense lava blocks. Closer to the eruption vent, block-and-ash flow deposits contain less ash and are referred to as *autoclastic lava breccias*. With decreasing distance from the vent they become a more welded lava breccia or *blocky lava*, grading eventually into massive *lava flows* (Sigurdsson et al., 2000). Lava flows consists of three parts which are most easily recognised in cross section: a *basal breccia* which forms as lava blocks on the top tumble down and are overridden by the slowly moving lava flow of which the *central* part consists of *massive lava,* in turn covered by a *capping breccia* of lava blocks (Schmincke, 2006).

The outcrops of Loutses South, which were recently classified as part of the oldest Phase A volcanic basement (Pe-Piper & Piper, 2013), are largely overgrown by vegetation. A few less weathered outcrops were found in a riverbed and can be described as block-and-ash flow deposits (Fig. 5.2A-B). The Phase B volcaniclastic apron is still preserved as jointed lava flows in the centre of the peninsula (Fig. 5.2C), but is represented by a *volcaniclastic conglomerate* nearer to the coast, at a larger distance from the vent (Fig. 5.2D). During the period of volcanic quiescence, these conglomerates formed through weathering and erosion of the Phase A and B volcanic rocks. The first effusive volcanics after an initially explosive renewal of volcanic activity are the jointed, massive lava flows of the enclave-bearing Phase C andesites (Fig. 5.2E) observed at Paleo Kastro and Ag. Varvara (see Fig. 5.1). The smaller flow at Paleo Kastro is the sampling location (41, Fig. 5.1) of a coarse-grained, angular xenolith with a quartz-rich vein, IM376, which is distinctly different from the less dense, more fine-grained sedimentary xenoliths observed in the Phase C pyroclastic deposits. The volcanic deposits from the younger Phases D to H are progressively less weathered and consist of autoclastic lava breccias and massive lava flows rather than block and ash flow deposits – unless they are part of the steep flanks of a dome (see Fig. 5.2F, G). Especially the 2200 year old Mavri Petra flow is near its vent a typical massive lava flow with a scoriaceous basal and capping breccia (Fig. 5.2H) but at more distal outcrops it is an autoclastic lava breccia (Fig. 5.2I).

The enclaves that are present throughout the effusive volcanic deposits described above are similar to the ones studied in the Delta 2 unit (Chapter 4, Fig. 5.3). Despite the different modes of deposition of their host lavas, they are often easily recognised by their different weathering colours (Fig. 5.3A-C); the fact that vesicular host rock around them is preferentially eroded away (Fig. 5.3D); their fresh, typical darker colour (Fig. 5.3E, F); or sometimes due to discolorations or a different texture

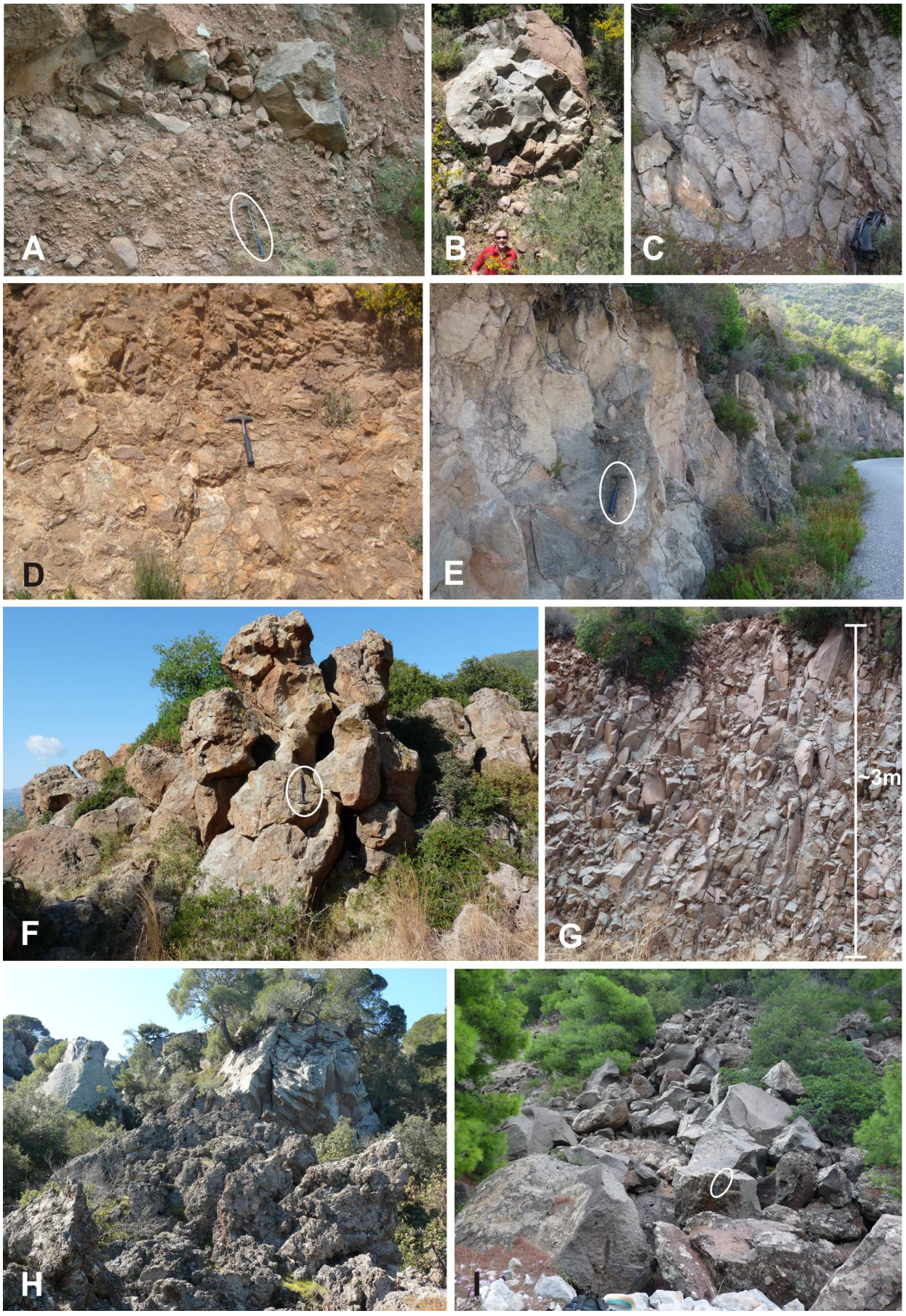
A
B
C
D
E
F
G
~3m
H
I

Figure 5.2 *Photographs of the andesitic to rhyodacitic host rock outcrops of volcanic phases A to H.*
(A) Phase A volcanic basement, location 9: block-and-ash flow deposit (hammer for scale). (B) Phase A volcanic basement, Loutses S, location 29: poorly exposed block-and-ash flow deposit with large juvenile lava block (author for scale). (C). Phase B volcaniclastic apron, location 33: massive lava flows with cooling joints (backpack for scale). (D) Phase B volcaniclastic apron: volcaniclastic conglomerate (hammer for scale) (E) Phase C, northern early andesites, location 36: road outcrop of massive lava with cooling joints (hammer for scale). (F) Phase G, central andesite volcanoes, location 48: slightly weathered blocky lava with some more scoriaceous parts (hammer for scale). (G) Phase G, central andesite volcanoes, location 49: massive lava flow, largely jointed and fractured (scale bar in image). (H) Phase H Mavri Petra flow, location 53: Near the eruption vent the deposit is a typical massive lava flow (background) with scoriaceous basal and capping breccias (foreground). (I) Phase H Mavri Petra flow, location 55: At the edge of the flow, the deposit is an autoclastic lava breccia (hammer for scale).

in the host rock around them (Fig. 5.3G, H). All enclaves are usually rounded, but some are slightly angular or elongated (Fig. 5.3). Their size typically varies between 1 cm to 30 cm but can sometimes reach up to 60 cm. Enclaves smaller than 1 cm are also present, but often only identified in thin section (see petrography sections 5.3.1 and 5.3.3). Individual enclaves usually have a homogeneous grain size which can vary from one enclave to the next from fine-grained to coarse-grained (Fig. 5.3B, D). Sometimes enclaves of two different grain sizes are in direct contact with one another (Fig. 5.3I, J), perhaps representing 'multiple generation enclaves' (Feeley et al., 2008), also known as 'sub-enclaves within main host enclaves' (Braschi et al., 2012).

5.1.2 Phase C fallout deposits

Pyroclastic deposits are formed by explosive activity during which volcanic gases quickly expand, leading to fragmentation of the magma in which they were hosted (Fisher & Schmincke, 1984). Two main types of pyroclastic deposits are *fallout deposits,* consisting of fragments that were transported through the air, and *pyroclastic density current (PDC) deposits* which are formed by energetic, fast, ground-hugging flows of hot gas and rock fragments. In the discussion of these pyroclastic rocks the nomenclature of Schmid (1981) is used to describe the individual pyroclast fragments according to their size (<2mm = *ash*; 2-64mm = *lapilli*, >64mm = *bomb* - plastically deformed during deposition as it was wholly or partially molten - or *block* - angular clast that was solid when touching the ground). *Tephra* is a collective term for all (usually unconsolidated) pyroclastic fragments generated during explosive eruptions; *tuff* is the term used for consolidated pyroclastic deposits composed of clasts smaller than 64mm; *juvenile* implies that the fragments represent the fresh magma that erupted during the explosive phase (Sigurdsson et al., 2000).The Phase C fallout deposits are indicated in bright red as 'pyroclastics and lapilli tuffs' on Fig. 5.1 and have been studied in detail during fieldwork on the Akri Pounda volcano (locations 32 and 34, Fig. 5.1). In addition, a small outcrop of fallout deposits was encountered during fieldwork on the Delta 2 unit, near the Chionessa dome (location 35, Fig. 5.1).

At Akri Pounda location 32, the light-grey coloured fallout deposit clearly drapes the topography defined by the older Phase B volcaniclastic deposits (Fig. 5.4A). This pyroclastic deposit consists mainly of well-sorted light grey pumice lapilli. A darker, light-brown layer visible within the lower part of this deposit (Fig. 5.4A) might represent either a palaeosol or a fine ash horizon. The uppermost two meters of this fallout deposit exhibit some parallel bedding due to grain size variation of the pumice lapilli (Fig. 5.4B) – it is however not clear whether this is primary bedding or secondary due to avalanching. At the top, these parallel graded deposits are immediately overlain by red PDC deposits of Phase C (location 34, Fig. 5.4B). The fallout deposits at Akri Pounda consist for 85-95% of pumice (mainly lapilli between 1 and 6 cm, but sometimes blocks as large as 15-20 cm) and 5-15% non-juvenile lithic clasts (up to 30cm). The lapilli sized pumice is usually angular and mostly cream-coloured to light grey. About 10% of the pumice lapilli have a distinctly darker grey colour and some show dark grey / light grey flow banding (Fig. 5.4C). The larger, light grey to cream-coloured pumice clasts tend to be more rounded, have multiple fractures and a pinkish-grey to brown-red discoloration

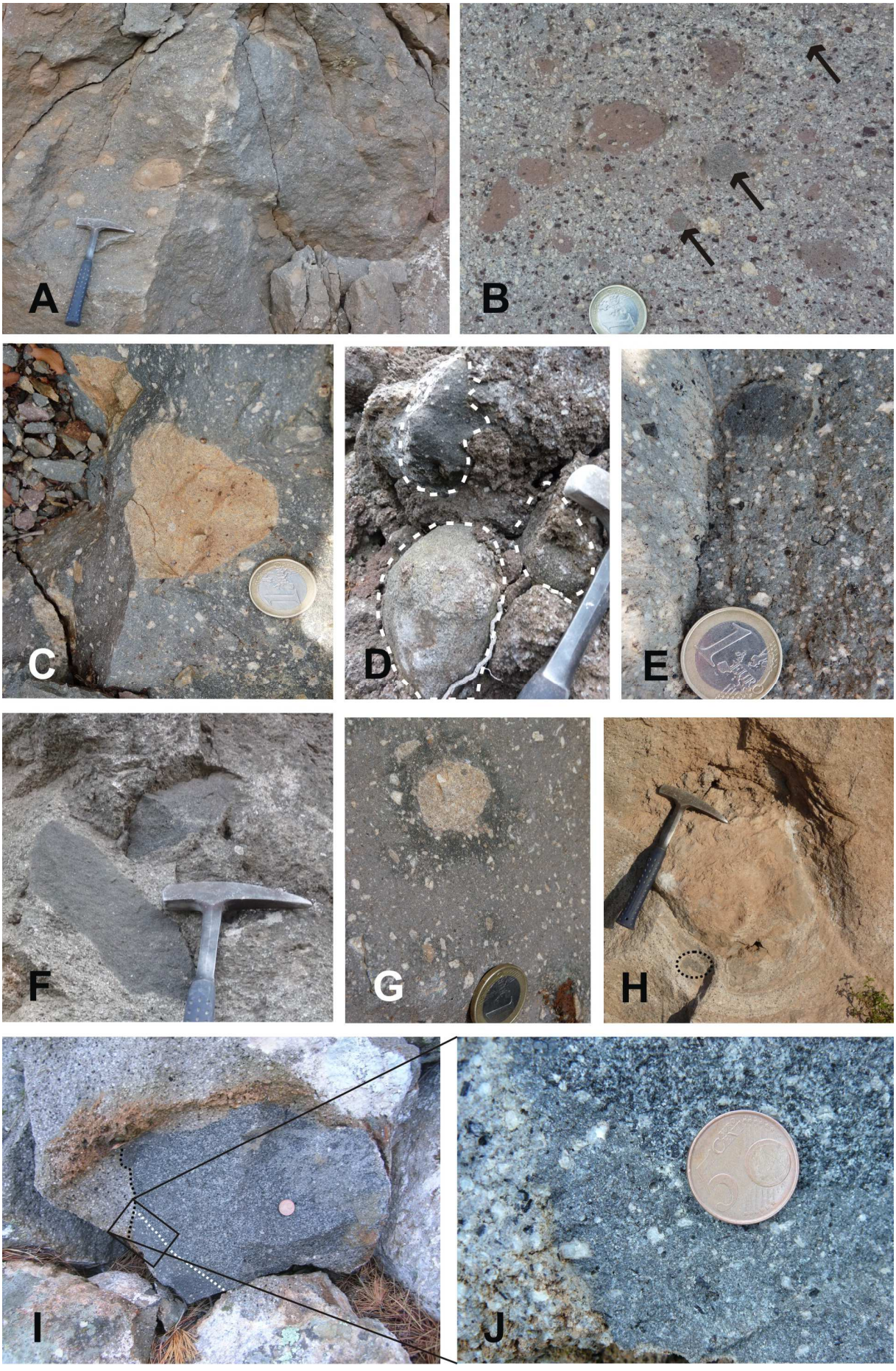
A
B
C
D
E
F
G
H
I
J

Figure 5.3 *Photographs of the enclaves observed in the lavas of the volcanic phases A to H* (hammer or coin for scale). (A) Phase C, northern early andesite, location 36: Enclaves are abundant (up to 10 vol%) and easily recognised due to their yellow-brown weathering colour. (B) Phase B volcaniclastic apron, location 33: The small, fine-grained enclaves have a brown-red colour due to weathering, whereas the more coarse-grained enclaves (black arrows) seem less altered and are therefore more difficult to distinguish. (C). Phase G, central andesite, location 49: The ubiquitous enclaves in this host rock are more often angular than anywhere else, and have a yellow-green (weathering?) colour. (D) Phase B volcaniclastic apron, location 32: three rounded enclaves (white dashed outlines) stick out due to preferential erosion of their vesicular host rock – the top one is more fine-grained, the two lower ones are more coarse-grained. (E) Phase D, NW andesites, location 45: small, dark grey enclave in a phenocryst-rich host lava. (F) Phase G, EW fissure volcanoes, location 52: two larger, fine-grained and elongated enclaves. (G) Phase G, central andesite, location 49: this rounded enclave has caused a corona of darker groundmass in the host rock directly enclosing it. (H) Phase D, southern dacites, location 46: The groundmass of the host shows a different texture in the immediate vicinity of a large enclave –within this area, a smaller and elongated enclave (black dotted oval) is oriented parallel to the larger enclave's outer boundary. (I) Phase H, Mavri Petra flow, location 53: Large, somewhat angular enclave shows a sharp contact with its host lava (black dotted line) but has a less obvious boundary between the two different grain sizes it exhibits (white dotted line) – a close-up of the contacts between the two enclave types and the host rock is shown in (J).

in their centre (Figure 5.4D). The (non-juvenile) lithics within this fallout deposit are mostly clasts of porphyritic, grey to red oxidised lava and enclaves, similar to the Phase A and B deposits. Small (1-3 cm) sedimentary lithics are occasionally observed, for example an angular pelitic clast or a quartz-rich xenolith. Based on field observations and the topographic contour lines on the geological map, the pumice fallout deposit at Akri Pounda volcano (locations 32 & 34, Fig. 5.1) is estimated to be 5-10 m thick.

The fallout deposit along the unpaved road near Chionessa (location 35, Fig. 5.1) is significantly smaller than the one at Akri Pounda. At the base of this approximately 6-7 m wide outcrop a light beige ash layer (10-15cm thick) is draped over the irregular topography of a lava breccia (Fig. 5.4E). This light-coloured ash layer changes upwards into a more orange-brown ash bed of similar thickness and is overlain by a thick bed of pumice lapilli (Fig. 5.4E). This main part of the fallout deposit is well sorted, with some larger lithics of porphyritic lavas and their enclaves concentrated towards the base (Fig. 5.4E). Lapilli mainly consist of 1 to 6 cm beige, grey or orange-pink pumice fragments embedded in small amounts of ash. The 1-2 m thick pumice-rich lapilli layer does not show internal bedding (Fig. 5.4E,F). A thin white ash layer marks the upper boundary of the pumice-rich lapilli deposit, itself overlain by a brown-red, finely laminated, up to 30cm thick ash bed (Fig. 5.4F). Large lava blocks from the overlying brecciated lava flow represent the upper boundary of this fallout deposit (Fig. 5.4F).

5.1.3 Phase C pyroclastic density current deposits & associated lava flows

These pyroclastic deposits concern the outcrops of Phase C 'Akri Pounda volcano' and 'Northern early andesites' indicated on Figure 5.1 in green-and-black-speckles. At Akri Pounda volcano they overlie the Phase C pumice fallout deposits; in the northern part of Methana they are restricted to the area around Ag. Andreas, west of Mavri Petra. At both localities, the PDC deposits directly overly local limestone basement and are spatially associated with the only two outcrops of basaltic andesite lava flows that occur on Methana.

At Akri Pounda (location 38, Fig. 5.1), the PDC deposits overlie the Phase B volcaniclastic basement, the Phase C lapilli tuffs (Fig. 5.4B) or the limestone basement (Fig. 5.5A). They are interpreted to be pyroclastic density current (PDC) deposits because they are very poorly sorted, partially welded and they have little to no internal bedding (Fig. 5.5A-D, Fisher & Schmincke, 1984). The deposits at Akri Pounda contain beds of varying grain size, sorting and thickness, with either black or red juvenile clasts (Fig. 5.5A-D). According to the terminology of Wright et al. (1980), they can be described as *scoria-and-ash deposits* (small-volume, unsorted ash deposits with vesicular lapilli of basaltic and andesitic composition - Fig. 5.5C) and *block-and-ash deposits* (more specifically 'semi-vesicular andesite-and-ash deposits': small-volume, unsorted ash deposits with moderately vesicular

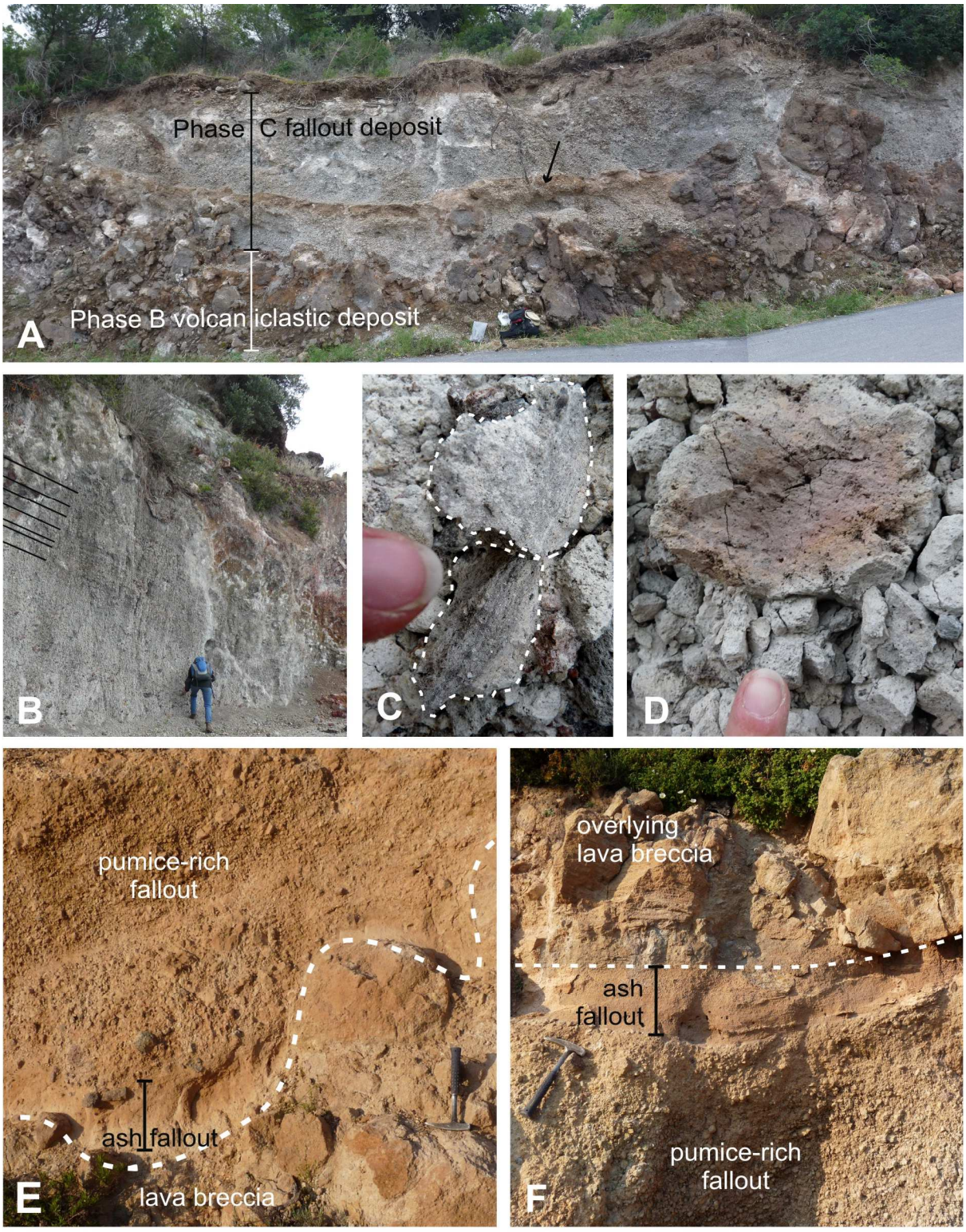

Figure 5.4 *Photographs of the fallout deposits.* (A) Akri Pounda, location 32. The Phase C fallout deposit drapes the topography of the Phase B volcaniclastic apron. Black arrow indicates possible paleosol between pumice lapilli beds. Back-pack for scale at centre of image. (B) Akri Pounda, location 34. The Phase C fallout deposit is overlain by the younger Phase C PDC deposit (orange-red unit to the right). Black lines in the upper 2 m of the pumice deposit trace parallel bedding visible to their right. 1.7 m supervisor for scale. (C) Akri Pounda, white dashed lines delineate two banded pumice lapilli. Index finger for scale. (D) Akri Pounda, fractured pumice bomb with orange-red interior. Index finger for scale. (E) Near Chionessa. The lower part of the fallout deposit drapes a brecciated lava flow. Black vertical bar indicates the beige and beige-brown ash layers that represent the base of this fallout deposit. Hammer for scale. (F) Near Chionessa. The upper part of the fallout deposit is overlain by a brecciated lava flow. Black vertical bar indicates the brown ash bed at the top. Hammer for scale.

andesitic lapilli and bombs – Fig. 5.5D). Both types of deposits often have fine-grained basal layers and sometimes contain over 1 m large, poorly vesicular juvenile bombs with a scoriaceous ropey surface (Fig. 5.5B, D). Besides these dense juvenile bombs, the PDC deposits also contain *lithics*: angular blocks of a different lithology - either magmatic rocks similar to those of the underlying Phase B (Fig. 5.5E) or light-coloured sedimentary rocks (Fig. 5.5F).

The PDC deposits in the north-western part of Methana near Ag. Andreas (locations 43 and 44, Fig. 5.1), are very similar to the ones at Akri Pounda: black and brown-red scoria-and-ash or andesitic block-and-ash deposits, often containing poorly vesicular bombs with a scoriaceous rim (Fig. 5.5G). At this location, the PDC deposits are all directly overlying the limestone basement, and commonly enclose angular carbonate lithics (Fig. 5.5H). Another type of light-coloured, fragile, sedimentary lithic (similar to some xenoliths at Akri Pounda) was also sampled (Fig. 5.5I), but in contrast with Akri Pounda, no igneous lithics were observed within the Ag. Andreas PDC deposits.

In both locations, the scoria and bombs look similar to the Delta 2 lavas: porphyritic, with prismatic black and white phenocrysts floating in a red or dark grey matrix. But in contrast to the Delta 2 host rocks, no mafic enclaves have been observed within the juvenile material of the studied PDC deposits. In close proximity to the PDC deposits of Akri Pounda and near Ag. Andreas, Methana's basaltic andesitic lava flows are found. These brecciated lavas are dark grey to black porphyritic rocks with white and black phenocrysts and rarely contain enclaves (only one small, coarse-grained enclave was observed during fieldwork). Based on their macroscopic similarity to the dark grey PDC deposits, as well as their spatial correlation with them, the basaltic andesitic lava flows have been interpreted as their effusively deposited equivalents.

5.2 Petrography

The nomenclature introduced in Chapter 4 is also used in the following petrographic descriptions: *macro-phenocrysts* are the largest crystals within the rock (usually ≥ 500µm) which were already identifiable in the field; *phenocrysts* are the intermediate-sized crystals (about 100-500 µm) that were (just) distinguishable as such in a hand specimen and which form a flow texture in the host rocks but a randomly oriented framework in the enclaves; *microlites* are the smallest, often needle-shaped, crystals (≤ 100 µm) that together with *volcanic glass* make up the *groundmass*. The petrography of 58 thin sections of igneous rock samples from Methana is presented below. Estimates of plagioclase and olivine compositions are based on optical methods (Nesse, 2004). The petrography of sedimentary xenoliths and basement rocks is not discussed as these lithologies were merely sampled to investigate their potential role as crustal contaminants.

5.2.1 Effusive deposits of Phases A to H

Despite their macroscopic similarity to the Delta 2 lavas, the Phase A to H effusive rocks have a more varied petrography which represents two distinct mineralogical compositions. The majority of Phase A to H host rocks are 'amphibole-rich' type 1 lithologies which contain the same minerals as the Delta 2 host rocks. These amphibole-rich lavas also display disequilibrium features similar to the ones observed in the Delta 2 unit. (Macro-) phenocrysts in such host rocks include embayed quartz grains with and/or without a mantle of prismatic clinopyroxene (Fig. 5.6A); olivine with Cr-spinel inclusions and overgrown by clinopyroxene or amphibole; clusters of tabular clinopyroxene crystals; prismatic orthopyroxene crystals; amphibole and biotite that range from intact crystals with or without new amphibole overgowth (Fig. 5.6B) to partial or complete replacement by anhydrous minerals (Fig. 5.6A); and plagioclase crystals with simple and/or polysynthetic twins, varying extents of sieve textures and some oscillatory zoning. Euhedral crystals of zircon and apatite are occasionally included in plagioclase (Fig. 5.6C, D), amphibole or biotite. Both plagioclase and amphibole typically display a seriate crystal size distribution from (macro-) phenocryst to microlite grainsize (Fig. 5.6E-F). Opaque

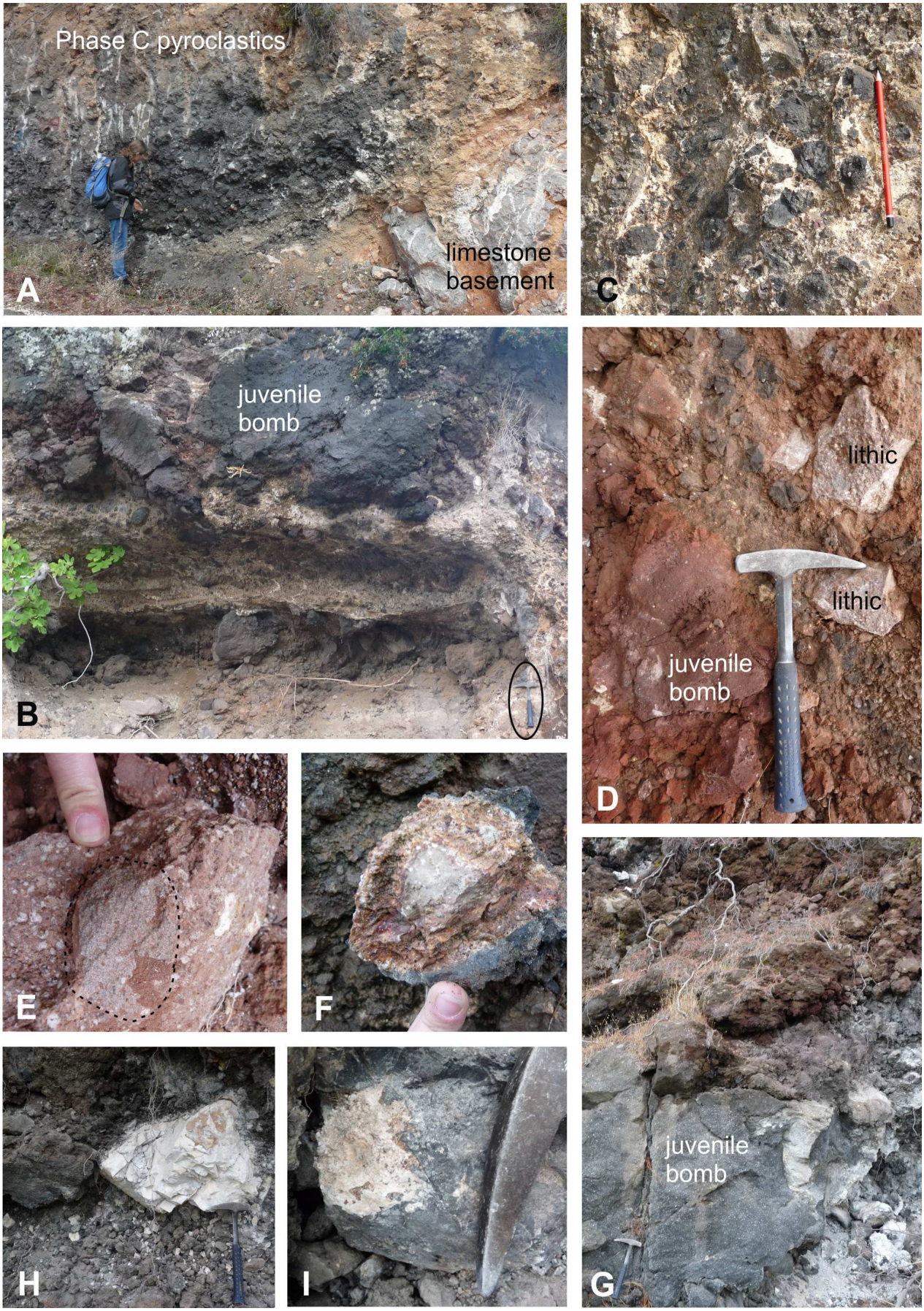
Phase C pyroclastics
limestone basement
A
C
juvenile bomb
B
lithic
lithic
juvenile bomb
D
E
F
H
I
juvenile bomb
G

Figure 5.5 *Photographs of the PDC deposits of phase C.* (A) Akri Pounda. The basis of the PDC deposit (here a dark grey to black scoria and ash deposit) covers the local limestone basement, 1.7m supervisor for scale. (B) Akri Pounda. The PDC deposit consists of different beds of scoria-and-ash or block-and-ash deposits, each with a more fine-grained base and sometimes containing large bombs. Hammer for scale. (C) Akri Pounda. A typical scoria-and-ash deposit. (D) Akri Pounda. Block-and-ash deposit, with a red bomb, some dark grey to black scoria lapilli and two angular lithics similar to the older Phase A and B lavas. (E) Akri Pounda. Angular lithic block of a porphyritic lava similar to the rocks of Phase A and B, containing a fine-grained enclave (delineated by black dashed line). Index finger for scale. (F) Akri Pounda. Sedimentary xenolith within dark grey scoriaceous lava, showing alteration zones. The core of this lithic = 'IM363 core'; its altered rim = 'IM363 rim'. Index finger for scale. (G) Near Ag. Andreas. Typical appearance of the PDC deposit, with both red and dark grey layers of scoria-and-ash as well as block-and-ash deposits, containing juvenile bombs. (H) Near Ag. Andreas. Limestone xenolith within a scoria-rich block-and-ash deposit. Fragment of this carbonate = sample IM396. (I) Porous, soft sedimentary xenolith enclosed by dark grey lava. Fragment of this xenolith = sample IM394. Point of hammer for scale.

Fe-Ti-oxides are always present as smaller phenocrysts to microlites (Fig. 5.6A, B, E, F). Within a single sample, the composition of plagioclase and olivine macro-phenocrysts is homogeneous. Between samples, plagioclase compositions vary from An_{45} to An_{65} (andesine to labradorite) and olivine can be either Mg-rich (Fo_{100} to Fo_{85}) or more Fe-rich (< Fo_{85}). Many of these host rocks also contain at least one micro-enclave with a mineralogical composition and texture similar to the larger enclaves identified during fieldwork (Fig. 5.6G). Holocrystalline clusters of eu- to anhedral clinopyroxene and plagioclase grains are sporadically observed in a few amphibole-rich host rocks.

The less common 'amphibole-poor' type 2 host rocks differ from the amphibole-rich type 1 host rocks due to their distinct lack of primary anhydrous minerals. In amphibole-poor host rocks, the presence of amphibole ± biotite is limited to only a few (macro-) phenocrysts which always show disequilibrium features that range from a thick opaque reaction rim to complete replacement by a fine-grained aggregate of anhydrous minerals (Fig. 5.6H). Dehydration of the biotite usually manifests itself in the replacement, from the outer rim inwards, by an aggregate of plagioclase, Fe-Ti-oxides and pyroxene. Pseudomorphs of amphibole are often epitaxial, fine-grained aggregates of ortho- and/or clinopyroxene. Some crystals are even totally replaced by an opaque, very fine-grained mineral assemblage (opacite), in which case it can be difficult to determine whether the original mineral was amphibole or biotite (Fig. 5.6H). In the absence of amphibole, plagioclase is the main mineral with a seriate crystal size distribution from microlite to macro-phenocryst (Fig. 5.6I). When orthopyroxene is present in large amounts it can also show such a continuous range in crystal size (Fig. 5.6J). The groundmass of these amphibole-poor lavas consists of glass and microlites of plagioclase, orthopyroxene and Fe-Ti-oxides (Fig. 5.6J). Besides plagioclase and minor amounts of dehydrated amphibole ± biotite, amphibole-poor host rocks contain the same (macro-) phenocrysts as the amphibole-rich host rocks as well as occasional zircon and apatite inclusions in large plagioclase crystals.

Type 1 and 2 host rocks can be both present within one eruptive phase. Samples from Phase G 'E-W fissure volcanoes', for example, all belong to the amphibole-rich host rocks (Fig. 5.6E) whereas the different localities of Phase G 'central andesite volcanoes' all have an amphibole-poor mineralogy (Fig. 5.6I, J). Depending on sampling location, the Phase D group of 'North-western andesite flows' contains amphibole-rich (location 46) or amphibole-poor (location 45) host rocks. The single locality of most recent Phase H Mavri Petra complex even contains host rocks of both mineralogical types: the more centrally sampled massive lavas (location 53) have an amphibole- (and biotite-) rich mineral assemblage with an An_{65} plagioclase macro-phenocryst composition (Fig. 5.6B); but blocks from the lateral lava breccia (location 55) show intense dehydration of both amphibole and biotite, increased amounts of ortho-and clinopyroxene phenocrysts and An_{50} plagioclase macro-phenocrysts (Fig. 5.6H). Another such block sampled at the outer margin of the Mavri Petra flow (location 56) shows complete replacement of initially hydrous minerals by an opaque mineral assemblage.

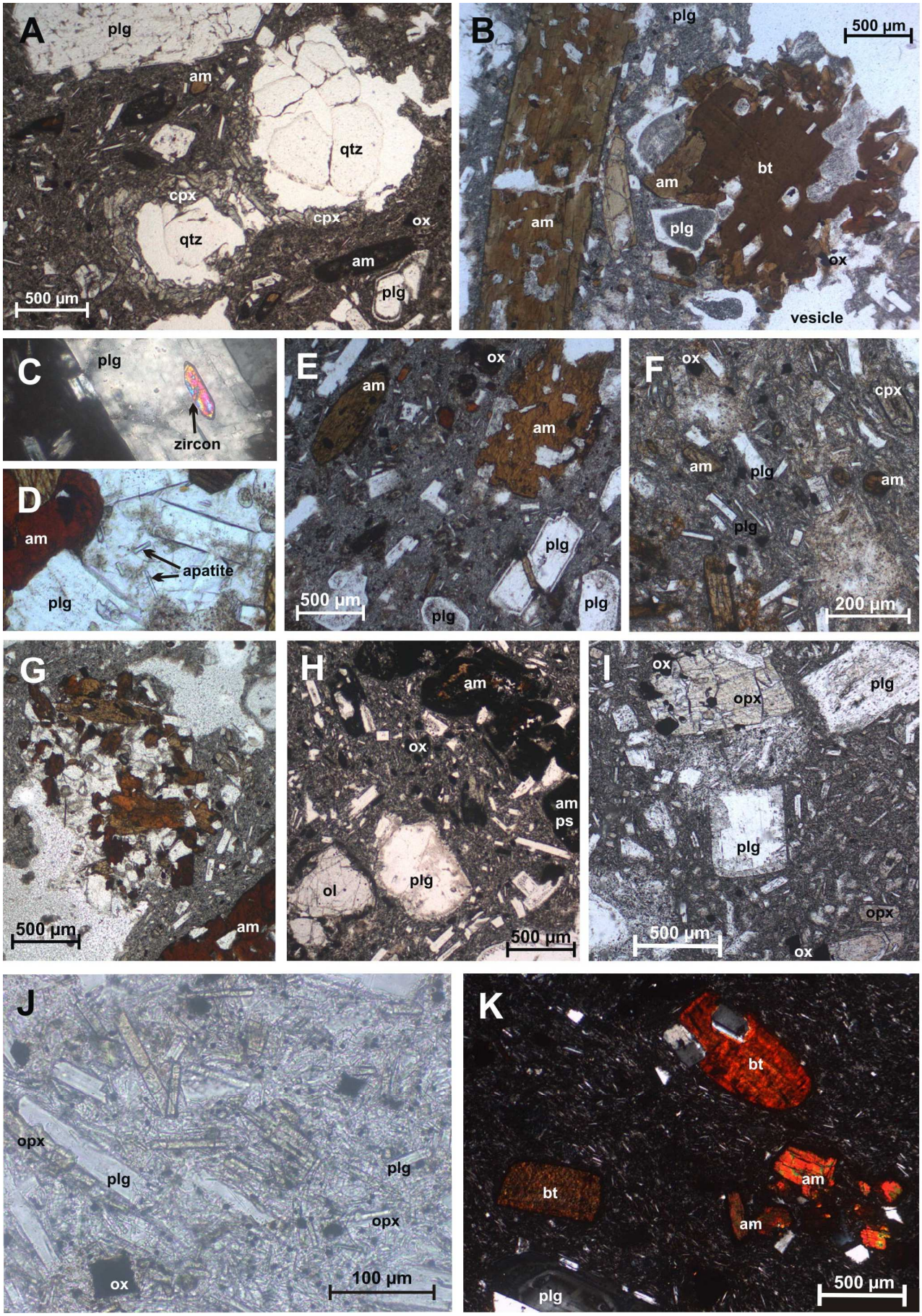
A
plg
am
qtz
cpx
cpx
ox
qtz
am
plg
500 µm
B
plg
500 µm
bt
am
am
plg
ox
vesicle
C
plg
zircon
D
am
apatite
plg
E
ox
am
am
plg
500 µm
plg
plg
F
ox
cpx
am
plg
am
plg
200 µm
G
500 µm
am
H
am
ox
am
ps
ol
plg
500 µm
I
ox
opx
plg
plg
opx
500 µm
ox
J
opx
plg
plg
opx
ox
100 µm
K
bt
bt
am
am
plg
500 µm

Figure 5.6 *Photomicrographs of the phase A to H host rocks.* ppl = under plane polarised light, xpl = under crossed polars, qtz = quartz, plg = plagioclase, am = amphibole, px = pyroxene, opx = orthopyroxene, cpx = clinopyroxene, ox = Fe-Ti-oxides, bt = biotite, ol = olivine, ps = pseudomorph. (A) Type 1 IM317, ppl. Two quartz ocelli with plg- and am-defined flow texture around them. (B) Type 1 IM29, ppl. Macro-phenocrysts of am and bt with new rim or overgrowth of am. (C) Type 1 IM313, xpl. 100 µm long euhedral zircon in plg macro-phenocryst. (D) Type 1 IM313, ppl. Euhedral apatite crystals (30 to 60 µm long) in plg macro-phenocryst. (E) Type 1 IM295, ppl. Major minerals plg and am show a seriate crystal size distribution from macro-phenocryst to large microlite. (F) Type 1 IM23, ppl. Groundmass with prismatic microlites of am, plg and ox. (G) Type 1 IM389, ppl. Coarse-grained micro-enclave with mainly am and plg. (H) Type 2 IM399, ppl. (Macro-) phenocrysts of ol, plg and am with am crystals almost completely dehydrated into opaque pseudomorphs. (I) Type 2 IM303, ppl. Major minerals plg and opx show a seriate crystal size distribution from macro-phenocryst to large microlite. (J) Type 2 IM21, ppl. Groundmass with microlites of opx, plg and ox. (K) Type 3 IM42, xpl. The groundmass represents up to 60% of the rock and is rich in acicular plg microlites which define a magmatic flow around the (macro-) phenocrysts.

A third type of host rock is encountered in one locality only (IM42). This rock shows an almost bimodal grain size distribution of microlites and macro-phenocrysts (Fig. 5.6K). Less than 30-40% of the sample are euhedral macro-phenocrysts of plagioclase (An_{40}), amphibole and biotite – with the hydrous minerals only showing opaque reaction rims as minor disequilibrium feature. The groundmass on the other hand is charged with acicular microlites of plagioclase only (no amphibole), which now define the magmatic flow texture instead of the phenocrysts present in other samples (Fig. 5.6K). All Phase A to H lavas furthermore show some subtle petrographic clues to whether a host rock is overall more mafic or more felsic. For example, when a rock contains large amounts of olivine its quartz occurs as embayed grains mantled by a pyroxene reaction rim. When a sample shows quartz as anhedral grains without a pyroxene mantle, olivine is scarcer (if present at all) and often overgrown by amphibole and/or pyroxene. Host rocks in which euhedral zircon inclusions were identified usually also contain quartz grains without reaction rim and little to no olivine. Large skeletal (hopper) crystals of olivine usually occur in samples with an overall more mafic mineral composition.

Enclaves show a dual distribution of their mineral assemblage that is similar to their host rocks. Amphibole-rich type 1 enclaves consist of plagioclase and amphibole phenocrysts (± clinopyroxene, ± olivine) that usually lack disequilibrium features, are randomly oriented and form a crystal framework (Fig. 5.7A, B). In comparison to the Kossona Vouno enclaves of the Delta 2 unit, these amphibole-rich enclaves contain more olivine. (Macro-) phenocrysts of this magnesium-rich mineral (Fo_{85} – Fo_{100}) include octahedral, dark brown Cr-spinel and are often overgrown by tabular clinopyroxene (sometimes orthopyroxene), which in turn can be mantled by amphibole (Fig. 5.7C). Besides olivine, common macro-phenocrysts are plagioclase (often with complex zoning and sieve textures - Fig. 5.7D), amphibole and biotite (to varying extents replaced by anhydrous aggregates - Fig. 5.7E, F) and anhedral quartz grains with a pyroxene reaction rim. The macro-phenocrysts of the enclaves are overall very similar to those observed in the host rocks, but they are present in smaller amounts.

Whereas the crystal framework of amphibole-rich type 1 enclaves is mainly built up by plagioclase and amphibole, the phenocrysts of amphibole-poor type 2 enclaves are mainly plagioclase and orthopyroxene (± clinopyroxene, ± olivine) (Fig. 5.7G, H). If prismatic amphibole phenocrysts are present, they are largely replaced either by opacite (Fig. 5.7H) or by pyroxene pseudomorphs (Fig. 5.7G). Macro-phenocrysts are also scarce in these amphibole-poor enclaves and mainly represent plagioclase (Fig. 5.7G) or amphibole crystals with pronounced disequilibrium features (Fig. 5.7I, J).

Type 1 enclaves are usually contained within type 1 host rocks and type 2 enclaves within type 2 lavas. The only exception are the amphibole-rich (micro-) enclaves found within the amphibole-poor host lavas of the small Paleo Kastro outcrop near Akri Pounda volcano (location 41). When a host rock and enclave are sampled together at a certain location, the enclave's olivine always shows the same (optically determined) forsterite content as the olivine in its host rock. The optically determined composition of an enclave's plagioclase macro-phenocrysts is usually also similar to that of its host rock. All enclaves furthermore contain small phenocrysts of Fe-Ti-oxides. As described for the Delta 2

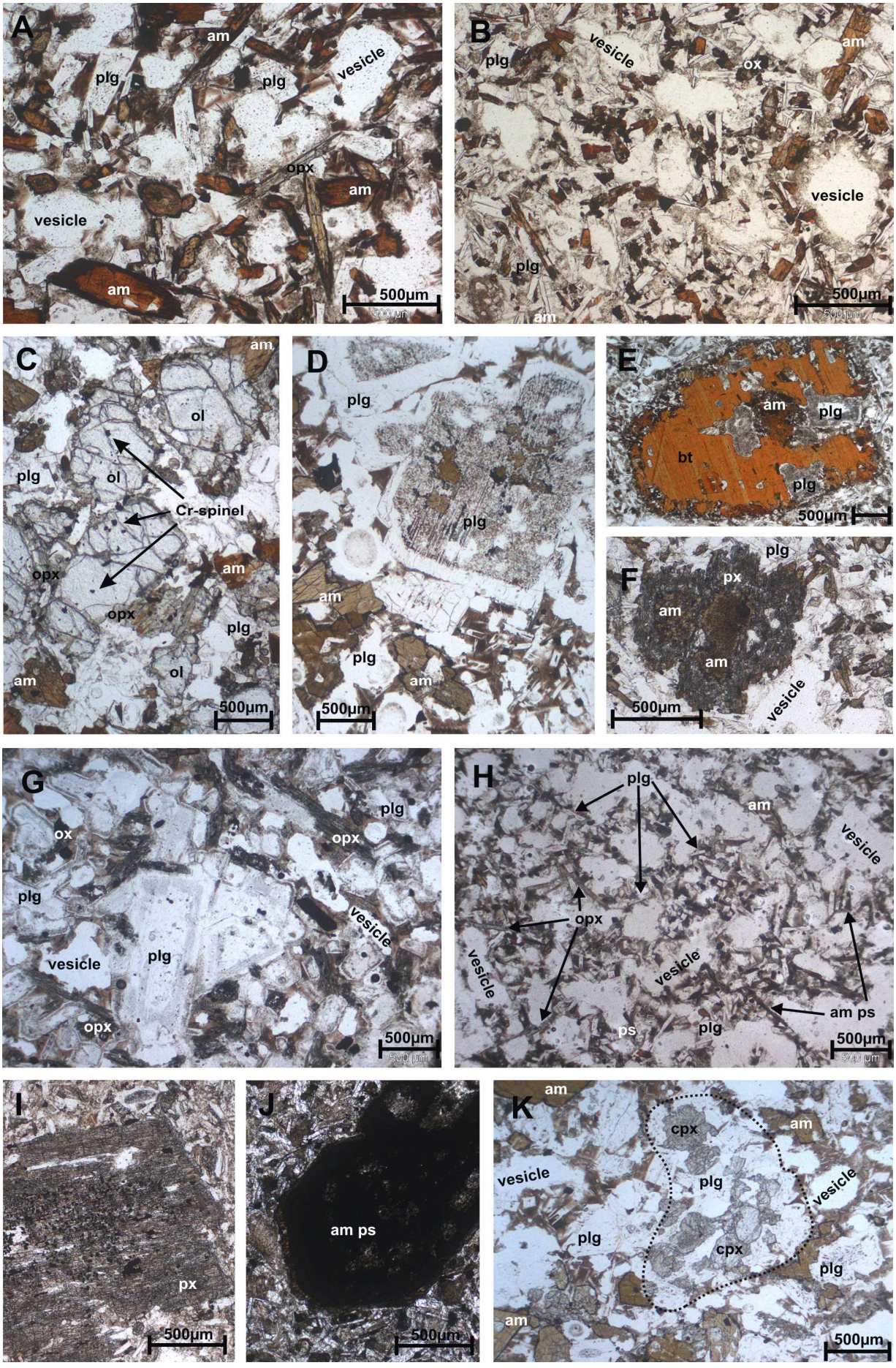
A
am
plg
plg
vesicle
opx
am
vesicle
am
500µm
B
plg
vesicle
ox
am
vesicle
plg
am
500µm
C
am
ol
plg
ol
Cr-spinel
opx
am
opx
plg
ol
am
500µm
D
plg
plg
am
plg
am
500µm
E
am
plg
bt
plg
500µm
F
plg
px
am
am
vesicle
500µm
G
ox
plg
opx
plg
vesicle
vesicle
plg
opx
500µm
H
plg
am
vesicle
opx
vesicle
vesicle
am ps
ps
plg
500µm
I
px
500µm
J
am ps
500µm
K
am
cpx
am
vesicle
plg
vesicle
plg
cpx
plg
am
500µm

Figure 5.7 *Photomicrographs of Phase A to H enclaves.* All images ppl, acronyms as in Fig. 5.6. (A) Type 1 IM40. Coarse-grained crystal framework of mainly plg and am ± opx. (B) Type 1 IM312. Fine-grained framework of more prismatic to acicular plg and am phenocrysts. (C). Type 1 IM369, ppl. Olivine macro-phenocrysts with octahedral Cr-spinel, some cpx overgrowths and am. (D) Type 1 IM373. Large plg macro-phenocrysts with sieve-textured cores and anhedral am inclusions. Note skeletal plg phenocrysts in brown glass in the lower right corner. (E) Type 1 IM312. The rim of a large bt macro-phenocryst is partially replaced by an anhydrous aggregate. (F) Type 1 IM368. An am macro-phenocrysts largely replaced by a fine-grained epitaxial aggregate of px and overgrown by smaller am grains. (G) Type 2 IM291. A few plg macro-phenocrysts within a very coarse-grained crystal framework that consists of plg and fine-grained, epitaxial px pseudomorphs after am. (H) Type 2 IM44. Very vesicular enclave with fine-grained crystal framework of plg and opx. (I) Type 2 IM301. Amphibole macro-phenocryst entirely replaced by epitaxial opx/cpx, ox and plg. (J) Type 2 IM316. Opaque pseudomorph after am macro-phenocryst. (H) Type 1 IM373. Black dashed line points out holocrystalline aggregate of eu- to anhedral plg and cpx. Note skeletal plg phenocrysts near the vesicles in the left and right middle part of the image.

enclaves, their crystal framework shows a range in grain size with the more fine-grained samples showing a higher aspect ratio for their framework-building phenocrysts (Fig. 5.7B, H). Fine-grained enclaves commonly have a higher amount of vesicles than more coarse-grained enclaves (Fig. 5.7 A-B, G-H). Besides macro-phenocrysts, phenocryst framework and rounded vesicles, all enclaves contain minor amounts of groundmass which is composed of glass and some prismatic to acicular plagioclase and pyroxene microlites. Some enclaves have heterogeneously distributed areas of a glassy groundmass with skeletal plagioclase microlites (Fig. 5.7G, K). A few enclaves also contain holocrystalline aggregates of eu- to anhedral plagioclase and clinopyroxene (Fig. 5.7K), similar to the few plagioclase-clinopyroxene clusters observed in the host rocks.

5.2.2 The pyroclastic deposits of Phase C

Pumice lapilli from both fallout deposits have the same mineralogy, but samples from the Chionessa location are slightly more vesicular (up to 45 vol.% vesicles) than the Akri Pounda pumice (up to 35 vol.% vesicles). Compared to a typical pumice vesicularity of more than 60 vol% (Siggurdson et al., 2000), the pumiceous lapilli from Methana have a rather low vesiuclarity which is reflected in the fact that they do not float on water, but immediately sink. Their vesicles are overall irregularly shaped and somewhat elongated (Fig. 5.8A, B). The groundmass represents 70 to 85% of the rock volume of the pumice samples and mainly consists of volcanic glass with concentric cracks that define a perlitic texture (Fig. 5.8A). The difference between the lighter and darker coloured Akri Pounda pumice microscopically translates into a clear volcanic glass (Fig. 5.8A) or a rather cryptocrystalline groundmass (Fig. 5.8E), respectively. Minor amounts of prismatic microlites of plagioclase and orthopyroxene are also present, besides equidimensional crystals of opaque Fe-Ti-oxides (Fig. 5.8A). Common phenocrysts are prismatic crystals of orthopyroxene and plagioclase, more or less aligned and defining a magmatic flow texture (Fig. 5.8B). Plagioclase displays the largest range in grain size, from tabular microlites to somewhat sieve-textured macro-phenocrysts. Orthopyroxene is also present as fine-grained, epitaxial replacements of (formerly) hydrous macro-phenocrysts and as an overgrowth onto olivine. The latter is present as (macro-)phenocrysts with inclusions of Cr-spinel and usually mantled by orthopyroxene and plagioclase (Fig. 5.8C, D). Some of such olivine-orthopyroxene-plagioclase aggregates resemble the olivine-rich type 2 enclaves from the effusive volcanic deposits (Fig. 5.8E). Amphibole and biotite are only rarely present as macro-phenocrysts, and if so with clear disequilibrium features (epitaxial replacement by mainly orthopyroxene ± clinopyroxene ± Fe-Ti oxides ± plagioclase for amphibole (Fig. 5.8F); replacement of biotite by orthopyroxene, plagioclase and Fe-Ti-oxides from the rim inward (Fig. 5.8G)). Quartz is observed in a few pumice lapilli as resorbed, embayed macro-phenocrysts which are never mantled by clinopyroxene crystals (Fig. 5.8H). Iron-Ti-oxides are always present as accessory phenocrysts and microlites.

Given the pronounced disequilibrium textures that mark the few hydrous minerals present and the fact that plagioclase and orthopyroxene are the main mineral phases for phenocrysts and microlites,

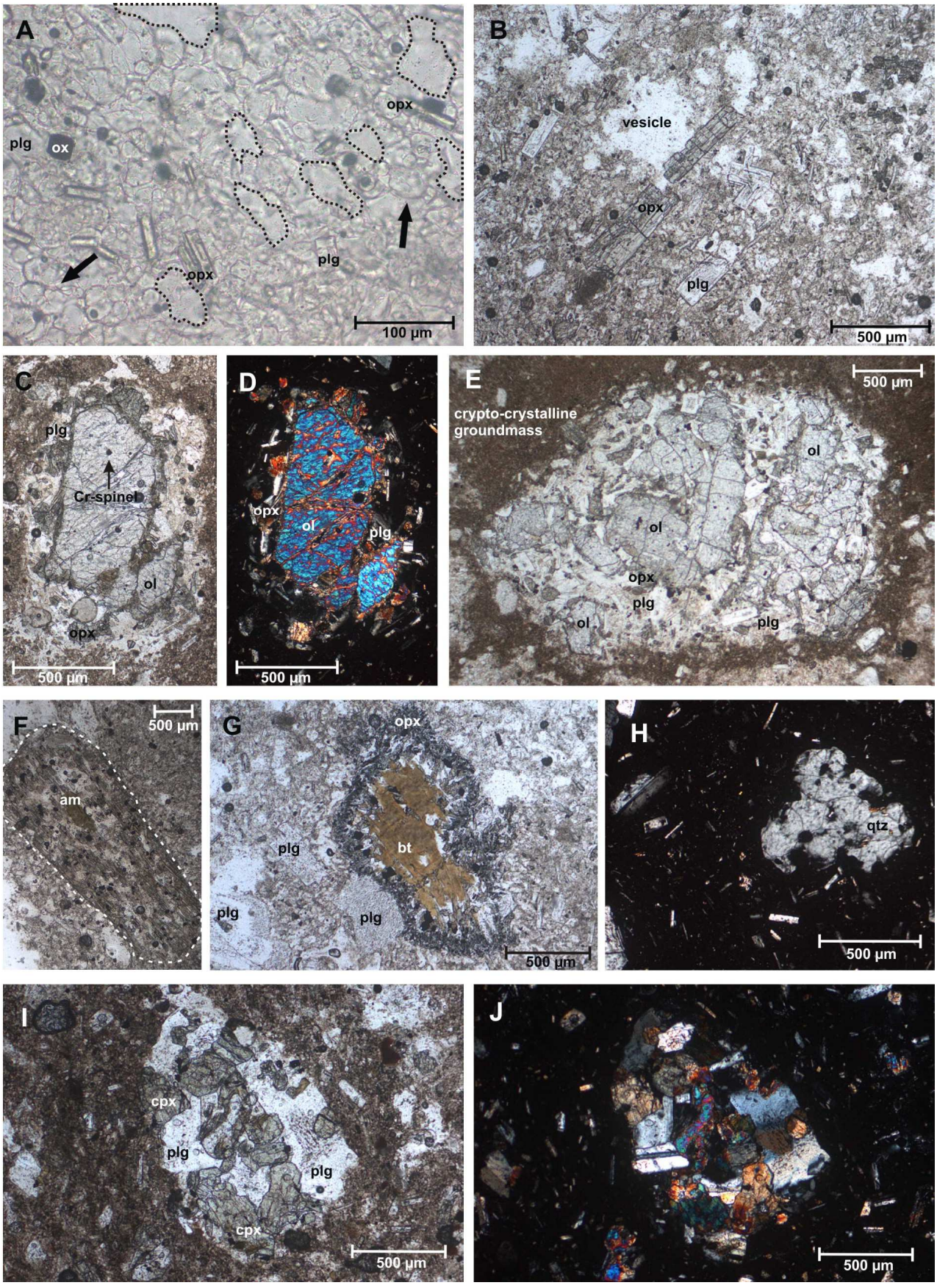
A
plg
ox
opx
plg
opx
100 µm
B
vesicle
opx
plg
500 µm
C
plg
Cr-spinel
ol
opx
500 µm
D
opx
ol
plg
500 µm
E
crypto-crystalline
groundmass
500 µm
ol
ol
opx
plg
ol
plg
F
500 µm
am
G
opx
plg
bt
plg
plg
500 µm
H
qtz
500 µm
I
cpx
plg
plg
cpx
500 µm
J
500 µm

Figure 5.8 *Photomicrographs of the pumice from the Phase C fallout deposits.* Acronyms as in Fig. 5.6. (A) Pumice IM17A, ppl. Close-up of clear glassy groundmass with concentric cracks (indicated by black arrows) and some microlites of plg, opx and ox. Vesicles are outlined by black dots. (B) Pumice IM17B, ppl. Groundmass with clear glass, microlites and aligned (macro-) phenocrysts of plg and opx. (C). Pumice IM388, ppl. Olivine macro-phenocryst with Cr-spinel, mantled by opx and plg. (D) Same as (C) but xpl. (E) Pumice IM17A, ppl. Micro-enclave with crystal framework primarily of plg and (macro-) phenocrysts of ol and minor opx. Note the cryptocrystalline groundmass around this micro-enclave. (F) Pumice IM383, ppl. White dashed line delineates a large am macro-phenocryst almost completely replaced by a fine-grained, epitaxial aggregate of plg, px and ox. (G) Pumice IM17B, ppl. Biotite macro-phenocryst whose rim is replaced by a fine-grained aggregate of (non-epitaxial) plg, opx and ox. (H) Pumice IM17B, xpl. Embayed qtz macro-phenocryst with clear conchoidal fracture pattern. (I) Pumice IM388, ppl. Small, holocrystalline aggregate of sub- to anhedral plg and cpx. (J) Same as (I) but xpl.

the pumice lapilli of Methana are petrographically more equivalent to the 'amphibole-poor' type 2 than the 'amphibole-rich' type 1 host rocks of the effusve volcanic deposits. Although no enclaves were macroscopically observed in the fallout deposits, the pumice lapilli all contain micro-enclaves composed of olivine, plagioclase and orthopyroxene. One of the pumice samples furthermore contains a few holocrystalline aggregates of sub- to anhedral plagioclase and clinopyroxene (Fig. 5.8I, J), similar to the holocrystalline plagioclase-clinopyroxene clusters sporadically observed in the effusive host rocks and enclaves (Fig. 5.7K).

The pyroclastic density current deposits at Akri Pounda and near Ag. Andreas are petrographically very similar to one another. The difference between scoria samples and denser bombs is mainly the higher vesicularity and the higher amounts of dark cryptocrystalline groundmass for the former - their mineralogy is essentially the same (Fig. 5.9A, B). The amount of groundmass varies from one sample to the next, but always represents more than 50 vol.% of the rock. The groundmass is charged with prismatic microlites of plagioclase in between which there are only minor amounts of glass (Fig. 5.9C). Besides plagioclase and some Fe-Ti-oxides, clinopyroxene is also present as a (minor) microlite phase of euhedral short prismatic to tabular crystals (Fig. 5.9C). Similar to the groundmass, the (macro-)phenocryst assemblage of these pyroclastic flow deposits is also characterised by plagioclase (An_{45}) and clinopyroxene. Plagioclase is the dominant mineral besides short prismatic to tabular clinopyroxene (Fig. 5.9A, B, D). The third major mineral phase is olivine (colourless, with Cr-spinel inclusions, Fo < 85%) – sometimes even present in higher amounts than clinopyroxene (greenish hue) (Fig. 5.9D, E). Iron-Ti-oxides are always present as a minor mineral of the phenocryst and microlite phase. The holocrystalline aggregates of sub- to anhedral plagioclase and clinopyroxene, only sporadically present in host rocks, enclaves and pumice lapilli, are ubiquitously present in both the scoria and juvenile bomb samples from the PDC deposits and resemble cumulate rocks (Fig. 5.9B, D, E). In these aggregates, clinopyroxene reaches macro-phenocryst dimensions and shows multiple twinning besides the more commonly present simple twins (Fig. 5.9F). These holocrystalline clusters can furthermore contain olivine and Fe-Ti-oxides (Fig. 5.9B, D-G). No mineral aggregates with vesicles and/or a typical (micro-) enclave texture have been found in any of the PDC deposits. Apart from a few fine-grained pseudomorphs after biotite or amphibole (Fig. 5.9A), these samples also lack hydrous minerals. At least half of the studied thin sections contain (macro-)phenocrysts of quartz with a (clino-)pyroxene corona texture (Fig. 5.9E). Most samples from the PDC deposits show a seriate crystal size distribution for plagioclase, in which case both the prismatic phenocrysts and the more acicular microlites define a flow texture around the macro-phenocrysts (Fig. 5.9C-E). There are, however, also samples with a nearly bimodal grain-size distribution of macro-phenocrysts and microlites in which only the plagioclase microlites are aligned (Fig. 5.9B), similar to the 'type 3' host rock IM42 (Fig. 5.6K).

The basaltic andesite autoclastic lava breccias closely associated with the PDC deposits at Akri Pounda and near Ag. Andreas all show a very similar mineralogy of plagioclase, clinopyroxene, olivine (Fo < 85%)) and Fe-Ti-oxides ± quartz with a reaction rim ± dehydrated amphibole or biotite (Fig. 5.8H). They also contain holocrystalline aggregates of eu- to anhedral plagioclase and clinopyroxene ± olivine. The basaltic andesites sampled near Ag. Andreas seem to contain slightly more clinopyroxene

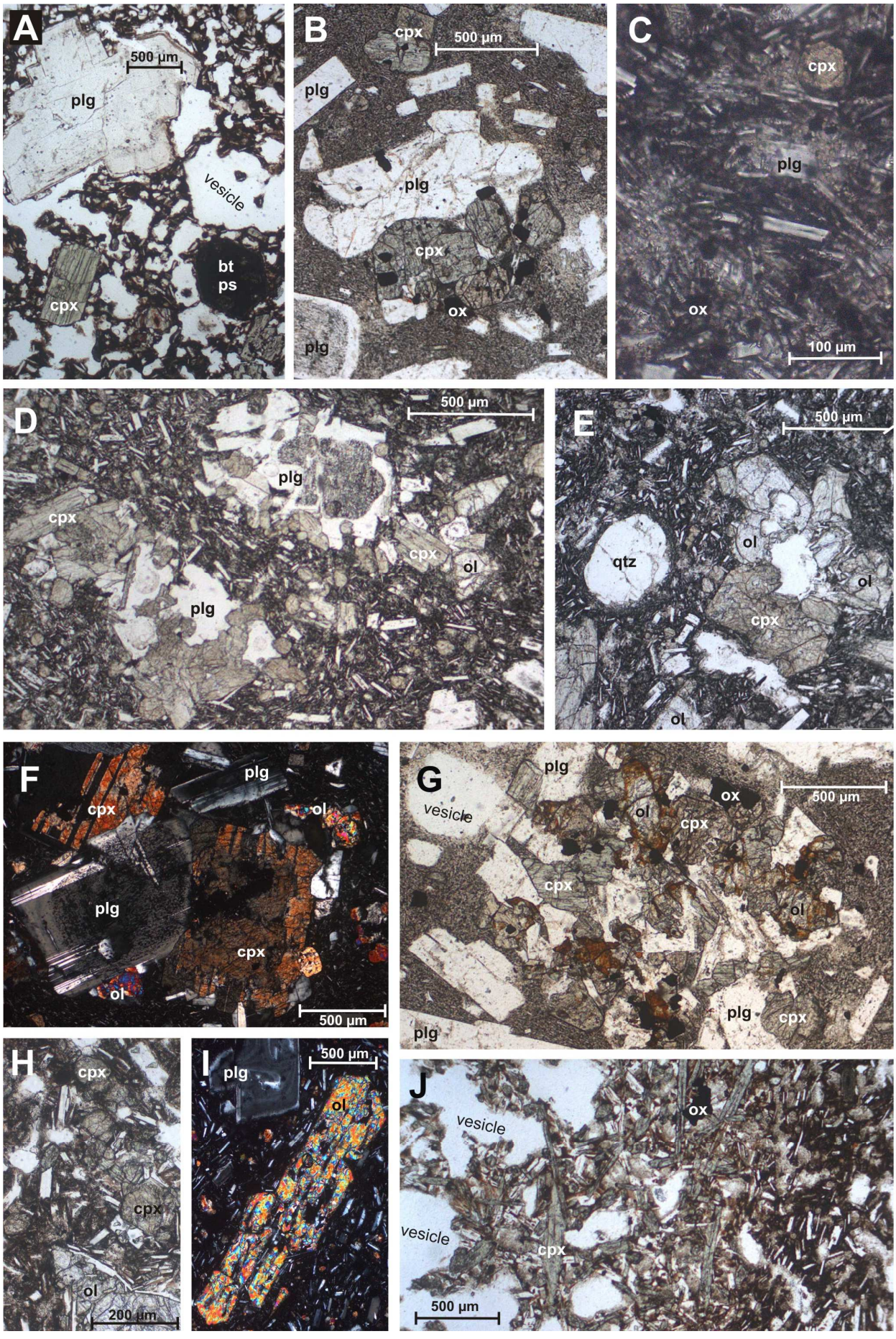
A
500 µm
plg
vesicle
bt
ps
cpx
B
cpx
500 µm
plg
plg
cpx
ox
plg
C
cpx
plg
ox
100 µm
D
500 µm
plg
cpx
cpx
ol
plg
E
500 µm
ol
qtz
ol
cpx
ol
F
plg
cpx
ol
plg
cpx
ol
500 µm
G
plg
ox
500 µm
vesicle
ol
cpx
cpx
ol
plg
cpx
plg
H
cpx
cpx
ol
200 µm
I
500 µm
plg
ol
J
ox
vesicle
vesicle
cpx
500 µm

Figure 5.9 *Photomicrographs of the Phase C pyroclastic density current deposits and associated basaltic andesites.* Acronyms as in Fig. 5.6; ps = pseudomorph. (A) Scoria IM394, ppl. Highly vesicular sample with a dark cryptocrystalline groundmass and plg microlites, surrounding (macro-) phenocrysts of plg, cpx and a bt ps. (B) Juvenile bomb IM13, ppl. Non-vesicular sample with a plg-rich groundmass and (macro-)phenocrysts of plg, cpx and ox. (C). Juvenile bomb IM359, ppl. Close-up of groundmass rich in prismatic to acicular plg microlites, besides cpx and ox. (D) Juvenile bomb IM359, ppl. Overview of this sample, rich in (holocrystalline aggregates of) plg and cpx macro-phenocrysts. (E) Juvenile bomb IM359, ppl. Embayed qtz grain with fine-grained cpx mantle next to a cluster of ol and cpx. (F) Juvenile bomb IM13, xpl. Aggregate of large subhedral macro-phenocrysts of plag and cpx - both with multiple twins - and some smaller ol. (G) Juvenile bomb IM13, ppl. Holocrystalline aggregate of sub- to anhedral plg, cpx, ol and ox. (H) Basaltic andesite IM36, ppl. Skeletal ol phenocryst in bottom right corner, groundmass with white, prismatic plg and euhedral, equidimensional cpx microlites. (I) Basaltic andesite IM36, xpl. Large skeletal ol macro-phenocryst and plg macro-phenocryst with some oscillatory zoning. Note orange-coloured cpx microlites and flow texture of plg microlites. (J) Basaltic andesite IM37, ppl. Highly vesicular enclave (left 3/4 of frame) with prismatic framework phenocrysts of plg and cpx, in contact with its host rock (right 1/4 of frame).

microlites in the groundmass than the equivalent rocks at Akri Pounda. Olivine (macro-)phenocrysts sometimes show a skeletal (hopper) crystal shape (Fig. 5.9I), especially in the lavas near Ag. Andreas. This is also the only location where a micro-enclave with round vesicles and prismatic clinopyroxene and plagioclase phenocrysts was observed (Fig. 5.9J).

5.2.3 Igneous xenolith IM376

Besides the unusual combination of type 1 enclaves in a type 2 host rock, the Paleo Kastro lavas also yielded the only igneous xenolith found on Methana. This coarse-grained sample of about 11 cm x 8 cm x 5 cm exhibits a sharp contact between two different holocrystalline lithologies, with a quartz-rich vein cross-cutting both lithologies as well as their contact. The contact with the surrounding lava is also sharp and without quenched margins in either xenolith or host rock (Fig. 5.10A). The more felsic variety (IM376A) mainly consists of 0.1 to 1mm sub- to anhedral plagioclase prisms and 100 – 250 µm anhedral quartz grains (Fig. 5.11A-E). Both quartz and plagioclase also occur as larger crystals – the latter with an An_{50} composition, polysynthetic twinning and rare oscillatory zoning (Fig. 5.10C). The smaller plagioclase grains have a lower anorthite content. Greenish clinopyroxene occurs as sub-to anhedral prismatic grains and as an epitaxial replacement of what could have been amphibole (Fig. 5.10D, E). Some Fe-Ti-oxides are spatially linked to clinopyroxene clusters. The contact with the more mafic part of this xenolith (IM376B) is very sharp (no chilled margins – Fig. 5.10F, G). The grain size of this mafic part of the holocrystalline xenolith is significantly smaller than that of its felsic counterpart, with the majority of the grains being smaller than 200 µm. It consists mainly of eu- to subhedral plagioclase with a prismatic to acicular habit. Eu- to subhedral clinopyroxene is the second major mineral and Fe-Ti-oxides are present in minor amounts (Fig. 5.10H). Large crystals (≤ 1 mm) include plagioclase, multiply twinned clinopyroxene and pseudomorphs of epitaxial clinopyroxene. Some clusters of medium-sized amphibole crystals are only replaced by clinopyroxene at their outer rim (Fig. 5.10I). Quartz is not present as either phenocryst or macro-phenocryst. The quartz-rich vein that cross-cuts both the felsic and mafic lithology consists of anhedral quartz and some feldspars and clinopyroxene grains. Its more or less equigranular grain size is similar to that of the felsic holocrystalline lithology: about 0.5 to 1 mm (Fig. 5.10J, K).

Based on the holocrystalline texture of this xenolith and the mineralogical composition of its two lithologies, felsic part IM376A is classified as a granite whereas the more mafic part IM376B is best described as a diorite.

5.3 Geochemical data

The major and trace element concentrations and Sr-Nd-Pb and Hf isotopic compositions analysed for igneous rocks from Methana (other than the Delta 2 unit) can be found in Appendices B2, C2, D2

and E, respectively. Since volcanism on Methana is less than 5 Ma old, age corrections have not been applied. The geochemical data of sedimentary basement rocks as well as of the non-igneous xenoliths found within the Phase C pyroclastic deposits are collected in Appendix F1.

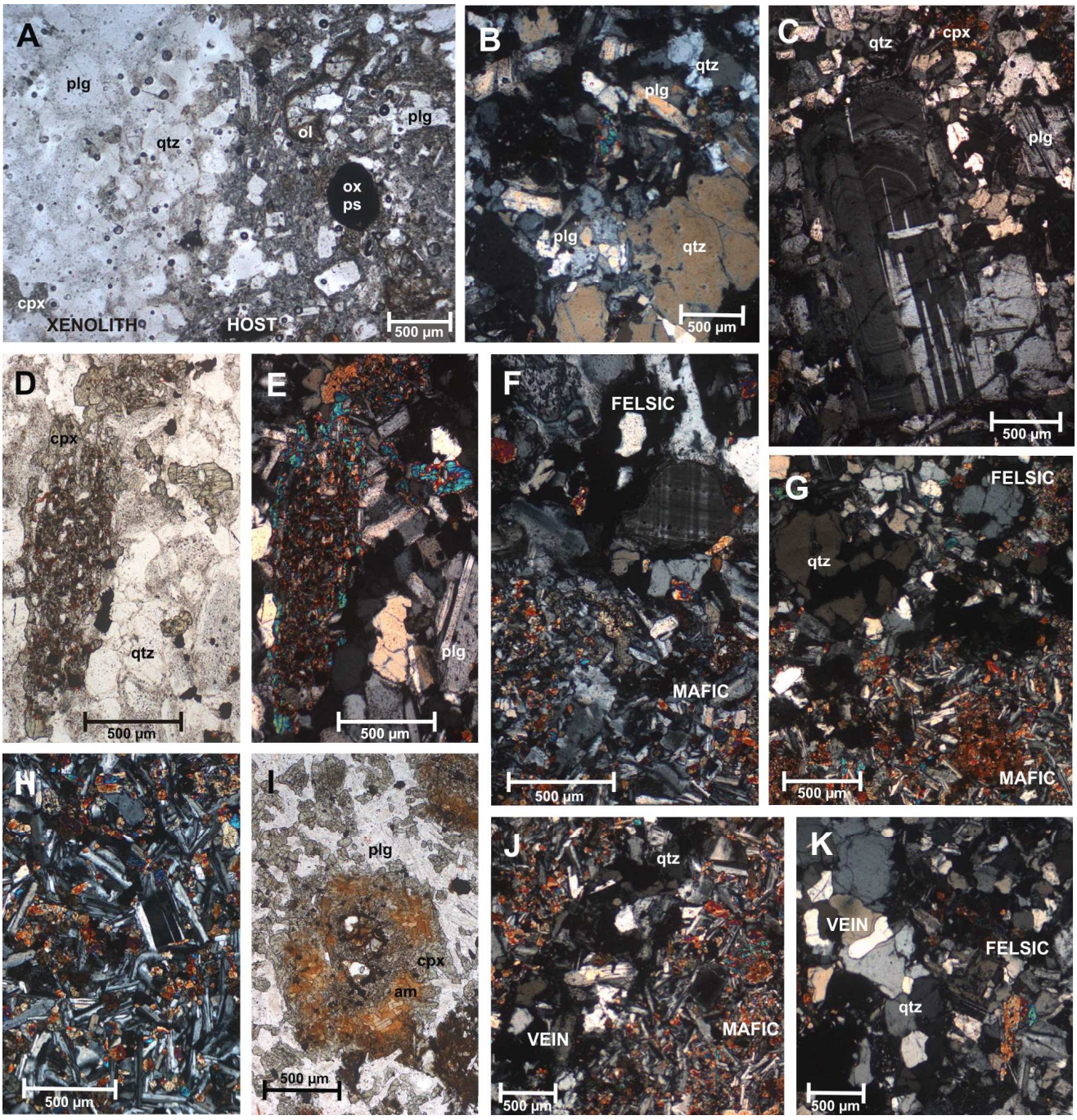

Figure 5.10 *Photomicrographs of holocrystalline, igneous xenolith IM376.* Acronyms as in Fig. 5.6. (A) IM376A, ppl. Contact between type 2 host rock (right) and felsic part of the xenolith (left). (B) IM376A, xpl. The felsic variety mainly consists of plg and qtz. (C). IM376A, xpl. Large euhedral plg crystal within felsic part of the xenolith. (D) IM376A, ppl. The felsic rock type also contains cpx, either as epitaxial pseudomorph (left part of image) or as primary crystals (top right part image). (E). IM376A – xpl image of (D). (F) IM376B, xpl. Contact between felsic and mafic parts of the holocrystalline xenolith, with a feldspar showing two perpendicular sets of polysynthetic twins. (G) IM376B, xpl. Contact between mafic and felsic varieties, with large qtz crystals in the latter. (H) IM376B, xpl. Overview of mafic part of holocrystalline xenolith. (I) IM376B, ppl. Cluster of am crystals, replaced by cpx at the rim. Also note higher amount of cpx in rest of mafic part (top left), compared to the felsic part in (A) and (D). (J). IM376B, xpl. Quartz-rich vein crosscutting the mafic part. (K) IM376A, xpl. Contact between felsic part and qtz-rich vein, note similar grain size.

The geochemical data presented below are grouped according to Methana's volcanic stratigraphy and eruptive style: phase A & B samples from the first period of activity (including the Loutses South samples from the Delta 2 unit); the pumice-rich fallout deposits; the PDC deposits and associated basaltic andesites; and the Phase C to H rocks from Methana's second period of volcanism. The Delta 2 samples discussed in Chapter 4 belong to the latter group but are shown separately to facilitiate comparison between their geochemical range and the compositional variety of Methana's other volcanic deposits. Enclaves and host rocks are indicated by different symbols, as are the two parts of the igneous xenolith found within the Paleo Kastro lavas (IM376A&B). Literature data on Methana's volcanic rocks are also given (Pe, 1971; Pe, 1974; Pe, 1975; Innocenti et al., 1981; Fytikas et al., 1987; Mitropoulos et al., 1987; Dietrich et al., 1988; Gülen, 1990; Clift & Blusztajn, 1999; personal communication G. Pe-Piper, June 2013).

5.3.1 Major element geochemistry

The K_2O-SiO_2 diagram (Gill, 1981) shows one continuous medium-K trend for nearly all volcanic rocks of Methana (Fig. 5.11). Only the two igneous xenoliths, IM376A&B, have significantly lower potassium contents (<0.20 wt%) and plot within the low-K field. The geochemistry of Methana's volcanic rocks presented in this study defines broadly the same geochemical range as literature data (grey field in Fig. 5.11) – which is as large as the compositional range observed within the Phase D 'Delta 2 unit' (black symbols in Fig. 5.11). Effusive volcanic products from the first (orange symbols in Fig. 5.11) and the second (green symbols in Fig. 5.11) period of volcanic activity overlap one another and neither show a compositional gap between enclaves and host rocks. In the Phase C pyroclastic deposits there is a distinct geochemical gap of ~4 wt% SiO_2 between the pumice-rich fallout deposits (red symbols in Fig. 5.11) on the one hand, and the PDC deposits and associated basaltic andesites (blue symbols in Fig. 5.11) on the other hand. Both types of pyroclastic deposits were sampled from two different locations, but whereas the pumice defines one compositional trend, the PDC deposits and associated basaltic andesites cluster into two small groups (see inset Fig. 5.11): a $K_2O \leq 1.28$ wt% cluster represents all samples from the southerly Akri Pounda volcano and a $K_2O \geq 1.28$ wt% cluster groups the rocks from the NW part of Methana peninsula near the Mavri Petra flow. The PDC

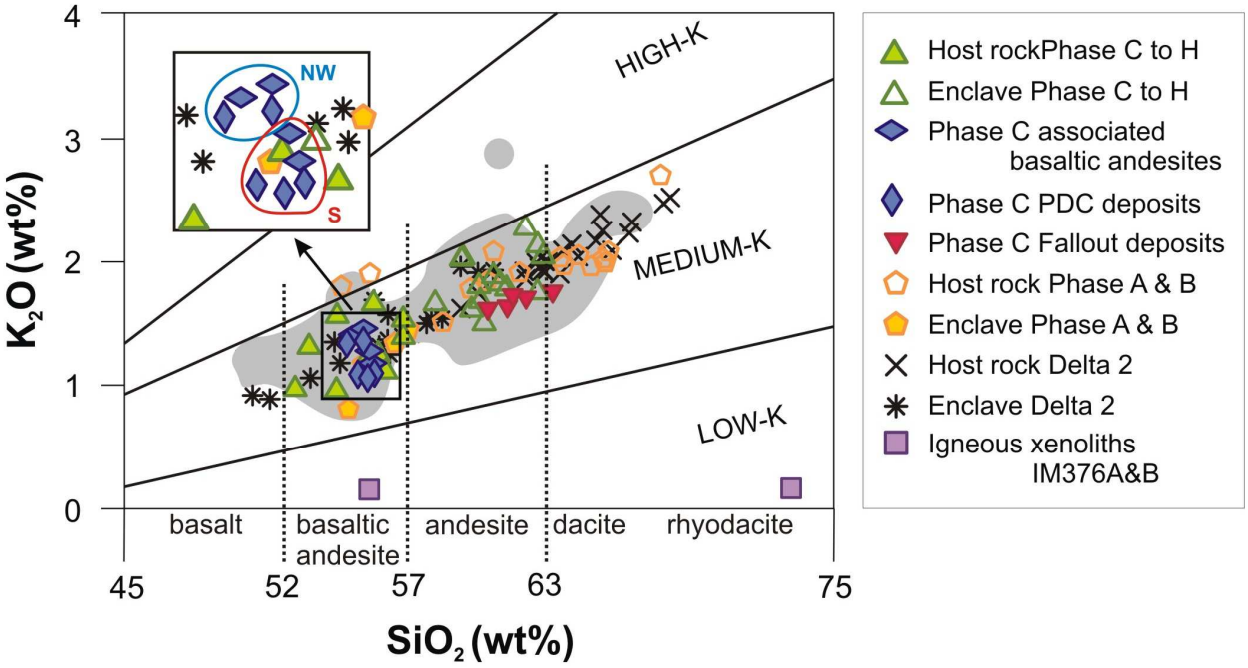

Figure 5.11. *Methana's volcanic rocks define a medium-K trend in the K_2O-SiO_2 classification diagram* of Gill (1981). Dotted lines indicate the silica ranges for basalts, basaltic andesites, andesites and dacites after Le Maitre et al. (2002). Grey fields = range of literature data.

deposits and associated basaltic andesites are furthermore geochemically identical to the enclaves from effusive volcanics. The fallout deposits represent intermediate magmas similar to the less felsic effusive host rocks. Based on the IUGS classification (Le Maitre et al., 2002), Methana's enclaves (and mafic pyroclastics) are mainly basaltic andesites, with minor basalts. The host rocks (and fallout

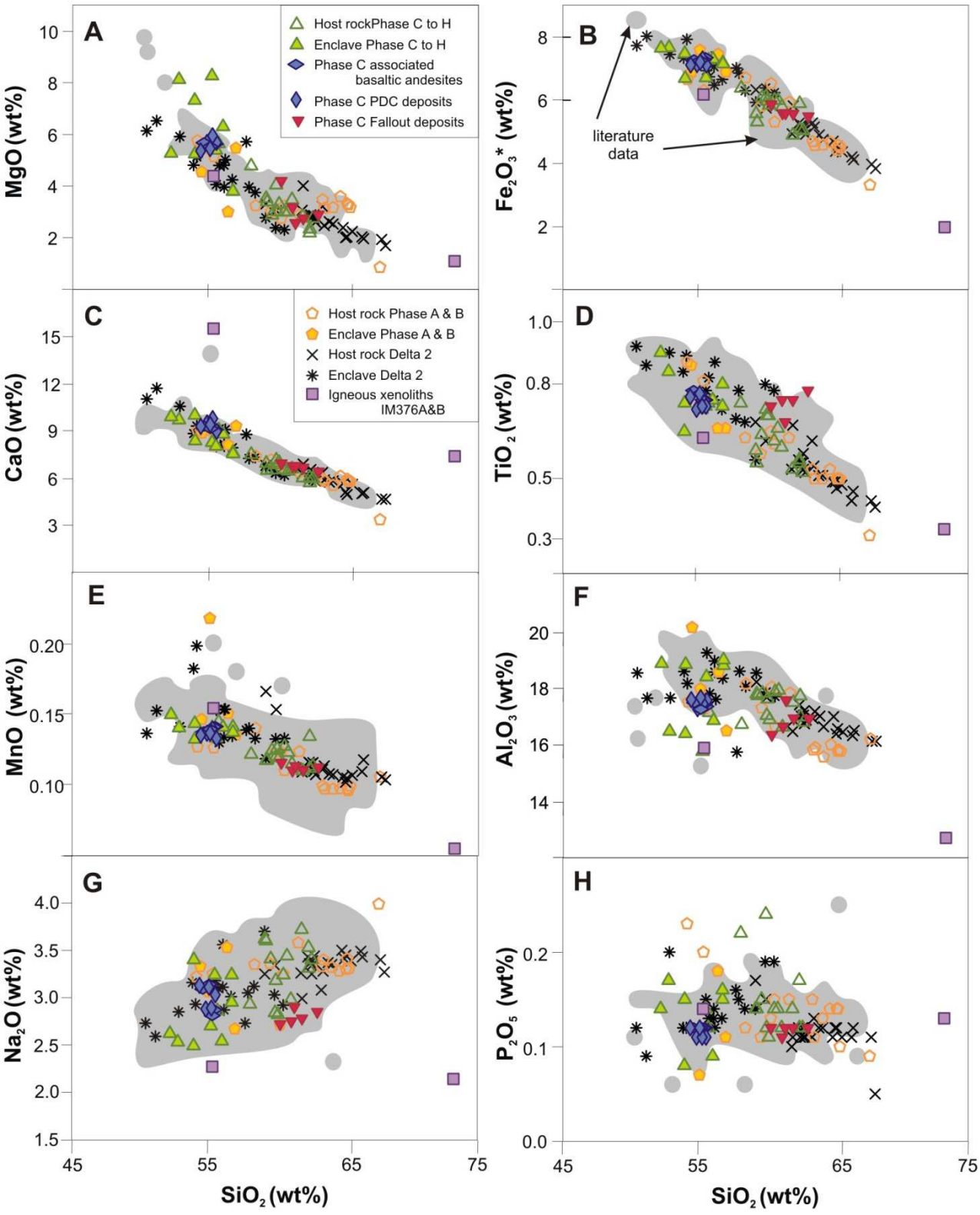

Figure 5.12. *Whole rock major element variation diagrams for all igneous rocks of Methana*, grouped according to the peninsula's volcanic stratigraphy. Fe_2O3* = all Fe presented as Fe_2O_3.

deposits) are andesites to (rhyo-)dacites. Mafic igneous xenolith IM376B has a basaltic-andesitic composition, and according to its geochemistry the felsic part IM376A is rhyodacitic. Geochemical data from this study as well as those from literature define a broad range of potassium contents (from medium-K towards high-K) for both basaltic andesitic enclaves with SiO_2 = 53-56 wt% and andesitic host rocks with SiO_2 = 59-63 wt%. The geochemistry of volcanic products 'bridging' these two silica ranges shows a much more restricted K_2O content for their SiO_2 = 56-59 wt% (Fig.5.11).

A more restricted compositional range bridging basaltic andesites and andesites is also present in the Harker variation diagrams of MgO and Fe_2O_3* (Fig. 5.12A, B). These diagrams furthermore show decreasing amounts of Mg and Fe with increasing silica contents for all of Methana's volcanic rocks. The CaO variation diagram (Fig. 5.12C) shows a very well defined trend of decreasing calcium (from CaO = 12 wt% to CaO = ~4 wt%) with increasing silica. The TiO_2 diagram (0.9-0.4 wt%) also shows lower titanium concentrations at increasingly higher differentiation levels (Fig. 5.12D). Despite a higher overall scatter of the data, the MnO-SiO_2 diagram also shows a negative trend with increasing differentiation (Fig. 5.12E). A similar negative correlation between Al and Si is present in the volcanic rocks with SiO_2 > 59 wt% (Al_2O_3 decreases from ~18.5 wt% to 16 wt%, Fig. 5.12F). For volcanic rocks near the silica-poor end of the diagram (SiO_2 < 59 wt%), aluminum contents show pronounced scatter, but seem to represent a more constant range of 17-19 wt% Al_2O_3 when taking into account the highest density of new data and the field of literature data. Na_2O defines a broadly positive, somewhat scattered trend with increasing silica contents (ranging from 2.5 to 4 wt%; Fig. 5.12G) but there does not seem to be any correlation between the phosphorus and silica content (P_2O_5 = 0.05-0.25 wt%, Fig. 5.12H). The two basaltic enclaves identified as the most primitive samples in Chapter 4 (DPM36 & DPM41A) remain the volcanic rocks with the lowest silica contents sampled from Methana (Fig. 5.11 & 5.12) but their MgO concentrations (~6 wt%) are not the highest. Instead, three enclaves from the 2nd period of volcanic activity have up to 8 wt% MgO (Fig. 5.12A), resulting in the highest Mg# values of the entire volcanic suite. The most evolved host rock from the Delta 2 unit (DPM42) still represents the most silica-rich sample of Methana's volcanics, but Phase B host rock IM42 has lower MgO, Fe_2O_3, CaO and TiO_2 combined with higher Na_2O, at similar SiO_2 contents (see Fig. 5.12).

The observations made for the volcanic rocks in Fig. 5.11 are also valid for the other major elements (Fig 5.12): i) the geochemical range defined for the Delta 2 unit (see Chapter 4) is as large as the variation in both the first and second phase of volcanic activity; ii) the geochemical fields defined by the newly presented data coincide with literature data; iii) the PDC deposits and associated basaltic andesites occupy a very small geochemical range within the 'enclave' field of the diagrams and are sometimes clustered according to their sampling locations (Na_2O, TiO_2); iv) the pumice samples define a much broader geochemical range, mostly unrelated to their sampling location, within the 'host rock' field of the diagrams. Among the 5 pumice samples, IM388 shows the lowest Al_2O_3 and highest MgO at the lowest silica content and DPM65 combines the highest SiO_2 and TiO_2 contents. The extremely low potassium contents of both igneous xenoliths (Fig. 5.11) are accompanied by higher amounts of CaO and somewhat lower Al_2O_3 and Na_2O concentrations than the volcanic samples (Fig. 5.12C,E,F). Their Mg, Fe, Ti, Mn and P concentrations, however, fall within the fields defined by Methana's volcanic deposits.

5.3.2 Trace element geochemistry

Whereas the variation in major element composition of the Delta 2 unit is nearly identical to that of all other extrusive rocks on Methana (Fig. 5.12), trace element data of the peninsula's volcanics cover a similar range as the Delta 2 unit but generally show more scatter (Fig. 5.13). Vanadium (Fig. 5.13A) and Sc concentrations show limited scatter, maintaining the strong negative correlation with increasing differentiation observed within the Delta 2 unit. Yttrium already showed a poor correlation with differentiation in the Delta 2 dataset, and this scatter increases when the other volcanic deposits are also taken into account (Fig. 5.13B). Nickel contents decrease with decreasing magnesium contents

(Fig. 5.13C), defining the same trend as Cr and Co. The three enclaves with the highest Mg# values (Fig. 5.12A) also show the highest abundance of Ni (Fig. 5.13C), Cr and Co. The Ni concentration of pumice IM388 is so elevated that it even exceeds that of the Loutses South host rocks which were

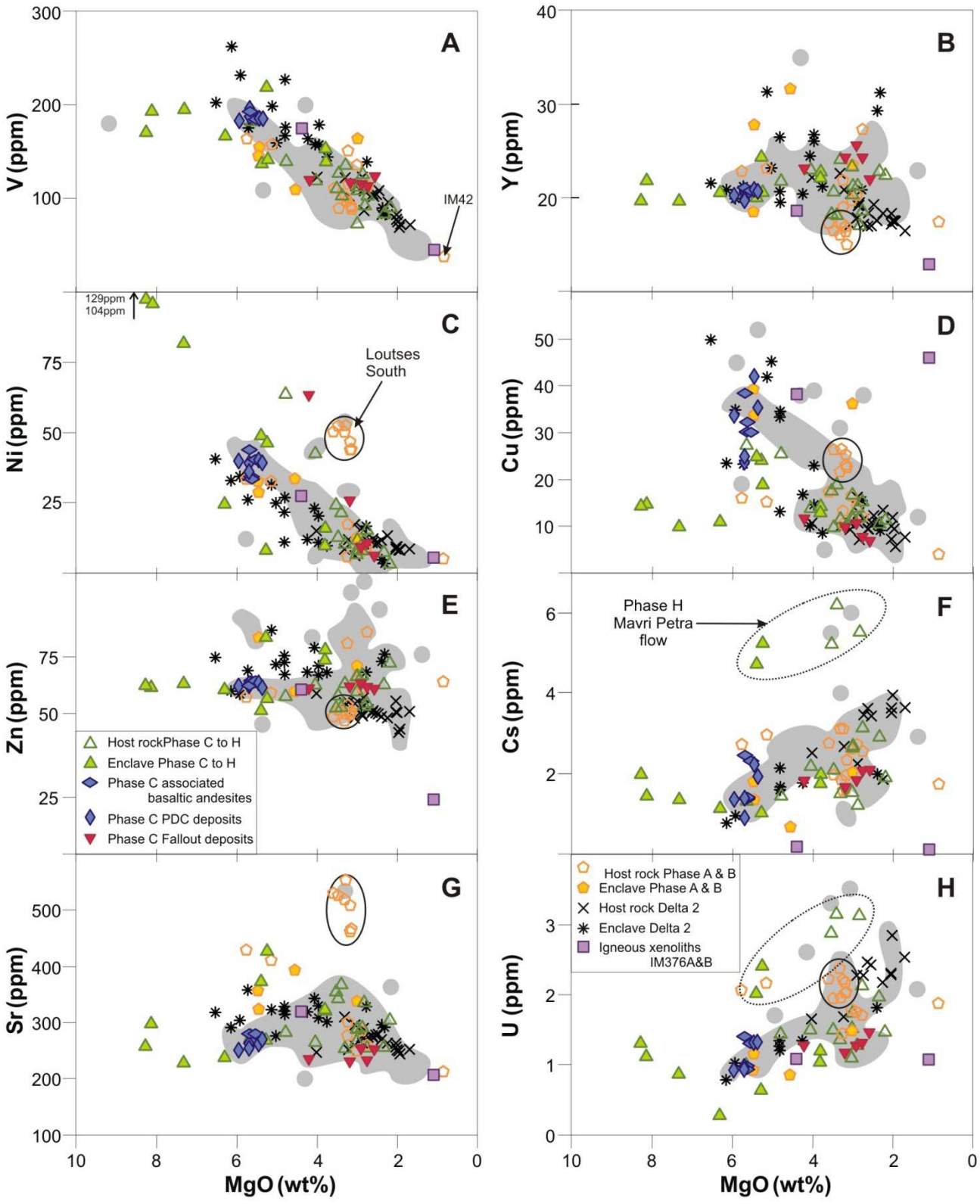

Figure 5.13. *Whole rock trace element concentrations plotted against MgO for all igneous rocks of Methana*, grouped according to the peninsula's volcanic stratigraphy.

identified in Chapter 4 as anomalously nickel enriched (Fig. 5.13C). The Cu and Zn concentrations of Methana's volcanic rocks show a lot of scatter, vaguely suggesting a negative correlation between differentiation and Cu contents (Fig. 5.13D) but no trend is observed in the Zn versus MgO diagram (Fig. 5.13E). Large ion lithophile elements Cs (Fig. 5.13F), Rb and Ba show similar trends of increasing concentrations towards lower magnesium contents. The PDC deposits and basaltic andesites thereby consequently define two clusters according to their sampling location: the samples near Mavri Petra show higher amounts of LILE than the rocks from Akri Pounda (Fig. 5.13F). Samples from the Mavri Petra flow itself (both enclaves and host rocks) also have higher LILE concentrations than other Methana samples (Fig. 5.13F). The Sr concentrations of the enclaves from the Mavri Petra flow are also elevated, but not as high as the Loutses South host rocks (Fig. 5.13G). The rest of Methana's volcanic rocks have a tendency towards lower Sr concentrations with increasing differentiation (Fig. 5.13G). The negative correlation between Cs and MgO is mirrored in the variation diagrams of U (Fig. 5.13H), Pb and Th. Uranium and lead furthermore show two distinct clusters of PDC deposits as well as elevated values for the Mavri Petra enclaves and host rocks (Fig. 5.13H).

Igneous xenoliths IM376A and IM376B plot within the geochemical range of Methana's volcanic rocks for V (Fig. 5.13A), Sc, Ni (Fig. 5.13C), Cr, Co and Sr (Fig. 5.13G). In these cases the

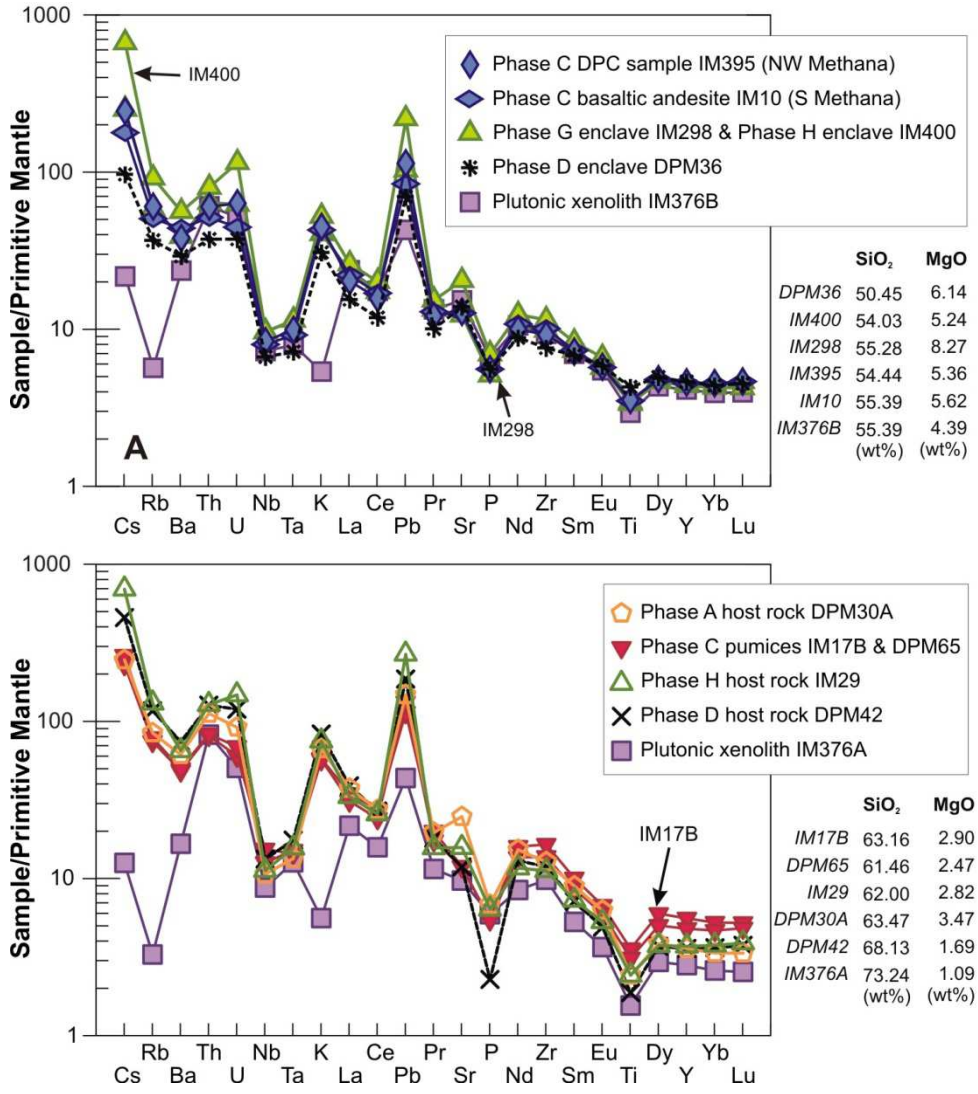

Figure 5.14. *Primitive Mantle-normalised trace element abundance patterns for representative volcanic rocks from Methana.* (A) Basaltic and basaltic andesitic compositions; (B) andesites to rhyodacites. Normalisation factors from Sun & McDonough (1989).

geochemistry of the more felsic igneous xenolith IM376A closely resembles that of Methana's most evolved volcanic rock IM42. However, IM376A shows lower Y (Fig. 5.13B), Zn (Fig. 5.13E), U (Fig. 5.13H) and Th concentrations than IM42. Both the mafic and the felsic igneous xenolith are furthermore enriched in Cu (Fig. 5.13D) and depleted in Cs (Fig. 5.13F), Rb, Ba and Pb in comparison to the volcanic deposits.

Primitive Mantle-normalised trace element abundance patterns of Methana's volcanics all show a downwards trend with increasing trace element compatibility, on which negative anomalies for Nb, Ta, P and Ti and a positive Pb anomaly are superimposed (Fig. 5.14). Amongst the more silica poor samples, the trace element composition of enclaves that contain notably high MgO, Cr, Ni and Co contents is otherwise identical to the Phase C mafic rocks (IM298 in Fig. 5.14A). These Phase C PDC bombs and basaltic andesites represent the average composition of Methana's enclaves. In comparison to these basaltic andesites, the normalised trace element pattern of most primitive enclave DPM36 is shifted to lower concentrations for the most incompatible elements (Cs to Zr, see Fig. 5.14A). The basaltic andesitic enclaves sampled from the youngest Mavri Petra flow show larger amounts of the most incompatible elements (IM400 in Fig. 5.14A) - although their major element composition is not different from other enclaves.

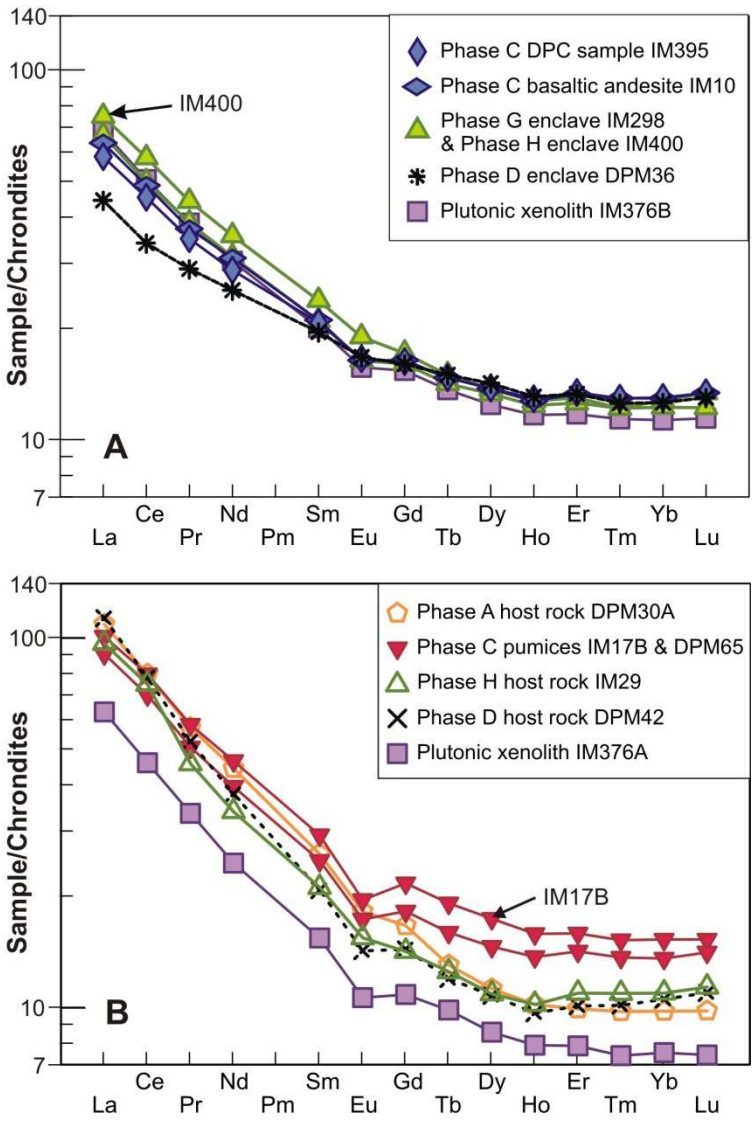

Figure 5.15. *Chondrite-normalised REE abundance patterns* for the same igneous rocks as in Fig. 5.14: (A) Basaltic and basaltic andesitic compositions; (B) andesites to rhyodacites. Normalisation factors from Sun & McDonough (1989).

Pumice lapilli sampled from the two different fallout deposits show identical Primitive Mantle-normalised trace element abundance patterns (IM17B & DPM65, Fig. 5.14B). These explosive intermediate volcanics are geochemically similar to the average andesitic host rock (DPM30A in Fig.5.14B) but have a somewhat flatter trace element pattern, with slightly lower Ba, Th and U and higher Ti and HREE contents. Compared to andesitic host rock DPM30A, the trace element pattern of most evolved host rock DPM42 shows higher concentrations of LILE, Th, U and Pb as well as a larger negative P and Ti anomaly (Fig. 5.14B). Despite its more silica-poor composition, the host rock from the youngest Mavri Petra flow (IM29 in Fig. 5.14B) contains similarly high LILE, Th, U and Pb concentrations as DPM42.

The two igneous xenoliths stand out amongst Methana's igneous lithologies due to their significantly lower Cs, Rb, K and Pb contents (Fig. 5.14). The Primitive Mantle-normalised trace element abundance pattern of mafic xenolith IM376B is otherwise similar to those of the Phase C basaltic andesitic rocks and most mafic enclave DPM36 (Fig. 5.14A). Felsic xenolith

IM376A is also poorer in Ba, U, Nb and Ta (Fig. 5.14B).

Figure 5.15 shows the chondrite-normalised REE abundance patterns of the rocks presented in Fig.5.14. Overall, the igneous rocks from Methana show slightly spoon-shaped REE patterns as well as small negative Eu-anomalies, with the latter more pronounced in intermediate to felsic lithologies (Fig. 5.15). All basaltic-andesitic samples have very similar REE patterns, with only minor LREE and MREE enrichment for Mavri Petra enclave IM400 and slightly lower MREE and HREE contents for xenolith IM376B (Fig. 5.15A). In comparison, basaltic enclave DPM36 shows a less steep REE pattern with lower amounts of LREE but similar MREE and HREE contents (Fig. 5.15A).

The REE patterns of the andesitic to rhyodacitic rocks are markedly steeper than those of the mafic lithologies, due to higher LREE and MREE concentrations (Fig. 5.15B). Despite their difference in silica contents, most evolved sample DPM42 and the young Mavri Petra host rock IM29 have almost identical REE contents. The chondrite-normalised REE pattern of average andesitic host lava DPM30A is also similar, apart from slightly higher MREE contents (Fig. 5.15B). The pumices sampled from the different localities (IM17B & DPM65) have identical patterns, which only differ from Methana's host rocks in their higher MREE and LREE contents (Fig. 5.15B). Felsic xenolith IM376A has a chondrite-normalised REE pattern that is clearly shifted downwards to lower REE concentrations in comparison to the felsic-intermediate volcanic samples (Fig. 5.15B).

5.3.3 Isotope geochemistry

The Sr, Nd, Hf and Pb isotope ratios analysed in this study are presented in figures 5.16 and 5.17 (uncertainties on the isotopic measurements are smaller than the symbol size). These figures also include the isotopic data available in literature, which are four $^{87}Sr/^{86}Sr$ ratios (Pe, 1975) and the Sr, Nd and Pb isotopic composition of one basaltic andesite (Gülen, 1990).

The Sr, Nd and Hf isotopic composition from samples representing Methana's entire volcanic history is similar to the range of isotope ratios encountered within the Delta 2 unit ($^{87}Sr/^{86}Sr$: 0.7050-0.7080, $^{143}Nd/^{144}Nd$: 0.51233-0.51267 and $^{176}Hf/^{177}Hf$: 0.28260-0.28294; see Fig. 5.16A, B and C, respectively). Only the pumice samples (and host rock IM303) plot outside the Delta 2 isotopic range, with higher $^{87}Sr/^{86}Sr$ (up to 0.7093) and lower $^{143}Nd/^{144}Nd$ (down to 0.51224) and $^{176}Hf/^{177}Hf$ (down to 0.28247) ratios. Despite scatter, the maximum $^{87}Sr/^{86}Sr$ ratio at a given SiO_2 concentration increases with increasing silica content (Fig. 5.16A), whereas $^{143}Nd/^{144}Nd$ and $^{176}Hf/^{177}Hf$ ratios show a negative correlation with silica contents (Fig. 5.16B, C). The main trend of Methana's volcanic rocks also shows a weak positive correlation between Pb isotope ratios and silica contents (Fig. 5.16D-F). The range of Pb isotope ratios observed within the Delta 2 unit is up to 5 times smaller than the variety present within the Pb geochemistry of Methana's entire volcanic stratigraphy (Fig. 5.16D-F) – which seems to confirm the decoupling between the Sr-Nd-Hf and Pb isotopic systems already observed in the Delta 2 unit. Igneous xenoliths IM376A and IM376B have Sr, Nd and Hf isotope ratios that plot within the compositional range of Methana's volcanic rocks (Fig. 5.16A-C). Their Pb isotope ratios, however, are much lower than those of any volcanic lithology (Fig. 5.16D-F). The Pb isotopic composition of Methana's volcanic rocks represent a straight line parallel to, but at higher $^{207}Pb/^{204}Pb$ and $^{208}Pb/^{204}Pb$ ratios than, the Northern Hemisphere Reference Line (NHRL – Hart, 1984) (Fig. 5.16G, H). Whereas mafic xenolith IM376B thereby represents the least radiogenic sample of Methana's trend of Pb isotope ratios, the Pb isotopic composition of felsic xenolith IM376A plots well below this trend and close to the NHRL (Fig. 5.16G, H).

The Sr-Nd isotopic composition of Methana's volcanic rocks are almost all enriched in comparison to bulk silicate earth (BSE, Fig. 5.17A). Two groups of samples plot off the $^{87}Sr/^{86}Sr$ – $^{143}Nd/^{144}Nd$ trend: the Loutses South host rocks plot below the main trend whereas the host rocks and enclaves from the youngest Mavri Petra flow plot above this main trend (Fig. 5.17A). There is a strong positive correlation between the Nd and Hf isotopic compositions for all igneous rocks (Fig. 5.17B). More

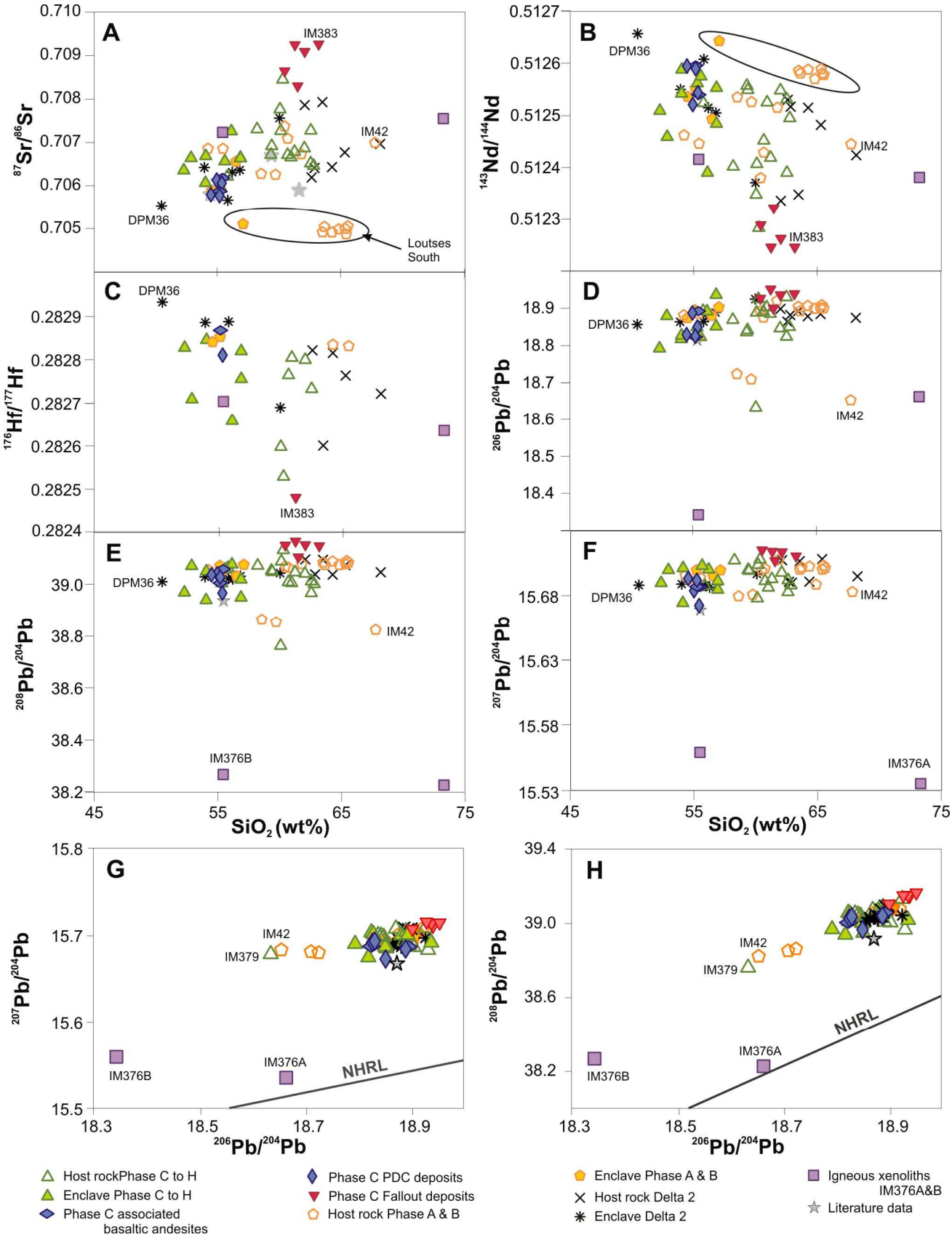

Figure 5.16. *Variation of Sr, Nd, Hf and Pb isotopic compositions with silica contents* for all igneous rocks of Methana. NHRL = Northern Hemisphere Reference Line (Hart, 1984).

evolved, silica-rich samples thereby coincide with the terrestrial array whereas intermediate to more more volcanics increasingly plot above the terrestrial array (Fig. 5.17B). Basaltic enclave DPM36 from the Delta 2 unit remains the most primitive sample as it combines the highest $^{143}Nd/^{144}Nd$ and $^{176}Hf/^{177}Hf$ ratios with a very low $^{87}Sr/^{86}Sr$ ratio (Fig. 5.16A-C & Fig. 5.17A,B). Andesitic pumice IM383 is the sample with the highest Sr and lowest Nd and Hf isotope ratios of the entire volcanic peninsula (Fig. 5.16A-C & Fig. 5.17A,B). The pumice samples also show the highest $^{206}Pb/^{204}Pb$, $^{207}Pb/^{204}Pb$ and $^{208}Pb/^{204}Pb$ ratios, whereas otherwise most primitive enclave DPM36 has rather radiogenic Pb isotope ratios (Fig. 5.16D-F & Fig. 5.17C-E). The volcanic lithology with the lowest Pb isotope ratios is IM379 – the host rock sampled within 20cm of igneous xenolith IM376. Phase B host rocks IM42, IM43 and IM317 (all from the northwestern part of the peninsula, sampling locations 28 to 30) also have Pb isotopic compositions that are distinctly less radiogenic than that of the other Methana volcanics (Fig. 5.17C-F).

Isotope geochemistry also groups the PDC deposits and associated basalts into two clusters according to their sampling locality: the rocks from Akri Pounda volcano in the south have higher $^{87}Sr/^{86}Sr$ and $^{206}Pb/^{204}Pb$ values, and lower $^{143}Nd/^{144}Nd$ and $^{176}Hf/^{177}Hf$ ratios, than the samples from the northwestern outcrop (Fig. 5.16A-D & Fig. 5.17). The red-oxidised scoria IM364 has distinctly lower $^{207}Pb/^{204}Pb$ and $^{208}Pb/^{204}Pb$ ratios and is therefore the sample that does not consistently plot within one of the two geographically-defined groups of the Phase C PDC deposits and associalted basaltic andesites.(Fig. 5.17C-E). Whereas the pumice samples represent one Sr-Nd-Hf isotopic trend regardless of their sampling locality, the one pumice analysed from the fallout deposit near Chionessa (DPM65) has a Pb isotopic composition that is distinctly less radiogenic than the four samples from Akri Pounda (Fig. 5.17C-E). Enclaves and host rocks from the youngest Mavri Petra flow also cluster together and have Pb isotope ratios very similar to those of the spatially close, but much older, Phase C basaltic andesites (Fig. 5.17C-E). As already pointed out in Chapter 4, the Pb isotope geochemistry of Methana therefore seems to reflect sampling locations rather than the difference between more mafic (enclaves) and more evolved (host rocks) lithologies.

The $^{87}Sr/^{86}Sr$ ratios of the limestone basements and xenolith are similar to the composition of Methana's intermediate volcanic rocks (0.7074 to 0.7078, see Appendix F1) but unfortunately, these samples did not contain enough Nd for isotope measurement. The other sedimentary samples contain more siliciclastic material than these limestones and show higher $^{87}Sr/^{86}Sr$ ratios which similar to the more evolved volcanic samples (0.7080 – 0.7101, Fig. 5.17A). The combination of their Sr and Nd isotope chemistry however reflects a different compositional range than that of the igneous rocks: whereas (calc-)siliciclastic samples plot within the main $^{87}Sr/^{86}Sr$-$^{143}Nd/^{144}Nd$ trend of Methana's volcanic deposits, calcareous and volcaniclastic samples plot above it at higher $^{143}Nd/^{144}Nd$ ratios (Fig. 5.17A). With regard to the Nd-Hf isotopic compositions, it is however a calcareous sample (IM394) that falls within the volcanic field and a calc-siliciclastic xenolith (IM386) that plots above the igneous trend (Fig. 5.17B). The one sedimentary xenolith which had Pb concentrations sufficiently high to allow isotopic analysis (IM362, a volcaniclastic greywacke) has a lead isotopic composition similar that of Methana's volcanic deposits (Fig. 5.17C-E).

5.4 Discussion of field observations and petrography

Field observations and petrographic descriptions are synthesised to give insights into Methana's magmatic plumbing system and its past eruption style. Potential changes of the magma system throughout Methana's volcanic history are also investigated, but information on the different magma sources and processes (and their evolution with time) is derived from whole rock geochemical data and discussed in subsequent section 5.5.

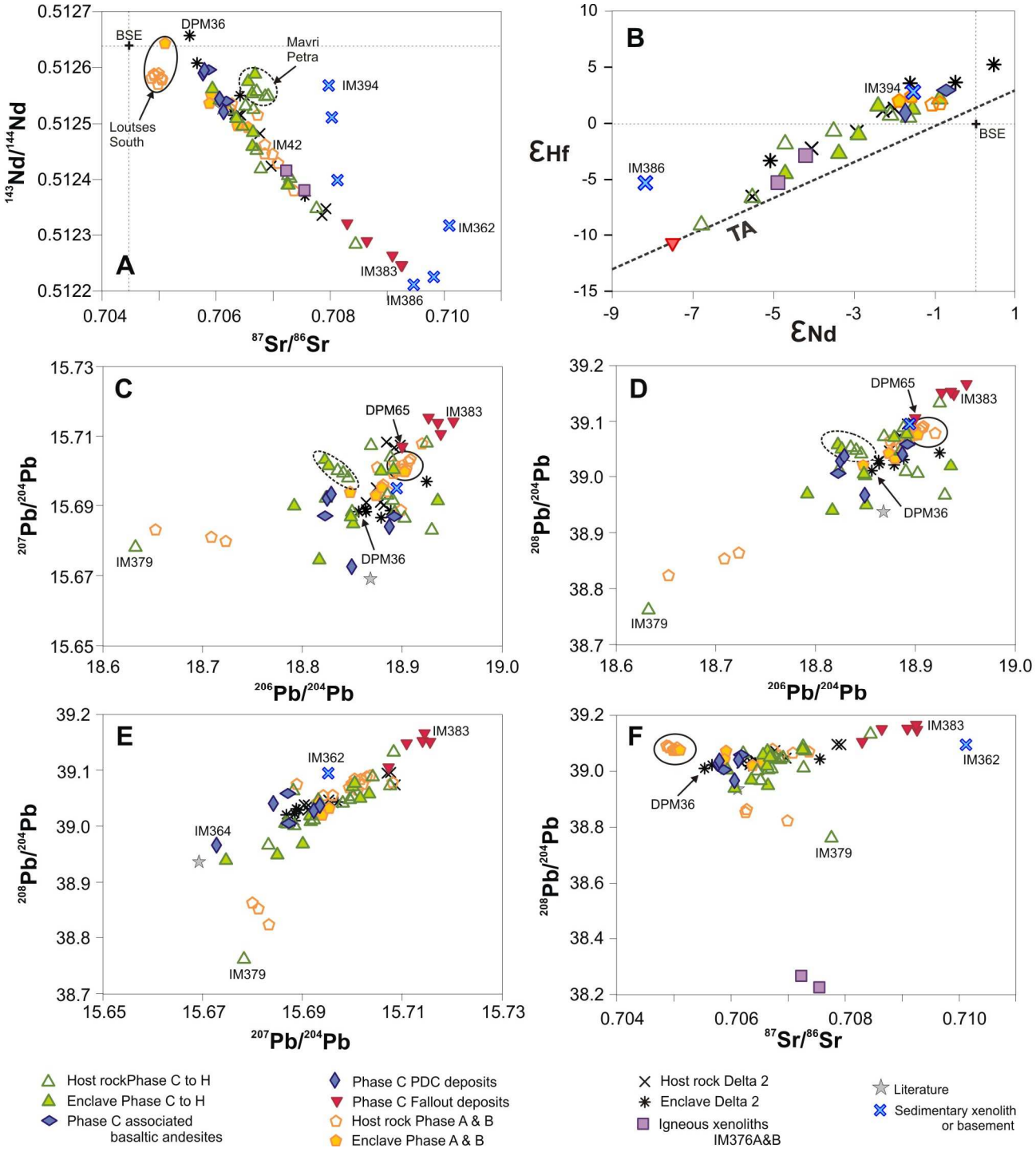

Figure 5.17. *Sr, Nd, Hf and Pb isotope ratios of Methana's volcanic rocks and sedimentary basement and xenoliths*. BSE = Bulk Silicate Earth (Workman & Hart, 2005), TA = Terrestrial Array (Vervoort et al., 2011, εNd and εHf values calculated using $^{143}Nd/^{144}Nd_{CHUR(0)}$ = 0.512630 and $^{176}Hf/^{177}Hf_{CHUR(0)}$ = 0.282785 (Bouvier et al., 2008).

5.4.1 Pyroclastic deposits: evidence of Methana's Plinian eruption(s)

The pyroclastic fallout deposit at Akri Pounda consists mainly of lapilli-sized pumice and contains up to 15% of lithic fragments, suggesting deposition relatively close to the eruptive vent (Schmincke, 2006; Houghton et al., 2000). Larger pumice clasts show internal fractures (Fig. 5.2D) that probably originate from impact upon ballistical ejection from the nearby vent. Their pink to red central part (Fig.

5.2D) is indicative of high-temperature emplacement, again suggesting a relatively short travel time and small distance from the eruption vent (Fisher & Schmincke, 1984; Houghton et al., 2000). The Akri Pounda deposits furthermore contain little to no fine-grained matrix between the angular, lapilli-sized pumice clasts and have an overall massive appearance and thickness – characteristics confirming their deposition by air fall (Fisher & Schmincke, 1984). The large thickness of this fallout deposit (ca. 5-10 m) suggest that it formed during a large explosive eruption (Cioni et al., 2000).

The Phase C fallout deposit near Chionessa is significantly smaller, but with a thickness of up to 2 m still indicative of a Plinian eruption. This pumice-rich lapilli deposit is similar to the one at Akri Pounda, but it does not contain fractured pumice clasts with red-oxidised cores. Other differences between the Akri Pounda and Chionessa fallout deposits are slight rounding of the pumice lapilli and the presence of a fine-grained matrix (5-10 vol%) and of differently coloured ash beds at the bottom and top of the latter deposit. Whether or not both fallout deposits originate from the same explosive eruption and/or were ejected from the same vent can not be determined from the field observations. However, the thickness of these fallout deposits and their rather coarse-grained character (lapilli and blocks) suggest that the eruptive vent(s) which ejected these Phase C fallout deposits were located nearby, on the volcanic peninsula of Methana (Houghton et al., 2000; Schmincke, 2006).

Despite the fact that pyroclastic fallout deposits are scarce on Methana, the few areas where they are exposed are scattered across the entire peninsula (Fig. 5.18) and their thickness in both studied outcrops suggests at least one major explosive eruption. The PDC deposits associated with these fallout deposits also suggest a Plinian eruption (Cioni et al., 2000; Schmincke et al., 2006). How long this explosive event lasted and whether it involved eruption from one or multiple vents is unclear. Field evidence at Akri Pounda and near Ag. Andreas indicates that it started with the ejection of a felsic magma (the pumice-rich fallout deposits) and continued with eruption of more mafic pyroclastic density currents that with time evolved into more effusive flows (the associated basaltic andesites). Whether the pyroclastic density currents graded into lava flows or the volcanic activity changed in character from explosive to effusive, is not clear.

The fact that Methana's Phase A volcanic basement is eroded and reworked into the widespread Phase B volcaniclastic apron (see Fig. 5.1) led to the interpretation that overlying Phase C pyroclastic deposits represent the start of volcanic activity after a period of eruptive quiescence. Pe-Piper & Piper (2013) define a time-frame for these two periods of volcanism by a 3.5±0.9 Ma K-Ar age for a Phase A rock and a 1.4±0.3 Ma K-Ar age for a Phase C early andesite dome which, based on field relations, is thought to be younger than the Phase C pyroclastics. They furthermore mention that the petrography and geochemistry of Methana's Phase C PDC deposits resemble those of Aegina's mafic Oros lavas which also represent a second period of volcanic activity (Pe-Piper et al., 1983). As these Oros lavas are dated at 2.1±0.1 Ma and deposition of the Phase C pyroclastic deposits occurred between 3.5±0.9 Ma and 1.4±0.3 Ma, renewal of volcanic activity seems to have occurred roughly within the same time-frame on both Aegina and Methana. Pe-Piper & Piper (2013) correlate the initiation of this second volcanic period with a regional change in tectonic style around the Pliocene-Pleistocene boundary. (At this time, the on-going collision between the Aegean-Anatolian microplate and the African promontory results in the onset of NE-SW strike-slip faulting in the westernmost part of the South Aegean Sea – parallel to the Kefalonian and the North Anatolian fault zones, see Fig. 2.5). The Phase C fallout deposits on Methana therefore represent explosive activity that marks the renewal of volcanism throughout the Saronic Gulf area.

5.4.2 Location of Methana's inferred collapse caldera

Based on the Phase C pyroclastic deposits, Pe-Piper & Piper (2013) inferred the development of a major collapse caldera in the centre of Methana peninsula approximately 2 – 3 Ma ago. However, reading Methana's geological map or studying its dominantly effusive rocks in the field gives the

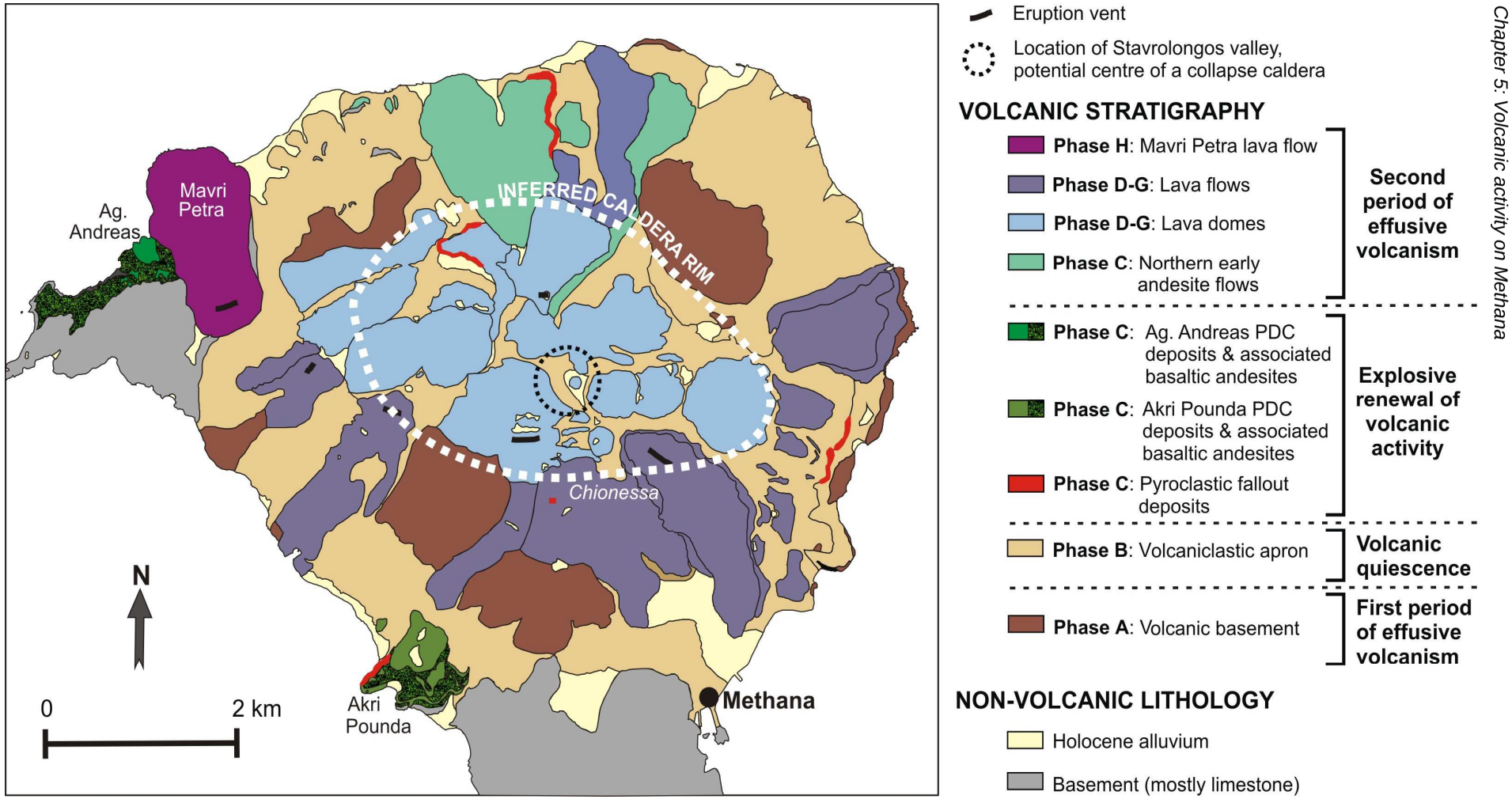

Figure 5.18 Adaptation of the geological map of Methana (after Pe-Piper & Piper, 2013) to bring out the different types and periods of volcanic activity throughout the peninsula's history. Differentiation between lava domes and flows from Phases D to H is based on fieldwork observations in combination with descriptions from Pe-Piper & Piper (2013) and the peninsula's topography as shown by Google Earth imaging.

impression that the volcanic centres of the Saronic Gulf lack large scale explosive eruptions similar to the ones that emplaced significant volumes of pumice fallout deposits in the younger central and eastern parts of the South Aegean arc (e.g. Minoan pumice on Santorini and Kos Plateau Tuffs, respectively, 0.3 Ma to present). Infilling of the Methana collapse caldera by the later Phase D to G domes, coverage of the caldera's flanks by Phase C to H lava flows (see Fig. 5.18 and Fig. 5.19) and erosion of the only slightly welded pumice deposits could explain why there is so little evidence left of Methana's Plinian eruption. Despite the absence of an obvious caldera on Methana, the peninsula's geological map does hold clues to the location and size of an older collapse caldera.

Figure 5.18 shows that the remaining lava domes and flows of the Phase A volcanic basement delineate a more or less NW-SE oriented oval shape around the central area of the volcanic peninsula. Deposits of the second period of volcanic activity within this area are mainly lava domes (Fig. 5.18) – indicating an original flat topography on which volcanic vents extruding viscous, crystal-rich magmas could form lava domes (Fig. 5.19). The younger Phase C to G volcanic deposits outside this ellipse are mostly lava flows (Fig. 5.18) – suggesting that the original topography had a certain inclination, so that viscous magma extruded from vents on the caldera's flanks would flow down towards the sea (Fig. 5.19). The white-dashed line in Figure 5.18 thus roughly represents the rim of a collapse caldera that was formed after Methana's Plinian eruption and subsequently filled-in and covered by the later volcanic deposits. The central area of this inferred collapse caldera is locally known as the 'Stavrolongos valley' (see black-dotted circle in Fig. 5.18) – and has been suggested as a small left-over of the former caldera floor amidst the new volcanic domes (personal communication Dr. Tom Pfeiffer). The inferred collapse caldera on Methana has a W-NW to E-SE orientation and is roughly 5km long and 3km wide. The collapse caldera formed by the Minoan eruption on Santorini, in comparison, also has an ellipse shape but is about 5 times larger (11.5km X 7km) and has a N-NW to S-SE orientation. The collapse caldera present on Nisyros is of similar size (3.5km X 3.5km) as the one inferred for Methana, but has a circular shape.

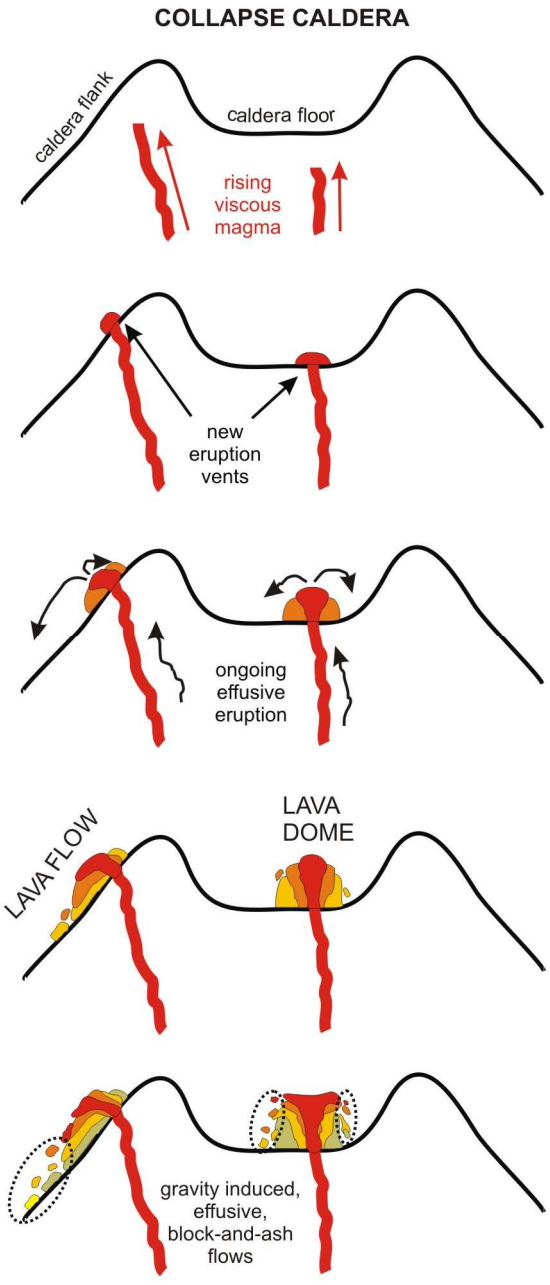

Figure 5.19. From top to bottom: sketch illustrating how the initial topographic surface influences the geometry of a viscous lava flow around its eruptive vent.

Only Methana's most recent (230 BC) Phase H Mavri Petra lava flow does not follow the general pattern of lava flows radiating outwards from the caldera rim and is instead located on the north-western edge of the peninsula (Fig. 5.18) – near the intensely fractured limestone basement. The Pausanias submarine volcano that is also linked to Methana's volcanism and thought to be younger still than the Mavri Petra flow is situated

even further to the north-west (Nomikou et al., 2013). This suggests that in historic times the active centre of Methana's magmatic complex has migrated towards the NW. The fact that Pausanias submarine volcano formed on a normal fault within a neotectonic graben, furthermore indicates that the locus of Methana's volcanic activity is still strongly controlled by the local tectonic regime.

5.4.3 Explosive volcanic deposits versus effusive lava domes and flows

Compared to the Phase C pyroclastics, Methana's effusive volcanic rocks are deposited during less violent eruptions, have an overall lower vesicularity, and contain numerous mafic enclaves which are virtually absent in the explosive deposits. Feeley et al. (2008) also observed that mafic enclaves are more often related to lava flows and domes than to pyroclastic deposits. Their 'gas bubble lifting model' describes how partially crystallised blobs of mafic magma cool upon entrapment in a more felsic magma and consequentially undergo *second boiling* (oversaturation of volatile contents in the residual melt due to crystallisation of volatile-free minerals) (see Fig. 5.20C-top). The rim of these enclaves is however semi-rigid due to the previously formed crystal framework, preventing the volatile bubbles formed within the interstitial melt from escaping. The bubbles thus reduce the enclaves' overall density, making them rise to the top of the magma chamber (Fig. 5.20C-top). Such concentration of enclaves near the roof of silicic reservoirs is thought to have a suppressing effect on eruption dynamics, favouring more quiet effusive eruptions (Feeley et al., 2008, Fig. 5.20D-top). This 'gas bubble lifting' process might have been involved in the petrogenesis of Methana's enclave-rich lava flows and domes. The petrogenesis of the enclave-poor Phase C pyroclastic deposits seems however different from that of the peninsula's dominantly effusive volcanic rocks.

The PDC deposits and associated basaltic andesites contain many holocrystalline aggregates of clinopyroxene + plagioclase ± olivine ± Fe-Ti-oxides (Fig. 5.8B, D, F, G) which petrographically resemble cumulates (Cox et al., 1979). Perhaps these holocrystalline clusters represent a mineral assemblage that formed at greater depths during polybaric crystallisation of rising mafic magma, which then reached the shallower crustal level of the more felsic magma that we now find as the pumice deposits (Fig. 5.20A). The presence of one such holocrystalline plagioclase-clinopyroxene cluster in a pumice lapilli (Fig. 5.8I, J) suggests that some of the (crystal cargo of the) mafic "PDC" magma mingled with the more felsic "pumice" magma. Mingling of the felsic pumice magma with a more mafic magma can also be inferred from the presence of micro-enclaves of olivine and plagioclase ± pyroxene within pumice lapilli (Fig. 5.8E). The fact that Methana's fallout deposits only contain mafic enclaves on the microscopic scale however suggests less interaction between both magmas than in the case of enclave-rich effusive deposits such as the Delta 2 unit (see Chapter 4). Juvenile bombs from the PDC deposits contain euhedral olivine phenocrysts together with antecrystic quartz grains mantled by a pyroxene reaction rim (Fig. 5.9E). In the pumice lapilli, embayed quartz phenocrysts coexist with olivine xenocrysts that show iddingsitisation and are overgrown by orthopyroxene and plagioclase crystals (Fig. 5.8C, D). The presence of both quartz and olivine in felsic pumice as well as in mafic PDC deposits is further evidence for pre-eruptive mixing and mingling between the magmas of these two pyroclastic deposits.

The PDC deposits (as well as the associated basaltic andesites) mainly contain phenocrysts of olivine, plagioclase and clinopyroxene similar to the ones in the pumice's micro-enclaves (compare Fig. 5.8E,I with Fig. 5.9D-G). Perhaps this indicates that the PDC deposits and associated basaltic andesites represent the more mafic magma from which the micro-enclaves in the pumice deposits originate. The volume of PDC deposits and associated basaltic andesites that erupted after the pumice lapilli is rather large. If these mafic rocks are derived from the same magma as the pumice's micro-enclaves, this would suggest a progressively tapped magma chamber with an upper felsic magma (the pumice) and a lower mafic magma (the PDC deposits and associated basaltic andesites)

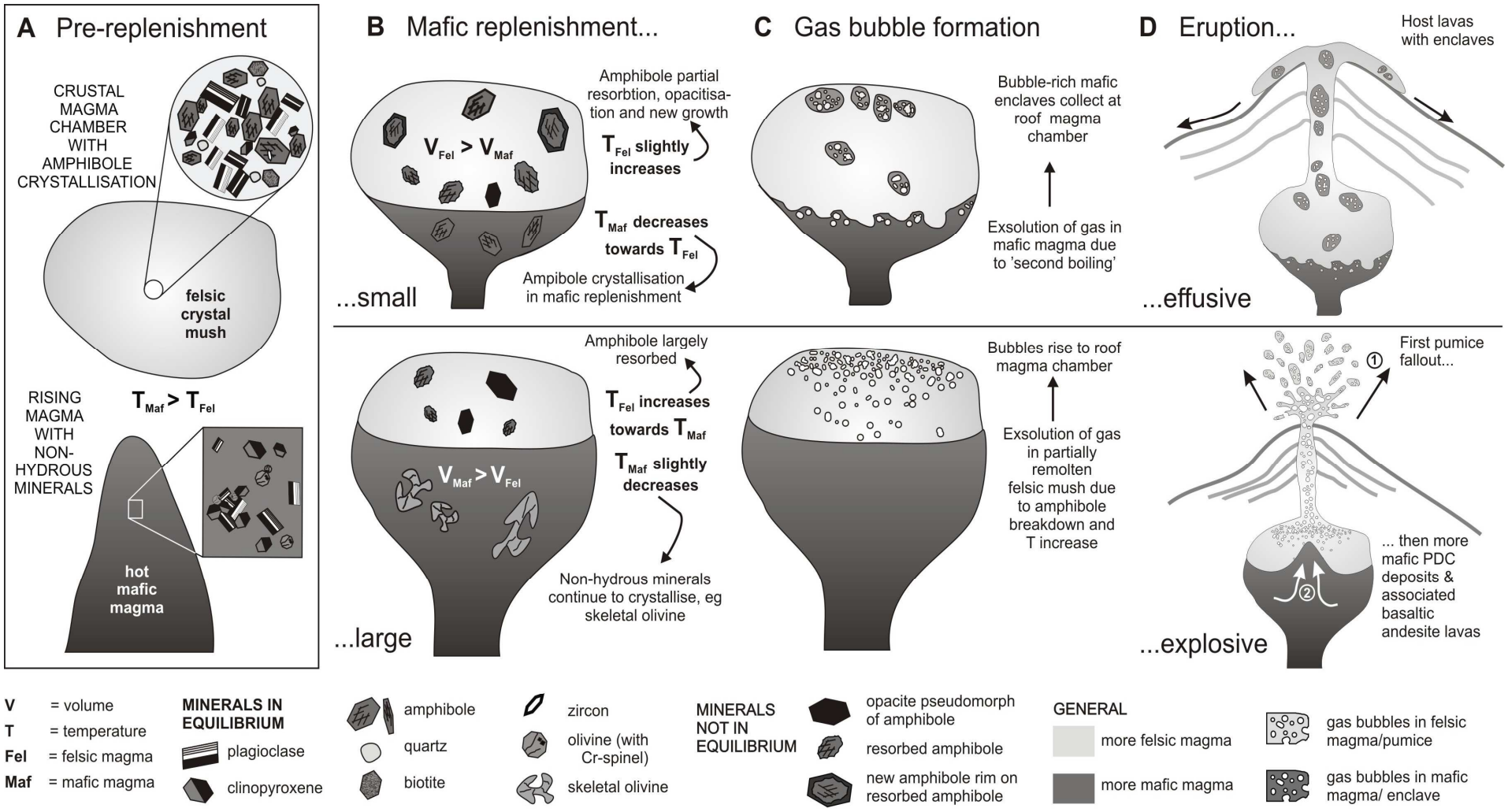

Figure 5.20. Hypothesis on the petrological reasons for the different eruption dynamics of Methana's effusive host rocks with enclaves, and the explosive Phase C pumice fallout, PDC deposits and associated basaltic andesites.

(Fig. 5.20D-down). The mineral assemblage of the pumice is overall similar to the minerals encountered in the effusive lavas on Methana (Fig. 5.20A) – the main difference between the two is the higher amount of glass and vesicles in the former. This high glass content of the pumice, together with its limited amounts of groundmass microlites (Fig. 5.8A), could result from sudden cooling after high degree melting of a more crystal-rich felsic magma, for example through heat transfer from a large batch of underlying mafic magma (Fig. 5.20B-down). The pumice lapilli contain some (relics of) large amphibole and biotite crystals, suggesting that hydrous minerals were crystallising from the felsic magma at a certain stage, likely prior to the mafic injection (Fig. 5.20A). These large crystals of biotite and amphibole, however, show intense disequilibrium features (Fig. 5.8F, G). This may indicate that the hydrous minerals of the felsic magma were no longer stable during the process of partial melting that followed upon the mafic replenishment (Fig. 5.20B-down). Dehydration of amphibole and biotite might, in turn, have triggered an explosive eruption due to H_2O-oversaturation and subsequent boiling of the felsic partial melt (Fig. 5.20C-D-down). According to Pistone et al. (2013), large explosive eruptions can result from even limited amounts of gas because bubbles significantly decrease a magma's viscosity. The highly explosive 2001 eruption of mixed magma at Etna (Italy), for example, is also partially ascribed to the formation of gas due to amphibole breakdown upon mixing of high T mafic magma with a more felsic magma (Viccaro et al., 2006).

The PDC deposits and associated basaltic andesites show a bimodal crystal size distribution between phenocrysts (crystal load of plagioclase + clinopyroxene + olivine + Fe- Ti-oxides) and microlites (present in large amounts, mostly plagioclase needles). Whereas (macro-)phenocrysts are often thought to form during isobaric cooling and crystallisation, microlites are commonly interpreted to represent final stages of crystallisation during decompression and ascent (Cox et al., 1979; Barclay & Carmichael, 2004; Vernon, 2004). This suggests that the microlites in the PDC deposits formed in response to a period of rapid ascent and extrusion of the mafic magma, given their orientation into a flow texture (Fig. 5.9C, D, J) probably by quenching of the mafic magma during ascent and extrusion. The (large) phenocrysts of sub-to euhedral olivine, clinopyroxene and plagioclase likely formed along with the holocrystalline cumulate clusters during slow cooling and crystallisation in a magma chamber at larger depth (Fig. 5.20A). The skeletal, hopper-like crystal habitus of some olivine phenocrysts (Fig. 5.9H, I) also suggests formation during rapid cooling – possibly during ascent towards the more shallow magma chamber and/or due to the onset of thermal equilibration upon mingling with the felsic crystal mush (Nixon, 1988; Holness & Bunbury, 2006; Fig. 5.20B-down). In comparison with the randomly oriented and overall more coarse-grained crystal framework of the mafic enclaves from the effusive volcanic deposits, the mafic pyroclastics (and associated basaltic andesites) seem to have undergone less crystallisation within an upper crustal magma chamber. The felsic pyroclastics contain significantly fewer phenocrysts and microlites than their effusive counterparts – indicating that they also experienced more rapid cooling (Buckley et al., 2006). The explosive mode of deposition of Methana's pyroclastic rocks agrees well with this inferred short residence time at shallow crustal levels, which led to limited mafic-felsic magma interaction and a rapid rise towards the surface.

The petrogenesis of the effusive volcanic rocks includes a mafic injection that is rather small compared to the volume of felsic crystal mush against which the mafic magma cools to form a randomly oriented crystal framework. Second boiling of this partially crystallised mafic magma induces mingling with and rise within the overlying more felsic crystal mush as mafic enclaves – eventually erupted during effusive volcanic activity (see Chapter 4, Fig. 4.17, Fig.5.20-top). The explosive volcanic deposits probably underwent a different petrogenesis in which a large mafic replenishment of a shallow magma chamber causes melting of the felsic crystal mush. Dehydration of the hydrous minerals within this felsic crystal mush is inferred to have led to exsolution of gases from the felsic partial melt, which in turn triggered an explosive eruption with progressive tapping, from the top down, of the zoned magma chamber (Fig. 5.20-down).

5.5 Discussion of geochemical data

5.5.1 Geochemical variation across Methana: comparison to the Delta 2 unit

The major and trace element composition of rocks extruded throughout Methana's volcanic history is similar to the geochemical range observed in the Delta 2 unit (Fig. 5.11 to 5.17). Host rocks from the first and second period of volcanic activity seem to be somewhat less differentiated (andesitic to dacitic) than the majority of the (dacitic to rhyodacitic) host rocks from Loutses, Tsonaka and Kossona Vouno. The geochemical variety present in Methana's entire volcanic stratigraphy (including the most felsic and most primitive compositions) was thus more or less obtained through detailed sampling of just one volcanic unit. This suggests that the common practice of taking just a few samples from different units could have led to misguided interpretations of Methana's volcanic rocks (for example observation of compositional gaps between enclaves and host rocks; different geochemistry for younger and older volcanic deposits; …). Whereas most volcanic studies report a geochemical gap between more mafic enclaves and their host rocks (see Chapter 4), the compositional ranges of these two rock types overlap one another in the effusive deposits of Methana. Prolonged interaction (mixing and mingling) between different batches of replenishing magma and more felsic crystal mushes could be responsible for the absence of this 'geochemical gap' as well as for the heterogeneous composition within one eruptive unit. This is inferred from the restricted compositional range of (and geochemical gap between) the two types of pyroclastic deposits: the pumice and PDC deposits are geochemically equivalent to host rocks and enclaves, respectively, - but their petrography indicates that they underwent only limited mixing and mingling with one another prior to their eruption (see section 5.4.3).

So in case of volcanic deposits showing signs of intense magma mixing and mingling prior to eruption (presence of more mafic enclaves, no correlation between mineralogy and geochemistry, lots of (different) disequilibrium textures, large scatter in variation diagrams, absence of geochemical gap between host rocks and enclaves,…) care should be taken with respect to defining a geochemical composition that is representative for a certain unit.

5.5.2 Late-stage differentiation processes in crustal magma chambers

Given the petrographic and geochemical similarities between the Delta 2 unit and Methana's entire volcanic stratigraphy, it is likely that the magma chamber processes modelled for the late-stage petrogenesis of the Delta 2 magmas also affected the final steps in the magma genesis of the other volcanic deposits. If this assumption is correct, the major and trace element composition of the pyroclastic deposits can be modelled with the same parameters as the ones defined for the Delta 2 unit (see Chapter 4). These models involve **equilibrium melting of more felsic crystal mushes** towards more intermediate compositions as well as **crystal fractionation of more mafic replenishments**. The more felsic end members of this petrogenesis are inferred to be crystal mushes rather than fully solidified granitoids because 1) just as in the Delta 2 volcanics, not a single K-feldspar was found in the thin sections of igneous rocks sampled across Methana, and 2) remobilisation of a still partially molten magmatic body is easier achieved as it requires less time and heat. Mixing and mingling between crystal mush and mafic injection as well as within a single batch of magma due to convection also takes place throughout crustal differentiation and explains the composition of more intermediate enclaves and host rocks (see Chapter 4). Mixing and mingling seem however less important for the petrogenesis of the pumice as well as the PDC deposits and associated basaltic andesites (see section 5.4.3).

The geochemistry of the Delta 2 enclaves defines two petrogenetic trends which involve fractional crystallisation of the same assemblage in different mineral proportions (see Chapter 4). Most other enclaves and the mafic pyroclastics fall within the 'Kossona Vouno series' (Fig. 5.12E & 5.13B), which was modelled by AFC of a crystallising assemblage rich in plagioclase and clinopyroxene (Chapter 4). Using the same mafic mineral compositions and calculations as for the Delta 2 modelling (see Table

4.2), the major element geochemistry of the **Phase C basaltic andesites** can be reproduced from most mafic enclave DPM36. However, this model involves less than 50% of remaining melt and up to 15% crystallisation of amphibole (see Table 5.1) – a mineral completely absent in these mafic samples (see Fig. 5.9). Since geochemical modelling of the Delta 2 rocks suggested that their mineralogy is representative of their crystallising assemblage (see Chapter 4), amphibole is replaced by olivine in the crystallising mineral assemblage. This amphibole-free assemblage requires only ~40% of fractional crystallisation from DPM36 to obtain a residual melt that is geochemically similar to the Phase C basaltic andesites (see Table 5.1) This larger fraction of remaining melt makes it physically easier for the residual liquid to segregate and an olivine-containing mineral assemblage is in agreement with the observed phenocrysts (Fig. 5.9). This suggests that the Phase C basaltic andesites and most enclaves underwent a stage of fractional crystallisation of plagioclase and clinopyroxene, as well as some Fe-Ti-oxides, olivine and apatite, before they replenished the magma chamber of a more felsic crystal mush.

The petrogenesis inferred from the petrographic study of **the Phase C pumice** suggests that this fallout deposit represents a remobilised felsic crystal mush similar to the effusive host rocks but which underwent a higher degree of partial melting. To test this hypothesis, the whole rock major element composition of the pumice samples was calculated from most felsic host rock DPM42, using the same felsic mineral compositions as those chosen for the Delta 2 host rocks. Crystallisation from a pumice sample towards the composition of most felsic host rock DPM42 was thereby successfully used as inversed model for equilibrium melting (SSR = 0.09, see Table 5.1). The whole rock major element geochemistry of the pumice can thus be depicted as a ~40% volume increase of a DPM42 magma by addition of a liquid formed from melting a gabbroic to dioritic mineral assemblage (see Table 5.1 - crystallising assemblage recalculated to 100%: ~54% plagioclase, ~23% clinopyroxene, ~17% amphibole, ~5% Fe-Ti-oxides, ~1% apatite). Instead of completely melting a mafic-intermediate rock, it is however more likely that (nearly) holocrystalline parts of the magma chamber (cumulates, chilled walls, …) underwent partial melting which involved resorption of plagioclase, clinopyroxene, amphibole, Fe-Ti-oxides and apatite.

The pumice's geochemistry is sometimes slightly different from the compositional range of host rocks with similar silica contents (Fig. 5.12 to 5.17). Some of these geochemical differences can be explained by the stability of residual minerals, for example lower K_2O, Cs and Rb due to residual

Phase C basaltic andesites	**Fe-Ti-oxide-1**	**Plag-An90-1**	**Clino-PX-1**	**Amph-Hbl-1**	**Oliv Fo87-1**	**Apatite**	**F**	**SSR**	**EV**
FC from a DPM36 melt	~2%	~23%	~6%	~15%	NA	~1.2%	0.53	0.91	**X**
FC from a DPM36 melt	~2.5%	~22%	~13%	NA	~1.5%	~1.2%	0.60	1.65	**V**
Phase C pumice	**Fe-Ti-oxide-2**	**Plag-An50-2**	**Clino-PX-2**	**Amph-Hbl-2**	**Apatite**	**F**	**SSR**	**EV**	
FC from IM17B to obtain DPM42	*1.4%*	*16%*	*7%*	*5.2%*	*~0.2%*	*0.70*	0.09	**V**	

Table 5.1. Results of the geochemical modelling of the Phase C pyroclastic deposits and associated basaltic andesites using the IgPet software and the same mineral compositions as in Chapter 4 (see table 4.2 for references). Phase C basaltic andesites = PDC deposits and associated basaltic andesites; F = fraction of remaining melt; SSR = sum of squared residuals (calculated using a weighting factor of 0.4 for SiO_2; 0.5 for Al_2O_3 and 1 for all other major element oxides); EV = evaluation, indicating the models interpreted to be less realistic with a red cross, and the ones that are plausible with a green V – the main reasons to reject or accept certain models are also indicated in red or green, respectively.

biotite and lower Na_2O, Sr, Eu and Ba due residual plagioclase. The relatively low U and Th contents are however not due to retention of zircon in the solid residue, because the pumice samples have amongst the highest Zr concentrations found on Methana. The higher Y and TiO_2 contents of the pumice samples in comparison to the host rocks can reflect more partial melting for the former than the latter, resulting in larger additions of amphibole-clinopyroxene melts to the pumice magma. Pumice samples furthermore have significantly smaller LREE/MREE and LREE/HREE ratios than the vast majority of effusive host rocks (Fig. 5.21), resulting from similar LREE concentrations as most felsic host rock DPM42 but significantly more MREE and HREE. This also points towards significant involvement of amphibole- and clinopyroxene-derived melts in the pumice's petrogenesis, as HREE and MREE are significantly more compatible in these minerals than LREE (Davidson et al., 2007). The process of partial melting shown to be involved in the final steps of the petrogenesis of the Delta 2 host rocks is thus also identified in the pumice fallout deposits which seem to have undergone an altogether higher degree of partial melting prior to eruption.

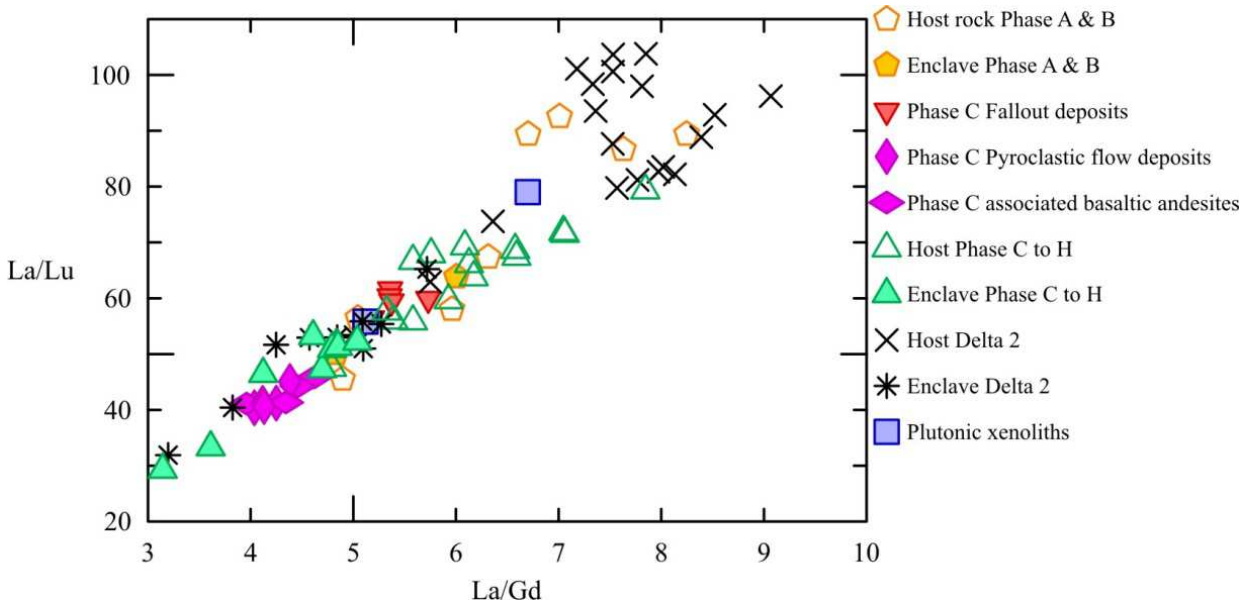

Figure 5.21. *LREE/HREE versus LREE/MREE diagram of all igneous rocks from Methana*. Note how the pumice lapilli plot among the less evolved samples of the overall host rock compositional range, despite their isotopically enriched signature and otherwise more differentiated characteristics.

5.5.3 Different sources reflected in the Sr-Nd-Hf-Pb isotopic composition

Arc magmas may undergo a number of differentiation steps before they finally reach the earth's surface. A variety of sources can thereby contribute to the whole rock geochemistry of the finally erupted lavas: partial melts and/or hydrous fluids from the down-going oceanic crust, partial melts and/or hydrous fluids from subducted sediments, partial melts from the mantle wedge, assimilated magma chamber wall rock at different crustal levels, and perhaps hydrothermal fluids in the uppermost part of the sub-volcanic system. The relative importance of the contributions of these different sources can be judged by trace element ratio diagrams, while the identity of the different sources is best assessed using the isotopic composition of the volcanic rocks (Elburg, 2010). As the Sr-Nd-Hf isotopic composition seems to be decoupled from the Pb isotopic composition, these two isotopic systems may shed light on different aspects of the petrogenesis of Methana's volcanic rocks.

According to the Nd-Hf isotopic system, basaltic enclave DPM36 is the most primitive end member of Methana's volcanic rock series, whereas pumice sample IM383 represents the most crustally enriched magma (Fig. 5.16B-C). The aberrant $^{87}Sr/^{86}Sr$ and $^{143}Nd/^{144}Nd$ compositions of the Loutses

South host rocks and of the Mavri Petra flow (Fig. 5.17A) however infers involvement of (at least) 3 different end members besides DPM36 in the volcanics' petrogenesis. The igneous rocks from Methana occupy triangular shaped fields in the Pb isotope diagrams, which also points to three different sources. A diagram of **$^{87}Sr/^{86}Sr$** versus Sr (Fig. 5.22) indeed shows three different trends: 1) the main trend which is followed by most effusive rocks as well as the pyroclastic deposits starts from a mafic magma with the relatively low Sr contents and isotopic composition of DPM36 (290 ppm; $^{87}Sr/^{86}Sr$ = 0.70554) and evolves to more crustal Sr isotope compositions at increasingly lower Sr concentrations (IM383: 230 ppm, $^{87}Sr/^{86}Sr$ = 0.70925); 2) the Loutses South host rocks represent the least radiogenic Sr composition combined with the highest Sr concentrations (550 ppm, $^{87}Sr/^{86}Sr$ = 0.70487), suggesting a different magma genesis for these host rocks prior to their remobilisation by a mafic replenishment similar to DPM36 (the Sr geochemistry of the Loutses South enclaves reflects mixing/mingling between a DPM26 crystal mush and DPM36 magma); and 3) enclaves and host rocks of the most recent Mavri Petra flow define a trend which starts from a different Sr geochemical composition (IM400: 430 ppm, $^{87}Sr/^{86}Sr$ = 0.70668) but evolves towards the intermediate effusive lavas from Methana. Figure 5.22 furthermore shows all sedimentary basement lithologies and xenoliths sampled on Methana. These rocks, however, combine similar to lower concentrations of Sr with a similar to only slightly more radiogenic composition compared to the volcanic rocks, which makes them unlikely crustal end members to explain the high $^{87}Sr/^{86}Sr$ ratio of the pumice lapilli. Simple mixing between volcaniclastic greywacke IM362 and a mafic magma such as DPM36, for example, would require unrealistically large amounts of this greywacke in order to reproduce Methana's high $^{87}Sr/^{86}Sr$ magmas (90% IM362 and 10% DPM36 renders the WR Sr geochemistry of pumice sample IM383 – Fig. 5.22). In case of the more probable process of AFC, however, only 5 – 10 % of crystallisation suffices for the residual melt to obtain the WR Sr isotopic composition of Methana's more primitive enclaves and of the PDC deposits (and associated basaltic andesites) from which xenolith IM362 was retrieved (Fig. 5.22). The AFC process involving 10-30% of fractional crystallisation of a mafic magma similar to Mavri Petra enclave IM400 and assimilation of IM362 could also explain the WR Sr geochemistry of the 'Mavri Petra trend' and of the more intermediate host rocks and enclaves (Fig. 5.22). The volcaniclastic xenolith found in the pyroclastic deposits might therefore represent a crustal level where more primitive magmas differentiate towards basaltic-

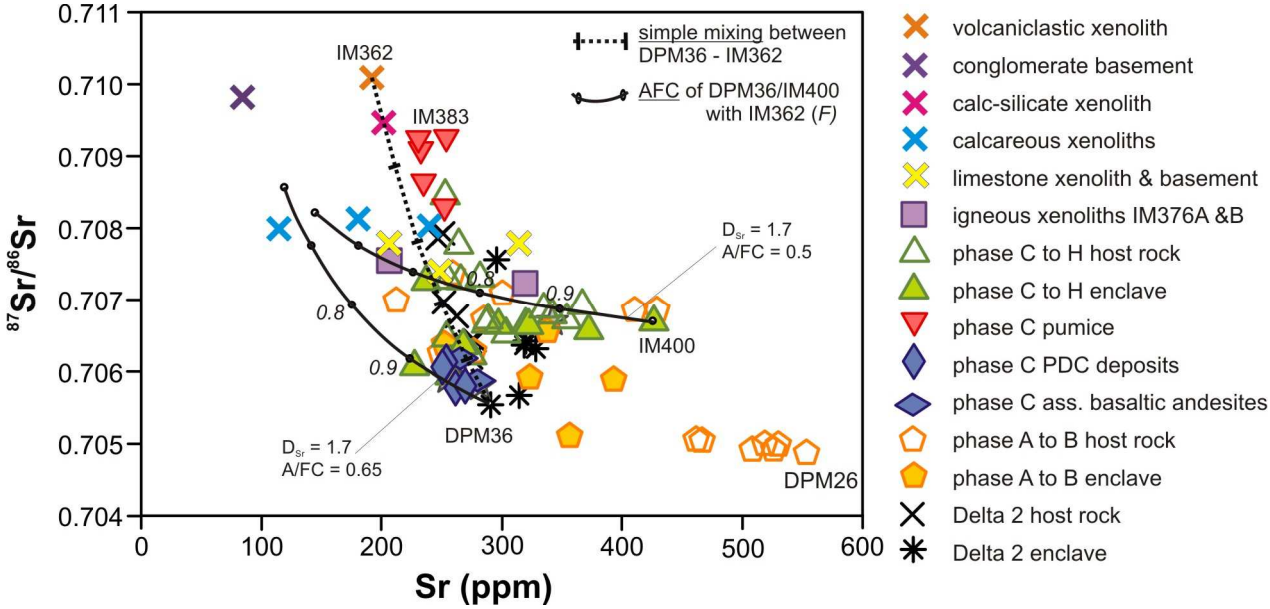

Figure 5.22. *Sr geochemistry of Methana's igneous and sedimentary rocks.* The limestone xenoliths and basement rocks can not be the main crustal end member of the Sr geochemistry of the volcanic rocks. The Sr geochemistry of the calc-silicate xenoliths might be reflected in the mafic pyroclastic rocks and intermediate host rocks and enclaves. The very radiogenic Sr composition of the pumice can not be reproduced by AFC processes using any of the sedimentary samples. F = fraction of residual melt.

andesitic 'enclave' magmas or intermediate 'host rock' magmas, but it can not account for the high $^{87}Sr/^{86}Sr$ ratios of the pumice deposits and more evolved host rocks.

Figure 5.23 shows that the Nd geochemistry of the sedimentary basement and xenolith samples also represents a compositional range similar to Methana's igneous rocks. The sampled limestones contain insufficient Nd to allow precise isotopic measurements and the calcareous xenoliths which could be analysed combine too little Nd with **$^{143}Nd/^{144}Nd$** ratios that are too high, rendering them unlikely major contributors to the Nd geochemistry of the volcanic rocks. Conglomerate IM26 does have a more crustal Nd isotopic composition similar to the pumice samples, but too small amounts of Nd. Volcaniclastic xenolith IM362 and calc-silicate xenolith IM386 are the only sedimentary samples which might be representative of crustal material involved in the petrogenesis of the enclave magmas and intermediate host rocks (Fig. 5.23). The Nd geochemistry of the pumice deposits can however not be modelled with any of the sedimentary rocks sampled from Methana.

The strong positive correlation between the Hf and Nd isotopic composition of Methana's igneous rocks (Fig. 5.17B) suggests that their $^{176}Hf/^{177}Hf$ values should behave in a similar way as the Nd geochemical models. The single calcareous xenolith analysed for its Hf isotopic composition has a $^{176}Hf/^{177}Hf$ ratio that is indeed too high to be a plausible crustal contaminant of Methana's volcanic rocks. In line with the Nd geochemical model (Fig. 5.23), fractional crystallisation and assimilation of calc-silicate xenolith IM386 was attempted to also reproduce the **$^{176}Hf/^{177}Hf$** ratios of enclaves and intermediate host rocks (Fig. 5.24A). Bulk distribution coefficients for Hf varying from 0.06 to 2.5 give AFC trends that seem to reproduce the Zr-Hf geochemistry of the more mafic volcanic rocks (Fig. 5.24A). However, the models in wich Hf is incompatible infer significant calc-silicate assimilation which is not reflected in the mafic samples' geochemistry, and more realistic amounts of AFC are only obtained when Hf is compatible (Fig. 5.24A). A bulk distribution coefficient of 2.5 for Hf requires crystallisation of zircon (the zircon-melt distribution coefficient of Hf is about 1000 in basaltic to andesitic magmas, http://earthref.org/KDD/). Although some euhedral zircon is observed in Methana's

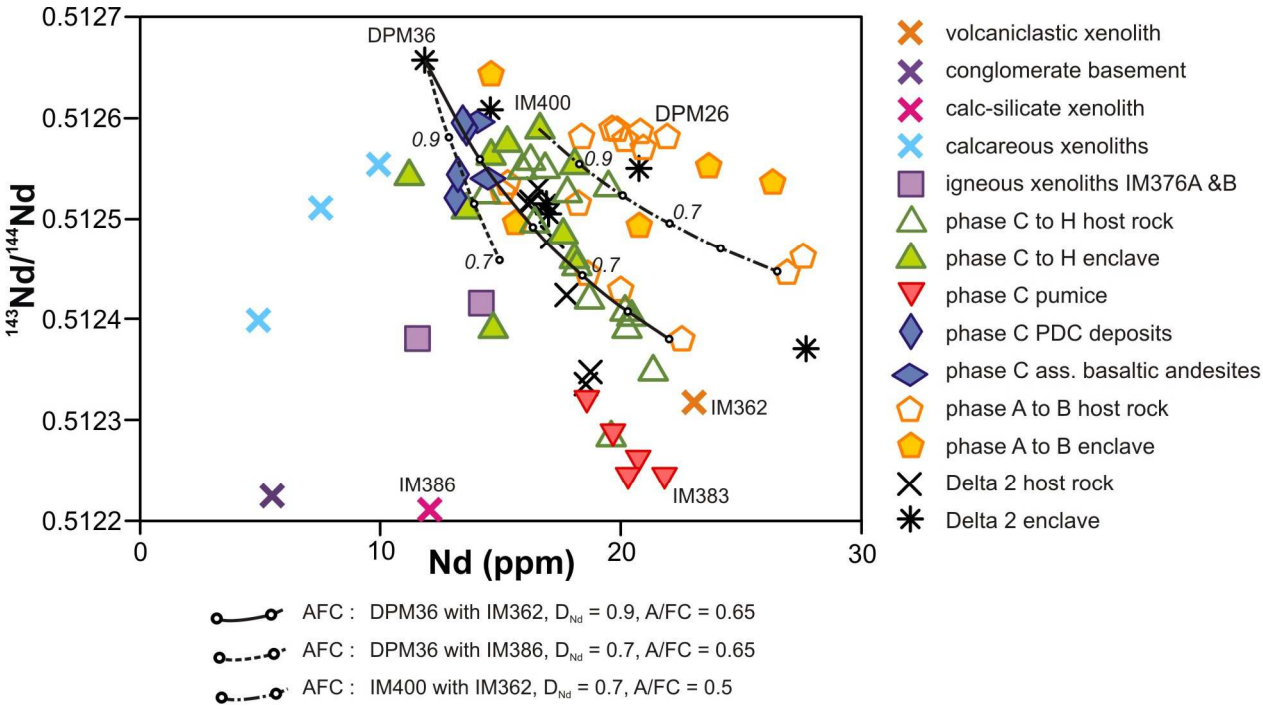

Figure 5.23. *Nd geochemistry of igneous and sedimentary rocks from Methana.* Geochemical models involving fractional crystallisation of DPM36 or IM400 (D_{Nd} 0.5 to 0.9) together with assimilation of either calc-silicate xenolith IM362 or IM386 (A/FC 0.5 to 0.65) successfully reproduce Methana's more mafic lithologies and host rocks - but the pumice deposits can not be modelled.

volcanic rocks, the Harker variation diagram suggests that zirconium is incompatible in the enclave series, with a sudden switch to increased compatibility, likely linked to zircon crystallisation, only for the host rocks (Fig. 5.24B). Whereas the Sr and Nd geochemistry of Methana's enclaves and more mafic host rocks could be reproduced by AFC within a volcaniclastic or calc-silicate wall rock, this model is not valid for their Hf isotopic compositions.

Decoupling between Nd and Hf isotopes observed in marine and riverine sediments is thought to reflect continental weathering which hydrodynamically fractionates heavy minerals such as zircon, the main Hf repository, from lighter minerals (Carpentier et al., 2009; Vervoort et al., 2011; Garçon et al., 2013). Zircon is the key mineral in Hf isotope systematics, leading to low $^{176}Hf/^{177}Hf$ ratios in zircon-rich sediments which are preferentially retained on or near the continents leading to a complementary high $^{176}Hf/^{177}Hf$ isotopic composition for marine sediments. The terrestrial ε_{Hf}-ε_{Nd} array represents the correlation between Hf and Nd isotope ratios present in marine sediments (Vervoort et al., 2011) and is nearly identical to the linear trend of the mantle array (Chauvel et al., 2007). The Hf-Nd isotopic

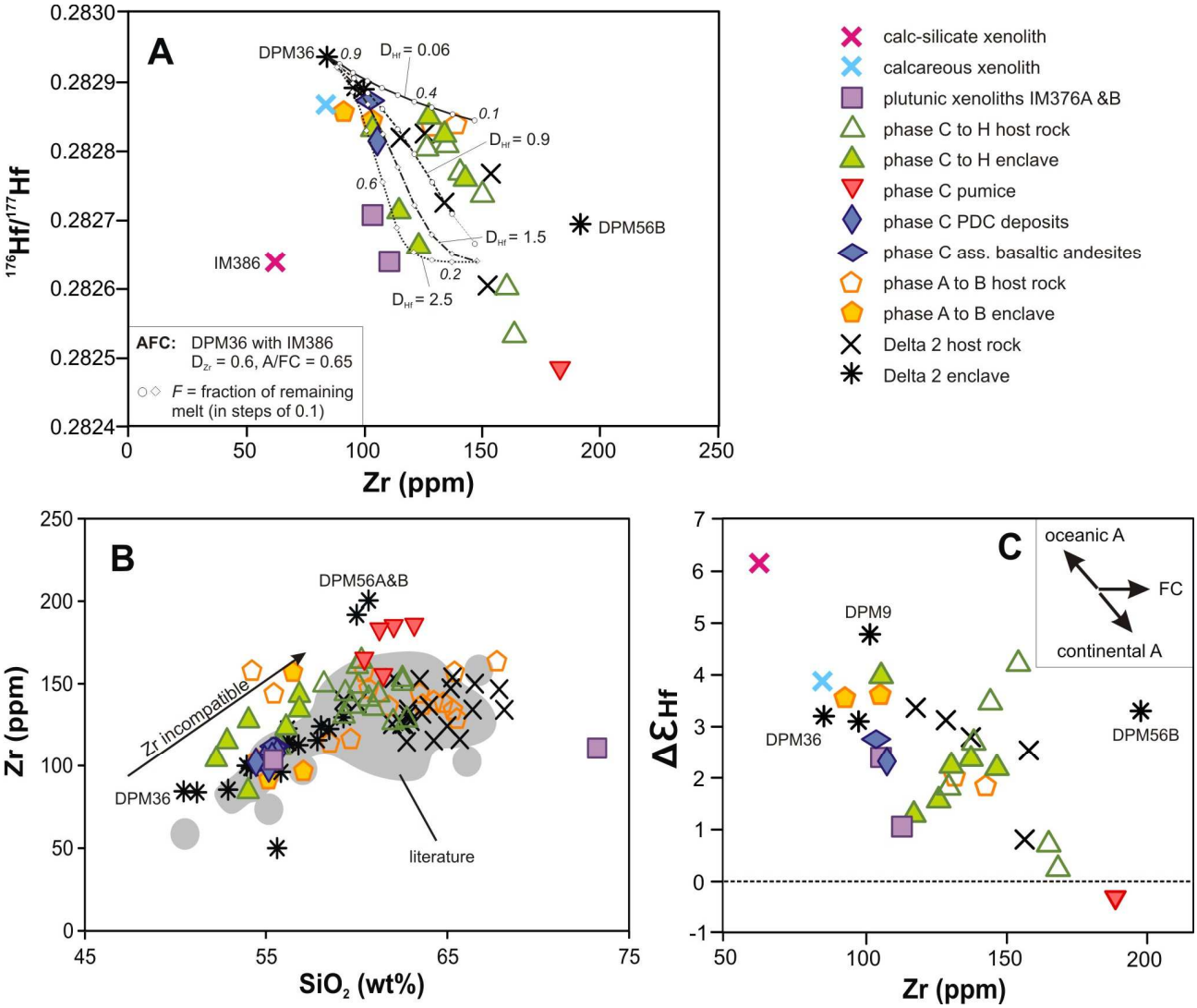

Figure 5.24. *Hf geochemistry of the igneous rocks and two sedimentary xenoliths from Methana.* (A) Some of the more successful modelling calculations can partially reproduce the Zr contents and $^{176}Hf/^{177}Hf$ ratio of Methana's volcanic deposits. (B) Variation diagram of zirconium, suggesting that Zr was incompatible throughout the enclaves' differentiation but that at least some zircon crystallised during the crystal fractionation of the more felsic host rock magmas. (C) The volcanic deposits of Methana show a negative correlation between Zr contents and vertical offset from the terrestrial ε_{Hf} - ε_{Nd} array. $\Delta\varepsilon_{Hf} = \varepsilon_{Hf} - (1.55^* \varepsilon_{Nd} + 1.21)$ (Carpentier et al., 2009), A = assimilation, FC = fractional crystallisation.

compositions of Methana's volcanic rocks are similar to the terrestrial array but their linear ε_{Hf}-ε_{Nd} trend is steeper as less differentiated volcanic rocks plot increasingly above the terrestrial array (Fig. 5.17B). There is a negative correlation between this deviation from the terrestrial array towards more radiogenic Hf (Fig. 5.17B) and the samples' Zr concentration (Fig. 5.24A) and silica contents (Fig. 5.16C & Fig. 5.24B). The whole rock Hf isotopic composition of the more primitive magmas (DPM36) thus seems to reflect a radiogenic Hf contribution from partial melts of the subducted oceanic crust and/or subducted marine sediments. Throughout subsequent differentiation in crustal magma chambers, this initially high $^{176}Hf/^{177}Hf$ ratio is increasingly overprinted due to assimilation of crustal wall rock with less radiogenic Hf compositions.

The vertical deviation of the samples' Hf isotopic composition from the terrestrial array of Vervoort et al (2011) ($\Delta\varepsilon_{Hf}$, = $\varepsilon_{Hf} - (1.55* \varepsilon_{Nd} + 1.21)$) is plotted against Zr to further examine the effect of crustal assimilation on Hf isotopes (Fig. 5.24C). Carpentier et al. (2009) used a similar diagram to discriminate between contributions of clay-rich, zircon-poor sediments (positive $\Delta\varepsilon_{Hf}$) and zircon-rich, more coarse-grained sediments (negative $\Delta\varepsilon_{Hf}$). Figure 5.24C shows that the more Zr-poor volcanic rocks display the largest vertical deviation from the terrestrial array and that those samples with the highest amounts of zirconium show almost no vertical deviation. This seems to confirm the hypothesis described above: Methana's most mafic magmas reflect incorporation of clay-rich, zircon-poor sediments but as crustal differentiation proceeds, this 'marine' signature evolves towards less radiogenic Hf compositions due to assimilation of zircon-rich, continental crust. The majority of volcanic rocks thereby follows the trend of less radiogenic Hf with increasing amounts of Zr defined by basaltic enclave DPM36 and pumice lapilli IM383, suggesting that crustal contamination is dominated by a single upper crustal end member which is most recognisable in the pumice deposits.

Scatter around this main DPM36-IM383 trend reflects both the geochemistry of varying source materials (subducted slab melt, mantle wedge, different crustal levels, …) and different origins for the zirconium and hafnium contents (in zircon or in groundmass). If the difference between the ICP-OES and ICP-MS analysed Zr concentrations is used to estimate the ratio Zr-in-zircon to Zr-in-groundmass, the position of certain samples off the main trend gives further insight into the petrogenesis of these samples. Granitic xenolith IM376A, for example, displays intermediate amounts of Zr in combination with a relatively low $^{176}Hf/^{177}Hf$ ratio, which can be explained by the fact that up to 70% of DPM56A's zirconium is hosted in zircon crystals (Fig. 5.24C). Anomalous enclave DPM56B has the overall highest concentrations of zirconium and contains nearly all its Zr in the groundmass (compare ICP-OES and ICP-MS analysed Zr concentrations in Appendices B and C, respectively). The inferred lack of zircon crystals in this enclave and its relatively radiogenic Hf composition suggests that its whole rock geochemistry is representative of an interstitial melt that remained after crystal fractionation (Fig. 5.24C). The small discrepancy between ICP-OES and ICP-MS obtained Zr concentration of pumice lapilli IM383 also indicates that its high zirconium contents are hosted in its groundmass rather than in zircon. The very low $^{176}Hf/^{177}Hf$ ratio of pumice IM383 however indicate that it obtained these large amounts of Zr through assimilation of crustal, zircon-rich lithologies rather than through fractional crystallisation (Fig. 5.24C).

Pumice lapilli IM383 also contains the most **radiogenic Pb composition** besides the highest $^{87}Sr/^{86}Sr$ value and the low Nd and Hf isotope ratios. Whereas most mafic enclave DPM36 has a relatively intermediate Pb isotopic composition (Fig. 5.17 C-E), plutonic xenolith IM376 combines an intermediate Sr-Nd-Hf isotope geochemistry with the lowest Pb isotope ratios (Fig. 5.16D-F). The spatial distribution of the Sr and Pb isotopic composition of the samples is shown in Figure 5.25, in which the rainbow colour-coding represents the composition of a sample relative to the volcanic rock with the highest (red) and lowest (purple) isotope ratio. Lead isotope ratios thereby show a tendency to correlate with the sampling locality rather than with the sample's level of differentiation.This spatial correlation is most pronounced in the $^{208}Pb/^{204}Pb$ ratios (Fig. 5.25B) and contrasts to the positive correlation between a samples level of differentiation and its $^{87}Sr/^{86}Sr$ ratio (Fig. 5.25A). The more

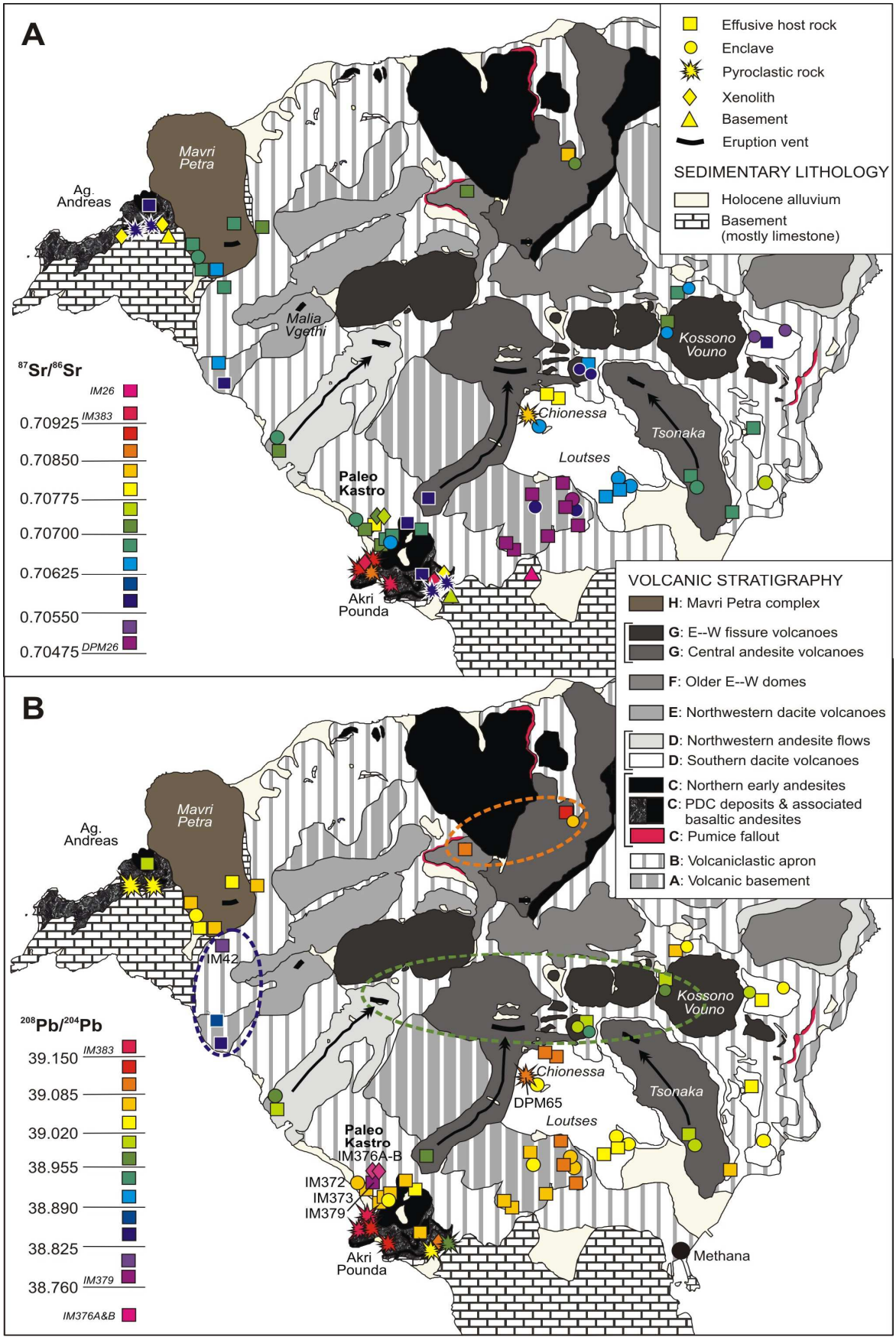

Figure 5.25. *Isotope geochemistry of the different lithologies on Methana visually linked to their sampling localities*. Comparison between (A) $^{87}Sr/^{86}Sr$ and (B) $^{208}Pb/^{204}Pb$ compositions shows decoupling between the Pb and the Sr(-Nd-Hf) isotopic systems.

mafic lithologies of enclaves, PDC deposits and associated basaltic andesites, for example, have low $^{87}Sr/^{86}Sr$ ratios (from dark blue over light blue to green-blue in Fig. 5.25A), but their Pb isotopic composition is clearly more radiogenic (from dark green over yellow to light orange in Fig. 5.25B). The location from where the samples were collected thereby roughly represents areas of similar Pb isotopic compositions for host rocks and enclaves alike – regardless of the stratigraphic age of the deposits. If the rocks sampled at locations 45, 48 and 50 are traced back to their respective eruption vents (see black arrows in Fig. 5.25), it becomes clear that they originate from a central area of the peninsula which seems to erupt lavas with similar Pb isotopic compositions (see dark green ellipse in Fig. 5.26B). The domes and (vents of the) lava flows that represent this area of homogeneous intermediate $^{208}Pb/^{204}Pb$ ratios are of different volcanic phases (D and G) but have a very similar degree of differentiation (SiO_2 = 60.1-62.8 wt% for host rocks). The few volcanic rocks sampled to the north of this area have the same silica content and are also from different phases (E and G), but their Pb isotopic signature is considerably more radiogenic (see orange ellipse in Fig. 5.25B). Three host rocks from the first period of volcanic activity sampled in the northwestern part of Methana have comparably low $^{208}Pb/^{204}Pb$ ratios (see dark blue ellipse in Fig. 5.25B) despite their large difference in silica contents (58.5, 59.7 and 67.7 wt% SiO_2, with the latter - IM42, purple – combining the overall highest SiO_2 concentration with the second lowest $^{208}Pb/^{204}Pb$ ratio). The fact that two host rocks are thereby sampled from the same volcanic unit does not explain their similar Pb geochemistry as two Paleo Kastro host rocks sampled from the same outcrop (spatially a lot closer to one another) have very different Pb isotope ratios. Indeed, host rock IM372 and its enclave IM373 have the same $^{208}Pb/^{204}Pb$ composition (Fig. 5.25B) which is significantly more radiogenic than the Pb isotopic composition of the host rock sampled from the same outcrop merely 10-15m away (IM379, Fig. 5.25B). The latter host rock thereby has the lowest Pb isotope ratios of the volcanic rocks and was sampled within 20 cm of igneous xenolith IM376, whose Pb geochemistry is the least radiogenic found on Methana (Fig. 5.16D-H).

The Pb isotopic composition is thus 1) similar for enclaves and host rocks from a certain sampling location, 2) rather homogenous across larger areas regardless of relative age or differentiation of the volcanic rocks, and 3) heterogeneous in the vicinity of a xenolith with distinctly different Pb isotope ratios. The fact that Pb isotope ratios of Methana's volcanic rocks do not correlate with their age or degree of differentiation, but rather with their geographical location or the presence of distinctly different xenoliths, suggests that they are derived in the very final stages prior to eruption. Basaltic andesites and andesites erupted near the limestone basements in the south and northwest parts of the peninsula are characterised by similar $^{208}Pb/^{204}Pb$ ratios and the different domes and vents of lava flows defining the 'green' Pb geochemistry in the centre of Methana are organised parallel to large east-west oriented faults. So perhaps the final lead isotopic composition was only established in the upper parts of the continental crust, which is transected by multiple faults acting as magma pathways towards the surface. Final Pb isotopic overprinting could then have occurred in a closed system through binary mixing or assimilation during fractional crystallisation. In this case, a correlation between Pb concentration and isotopic composition, similar to the trends observed for the Sr and Nd geochemistry, would be expected. Comparison between Fig. 5.22-5.23 and Fig. 5.26A however reveals that there is no such correlation. Figure 5.26 also shows that whereas different effusive rocks from a certain location tend to have similar Pb isotope ratios, enclaves systematically contain less lead than their host rocks. This suggests that the longer residence times in the upper crust inferred for crystal mushes give rise to higher Pb contents rather than to more radiogenic Pb isotope. But which crustal source could be responsible for a Pb enrichment that also adds a radiogenic isotope fingerprint which varies from one eruption area to the next?

Nearly all sedimentary basement and xenolith samples can be ruled out as possible contaminants as they have too little lead to even allow precise determination of their Pb isotopic composition. Only volcaniclastic xenolith IM362 could be analysed and has a Pb isotopic composition in the range of Methana's intermediate volcanic rocks (Fig. 5.26B). Despite the decoupling between Sr-Nd-Hf and Pb

isotope ratios, geochemical models introduced to explain the trends in the former isotopic systems seem to also apply to the lead geochemistry: fractional crystallisation of more mafic enclaves with concurrent assimilation of IM362 reproduces the $^{208}Pb/^{204}Pb$ ratios and Pb contents of more evolved enclaves and Loutses South host rocks (Fig. 5.26B). Even the more Pb-enriched effusive rocks of Mavri Petra can be generated via AFC process if lead is incompatible ($D_{bulk}^{(Pb)} \leq 0.1$) within the crystallising mineral assemblage. Whereas igneous xenoliths IM376A and IM376B plot within the Sr-Nd-Hf geochemical range of all other samples, they have lower Pb contents as well as significantly lower $^{208}Pb/^{204}Pb$ ratios (Fig. 5.26B). The aberrant $^{208}Pb/^{204}Pb$ composition of their host lava IM379

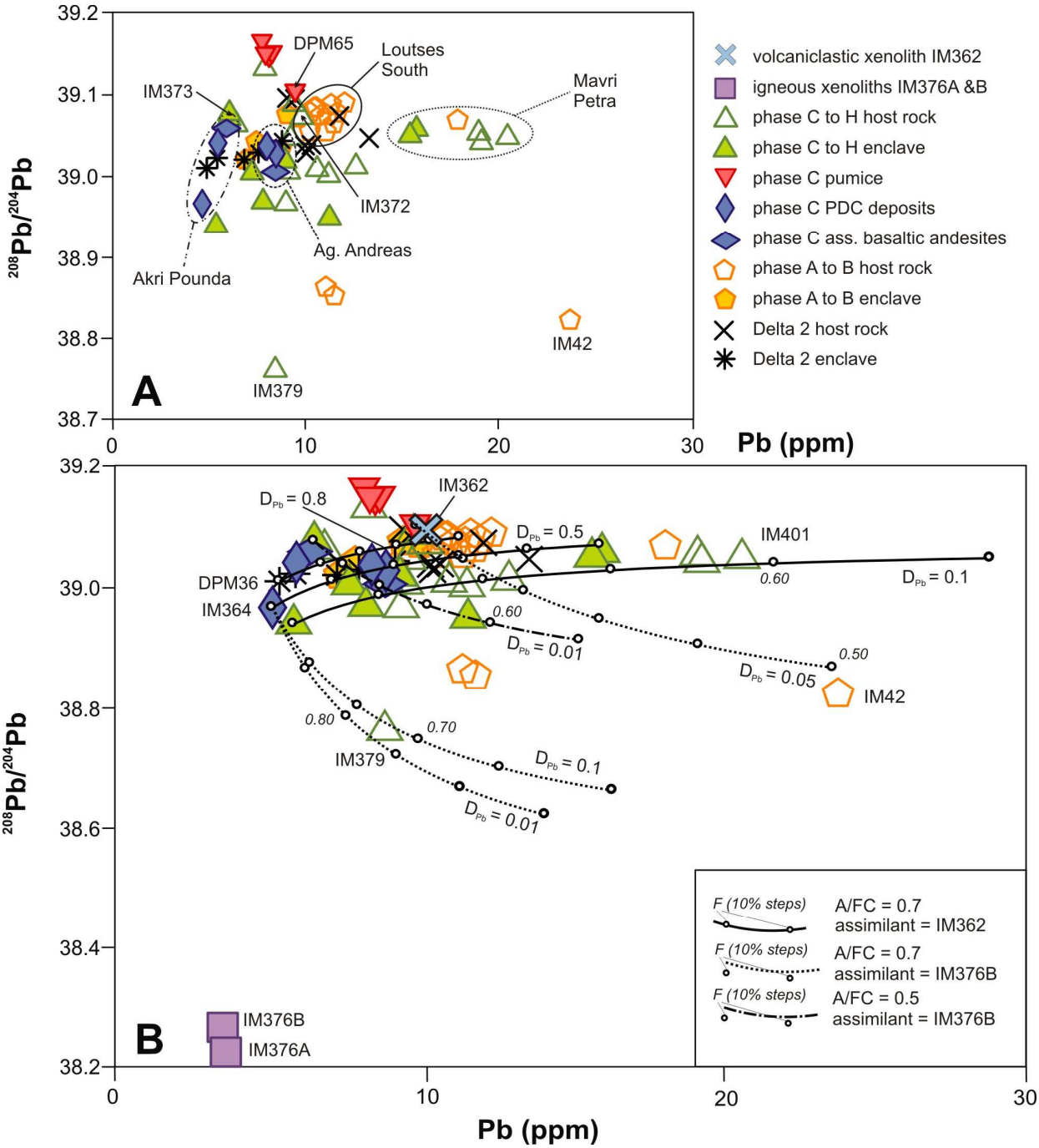

Figure 5.26. *$^{208}Pb/^{204}Pb$ versus Pb contents of the main igneous rocks and one volcaniclastic xenolith from Methana.* (A) The isotopic composition shows no correlation with Pb contents, but seems to cluster according to sampling locality. (B): Geochemical modelling of AFC processes, involving more primitive enclaves and the only two xenoliths which Pb isotopic composition could be determined, is able to reproduce the Pb geochemistry of most volcanic deposits on Methana, apart from the pumice samples.

can be modelled from more mafic enclave magmas which partially assimilate IM376B whilst Pb is incompatible ($D_{bulk}^{(Pb)}$ 0.1-0.01). Assimilation of igneous xenolith IM376B in a system where Pb is incompatible can furthermore reproduce the $^{208}Pb/^{204}Pb$ composition of other aberrant volcanic rocks with Pb > 10 ppm but a $^{208}Pb/^{204}Pb$ ratio below the more primitive enclaves. The low bulk distribution coefficient for lead derived from geochemical modelling agrees with the moderate to strong incompatibility of Pb in the main mineral phases inferred to play a role in the upper crustal AFC processes (see section 5.5.2 and GERM Partition Coefficient Database). The systematic difference in Pb contents between enclaves and host rocks can thus be explained by incompatibility of Pb during late-stage differentiation processes. But what causes the correlation between geographical location and similar Pb isotopic composition of host rocks and enclaves (Fig. 5.25B)?

McCulloch and Woodhead (1993) ascribe significant Pb mobility in deep, crustal-scale fluid advection systems to the extremely high solubility of $PbCl^+$ in sulfur- and chlorine-enriched brines at elevated temperatures (>300°C). Such a type of aqueous fluid is probably also present within the upper crustal differentiation levels of Methana's magmas as there is a hydrothermal reservoir below the centre of the peninsula (Dotsika et al., 2010). The temperature of Methana's geothermal reservoir is estimated to be about 210°C and the spring waters associated with it are indeed enriched in both H_2S and NaCl (D'Alessandro et al., 2008). The centrally located reservoir is imaged through magneto-telluric data down to a depth of about 1.5 km, as well as a continuation of this hydrothermal system to greater depths (3 km) along WNW-ESE oriented faults that crosscut the southern limestone basement (Efstathiou et al., 2012). Shallow magmatic intrusions imaged below Methana are mainly associated with E-W and N-S oriented normal faults (Efstathiou et al., 2012), which suggest that magmas also move along the upper crustal fractures. Hydrothermal fluids are thus proposed as the cause for the specific Pb geochemistry of Methana's igneous rocks. Such fluids are capable of dissolving Pb from the sedimentary basement lithologies and homogenising the Pb isotopic signature within certain crustal segments. This specific Pb isotopic composition will then be passed on by wall rock assimilation – resulting in a different Pb geochemistry for shallow intrusions at different geographic locations. Hydrothermally contaminated plutons can in turn also influence the Pb geochemical signature of younger upper-crustal magma intrusions in their final stages prior to eruption. The Pb isotopic signature of host rock IM379, for example, reflects interaction with its igneous xenolith IM376 whilst carrying it to the surface. Hydrothermal fluids transporting Pb along the crustal fault systems could also directly come into contact with rising magma. The different behaviour of Pb relative to Sr, Nd and Hf thus originates from the fact that in the upper continental crust Pb is redistributed by hydrothermal fluids, whereas the behaviour of Sr, Nd and Hf remains mainly controlled by magmatic melts and minerals. Decoupling between the different isotopic systems does therefore not necessarily reflect magmagenesis at varying crustal levels, nor different (upper) crustal contaminants, but different mobility of the key chemical elements in the upper 3 km of the crust. The crustal level represented by volcaniclastic xenolith IM362, for example, seems to have influenced the Sr-Nd as well as Pb isotopic composition of a number of Methana's volcanic rocks.

5.6 Further integration of field observations, petrography and geochemistry

5.6.1 Amphibole-rich and amphibole-poor mineralogy reflected in geochemistry?

All volcanic rocks of Methana contain amphibole and can be accordingly subdivided into amphibole-rich and amphibole-poor types based on the amount of disequilibrium features shown by their hydrous minerals, as well as the presence or absence of amphibole phenocrysts and microlites (see section 5.2.1). Geochemical modelling also points to a key role for amphibole in the petrogenesis of most volcanic rocks: (1) amphibole fractionation from more intermediate magmas is involved in the differentiation process towards more felsic magmas (see Chapter 4), (2) the presence of amphibole in upper crustal magma chambers prohibits the resulting viscous crystal mushes from erupting, (3) subsequent partial melting induced by mafic injections leads to amphibole breakdown, lowering the host magma's viscosity and triggering its effusive eruption (see Chapter 4), and (4) significant partial

melting of such an intermediate to felsic crystal mush causes large scale amphibole resorption and a violent explosive eruption (see section 5.4.3). But does the geochemistry of Methana's volcanic rocks actually reflects their observed amphibole-poor and amphibole-rich mineral assemblage?

Hornblende-melt partition coefficients for subduction-related basaltic andesites to dacites show that MREE are generally more compatible in amphiboles than HREE (Sisson, 1994). A rock rich in amphibole is thus expected to have a higher Dy/Lu ratio than its residual melt which will be more depleted in Dy than in Lu. Figure 5.27A shows the Dy/Lu versus SiO_2 diagram for all volcanic rocks of Methana, grouped according to their amphibole content. This shows that amphibole-rich volcanic rocks have any silica content ranging from most mafic enclave DPM36 to most felsic host rock DPM42, whereas amphibole-poor volcanics represent a more restricted SiO_2 composition (~54-63wt%, Fig. 5.27A). Overall, the volcanic rocks of Methana show no correlation between their REE geochemistry and their mineral assemblage (Fig. 5.27A). However, clinopyroxene has a similar trend for its REE distribution coefficients (Fig. 5.27A, Davidson et al., 2007) and so its imprint is difficult to distinguish from that of amphibole. Discrimination between the two minerals might still be possible as Y can be up to 5 times more compatible in amphibole than in clinopyroxene (GERM database, 2013). A rock with amphibole as major mineral phase would thus show high Dy/Lu ànd high Y contents whereas a rock with clinopyroxene as dominant mafic mineralogy might contain lower amounts of Y at similar Dy/Lu ratios. In case of Methana's volcanic rocks the presence or absence of amphibole does not correlate with higher Dy/Lu and Y contents (Fig. 5.27B): apart from the Loutses South host rocks, the entire Methana volcanic suite shows a positive correlation between Y contents and Dy/Lu ratio – again suggesting a key role for amphibole in their petrogenesis. The petrographic classification of Methana's volcanic rocks according to their hydrous mineral contents thus mainly seems to reflect

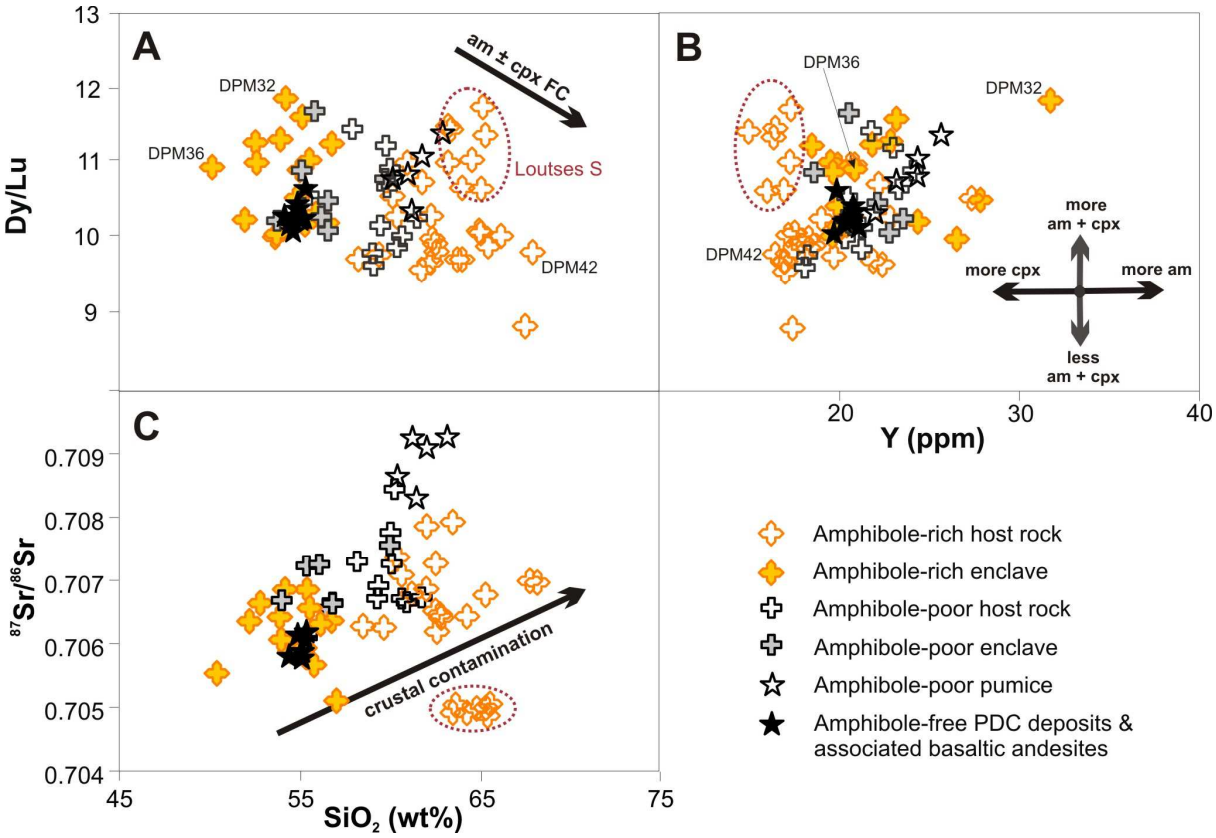

Figure 5.27. *The petrographically defined amphibole-poor and amphibole-rich volcanic rock types do not correlate with their geochemical composition*, despite the fact that their REE and Y contents do reflect crustal processes involving amphibole (and clinopyroxene).

amphibole stability at the last differentiation level prior to eruption, and is not an indication for significantly different magma compositions.

The amphibole-poor pumice deposits, for example, contain high Dy/Lu ratios and elevated Y contents probably derived from incorporation of amphibole (and clinopyroxene) melt, rather than reflecting a large population of amphibole (macro-)phenocrysts. Davidson et al. (2007) introduced the term 'cryptic amphibole fractionation' for this contradiction between the limited amounts of amphibole present in arc volcanic rocks worldwide and the strong geochemical indication that this mineral plays an important role in the (earlier stages of the) petrogenesis of arc-related magmas. The only minor correlation observed between the hydrous mineralogy of the effusive volcanic rocks and their geochemistry is the fact that amphibole-poor samples usually have higher $^{87}Sr/^{86}Sr$ ratios (0.7065-0.7095) whereas the amphibole-rich lithologies are shifted towards less radiogenic Sr isotopic compositions (0.7045-0.7080) (Fig. 5.27C). This confirms that amphibole-poor rocks reflect a final differentiation stage in the uppermost part of the crust, which apparently contributes most to crustal contamination of $^{87}Sr/^{86}Sr$. The PDC deposits and associated basaltic andesites show less radiogenic Sr contents suggesting fast migration through the crust without much crustal assimilation (Fig. 5.27C).

5.6.2 Amphibole differentiation at multiple crustal levels

The 'amphibole-rich' and 'amphibole-poor' classification for the host rocks and its extension to the enclaves ('type 1' enclaves contain plagioclase + amphibole ± pyroxene whereas 'type 2' enclaves contain plagioclase + pyroxene) is already described by Pe (1974). Since hydrous minerals are only stable under certain pressure-temperature conditions, this dual mineral assemblage of Methana's volcanic deposits might indicate different crustal levels at which magmas fractionate. On one hand, there is the crustal differentiation level at which amphibole-rich rocks resided prior to their eruption. The presence of amphibole microlites and of pristine amphibole ± biotite phenocrysts indicates that the type 1 magmas mainly crystallised within the stability field of amphibole. This suggest that the amphibole-rich magmas, if they had roughly the same H_2O content and chemical composition as the WR contents of the erupted type 1 host rocks, evolved at considerable depths (pressures greater than 75-100 MPa corresponding to a minimum depth of ca. 3 km) and within a temperature range of 800-1050°C (Moore & Carmichael, 1998; Best, 2003). The amphibole-poor mineral assemblage suggests a crustal differentiation level outside the amphibole stability field. The presence of hydrous minerals with disequilibrium features implies that magma rose to a shallower level in the crust where hydrous minerals were no longer stable (at pressures lower than 75-100 MPa) after an initial phase of amphibole stability at greater depth.

Amphiboles with dehydration and reaction rims are common in volcanic rocks and often attributed to slow ascent and extrusion. Thin opaque rims are thought to result from late-stage oxidation upon extrusion, whereas more coarse-grained anhydrous aggregates replacing amphibole from the rim inwards are interpreted as decompression reactions during slow ascent or pre-eruptive storage (Buckley et al., 2006; Ridolfi et al., 2008). The thickness of an amphibole's reaction rim can therefore be interpreted as a measure for the decompression rate, and thus for the speed at which its host magma ascended during eruption (Rutherford & Hill, 1993). From this point of view, the petrographic difference between amphibole-rich and amphibole-poor effusive lavas could reflect a variation between fast and slow magma ascent, respectively. Within the Phase H Mavri Petra deposits, a gradual change is observed from amphibole-poor host rocks on the outer flanks of the lava flow to amphibole-rich host rocks near the eruptive vent (Fig. 5.28). This could thus be interpreted as progressive tapping of magma from deeper crustal levels, a gradual increase with time in magma ascent rate – or a combination of both.

Since the stability of amphiboles formed in equilibrium with their melt is confined to small ranges near their dehydration curves, amphiboles are reliable indicators of the physical-chemical conditions under which the magma crystallised. Ridolfi et al. (2010) combined this knowledge with literature data on subduction-related, calc-alkaline volcanic rocks and their amphiboles from around the world, as well as with experimental data, to formulate new thermobarometric equations. The resulting 'one amphibole' geo-thermobarometer can be applied to all deposits of calc-alkaline volcanoes, including hybrid intermediate lavas, with a precautionary restriction to upper- and mid-crustal settings (<40km, i.e. <1GPa) for continental arcs (Ridolfi et al., 2010). The chemical composition of Methana's volcanic amphiboles is thus suitable for investigation of their pre-eruptive physical-chemical conditions using this geothermobarometer (Elburg et al., 2013). Such geochemical data are available in literature: Mitropoulos & Tarney (1992) published the mineral composition of amphibole phenocrysts from three different lavas whereas Pe (1974) analysed the composition of hornblende from three different enclaves. Micro-probe analysis was also carried out on three Methana amphiboles for the geo-archeological provenance study of Dorais & Shriner (2002). From these three studies, 8 out of 9 amphiboles plot closely together and define two different P-T fields (Fig 5.29). The only amphibole analysis that plots in between these two pressure-temperature fields (Fig. 5.29) likely reflects measurement across a zoned crystal, as Dorais & Shriner (2002) report that "in order to avoid potential operator bias in sample spot collection of zoned grains, traverses were conducted across numerous grains". Methana's bimodal amphibole geochemistry thus seems to be supported by three unrelated studies and is therefore interpreted to reflect amphibole crystallisation in equilibrium with magmas that are stalled at two distinct crustal levels, represented by two P-T fields: one at 988-1050°C at 440-500MPa and second one at 814-837°C at 120-146MPa, corresponding to depths of about 5km and 18km, respectively, when a crustal density of 2.7g/cm³ is assumed (Fig. 5.29).

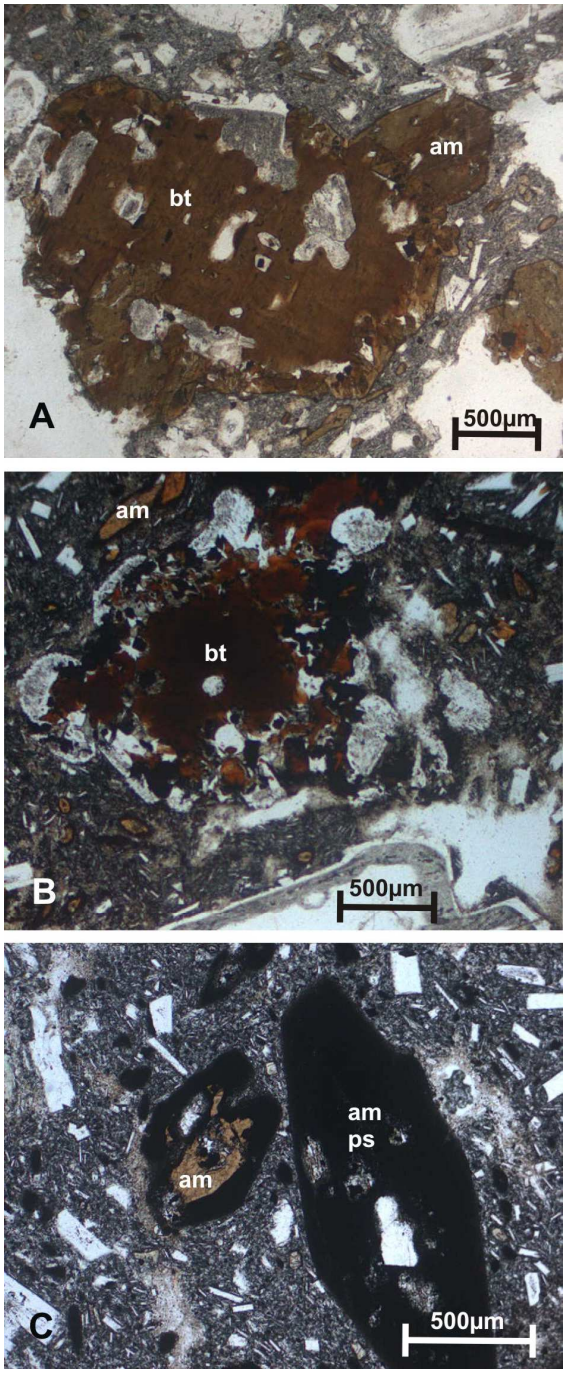

Figure 5.28. *Photomicrographs of Phase H Mavri Petra host rocks under plane polarised light.* Samples taken from the flanks of the lava flow are interpreted to have been extruded prior to those taken near the eruptive vent (see Fig. 5.1). bt = biotite; am = amphibole; ps = pseudomorph. (A) Amphibole-rich IM29, sampled near the eruptive vent. Note the lack of opaque reaction rims around either am or bt phenocrysts and the presence of euhedral, unaltered am microlites. (B) Amphibole-rich IM40, sampled between the vent and outer flanks of the lava flow. The bt crystal is partially replaced from the rim inwards by a fine-grained plagioclase, pyroxene and Fe-Ti-oxide mineral assemblage. Note the opaque reaction rims around am phenocrysts and microlites. (C) Amphibole-poor IM399, sampled at the bottom of the lava flow's flank. Amphibole phenocrysts show thick opaque reaction rims or are totally replaced by fine-grained anhydrous minerals; hydrous microlites are totally replaced by an opaque aggregate.

Geophysical studies of the South Aegean region seem to agree well with these mineralogically derived crustal levels of magma storage. Slowing down of S-wave velocities is imaged by Karagianni et al (2005) at depths between 15-20km below the Peloponnesus and the westernmost part of the South Aegean arc. The depths cal-culated on the basis of geophysical (15-20 km) and of mineralogical (18km) data are thus very similar. Given the common interpretation of S-wave speed reduction as indicators of molten rock, it seems that at about 18±2km below Methana subduction-related magmas are stalled and undergo amphibole fractionation. The inferred amphibole fractionation level at a depth of 5±1km (see Fig. 5.29) agrees well with geophysical imaging of the upper crust below Methana peninsula (Fig. 5.30, Efstathiou et al. 2012). Derived through 3D inversion of aeromagnetic data, this 3D model of Methana's subvolcanic system shows a flattened, ellipsoidal body at the 4-6 km depth interval, which could be one large or several smaller (interconnected?) magma chambers. The depth at which this magma chamber is located corresponds to the lower pressure limit for amphibole (ca. 75-100 MPa). Magmas (of the right chemical composition) that differentiate at this level (4-6 km depth) are therefore indeed likely to have amphibole in their crystallising mineral assemblage.

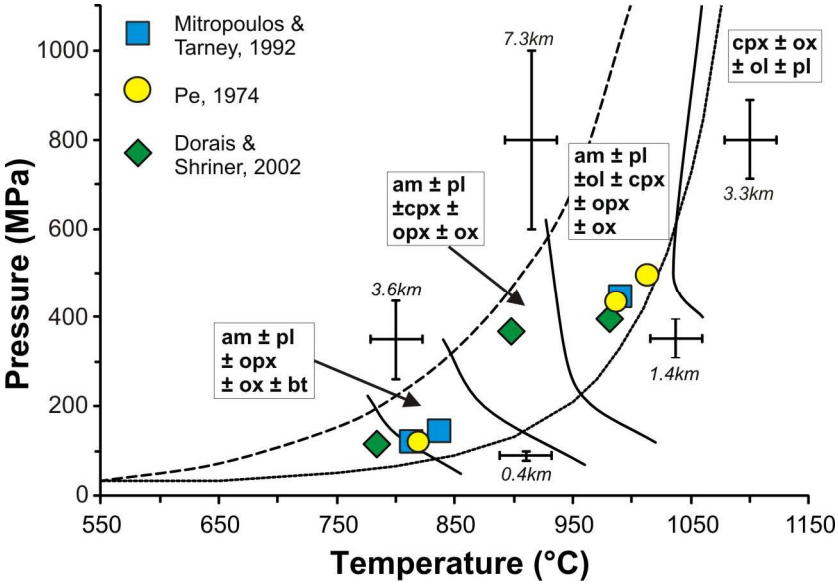

Figure 5.29. *P-T diagram for the volcanic amphiboles from Methana as calculated by the geothermobarometer of Ridolfi et al. (2010). Black dotted line* represents the maximum thermal stability curve for amphibole; *black dashed line* indicates the upper limit of amphiboles with a composition consistent with their host rock; *full black curves* delineate P-T stability limits for equilibrium phases such as amphibole (am), clinopyroxene (cpx), orthopyroxene (opx), olivine (ol), plagioclase (pl), Fe-Ti-oxides (ox) and biotite (bt). *Error bars* represent the expected σ_{est} for estimated temperatures (22°C) and pressures (varies with P-T conditions, written in italic above/below respective error bar and presented as uncertainties of depth, calculated using a crustal density 2.7 g/cm³). Amphibole geochemical data retrieved from literature, see graph for references. Figure drawn after Ridolfi et al. (2010).

Figure 5.30 also shows a set of shallow magma chambers and/or plutons located directly below Methana (~0-3 km, outside the amphibole stability field). Geophysical data therefore support the hypothesis, based on petrographic observations, that some magmas are stored within the upper 3 km of the crust below Methana - outside the amphibole stability field. The two geophysically imaged, sub-volcanic structures are separated from one another by about one km of 'normal' upper crust – with only a few funnel-shaped connections between them, interpreted as sub-volcanic conduits between the upper crustal magma chamber(s) and the shallow magmatic system directly below Methana (Efstathiou et al., 2012).

5.6.3 Igneous xenolith IM376

The non-sedimentary xenolith found on Methana consists of a felsic part (IM376A) in contact with a more mafic part (IM376B), both crosscut by a quartz-rich vein (Fig. 5.10). The holocrystalline texture of both IM376A and IM376B, and the random orientation of their sub-to anhedral crystals, is characteristic for plutonic rocks (Cox et al., 1979; Vernon, 2004). The granitic part of IM376 is significantly coarser grained than the dioritic part (Fig. 5.10) – suggesting that the thermal gradient

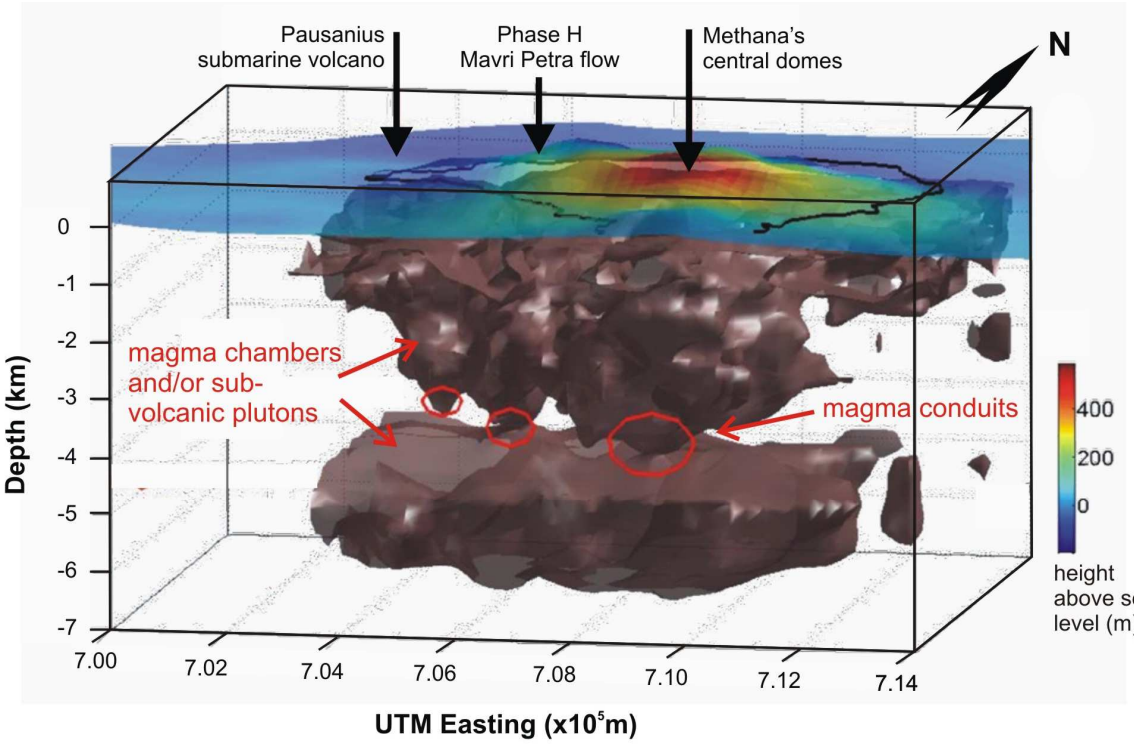

Figure 5.30. *The geophysical model of the upper crust below Methana* (Efstathiou et al., 2012) suggests the presence of two distinct levels of sub-volcanic plutons and/or magma chambers which are interconnected by magma conduits. The black line on the coloured topographic map on top of the 3D model represents the coastline of Methana peninsula.

between magma and surrounding country rock was smaller for the felsic than for the mafic magma. These two compositionally different igneous rocks might therefore be equivalent to solidified magmas of a felsic crystal mush (IM376A) and a more mafic replenishment (IM376B). The few larger crystals present in these rocks (e.g. Fig. 5.10C, D, E) are probably (macro-)phenocrysts from an earlier crystallisation phase. Similar plutonic xenoliths are described for volcanic rocks from different tectonic settings: they usually have a hydrous modal composition and are referred to as amphibole gabbro (e.g. Holness & Bunbury, 2006; Ridolfi et al., 2008; Smith et al., 2009). In the case of Methana, the felsic rock is however completely amphibole-free, with clinopyroxene pseudomorphs as the only trace for a once hydrous mineralogy (Fig. 5.10D-E). The mafic rock only has some relic amphiboles in the cores of large clusters of hydrous minerals, otherwise replaced by a clinopyroxene aggregate (Fig. 5.10L) The evolved dehydration of these two holocrystalline rocks indicates prolonged crystallisation at shallow crustal levels where amphibole is no longer stable (at pressures lower than 75-100 MPa, depths of 0-3 km). This igneous xenolith therefore seems to have solidified within one of the shallow magma chambers imaged in Fig. 5.30, but whether it represents a 'true' pluton or the chilled margin of a shallow magma chamber is unclear. Both plutonic bodies and chilled margins of magma chambers are known to be intruded by quartz-rich veins (Cox et al., 1979).

The two parts of xenolith IM376 have a major and trace element composition overall similar to a basaltic andesitic enclave (in case of IM376B) and a very evolved rhyodacitic host rock (in case of IM376A) (see Fig. 5.12 & 5.13). Some of their element concentrations are however significantly different from Methana's volcanic rock suite: they have higher amounts of Cu and Ca and the by far lowest amounts of K_2O, Cs, Ba, Rb and Pb – Fig. 5.12-5.14). Throughout crystallisation of a chilled margin, incompatible elements are gradually concentrated in the interstitial melt and exchanged with magma further away from the wall rock for elements that are compatible in the crystallising minerals. This could be the mechanism that depleted IM376A and IM376B in Cs, Rb, Ba, K and Pb – but it is odd that it would not have affected similarly incompatible elements such as Th, U, Nb and Ta (Fig.

5.14). Expulsion of interstitial melt from a solidifying chilled margin can also not explain the anomalously low Na_2O and Al_2O_3 contents, nor the extremely high CaO contents or elevated Cu concentrations (Fig. 5.12 and 5.13).

Besides incompatible, K, Cs, Ba, Rb and Pb are also fluid-mobile elements, suggesting a hydrous fluid could have caused the aberrant chemical composition of igneous xenolith IM376. The petrography of this xenolith suggests final crystallisation in the upper 3 km of the crust, which is also the area where geothermal fluids are present. The aberrant high concentration of Cu within IM376A also suggests influence of geothermal fluids (Fig. 5. 13D), as well as the presence of a quartz-rich vein that crosscuts both the felsic and mafic parts of IM376 (Fig. 5.10). Petrographic textures, however, do not show any signs of post-solidification geothermal alteration (see Fig. 5.10). So if a geothermal fluid is responsible for 'leaching' K, Cs, Rb, Ba, K and Pb from IM376A&B, it must have happened during solidification of the xenolith due to interaction between co-existing crystallising magma and geothermal fluid. Interpretation of the xenolith as a chilled margin could support this hypothesis, since geothermal fluids are concentrated in upper crustal fractures which also represent magma pathways. Intrusion along fractures of a hot magma will heat up circulating geothermal fluids, making them more chemically reactive and thus facilitating interaction with the magma nearest to the wall rock. The smaller grain-size of mafic xenolith IM376B represents faster cooling and solidification, limiting the time and thus amount of interaction it had with a co-existing geothermal fluid. The larger grain-size of felsic xenolith IM376A is inferred to represent slower and longer solidification, which seems reflected in the larger enrichment/depletion of specific element concentrations compared to IM376B (see Fig. 5.12 – 5.15). Another hypothesis is that the magma's hydrous phase escaped before IM376 was completely solidified, thereby depleting its residual melt from fluid-mobile elements as well as further destabilising any hydrous minerals present. The distinct Pb geochemistry of IM376A and IM376B with little amounts of Pb and distinctly low isotopic ratios could thus reflect lead loss due to expulsion of magmatic water, leaving only the small fraction of Pb that was incorporated in crystals and possibly reflects the isotopic composition of the primitive source (Fig. 5.16 & Fig. 5.17). Non-fluid mobile elements Nd and Hf, as well as fluid-mobile but compatible element Sr, are however not effected by this loss of magmatic fluid: the Sr-Nd-Hf geochemistry of IM376A&B plot within the range of Methana's volcanic deposits (Fig. 5.16 & 5.17).

The geothermal reservoir below Methana is already inferred as an indirect cause of decoupling between the Sr-Nd-Hf and Pb isotopic composition of Methana's volcanic rocks (section 5.5.3). A combination of interaction with geothermal fluids and loss of magmatic fluid is therefore preferred to explain the aberrant geochemistry of igneous xenolith IM376. Thermal spring waters on Methana are shown to contain about 23% arc-type magmatic water besides local groundwater and seawater (Dotsika et al., 2012). A combination of these three hydrous fluids, the 'hydrothermal fluid', is proposed to partially inherit the chemical composition from the local basement it is stored in and circulates through. Sedimentary basement samples and xenoliths are mainly limestone, calc-arenites and volcaniclasts with overall high Ca and Sr, low Na, K and Al, and a locally specific Pb isotopic composition (see Appendix F1) - elements that can be mobilised by interaction with a hot hydrous fluid. Convection is likely to homogenise this chemical signature within the distinct parts of the upper crust where local lithologies are being hydrothermally altered. Wall rock assimilation will then lead to a specific chemical signature for host rocks and enclaves which underwent differentiation in the same shallow crustal area. For example, the PDC deposits and associated basaltic andesites have an overall very similar chemical composition - except for those elements identified in IM376A&B to have been influenced by hydrothermal fluids. According to the area where they erupted, these mafic Phase C rocks define two separate clusters of K, Na, Cs, Rb, Ba, Pb and Cu contents and Pb isotope ratios and thus reflect the different chemistry of the shallow crust in the NW and S parts of Methana. Magma which remains in contact with the wall rock undergoes more intense modification of its geochemistry as it is more and longer exposed to hydrothermal fluids and their alteration products.

Igneous xenolith IM376 probably represents such a chilled margin whose Pb escaped with the magmatic liquid during complete solidification, whereas Ca and Cu seem to have been added through interaction with the hydrothermally altered wall rock.

5.6.4 Mavri Petra flow

It has been shown that the that the PDC deposits and associated basaltic andesites are geochemically comparable to the more mafic enclaves present throughout Methana's effusive volcanic deposits. Compositional differences between pumice and effusive host rocks seem to result from a larger degree of partial melting of an intermediate-to-felsic crystal mush for the former than for the latter. Decoupling between the Sr-Nd-Hf and the Pb isotopic system, together with correlations between certain (fluid-mobile) element concentrations and specific areas in Methana, seem to reflect (indirect) involvement of the hydrothermal system during final differentiation within upper crustal magma chambers and conduits. Igneous xenolith IM376 is thereby interpreted as a chilled margin whose proximity to the wall rock lead to a larger influence of hydrothermal fluids during (and perhaps also after) its solidification. Amongst the different sedimentary xenoliths and basement rocks encountered on Methana mainly volcaniclastic and calc-arenitic lithologies seem to have influenced the host rocks' chemical composition via assimilation during fractional crystallisation (section 5.5.3). The most incompatible element throughout Methana's volcanic rocks seems to be Th as it shows a single trend with limited scatter, representing a five-fold increase with progressive differentiation (Fig. 5.31A). Thorium is however known to be (slightly) fluid mobile so that the whole rock Th concentrations of Methana's volcanic deposits might also be influenced by late stage differentiation in the presence of hydrothermal fluids. Fluid immobile element tantalum shows an incompatibility in Methana's volcanic suite that is comparable to the incompatibility of Th (Fig. 5.31B) and is therefore chosen to represent incompatible elements which prefer the melt fraction in order to distinguish between additions of a dominantly melt or fluid character (Fig. 5.31C-E).

All host rocks and enclaves from the 2200 year old Mavri Petra flow are geochemically distinct from Methana's main volcanic suite as they contain the highest Cs, Be, Pb and U contents, high Sr, Rb and Th concentrations and elevated amounts of K_2O, Na_2O, Ba and Li besides a distinct $^{143}Nd/^{144}Nd$-to-$^{87}Sr/^{86}Sr$-ratio (Fig. 5.12-5.17). Figure 5.31C shows that the volcanic rocks on Methana display a (weak) positive correlation between Ba/Ta and Cs/Ta ratios. The Cs/Ta ratios furthermore show a bimodal distribution with values above 8 characteristic of the Mavri Petra deposits whereas all other igneous rocks have a Cs/Ta ratio lower than 6. Subtle differences between location-correlated clusters in the latter group have been ascribed to the presence of a hydrothermal system (section 5.6.3), but the significantly different Cs/Ta composition of the Mavri Petra flow infers involvement of another fluid-influenced source. Since overprinting of the magmas' chemical composition by the geothermal system is most clearly identified in the lead geochemistry, Methana's Cs/Ta ratios are plotted against their Pb/Ce ratios in Fig. 5.31D. This diagram shows a single trend of positive correlation between the Cs/Ta and Pb/Ce compositions but with distinctly higher Pb contents for the Mavri Petra deposits (Fig. 5.31D). If the Pb/Ce composition of the Phase A-G deposits reflects contamination by the shallow geothermal system, the yet higher Pb concentrations of the Mavri Petra lavas infer that another hydrous source was involved in their petrogenesis. Dehydration of the subducted slab is commonly thought to induce partial melting of the mantle wedge as well as transfer a fluid-mobile chemical signature to this primitive magma source. The distinct fluid-mobile element composition of the Mavri Petra flow could therefore be inherited from such dehydration fluids, but it is difficult to distinguish this initial fluid-mobile fingerprint from the final geothermal overprint as they seem to both have modified the magmas' Cs, Ba and Pb concentrations (Fig. 5.31C-D).

The Mavri Petra volcanic deposits however also show elevated amounts of Li, Be and U, trace element contents inferred not to be influenced by differentiation in the hydrothermally alterd upper portion of the crust. This distinct geochemical signature is thus most likely inherited from the

subducted slab. Subducted sediments are thereby the obvious reservoir for these elements, but they do not contain the amount of water necessary for fluid-absent melting by the time they reach sub-arc depths (Hermann et al., 2006). Aqueous fluids derived from the subducted oceanic crust, on the other hand, will transport certain fluid-mobile elements at sub-arc depths, but their initially low amounts of total dissolved solids will be progressively diluted during upward migration through the slab and mantle wedge (Manning, 2004). So how could the 'subducted sediments' signature observed in the Mavri Petra deposits be transferred from the subducted slab into the sub-arc mantle?

Natural and experimental data from high pressure and ultra-high pressure rocks suggest that dehydration of subducted oceanic crust at sub-arc depths (100-150 km) generates 700-800°C aqueous fluids (Fig. 5.32A). As these altered MORB-derived fluids rise within the subducted slab they induce melting in sediments and altered oceanic crust at the hotter top of the slab (Fig. 5.32A,

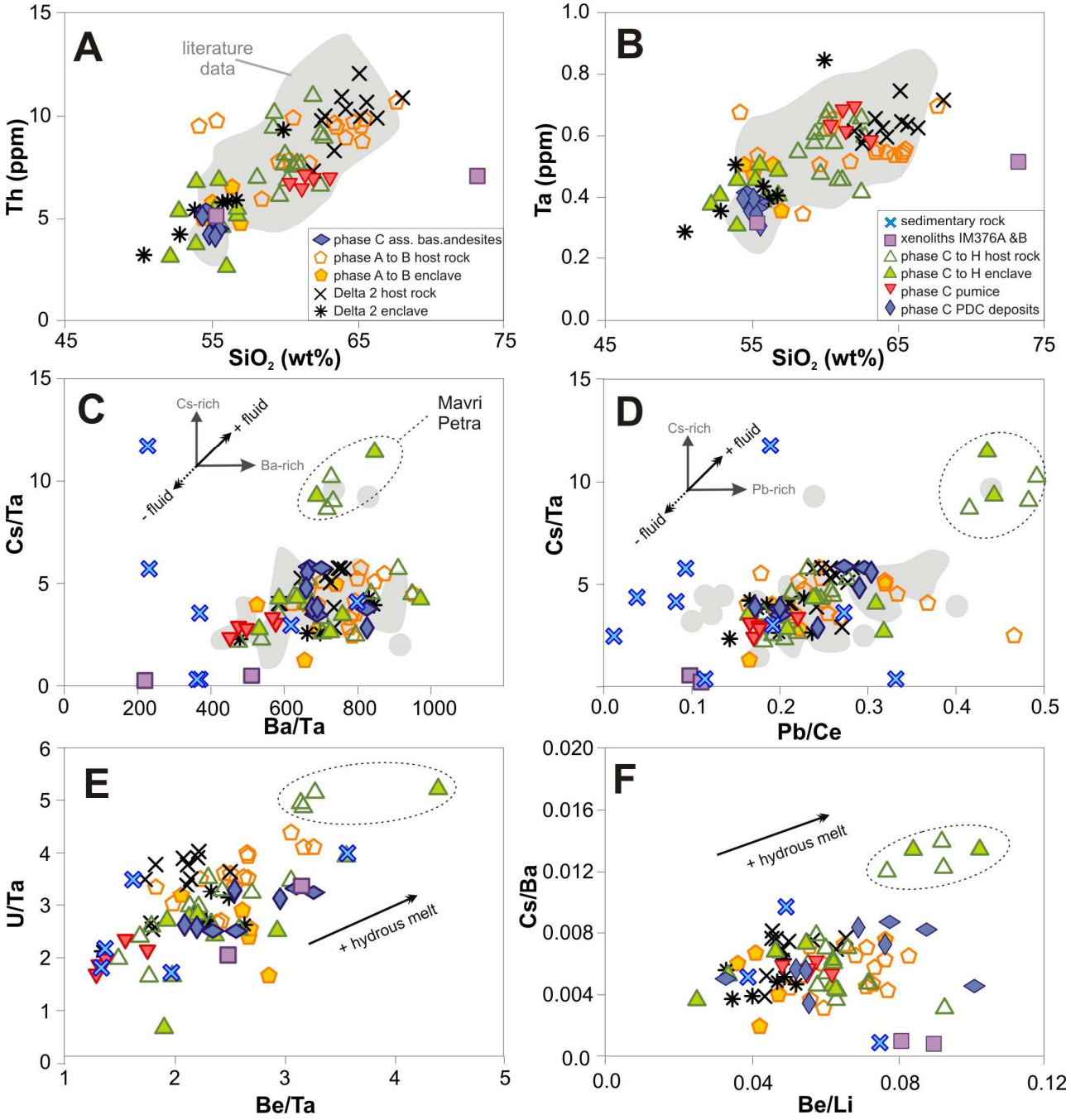

Figure 5.31. *Variation diagrams with ratios of different incompatible elements, used to distinguish between influence of geothermal fluids and hydrous melts.*

Hermann et al., 2006). Experimental fluid-solid partition coefficients for average MORB indicate that at 700-800° C and 4 GPa, the aqueous fluids are mainly enriched in Cs, Ba and Pb whereas a hydrous melt at 1000°C also contains elevated amounts of Li, Be and U (compare these elements' fluid-solid partition coefficients at 700-800°C with the values at 1000°C, Fig. 5.32B) (Manning, 2004; Kessel et al., 2005). These elements are therefore commonly used in diagrams that aim at identifying the subduction component as being rather an aqueous fluid or more of a hydrous melt. Plotting the volcanic rocks of Methana in these diagrams thereby also suggests involvement of a hydrous melt in the petrogenesis of the Mavri Petra deposits (Fig. 5.31E-F).

The distinct enrichment of incompatible elements in the younger Mavri Petra flow compared to all other volcanic rocks of Methana is thus proposed to reflect the contribution of a hydrous subducted sediment melt to the mantle source. Geochemical modelling of this process is not attempted because the composition of both the mantle source and the subducted sediment is unknown and because subsequent crustal petrogenesis of the Mavri Petra flow largely obliterated this initial contribution of hydrous melt. The absence of this subducted sediment signature in all older volcanic rocks however suggests that partial melting of subducted sediments did not occur during the first 4 to 5 Ma of arc-related volcanism. It is thereby unclear why subducted sediment melts have been added to the mantle wedge since historic times. Perhaps this reflects an increase in temperature of the subducted slab? Or perhaps this slab melting is triggered by slab roll back which leads to derivation of the subduction component from a deeper section of the slab? Or is it the location of the Mavri Petra vent, further towards the rear of the arc? The geochemistry of the even more recently erupted submarine Pausanias volcano, located NW of Methana offshore from the Mavri Petra flow, could shed more light on these hypotheses.

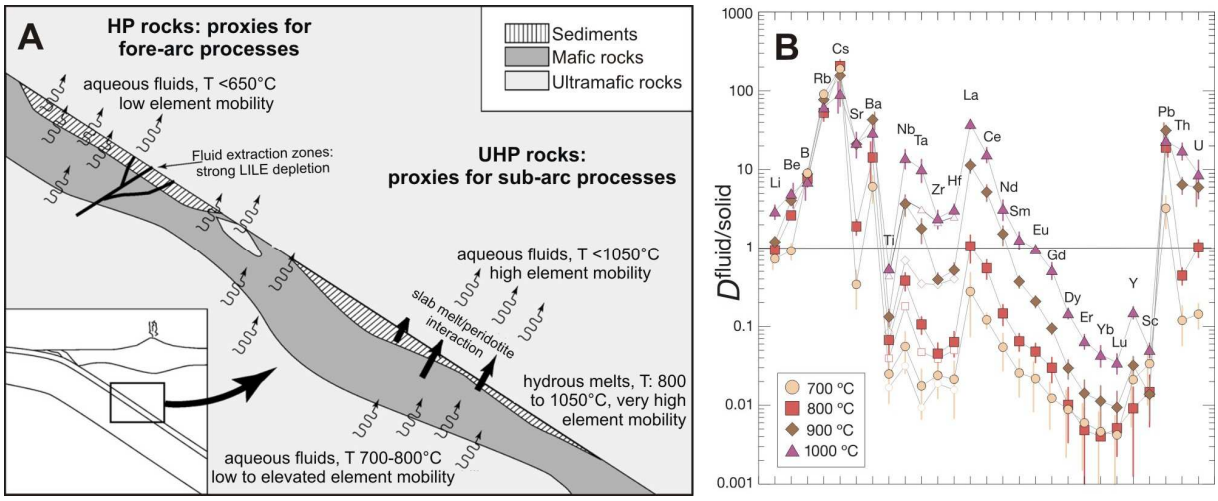

Figure 5.32. *Origin and composition of the aqueous fluids and hydrous melts derived from the subducted slab.* (A) Dehydration of the oceanic crust delivers the aqueous fluids that allow melting of the overlying sediments (Hermann et al., 2006). (B) Experimental fluid-solid partition coefficients at 4GPa, between average MORB and an aqueous fluid (700-900°C) and hydrous melt (1000°C) (Kessel et al., 2005). See text for discussion.

5.6.5 Loutses South host rocks

The diagrams of Fig. 5.31 don't show volcanic rocks with a geochemical composition distinctly different from the general igneous trend apart from the Mavri Petra host rocks and enclaves. The aberrant geochemistry of the Loutses South host rocks is thus probably not reflecting the influence of a hydrous melt from the subducted slab. In contrast to the Mavri Petra flow, only the host rocks from the Loutses South flows have a distinct geochemistry whilst their enclaves fall within Methana's general trend. This suggests that a 'normal' basaltic to andesitic magma replenished the magma chamber of a crystal mush which had a petrogenetic history different from the other effusive host rocks.

The Loutses South host rocks are geochemically defined by the overall highest Sr concentrations, very high amounts of Ni, Cr and Cu, elevated Co, MgO and MREE contents but some depletion of Al, Mn, Mo, Y, Nb, Ta, HREE relative to the other host rocks (Fig. 4.9-4.12 and Fig.5.12-5.15). The elevated Ni, Co and MgO contents could result from the presence of olivine xenocrysts, but nearly no olivine is observed within the Louts South samples. These rocks do contain many clusters of clinopyroxene phenocrysts which might explain their high Cr contents. Whereas the Mavri Petra lithologies are enriched in the most incompatible and fluid-mobile elements (LILE, LREE, Na, K, Th, U, Pb, Be and Li), the specific elements defining the chemical signature of the Loutses South host rocks are more typical for the mantle (Mg, Mn, Ni, Cr, Co). This stronger mantle signature is also reflected in their $^{143}Nd/^{144}Nd$ - $^{87}Sr/^{86}Sr$ chemistry of least radiogenic Sr and rather primitive Nd compositions (Fig. 5.16 & 5.17). Could the Loutses South host rocks result from hybridisation with a primitive magma early on in their petrogenesis? Their silica and Zr contents are amongst the highest on Methana (SiO_2 = 63.5-65.5 wt%, Zr = 130-160 ppm), indicating overall strong differentiation which would have subdued the high amounts of Ni, Cr and MgO. Perhaps their high Sr, Mg, Ni and Cr contents represent assimilation of a mafic olivine-clinopyroxene-plagioclase cumulate? Besides the fact that nearly no olivine is observed in these rocks, their average CaO, relatively low Al_2O_3 and the lack of a positive Eu anomaly also do not support significant incorporation of xenocrystic plagioclase. The Loutses South host rocks seem to have inherited and/or conserved their more primitive signature through less straightforward processes than addition of a hydrous melt, mixing with primitive magmas or assimilation of mafic cumulates.

The specific trace element signature that defines the Loutses South host rocks seems derived from mafic rocks which, in a subduction zone setting, are either the (meta-)basalts of the subducted oceanic crust or basalts underplating the sub-arc crust. The mafic signature of the Loutses South host rocks is more likely derived from the sub-arc crust-mantle boundary than from the subducted oceanic slab given the difficulty to transfer the latter's geochemistry through fluids or to induce its partial melting (Hermann et al., 2006). The crust is relatively thick below Methana (~32 km, see Chapter 2) and most volcanic rocks atop such thick continental crusts show important overprinting of their geochemistry by crustal differentiation, rendering conservation of a geochemical signature inherited from the subducted oceanic crust even less likely.

Experimental data from Alonso-Perez et al. (2009) showed that garnet is an important phase in hydrous arc-related magmas that differentiate in the lower crust or near the crust-mantle boundary (25-40 km; 8-12 kbar). Dehydration melting experiments of metabasalts also indicated that garnet remains stable within the solid eclogite residue down to 12 kbar and 1050°C (Rapp & Watson, 1995). Magmas which underwent a stage of differentiation at the crust-mantle boundary below Methana could therefore have been influenced by garnet, either as a stable phase during fractional crystallisation or within the solid residue of partial melting. Whereas amphibole preferentially incorporates the MREE, garnet is an important host mineral for the HREE (Fig. 5.33A). Davidson et al. (2007) accordingly used La/Yb and Dy/Yb ratios of arc volcanic rocks worldwide to argue that most arc magma differentiation occurs at shallower depths where amphibole exerts a major influence, whereas petrogenesis at greater depth and in the stability field of garnet is less commonly observed. Using their discrimination diagram to distinguish the influence of amphibole from that of garnet during differentiation, most of Methana's effusive rocks seem to follow the 'amphibole' trend of relatively shallow differentiation (Fig. 5.33B). Two groups however plot above this main trend: 1) a more mafic cluster including all three Kossona Vouno enclaves, and 2) all Loutses South host rocks at the more silica-rich end of the diagram. (The pumice samples derive higher Dy/Yb ratios because they represent more significant partial melting which added amphibole melt to their magma – giving the inverse trend of amphibole fractionation – see section 5.5.2). Figure 5.33B thus suggests that shallow differentiation with amphibole fractionation indeed prevails in the petrogenesis of Methana's volcanic rocks, but that for some lithologies, for example the Loutses South host rocks, garnet fractionation in a deeper magma chamber can not a priori be ruled out. Other tell-tale signs of the involvement of garnet in the petrogenesis of arc volcanic deposits are low Y contents and high Sr/Y ratios (Rapp & Watson, 1995).

The Loutses South host rocks also show distinctly high Sr/Y ratios at low Y contents (Fig. 5.33C). Amongst the most important effects of garnet fractionation on derivative magmas are MgO enrichment and Al_2O_3 depletion, due to garnet's high Fe/Mg solid/liquid partitioning coefficient and its incorporation of Al (Alonso-Perez et al., 2009). Besides their high Sr/Y ratios, the Loutses South host rocks also clearly show these hallmarks of garnet fractionation (Fig. 5.33D-F).

Together with their relatively primitive Sr-Nd isotope geochemistry, this seems to support a differentiation stage in the roots of Methana's arc volcanic system for the Loutses South host rocks. Their lower MnO contents can be furthermore explained by the fact that the crystallising garnets have a relatively large spessartine content (Alonso-Perez et al., 2009), whereas their depletion of HREE relative to MREE in comparison to the other host rocks reflects garnet instead of amphibole as main

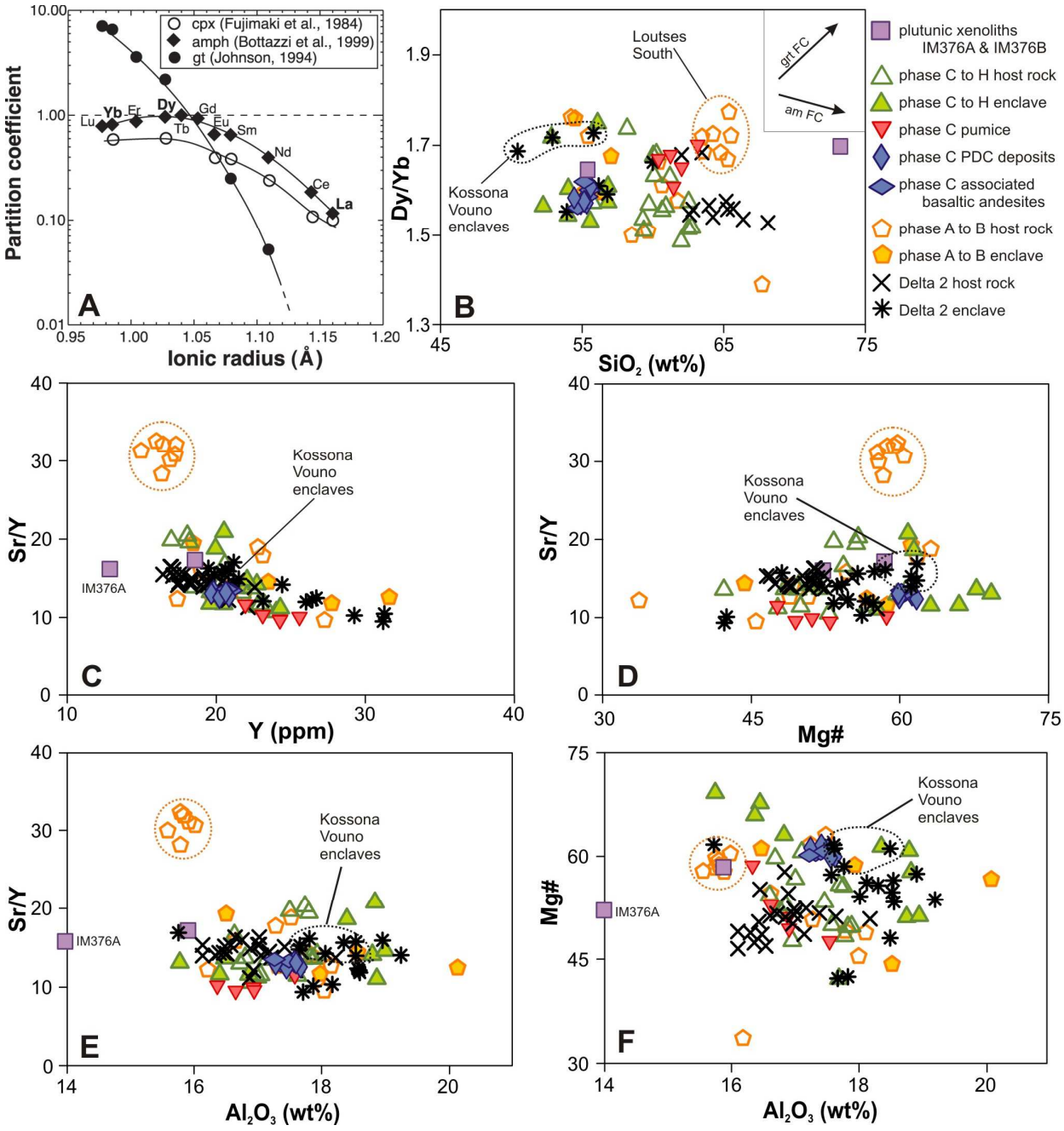

Figure 5.33. *Geochemistry of the Loutses South host rocks (and Kossona Vouno enclaves?) point towards involvement of garnet fractionation at the crust-mantle boundary* (A) Solid/melt distribution coefficients of the REE for garnet, amphibole and clinopyroxene (Davidson et al., 2007). (B-F) Whole rock major and trace element (ratio) diagrams commonly used to identify involvement of garnet fraction.

fractionating phase (Fig. 5.33A) and their elevated Ni (and Cr) contents could result from little to no fractionation of olivine (which is shown to commonly incorporate Cr-spinel crystals). At a depth of approximately 25-30 km, garnet is only stable at H_2O contents above 6 wt%, and constitutes an important crystallising phase together with amphibole. At depths of approximately 35-40 km garnet remains stable at lower water contents and represents, together with clinopyroxene, the first crystallising phase at high temperatures (1000°C), with amphibole and plagioclase only crystallising at lower temperatures (950°C) (Alonso-Perez et al., 2009). The Loutses South host rocks' high Sr contents and lack of Eu anomaly suggest little to no plagioclase fractionation and their relatively low Y concentrations infer only a minor role for amphibole fractionation in their petrogenesis. Garnet crystallisation at 1000°C and at a depth of approximately 35-40 km is therefore the most appropriate process to explain the distinct geochemistry of the Loutses South host rocks.

Geochemical modelling in Chapter 4 revealed differentiation with little to no amphibole fractionation for the Kossona Vouno enclaves and the question rises if they also reflect garnet fractionation. The Kossona Vouno enclaves indeed show relatively low Y contents, elevated Dy/Yb ratios and high Mg# values (Fig. 5.33) and the overall most primitive Sr-Nd-Hf isotopic signature (Fig. 5.16-5.17), but they lack significant Sr enrichment and Al_2O_3 depletion. The fact that plagioclase was modelled as a major crystallising phase could however reconcile their normal Sr contents, yet high Dy/Yb and overall most primitive isotopic signature with a stage of mainly plagioclase and some garnet fractionation at the crust-mantle boundary. The petrogenesis of both the Loutses South host rocks and Kossona Vouno enclaves is thus proposed to involve garnet fraction at large depth, a differentiation step that the majority of Methana's igneous rocks seem to have skipped. Detailed geochemical modelling of the REE contents of the Loutses South host rocks and Kossona Vouno enclaves is however not possible as there is no information on the chemistry of the inferred garnets, nor good estimates of the distribution coefficients of these elements in those differentiation levels at the crust-mantle boundary. Later AFC in the mid-to-upper crust will have furthermore overprinted most of the garnet-fractionation REE characteristics – as well as mixing with no-garnet fractionation magmas (enclaves in case of the Loutses South host rocks, and a felsic crystal mush in case of the Kossona Vouno enclaves).

5.6.6 A complex and long-lived magma plumbing system

Annen et al. (2006) propose the main chemical differentiation of intermediate to silicic magmas to happen at the crust-mantle boundary. Based on experimental and natural geochemical data as well as numerical modeling of subduction-related rocks, they argue that basaltic underplating leads to storage of large volumes of mafic magma in sill-like bodies in the sub-continental lithosphere and lower crust. High pressure differentiation of H_2O-rich magmas in these 'deep crustal hot zones' involves crystal fractionation of mainly ferromagnesian silicate minerals. Due to the elevated temperatures of the local geotherm (near the liquidus), this only leads to limited solidification after which the evolved residual liquid can be stored for prolonged periods of time. When mobilised, however, the low viscosity and density of these H_2O-rich andesitic to dacitic residual melts allows rapid ascent along dyke-like conduits towards upper crustal levels where they undergo further differentiation and subsequently either erupt or solidify as silicic plutons (Annen et al., 2006). This 'deep crustal hot zone' model is consistent with geophysical observations of low-velocity zones below arc systems around the world, usually reflecting areas of partial melts and/or the presence of fluid phases. Such low-velocity zones are thereby located both at or below the seismically defined Moho, suggesting that in some arcs the deep crustal hot zone may be located in the uppermost mantle. This would result from prolonged injection of hydrous mafic magmas that create a thick layer of basaltic sills, causing a discrepancy between the seismic Moho (top of sill complex) and the petrological Moho (base of sill complex) (Annen et al., 2006). High temperature and high pressure fractionation of hydrous mantle melts within a 'deep crustal hot zone' is for example inferred to play a major role in the petrogenesis of island arc magmas from the Solomon Islands (Smith et al., 2009).

The low-velocity layer observed by Karagianni et al. (2005) just below the Moho discontinuity (at depths of 30-40km) in the South Aegean region is proposed to also represent such a deep crustal hot zone where underplating of primitive arc-magmas thickened the crust (Fig. 5.34). A second crustal differentiation level is deduced from literature data on amphibole compositions at 18 ± 2 km depth and coincides with a geophysically detected anomaly 15 – 20 km below the western part of the South Aegean arc (section 5.6.2). This could be a second crustal hot zone where more intermediate magmas stall due to the chemical-physical changes at the boundary between lower and middle crust (Annen et al., 2006), or perhaps because their crystallinity increased drastically upon arrival of amphibole on the liquidus (Barclay & Carmichael, 2004). Since all three sets of Methana amphibole data identify this 18 km deep source (section 5.6.2), it is likely that a significant amount of host magma underwent differentiation with amphibole fractionation at this 'mid crustal hot zone' (Fig. 5.34). But the amphibole studies also identify a second, more shallow level of amphibole fractionation at approximately 5 km beneath the surface (section 5.6.2) – independently confirmed by geophysical imaging of what seems to be large magma chambers at this upper crustal level (Fig. 5.30). This depth represents the upper limit of fractional crystallisation of hydrous minerals where magmas evolve into more felsic crystal mushes (Fig. 5.34). There are also magma chambers outside the amphibole stability field, in the top 3 km of the crust (Fig. 5.30): the correlation between amphibole disequilibrium features and elevated $^{87}Sr/^{86}Sr$ suggest that the amphibole-poor lithologies underwent final differentiation at this shallow level (section 5.6.1). The geothermal system beneath Methana also extends down to 3 km due to circulation of hydrothermal fluids in the fractured basement. Decoupling between Sr-Nd-Hf and Pb isotopic data and the correlation of the latter with the location of eruption vents (section 5.5.3) suggest that hydrothermally altered basement rocks interact with the magmas as they either reside there or pass through them on their way to the surface (section 5.5.3, Fig. 5.34).

The following model for the petrogenesis of the Methana magmas seems most likely: All volcanic rocks erupted on Methana started out as partial melts of the hydrated mantle wedge which traversed the crust-mantle boundary and resided for a longer or shorter period of time at this 'deep crustal hot zone' (Fig. 5.34). Only fragments of the primitive magmas' geochemistry can be recognised in Methana's igneous rocks: 1) their major and trace element composition probably resembled that of DPM36 (see Fig. 5.11 – 5.15), which 2) is the basaltic enclave that also contains the most primitive $^{143}Nd/^{144}Nd$ and $^{176}Hf/^{177}Hf$ (Fig. 5.16), whereas 3) Sr-rich Loutses South host rock DPM26 seems to have buffered its primitive $^{87}Sr/^{86}Sr$ value (Fig. 5.16) and 4) Pb-poor igneous xenolith IM376 largely preserved its initial Pb isotopic composition (Fig. 5.16). As these mafic magmas continued their journey from the crust-mantle boundary towards the surface, they crossed the 'mid crustal hot zone' at ca. 18 km depth where some of them stalled and underwent assimilation and fractional crystallisation of an amphibole-bearing mineral assemblage which probably also included plagioclase, clinopyroxene, Fe-Ti-oxides, apatite ± olivine ± orthopyroxene (Fig. 5.34). Remobilisation of these intermediate crystal-rich magmas, either by a more mafic injection or due to a decrease in their density due to fractional crystallisation, allowed them to continue their ascent and replenish an upper crustal magma chamber at ca. 5 km depth. The crystallisation sequence under these upper crustal conditions seems to have included biotite, quartz and zircon besides plagioclase, Fe-Ti oxides, apatite, pyroxene and low P-T amphibole (Fig. 5.34). Resulting amphibole-rich crystal mushes were probably not eruptable due to their high crystal contents that hindered effective segregation of their felsic, viscous, interstitial melt (Barclay & Carmichael, 2004; Annen et al., 2006). Only partial melting and remobilisation due to a replenishing more mafic magma allowed them to continue their ascent and erupt as an amphibole-rich lava with more mafic enclaves – the dominant volcanic deposits on Methana. Some magmas got trapped as intrusions within the upper three km of the crust, where they assimilated hydrothermally altered basement rocks (Fig. 5.34). Under these shallow conditions the amphibole-rich magmas dehydrated and changed into amphibole-poor magmas with no hydrous microlites and only few amphibole ± biotite phenocrysts showing strong disequilibrium features. These dehydrated amphibole-poor magmas may eventually reach the surface due to remobilisation by ascending, more mafic and hotter magmas – or they might completely solidify and form holocrystalline

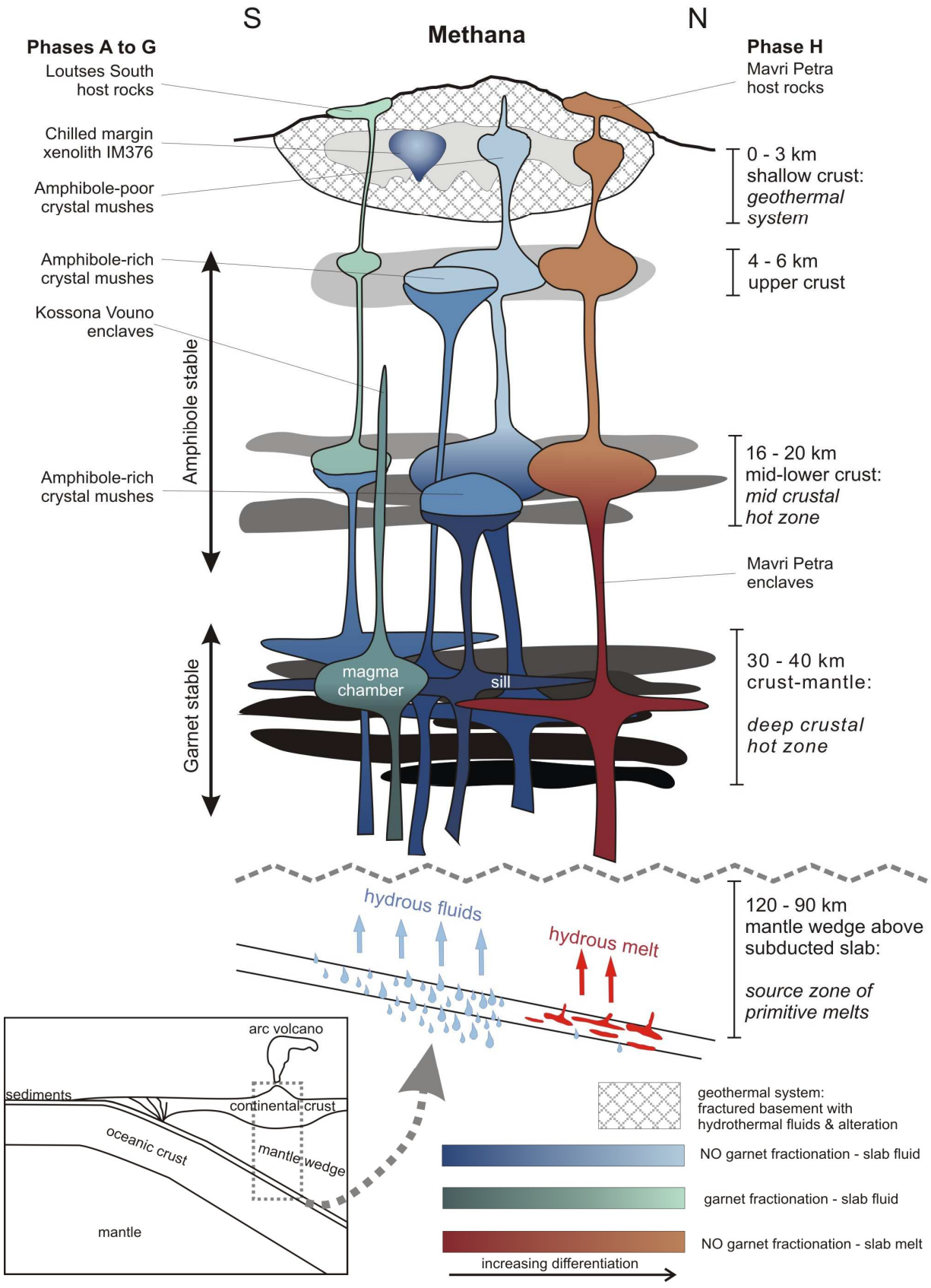

Figure 5.34. *Schematic representation of the petrogenesis of Methana's volcanic deposits*. Inset = general sketch of a subduction zone, main figure = proposed magma plumbing system beneath Methana. Vertical dimension represents key crustal levels (depths in km below sealevel), horizontal axis reflects evolution with time: the magmagenesis of the youngest Mavri Petra flows involved partial melts from the subducted sediments, but the primitive melts of all older volcanic lithologies seem to be contaminated by slab-derived fluids only.

sub-volcanic intrusions. However, not all of the enclave-bearing effusive rocks need to have undergone differentiation in upper crustal reservoirs: certain lavas may represent crystal mushes that mainly underwent differentiation at the 'mid crustal hot zone'. The above described petrogenetic model applies to the majority of the volcanic deposits on Methana, but it is likely that there are also a large number of magmas that completely solidified at any of the above described four crustal differentiation levels.

The lack of a geochemical gap between enclaves and host rocks identified in the Delta 2 unit is also observed for the effusive deposits of the first and second phase of volcanic activity– suggesting an important role for homogenisation by mixing and mingling between the more felsic crystal mushes and more mafic replenishments at mid and upper crustal levels. The fact that the geochemical composition of the effusive rocks are very similar throughout Methana's volcanic history indicates that for most of the time the same sources and processes were involved in their petrogenesis. A few rocks however show the geochemical signature of garnet fractionation, indicating that some magmas underwent important differentiation outside the amphibole stability field in lower crust or deep crustal hot zone (Loutses South host rocks and Kossona Vouno enclaves, section 5.6.5). The distinct geochemistry of both the host rocks and enclaves from the historically erupted Mavri Petra flow reflects addition of a hydrous melt to the mantle source (section 5.6.4). This suggests that whereas the subducted slab contributed hydrous fluids throughout most of the arc-related volcanism on Methana, an unidentified change in the subduction dynamics seems to have initiated hydrous melting of subducted sediments in more recent times. The presence of more mafic enclaves in each of Methana's andesitic to rhyodacitic lavas (section 5.1.1) strongly suggests that the latter all erupted due to injection of a less evolved magma.

The only lavas which do not contain enclaves are the basaltic andesites associated with the PDC deposits at Mavri Pounda and near Ag. Andreas (section 5.1.3). These amphibole-free lavas are however geochemically indistinguishable from the enclaves found in more silica-rich lavas. I thus propose that during their ascent, more mafic magmas are nearly always arrested as they encounter magma chambers with older, more felsic crystal mushes. If the volumes, temperatures and geochemical compositions of the felsic mush and mafic injection allow it, they will interact with one another by partial melting and crystallisation, respectively, which leads to mixing, mingling and eventually effusive eruption as host rocks and enclaves (Chapter 4). Mafic magma batches below a certain critical size probably 'freeze' against the more felsic crystal mush, as is probably reflected in the contact between the felsic and mafic parts of IM376, the igneous xenolith which is interpreted as a chilled margin (section 5.6.3). A significantly larger volume of mafic magma, however, will induce so much partial melting in the felsic crystal mush that dehydration of the latter's amphibole crystals results in exsolution of volatiles, overpressure and eventually a major explosive eruption (section 5.4.3 and Fig. 5.20). Such a Plinian eruption gave rise to the Phase C pyroclastic deposits, which represent gradual tapping of a two-layer magma chamber. The (partially) molten felsic crystal mush, located near the top of the chamber, was first erupted as Phase C pumice fallout before the underlying large mafic replenishment was erupted as Phase C pyroclastic density currents. As the eruption continued and the driving force of its explosiveness subdued, eruption of these basaltic andesitic magmas probably evolved from pyroclastic density currents into the effusive lava flows of the Phase C associated basaltic andesites.

Pe-Piper & Piper (2013) already identified two main periods of volcanic activity on Methana and recognised the explosive eruption of the Phase C pyroclastic deposits as the initiation of the second period, related to the onset of crustal-scale NE-SW faulting after prolonged volcanic quiescence. Throughout Methana's volcanic history, effusive domes and flows seem to have erupted from vents along the fault systems that were active at their time of extrusion (Pe-Piper & Piper, 2013). The most recent volcanic eruption emplaced the submarine Pausanias volcano in a graben right next to the boundary normal fault (Chapter 2). This confirms what other scientists already suggested: there is a link between the timing and location of volcanic activity on and around Methana on the one side, and

the (changes of) the regional stress regime on the other. The magmas themselves have an undoubtedly subduction-zone derived geochemical signature, but it seems that mainly the tectonic structures of the Saronic Gulf created the pathways for these magmas to ascent towards the surface and erupt.

Chapter 6: Petrography and geochemistry of the volcanic deposits on Aegina and Poros

The island of Aegina represents the second most important magmatic centre of the Saronic Gulf and is covered for two thirds with volcanic deposits. These volcanic rocks erupted during two periods of volcanic activity which were separated by a prolonged time of volcanic quiescence and are thought to have largely coincided with the two volcanic phases on the neighbouring peninsula of Methana (Dietrich et al., 1988; Pe-Piper & Piper, 2013). Methana is however regarded as a present-day magmatically active centre, whereas volcanic activity on Aegina ceased shortly after the start of the second volcanic phase (2.1±0.1 Ma - Pe-Piper et al., 1983). The majority of volcanic deposits exposed on Methana thus represent products from the second period of volcanic activity, but as this second phase was rather short-lived on Aegina, most volcanic deposits exposed on this island date back to the first volcanic phase. On Aegina, the main products of the first volcanic phase are amphibole(-biotite)-bearing andesite flows and plugs with abundant more mafic enclaves and the second phase is characterised by basaltic andesitic lava flows with few or no enclaves. For each volcanic unit on Aegina, up to four samples were collected from 1 to 2 locations and their petrography and geochemistry is presented in this chapter. A larger number of samples (from more locations) was collected for the geographically isolated Kokkinovrahos dacite in order to assess the mineralogical and geochemical variability within a single unit. Four basement lithologies were sampled and analysed to assess their involvement in the magma genesis below Aegina. As this volcanic centre is slightly better studied than Methana, there are already a few petrogenetic models proposed in older studies (Pe, 1973; Dietrich et al., 1988; Dietrich et al., 1993b; St. Seymour, 1996). Petrographic information and geochemical data from literature and this study are therefore combined to further explore these existing petrogenetic models and, if necessary, modify them.

The 1 km² volcanic deposits located in the southern part of Poros island represent the third volcanic centre of the Saronic Gulf. These volcanic rocks are andesitic lavas containing more mafic enclaves which erupted during a single volcanic event ca. 2.7 Ma (Fytikas et al., 1987; Matsuda et al., 1999). Their petrography and geochemistry is presented and, in combination with the small amount of data available in literature, subsequently used to infer a petrogenesis for the volcanic rocks of Poros which is in-keeping with the magma genesis below Aegina and Methana.

6.1 Observations during fieldwork on Aegina

All sampling work was carried out on the basis of the most recent geological map of Aegina (Dietrich et al., 1993a). Figure 6.1 shows the volcanic stratigraphy of Aegina according to Dietrich et al. (1993a, 1993b) as well as all the locations from where samples were collected during this study. Whereas most volcanic units are located in the southern part of Aegina where they overlap one

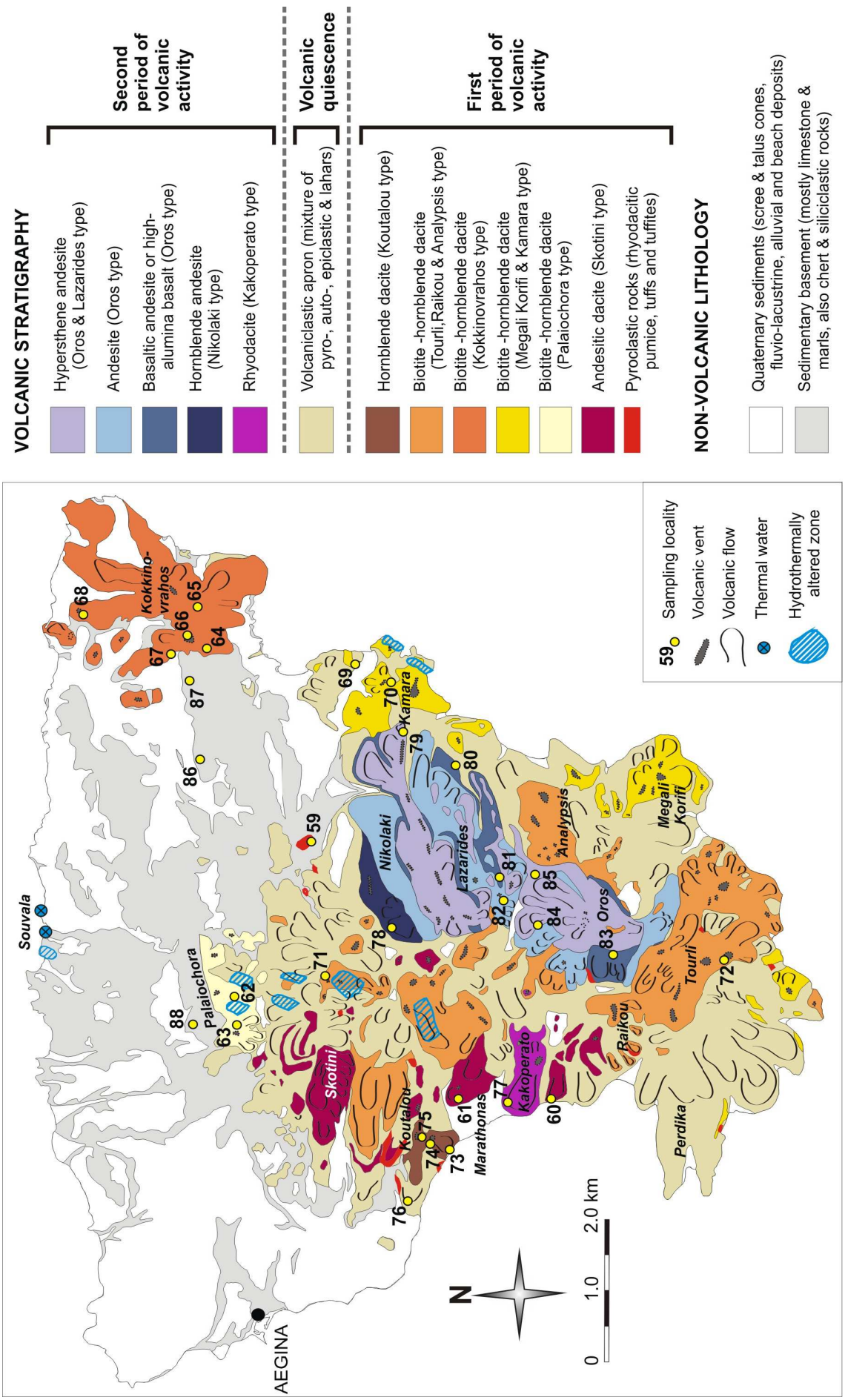

Figure 6.1. *Geological map of Aegina island, presenting the volcanic stratigraphy according to Dietrich et al. (1993a).* The different sampling locations of this study are given in order to illustrate the sampling strategy applied during fieldwork, which was to collect at least one sample from each volcanic unit (Dietrich et al., (1993a).

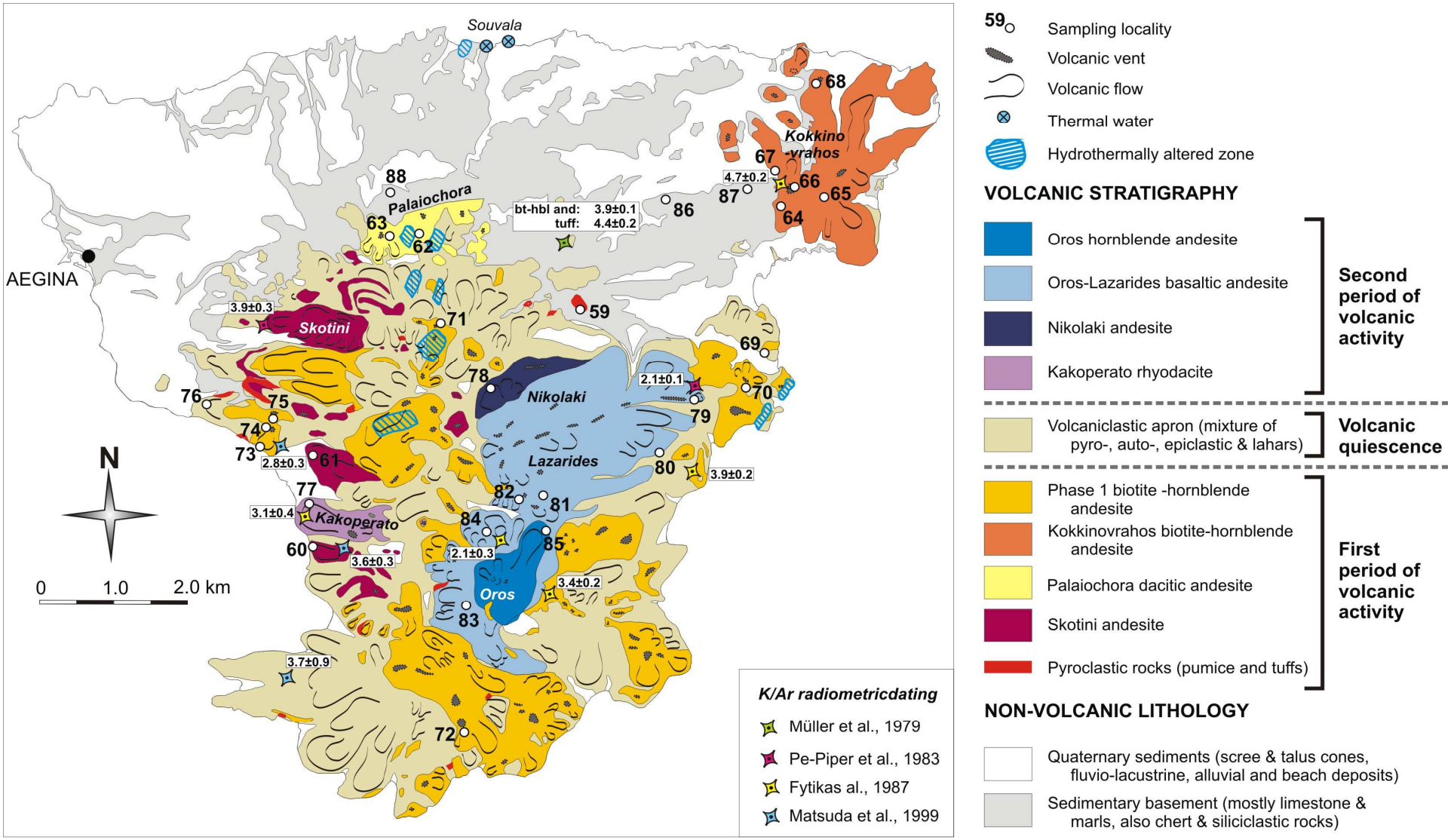

Figure 6.2. *Proposed geological map of Aegina,* modified after Dietrich et al. (1993a) on the basis of petrographic and geochemical observations from this study. Also shown are sampling locations (see Appendix A3) and literature ages. See section 6.5.1 and Table 6.2 for information on the proposed changes to the geological map of Dietrich et al. (1993a).

another and/or laterally grade into a volcaniclastic apron, the Kokkinovrahos biotite-hornblende dacite is geographically isolated within the northern part of the island, which is dominated by sedimentary rocks. More samples were therefore collected from the Kokkinovrahos biotite-hornblende dacite in order to define the petrographic and geochemical variety within a single unit. Despite the fact that Dietrich et al. (1993b) describe minor pyroclastic deposits (pumice, scoria, lapilli and bombs) at the base of both the first and second period of volcanic activity, none were observed during fieldwork apart from a fine-grained tuff at location 59 (see Fig. 6.1) which represents the stratigraphically oldest sample of this study. All other volcanic samples are derived from effusive deposits: 33 host rocks and 16 enclaves in total. No sedimentary, metamorphic or plutonic xenoliths were found in any of the outcrops apart from one coarse-grained, quartz-rich xenolith in the Skotini lavas.

After fieldwork and sampling, petrographic and geochemical research revealed that a large number of the volcanic samples show inconsistencies between the name of their stratigraphic units according to Dietrich et al. (1993a) and their composition. There were also a few significant geochemical heterogeneities within single units and uniform compositions across supposedly different units. These observations led to adaptations of the geological map of Dietrich et al. (1993a) and the proposal of a new volcanic stratigraphy which partially reflects older geological maps from Davis (1957) and Gaitanakis (1984). The proposed changes to Aegina's volcanic stratigraphy are discussed in detail in section 6.6.1, along with the petrographic and geochemical arguments for these alterations. However, to avoid confusion between the volcanic stratigraphy according to Dietrich et al. (1993a) and the one proposed in this study, Figure 6.2 already introduces the modified geological map. It also indicates the sampled outcrops, the exact locations of which are presented in Appendix A3 together with the proposed volcanic stratigraphy and a short description of the respective outcrop and/or sample(s).

All sampling localities on Aegina represent relatively viscous lava flows: from lava plugs in eruption vents over massive, jointed lava in a flow's central parts to brecciated lava and autoclastic lava breccia at the top and margins of a flow (Fig. 6.3). Due to their age, volcanic deposits facing N to NW are strongly weathered and covered with lichen, hindering observations on the amount, type and size of enclaves. The physical appearance of the different outcrop types are first discussed for the more intensely sampled Kokkinovrahos biotite-hornblende andesite (location 64 to 68, Fig. 6.1). Field observations of the other volcanic units are subsequently discussed according to their stratigraphic age.

6.1.1 Sampling locations of the Kokkinovrahos biotite-hornblende andesite

Southernmost sampling location 64 is a 1-1.5 m high road cut into a massive lava with cooling joints (Fig. 6.3A). The rock has a grey groundmass with many large sub- to euhedral phenocrysts of plagioclase, as well as some amphibole, biotite and green (clino-?)pyroxene (Fig. 6.3B-C). The host rock has a coarse-grained texture and 'crumbles' relatively easy when hammered. Enclaves represent up to 8 vol% and stand out on this fresh host rock due to their darker colour. They range in size from 1 cm up to 40 cm, with the larger enclaves usually being more fine-grained than the smaller ones (Fig. 6.3B-C). Prismatic plagioclase and amphibole phenocrysts are the main components of most enclaves, but some of the coarse-grained, smaller (up to 5 cm) enclaves also contain large amounts of green (clino-?)pyroxene. Macro-phenocrysts of plagioclase, amphibole or biotite that look similar to the ones present in the host rock are also occasionally observed in enclaves (Fig. 6.3C). A group of up to 30 coarse-grained enclaves are arranged in such a way that they seem 'frozen' whilst mechanically breaking up into smaller parts, also known as 'enclave crumbling' (Braschi et al., 2012) (Fig. 6.3C). Host rocks and enclaves at the other sampling points in the SW part of the Kokkinovrahos unit have the same characteristics. The road cut at location 67 reveals massive, jointed lava near the capping breccia of that flow (Fig. 6.3D), whereas locations 65 and 66 represent in-situ brecciated lava as bed rock of a minor road (Fig. 6.3E).

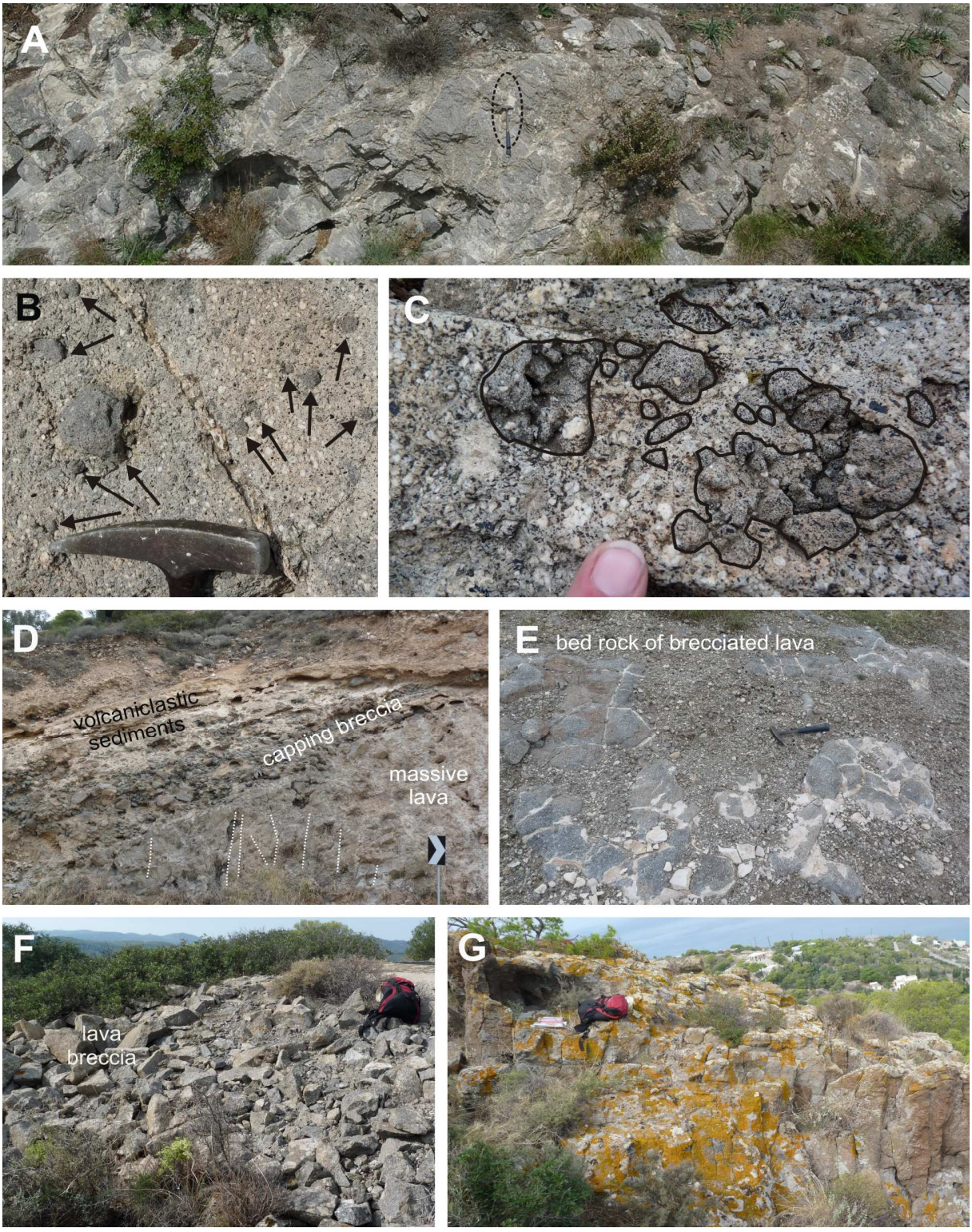

Figure 6.3. *Macroscopic appearance of the Kokkinovrahos biotite-hornblende.* (A) massive lava flow with sub-vertical cooling joints at location 64. Hammer for scale. (B) The grey host rock at location 64 contains many darker grey enclaves (black arrows) of varying dimensions and grain size. Hammer for scale. (C) A group of up to 30 smaller enclaves, interpreted to represent the process of 'enclave crumbling'. Location 64, index finger for scale, black lines represent the contact between host rock and enclave(s). (D) Location 67 where the capping breccia of a massive lava flow with cooling joints (white dashed lines) is overlain by sedimentary deposits with volcaniclastic fragments. (E) Location 65 is a brecciated lava flow in the bed rock of small road. Hammer for scale. (F) Sampling area 68 is a relatively fresh lava breccia at the top, near the vent, which changes downhill into (G) a massive, jointed lava which is largely covered with yellow-green lichen. Backpack for scale in both images.

The N to NE half of the Kokkinovrahos andesite is fenced off as a military domain. Located near the border of this domain, sampling area 68 represents a lava breccia at the eruption vent (Fig. 6.3F) and the downhill more massive lava flow with vesicular basal and capping breccia (Fig. 6.3G). The mineralogy and texture of these lavas is the same as described above, but there appeared to be less enclaves – and none with green pyroxene. This could however be due to the strong weathering and lichen overgrowth of these northerly oriented rocks (Fig. 6.3G).

6.1.2 Other lava flows and plugs from the first period of volcanic activity

The oldest lavas on Aegina are preserved along the western coastline as flows of the Skotini andesite (Fig. 6.2). These rocks have a heterogeneously grey and red coloured groundmass which is interpreted to reflect variable oxidation and which sometimes shows flow-banding (Fig. 6.4A-B). A light-grey, felsic dike was observed at location 60, crosscutting the Skotini andesite sub-parallel to this grey-red flow banding (Fig. 6.4A-B). At both sampling locations, the Skotini rocks are massive to brecciated lavas which contain many plagioclase phenocrysts as well as some amphibole, biotite and yellowish olivine (Fig. 6.4A-C). Approximately 3 vol% of the rocks are fine-grained and coarse-grained enclaves with a diameter of up to 15 cm. A quartz-rich, angular clast engulfed by the Skotini lavas at location 61 is the only sedimentary xenolith observed on Aegina (Fig. 6.4C).

Both sampling locations of the Palaiochora dacitic andesite are very enclave-poor, containing at most one or two small (ca. 1 cm) enclaves. These porphyritic lavas have a light grey groundmass with abundant white phenocrysts of plagioclase, smaller and prismatic black amphibole and a few hexagonal dark brown biotite crystals (Fig. 6.4D).

The other units of the first phase of volcanic activity are biotite-hornblende andesites similar to the Kokkinovrahos rocks discussed in section 6.1.1. The sampled outcrops range from lava breccia to massive lava with cooling joints, as well as a lava plug in the centre of a vent. Its subvertical, parallel and very closely spaced fractures show small kinks and curvatures which represent the flow foliation as magma was squeezed out and which distinguishes them from (more widely spaced) cooling joints (Fig. 6.4E). The groundmass of these andesites can be both grey and red-oxidised, sometimes showing flow-banding but always containing many phenocrysts of plagioclase besides varying amounts of amphibole and biotite (Fig. 6.4F). Green pyroxene and pinkish quartz are also sporadically present. Most andesites furthermore contain up to 8 vol% of more mafic enclaves, both large (up to 70 cm) fine-grained and small (down to 1 cm) coarse-grained ones (Fig. 6.4G-H) – but none of these enclaves contain green pyroxene. Besides white and black prismatic phenocrysts (plagioclase and amphibole) the enclaves sometimes contain large, more equidimensional crystals which are usually mantled by reaction rim (Fig. 6.4I) and seem similar to larger crystals in the host rocks.

The volcaniclastic apron, formed during prolonged volcanic quiescence by erosion and re-deposition of products from the first volcanic period, was sampled at location 76 from large boulders at a topographically elevated point. The grey host rock contains plagioclase, amphibole and biotite as well as up to 8 vol% of large, dark grey enclaves.

6.1.3 Lava flows and plugs of the second volcanic phase

The Kakoperato rhyodacite is a light grey lava flow that contains many phenocrysts of plagioclase and amphibole besides minor amounts of biotite, green pyroxene and pinkish quartz (Fig. 6.2, location 77). The groundmass is glassy and slightly vesicular, making the overall coarse-grained lava ‘crumbly’ so that it shatters easily upon hammering. The Kakoperato flow is the host rock of both coarse- and fine-grained enclaves, which are up to 50 cm large and represent approximately 8 vol% of the lava. These enclaves mainly consist of prismatic white (plagioclase) and black (amphibole) phenocrysts and

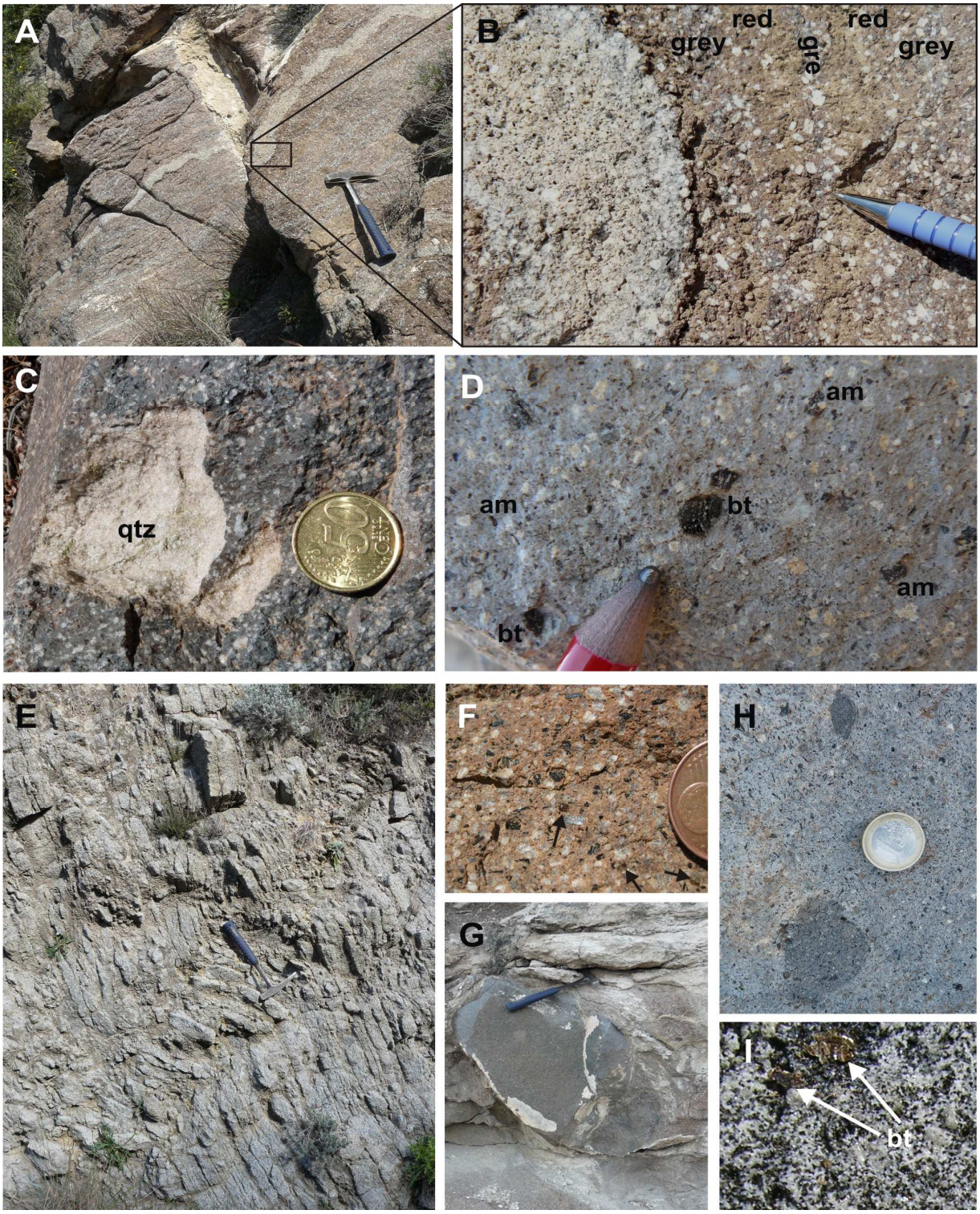

Figure 6.4. *Field observations of rocks from the first period of volcanic activity.* am = amphibole, bt = biotite, hbl = hornblende, plg = plagioclase, qtz = quartz (A) The Skotini andesite at location 60 shows alternating red and grey groundmass, interpreted to reflect flow-banding. A felsic dike crosscuts the lava roughly parallel to this banding. (B) Close-up of (A). (C) Quartz-rich xenolith within the Skotini andesite at location 61. (D) Close-up image of the Palaiochora dacitic andesite at location 62. The light grey rock contains mainly plg (white crystals) as well as am (small black speckles) and some larger, eu-to subhedral bt. (E) Outcrop 70 represents a plug, showing very closely-spaced, sub-vertical partings which are interpreted to reflect flow foliation. (F). The red-oxidised coarse-grained bt-hbl andesite at location 72 contains phenocrysts of plg (white crystals) and am (black prismatic crystals) besides a few bronze-coloured bt (black arrows). (G) Very large, fine-grained enclave within the Phase 1 bt-hbl andesite at location 69. (H) Two enclaves in the bt-hbl-andesite at location 74. This host contains very few, small enclaves. (I) Enclave of the bt-hbl andesite at location 70: a 1 cm bronze bt grain with a dark rim.

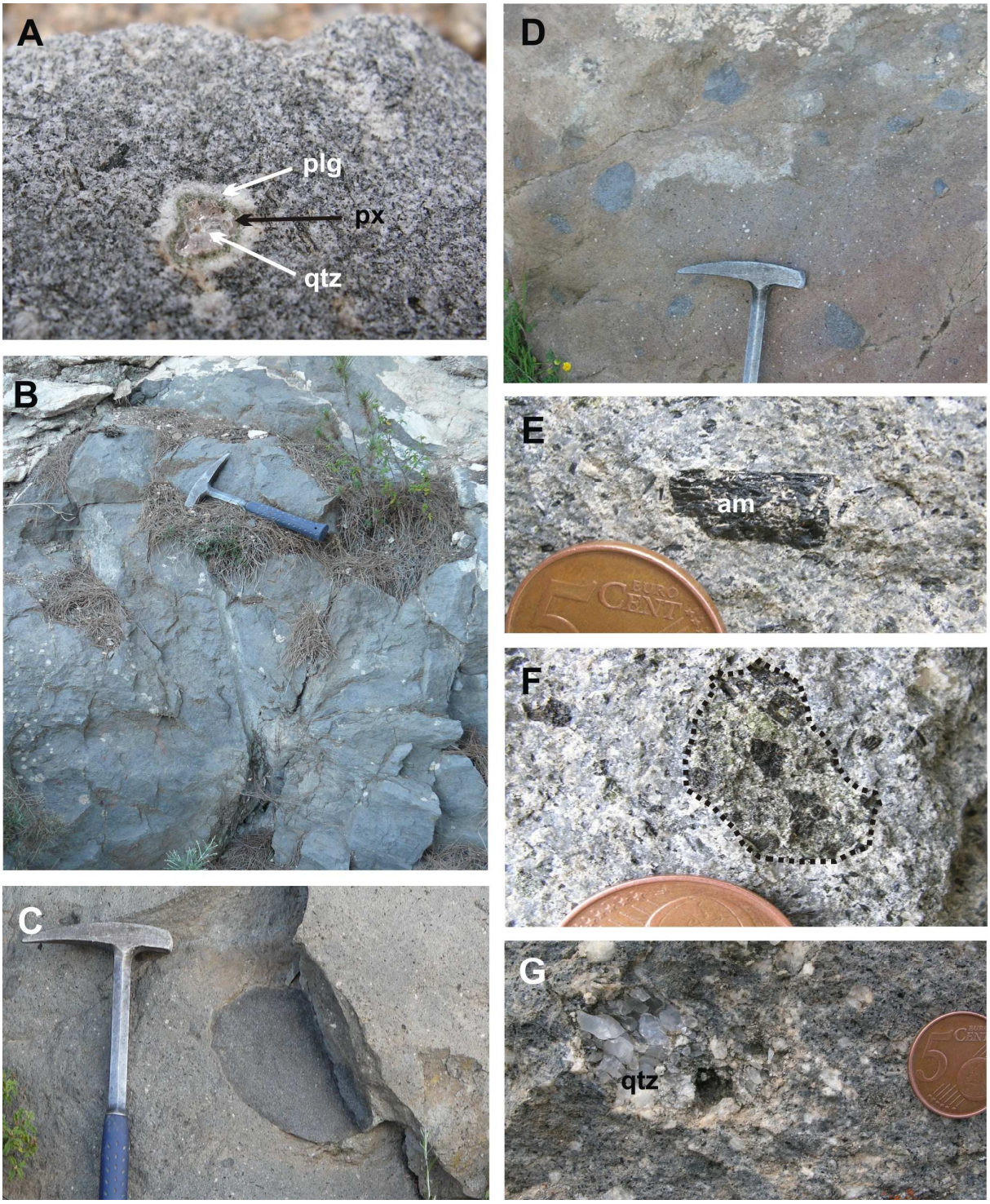

Figure 6.5. *Field observations of the rocks from the second period of volcanic activity.* am = amphibole, hbl = hornblende, plg = plagioclase, qtz = quartz, px = pyroxene (A) Quartz ocellus (ca. 1 cm) in a fine-grained enclave of the Kakoperato rhyodacite, location 77. (B) Massive dark grey lava of the Oros basaltic andesite at sampling location 79. (C) Large, fine-grained enclave within the Oros hornblende andesite at location 85. (D) The Oros hbl andesite contains up to 6 vol% of more mafic enclaves at location 85. (E) Close-up image of the Oros hbl andesite at location 85. The light grey, fine-grained rock contains mainly plg (white) as well as unidentified green, dark grey and black prismatic minerals (px?) and rare large, euhedral am. (F). Black dotted line indicates contact between Oros hbl andesite and a coarse-grained, (holo?)crystalline inclusion of green to black minerals. Location 85. (G) Cluster of large quartz crystals within the Oros hbl andesite at location 85, probably representing a small sedimentary xenolith.

some large, pinkish quartz with reaction rims of green pyroxene and white plagioclase (Fig. 6.5A).

The youngest volcanic deposits are the (basaltic) andesites of Nikolaki, Oros and Lazarides, located in the central to south-eastern parts of Aegina. The geological map shows that they originate from two main eruptive areas: 1) the Lazarides area in the north with elongated eruption vents and fissures, often aligned and parallel to NE-SW faults, and 2) the Oros mountain in the south with fewer and smaller, more circular vents (Fig. 6.2). The lavas are overall fine-grained, very dense and compact and contain few to no enclaves. The oldest in this series of mafic lavas is the Nikolaki andesite which contains phenocrysts of plagioclase, amphibole and green pyroxene besides minor amounts of quartz with and without a reaction rim.

The subsequently erupted Oros-Lazarides basaltic andesites are all fine-grained, dark grey, dense rocks with plagioclase and pyroxene phenocrysts (Fig. 6.5B). Some of them contain olivine, others quartz grains with a reaction rim. Except for the outcrop at location 80 where fine-grained, vesicular, darker grey enclaves are more common, these basaltic andesites rarely host any enclaves.

The youngest unit of the Oros hornblende andesite, on the other hand, contains up to 6 vol% of enclaves, both fine- and coarse-grained ones, up to 40 cm large (Fig. 6.5C-D). These lavas contain phenocrysts of plagioclase and greenish, dark grey to black pyroxenes as well as occasional large, euhedral amphibole crystals (Fig. 6.5E). Sampling location 85 shows a heterogeneous mineral distribution, with some very crystalline and coarse-grained inclusions of black and green (pyroxene?) crystals (Fig. 6.5F) and elsewhere increased amounts of quartz crystals, grouped into a cluster that resembling a small sedimentary xenolith (Fig. 6.5G).

6.2 Field observations on Poros

Located along the southern coastline of Poros island, the peninsula of Sferia is composed of about 1 km² of enclave-bearing lavas. Samples of these volcanic rocks were collected on the basis of the most recent geological map of Schwandner (1998), which divided the effusive rocks in dacites and andesites. Figure 6.6 shows the locations from which host rocks and/or enclaves were sampled; more detailed information on these 5 outcrops (GPS coordinates, macroscopic description of the rocks,…) can be found in Appendix A4. Published K/Ar ages for Poros' volcanic deposits are also given in Fig.6.6, but the exact locations from where the dated samples were collected could not be determined ('Poros Dome' Fytikas et al. (1987) and 'Poros Village' Matsuda et al., 1999). The four ages are however within analytical uncertainty of one another and suggest one main volcanic phase at ca. 2.7 Ma during which all Poros' lavas were deposited.

All volcanic units studied on Poros are massive lavas with cooling joints – the pyroclastic deposits indicated on Fig. 6.6 in the western corner of the peninsula were not observed. Due to the dense housing development of Sferia peninsula (more than half the population of Poros lives on the island's 1 km² volcanic deposits) the majority of the andesitic rocks is no longer visible except for a few relatively fresh outcrops along the main road (location 89, Fig. 6.7 A-B) and in between buildings (location 93, Fig. 6.7G). The areas indicated by Schwandner (1998) as dacites correlate with the topographic higher points of the peninsula and represent more weathered, rounded lavas which are easily accessible (locatios 90-91, Fig. 6.7C), except for outcrop 92 on which the island's landmark, a clock tower, is built (Fig. 6.7F).

The lavas studied at the different outcrops all have a very similar macroscopic appearance: porphyritic rocks with large phenocrysts of white plagioclase and bronze to dark brown biotite, besides some smaller, black amphibole crystals and scarce crystals of pinkish quartz (Fig. 6.7E). The groundmass of these lavas varies between outcrops from dark grey with minor red patches, interpreted to be the result of oxidation, to a mainly red groundmass with just a few grey areas.

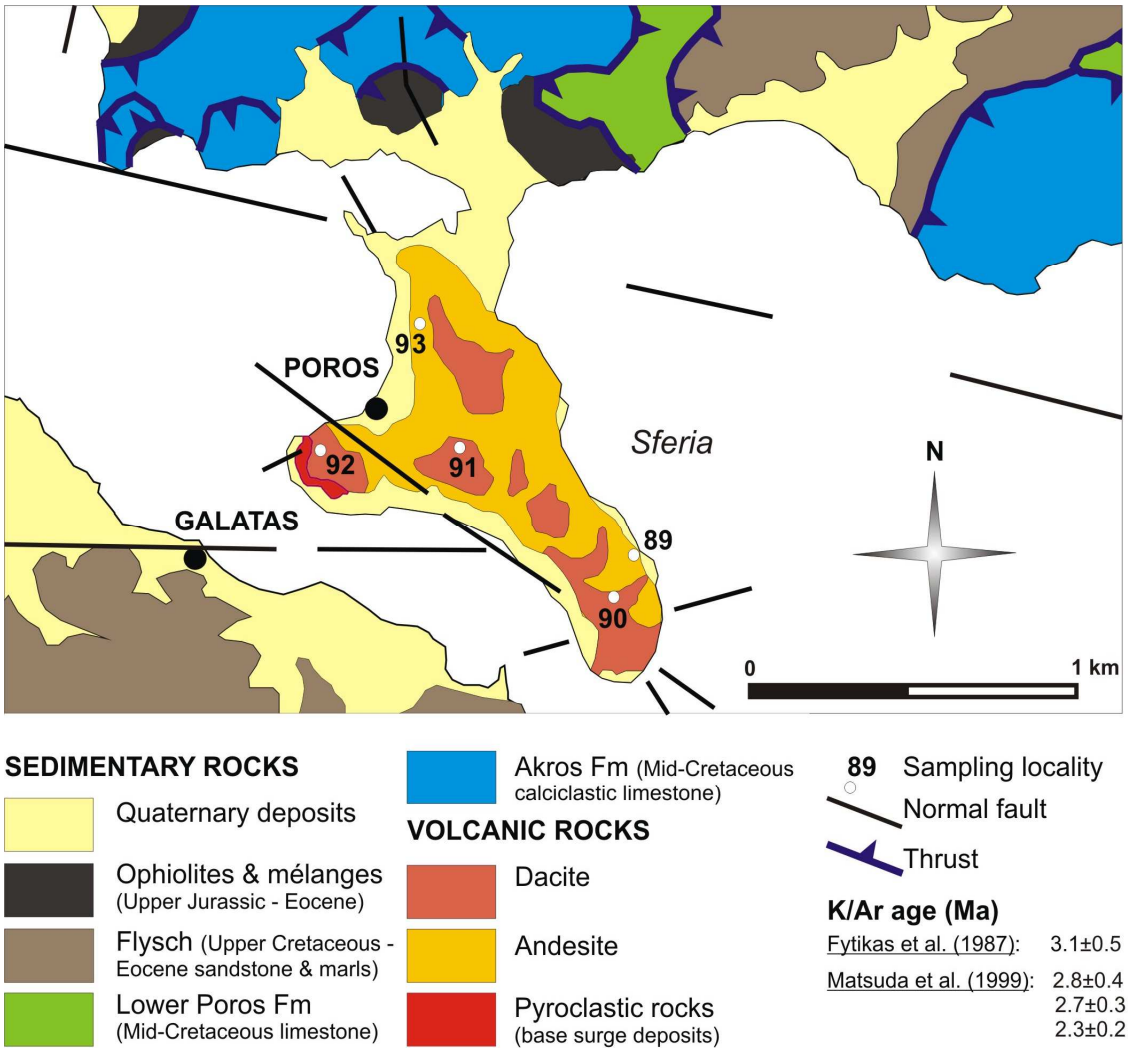

Figure 6.6. *Geological map of the volcanic peninsula of Sferia, along the southern coast of Poros*, with the locations from where this study's rock samples were collected (after Schwandner, 1998).

Rounded, more mafic inclusions are observed in dacites and andesites alike, but the andesitic lavas seem to contain fewer and smaller enclaves than the dacites do. These fine-grained to coarse-grained enclaves vary in size from 1 cm to 20 cm, represent up to 4 vol% of the volcanic rock and are mainly composed of smaller plagioclase and amphibole crystals but also sporadically contain larger crystals of plagioclase, amphibole, biotite or quartz with a reaction rim (Fig. 6.7D-E). No xenoliths were observed in any of the studied outcrops.

6.3 Petrographic study of the volcanic rocks of Aegina

The nomenclature applied to crystal sizes in Chapters 4 and 5 is again used in the following petrographic descriptions. First, the petrographic variety observed within the Kokkinovrahos biotite-hornblende andesite is discussed. Mineral contents and petrographic textures of the other igneous rocks are then summarised according to the island's volcanic stratigraphy. Estimates of plagioclase and olivine compositions of macro-phenocrysts are based on optical methods (Nesse, 2004). Sedimentary xenoliths and basement rocks are not included as they were sampled primarily to investigate their potential role as crustal contaminants.

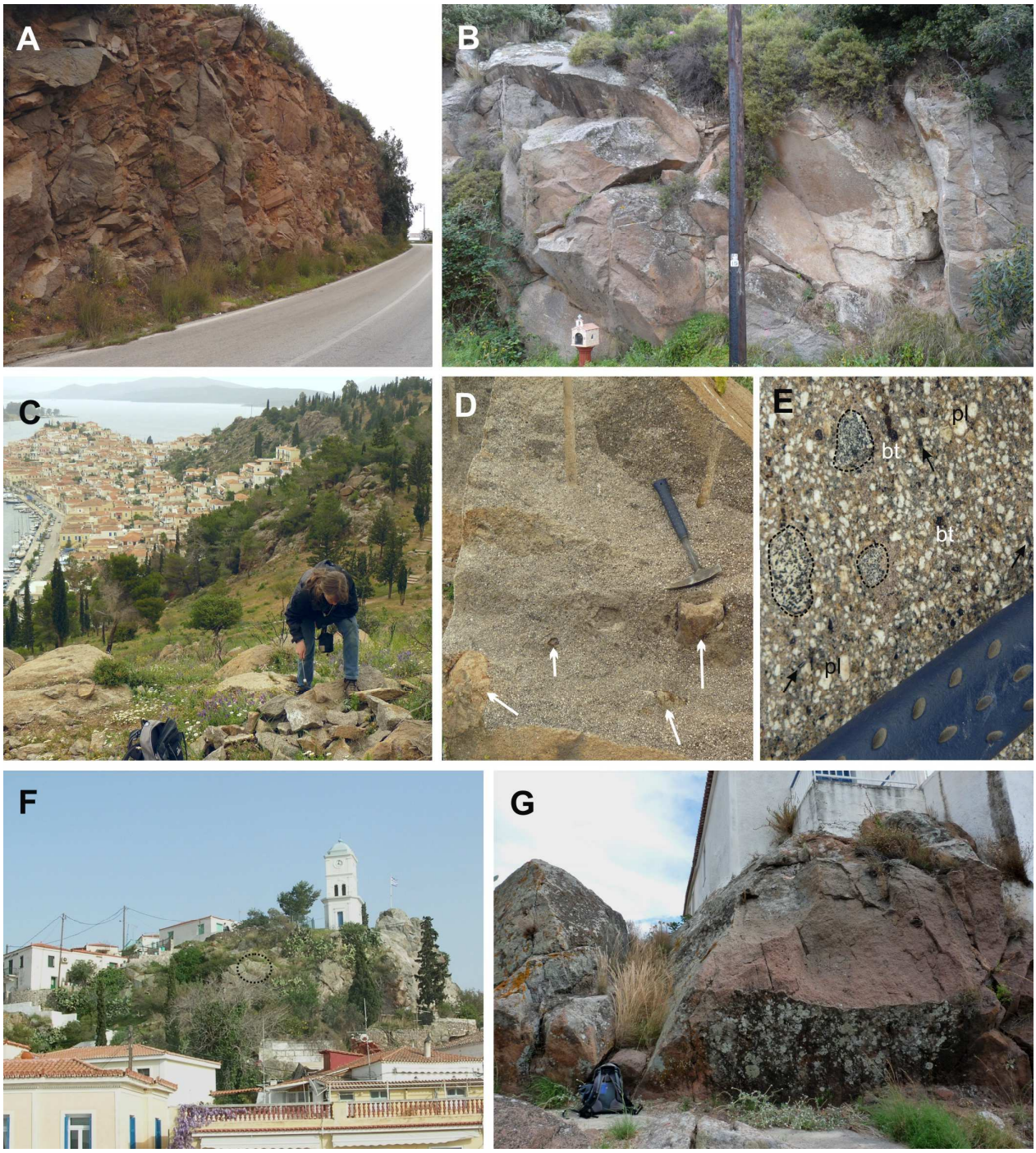

Figure 6.7. *Photographs of the sampled dacite and andesite outcrops on Poros.* (A) Andesite, SE tip of Sferia peninsula. Fresh, massive lavas with cooling joints form a 4-5 m high road cut. (B) Andesite, location 89. About 2-3 m high, slightly weathered massive lava flow with cooling joints along the road. (C) Dacite, location 90. This rounded, weathered dacite outcrop (bottom left) has been partially blasted apart, leaving behind fresh, angular pieces (bottom right) which were studied and sampled. (D) Dacite, location 90. Large block of fresh grey lava with a few heterogeneously distributed more mafic enclaves (white arrows). Hammer for scale. (E) Close-up of the dacite at location 90. Black dotted lines indicate the location of three small, rounded enclaves of varying grain size. Tabular white plagioclase crystals indicate with 'pl', euhedral, bronze-dark brown biotite crystals above 'bt', black arrows point out prismatic amphibole. Hammer handle for scale. (F) Dacite, location 92. Black dashed line indicates the location at which host rock IP299 was collected. (G) Andesite, location 91. This weathered outcrop of massive lava, preserved in between houses, is the sampling location of host rock IP300. Backpack for scale.

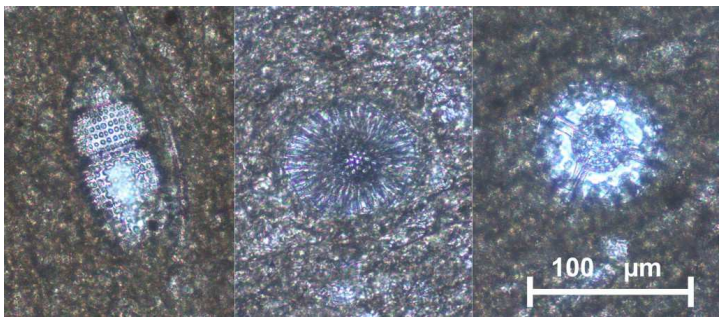

Figure 6.8. Examples of Radiolarian microfossils observed in tuff sample IA341.

The oldest volcanic deposit sampled on Aegina is tuff IA341. Petrographic study reveals that this sample mainly consists of cryptocrystalline material with only small amounts of crystals (mainly quartz, also a few amphiboles) – as well as Radiolaria (Fig. 6.8). The presence of these microfossils indicates that the tuff was initially deposited in an open marine environment. The whole rock geochemistry of sample IA341 therefore reflects a mixture of volcanic ash and marine sediments rather than a magmatic composition. This is confirmed by its high loss-on-ignition (25 wt%), high calcium contents (18 wt%) and relatively low amounts of silica (54 wt%). So although the geochemical composition of tuff IA341 is included in Appendices B3 and C3, this sample will not be further discussed and the Skotini andesite is thus the oldest volcanic rock studied in this work.

6.3.1 Host rocks and enclaves of the Kokkinovrahos biotite-hornblende andesite

The bachelor project of Eeckhout (2012) involved a detailed petrographic study of 7 host rocks and 10 enclaves from this geological unit, and the obtained point counting data are summarised in Table 6.1 as average volume percentages (number of points varying between 300 and 550 depending on the sample's grainsize).

All host rocks sampled from different flows of the Kokkinovrahos unit have the same mineral contents and very similar petrographic textures. Plagioclase (22%) is the dominant mineral and displays a seriate crystal size distribution from eu-to subhedral, tabular macro-phenocrysts over tabular to prismatic phenocrysts down to prismatic microlites. Larger grains (An_{65}) show polysynthetic and simple twinning, sometimes oscillatory zoning and often sieve-textured cores or rims (Fig. 6.9A). Amphibole is the second main mineral and almost as abundant as plagioclase (19%). The mostly euhedral, tabular to prismatic crystals range in size from macro-phenocrysts to large microlites and display a very strong green-brown to orange-brown pleochroism. Larger grains commonly show simple twinning and/or oscillatory zoning expressed as differently coloured rims of varying thickness (Fig. 6.9B). Faint greenish clinopyroxene (2%), biotite (2.5%) and Fe-Ti-oxides (2.5%) are present as minor mineral phases. Larger clinopyroxenes are usually euhedral, individual crystals (Fig. 6.9A) with occasional zoning whereas smaller, more subhedral grains tend to cluster and are sometimes mantled by amphibole (Fig. 6.9C). Very large (≤ 2 cm), euhedral clinopyroxene crystals which seem to have grown around largely resorbed amphibole grains are also observed (Fig. 6.9D). Biotite occurs as fresh, eu- to subhedral crystals ranging in size from very large macro-phenocrysts to small phenocrysts. The larger grains often have sub- to anhedral plagioclase inclusions (Fig. 6.9E). Eu- to anhedral, equidimensional Fe-Ti-oxides range in grain size from phenocrysts to microlites. Orthopyroxene, quartz, zircon and apatite are observed as accessory phases. Orthopyroxene phenocrysts are short prismatic, euhedral crystals (Fig. 6.9F). Quartz occurs as embayed grains without any reaction rim. Once, a euhedral zircon prism was observed within the sample's cryptocrystalline groundmass. Prismatic apatite needles commonly occur in the groundmass or within large plagioclase macro-phenocrysts – larger, euhedral crystals is are occasionally present as phenocrysts.

Crystals represents less than 50% of the host rock, which furthermore consists of up to 8% vesicles and about 46% groundmass, of which up to 3.5% is volcanic glass. Glass and vesicles are however

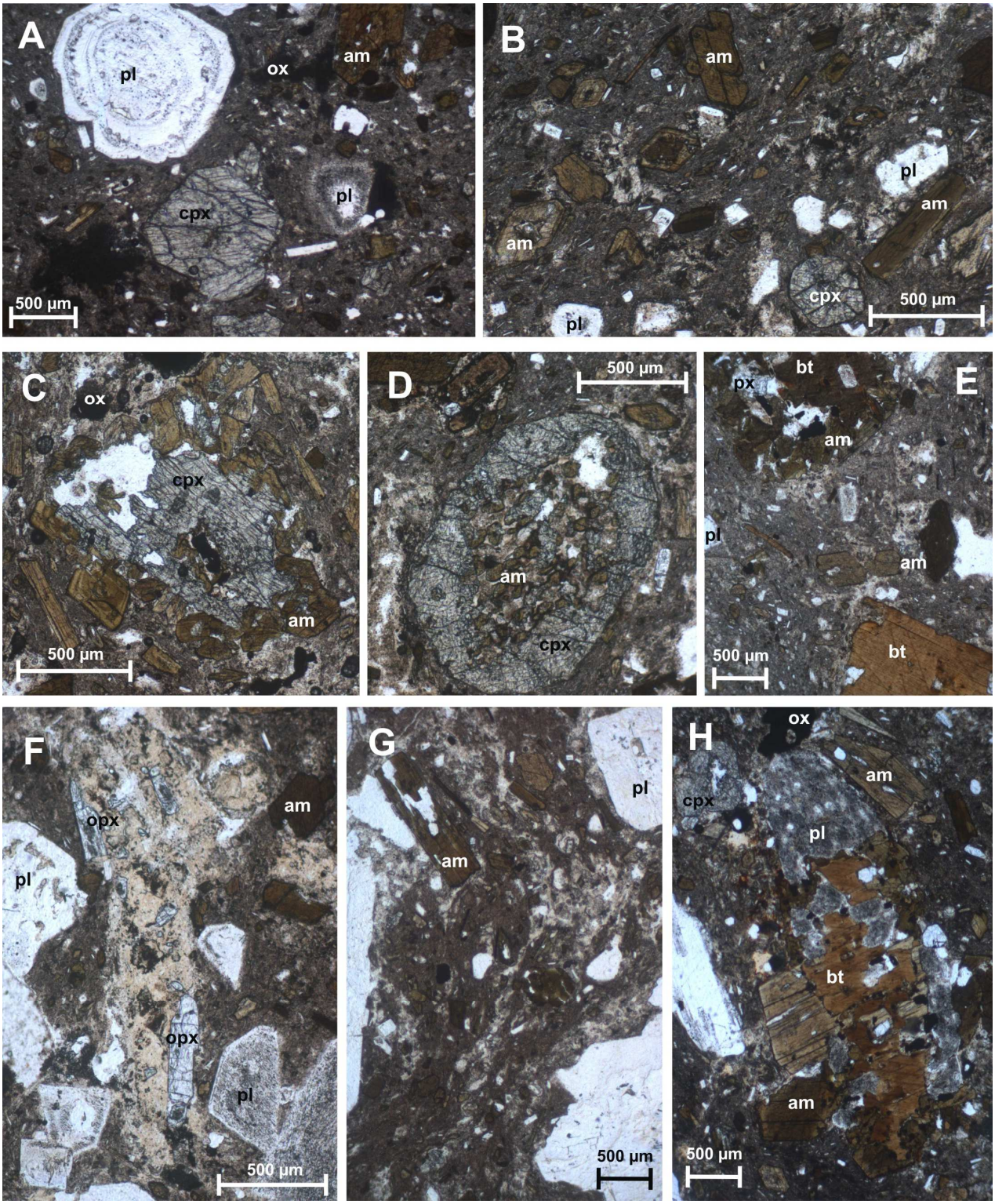

Figure 6.9. *Photomicrographs of host rock samples from the Kokkinovrahos biotite-hornblende dacite.* All images ppl. (A) IA350. Overview with cpx, am and two differently sieve-textured pl macro-phenocrysts. (B) IA55. Prismatic phenocrysts define a weak flow texture. Note the differently coloured rims on the am crystals. (C) IA346. Large cpx macro-phenocryst mantled by (oscillatory) zoned am phenocrysts. (D) IA56. Large cpx macro-phenocryst which seems to have grown around a partially resorbed/replaced am crystal. (E) IA56. Two bt macro-phenocrysts, one with and one without rim replacement/mantle of pl, ox and am. (F) IA344. Central zone of more translucent, vesicular groundmass containing prismatic opx phenocrysts. (G) IA55. Flow texture expressed by combined phenocryst alignment and alternation of more glassy and more cryptocrystalline groundmass bands. (H) IA344. Holocrystalline aggregate of am, bt, pl and ox.

not homogeneously distributed in the lavas. The grey and red lavas observed during fieldwork correspond to two petrographically distinct groundmass types: a glass-rich, translucent type which contains most of the irregularly shaped vesicles and a more 'dusty', cryptocrystalline type (Fig. 6.9F). As the groundmass is mostly cryptocrystalline, there are only few microlites and also not many prismatic phenocrysts so that their alignment texture around the larger crystals only vaguely defines a flow. In some places, however, magmatic flow is more pronounced through thin bands of alternating translucent and more cryptocrystalline groundmass wrapping around mineral clusters and large macro-phenocrysts (Fig. 6.9G). The Kokkinovrahos biotite-hornblende andesite contains few hydrous minerals with strong disequilibrium features such as nearly complete replacement by a fine-grained anhydrous mineral aggregate or thick opaque reaction rims – the ubiquitous amphibole and biotite grains even seldom show a thin opaque reaction rim. The only indications of disequilibrium are occasional corona textures of amphibole around clinopyroxene clusters and sporadic replacement of the rim of large biotite grains by plagioclase, pyroxene, Fe-Ti-oxides and amphibole (Fig. 6.9E). Besides sporadic micro-enclaves, most host rocks also contain cumulophyric clusters of clinopyroxene ± plagioclase (nearly holocrystalline aggregates of mostly euhedral crystals with little interstitial glass or groundmass) and sometimes holocrystalline aggregates of large, subhedral amphibole, plagioclase ± biotite (Fig. 6.9H).

The range of coarse-grained to more fine-grained enclaves sampled from the Kokkinovrahos andesite can be mineralogically divided into two groups. The majority of enclaves (type 1) largely consists of a framework of randomly oriented plagioclase (38%) and amphibole (28%) phenocrysts. The euhedral, prismatic plagioclase grains show simple twinning and often touch one another or the eu-to subhedral, larger, prismatic amphibole crystals (Fig. 6.10A). The latter show the same green-brown to orange-brown pleochroism as the amphiboles in the host rock, but little to no zoning. The third main component of the crystal framework consists of anhedral, fresh-looking biotite grains (5%) (Fig. 6.10A). Small Fe-Ti-oxides (1.5%) are scattered throughout the enclaves whereas pyroxene crystals are only occasionally present (<1%) (Fig. 6.10B). Quartz could not be unambiguously identified in any of these enclaves, but one of them did contain a euhedral zircon crystal within its groundmass (Fig. 6.10C). Prismatic apatite crystals are sporadically found as inclusions in plagioclase. Few to no microlites are present in the groundmass, which mainly consists of volcanic glass (15-20%) containing rounded, relatively small vesicles (Fig. 6.10B). Depending on the average grain size of the framework phenocrysts, coarse-grained enclaves tend to be less vesicular (10%) than more fine-grained ones (17%). Fine-grained enclaves also have 1) higher length-to-width ratios for their framework phenocrysts, 2) less glass or groundmass, 3) a higher proportion of irregularly shaped vesicles, and 4) more macro-phenocrysts than the coarse-grained varieties. Macro-phenocrysts are subhedral crystals of amphibole, biotite and sieve-textured plagioclase.

	pl	*am*	*cpx*	*bt*	*ox*	*opx*	*qtz*	*apt*	*zrc*	*Cr gm*	*Glass*	*Ves*
Host rock	22%	19%	2.0%	2.5%	2.5%	≤0.5%	≤0.5%	0.3%	≤0.1%	42%	3.5%	6%
Enclave type 1	38%	28%	≤0.5%	5%	1.5%	≤0.5%	/	0.2%	≤0.1%	/	18%	10-17%
Enclave type 2	25%	25%	5%	≤0.5%	1%	≤0.5%	/	0.2%	/	/	35%	9%

Cr gm = cryptocrystalline groundmass and microlites – together with the volcanic glass representing the total groundmass, Ves = vesicles. Amounts of each constituent expressed as average volume % counted across different samples of each host rock or enclave type.

Table 6.1. *Relative amounts of the minerals, glass, cryptocrystalline groundmass and vesicles in the rock types of the Kokkinovrahos biotite-hornblende dacite.* Summarised point counting results from Eeckhout (2012).

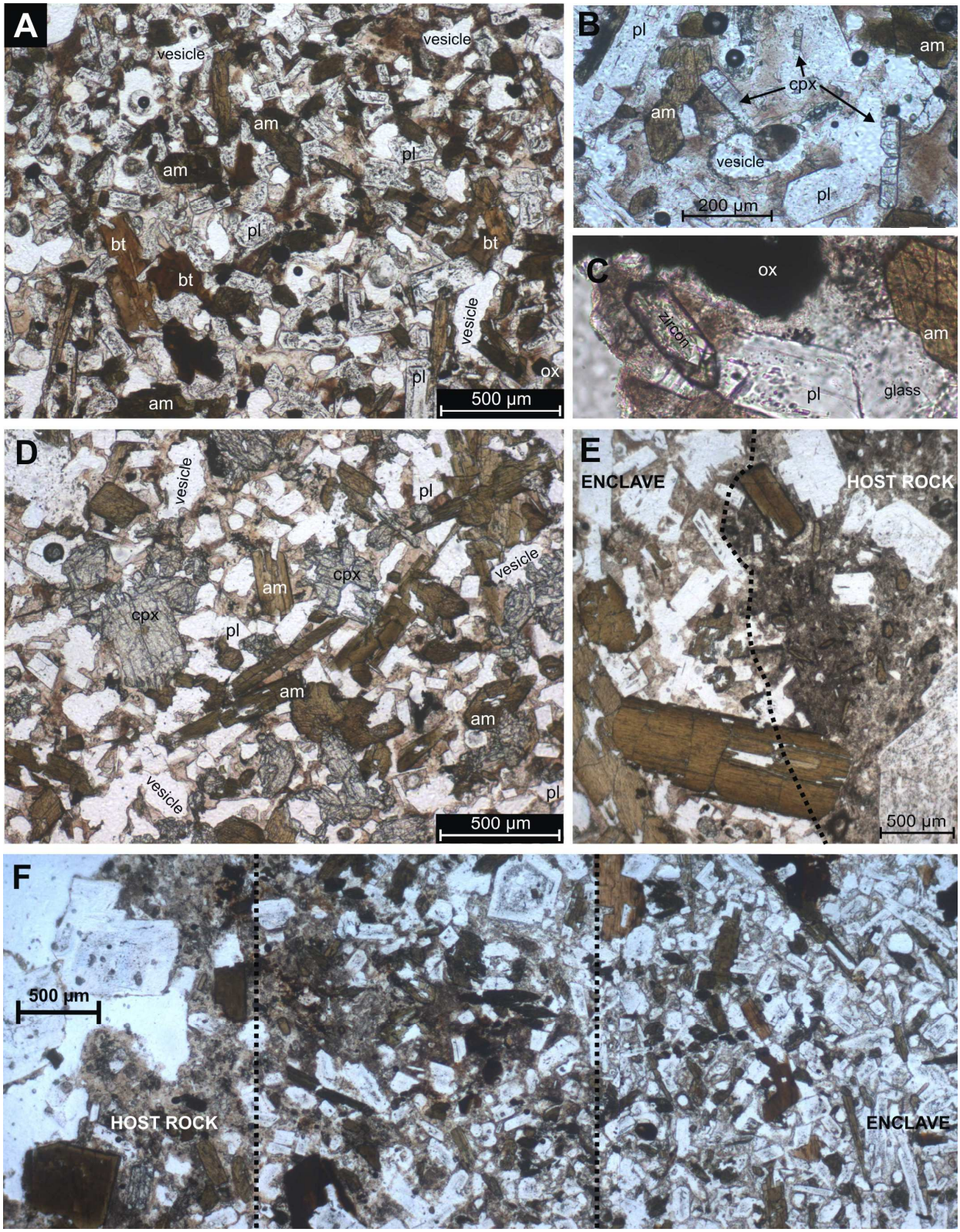

Figure 6.10. *Photomicrographs of type 1 and 2 enclaves from the Kokkinovrahos biotite-hornblende andesite.* All images ppl. (A) IA349. Overview of a coarse-grained type 1 enclave with pl, am and bt framework phenocrysts and rounded vesicles. (B) IA355B, type 1. Enlargement of the groundmass with pl, am and cpx phenocrysts. (C) IA345, type 1. 100 µm long zircon crystal in the enclave's groundmass. (D) IA336. Overview of a coarse-grained type 2 enclave with framework phenocrysts of pl, am and greenish cpx. (E) IA348, type 2. Example of a relatively sharp contact between enclave and its host. (F) IA338, type 1. Example of broad transition zone between enclave and its host, in which pl crystals seem to 'crumble' from the enclave into the host (enclave crumbling).

During fieldwork it was already noticed that on average 1 out of 10 enclaves shows homogeneously distributed green minerals. These overall more coarse-grained enclaves contain a higher proportion of glassy groundmass (35%) and higher mafic mineral content. As for the type 1 enclaves, the dominant phenocrysts are randomly oriented, eu-to subhedral plagioclase (25%) and amphibole (25%) grains, but they do not always form a touching crystal framework (Fig. 6.10D). Faint green clinopyroxene phenocrysts represent the third main component (5%) instead of biotite that is only scarcely present (Fig. 6.10D). These 'green clinopyroxene' type 2 enclaves have a similar vesicularity as type 1 enclaves of similar grain size (9%), despite their higher glass content. Observed macro-phenocrysts are amphibole, greenish clinopyroxene and sieve-textured plagioclase (Fig. 6.10E).

Contacts between host rocks and any of the two enclave types are usually sharp (Fig. 6.10E) – only in some enclaves are there contact zones where framework phenocrysts of the enclave seem to have been arrested in the process of being dispersed into the host rock (enclave crumbling) (Fig. 6.10F).

6.3.2 Other lava flows and plugs from the first period of volcanic activity

The detailed description of shape, pleochroism, zoning, alteration, twinning and colour of (macro-) phenocrysts and microlites in the Kokkinovrahos lavas and enclaves will not be repeated for similar-looking minerals in the other volcanic deposits. Only distinctions in comparison to the Kokkinovrahos volcanic rocks will be mentioned.

The Skotini andesite is a porphyritic lava with mainly plagioclase (An_{55}) and olivine macro-phenocrysts. The olivine (macro-) phenocrysts are euhedral, tabular crystals with Cr-spinel inclusions and red-brown to opaque iddingsitic alteration along the outer rim and main fractures (Fig. 6.11A). Many olivine crystals furthermore show large areas that are altered to orange-brown, translucent iddingsite which masks the mineral's birefringence colours (Fig. 6.11A) and probably causes the olivine's yellow appearance in the field. The third main mineral component are clinopyroxene phenocrysts which usually cluster together but also occur as individual crystals (Fig. 6.11B). Other (macro-)phenocrysts are pseudomorphs after amphibole and biotite, consisting of opacite and/or epitaxial (clino-)pyroxene (Fig. 6.11A, C, E). Large subhedral biotite crystals can be variably altered from the rim inwards by an anhydrous mineral assemblage of plagioclase, pyroxene and Fe-Ti-oxides (Fig. 6.11D. Rounded quartz macro-phenocrysts are heterogeneously distributed throughout the host rock. Prismatic plagioclase crystals are the dominant phenocrysts, showing a a seriate grain size distribution from macro-phenocrysts to microlites (Fig. 6.11E), with the smaller plagioclase grains forming a flow texture around the host rock's macro-phenocrysts. Groundmass represents up to 50 vol% of the Skotini andesite and mainly consists of acicular plagioclase and equidimensional Fe-Ti oxide microlites, besides minor clinopyroxene and glass (Fig. 6.11B).

Two types of enclaves were identified during fieldwork on the Skotini andesite: a coarse-grained rock composed of black and white minerals and a green-grey aphanitic rock. The former has a framework of tabular plagioclase phenocrysts and pseudomorphs after prismatic amphibole crystals (with sometimes patches of relic amphibole) (Fig. 6.11F-G) consisting of epitaxial pyroxene or opacite (Fig. 6.11F-G). The green-grey enclaves have a very fine-grained framework of prismatic plagioclase and clinopyroxene crystals, but no amphibole (or pseudomorphs thereafter) (Fig. 6.11H). Both enclave types furthermore contain macro-phenocrysts of olivine, plagioclase and pseudomorphs after hydrous minerals, round vesicles and a glassy groundmass (Fig. 6.11F-H). Additionally, the Skotini andesite has been observed to contain: 1) a fine-grained plagioclase-clinopyroxene-Fe-Ti-oxide micro-enclave; 2) cumulophyric aggregates of plagioclase, clinopyroxene (± olivine) (Fig. 6.11I), and 3) a sedimentary xenolith consisting of anhedral quartz grains. The host rock near the contact with this xenolith also contains a number of anhedral, rounded quartz grains without reaction rims (Fig. 6.11J).

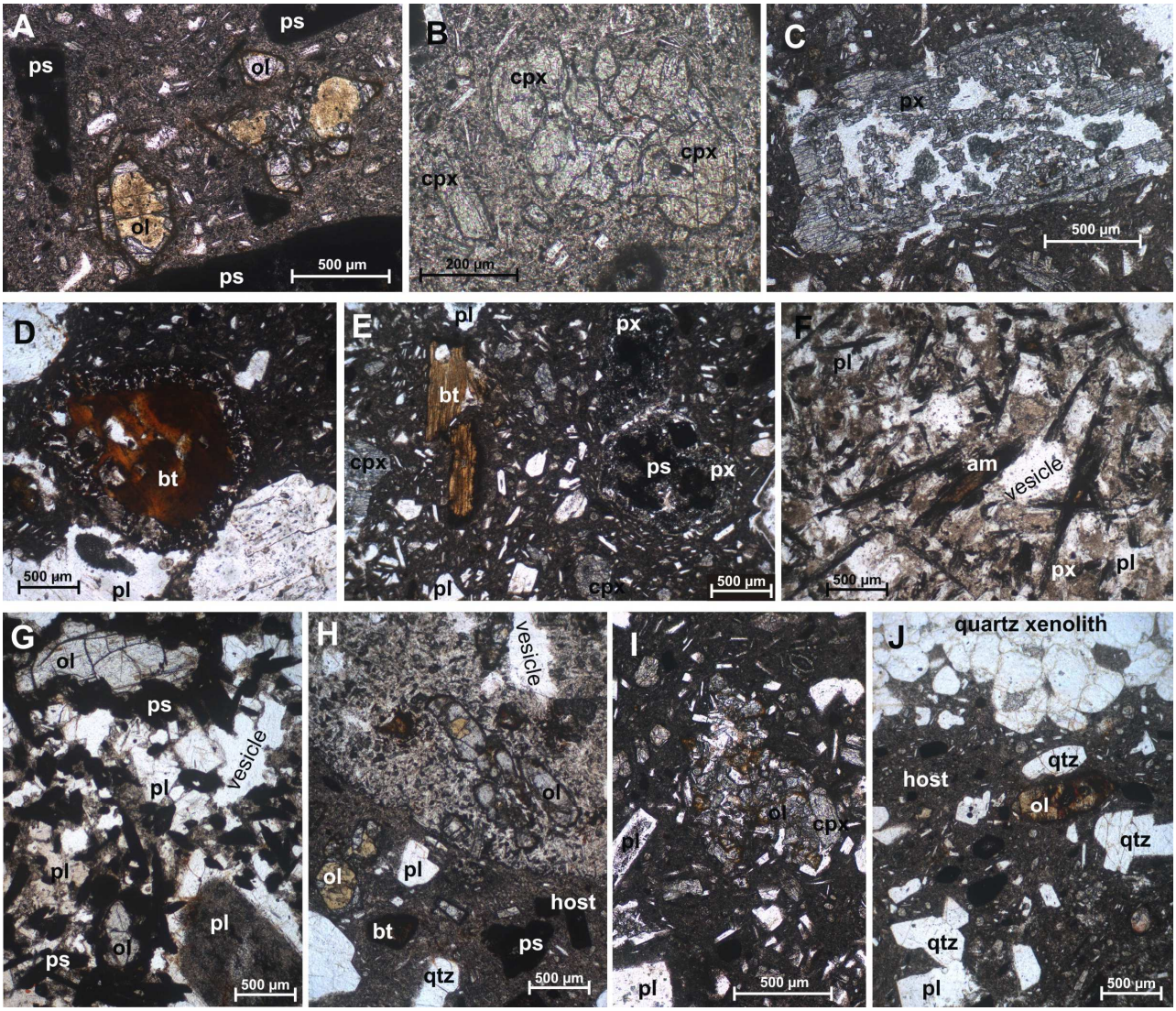

Figure 6.11. *Photomicrographs of host rock and enclaves of the Skotini andesite.* All images ppl. (A) Host IA329. Besides red-brown opaque iddingsite tracing their outline, many ol crystals also show orange-brown translucent iddingsite alteration in their core zone. Note the opacitised pseudomorphs after hydrous minerals. (B) Host IA329. Eu-to subhedral cpx phenocrysts occur both in clusters and as individual crystals. (C) Host IA102. Pseudomorph of fine-grained, epitaxial px replacing am. (light areas within the crystal are voids, likely introduced during thin section preparation) (D) Host IA102. Large bt macro-phenocryst with anhedral pl inclusions and replaced from the rim inwards by pl, ox and px. (E) Host IA102. Overview of the Skotini lavas with about 50 vol% groundmass, and cpx and pl phenocrysts weakly defining a flow texture around macro-phenocrysts of bt, cpx, pl and ps. (F) Enclave IA101. Coarse-grained framework of pl and am largely replaced by epitaxial px and opacite. (G) Enclave IA332. Coarse-grained framework of pl and ps after am, with macro-phenocrysts of pl and ol. (H) Enclave IA331B. Contact between host and very fine-grained (same scale as F and G) enclave. The latter has a framework of prismatic pl (white laths) and cpx (greenish grains in between). Macro-phenocrysts of ol in host rock and enclave are very similar. (I) Host IA102. Cumulophyric aggregate of cpx, pl and ol. Note flow texture around this small crystal group. (J) IA328B. Contact between quartz xenolith and host rock, with host containing rounded qtz very similar to the xenolith's grains.

The Palaiochora dacitic andesite and Phase 1 biotite-hornblende andesite, as well as the host rock sample from the volcaniclastic apron, have petrographic characteristics broadly similar to the Kokkinovrahos lavas. As suggested by their name, amphibole is a major mineral (besides plagioclase) whereas biotite often occurs as a minor mineral phase (beside Fe-Ti-oxides) (Fig. 6.12A). No olivine has been observed in these hydrous-mineral rich (dacitic) andesites. There are subtle differences between different units with respect to their pyroxene contents and the nature of their amphibole (macro-) phenocrysts. All biotite-hornblende lavas contain tabular, euhedral, clinopyroxene with a

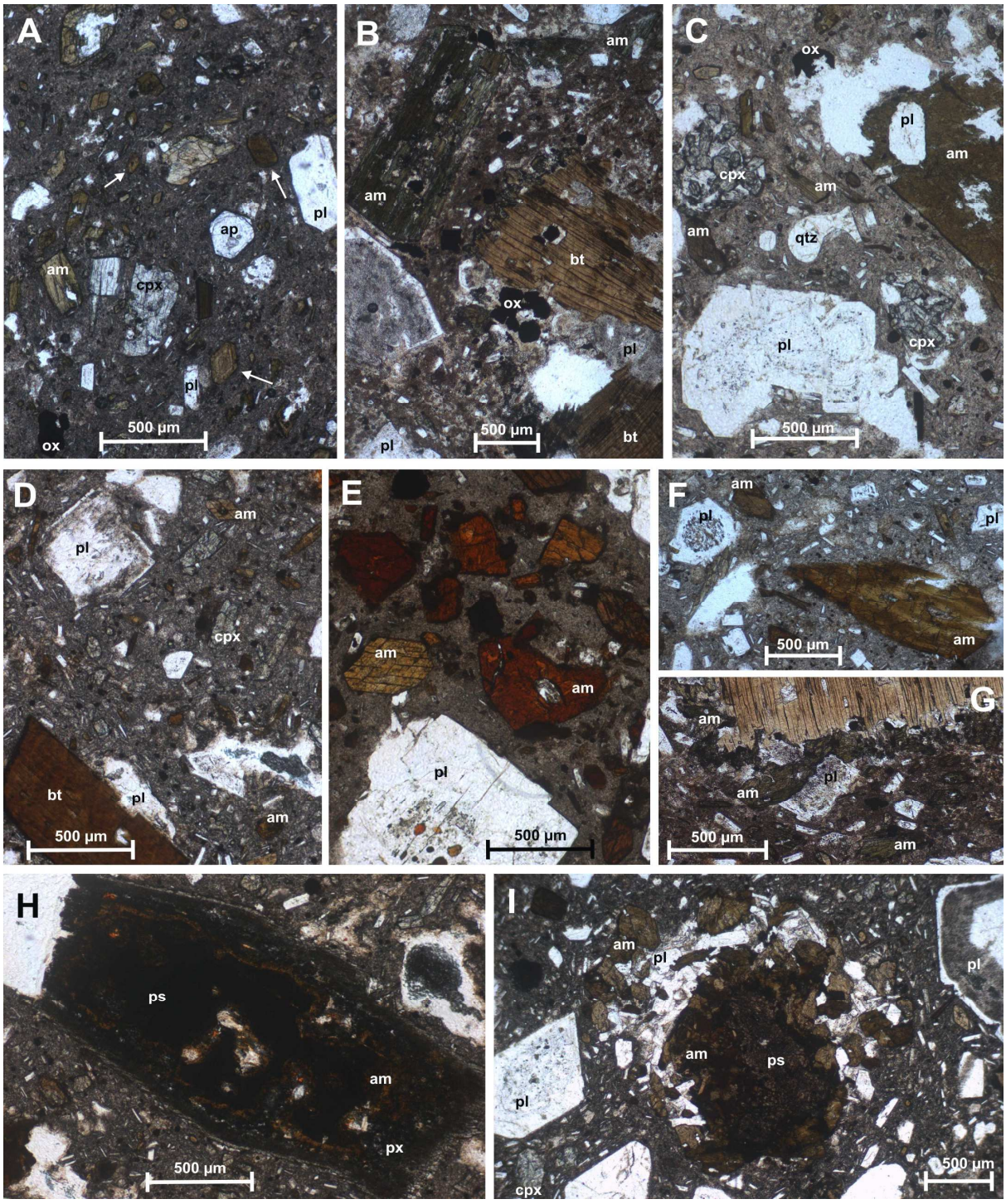

Figure 6.12. *Photomicrographs of the host rocks from the Palaiochora dacitic andesite, Phase 1 biotite-hornblende andesites and volcaniclastic apron.* All images ppl. (A) IA352, Kokkinovrahos bt-hbl and. Overview of (oscillatory) zoned (white arrows), green-brown to yellow-brown pleochroic am, greenish cpx, pl, ox, apt and flow texture. (B) IA61. The Palaiochora dac and is characterised by the absence of cpx, ample macro-phenocrysts of bt and typical brown-green to bluish-green am. (C) IA322, volcaniclastic apron. This sample contains embayed qtz. (D) IA103. This sample is a typical Phase 1 bt-hbl and with bt, unzoned am, pl and green cpx. (E) IA65. In comparison with (D), this Phase 1 bt-hbl and does not contain cpx and its am crystals have a distinct red colour. (F) IA325. This Phase 1 bt-hbl and does not contain bt; cpx and oscillatory zoned am are its main mafic minerals. (G) IA340, Palaiochora dac and. A large bt macro-phenocryst is at its rim overgrown by pl, ox and am. Note the bluish-green colour of the am, typical for this unit. (H) IA103, Phase 1 bt-hbl and. One of the rare hydrous minerals with pervasive alteration and dehydration features. (I) IA59, Phase 1 bt-hbl and. A fine-grained pseudomorphic aggregate is overgrown by am, then by pl and again by am.

greenish hue that frequently occurs as a minor mineral phase – either individual grains but often also as cumulophyric aggregates – except for the Palaiochora dacitic andesite in which no clinopyroxene was observed. The latter furthermore contains distinctly brown-green to bluish-green, strongly pleochroic amphibole crystals that do not show zoning (Fig. 6.12B). The amphibole crystals in host rocks from the Phase 1 biotite-hornblende andesites and the volcaniclastic apron do not show zoning either, but they have a green-brown to yellow-brown pleochroic colour (Fig. 6.12C). The mineral content and petrographic textures are typically homogeneous within one volcanic unit. Only the two host rocks from the lavas classified as 'Tourli dacites' by Dietrich et al. (1993a) differ from each other: the sample from the southern part of Aegina (IA103, location 72, see Fig. 6.1) is very similar to the other biotite-hornblende andesites (Fig. 6.12D), but the sample from the northern part (IA65, location 71, see Fig. 6.1), has a distinct mineralogy which lacks clinopyroxene, has fewer biotite grains and strongly pleochroic, orange-brown to deep red-brown amphibole crystals without zoning (Fig. 6.12E). The former sample is collected near an eruption vent of the unit, whereas the latter at lower elevation, next to the volcaniclastic apron and near hydrothermally altered volcanic rocks. The youngest effusive deposits from the first period of volcanic activity ('hornblende Koutalou dacite' according to Dietrich et al., 1993a) show a more restricted mineralogy of plagioclase, brown, unzoned amphibole, greenish clinopyroxene and Fe-Ti-oxides.

Orthopyroxene phenocrysts are sporadically observed in host rocks which contain relatively large amounts of clinopyroxene. Embayed quartz is occasionally observed as a minor or accessory phase across the Palaiochora lavas, Phase 1 andesites and volcaniclastic apron (Fig. 6.12C). Samples with embayed quartz often also contain euhedral zircon crystals in large plagioclase, amphibole or biotite macro-phenocrysts. All (dacitic) andesites from the first period of volcanic activity have abundant hydrous minerals which usually show no dehydration reactions or disequilibrium features. Biotite crystals are sometimes mantled by subhedral, smaller amphibole crystals (Fig. 6.12G). Epitaxial replacement of amphibole by fine-grained pyroxene occurs sporadically, in which case it is largely restricted to a pseudomorphic broad rim around a partially opacitised amphibole core (Fig. 6.12H). In some instances, pseudomorphs after hydrous minerals are mantled by multiple layers of different minerals, including amphibole (Fig. 6.12I).

The Palaiochora dacitic andesite and the hornblende andesite lavas that erupted at the end of Aegina's first volcanic phase (the 'Koutalou hornblende dacite' according to Dietrich et al., 1993a) do not host any enclaves apart from very rare micro-enclaves smaller than 1 cm. The Phase 1 biotite-hornblende andesites and volcaniclastic apron, however, contain up to 8 vol% of more mafic enclaves. The grain size of these enclaves varies from fine-grained to coarse-grained. The framework of the enclave sampled at location 69 consists of euhedral, short prismatic plagioclase phenocrysts and larger, subhedral, prismatic amphibole crystals (Fig. 6.13A). The latter have a strong orange-brown to deep red-brown pleochroic colour but no zoning. Tabular, eu-to subhedral clinopyroxene is present as a minor phenocryst phase as are small amounts of Fe-Ti-oxide (Fig. 6.13B). The host rock sampled near this enclave, however, contains a fine-grained micro-enclave that mainly consists of prismatic plagioclase and equidimensional Fe-Ti-oxides, some clinopyroxene and rare opaque pseudomorphs after hydrous minerals (Fig. 6.13C). Another outcrop of the Phase 1 biotite-hornblende andesites (location 70) contains the same fine-grained micro-enclaves (Fig. 6.13D) as well as larger coarse-grained ones similar to the plagioclase-amphibole enclave described above but in which the amphibole phenocrysts show green-brown to yellow-brown pleochroism (Fig. 6.13E). This green-brown to yellow-brown pleochroic amphibole is the most common type among all enclaves from the first period of volcanic activity, and often shows (oscillatory) zoning (Fig. 6.13F). More coarse-grained enclaves of the biotite-hornblende andesites contain small, round vesicles and more glass. More fine-grained enclaves contain significantly less glass and their vesicles are more irregularly shaped and partially bordered by mineral grains (compare Fig. 6.13D to 6.13B). The coarse-grained enclave sampled from the volcaniclastic apron also shows a high vesicularity, but in contrast with the coarse-grained enclaves described above little to no glassy groundmass – leading to irregularly shaped vesicles largely bordered by phenocrysts (dictytaxitic texture) (Fig. 6.13G). Its framework consists of

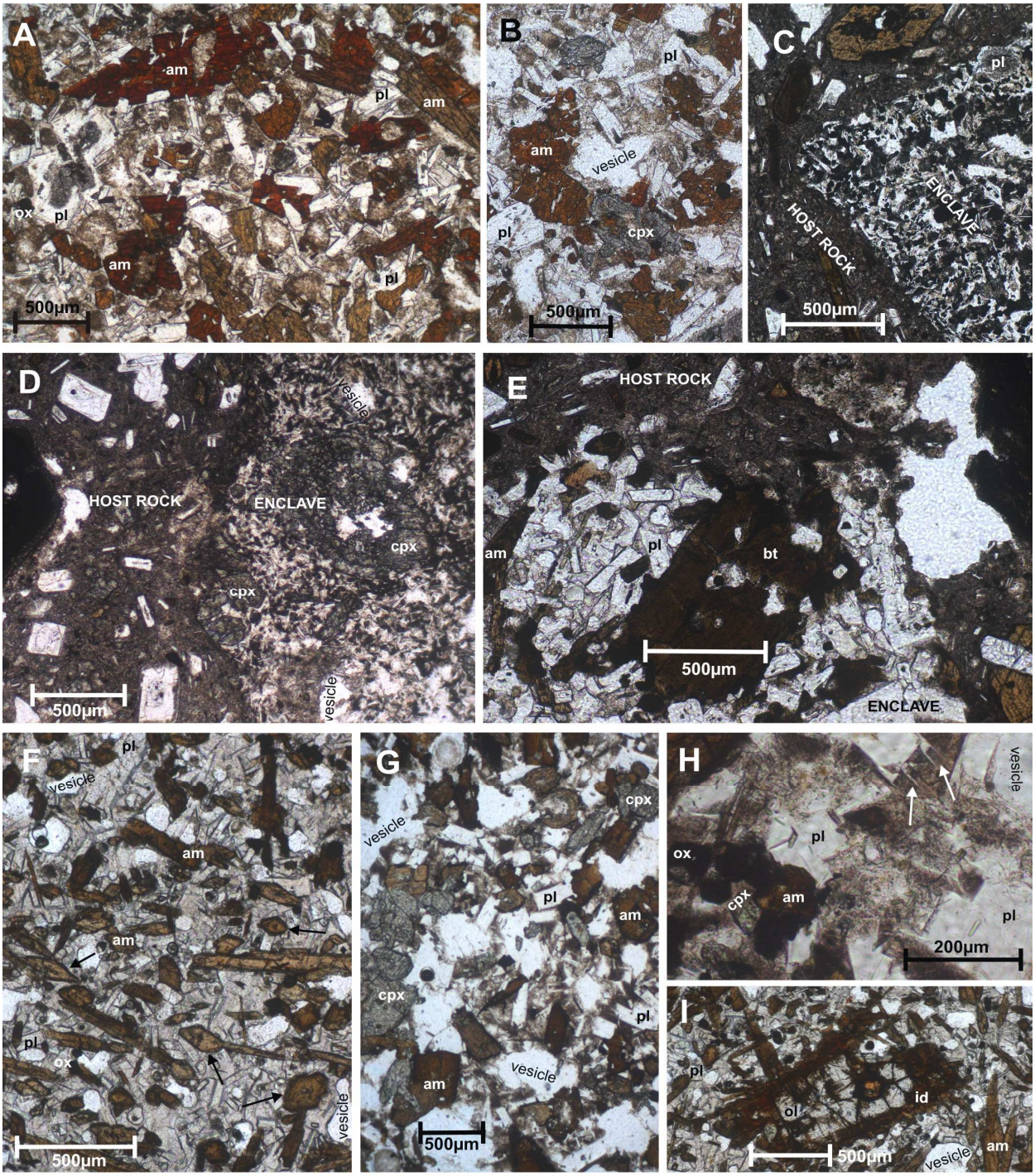

Figure 6.13. *Photomicrographs of enclaves from the Phase 1 biotite-hornblende andesites and volcaniclastic apron*. All images ppl. (A) IA60, Phase 1 bt-hbl and. Enclave with orange-brown to deep red-brown pleochroic am. (B) IA60, Phase 1 bt-hbl and. Enlarged view with cpx, am and pl phenocrysts. (C) IA59, Phase 1 bt-hbl and. Contact between host rock and fine-grained micro-enclave mainly consisting of pl and ox. (D) IA67, Phase 1 bt-hbl and. Contact between host rock and fine-grained micro-enclave with cpx macro-phenocrysts. (E) IA67, Phase 1 bt-hbl and. Contact between host rock and coarse-grained micro-enclave containing a bt macro-phenocryst. (F) IA104, Phase 1 bt-hbl and. Coarse-grained enclave, note zoning of the green-brown to yellow-brown pleochroic am phenocrysts (black arrows) and rounded vesicles. (G) IA321, volcaniclastic apron. Coarse-grained enclave with green-brown to yellow-brown pleochroic, occasionally zoned am phenocrysts, green cpx, white pl and irregular shaped vesicles . (H) IA321, volcaniclastic apron. Close-up of groundmass with microlites of ox, am, cpx and skeletal pl (white arrows). Note dictytaxitic texture. (I) IA104, Phase 1 bt-hbl and. Macro-phenocryst of ol with red iddingsite around its outer rim.

euhdral, tabular plagioclase, prismatic amphibole and eu- to subhedral greenish clinopyroxene (Fig.6.13G). The groundmass contains mainly plagioclase microlites (the smaller ones being skeletal crystals) besides Fe-Ti-oxides, amphibole and clinopyroxene (Fig. 6.13H). Overall, most enclaves are coarse-grained and similar to the green clinopyroxene type 2 enclaves in the Kokkinovrahos andesite (see section 6.3.1). Micro-enclaves of fine-grained plagioclase and Fe-Ti-oxide are sporadically present, but no biotite-rich enclave similar to the Kokkinovrahos type 1 enclaves is observed. Apart from a large subhedral olivine grain in enclave IA104 (Fig. 6.13I), macro-phenocrysts are similar to the ones present in the enclaves' host rocks: plagioclase (Fig. 6.13C), amphibole with and without disequilibrium features, biotite (Fig. 6.13E) and green euhedral clinopyroxene (Fig. 6.13D). Contacts between host rocks and their enclaves are usually sharp (Fig. 6.13C-E).

6.3.3 Lava flows and plugs from the second period of volcanic activity

The Kakoperato rhyodacite is composed of a porphyritic host rock with macro-phenocrysts of mainly plagioclase and amphibole besides minor biotite and quartz. Plagioclase crystals are commonly subhedral with rounded edges and can be difficult to distinguish from quartz when they are anhedral grains without zoning, twinning or sieve texture (Fig. 6.14A). Amphibole crystals are commonly euhedral and show green-brown to yellow-brown pleochroism and zoning (Fig. 6.14B). Biotite crystals are often also rounded and occasionally intergrown with a single euhedral amphibole crystal (Fig. 6.14C). Quartz grains are all rounded to embayed and never mantled by a corona of mafic minerals (Fig. 6.14D). None of these minerals show a seriate crystal size distribution and there are only few phenocryst-sized crystals present. These include sub- to anhedral plagioclase, euhedral and zoned amphibole, tabular crystals of green clinopyroxene, colourless subhedral orthopyroxene and Fe-Ti-oxides (Fig. 6.14B-E). The total volume represented by the lavas' (macro-)phenocrysts is less than 40% and they are enclosed by a translucent, fine-grained groundmass that is charged with small, prismatic to acicular plagioclase microlites, small amounts of very fine-grained Fe-Ti-oxides and volcanic glass (Fig. 6.14F). The plagioclase microlite population has a homogeneous size and defines a flow texture around the (macro-)phenocrysts (Fig. 6.14F). Euhedral apatite crystals are occasionally present as phenocrysts in the groundmass or as inclusions in plagioclase (Fig. 6.14F). The fine-grained groundmass has many irregular, heterogeneously distributed cracks running through it (Fig. 6.14A-C & E) - probably the cause for the rhyodacite's low resistance to hammering (see section 6.1.3).The thin section of host rock sample IA97 contains an irregular area of ca. 2.5 x 1.5 cm which for two-thirds consists of groundmass fragments, a piece of embayed quartz and phenocryst-sized pieces of amphibole set in a transparent glassy matrix (Fig. 6.14G). The remaining one third represents most of the outer rim of this area and consists of microlite-sized plagioclase, pyroxene and amphibole crystals which become more fine-grained nearer the sharp contact between this xenolithic fragment and the host rock (Fig. 6.14G).

The Kakoperato rhyodacite is riddled with coarse-grained enclaves of which the dimensions vary between 1 mm (Fig. 6.14H) and 50 cm (Fig. 6.14I). These enclaves all have the same mineralogy of a euhedral plagioclase and (oscillatory) zoned amphibole framework with Fe-Ti-oxides and rare pyroxene (Fig. 6.14H-I). Their groundmass mainly consists of volcanic glass with rounded vesicles (Fig. 6.14H-I). Macro-phenocrysts are subhedral plagioclase (often sieve-textured), large euhedral and zoned amphibole (Fig. 6.14I), euhedral biotite overgrown by a rim of optically continuous euhedral amphibole (Fig. 6.14I) and rounded quartz grains that are always mantled by green clinopyroxene in turn overgrown by plagioclase (Fig. 6.5A).

The Nikolaki andesite is an enclave-free, porphyritic lava in which plagioclase is the main mineral, displaying a seriate crystal size distribution ranging from acicular microlites over more prismatic phenocrysts to tabular An_{45} macro-phenocrysts (Fig. 6.15A). Simple and polysynthetic twinning commonly occurs, as well as varying degrees of sieve texture, but oscillatory zoning is only sporadically observed. Prismatic plagioclase phenocrysts and microlites are very abundant and form a

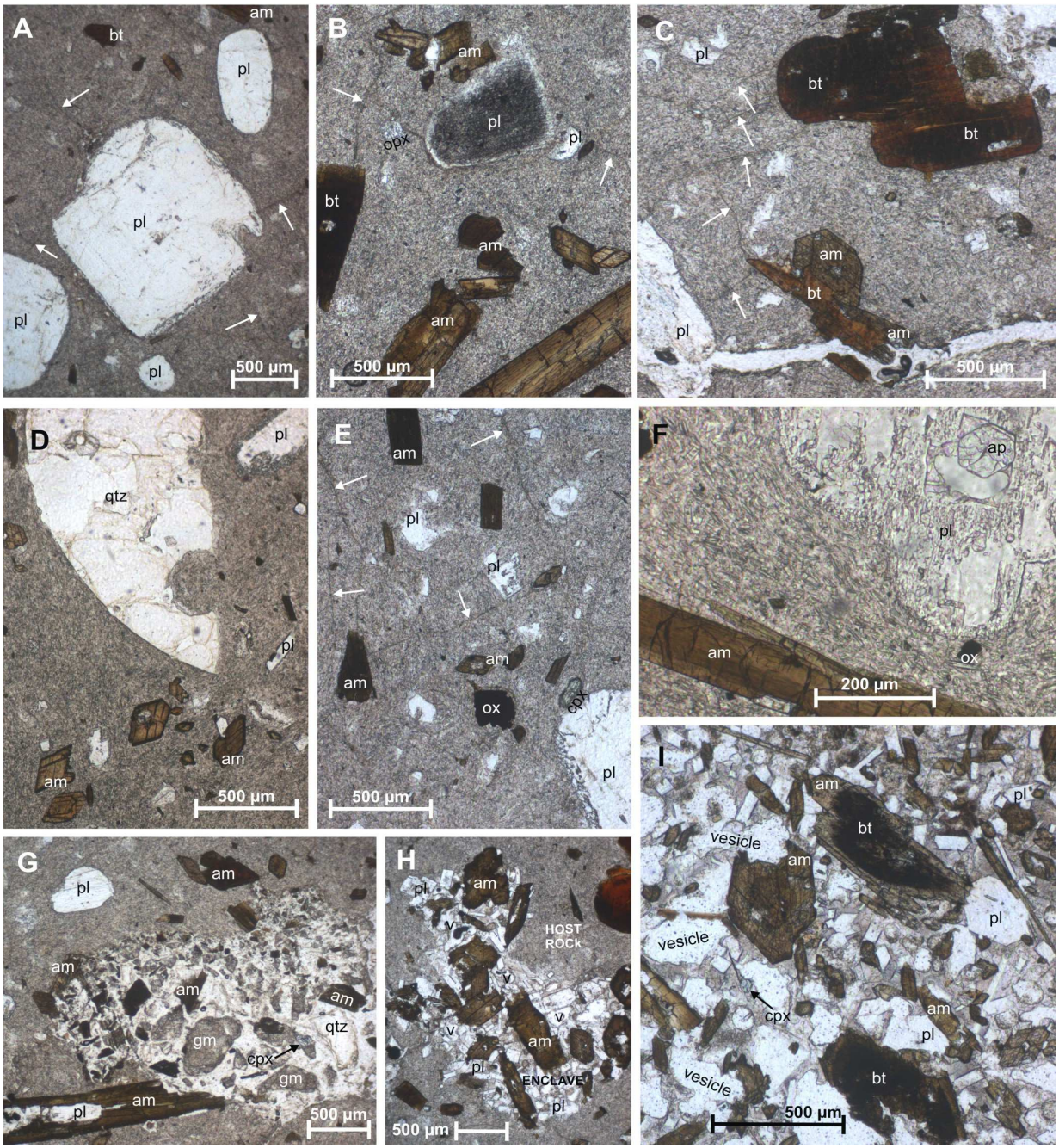

Figure 6.14. *Photomicrographs of the Kakoperato rhyodacite*. All images ppl. White arrows are perpendicular to the groundmass cracks they point out. (A) Host rock IA97. Rounded (macro-) phenocrysts of pl without sieve texture. (B) Host rock IA97. Macro-phenocrysts of green-brown to yellow-brown pleiochroic, zoned am and a sieve-textured, rounded pl. (C) Host rock IA97. Large subhedral, rounded bt macro-phenocrysts and a smaller, more euhedral bt crystal overgrown by am. (D) Host rock IA333. Very large embayed qtz macro-phenocryst and phenocrysts of pl and zoned am. (E) Host rock IA97. Phenocrysts of pl, am, ox and a green cpx (bottom right corner above pl macro-phenocryst). (F) Host rock IA333. Macro-phenocryst of pl (with a euhedral ap in the top right corner) and prismatic am in between which prismatic pl microlites of the groundmass form a flow texture. (G) Host rock IA97. Angular, irregular xenolithic area with pieces of the host rock groundmass and fragments of larger qtz and am grains (partially) mantled by a more fine-grained aggregate of randomly oriented am, pl and px fragments. (H) Coarse-grained micro-enclave in host rock IA97. (I) Enclave IA98. Glassy groundmass with rounded vesicles in between a medium-grained am and pl framework with zoned am and am overgrown bt macro-phenocrysts.

flow texture around the macro-phenocrysts (Fig. 6.15A-C). The second main mineral is greenish, short prismatic clinopyroxene – often in cumulophyric aggregates but also as individual crystals (Fig. 6.15A-B). It occurs as (very large) euhedral macro-phenocrysts, more subhedral phenocrysts and rare microlites. Anhydrous, opaque pseudomorphs after amphibole are the third most common (macro-) phenocrysts (Fig. 6.15A-E). In rare pseudomorphic aggregates of opaque minerals the core of the amphibole is sometimes preserved, showing (oscillatory) zoning (Fig. 6.15C). Orthopyroxene (macro-) phenocrysts are present as colourless to yellowish, euhedral crystals with somewhat darker rims (Fig. 6.15D). Small amounts of subhedral, colourless olivine (macro-)phenocrysts are recognised by orange-brown iddingsite rims (Fig. 6.15E). The groundmass represents less than 40 vol% of the lava and consists almost completely of prismatic plagioclase microlites of varying size, Fe-Ti-oxides and rare clinopyroxene. Volcanic glass is thereby only sporadically observed in between the microlites and vesicles are rare. All host rocks of the Nikolaki andesite show the same mineralogy and petrography

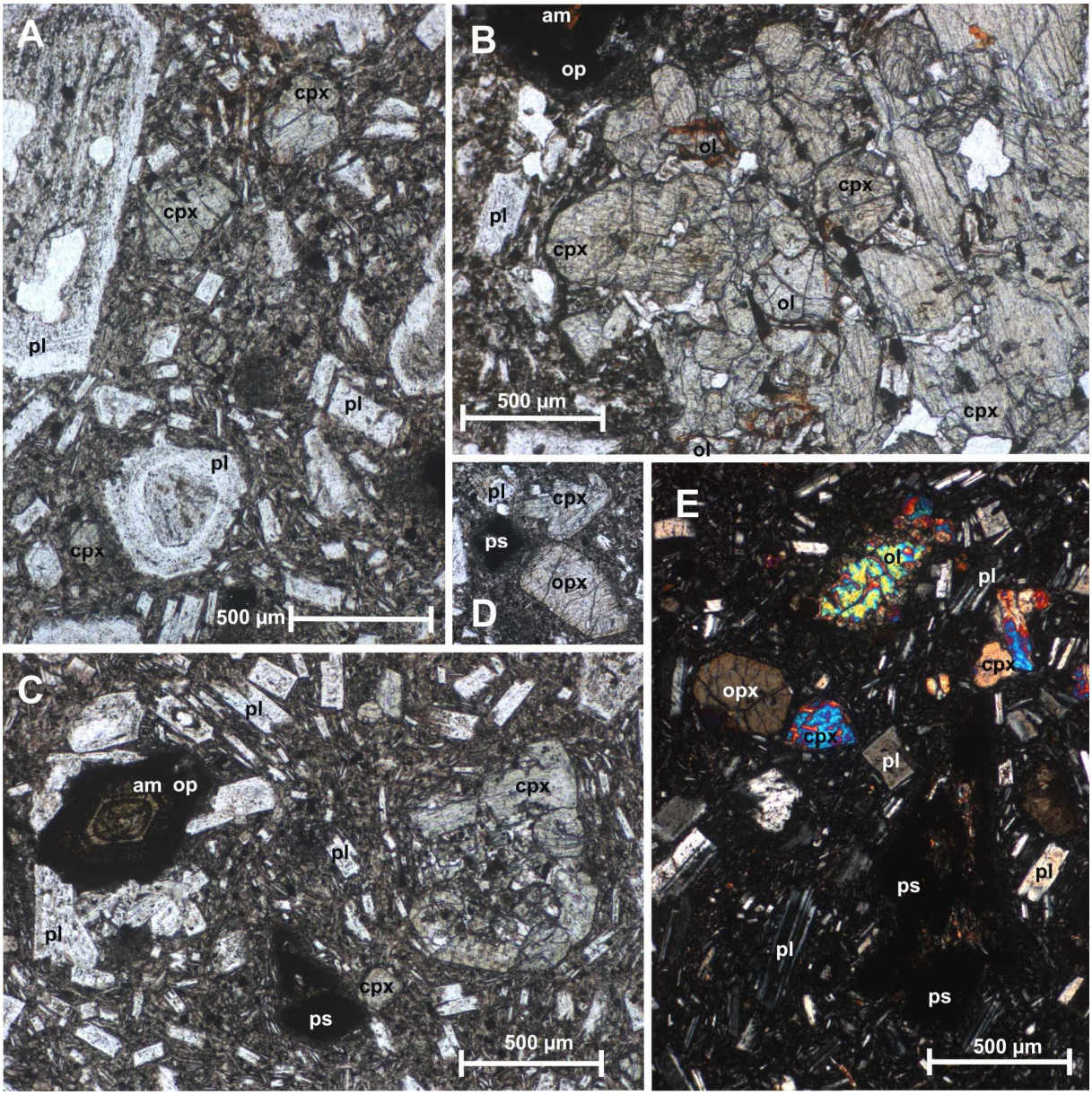

Figure 6.15. *Photomicrographs of the Nikolaki andesite*. (A) IA73, ppl. Seriate texture of pl with sieved macro-phenocrysts. Second main mineral is greenish cpx. (B) IA73, ppl. Cumulophyric aggregate of cpx and ol macro-phenocrysts. (C) IA74, ppl. Flow texture of prismatic pl phenocrysts around holocrystalline aggregate of pl and oscillatory zoned, brown-green pleochroic am, opacite pseudomorphs and cumulophyric cpx aggregate. (D) IA73, ppl. ca. 350 µm long, euhedral, colourless opx crystal with yellowish rim and subhedral, greenish cpx. (E) IA74, xpl. Overview with pl flow texture, am ps, ol, cpx and opx.

as the one described above. The felsic crystals mantled by a reaction rim of mafic minerals identified in the field were not observed during the petrographic study. Thin sections however do contain cavities rimmed by clinopyroxene which might represent such a corona texture from where the felsic minerals are lost. No macro- or microscopic enclaves have been observed in the Nikolaki andesite, but cumulophyric aggregates of eu-to subhedral clinopyroxene which sometimes also include minor orthopyroxene and olivine are common (Fig. 6.15B-C).

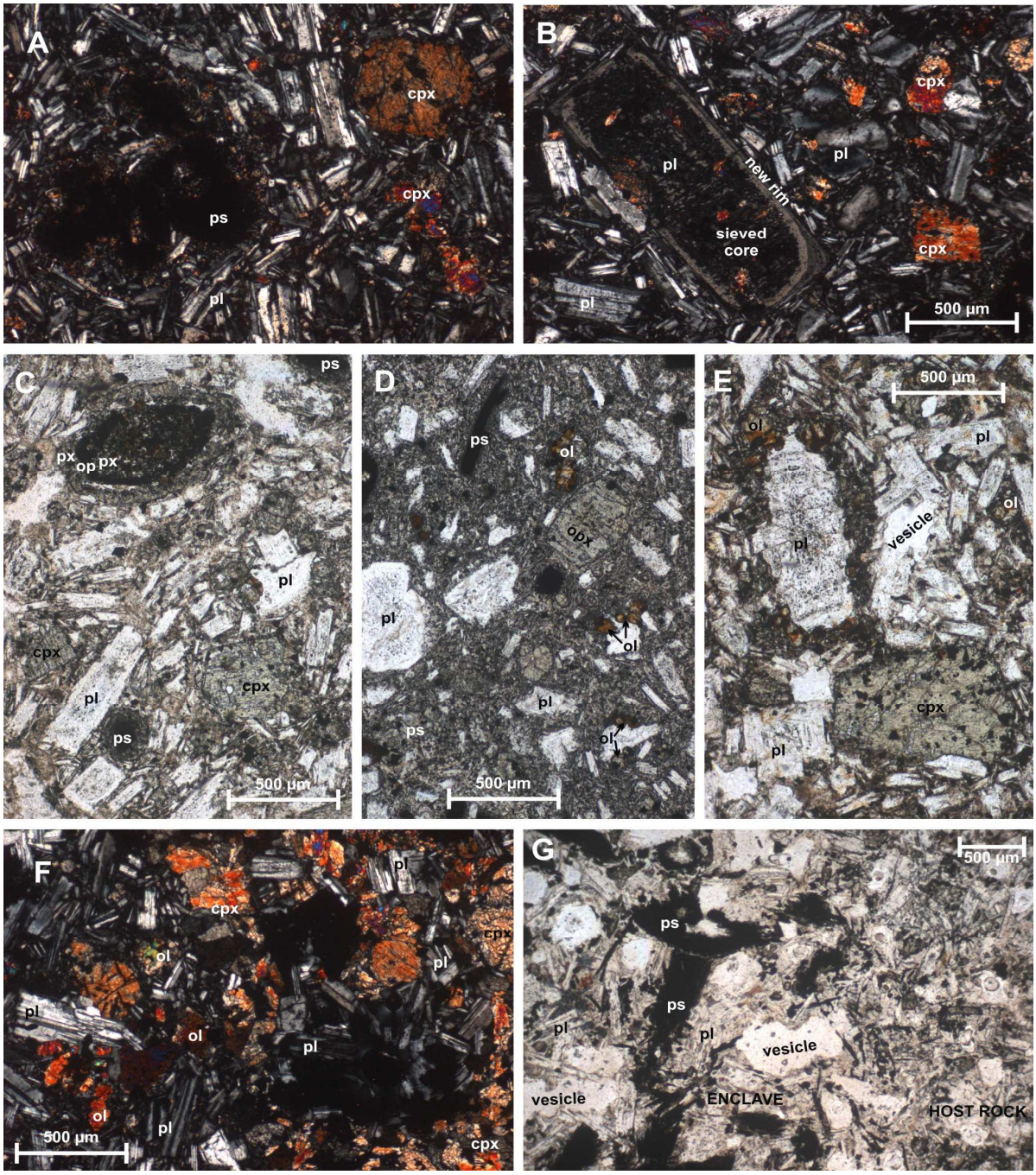

Figure 6.16. *Photomicrographs of the Oros-Lazarides basaltic andesites.* (A) Host rock IA80, xpl. Large microlites and phenocrysts of prismatic pl are aligned and oriented around macro-phenocrysts of cpx and ps of am. (B) Host rock IA68, xpl. Rare pl macro-phenocryst showing anhedral, sieved core and oscillatory zoned rim. (C) Host rock IA71, ppl. Macro-phenocrysts of cpx and a ps of alternating op and px. (D) Host rock IA88, ppl. Overview with small phenocrysts of iddingsite-rimmed ol and macro-phenocrysts of pl and opx. (E) Host rock IA93, ppl. Macro-phenocrysts of cpx and of anhedral pl with ol and ox mantle. (F) Host rock IA93, xpl. Bottom right shows cluster of An_{35} pl phenocrysts in glass, rimmed by cpx and some ol. Pl phenocrysts of the host rock (top left) are An_{50}. (G) Enclave IA72, ppl. Sharp contact between host and enclave.

The Oros-Lazarides basaltic andesites also contain plagioclase as a major mineral phase which ranges in size from microlite to macro-phenocryst. Unlike the Nikolaki andesites, however, the dominant plagioclase population are large prismatic phenocrysts (An_{50} to An_{60}) with simple and polysynthetic twins, aligned closely to one another around macro-phenocrysts (Fig. 6.16A). The volume of groundmass varies between samples from approximately 40% to less than 15%. Macro-phenocrysts of plagioclase become scarcer with decreasing volume of the groundmass and often show a resorbed core with strong sieving and a euhedral, oscillatory zoned outer rim (Fig. 6.16A). The second most common mineral phase are either amphibole pseudomorphs (of opaque grains or with alternating rims of opacite and fine-grained pyroxene) or euhedral, greenish clinopyroxene (individual grains or cumulophyric clusters) (Fig. 6.16A-C). Phenocrysts of slightly yellowish, euhedral orthopyroxene are also commonly present (Fig. 6.16D). All basaltic andesite samples furthermore contain minor amounts of olivine which is usually present as small, subhedral phenocrysts with strong orange-red iddingsitisation (Fig. 6.16D) and sometimes as large, more colourless grains similar to the ones in the Nikolaki andesite. Occasionally an anhedral plagioclase grain is mantled by small, iddingsitic olivine grains and Fe-Ti-oxides (Fig. 6.16E). Recurring mineral aggregates are mafic cumulophyric clusters of clinopyroxene ± olivine ± orthopyroxene and felsic grains (quartz, An_{35} plagioclase) mantled by clinopyroxene ± olivine (Fig. 6.16F). Enclaves were only sporadically

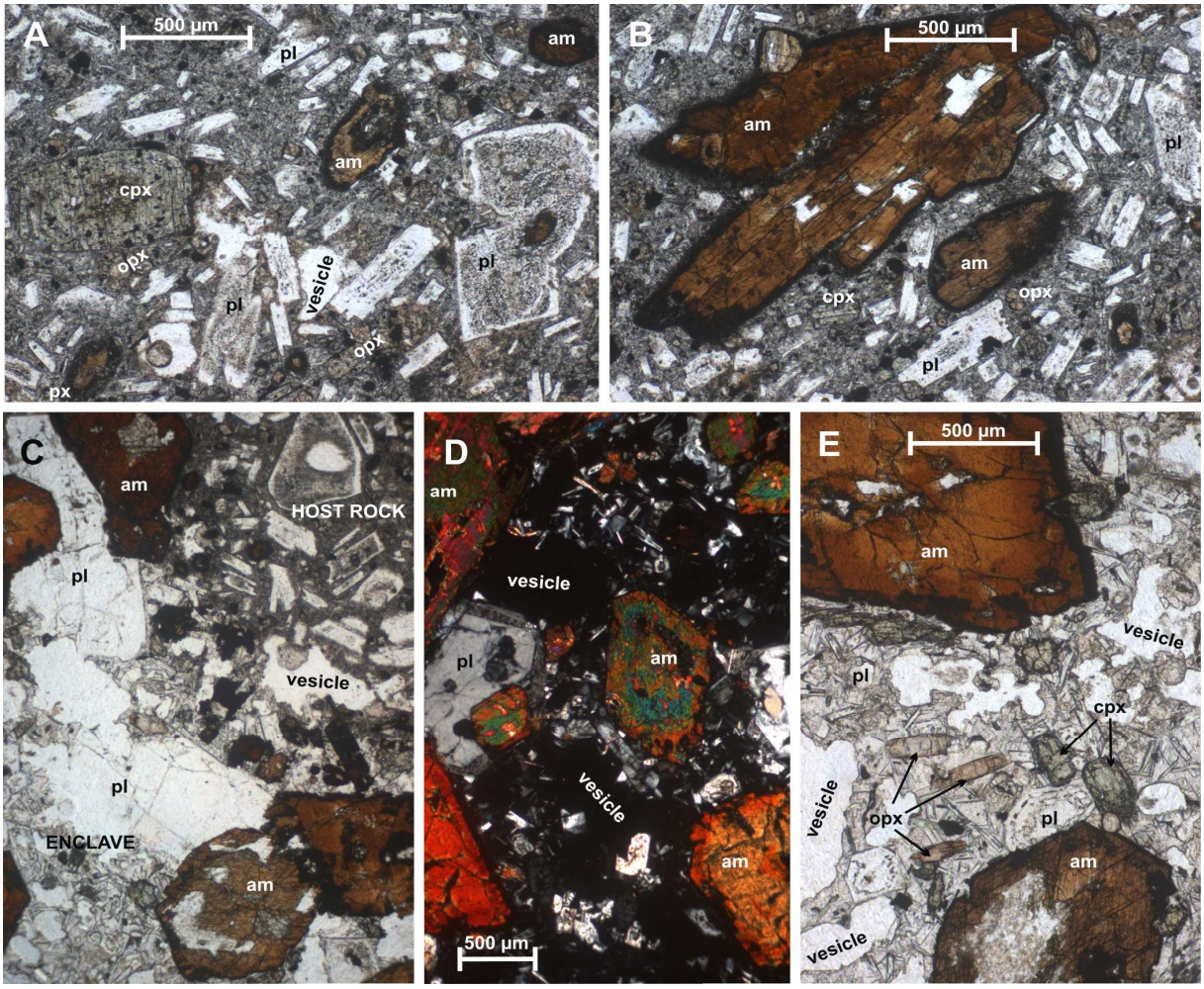

Figure 6.17. *Photomicrographs of host rock and enclave of the Oros amphibole andesite.* (A) Host rock IA75, ppl. Prismatic phenocrysts of am and pl define a flow texture around macro-phenocrysts of pl and cpx. (B) Host rock IA75, ppl. Large macro-phenocrysts of am with relatively thin opacite rims. (C) Enclave IA78, ppl. Sharp contact between very coarse-grained enclave and its host rock. (D) Enclave IA78, xpl. The framework consists mainly of large macro-phenocrysts of zoned am besides some euhedral pl. The 'groundmass' in between the framework crystals contains large vesicles and large amounts of prismatic pl phenocrysts. (E) Enclave IA78, ppl. Close-up of the vesicular, glassy groundmass with prismatic phenocrysts of pl, cpx and opx.

observed during fieldwork and none of the 9 Oros-Lazarides basaltic andesites contains micro-enclaves. Petrographic study of enclave IA72 reveals a framework of euhedral plagioclase, pseudomorphs of fine-grained opaque aggregates and subhedral clinopyroxene surrounding many large vesicles but little to no cryptocrystalline groundmass (Fig. 6.16G).

The Oros amphibole andesite at location 85 contains significantly more enclaves than the basaltic andesites as well as small clusters of quartz crystals which look similar to the larger quartz xenolith in the Skotini andesite (Fig. 6.5G). Its host rock mainly consists of prismatic plagioclase (macro-) phenocrysts but contains more groundmass than the Oros-Lazarides basaltic andesites (Fig. 6.17A). The large, prismatic phenocrysts have an An_{45} to An_{60} composition and define a flow texture around the macro-phenocrysts (Fig. 6.17B). Amphibole is the second major mineral phase with a seriate texture and, in contrast to the strongly dehydrated hydrous minerals of the Oros-Lazarides basaltic andesites, only shows relatively thin opaque reaction rims or limited replacement by fine-grained pyroxene (Fig. 6.17A-B). Clinopyroxene mostly occurs as euhedral macro-phenocrysts and orthopyroxene is usually present as phenocrysts (Fig. 6.17A). The groundmass of this Oros amphibole andesite consists of volcanic glass with large to small microlites of prismatic plagioclase, larger prismatic orthopyroxene, tabular microlites of clinopyroxene and Fe-Ti-oxides. Very coarse-grained enclave IA78 shows a sharp contact with its host rock (Fig. 6.17C) and consists of a crystal framework of mainly macro-phenocryst sized amphibole and some large, tabular plagioclase crystals (Fig. 6.17D). The euhedral framework amphiboles display a strong orange-brown to deep red-brown pleochroism and are zoned (Fig. 6.17D). This macro-phenocryst framework encloses a glassy groundmass which contains phenocryst-sized grains of plagioclase, clinopyroxene, orthopyroxene, smaller Fe-Ti-oxides and large, rounded vesicles (Fig. 6.17E).

6.4 Petrography of the Poros lavas and their enclaves

The same nomenclature applied to describe the grain size of primary crystals in the volcanic deposits of Methana and Aegina is also used throughout the following petrographic descriptions. Microscopic study of 11 host rocks suggests a homogeneous mineralogy for the dacites and andesites alike, despite the fact that they were classified as two distinct volcanic units on the geological map of Schwandner (1998) (Fig. 66).

All host rocks have plagioclase and amphibole as main mineral phases with a seriate crystal size distribution from large eu-to subhedral macro-phenocrysts over phenocrysts down to microlites (Fig. 6.18A). The prismatic plagioclase and amphibole phenocrysts thereby always form a magmatic flow texture (Fig. 6.18A-B). Plagioclase macro-phenocrysts (An_{45-55}) are tabular and their rims and/or cores can be sieve textured (Fig. 6.18A). They commonly show polysynthetic twinning but oscillatory zoning is only rarely present (Fig. 6.18C). Amphibole (macro-)phenocrysts are usually (oscillatory) zoned (Fig. 6.18A-B). They commonly show pale green-brown to orange-brown pleochroic colours (Fig. 7.3A) which can be more intense, ranging to deep red-brown, in lavas with a red-oxidised groundmass (Fig. 7.3B). Dehydration of amphibole crystals mainly occurs as opaque reaction rims of varying thickness (Fig. 6.18D) – replacement by a more fine-grained epitaxial pyroxene aggregate is sometimes observed in the vicinity of enclaves (Fig. 6.18E). Biotite is the third most abundant mineral and occurs as eu- to anhedral (macro-)phenocrysts with intense orange-brown to deep-red brown pleochroic colours (Fig. 6.18E-G). It only rarely shows replacement by fine-grained opaque minerals or a reaction rim of amphibole (±plagioclase ± Fe-Ti-oxides) (Fig. 6.18G). Quartz is the fourth mineral observed in all studied host rocks and always occurs as rounded, up to 5 mm large macro-phenocrysts without reaction rim (Fig. 6.18H). Two thirds of the host rocks furthermore contain significant amounts of eu-to subhedral clinopyroxene. This mineral is usually present as tabular, faint green phenocrysts clustered together in groups but single macro-phenocrysts also occur. Sometimes these clinopyroxene clusters are (partially) overgrown by amphibole (Fig. 6.18I), whereas the single, isolated clinopyroxene crystals can show anhedral amphibole inclusions in their core (Fig. 6.18J). These clinopyroxene-bearing lavas

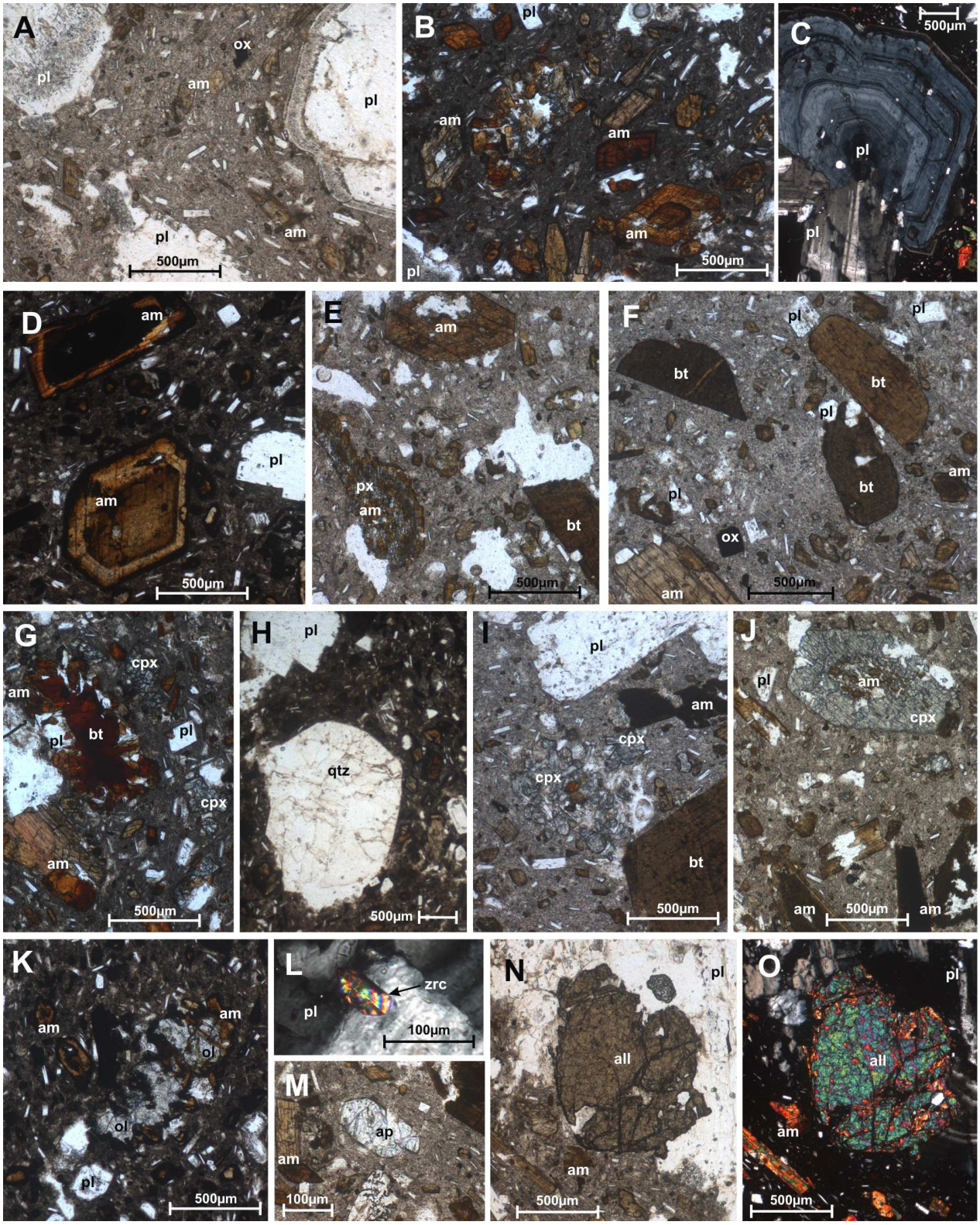

Figure 6.18. *Photomicrographs of the Poros dacitic and andesitic host rocks.* (A) dac IP49, ppl. Three differently sieve-textured pl macro-phenocrysts with flow texture in between. (B) dac IP298, ppl. Euhedral am crystals showing pleochroism and zoning. (C) dac IP45, xpl. Aggregate of tabular pl with polysynthetic twinning (bottom) and with oscillatory zoning (top). (D) dac IP45, ppl. Zoned am crystals with thick opacite rims. (E) and IP47, ppl. Epitaxial px pseudomorph with residual anhedral am besides not replaced am and bt macro-phenocrysts. (F) dac IP49, ppl. Subhedral bt crystals without alteration rim. (G) dac IP298, ppl. Anhedral bt crystal with rim of pl, am and ox. (H) dac IP45, ppl. Round qtz macro-phenocryst without reaction rim. (I) dac IP49, ppl. Cluster of faintly green, euhedral cpx. (J) and IP47, ppl. Large, euhedral cpx crystal with anhedral am. (K) dac IP45, ppl. Subhedral ol crystals with am mantle. (L) dac IP48, xpl. Euhedral zrc inclusion in pl. (M) and IP46, ppl. Euhdral, short prismatic phenocryst of ap in groundmass.(N) and IP46, ppl. Subhedral all crystal in pl. (O) Same as (N), xpl.

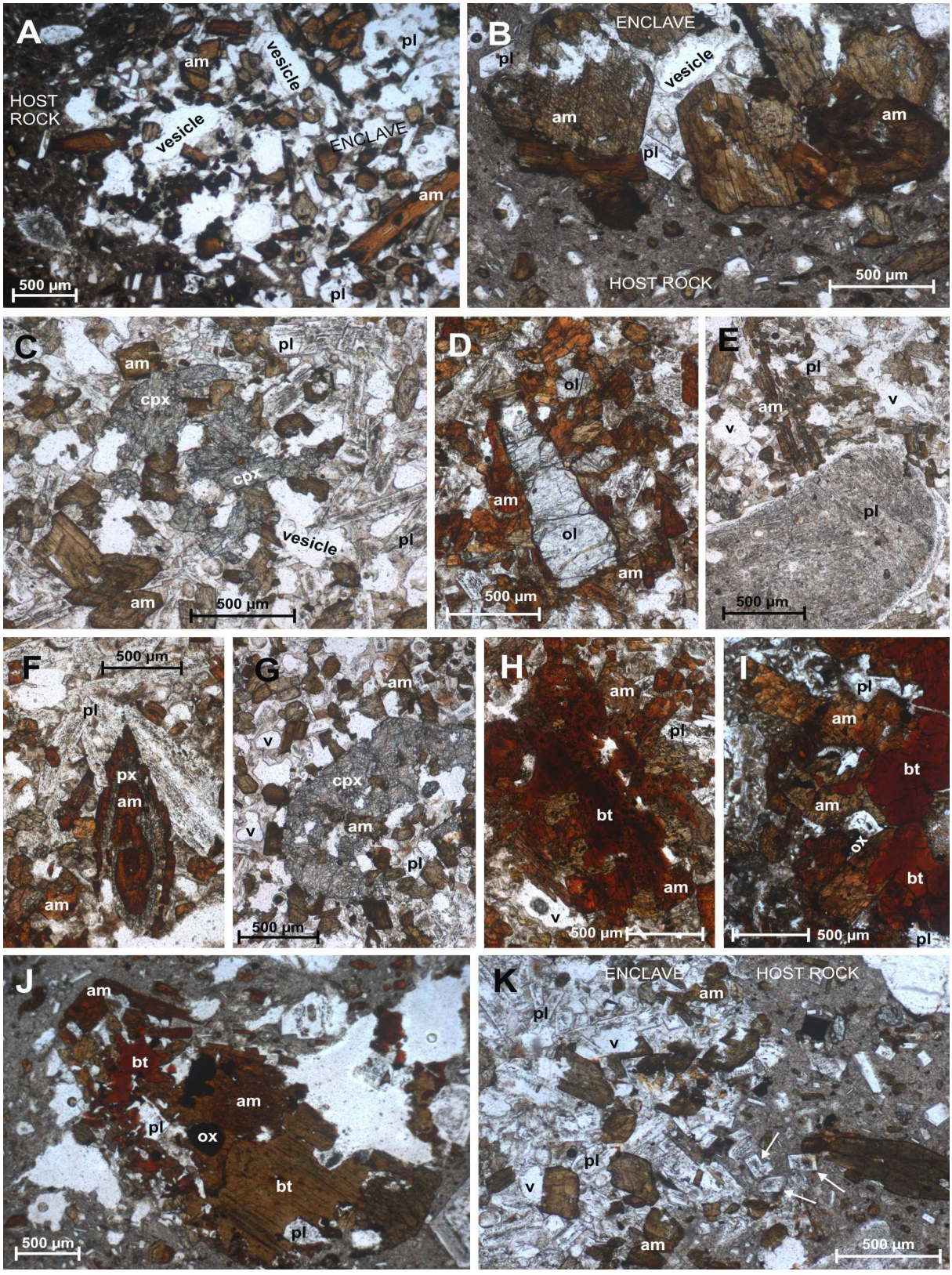

Figure 6.19. *Photomicrographs of enclaves and holocrystalline aggregates in Poros' lavas*. (A) Coarse-grained pl-am micro-enclave in dacite IP45. (B) Extremely coarse-grained pl-am micro-enclave in andesite IP46. (C) Enclave IP47, coarse-grained pl-am-cpx enclave. (D) Enclave IP50, macro-phenocryst of ol, mantled by am. (E) Sieve-textured pl crystal in enclave IP47. (F) Enclave IP50, zoned am crystal partially altered to px. (G) Large cpx crystal in enclave IP47. (H) Enclave IP50, anhedral bt crystal mantled by am. (I) Holocrystalline aggregate of pl + am + bt + ox in enclave IP53. (J) Holocrystalline aggregate of pl + am + bt + ox in host rock IP51. (K) Crumbling of enclave IP47 into its host rock.

do not contain olivine, which, however, does appear as a minor mineral phase in the host rocks without clinopyroxene (Fig. 6.18K). Fe-Ti-oxides are a minor mineral phase in all host rock samples and occur as eu-to anhedral microlites and small phenocrysts (Fig. 6.18A&F). Whereas apatite was an accessory microlite phase in the volcanic deposits of Aegina and Methana, it commonly present as euhedral phenocrysts in the host rocks of Poros (Fig. 6.18L). Zircon is observed in nearly all host rocks as euhedral inclusions in plagioclase, amphibole or biotite macro-phenocrysts (Fig. 6.18M). One of the clinopyroxene-bearing host rocks contains a large, subhedral allanite crystal included in a plagioclase macro-phenocryst (Fig. 6.18N-O). Orthopyroxene has not been identified in any of the Poros lavas.

Amphibole and plagioclase are also the main mineral phases in all enclaves collected from the Poros lavas. Micro-enclaves are abundantly present and usually consist of a coarse-grained amphibole-plagioclase crystal framework in a glassy groundmass with round vesicles (Fig. 6.19A-B). The micro-enclaves do not contain other mineral phases apart from those in the crystal framework, which can be so coarse-grained that its crystals resemble the host rocks' macro-phenocryst population (Fig. 6.19B). The enclaves identified during fieldwork have fine-to coarse-grained crystal frameworks that also consist of plagioclase and amphibole, but in addition contain significant amounts of greenish clinopyroxene (Fig. 6.19C). The fourth mineral present in all macroscopic enclave samples is olivine, occurring as heterogeneously distributed eu-to subhedral (macro-)phenocrysts that are mantled by amphibole (Fig. 6.19D). Rarely observed macro-phenocrysts of sieve-textured plagioclase (Fig. 6.19E), amphibole partially replaced by pyroxene (Fig. 6.19F), clinopyroxene with anhedral amphibole inclusions (Fig. 6.19G) and biotite mantled by amphibole (Fig. 6.19H) look very similar to macro-phenocrysts in the host rocks (see Fig. 6.18). Despite the fact that a few quartz quartz grains with clinopyroxene reaction rim were observed in enclaves during fieldwork, none of the thin sections contains one. Apatite, zircon and allanite were not identified in any of the enclaves either. A few prismatic orthopyroxene crystals occur together with clinopyroxene in enclave IP50.

One enclave contains a holocrystalline aggregate of eu- to anhedral biotite, amphibole and plagioclase (Fig. 6.19I). Such holocrystalline mineral aggregates also occur in Poros' volcanic host rocks (Fig. 6.19J). The contact between enclave and host rock is usually sharp and without chilled margin, but in some cases the framework crystals seem to be dispersed into the host rock's groundmass, representing enclave crumbling (Fig. 6.19K).

6.5 Geochemical data

All major and trace element concentrations and Sr-Nd-Pb and Hf isotopic compositions analysed for volcanic rocks from Aegina can be found in Appendices B3, C3, D3 and E ,respectively – the geochemical composition of the volcanic deposits on Poros is presented in Appendices B4, C4, D4 and E. As the K/Ar ages defined for all the volcanic rocks on these two islands are younger than 5 Ma (Fig. 6.3 & 6.6), age corrections have not been carried out. The geochemical data of sedimentary basement rocks of from Aegina and of the quartz-rich xenolith found in the Skotini andesitic dacite are collected in Appendix F2.

The geochemical data of Aegina's volcanic deposits are grouped and presented according to the island's volcanic stratigraphy and the samples' petrographic characteristics. Colour-coding is thereby similar to the colours used on the geological map (Fig. 6.2): 1) deposits from the first period of volcanic activity are red, except for 2) the more densely sampled Kokkinovrahos flow which is orange and used as measure for the geochemical range observed in products from a single eruption, 3) host rocks and enclave from the Kakoperato rhyodacite which mark the beginning of the second volcanic phase are purple and 4) lavas erupted from the Lazarides and Oros area during the second period of volcanic activity are all blue (see Fig. 6.20). All enclaves and host rocks from a certain flow or group of deposits are always indicated with the same symbol but which is unfilled for host rocks and filled for enclaves. Major and some trace element data for Aegina's volcanic rocks available in literature are also given

(Paraskevopoulos, 1958; Pe, 1973; Innocenti et al., 1981; Fytikas et al., 1987; Mitropoulos et al., 1987; Dietrich et al.,1988; Mitropoulos & Tarney, 1992; St. Seymour, 1996; Clift & Blusztajn, 1999) as well as the handful of published Sr-Nd-Pb isotope ratios (Pe, 1975, Gülen 1990).

The geochemical composition of the volcanic deposits of Poros is represented by green symbols: '**Δ**' in case of the 4 host rock samples and '**+**'for the 2 enclaves. To avoid obscuring the different volcanic trends on Aegina and cluttering the graphs, the major and trace element compositions published in literature or not included in the following diagrams. They define, however, the same compositional range as the samples studied in this work, as shown in the geochemistry graphs of Chapter 7.

6.5.1 Major and minor element geochemistry

The major element geochemistry obtained in this work for the volcanic centre of Aegina overlaps with the data available in literature. Aegina's volcanic deposits define a double trend: the Kakoperato host rocks are high-K rhyodacites whereas all other rocks are medium- and high-K basaltic andesites to andesitic dacites (Gill, 1981) (Fig. 6.20). The host rocks of the Kokkinovrahos lavas show a relatively uniform geochemical composition similar to all other biotite-hornblende andesites (Fig. 6.20). The host rocks of the Oros-Lazarides basaltic andesites define an even narrower geochemical range whereas both host rocks and enclaves from the Skotini andesite have distinctly different K contents depending on their sampling locality (medium-K for the host and enclave from the outcrop at point 60 but high-K for the two enclaves and two host rocks from sampling point 61- Fig. 6.20). The Kokkinovrahos deposits furthermore show a distinct geochemical gap between host rocks (60-63 wt% SiO_2) and enclaves (53-55 wt% SiO_2) and this feature is present throughout all deposits from the first period of volcanic activity: there is a geochemical gap of ca. 3 wt% SiO_2 between the andesitic host rocks and their basaltic andesitic to basaltic enclaves (Fig. 6.20). Besides a geochemical gap between the Kakoperato rhyodacites and all other volcanics, there is also a large geochemical gap between the Kakoperato host rocks (ca. 70 wt% SiO_2) and their andesitic enclave (ca. 57 wt% SiO_2) (Fig. 6.20).

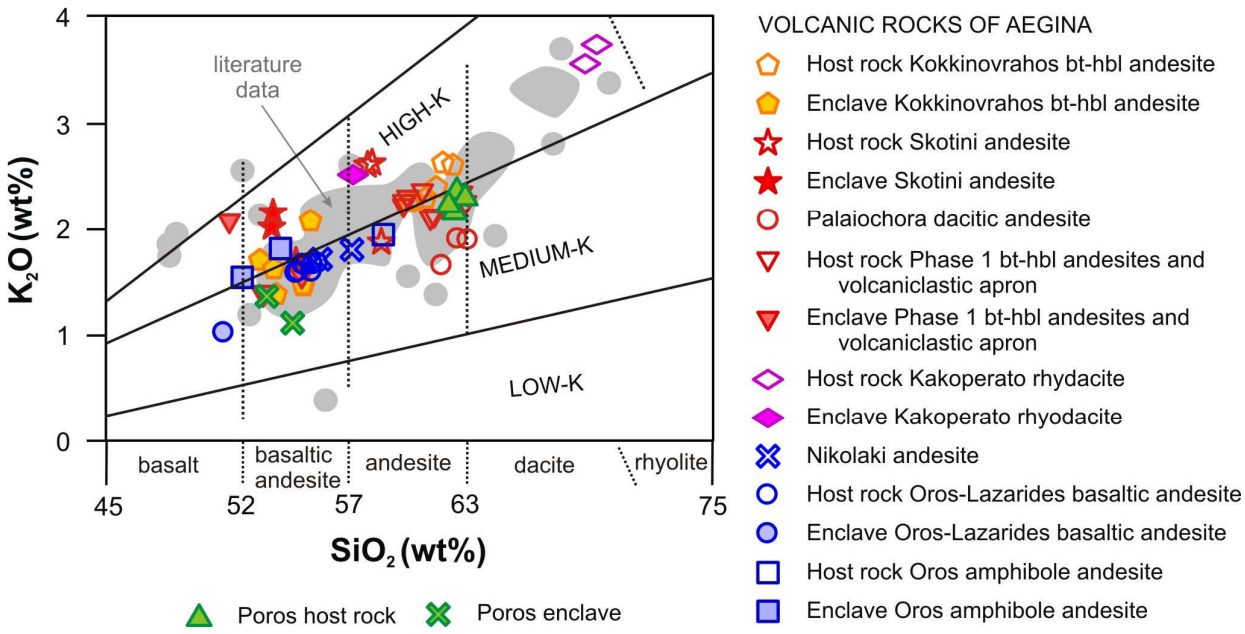

Figure 6.20. *K_2O-SiO_2 classification diagram of Gill (1981)*. Whereas Aegina's volcanic deposits and Poros host rocks straddle the boundary between medium-K and high-K rocks, the Poros enclaves plot at lower potassium contents in the medium-K field. Dotted lines indicate the silica ranges for basalts, basaltic andesites, andesites, dacites and rhyodacites after Le Maitre et al. (2002). Grey fields = literature data.

The enclave-poor mafic deposits of the Lazarides and Oros eruption areas define a continuous trend from basaltic andesites to andesites and are also separated from their mafic enclaves by a geochemical gap (Fig. 6.20).

The volcanic deposits of Poros show a bimodal distribution for their potassium contents. Their host rocks define a relatively narrow compositional range which straddles the boundary between medium-K and high-K compositions whereas the enclaves' medium-K geochemistry show somewhat more scatter (Fig. 6.20). Geochemical classification of the volcanic rocks from Poros identifies enclaves as basaltic andesites and host rocks as dacitic andesites (Fig. 6.20).

Harker variation diagrams for Aegina's volcanic rocks show little scatter and the same systematics as those observed in the potassium versus silica diagram (Fig. 6.20 – 6.21). The two Kakoperato rhyodacitic host rocks remain separated from all the other volcanic rocks, the latter of which show a well-defined trend of decreasing MgO, Fe_2O_3*, CaO, TiO_2 and MnO with increasing silica contents (Fig. 6.21A-E). Sodium contents of Aegina's basalts to dacitic andesites show a positive correlation with increasing differentiation (Fig. 6.21F). Host rocks from the first volcanic phase have distinctly higher silica contents than the range defined by the Phase 1 enclaves. The Oros amphibole andesite plots within the field of the andesitic host rocks of the first volcanic phase, whereas the Nikolaki enclave-free lavas (together with the Kakoperato enclave) plot between the Phase 1 andesites and their basaltic andesitic enclaves. Despite larger distances between their sampling localities, the Oros-Lazarides basaltic andesites always cluster very close to one another and within the compositional range of the Phase 1 enclaves. Aluminium and phosphor contents show significantly more scatter than other major and minor elements (Fig. 6.21F-G). This scatter is most pronounced at the silica-poor end of the variation diagrams: Oros amphibole andesite enclave IA78 combines relatively low Al_2O_3 with the highest P_2O_5 contents whereas Oros-Lazarides basaltic andesite enclave IA72 shows higher aluminium and lower phosphor contents (Fig. 6.21F-G). Besides elevated K_2O contents (Fig. 6.21), all samples from the Skotini andesite at sampling point 61 as well as volcaniclastic apron enclave IA321 contain very high amounts of P_2O_5 which are also reflected in some literature data (Fig. 6.21G), and is matched by a mineralogy with high abundances of apatite. The Palaiochora lavas combine elevated aluminium contents with low MnO concentrations as well as slightly higher TiO_2 and lower Na_2O and MgO (Fig. 6.21A, D-F).

The major element composition of the Poros host rocks and enclaves define the same trends with increasing silica contents as the volcanic series of Aegina do (Fig. 6.21). Their major element geochemistry usually falls within the range defined by the volcanic deposits of Aegina (TiO_2, MnO and Al_2O_3 – Fig. 6.21 D,E,G), plots near the higher concentrations observed on Aegina for (MgO and CaO – Fig. 6.21A,C) or coincides with Aegina's lower contents (Fe_2O_3* and Na_2O – Fig. 6.21B,F).

Based on MgO, SiO_2 and Fe_2O_3* concentrations, the most mafic rocks on Aegina are basaltic enclaves IA72, IA321 and IA78 and the rhyodacitic host rocks from the Kakoperato lava flow represent the most silica-rich samples of this volcanic centre (Fig. 6.20). Based on the Mg#, however, the Palaiochora dacitic andesites are the most evolved rocks instead of the Kakoperato rhyodacites, and enclave IA72 is not as mafic as the most primitive compositions represented by enclaves IA78 and IA321 (Fig. 6.22). The Mg# of the volcanic rocks of Poros is slightly higher than that of the main trend of the Aegina volcanic suite, in keeping with their magnesium, silica and iron contents (Fig. 6.22).

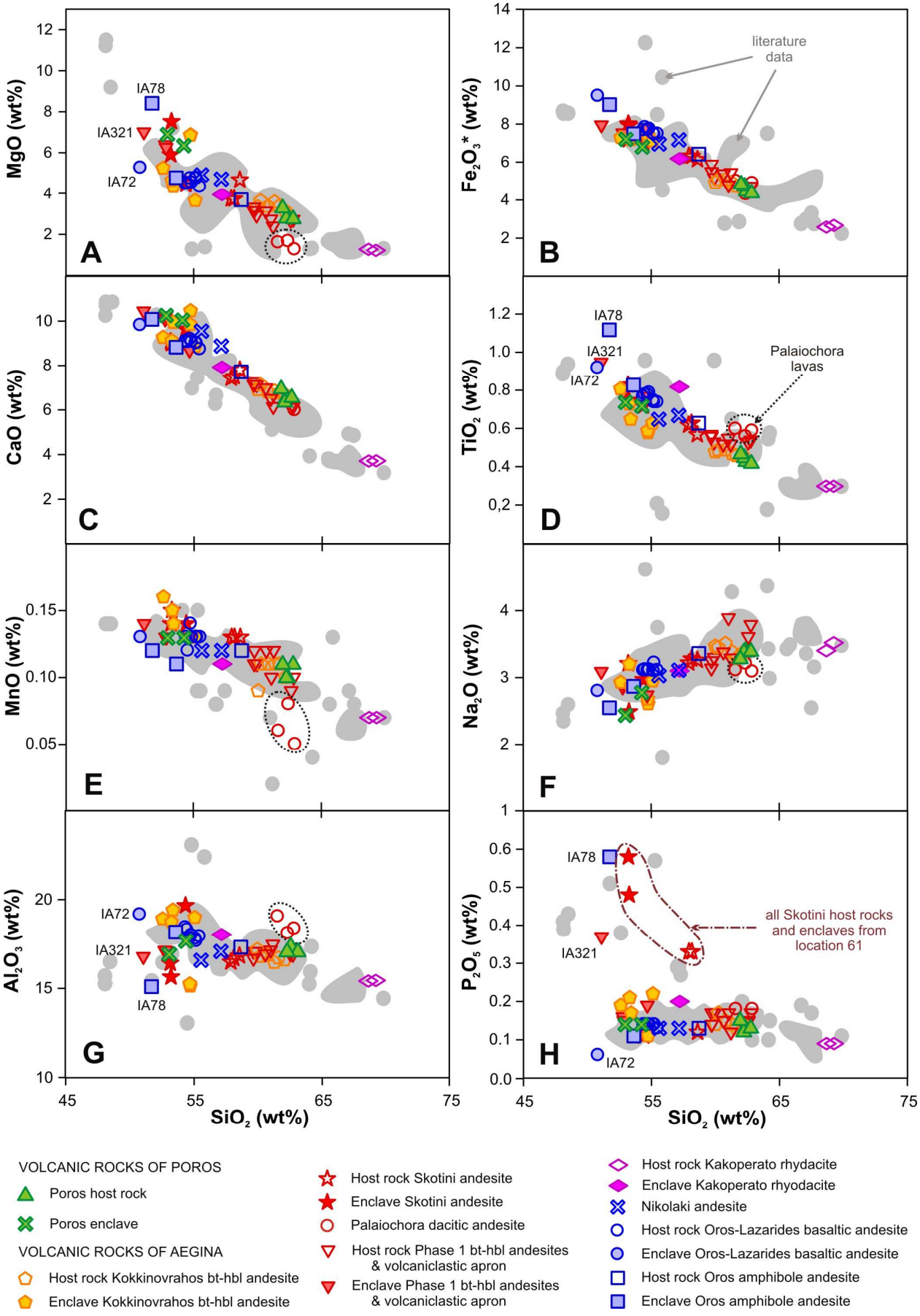

Figure 6.21. *Whole rock major and minor element variation diagrams for all volcanic rocks of Aegina of Poros.* Fe_2O3^* = all Fe presented as $Fe_2O_3^*$.

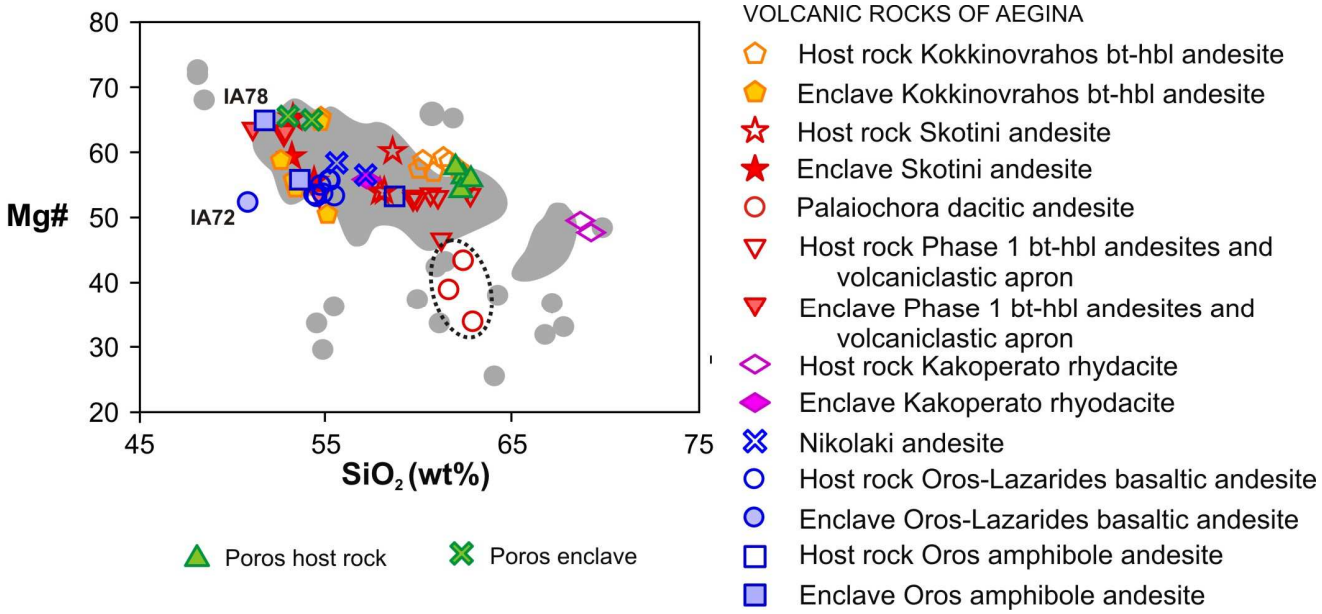

Figure 6.22. *Mg# (molar Mg/(Mg+Fe$_{tot}$)) versus silica contents* suggests that not the Kakoperato rhyodacites but the Palaiochora dacitic andesites are the most differentiated lavas.

6.5.2 Trace element geochemistry

With increasing differentiation, Aegina's mafic to intermediate volcanic rocks show decreasing **Sc** contents (ca. 45 to 12 ppm) in a well-defined trend on the extension of which the Kakoperato rhyodacites plot (ca. 8 ppm) (Fig. 6.23A). A similar negative correlation is observed for **Co**, **V** and **Cu**, but vanadium (cobalt and cupper, not shown) contents seem to be higher for the enclaves of the second period of volcanic activity (up to 310ppm instead of 220 ppm for the most V-rich rock from the first phase (Fig. 6.23B). **Y**ttrium contents show a scattered negative correlation with increasing silica contents (ca. 27 ppm down to ca. 12 ppm) – apart from the Palaiochora dacitic andesites which contain similar Y concentrations as the basaltic andesitic enclaves (Fig. 6.23C). Increasing differentiation also correlates with strongly decreasing **Cr** concentrations, but whereas it is always one of the basaltic enclaves from the second volcanic phase that contains the highest Sc, Co, V, Cu or Y concentrations, the basaltic enclave from the first phase shows the highest Cr concentration (210 ppm) amongst the most mafic rocks (Fig. 6.23D). The two Skotini enclaves from sampling point 61 and the 'green clinopyroxene' enclaves from Kakoperato are significantly Cr-enriched (up to 320 ppm) compared to rocks with similar silica contents. All Kakoperato lavas, the Skotini andesite from outcrop 61 and both Nikolaki andesites also show elevated Cr concentrations (Fig. 6.23D). **Ni**ckel (not shown) displays an overall similar negative trend with increasing silica as Cr does (from 70 to 5 ppm), except for the fact that only the Skotini host rocks and enclaves from location 61 are significantly Ni-enriched (up to 125 ppm). Increasing differentiation seems to coincide with enrichment of the high field strength elements. This positive correlation is expressed in a well-defined trend for **Ta** concentrations, apart from the Skotini host rocks and enclaves collected at outcrop 61 which are enriched relative to other volcanics with similar silica contents (Fig. 6.23E). The Palaiochora lavas have the highest **Zr** concentrations (up to 165 ppm) whereas the Kakoperato rhyodactites contain only slightly more Zr (120 ppm) than the basaltic andesites of the second volcanic phase (95-110 ppm). The 'outcrop 61' Skotini samples also show elevated Zr contents and the Kokkinovrahos enclaves define one Zr-enriched (120-130 ppm) and one Zr-depleted (80 ppm) cluster (Fig. 6.23F). The **Sr** concentrations of Aegina's volcanic rocks seem to vary randomly between 300 and 1000 pm, without clear correlation with eruption age or sampling location – a negative correlation between Sr and increasing silica is weakly recognisable in Fig. 6.23G. **Ba**rium concentrations also show large variations across Aegina

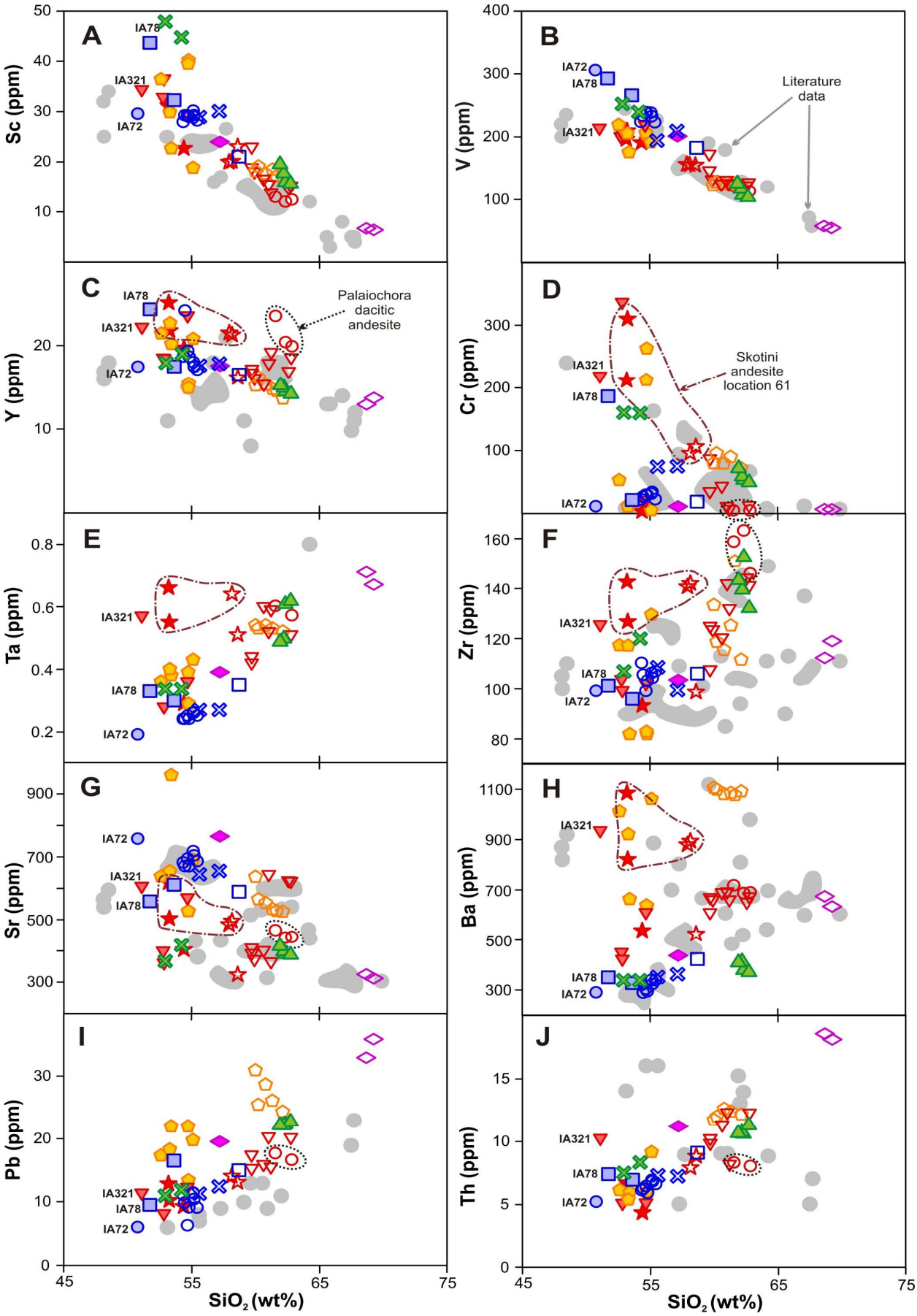

Figure 6.23. *Whole rock trace element Harker variation diagrams for all volcanic rocks of Aegina and Poros.* Symbols as in Fig. 6.21.

(250-1100 ppm) with a weak positive correlation with increasing silica, but they seem to mainly reflect the volcanic deposits' age as well as their geographic location (Fig. 6.23H). On the one hand, there is a distinct difference between the Ba contents of the first phase volcanics (450-1100 ppm) and those of the second volcanic period (250-450 ppm). On the other hand, host rocks erupted from different areas on Aegina cluster together at distinct Ba concentrations (Kokkinovrahos lavas, Skotini outcrop 61 rocks, … - Fig. 6.23H). **Be**ryllium concentrations (not shown) display a distribution very similar to that of Ba. Lead concentration data define two trends of increasing **Pb** contents with increasing silica: all basaltic andesitic lavas located in the central and southern parts of Aegina represent one trend which ranges from 5 to 25 ppm Pb, and the Kakoperato rhyodacite and north-easterly located Kokkinovrahos lavas define a second, parallel trend at higher Pb contents (15-35 ppm) (Fig. 6.23I). **Th**orium shows a single trend, with higher concentrations for more silica-rich host rocks (up to 18.5 ppm Th for the Kakoperato rhyodacites) – only the Palaiochora dacitic andesites plot below this trend at 8.5 ppm (Fig. 6.23J). Enclaves display scattered Th contents which range between 4 and 12 ppm. **U**ranium contents (not shown) behave similarly to thorium.

The volcanic series of Poros shows a distict geochemical gap between host rocks and enclaves, with its host rock trace element geochemistry coinciding with the compositional range of the Aegina lavas and their enclave trace element concentrations being overlapped by the geochemistry of Aegina's enclaves (Fig. 6.23). Poros volcanic rocks thereby show significantly less scatter than some individual volcanic units on Aegina such as the Kokkinovrahos biotite-hornblende andesite or the Skotini andesite (Fig 6.23). Their more narrow defined trend coincides with the average Ta, Nb, Th and Pb contents observed on Aegina, but shows elevated mounts of Sc, V, Cr, Zr, Cs and Li and lower concentrations of Y, Sr and Ba (Fig. 6.23 & Fig. 7.3).

Primitive mantle-normalised trace element abundance patterns of representative intermediate to felsic host rocks from Aegina show a trend of decreasing concentrations with increasing compatibility on which large negative anomalies of Ti, Nb and Ta, as well as strong positive anomalies of Pb and K, are imposed (Fig. 6.24A). Except 'outcrop 61' Skotini andesite IA331A these host rocks furthermore have a strong negative P anomaly and, apart from the Palaiochora lava IA61, a positive anomaly for U. The Kakoperato rhyodacite IA97 thereby shows the most extreme pattern with often the highest positive as well as lowest negative anomalies. Oros amphibole andesite IA75 has a pattern with overall modest peaks, apart from its distinctly stronger Nb-Ta depletion (Fig. 6.24A). Positive and negative anomalies are smallest in the Palaiochora lavas, which furthermore display the lowest concentrations of the most incompatible elements and somewhat elevated REE contents. These four types of intermediate to felsic host rocks have Primitive mantle-normalised abundance patterns that are parallel to one another – except for the apparently random variation of their Ba, and to a lesser extent Sr, concentrations (Fig. 6.24A). Aegina's basaltic andesites have a Primitive mantle-normalised trace element abundance pattern similar to that of the intermediate to felsic host rocks, but which is not as steep and with less pronounced Ti, Pb and U anomalies but a larger negative P anomaly (Fig. 6.24B). Amongst these mafic volcanics, the pattern with the smallest slope belongs to enclave IA72 from the Oros basaltic andesites. Its host rock IA71 shows more characteristics towards the intermediate lavas (larger amounts of the most incompatible elements, Cs to K, and a more positive Pb, less negative P and more negative Ti anomaly) (Fig. 6.24B). The dominant enclave type of the Kokkinovrahos deposits (IA338) displays an even steeper pattern with more pronounced anomalies – which is distinctly different from the less common 'green clinopyroxene' enclaves (e.g. IA336) from this unit (Fig. 6.24B). The Skotini andesite at sampling locality 61 also contains both 'normal' (IA331B) and 'green clinopyroxene' (IA332) enclaves, but these are identical to one another and distinguishable from the other basaltic andesites by their smaller negative Nb-Ta anomaly and weak positive (instead of strong negative) P anomaly (Fig. 6.24B).

As already shown by the trace element variation diagrams in Gif. 6.23, the primitive mantle-normalised trace element abundance patterns of Poros host rocks and enclaves coincide with the patterns that represent the main volcanic trends on Aegina (Fig. 6.24).

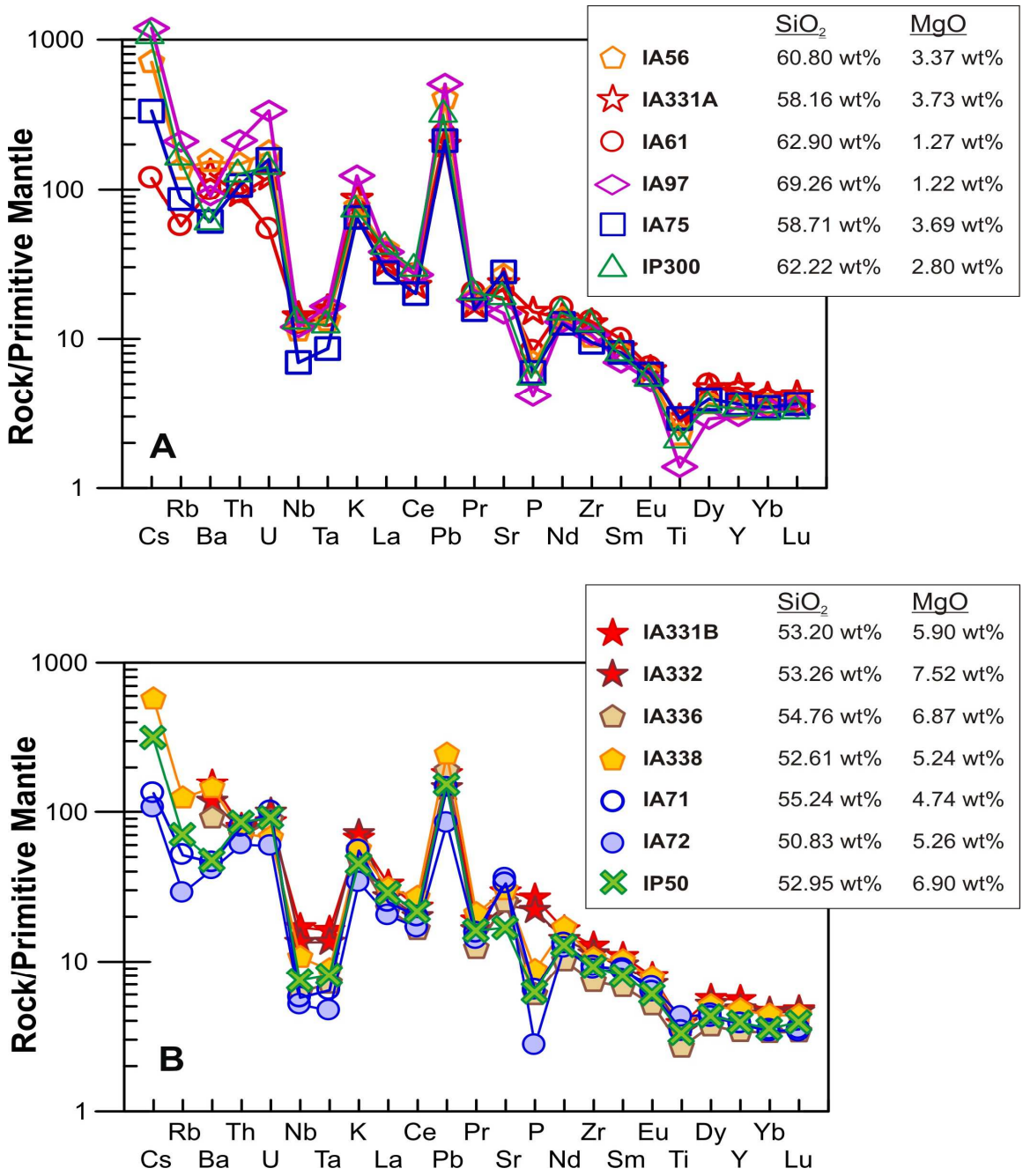

Figure 6.24. *Primitive mantle-normalised trace element abundance patters for representative samples from the volcanic islands of Aegina and Poros.* (A) Intermediate to felsic host rocks. (B) Basaltic andesitic host rocks and enclaves. Normalisation factors from Sun & McDonough (1989).

Figure 6.25 presents the chondrite-normalised rare earth element abundance patterns for the same host rocks and enclaves as presented in Fig. 6.24. Aegina's intermediate lavas show nearly identical chondrite-normalised REE patterns which are gently sloping from the LREE to the MREE, with a small negative Eu anomaly, and then continue sub-horizontally towards the HREE (Fig. 6.25A). The felsic Kakoperato rhyodacite starts and ends at similar La and Lu contents, respectively, but has a distinct pattern without Eu anomaly and a slight spoon-shape as REE contents increase somewhat from MREE to HREE (Fig. 6.25A). Despite some significant differences between their Primitive mantle-normalised trace element abundance patterns, the basaltic andesites have very similar chondrite-normalised REE patterns, which are nearly identical to those of the andesitic host rocks (Fig. 6.25B).

Their REE patterns are all parallel to one another, except for basaltic enclave IA72 which is slightly flatter. The most common and 'green clinopyroxene' enclaves from the Skotini andesite have the same REE composition whereas those from the Kokkinovrahos lavas are parallel but shifted relative to one another (Fig. 6.25B).

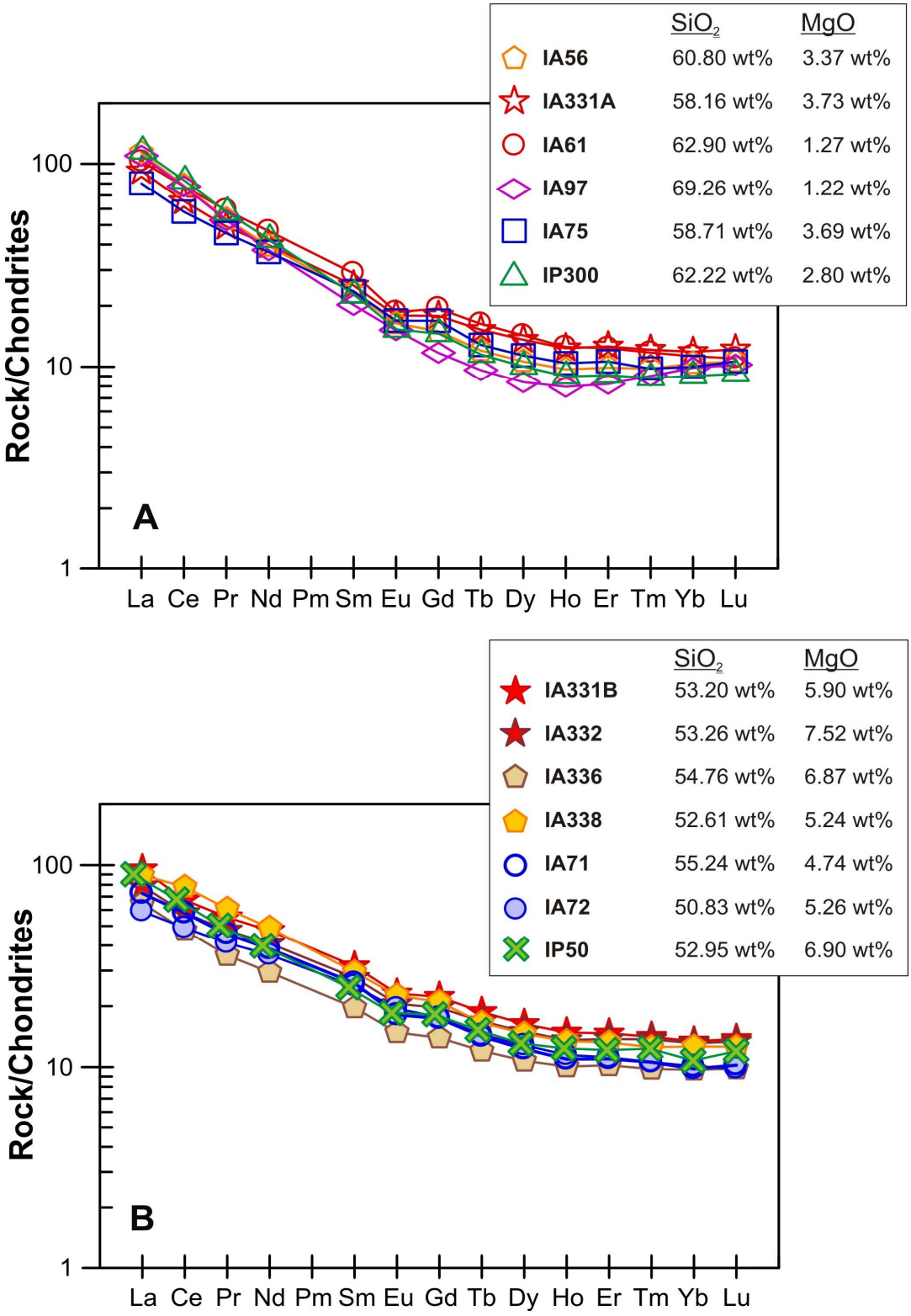

Figure 6.25 *Chondrite-normalised rare earth element diagrams for representative samples from the volcanic islands of Aegina and Poros.* (A) Intermediate to felsic host rocks. (B) Basaltic andesitic host rocks and enclaves. Normalisation factors from Sun & McDonough (1989).

Poros host rock IP300 has a chondrite-normalised REE abundance pattern very similar to that of Aegina's intermediate host rocks and also lacks the spoon-shaped curvature observed in the Kakoperato rhyodacite (Fig. 6.25A). The REE composition of host rocks from Poros are however slightly steeper than those from Aegina's lavas as they combine the highest La contents with the lowest amounts of Lu (Fig. 6.25A). The REE geochemistry of Poros enclaves, on the other hand, is not distinguishable from the chondrite-normalised REE abundance patters of Aegina's basaltic andesites (Fig. 6.25B).

6.5.3 Sr-Nd-Hf-Pb isotope geochemistry

The $^{87}Sr/^{86}Sr$ ratios of lavas from Aegina's first period of volcanic activity range from 0.7057 to 0.7076 which is higher than the Sr isotope ratios of the second phase volcanic deposits (0.7041-0.7048) (Fig. 6.26A). Only the Kakoperato rocks don't follow this simple scheme: whereas the enclaves indeed plot within the range of the second phase, the rhyodacitic host rock has a $^{87}Sr/^{86}Sr$ ratio typical of the average phase 1 host rock (Fig. 6.26A). The Sr isotopic ratios do not show any correlation with silica content (Fig. 6.26A). Although also not scatter-free, the $^{143}Nd/^{144}Nd$ and $^{176}Hf/^{177}Hf$ values define a negative correlation with increasing SiO_2 concentrations but do not display a geochemical gap between the first and second phase deposits (Fig. 6.26B-C). The ranges of Nd and Hf isotope ratios of the two different volcanic periods however only overlap partially, with the second phase basaltic andesites plotting at higher$^{143}Nd/^{144}Nd$ and $^{176}Hf/^{177}Hf$ ratios (0.51253 - 0.51263 and 0.28287 – 0.28292, respectively) than the Kakoperato rhyodacite and first phase andesites (0.51233 - 0.51257 and 0.28264 - 0.28289, respectively) (Fig. 6.26B-C). In a $^{143}Nd/^{144}Nd$ versus $^{87}Sr/^{86}Sr$ diagram, Aegina's volcanic deposits define two linear trends that are shifted parallel to one another: the first phase volcanics (including the Kakoperato rhyodacite) represent a trend of higher Sr isotopic ratio for a given Nd isotopic ratio, compared to the second phase lavas (Fig. 6.26D). Since Aegina's volcanic deposits represent a single linear trend in an εHf versus εNd diagram (Fig. 6.26E), the two trends in the $^{143}Nd/^{144}Nd$ versus $^{87}Sr/^{86}Sr$ diagram is due to the decoupling between the Sr and Nd-Hf isotopic systems. The singe, well-defined εHf - εNd trend reflected in the volcanic rocks from Aegina furthermore plots distinctly above and parallel to the terrestrial array (Vervoort et al., 2011) (Fig. 6.26E). Figure 6.26F shows that the strong correlation between timing of eruption (first or second volcanic phase) and Sr isotopic composition does not correlate with the lavas' whole rock Sr contents. The relatively unradiogenic lavas from the second volcanic period have Sr concentrations that vary from ca. 550 to 750 ppm and which are overlapped by the range of Sr concentrations observed in the first phase samples (ca 350-950 ppm) (Fig.6.26F). The sample with both the highest $^{143}Nd/^{144}Nd$ and $^{176}Hf/^{177}Hf$ ratios and lowest $^{87}Sr/^{86}Sr$ is Oros-Lazarides basaltic andesite IA80, whereas Palaiochora andesite IA61 shows the least radiogenic Nd-Hf and most radiogenic Sr composition of all volcanic rocks from Aegina (Fig. 6.26).

The Sr-Nd-Hf isotopic composition of the volcanic deposits on Poros coincides with the $^{87}Sr/^{86}Sr$, $^{143}Nd/^{144}Nd$ and $^{176}Hf/^{177}Hf$ ratios of the main trend of Aegina's first phase of volcanic activity (Fig. 6.26). Poros lavas are thereby very similar to the Palaiochora dacitic andesite whereas their enclaves reflect more scatter as they plot within the relatively large compositional range of Aegina phase 1 enclaves (Fig. 6.26). With increasing silica contents, there are clear positive and negative correlations between respectively Sr and Nd-Hf isotopic compositions of Poros' volcanic deposits (Fig. 6.26A-C)

The Pb isotopic systematics of the volcanic deposits of Aegina show that Kokkinovrahos enclave IA345 has the lowest $^{206}Pb/^{204}Pb$, $^{207}Pb/^{204}Pb$ and $^{208}Pb/^{204}Pb$ ratios (Fig. 6.27). Whereas there is no correlation between silica content and $^{206}Pb/^{204}Pb$ ratio, both $^{207}Pb/^{204}Pb$ and $^{208}Pb/^{204}Pb$ ratios seem to become increasingly radiogenic at higher SiO_2 concentrations (Fig. 6.27A-C). Whereas Aegina's most radiogenic sample is again Palaiochora andesite IA61 for the $^{207}Pb/^{204}Pb$ and $^{208}Pb/^{204}Pb$ ratios, it is the enclave sampled from the volcaniclastic apron, IA321, that shows the highest $^{206}Pb/^{204}Pb$ ratio

(Fig. 6.27D-E). Plotting the geochemical data of the latter two radiogenic Pb ratios against one another indeed results in two distinct linear trends that intersect: the Pb isotopic composition of volcanic rocks from the first period of volcanic activity define a steeper trend than the deposits from the second volcanic phase (Fig. 6.27F).

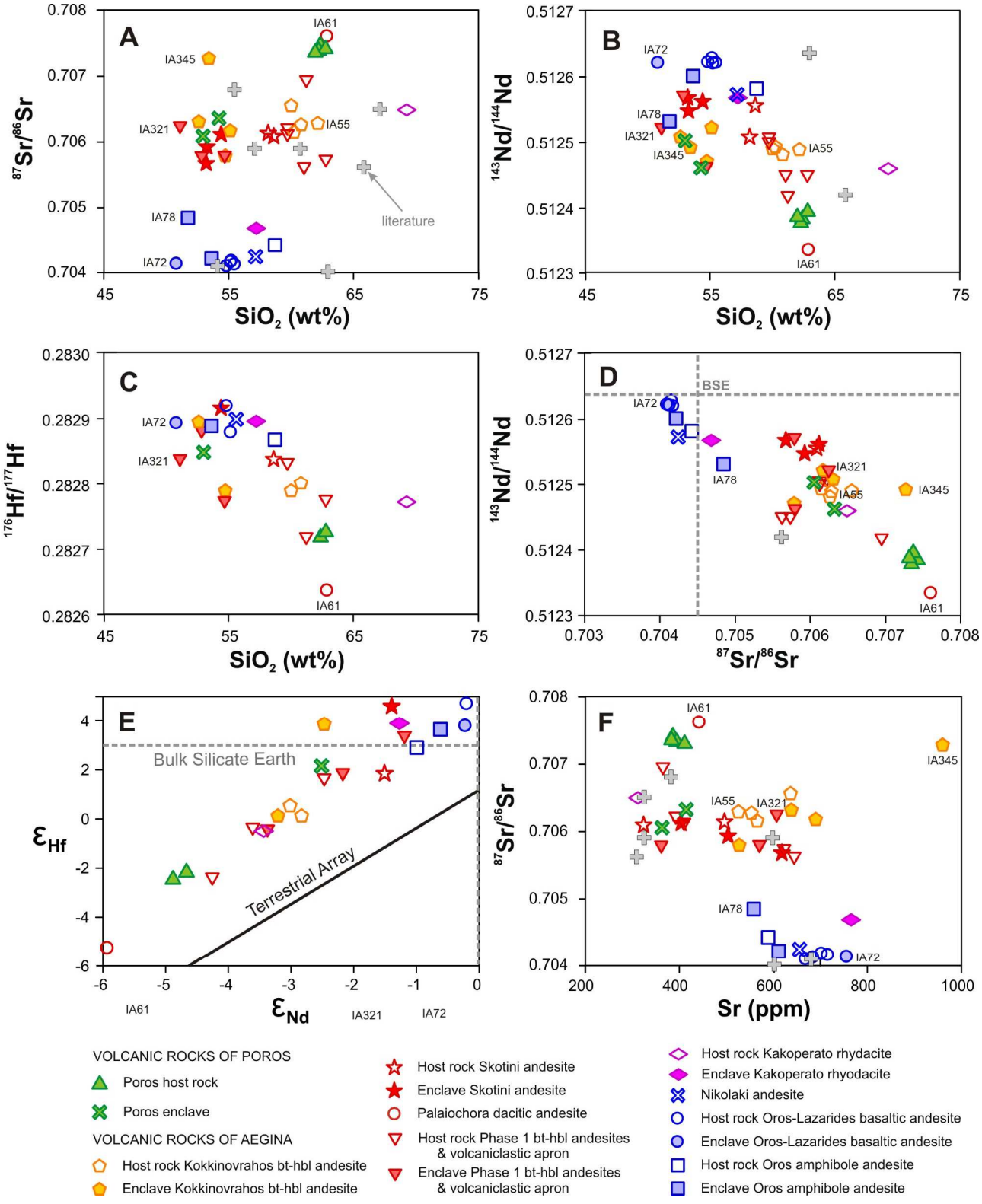

Figure 6.26. *Sr, Nd and Hf isotopic composition of the volcanic rocks from Aegina and Poros.* BSE = Bulk Silicate Earth (Workman & hart, 2005), Terrestrial Array from Vervoort et al. (2011).

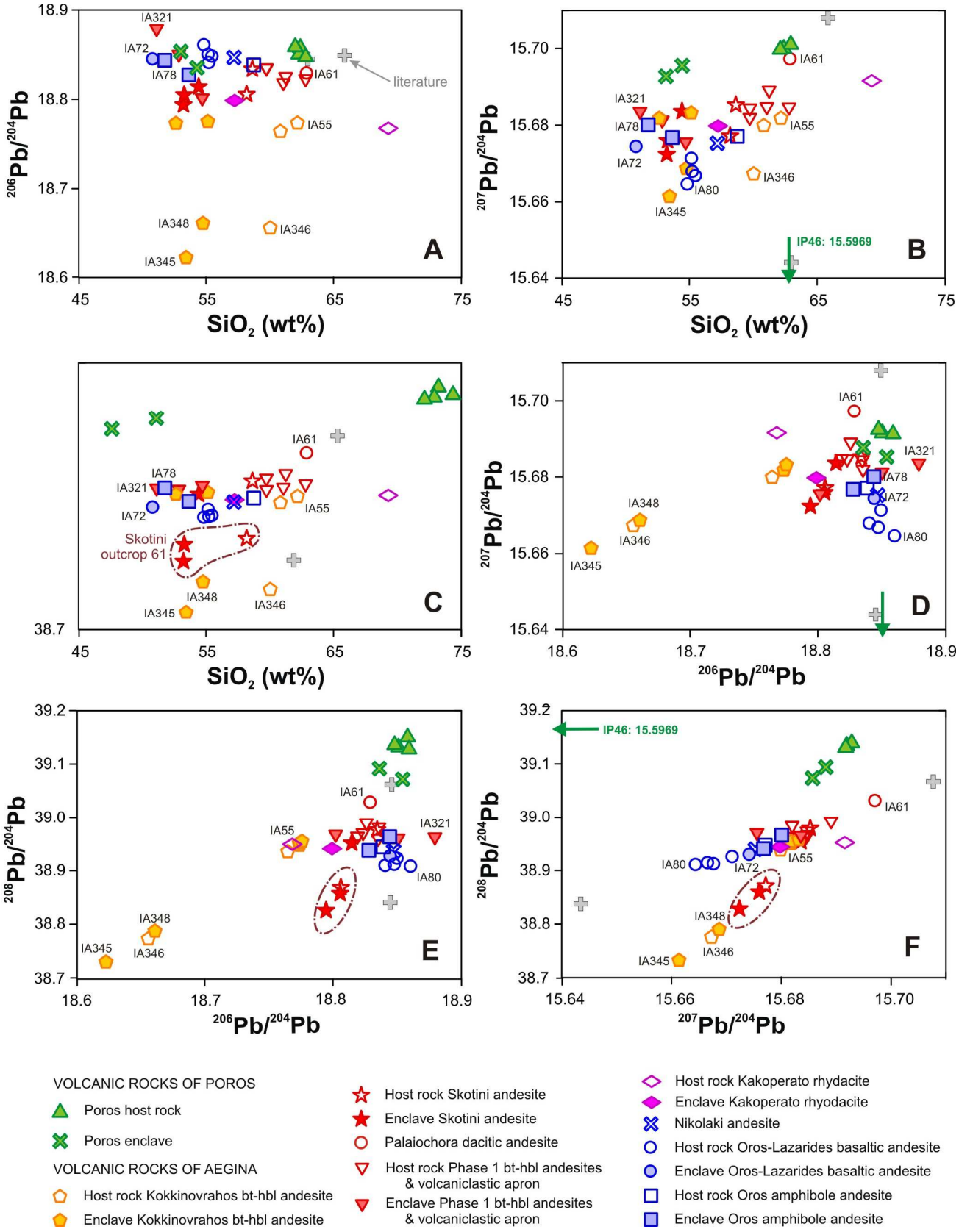

Figure 6.27. *Pb isotopic composition of the volcanic rocks from Aegina and Poros.*

The volcanic rocks on Poros also reflect a discrepancy between their $^{206}Pb/^{204}Pb$ ratios and their $^{207}Pb/^{204}Pb$ and $^{208}Pb/^{204}Pb$ ratios: whereas the former plot amongst the most radiogenic compositions of Aegina's first phase volcanics, the latter are distinctly higher for Poros than for any deposit on Aegina (Fig. 6.27A-C). Host rocks and enclaves from Poros usually show very similar Pb isotopic compositions, except for the anomalously low $^{207}Pb/^{204}Pb$ ratio of host rock IP46 (Fig. 6.27B).

6.6 Discussion of petrographic observations and geochemistry of Aegina

The modifications to the geological map of Dietrich et al. (1993a), already introduced in section 6.1, are clarified with the petrographic observations and geochemical data that led to them. Literature microprobe data of amphiboles from Aegina are used to obtain estimates of the pressure and depth at which they crystallised. Literature data on the composition of Aegina's other minerals are used for the calculation of crystallisation models. Existing hypotheses concerning the petrogenesis of some of Aegina's lavas are assessed with the new geochemical data obtained in this study. The sedimentary basement samples and quartz-rich xenolith from the Skotini andesite are tested as potential upper crustal contaminants. Finally, all data and interpretation will be synthesised into a model for the magma plumbing system below Aegina.

6.6.1 Suggested modifications to the geological map of Aegina

The geological map and volcanic stratigraphy from Dietrich et al. (1993a) were the basis of this study and used to target at least one outcrop of each volcanic unit for sampling (Fig. 6.1). Microscopic and geochemical study of the volcanic rock samples however revealed a heterogeneous composition between different samples from a single outcrop or between different outcrops of a single volcanic unit, as well as petrographic and geochemical homogeneity across supposedly different units. Furthermore, the names given to certain units on the geological map of Dietrich et al. (1993a) do not agree with the geochemical classification of Aegina's volcanic deposits in the TAS-diagram of Le Maitre et al. (2002) (see Fig. 6.20 in which dotted lines represent the silica ranges for basalt, basaltic andesites, andesites, dacites, rhyodacites and rhyolites). Dietrich et al. (1988) discuss the discrepancy between nomenclature based on whole rock major element chemistry (andesite) or on groundmass composition and inferred phenocrysts (dacites), and eventually prefer the second classification for the identification of Aegina's intermediate lavas. However, this discrepancy is not observed for Methana's volcanic deposits, which have been classified according to their whole rock geochemistry.

In order to apply the same classification for all volcanic rocks in the Saronic Gulf and thereby facilitate comparison between them, Aegina's volcanic deposits have been re-classified on the basis of their whole rock major element concentrations in the present work. This results in slight adaptations of the geological map (Fig. 6.2) which partially reflect older geological maps of Davis (1957) and Gaitanakis (1984). The correlation between the proposed volcanic stratigraphy and the one of Dietrich et al. (1993a) is presented in Table 6.2, in which the colour shading matches the colours on the modified geological map (Fig. 6.2) and indicates which older volcanic groups belong to the newly proposed units. This table also shows the K/Ar radiometric ages that have been obtained for some of Aegina's volcanic rocks: the ages suggested (but apparently not published) by Dietrich et al. (1993a) are presented together with their volcanic stratigraphy, whereas the K/Ar dating of four other publications are, where possible, linked to the old volcanic stratigraphy and presented separately. More K/Ar radiometric analyses are however needed to further define the ages of Aegina's magmatic deposits and clarify its volcanic evolution. The basis of the modified stratigraphy is explained below. Some simplifications have been carried out in the form of either dropping a geographical name if there are more than two areas at which the respective volcanic deposits are located, or placing the geographic name in front of the (petrographic-)geochemical classification if the unit is specific for certain areas.

	Revision based on this study		Dietrich et al. (1993a)	
	Volcanic stratigraphy	***Age*** ^{Literature}	***Volcanic stratigraphy***	***Age*** ^{4}
SECOND PERIOD OF VOLCANIC ACTIVITY	Oros hornblende andesite		Hypersthene andesite (Oros & Lazarides type)	~ 1.6 Ma
	Oros-Lazarides basaltic andesite	2.1±0.1 Ma [2] 2.1±0.3 Ma [3]	Andesite (Oros type)	~ 1.6 Ma
			Basaltic andesite or high-alumina basalt (Oros type)	~ 1.6 Ma
	Nikolaki andesite		Hornblende andesite (Nikolaki type)	~ 1.6 Ma
	Kakoperato rhyodacite	3.1±0.4 Ma [3]	Rhyodacite (Kakoperato type)	~ 1.6 Ma
VOLC. PAUSE				
	Volcaniclastic apron	3.9±0.1 Ma [1]	Epiclastic flows	
			Volcaniclastic flows	
FIRST PERIOD OF VOLCANIC ACTIVITY	Phase 1 biotite-hornblende andesite	2.8±0.3 Ma [5]	Hornblende dacite (Koutalou type)	~ 2.0 Ma
		3.4±0.2 Ma [3]	Biotite-hornblende dacite (Tourli, Raikou & Analypsis type)	2.0-3.4 Ma
		3.7±0.9 Ma [5] 3.9±0.2 Ma [3]	Biotite-hornblende dacite (Megali Korifi & Kamara type)	3.8-4.2 Ma
	Kokkinovrahos biotite-hornblende andesite	4.7±0.2 Ma [3]	Biotite-hornblende dacite (Kokkinovrahos type)	3.8-4.2 Ma
	Palaiochora dacitic andesite		Biotite-hornblende dacite (Palaiochora type)	4.2-4.4 Ma
	Skotini andesite	3.6±0.3 Ma [5] 3.9±0.3 Ma [2]	Andesitic dacite (Skotini type)	4.2-4.4 Ma
	Pyroclastic rocks	**4.4±0.2 Ma [1]**	**Pyroclastic rocks**	

K/Ar radiometric dates: [1] Müller et al., 1979; [2] Pe-Piper et al., 1983; [3] Fytikas et al., 1987; [4] Dietrich et al., 1993a; [5] Matsuda et al., 1999.

Table 6.2. *Correlation between the newly proposed volcanic stratigraphy and the older one* from Dietrich et al. (1993a), including the K/Ar ages of Aegina's volcanic deposits available in the literature.

Only one tuff was observed during fieldwork and its microfossil content (Radiolarian, Fig. 6.8) suggested that its geochemistry is not representative of an original magma composition. The oldest volcanic unit on Aegina therefore remains known as the 'Pyroclastic rocks' unit.

Different samples from the Skotini andesite unit are petrographically very similar (Fig. 6.11), but their host rocks are not 'andesitic dacite' since they all plot in the andesite field, near the boundary with the basaltic andesites, to which all Skotini enclaves belong (Fig. 6.20). Despite the petrographic homogeneity across the two Skotini outcrops, host rocks and enclaves from location 61 display a distinctly different geochemistry from the samples taken at location 60 (in case of MgO, Mg#, Sc, Y,

Sr, and $^{87}Sr/^{86}Sr$-$^{143}Nd/^{144}Nd$) and sometimes even from the main Aegina trend (in case of K_2O, P_2O_5, Cr, Ta, Zr, Ba, and Pb isotopic composition) (Fig. 6.20-23 an Fig. 6.26-6.27).

The Palaiochora dacitic andesite has a distinct petrography as it is the only rock with strong brown-green to bluish-green pleochroic amphibole (Fig. 6.12B & G). It is furthermore the only unit of the first volcanic period with few to no enclaves and besides the Kokkinovrahos deposits, the only other volcanic unit which is geographically isolated within the northern area of Aegina (Fig. 6.2). Geochemically, it straddles the border between andesites and dacites instead of representing a true dacite (Fig. 6.20). This volcanic unit furthermore has a geochemical composition that is distinct from the other Aegina volcanics in terms of its K_2O, MgO, TiO_2, MnO, Na_2O, Al_2O_3, Mg#, Y, Zr, Th concentrations and $^{87}Sr/^{86}Sr$, $^{143}Nd/^{144}Nd$, $^{176}Hf/^{177}Hf$, $^{207}Pb/^{204}Pb$ and $^{208}Pb/^{204}Pb$ ratios (Fig. 6.20-6.23 an Fig. 6.26-6.27).

Despite the larger number of samples collected from the Kokkinovrahos biotite-hornblende andesite, the mineralogy of the host rocks of this unit is homogeneous, and the petrography of its enclaves defines only two distinct groups (Fig. 6.9 – 6.10). Although relatively close to the boundary of the dacite field, the host rocks are geochemically all andesites (Fig. 6.20). Whereas the geochemistry of their enclaves displays some scatter, the Kokkinovrahos host rocks always cluster together and represent a geochemical composition often similar to the "Phase 1 biotite-hornblende andesites" (see below), except for their different Mg#, Y, Cr, Ba, Pb concentrations and distinct $^{206}Pb/^{204}Pb$ ratios (Fig. 6.22-6.23 & Fig. 6.26-6.27). Despite their overall geochemical homogeneity across the different sampling outcrops, the Pb isotopic composition of the northward directed flows (locations 67-68) is distinctly different from those in the southern part of the Kokkinovrahos deposits (Fig. 6.27).

The Phase 1 biotite-hornblende andesite unit encompasses both the two younger 'biotite-hornblende dacite' units and the 'Koutalou hornblende dacite' from Dietrich et al. (1993a) since the samples from these enclave-bearing units all display similar microscopic characteristics (compare Fig. 6.1 to 6.2). Their petrography only shows slight variations in the amount of biotite, the presence or absence of zoning in amphiboles and the fact that whereas most amphiboles display green-brown to yellow-brown pleochroism, some samples have distinct orange-brown to deep-red brown pleochroic amphibole (Fig. 6.12 A, C-F, H-I & Fig.6.13). Geochemically, they are andesites (instead of dacites) (Fig. 6.20). They are homogeneous with respect to major, minor and trace elements and resemble the Kokkinovrahos and Palaiochora deposits, defining the 'main Aegina trend' for the intermediate to more felsic volcanic rocks (Fig. 6.20-6.23). On the one hand, their Sr-Nd-Hf isotopic compositions show more scatter than the Kokkinovrahos deposits and probably reflect different sampling locations (Fig. 6.26). Their Pb isotopic geochemistry, on the other hand, is homogeneous, especially in comparison to that of the Kokkinovrahos rocks (Fig. 6.27).

The only sampling location of the volcaniclastic apron was near an outcrop of the Phase 1 biotite-hornblende andesites. Given the inferred petrogenesis of this unit (through erosion and deposition of older volcanic deposits during a prolonged period without volcanic activity) it is no surprise that the petrography and geochemistry of the sampled volcaniclastic host rock and enclave are similar to those of the nearby Phase 1 unit. Whereas the original Aegina geological map (Dietrich et al., 1993a) made a distinction between "volcaniclastic flows – often mixture of pyroclastic, autoclastic and epiclastic processes, partially lahars" and "epiclastic flow", no clear differences were observed during fieldwork and both types of deposits are thus grouped together within the unit of the volcaniclastic apron.

The Kakoperato rhyodacite lava flow displays a homogenous petrography (very large volume of cryptocrystalline groundmass with minor amounts of clearly resorbed, rounded phenocrysts – Fig. 6.14) and geochemistry (very felsic, only rhyodacite and even near the border of the rhyolite field – Fig. 6.20) which is distinct from any other volcanic deposits on Aegina. This unit's name according to Dietrich et al. (1993a) is thus preserved.

The enclave-free rocks from the Nikolaki andesite have a whole rock geochemistry that plots close to or within the basaltic andesite field (Fig. 6.20) – but their classification as overall andesitic rocks is maintained. However, given the absence of amphibole as a microlite or phenocryst phase and the fact that its rare hydrous macro-phenocrysts are usually completely replaced by opaque aggregates (Fig. 6.15), 'hornblende' was omitted from this deposit's name. The geochemical composition of these Nikolaki andesites usually plots between the more mafic basaltic andesites and the main trend of Aegina's more felsic magmas (Fig. 6.21-6.23 and Fig. 6.26-6.27).

The three volcanic units which are the youngest on Aegina according to Dietrich et al. (1993a) are located near the Oros and Lazarides eruptive centres (Fig. 6.1). Samples for each of these three supposedly distinct basalts, basaltic andesites and andesites however display very similar microscopic and geochemical characteristics. Volcanic rocks from sampling points 79 to 84 are therefore grouped together in one unit, the Oros-Lazarides basaltic andesites (Fig. 6.2). They are petrographically rather similar to the Nikolaki andesites, except for the fact that 1) their olivine crystals are usually small and with red iddingsite rims instead of large, colourless and eu-to subhedral crystals, 2) they have significantly more groundmass, mainly more plagioclase phenocrysts which display a seriate crystal size distribution and magmatic flow foliation and 3) instead of greenish clinopyroxene, the second most common minerals are pseudomorphs after hydrous phases (compare Fig. 6.15 to Fig. 6.16). Also in contrast to the enclave-free Nikolaki andesite, the Oros-Lazarides basaltic andesites contain rare basaltic enclaves (Fig. 6.20). The main reason, however, to group all host rocks sampled from these different locations into one unit is their extremely homogeneous major, minor and trace element concentrations and Sr-Nd-Hf-Pb isotopic composition, showing less geochemical variation than the Kokkinovrahos host rocks, sampled from geographically more clustered outcrops (Fig. 6.20-6.23 and Fig. 6.26-6.27).

Whereas the outcrop sampled at location 85 should, according to Dietrich et al. (1993a – Fig. 6.1) also represent the above described unit, this lava contains significantly more enclaves (Fig. 6.5C-D) as well as small clusters of quartz crystals which look similar to the larger quartz xenolith in the Skotini andesite (Fig. 6.5G) but are not observed in the Oros-Lazarides basaltic andesites. Besides its distinct macroscopic appearance, the Oros hornblende andesite also has petrographic characteristics different from the basaltic andesites (compare Fig. 6.16 to Fig. 6.17): 1) no olivine was observed in either host rock or enclave samples, 2) its host rock contains amphibole as second most important mineral, showing a seriate crystal size distribution and few to no disequilibrium features, 3) its rounded quartz crystals are not mantled by mafic minerals, and 4) its enclaves have a distinct texture with macro-phenocryst sized, orange-brown to deep red-brown pleochroic, oscillatory zoned amphiboles that dominate the crystal framework. Its major, minor and trace element contents are similar to the andesites of the first phase of volcanic activity (Fig. 6.20-6.23), but its $^{87}Sr/^{86}Sr$ composition clearly shows its affiliation with the other magmas from the second period of volcanism (Fig. 6.26). The lavas at location 85 are therefore classified as a new volcanic unit of which the boundaries are temporarily drawn based on the classification of nearby outcrops 81 to 84 as well as the extent of whitish discoloration observed at this locality on Google Earth (Fig. 6.2). More samples need to be collected and analysed from this Oros hornblende andesite in order to define its geographical extent. K/Ar radiometric dating should also be carried out on this new volcanic unit to allow identification of its relative position within the eruptive history of the second phase volcanics, but for now it is interpreted as the youngest volcanic deposit based on the outcrop's topography.

6.6.2 Different types of amphibole and their crystallisation conditions

Petrographic study shows that all host rocks from the first period of volcanic activity contain (traces of) amphibole. Within the more mafic Skotini volcanics, amphibole and biotite are partially to completely replaced by a pseudomorph of fine-grained opaque minerals, pyroxene (± plagioclase) or a combination of both (Fig. 6.11A, C-E, H). Enclaves from these Skotini lavas contain even less relic hydrous phases as their prismatic amphibole phenocrysts are often completely replaced by opacite

(Fig6.11 F-G). The disequilibrium features of the vast majority of hydrous minerals in the Skotini lavas are in sharp contrast with the eu- to subhedral and often completely unaltered amphibole (and biotite) crystals abundantly present in both host rocks and enclaves of all other, more felsic lavas of the first volcanic phase (Fig 6.9-6.10-6.12-6.13). Petrographic characteristics of these amphiboles suggest three distinctly different types of amphibole. Deposits of the enclave-free Palaiochora lavas contain amphibole (macro-)phenocrysts with a very distinct brown-green to bluish-green colour and pleochroism (Fig. 6.12B & G). Amphiboles in both host rocks and enclaves from most other (biotite-) hornblende lavas show a green-brown to yellow-brown pleochroism. (Oscillatory) zoning is thereby occasionally observed in the host rocks and occurs more frequently in enclaves (Fig. 6.12A, C-D, F & Fig. 6.13 F-I). Crystals with a strong orange-brown to deep red-brown pleochroism represent a third type of amphibole which is only present in certain coarse-grained enclaves from the Phase 1 biotit-hornblende andesites (Fig. 6.12E & 6.13A-B).

Lavas from the second period of volcanic activity are commonly more mafic in com-position than the Phase 1 vol-canic deposits and contain pseudomorphs of opacite and/or pyroxene with only minor relic amphibole (Fig. 6.15 & 6.16). Exceptions are the Kakoperato rhyodacite and the the Oros hornblende andesite. Amphibole present in both host rocks and enclaves from the Kakoperato rhyodacite and in the Oros horn-blende andesitic host rock are similar to the type dominantly present in the first volcanic phase: green-brown to yellow-brown pleochroism and occa-sional (oscillatory) zoning (Fig. 6.14 & 6.17A-C). Enclaves from the Oros hornblende andesite, however, contain amphiboles which display a distinct orange-brown to deep red-brown pleochroism, similar to the third amphibole type of the first volcanic phase (Fig. 6.15C-E).

The amphibole (macro-) phenocrysts with pervasive disequilibrium features, present in the more mafic lavas, are indicative of a period in their host magma's petrogenesis during which chemical and/or physical conditions were no longer within the stability field of amphibole. The three distinct types of amphiboles within the more felsic lavas (Fig. 6.28) suggest (at least) three different physico-chemical conditions of amphibole stability and crystallisation. Previous studies on Aegina's volcanic rocks also report the presence of different types of amphibole. Pe (1973) describes Aegina's amphiboles as showing various shades and depths of brown, yellow and green or even reddish brown, with strong pleochroism and very common zoning. Both Dietrich et al. (1988) and Mitropoulos and Tarney (1992) describe the amphiboles as green or brown, highly

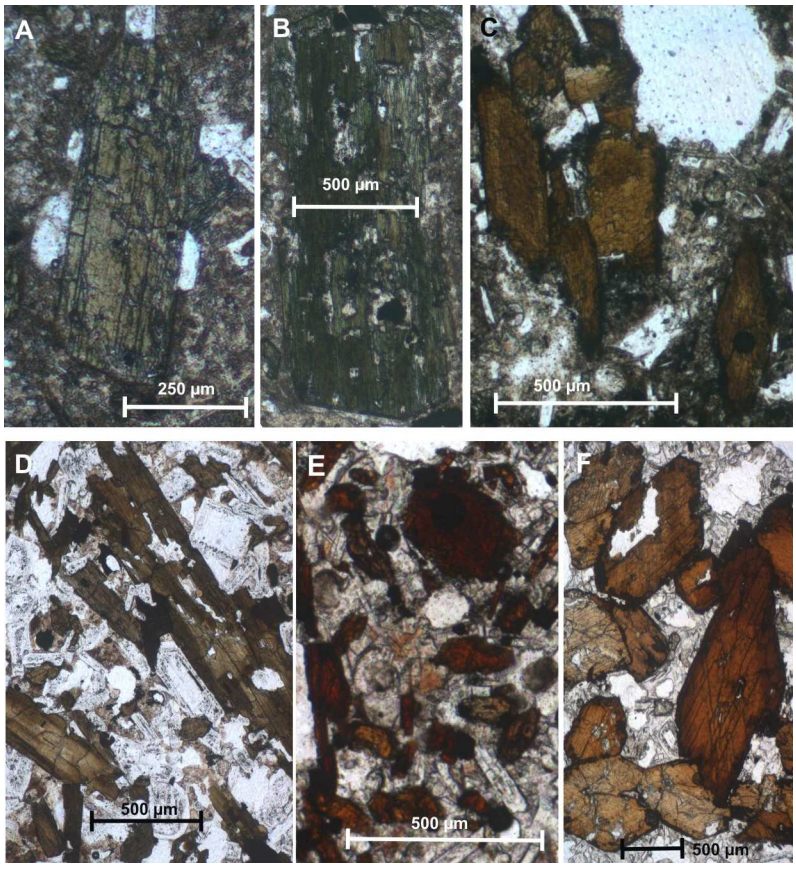

Figure 6.28. *Examples of the petrographically defined three different types of amphibole.* Yellow-green to bluish green pleiochroic type 1 amphibole: (A) Palaiochora host rock IA340, and (B) Palaiochora host rock IA61. Green-brown to yellow-brown pleiochroic with occasional oscillatory zoning: (C) Koutalou host rock IA94, and (D) Kokkinovrahos enclave IA345. Orange-brown to deep red-brown pleiochroic with occasional oscillatory zoning: (E) Micro-enclave in host rock IA65, and (F) Oros amphibole andesite enclave IA78.

pleochroic eu-to subhedral crystals. Dorais and Shriner (2002) divided the more felsic lavas form Aegina's first volcanic phase into those containing green pleochroic amphibole and those with red to brown pleochroic amphibole. In her study of the Kakoperato rhyodacite, St. Seymour (1996) notes that the amphiboles of host rocks and enclaves alike show greenish or reddish pleochroism and that reverse zoning is commonly present, with increasing Mg contents towards the rims of the amphiboles.

Plotting mineral composition from Pe (1973), Müller et al., (1979), Mitropoulos & Tarney (1992), St. Seymour (1996) and Dorais & Shriner (2002) into the amphibole geothermobarometer of Ridolfi et al (2010) indicates that most amphiboles on Aegina crystallised in either one of two temperature-pressure ranges (820-880°C at 120-200 MPa or 950-1050°C at 300-750 MPa, Fig. 6.29). The only two amphiboles that plot in the intermediate pressure-temperature field are from Dorais and Shriner (2002), which report that "in order to avoid potential operator bias in sample spot collection of zoned grains, traverses were conducted across numerous grains". This implies that some of their intermediate amphibole compositions could actually represent a mixture of geochemically distinct cores and rims. Therefore, if such intermediate compositions are not supported by similar compositional data from other amphibole studies, they are discarded for further interpretations (Fig. 6.29).

Translating the calculated pressures to depths below an average continental crust and looking more closely at the clusters formed by the amphibole data of Pe (1973), Mitropoulos and Tarney

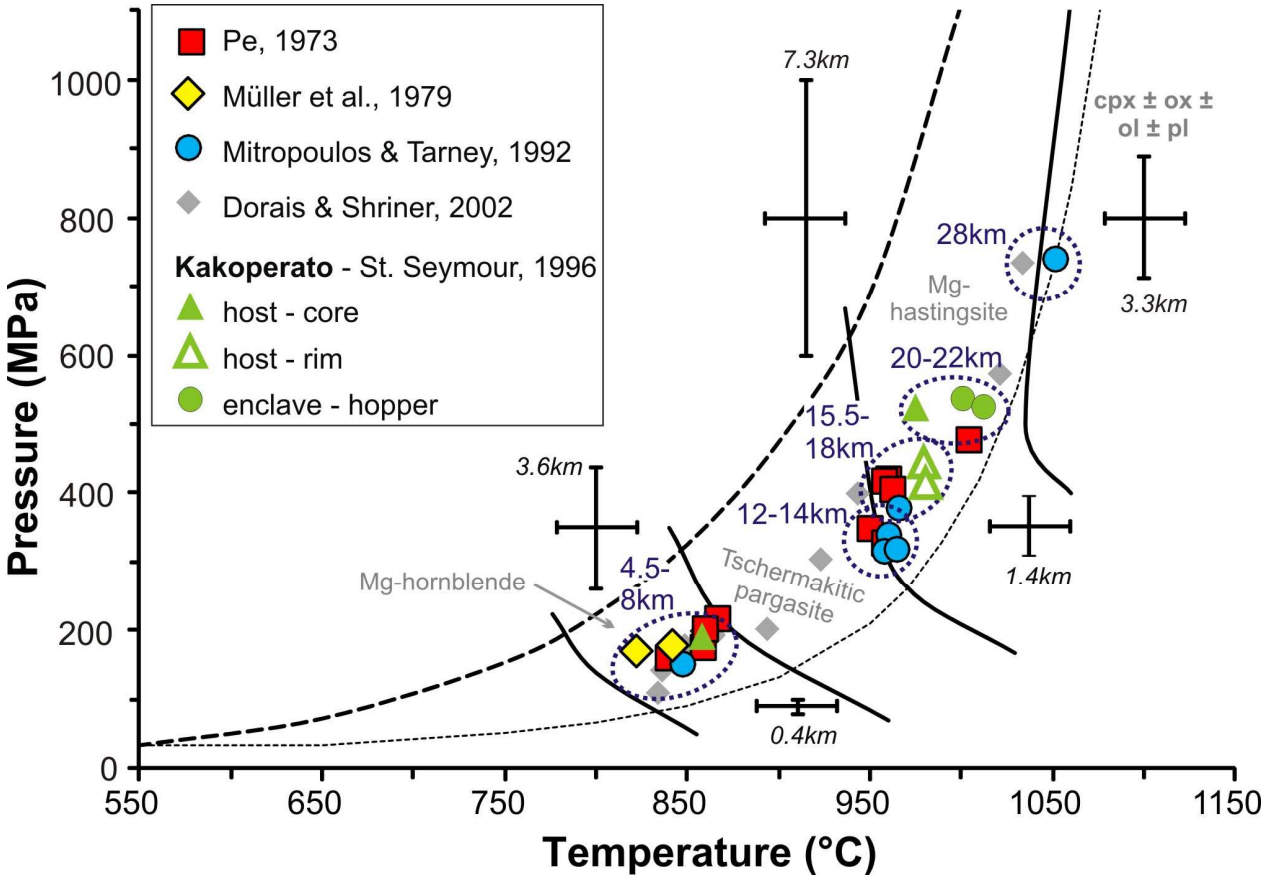

Figure 6.29. *P-T diagram for the volcanic amphiboles from Aegina as calculated by the geothermobarometer of Ridolfi et al. (2010). Black dotted line* represents the maximum thermal stability curve for amphibole; *black dashed line* indicates the upper limit of amphiboles with a composition consistent with their host rock; *full black curves* delineate approximate P-T stability limits for the three different types of amphibole (written in grey). *Error bars* represent the expected σ_{est} for estimated temperatures (22°C) and pressures (varies with P-T conditions, written in italic above/below respective error bar and presented as uncertainties of depth, calculated using a crustal density 2.78 g/cm³) – see Ridolfi et al. (2010) for further details. Amphibole geochemical data retrieved from literature, see graph for references. Figure drawn after Ridolfi et al. (2010).

(1992) and St Seymour (1996) suggests the presence of three different zones of amphibole crystallisation: 1) a minority of amphibole grains seem to have formed at a depth of 28 km, at ca. 1050°C, 2) the majority of amphiboles, including those from the Kakoperato lava flow, crystallised between ca. 1025°C at 22 km depth and ca. 950°C at 12 km depth, and 3) the second largest group formed near the upper boundary of amphibole stability, at ca. 4.5-8 km depth and temperatures ranging from 840 to 875°C (Fig. 6.29). It is not clear whether these three crustal levels of amphibole crystallisation coincide with the three petrographically distinct types of amphibole. Description of green, brown and red pleochroism is rather subjective to the researcher's definition of these colours and most studies also don't specifically mention the (pleochroic) colour of the analysed amphibole crystals. The detailed study of the Kakoperato rhyodacite (St. Seymour, 1996), however, does specify the origin of the analysed amphibole grains. Calculation of their crystallisation P-T estimates suggests that skeletal amphibole from Kakoperato enclaves formed at ca. 1010°C and 20 km depth, whereas the amphibole crystals in the host rock represent different populations (Fig. 6.29). The cores of the first type of amphiboles seem formed at depths similar to the enclaves, but at lower temperatures (975°C) - their compositionally distinct rims in turn crystallised at a similar temperature, but at shallower depth (16-17 km) (Fig. 6.29). The second amphibole population from the Kakoperato host rock has a geochemical composition consistent with formation at 860° C and relatively shallow depth (7 km).

6.6.3 Processes involved in the petrogenesis of Aegina's volcanic deposits

The negative correlation between $^{143}Nd/^{144}Nd$ or $^{176}Hf/^{177}Hf$ ratios and SiO_2 contents suggest a role for **crustal contamination** in the petrogenesis of Aegina's volcanic deposits (Fig. 6.26B-C). There also seems to be a trend of increasing $^{207}Pb/^{204}Pb$ and $^{208}Pb/^{204}Pb$ ratios with increasing differentiation (Fig. 6.27B-C), but no clear correlation is shown in the silica versus $^{206}Pb/^{204}Pb$ or $^{87}Sr/^{86}Sr$ diagrams (Fig. 6.26A & 6.27A). Decoupling between the $^{87}Sr/^{86}Sr$, $^{143}Nd/^{144}Nd$-$^{176}Hf/^{177}Hf$, $^{206}Pb/^{204}Pb$ and $^{207}Pb/^{204}Pb$-$^{208}Pb/^{204}Pb$ radiogenic compositions thus seems connected to assimilation of crustal material during magma differentiation. Reflected in only some of the radiogenic isotope compositions, this suggests that the specific crustal end-member has a similar $^{206}Pb/^{204}Pb$ composition as the more primitive magmas and either also similar $^{87}Sr/^{86}Sr$ contents or not enough Sr to appreciably change the magmas' Sr isotope ratios. Little to no evidence of crustal assimilation was observed during fieldwork apart from one cluster of coarse-grained quartz crystals in the Oros hornblende andesite (Fig. 6.5G) and a quartz-rich, angular sedimentary xenolith in the Skotini andesite (Fig. 6.4C). Near the boundary between the latter xenolith and its host rock, individual, rounded quartz grains seem arrested during their dispersal into the lava (Fig. 6.11J) – attesting to the foreign origin of rare rounded quartz found elsewhere in this intermediate to mafic Skotini andesite. The absence of a mafic mineral reaction rim mantling any of these quartz xenocrysts and the preservation of the angular quartz-rich xenolith suggest that this specific contamination of the magmas with quartz-rich sedimentary material occurred in the very final stages of ascent and eruption.

Besides the rare sedimentary quartz-rich xenoliths mentioned above, fieldwork and petrographic study also revealed the presence of very coarse-grained, (nearly) holocrystalline mineral aggregates. Within the more silica-poor (basaltic) andesitic lavas, these aggregates are mainly composed of mafic minerals (amphibole + Fe-Ti-oxides ± clinopyroxene ± olivine ± plagioclase) and range from micro- to macroscopic dimensions (Fig. 6.15B & Fig.6.5F, respectively). Crystals in these aggregates are commonly eu-to subhedral and occasionally contain a little interstitial groundmass. Based on their high crystallinity, large average grain size, eu-to subhedral crystal shapes and the absence of vesicles, these mafic aggregates are interpreted as cumulates resulting from crystal fractionation. Pe (1973) also described the occasional presence of such 'gabbroic' textured mineral aggregates and interpreted them as representing crystal accumulation, unlike the non-accumulative origin she inferred for the ubiquitous porphyritic, vesicular 'cognate xenoliths' (= the more mafic enclaves). The more felsic andesites of Aegina, on the other hand, sporadically contain holocrystalline aggregates of plagioclase + Fe-Ti-oxides + amphibole ± biotite (Fig. 6.9H). The crystals in these aggregates range from eu-to anhedral and completely interlock, with plagioclase often being sieve-textured and amphibole and

biotite showing disequilibrium features. These hollocrystalline aggregates are interpreted as remnants from either a very melt-poor crystal mush or a completely solidified sub-volcanic intrusive body. The same origin is inferred for the large, subhedral macro-phenocrysts of plagioclase, amphibole and biotite that show a variety of disequilibrium features and occasionally contain inclusions of euhedral zircon or apatite (Fig. 6.9A & C-D, Fig. 6.11C-D, Fig. 6.12B-H, Fig. 6.14A-C & F, Fig. 6.15A,C and Fig. 6.16B-C, E).

Sporadic observations of (nearly) holocrystalline mafic and felsic cumulates are however not the only indication for **significant incorporation of** cumulate material in Aegina's lavas. Structural/mineralogical criteria defined by Vernon and Collins (2011) for the identification of cumulates include: 1) locally high concentrations of particular minerals relative to concentrations in the bulk rock, 2) abundant euhedral crystals in contact with one another, 3) abundant crystals with reaction rims, 4) adjacent plagioclase crystals with different zoning patterns, and 5) glomeroporphyritic mineral aggregates. All volcanic deposits on Aegina meet at least three of the above criteria, mainly with respect to heterogeneous distribution of euhedral clinopyroxene ± olivine clusters (more mafic lavas) or of euhedral plagioclase ± biotite ± amphibole clusters (more felsic lavas), and minerals with reaction rims (amphibole overgrowth on biotite, clinopyroxene overgrowth on amphibole and olivine, quartz mantled by clinopyroxene). It is therefore likely that many of the larger crystals that could already be identified in hand specimen (olivine, clinopyroxene, amphibole, plagioclase and quartz) (Fig. 6.4E & I and Fig. 6.5A & E) are **antecrysts** inherited from magmatic bodies whose differentiation preceded that of the more intermediate magma that these crystals are found in now Charlier et al., 2005; Jerram & Martin, 2008; Larrea et al., 2013 – see section 4.4.5). Whether these antecrysts represent earlier differentiation stages of the finally erupted lavas, or whether they are derived from different, older magmatic bodies is not clear.

When there are no significant whole rock compositional differences between the magmas from which the cumulates formed and their final host magma, it can be very difficult to geochemically identify assimilation of even significant amounts of antecrysts (Vernon & Collins, 2011). However, aberrantly high (in comparison to other Aegina lavas with similar silica content) P_2O_5 and Cr concentrations in Skotini host rocks and enclaves from outcrop 61 go along with the microscopic observation of hexagonal apatite phenocrysts and (Cr-spinel bearing) olivine as second most common (macro-)phenocryst, respectively. The occurrence of euhedral zircon within large plagioclase and biotite macro-phenocrysts of the Palaiochora dacitic andesite seems to be reflected in their high Zr concentrations. The presence of antecrysts in Aegina's lavas thus seem responsible for the scatter observed in some of the geochemical whole rock data, but the extent of their influence on the lavas' composition is uncertain. A study into the role of cumulate crystals in the petrogenesis of volcanic rocks from the Azorean island of Corvo shows that significant antecryst accumulation can strongly affect the magma's bulk composition. Olivine antecrysts thereby show the by far largest influence on the rocks' whole rock major element geochemistry and clinopyroxene cumulates have a minor influence but accumulation of plagioclase has only little effect (Larrea et al.,2013).

Pe (1973) reports that most of Aegina's plagioclase phenocrysts show normal zoning with a maximum compositional difference between core and rim of 13 wt% anorthite. This suggests a role for closed-system plagioclase crystallisation in the petrogenesis of Aegina's magmas. However, Pe (1973) also observed eu- to anhedral plagioclase crystals with a distinct new rim, showing reverse zoning with up to 25 wt% more anorthite in the rim than in their sodic cores. Narrow rims of large plagioclase crystals in the Kakoperato rhyodacite are even equally Ca-rich (An_{80}) as the plagioclase phenocrysts of the Oros-Lazarides basaltic andesites (An_{79}) (Pe, 1973). The common presence of larger plagioclase crystals with a core that crystallised in a more evolved magma but a Ca-rich rim in equilibrium with a more primitive melt suggests **mafic replenishment of a more felsic crystal mush** is a recurrent petrogenetic process. This is also suggested by the ubiquitous presence of more mafic enclaves across Aegina's volcanic deposits (with exception of the virtually enclave-free Palaiochora dacitic andesite and Nikolaki andesite). Most of these enclaves have a framework of randomly

oriented phenocrysts with interstitial glassy groundmass, a high vesicularity, sharp contact with their host lava (but no chilled margins) and a few large crystals of plagioclase, amphibole, biotite or anhydrous pseudomorphs very similar to the macro-phenocryst population of their host rock (Fig. 6.10A-E, Fig. 6.11F-I, Fig. 6.13, Fig. 6.14G-I and Fig. 6.16G). These characteristics suggest an origin as small volumes of partially solidified (phenocryst framework) magma for which crystallisation lead to exsolution of volatiles (vesicles) and subsequent dispersal into a more felsic, cooler crystal rich mush (eventual host rock) from which it incorporates minor amounts of macro-phenocrysts (Coombs et al., 2002; Martin et al., 2006a). Exceptions to the above described petrographic characteristics are rare enclaves with a broad transition zone in which their framework phenocrysts crumble into the host rock (Fig. 6.10F) and enclave IA78 of which the euhedral amphibole framework is so coarse-grained that the crystals are larger than most macro-phenocrysts of its host rock (Fig. 6.17). These 'enclaves' are therefore interpreted to represent the transition between cumulates from the margins of a magma chamber and enclaves from a crystal-rich but less solidified mafic magma. Enclave formation from a mafic replenishment by dispersion into an overlying, more felsic crystal mush is a not uncommon phenomenon inferred for magmatic deposits around the world, including the other volcanic centres of the South Aegean arc (for example Didier & Barbarin, 1991; Feeley & Dungan, 1996; Mortazavi & Sparks, 2004; Zellmer & Turner, 2007; Feeley et al., 2008; Davi et al., 2010; Kocak et al., 2011; Braschi et al., 2012; van der Zwan et al., 2013).

These less evolved enclaves are thereby usually interpreted as evidence for **mingling and mixing** between compositionally different magmas. Another indication for magma mingling in Aegina's volcanic deposits, besides the ubiquitous more mafic magmatic enclaves, is the macroscopic flow-banding of alternating grey and red lava (Fig. 6.4A-B) which is also observed on the microscopic scale as alternating bands of more glassy and more cryptocrystalline groundmass (Fig. 6.9F-G). Petrographic indications of crystal mingling and magma mixing are however less abundant. The presence of both quartz and olivine crystals in the same groundmass, commonly interpreted as clear evidence for mixing of a mafic and felsic magma, is restricted to just a handful field and petrographic observations of quartz in olivine-bearing rocks, but never was olivine observed in quartz-bearing lava. Although the Skotini andesite contains both olivine and quartz, the lack of a reaction rim around the rounded quartz crystals and the presence of a quartz-rich xenolith suggests that in these deposits the quartz crystals are derived from late-stage sedimentary contamination, instead of mixing with a felsic crystal mush (Fig. 6.4C and Fig. 6.11H,J). Within more mafic enclaves from the second period of volcanic activity, quartz crystals with a mafic reaction rim are likely antecrysts from their host after incorporation of enclave magma into the more felsic crystal mush (Fig. 6.5A). Only in the olivine-bearing Oros-Lazarides basaltic andesites is the presence of pyroxene-mantled quartz, accompanied by anhydrous pseudomorphs and glomerophyric clusters of plagioclase with interstitial glass and a clinopyroxene reaction rim, interpreted as evidence for mixing between a mafic injection and more felsic crystal mush (Fig. 6.16). The geochemical gap present between enclaves and host rocks from all volcanic units on Aegina, and the relatively narrow geochemical ranges shown by the different types of host rocks, also suggest that mixing/hybridisation between the mafic replenishments and more felsic, crystal-rich magmas was minor (Fig. 6.20-6.23). The larger geochemical spread amongst enclaves from a specific unit or even outcrop can be partially explained by the macro- and microscopic observation of host rock antecrysts and the varying origin of these rocks as either mafic injection or crystal cumulate. Dietrich et al. (1988) also interpret the majority of enclaves as globules of partially solidified mafic magma that mingled with a more felsic crystal mush but describe some of them as cumulates of hornblende gabbro. The petrogenesis they propose for Aegina's volcanic deposits furthermore also involves interaction between mafic injections and felsic crystal mushes that is limited to mechanical mixing (mingling) for the lavas of the first period of volcanic activity, but involves more intense chemical mixing and hybridisation for the volcanic rocks of the second volcanic phase (Dietrich et al., 1988).

The fact that the lavas have a high crystallinity and contain crystal cumulates as well as different populations of pheno- and antecrysts which display both normal and inverse zoning patterns indicates

that **crystal fractionation** is an important differentiation process for all Aegina's magmas. Pe (1973) came to the same conclusion based on field observation of continuous series from more mafic to more felsic deposits and fractional crystallisation calculations. She suggests that all host rocks and enclaves throughout Aegina's volcanic history are derived from very similar primitive magmas through different steps of fractional crystallisation and successive separation. Petrographic and geochemical evidence indicates hornblende and Fe-Ti-oxides make an early appearance in the magmas' crystallisation assemblage and continue to precipitate (Pe, 1973). Dietrich et al. (1988) infer two distinct phases of fractional crystallisation from an initial primitive magma represented by nepheline-normative mafic enclaves. A first phase of fractional crystallisation involves precipitation of mainly Mg-rich olivine (Fo_{88-90}) and Cr-spinel - with minor amounts of Ca-rich plagioclase (An_{79-80}), Al- and Ti-rich clinopyroxene and Mg-hastingsitic amphibole. The mineral assemblage that crystallises from the resulting intermediate magmas comprises mainly amphibole, plagioclase (An_{35-45}), clinopyroxene and Fe-Ti-oxides, and possibly minor amounts of Fe-rich olivine (Fo_{66}) (Dietrich et al., 1988). They furthermore stress that all crystallisation, mingling and mixing took place in magma chambers at significant depth, with the first phase of fractional crystallisation potentially as deep as the crust-mantle boundary.

Using mineral compositions available in literature and the least squares regression of the major elements (after Bryan et al., 1969) implemented in the RockWare IgPet software (2012 version), an attempt was made to model the geochemistry of Aegina's volcanic rocks solely by crystal fractionation (mixing is shown to play a less important role), taking into account the hypotheses of Pe (1973) and Dietrich et al. (1988). Up to 6 different microprobe analyses on olivine, plagioclase, amphibole, clinopyroxene and biotite from Aegina were selected from literature (representing the entire geochemical variety of this volcanic centre) and subsequently tested in the FC geochemical calculations - those mineral compositions that led to plausible models are presented in Table 6.3. One Fe-Ti-oxide composition from Aegina and one orthopyroxene analysis from Methana are also used,

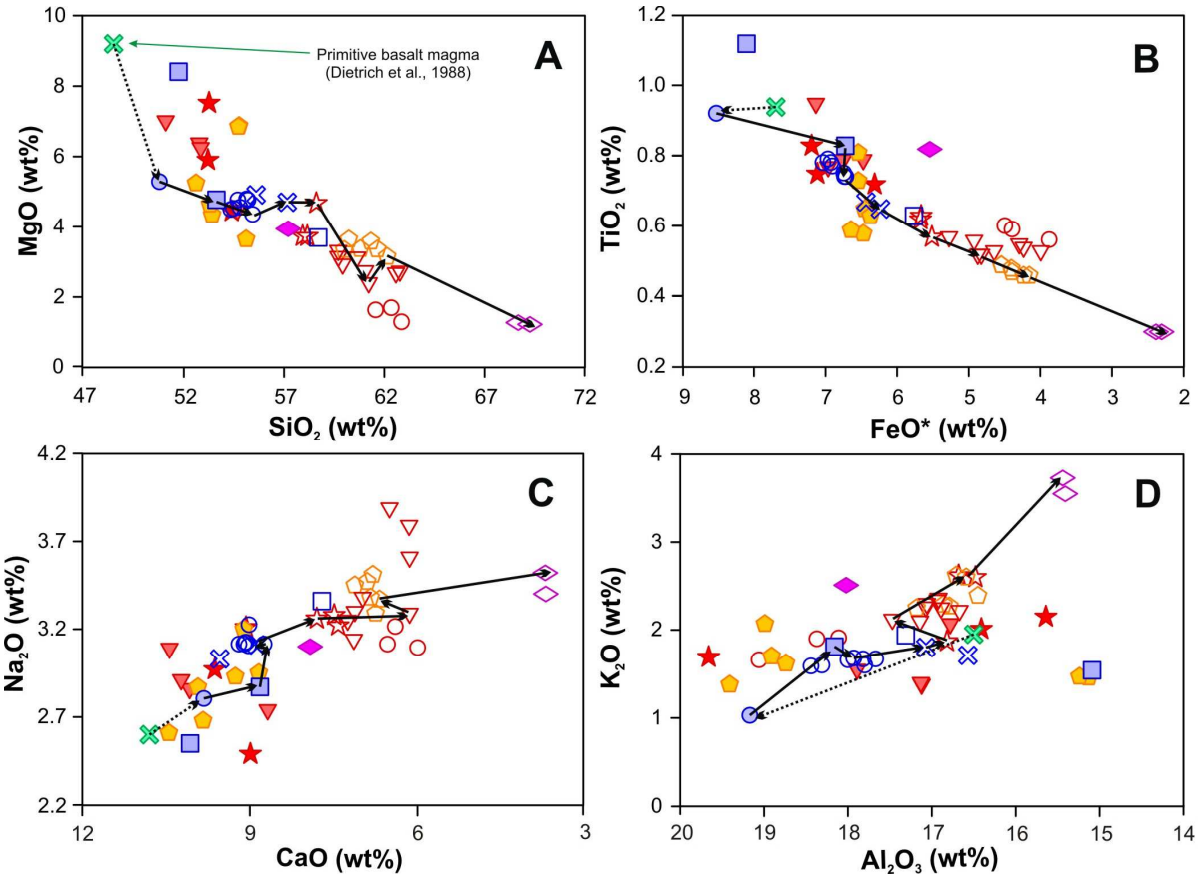

Figure 6.30. *Illustration of the WR major element compositions succesfully reproduced* by 8 successive fractional crystallisation steps, each involving a different crystallising mineral assemblage. See text for discussion.

but since no geochemical data for Cr-spinel and apatite from the Saronic Gulf are available, a composition from the nearest volcanic centre (Santorini) is used instead (Table 6.3). The main goal of this modelling exercise is to assess the plausibility of reproducing the geochemical range of Aegina's 'main trend' through successive steps of fractional crystallisation of different mineral assemblages (see Fig. 6.30) and identify the mineral compositions most likely to have played a role in these differentiation processes. (Aegina's 'main trend' refers back to those samples that define a single volcanic series that largely overlaps the literature data in Fig. 6.21-6.23 - exceptions are a number of possibly accumulative enclaves, the Palaiochora dacitic andesite and location 61 Skotini lavas).

Since most rocks from the first period of volcanic activity have a rather intermediate character and those of the second volcanic phase are more mafic, key whole rock compositions from the latter are selected for calculations of the silica-poor part of the trend, and a number of host rocks from the first phase for modelling of the silica-enriched lavas (Fig. 6.30). Oros-Lazarides basaltic andesite enclave IA72 is thereby the most mafic sample from this study, whereas the Kakoperato rhyodacite host rock IA97 represents the most felsic composition (Fig. 6.30). The 'primitive basalt' composition suggested by Dietrich et al. (1988) as the initial magma from which all other volcanic rocks on Aegina are derived is not matched by any sample analysed in this study but there are a few similar literature compositions, so a first modelling step involved derivation of basaltic enclave IA72 (this study's most mafic sample) from Dietrich et al. (1988)'s primitive basalt (green cross in Fig. 6.30). For every step of fractional crystallisation, the plausibility of a calculated model was judged on the basis of 1) the fraction of remaining melt (F) that would need to segregate, 2) the sum of squared residuals (SSR) which represents the difference between calculated and observed major element contents, 3) the relative proportions of the different minerals in the crystallising assemblages (are they similar to petrographic observations?) and 4) closeness-of-fit between the measured and modelled trace element concentrations, automatically calculated by IgPet whenever a combination of minerals results in a mathematically plausible model.

This step-wise fractional crystallisation modelling could successfully reproduce the main trend of major element compositions of Aegina's volcanic rocks, as illustrated in Fig. 6.30. The specific mineral assemblages involved in the successive crystallisation steps are presented in Table 6.4 and reflect a crystallisation sequence from mafic to more felsic minerals, as well as a gradual change for olivine-amphibole-clinopyroxene/plagioclase from more magnesium- and anorthite-rich to more iron- and albite-rich compositions for the dominant mineral phases.

A combination of the most plausible geochemical models for each fractional crystallisation step results in the following petrogenetic history: differentiation from the primitive Aegina magma inferred by Dietrich et al. (1988) to the most mafic sample in this study (IA72) indeed involves fractional crystallisation of mainly Mg-rich olivine, Ca rich plagioclase and Ti-Al-rich clinopyroxene. Supporting petrographic evidence of this fractionation is given by small cumulophyric aggregates, composed of similar amounts of olivine, clinopyroxene and plagioclase, that have been sporadically observed in the Skotini andesite (Fig. 6.11I). Although Dietrich et al. (1988) suggested important precipitation of Cr-spinel in this first crystallisation assemblage, none of the modelling calculations allowed formation of this mineral – supported by the lack of Cr-spinel inclusions in Aegina's olivine crystals. Despite the fact that this geochemical model involves a large enough fraction of residual melt (allowing for efficient melt segregation) and that the discrepancy between calculated and observed major element geochemistry is relatively small (Table 6.4), the 'primitive magma' of Dietrich et al. (1988) shows aberrantly high MgO and low FeO* and Al_2O_3 that do not fit within the general differentiation trend defined by the samples from this study (Fig. 6.30A,B&D). The geochemistry of this 'primitive magma' is therefore likely to reflect a cumulate composition, similar to enclave IA78 for example, rather than a liquid composition. The most primitive magma is thus represented by enclave IA72, from which the more evolved geochemistry of IA77 can be obtained through *either* an anhydrous mineral assemblage of Fe-rich olivine and Ca-rich plagioclase, *or* Mg-rich amphibole, Mg-rich clinopyroxene and Ca-rich

Mineral/**Oxide**	SiO_2	TiO_2	Al_2O_3	FeO	MnO	MgO	CaO	Na_2O	K_2O	P_2O_5	Cr_2O_3
[2] *Olivine* $_{Fo90}$	40.87	0	0	9.77	0	49.35	0	0	0	0	0
[2] *Olivine* $_{Fo66}$	37.06	0	0	30.13	0	32.81	0	0	0	0	0
[3] *Am* $_{FeO/MgO=0.44}$	43.97	1.76	11.51	7.3	0	16.78	12.44	2.08	0.74	0	0
[1] *Am* $_{FeO/MgO=0.53}$	41.47	2.32	13.08	8.51	0.13	15.97	11.92	2.17	0	0	0
[1] *Am* $_{FeO/MgO=1.53}$	44.82	1.45	9.06	16.78	0.55	12.43	12.03	1.36	0	0	0
[1] *Cpx* $_{FeO/MgO=0.43}$	49.53	1.21	7.17	6.13	0.17	14.28	22.38	0.36	0	0	0
[3] *Cpx* $_{FeO/MgO=0.62}$	53.26	0	0.82	9.18	0.58	14.91	21.65	0.6	0	0	0
[1,2] *Plagioclase* $_{An80}$	59.56	0	30.32	0	0	0	8.89	1.23	0	0	0
[1] *Plagioclase* $_{An54}$	60.34	0	30.72	0	0	0	6.08	2.86	0	0	0
[1] *Plagioclase* $_{An47}$	60.92	0	30.83	0	0	0	5.31	3.31	0	0	0
[2] *Plagioclase* $_{An35}$	60.55	0	31.01	0	0	0	3.98	4.08	0	0	0
[1] *Biotite* $_{FeO/MgO=1.16}$	36.02	4.81	14.36	15.83	0.25	13.63	0.12	0.69	9.02	0	0
[3] *Fe-Ti-oxide*	0.79	6.25	2.71	83.69	1.18	0.81	0	0	0	0	0
[3] *Orthopyroxene*	52.14	0	1.61	20.75	1.25	22.48	1.03	0.74	0	0	0
[4] *Cr-Spinel*	0	0.49	21.47	23.03	0.21	13.49	0	0	0	0	41.32
[5] *Apatite*	0.23	0	0.01	0.43	0.18	0.09	55.7	0.09	0.03	43.23	0

All iron expressed as FeO and all oxides recalculated to 100% (in accordance with IgPet requirements). FeO/MgO ratio of ferromagnesian minerals given as indication for the mafic character of their geochemistry. [1] Pe (1973); [2] Dietrich et al. (1988); [3] Mitropoulos & Tarney (1992); [4] Vagelli et al., 2009; [5] Gertisser et al., 2009.

Table 6.3. *Selection of literature mineral compositions used for the geochemical calculations of fractional crystallisation.* Olivine, amphibole, clinopyroxene, plagioclase, Fe-Ti-oxdes and biotite analyses from Aegina, orthopyroxene from Methana, apatite and Cr-spinel from Santorini. See text for discussion.

plagioclase (Table 6.4). Whereas the first model combines a realistic F with somewhat higher SSR, the better fit of the hydrous model (lower SSR) is accompanied by only 60% of residual melt, making it more difficult to efficiently segregate the liquid from the crystals (Table 6.4). No model calculation involving both olivine and clinopyroxene + amphibole was successful. Since most olivine observed in thin section is rather Fe-rich (<Fo_{85}) and Ca-rich plagioclase crystals are commonly present with large amphibole and clinopyroxene crystals, both models are interpreted as equally plausible. The possibility of two parallel crystal fractionation trends, one with amphibole and one with only anhydrous minerals, also emerges in the subsequent three steps of fractional crystallisation (Table 6.4). Geochemical differentiation from a magma with a composition similar to basaltic andesitic enclave IA77 to Skotini andesite host rock IA102, via basaltic andesites IA68 and IA74, can be achieved *either* via successive crystal fractionation of plagioclase + clinopyroxene (± orthopyroxene) *or* of plagioclase + amphibole (Table 6.4). Mineral compositions thereby become increasingly more felsic (An_{80} plagioclase is replaced by An_{54}, and the initially Mg-rich amphibole becomes richer in Fe) and in each step the relative amounts of plagioclase and mafic minerals in the hydrous and anhydrous mineral assemblage is comparable. Calculated fractions of remaining melt furthermore allow efficient separation of evolved liquid from crystal cumulates (Table 6.4). Petrographic observation of similar mineral aggregates, An_{55} phenocrysts in the Oros-Lazarides basaltic andesites and zoned amphibole seem to support these geochemical modelling calculations. Further differentiation, from the Skotini andesite lavas to the Kokkinovrahos andesites, is successfully reproduced by fractional crystallisation of both amphibole and pyroxene (either clino-or orthopyroxene – Table 6.4) and plagioclase. The latter thereby becomes

abs% *(rel%)*	**[1]Prim → IA72**	**IA72 → IA77**		**IA77 → IA68**		**IA68 → IA74**		**IA74 → IA102**		**IA102 → IA65**	**IA65 → IA55**	**IA55 → IA98**
Fo_{90}	7.6 *(37.0)*	NOT	NOT									
Fo_{66}	NOT	3.9 *(17.7)*	NOT	NOT	NOT							
$Am_{0.44}$	NOT	NOT	10.9 *(26.7)*	NOT	6.2 *(47.1)*	1.1 *(10.4)*						
$Am_{0.53}$								3.6 *(37.2)*	NOT	12.4 *(68.6)*	NOT	
$Am_{1.53}$											3.1 *(23.2)*	9.9 *(24.2)*
$Cpx_{0.43}$	9.3 *(44.9)*	NOT	4.0 *(9.9)*	2.8 *(25.5)*	NOT		1.8 *(13.7)*	NOT	6.4 *(39.4)*	4.4 *(24.6)*	NOT	
$Cpx_{0.62}$											NOT	8.4 *(20.5)*
An_{80}	2.3 *(11.4)*	14.1 *(63.4)*	21.4 *(52.4)*	5.7 *(52.5)*	6.2 *(47.1)*	8.6 *(78.1)*						
An_{54}							9.6 *(74.8)*	3.7 *(38.3)*	7.7 *(47.8)*			
An_{47}										0.9 *(5.0)*		
An_{35}											9.9 *(74.9)*	20.2 *(49.5)*
Bt												1.4 *(3.5)*
Ox	NOT	2.4 *(10.7)*	4.0 *(9.8)*	0.4 *(3.4)*	0.6 *(4.7)*	1.2 *(10.6)*	1.3 *(9.9)*	1.2 *(12.4)*	1.6 *(9.8)*	0.1 *(0.6)*	NOT	NOT
Opx				1.9 *(17.5)*		NOT	NOT	NOT	NOT	NOT	0.2 *(1.9)*	NOT
Apatite	1.4 *(6.7)*	1.8 *(8.2)*	0.5 *(1.2)*	0.1 *(1.1)*	0.1 *(0.4)*	0.1 *(0.9)*	0.2 *(1.5)*	1.2 *(12.2)*	0.5 *(3.0)*	0.2 *(1.1)*	NOT	0.9 *(2.2)*
F	**0.79**	**0.78**	**0.59**	**0.89**	**0.87**	**0.89**	**0.87**	**0.90**	**0.84**	**0.82**	**0.87**	**0.59**
SSR	**1.730**	**1.750**	**0.519**	**0.349**	**0.156**	**0.106**	**0.075**	**0.477**	**0.140**	**0.118**	**1.328**	**0.371**

Basaltic composition inferred by [1] Dietrich et al. (1988) to represent Aegina's primitive magmas. Abs% = absolute amount of specific mineral that is calculated to crystallise; (*Rel%)* = relative percentage of this mineral within the crystallising assemblage. When a mineral crystallised more than one geochemical composition, these are ordered from the top down from more mafic to more felsic geochemistry. Details on the exact geochemistry of these minerals, as well as the sources for the micro-probe data, can be found in Table 6.3. NOT indicates that a certain mineral (composition) did not fit any potential scenario of the specific differentiation step. F : fraction of remaining melt, interpreted to segregate from the crystal mineral assemblage and move on to the next differentiation step. SSR = sum of squared residuals, indicates how well model calculations fit the observed WR compositions.

Table 6.4. *Details on the different steps of fractional crystallisation that successfully reproduced the geochemical range in Aegina's major element contents*. See text for discussion.

increasingly more Na-rich, with compositions that match those optically determined (An_{47}-An_{35}), whilst the precipitating amphiboles show a drastic increase in Fe/MgO ratios (FeO*/MgO 0.53 to 1.53 –Table 6.4). The main geochemical trend defined by most samples from both this study and literature with basaltic enclave IA72 as mafic starting point and Kokkinovrahos andesite IA55 as most evolved composition is thus relatively easily reproduced by a number of realistic fractional crystallisation steps. Apatite is from the start present as accessory phase in nearly each crystallisation assemblage and Fe-Ti-oxides start to precipitate slightly later but then persist throughout further differentiation (Table 6.4). Orthopyroxene is only sporadically present as a crystallising phase – in agreement with its rare occurrence (Pe, 1973). Although often present as a minor mineral phase, biotite and quartz precipitation was never successfully modelled – nor did any calculations agree with the sporadic occurrence of zircon (Table 6.4). Even the distinctly more evolved composition of the Kakoperato rhyodacite can be reproduced by fractional crystallisation from a magma with a composition similar to

Kokkinovrahos andesite IA55 (Table 6.4). The minerals calculated to take part in the crystallising assembly thereby show high Fe/Mg and Na/Ca ratios and all observed as (macro-) phenocrysts in the rhyodacite (Fig. 6.14). The chondrite-normalised REE pattern of the Kakoperato rhyodacite is furthermore distinct by its lack of a negative Eu-anomaly and clear spoon-shape (Fig. 6.25A) – in agreement with fractionation of Ca-poor plagioclase and significant amounts of amphibole. Only the large embayed quartz grains can not be linked to the geochemical modelling calculations. Despite the good agreement between calculated and observed WR major element contents, the fraction of remaining melt is only 59% - making it more difficult to allow efficient segregation from the crystal cumulates which is inferred from the rhyodacite's large volume of cryptocrystalline groundmass (Fig. 6.14).

This suggests that the Kakoperato rhyodacitic magmas would have been uneruptable, due to their high degree of crystallinity – and required a large mafic replenishment to trigger **partial melting**, necessary to decrease their viscosity and allow ascent and eruption. A large volume of more mafic enclaves in the Kakoperato lava flow have been observed – indicative of mafic injection and mingling (see above). Petrographic study furthermore revealed that the degree of rounding of large macro-phenocrysts is significantly larger in the Kakoperato lavas than in any other Aegina volcanic deposits and likely reflecting resorption during partial melting (Fig. 6.14). The Kakoperato rhyodacites are compositionally distinct due to the large geochemical gap between them and the intermediate (dacitic) andesites which represent the most evolved end of Aegina's main differentiation series and their large amounts of groundmass and embayed quartz. These characteristics are interpreted as evidence for pro-longed cooling and differentiation to rhyolitic compositions (through crystallisation of amphibole, plagioclase, clinopyroxene, biotite, apatite, quartz and even zircon) before re-heating by a mafic injection remobilised the rhyodacitic partial melt (including remaining crystals) and triggered its eruption at the start of the second period of volcanic activity. So although not a generally important process for the petrogenesis of Aegina's magmas, partial melting is inferred to have played a major role in the formation of the Kakoperato rhyodacite lavas. This hypothesis is furthermore supported by the common presence of randomly oriented plagioclase crystals in a glassy groundmass, mantled by clinopyroxene (Fig. 6.16F) in the Oros-Lazarides basaltic andesites. The optically determined composition of the plagioclase in these corona textured inclusions (An_{35}) is thereby significant lower than that of the plagioclase phenocrysts of its host rock (An_{50}) and identical to the Na-rich plagioclase composition calculated to precipitate during differentiation towards the Kakoperato magmas (Table 6.4). So if the Oros-Lazarides basaltic andesites would represent a portion of the mafic injection that remobilised the Kakoperato rhyodacite, this would explain the presence of these plagioclase-glass inclusions with clinopyroxene reaction rim as contamination from the Kakoperato felsic crystal mush.

This petrogenesis is in agreement with the hypothesis of St. Seymour (1996) in which a zoned magma chamber containing a rhyolitic crystal mush is replenished by a hotter, basaltic magma that ponds below the felsic mush. Crystallisation of the basaltic magma led to its vesiculation and subsequent dispersion of mafic droplets in the overlying rhyolitic magma (mingling). As these mafic enclaves continue to cool down and solidify within the felsic host, chemical mixing between the two magmas is facilitated through elemental **diffusion** across the contact boundaries (St. Seymour, 1996). Felsic melt directly in contact with the mafic inclusions thereby becomes more oxidised, as evidenced by the presence of fine oxide dusting and oxy-hornblende in the groundmass enveloping the enclaves. This diffusional modification of the felsic magma does not cause significant geochemical changes, but it does change the groundmass colour from grey to red, defining flow banding during ascent and eruption by mingling of the two physically distinct magmas (St. Seymour, 1996). Diffusion-driven oxidation of groundmass in the vicinity of mafic enclaves is thus also a likely cause for the heterogeneously grey and red groundmass, frequently observed during this study in Aegina's intermediate lavas in which it sometimes defines flow banding (Fig. 6.4A-B). St Seymour (1996) furthermore suggests that despite the large geochemical gap between the basaltic andesitic enclaves and the Kakoperato rhyodacitic lava, both their bulk chemistries are controlled by amphibole-pyroxene-plagioclase fractionation, and explains their similar REE, Zr, Y and Nb contents to

fractionation of accessory zircon from the initial rhyolite magma. The main difference between St. Semour's (1996) petrogenetic interpretation of the Kakoperato deposits and the petrogenesis suggested in this study is that whereas the former focuses on an important role for diffusion in order to explain the disequilibrium features and resorption of the host rock's macro-phenocrysts, the latter prefers partial melting through heat transfer from the hot (and crystallising) ponding mafic injection.

6.6.4 Sources contributing to Aegina's magmas throughout its volcanic history

Primitive mantle-normalised trace element patterns of both host rocks and enclaves show the classic hallmarks of subduction-related magmatism: a steep pattern due to enrichment of the most incompatible LILE and a combination of negative Nb-Ta, P and Ti with positive U, Pb and Sr anomalies (Fig. 6.24) (Elburg, 2010). All volcanic rocks on Aegina thus originate from a 'metasomatised mantle' source – partial melting of the mantle wedge induced by hydrous additions from the subducted slab, either in the form of hydrous fluids or as partial melts themselves. But is this primitive source magma the same for lavas of the first and second period of volcanic activity? Major element modelling suggests that most geochemical compositions encountered in Aegina's volcanic deposits can indeed be explained by successive fractional crystallisation steps of different mineral assemblages starting from the most mafic sample (Fig. 6.30). The strontium isotopic compositions of these lavas, however, show a clear distinction between deposits from the first period of volcanic activity ($^{87}Sr/^{86}Sr$ = 0.7055-0.7075) and the less radiogenic lavas of the second volcanic phase ($^{87}Sr/^{86}Sr$ = 0.7040-0.7050) (Fig. 6.26A & F). The only exception to these Sr systematics are the Kakoperato deposits, of which host rocks plot within the Sr isotopic field of the first volcanic phase, but the enclaves show lower $^{87}Sr/^{86}Sr$ ratios characteristic of the second volcanic phase. The Kakoperato eruption marks the very start of the second period of volcanism and was generated through partial melting of an uneruptable, rhyolitic crystal mush that is remobilised by a more mafic injection. In this way, the different Sr isotopic compositions of host rocks and enclaves can be easily reconciled: the rhyolitic crystal mush that is the protolith of the eventual Kakoperato rhyodacite lavas represents a magma body from the first period of volcanic activity that got stuck in the crust whereas the enclaves represent the uprising mafic magmas that initiated the renewal of volcanism and remobilised the 'first phase' crystal mush on their way to the surface.

Dietrich et al. (1988) interpret all (basaltic) andesites from the second period of volcanic activity as the successive compositions tapped from a zoned magma chamber in which a mafic replenishment underwent significant mixing and homogenisation with the overlying Kakoperato felsic mush. Indeed, simple mixing of ca. 60% of a mafic magma represented by basaltic enclave IA72, identified as the most primitive sample of this study, with up to 40% of a felsic crystal mush compositionally similar to Kakoperato host rock IA97 reproduces the Sr isotope geochemistry of all second phase volcanic deposits (Fig. 6.31A). The felsic crystal mush that was solidifying in a crustal magma chamber (at about 15.5-18 km depth, Fig. 6.29) and eventually erupted as the Kakoperato rhyodacite thus seems to represent the Sr-geochemical end-member which 'contaminated' the mafic melts of the second period of volcanic activity. Despite the marked shift in the $^{87}Sr/^{86}Sr$-$^{143}Nd/^{144}Nd$ trend between the volcanic series of the first and second period (Fig. 6.26D), the straightforward model of binary mixing between the mafic magma of IA72 and felsic crystal mush IA97 can also reproduce the Sr-Nd isotopic composition of all second phase lavas (Fig. 6.31C). Even most of the younger (basaltic) andesites' Nd geochemistry can be explained by mixing between basaltic enclave IA72 and Kakoperato rhyodacite IA97 (Fig. 6.31D). The Sr-Nd geochemical composition of the lavas from the second volcanic phase thus supports the petrogenesis, suggested by Dietrich et al. (1988), of hybridisation between a mafic magma and a felsic crystal mush.

The Sr-Nd geochemistry of host rocks and enclaves from the first period of volcanic activity displays significantly more scatter than those from the (short-lived) second volcanic phase – could these magmas still be derived from a primitive melt similar to basaltic enclave IA72? These magmas probably spend prolonged time at a range of different crustal levels (at ca. 28 km, 22-12 km and 4.5-8

km depth – see Fig. 6.29) as they evolved through fractional crystallisation to more intermediate compositions. Undoubtedly, these first phase magmas would have assimilated local magma chamber wall rock during their differentiation to more felsic compositions. The only xenolith encountered, however, is the quartz-rich sedimentary rock in the Skotini andesite. Its unaltered appearance and sharp contact with the host lava (without reaction rim) suggests it was picked up by the magma from a very shallow level and only shortly before eruption. The geochemical composition of this xenolith (IA328A – see Appendix F2) furthermore shows that it is consists mainly of quartz (98 wt% SiO_2) with trace element concentrations too low to permit determination of its Sr, Nd, Hf or Pb isotopic composition – effectively ruling out this shallow, quartz-rich lithology as potential source of contamination. Aegina's sedimentary basement is mainly exposed in the northern part of the island where it comprises limestone and minor amounts of siliciclastic rocks, from which respectively three and one sample were collected (Appendix F2). Figure 6.31A shows that the Sr contents and $^{87}Sr/^{86}Sr$ composition of the limestone samples are at the lower, respectively higher, end of the geochemical

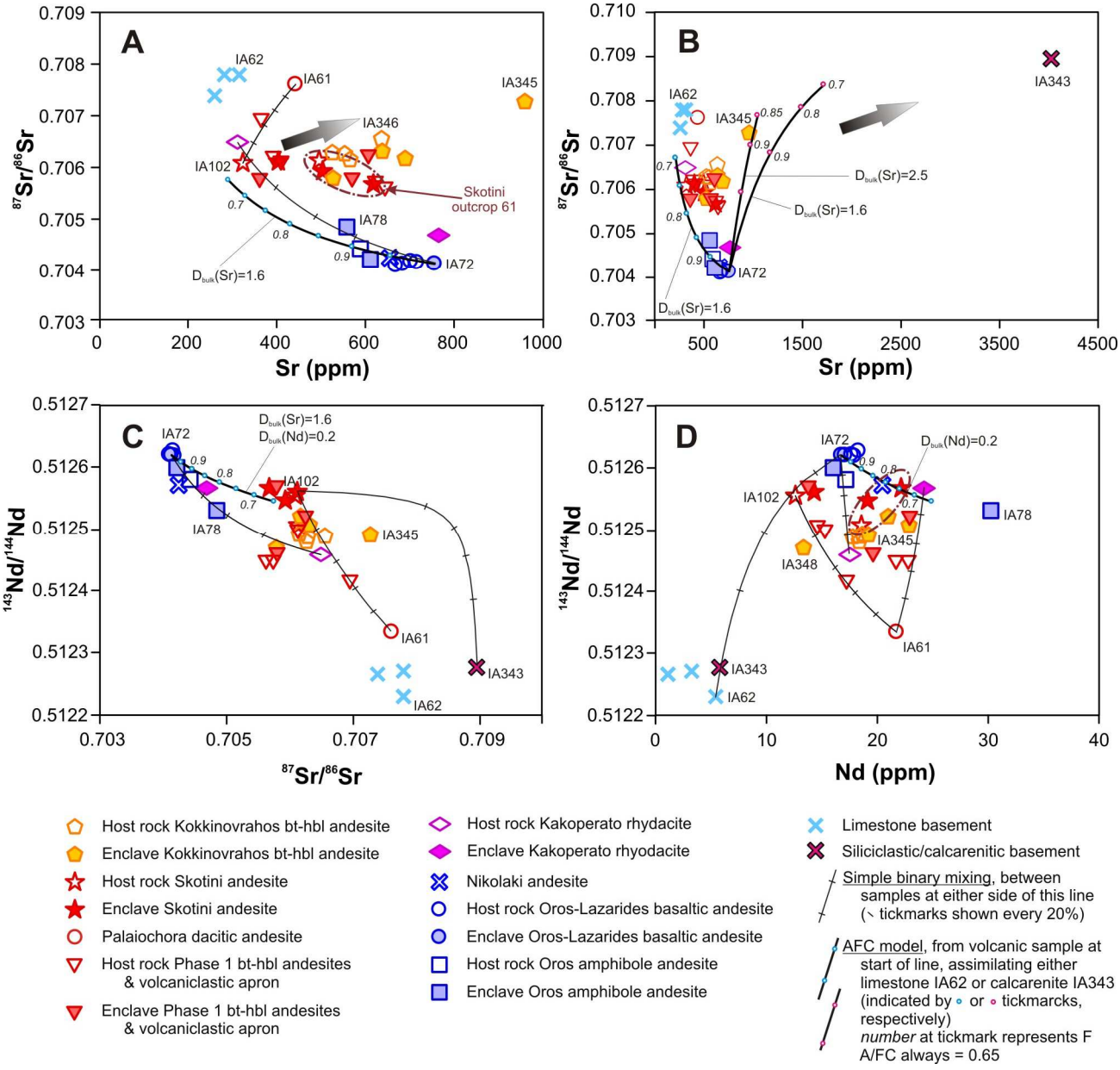

Figure 6.31. *Sr-Nd geochemistry of both volcanic and sedimentary samples collected from Aegina*. Geochemical models involving binary mixing and AFC with sedimentary basement rocks can partially reproduce the lavas of both the first and second period of volcanic activity.

range displayed by the volcanic deposits from the first period of activity. This means that the radiogenic Sr composition of the Palaiochora dacitic andesites and Kokkinovrahos andesites can not be explained by contamination with these carbonates. Most primitive samples of the first volcanic phase, the host rock (IA102) and enclave (IA101) of the Skotini andesite sampled at outcrop 60, can however be modelled by an AFC differentiation process involving contamination of overall most mafic basalt IA72 by limestone IA62 (Fig. 6.31A). The ratio of assimilation over fractional crystallisation (0.65), Sr bulk distribution coefficient (1.6) and fraction of remaining melt representing the Skotini magmas (0.65) are thereby all values in agreement with the major element modelling. Formation of the most mafic lavas from the first period of volcanic activity (the Skotini lavas) by fractional crystallisation from basaltic enclave IA72 with concurrent assimilation of a wall rock similar to limestone IA72 is also suggested by the rocks' $^{87}Sr/^{86}Sr$-$^{143}Nd/^{144}Nd$ composition (Fig. 6.31C). The Nd geochemistry of (outcrop 60) Skotini magmas can not be reproduced by AFC, but rather by simple mixing, between basalt IA72 and limestone IA62 (Fig. 6.31D). This simple mixing model however involves contamination of the primitive magma with up to 40% limestone or calcarenite which would result in elevated calcium contents for the resulting magmas. As the (outcrop 60) Skotini lavas do not contain higher CaO contents than the other Aegina volcanic deposits (Fig. 6.21C), the geochemical model involving assimilation of significant amounts of limestone is not valid. The sedimentary basement lithologies used for these geochemical modelling calculations are furthermore not likely to be present at the crustal depths were the first stages of magma differentiation occur. Successful reproduction of the geochemistry of some volcanic deposits (Fig. 6.31) is therefore interpreted to suggest that crustal differentiation levels had a Sr-Nd geochemical composition similar to Aegina's sedimentary basement rocks – not that crystal fractionation actually took place in exactly these basement rocks.

The host rock with the most enriched Sr and depleted Nd composition, Palaiochora dacitic andesite IA61, can not be modelled by contamination with any of the crustal rocks collected in this study (Fig. 6.31). These enclave-free lavas have a geochemical composition that is distinctly different from the other first phase intermediate lavas, with the by far lowest Mg#, low MgO, MnO, Na_2O, K_2O, Co, Cu, Ni, Cr and Th concentrations and high Al_2O_3, TiO_2, and Zr contents (Fig. 6.20 – 6.23). This characteristic geochemistry probably results from differentiation of a distinct batch of magma (also suggested by the geographical isolation of the Palaiochora lavas in the northern sedimentary part of Aegina – Fig. 6.2) at a specific crustal level and/or involving a slightly different crystallising mineral assemblage (as reflected in the strong brown-green to bluish-green pleochroic amphiboles that are only observed in these deposits (Fig. 6.28A,B). The Palaiochora dacitic andesites are the only intermediate-felsic lavas which do not contain enclaves – and could thus have ascended and erupted without the trigger mechanism of a mafic injection. The details on how exactly the petrogenesis of the Palaiochora magmas differs from that of the other first phase deposits is not entirely clear. Their geochemistry, however, seems to reflect the composition of a crustal end member that also influenced the geochemistry of most other first phase magmas. Since this crustal contaminant is not (yet) identified, the composition of most evolved Palaiochora host rock IA61 is used as end member instead as it successfully explains the $^{87}Sr/^{86}Sr$-$^{143}Nd/^{144}Nd$ composition of the majority of first phase volcanic deposits by simple mixing with the Skotini lavas (Fig. 6.31C). Binary mixing between the Palaiochora lavas and more mafic magmas, derived from basalt IA72 and a crustal rock with a Sr-Nd geochemistry similar to limestone IA62 by either AFC or mixing, also reproduces the Nd isotopic composition of most other, more intermediate lavas (Fig. 6.31D). However, many host rocks and enclaves from the first period of volcanic activity plot away from this Skotini-Palaiochora mixing line, towards higher Sr contents (see grey arrow in Fig. 6.31A). Interestingly, this is also the direction in which calcarenite IA343 plots, at up to 10 times higher Sr contents (ca. 4000 ppm) and slightly more radiogenic $^{87}Sr/^{86}Sr$ (0.708950). A minor role for this siliciclastic lithology is suggested by successful reproduction of enclave IA348 (representing the most 'aberrant' Sr geochemistry) by AFC from basalt IA72 involving ca. 12.5% crystallisation of a plagioclase-rich mineral assemblage and concurrent assimilation of calcarenite IA343 (Fig. 6.31B).

Table 6.5 presents the **geochemical composition of end-members** that are inferred to have played an important role in the petrogenesis of Aegina's magmas. The Sr and Nd systematics of these 'sources' were discussed above. The $^{176}Hf/^{177}Hf$ ratio is not separately mentioned, but its overall good positive correlation with the $^{143}Nd/^{144}Nd$ ratio (Fig. 6.26C & E) indicates a similar behaviour as discussed for the Nd isotopic. The Pb systematics within Aegina's volcanic deposits are however almost completely decoupled from the Sr and Nd-Hf system, with even a discrepancy between the $^{206}Pb/^{204}Pb$ ratio and the $^{207}Pb/^{204}Pb$-$^{208}Pb/^{204}Pb$ composition (Fig. 6.27). The only basement sample that contains just enough lead to allow analysis of its Pb isotopic composition is calcarenite IA343, but its Pb isotope ratios plot near the most radiogenic compositions of the volcanic rocks, ruling it out as potential contaminant. (see Appendix F2). Decoupling between the $^{206}Pb/^{204}Pb$ and $^{207}Pb/^{204}Pb$ systems is mainly expressed in the inversion of radiogenic composition for the first and second phase volcanic deposits: whereas the second phase magmas all show high $^{206}Pb/^{204}Pb$ ratios in comparison to the overall lower ratios of the first phase lavas, they contain the lowest $^{207}Pb/^{204}Pb$ ratios within the compositional range of the older phase 1 samples (Fig. 6.27A-B). The $^{208}Pb/^{204}Pb$ ratios of the first and second phase volcanic series show an arrangement intermediate to those of the $^{206}Pb/^{204}Pb$ and $^{207}Pb/^{204}Pb$ compositions (Fig. 6.27C). Samples thereby seem to cluster together according to their outcrop area: Kakoperato host rock and enclaves have virtually the same $^{208}Pb/^{204}Pb$ ratios, all phase 2 volcanics from the Oros and Lazarides areas plot within a relatively narrow range which is similar to that of most phase 1 magmas, with the distinct exception of the Palaiochora lavas, location 61 Skotini andesite samples and those Kakoperato host rocks and enclaves sampled near location 66. The latter two groups (outcrop 61 Skotini andesites and outcrop 66 Kokkinovrahos lavas) define a single trend within the $^{207}Pb/^{204}Pb$-$^{208}Pb/^{204}Pb$ diagram which deviates from Aegina's main trend (roughly defined by samples IA80 and IA61) towards less radiogenic compositions (Fig. 6.27D-F). These samples also showed the largest deviation from the Sr systematics within the first phase volcanic deposits (Fig. 6.27A) and furthermore contain Ba, Cr, Zr and P_2O_5 concentrations which are distinctly higher than other first phase lavas with similar amounts of silica (Fig. 6.21 & 6.23). These elements are compatible in specific minerals (biotite, amphibole-clinopyroxene-biotite, zircon and apatite, respectively – GERM distribution coefficient databe, http://earthref.org/KDD/) of which crystals observed in thin section have been interpreted as antecryst from earlier fractional crystallisation processes. Some of these antecrysts are also inferred to be present in thin sections from the outcrop 61 Skotini and outcrop 66 Kokkinovrahos lavas – leading to the interpretation of these samples' aberrant trace element and Pb isotopic composition as resulting from incorporation of (larger amounts of?) of crystals from previous differentiation processes. The fact that their Pb isotopic composition is less radiogenic than that of the 'normal' macro-phenocryst-bearing deposits suggests that the incorporated plagioclase-rich cumulates

End member	**Representa-tive sample**	**SiO_2 / MgO**	**$^{87}Sr/^{86}Sr$**	**$^{143}Nd/^{144}Nd$**	**$^{206}Pb/^{204}Pb$**	**$^{207}Pb/^{204}Pb$ $^{208}Pb/^{204}Pb$**	**Remark**
Primitive magma	**IA72**	lowest/ high	lowest	highest	~ highest	int. high	Most 'primitive' Sr, Nd & Hf isotopes
Phase 1 mafic magma	**IA101**	int. low / int. high	lowest in phase 1	highest in phase 1	int. high	int. high	AFC from IA72 with limestone
Phase 2 contaminant	**IA97**	highest / lowest	int. high	int. low	intermediat e	int. high	Furthest differen-tiated (lowest Mg#)
Phase 1 contaminant	**IA61**	high / lowest	highest	lowest	int. high	highest	Overall most 'crustal' isotope ratios
Pb-source	**IA345**	int. low / highest	~ highest	intermediate	lowest	lowest in phase 1	Most 'primitive' Pb isotopes
int. = intermediate, see Fig. 6.17-6.18-6.22-6.23.							

Table 6.5. *Geochemical characteristics of the different end-members identified within the Aegina's volcanic deposits.* See text for discussion.

formed early on in the petrogenesis, when the magmas Pb isotopic composition was still relatively primitive. The lowest Pb isotope ratios, analysed in outcrop 66 enclave IA345, are therefore combined with the overall most primitive composition of basaltic enclave IA72 to reflect the initial melt composition of Aegina's volcanic rocks (see Table 6.5).

6.7 Discussion on the petrography and geochemistry of the volcanic deposits of Poros

Although the Poros lavas are divided into andesites and dacites on the geological map of Schwandner (1998) (Fig. 6.6), fieldwork observations, petrography and geochemical analyses carried out during this study suggest that all host rocks have the same dacitic andesitic composition. This finding agrees with the older geological map of Fytikas et al. (1972) on which the volcanic peninsula of Sferia is indicated as one single volcanic unit. I therefore suggest to change the two different volcanic units proposed by Schwandner (1998) back to one single unit of effusive andesitic dacites.

All petrographic characteristics of the Poros host rocks and enclaves presented in this study (Fig. 6.18-6.19) furthermore agree with data available in literature. The petrographic study of Davis (1957) describes the Poros volcanic rocks as fissure eruption products with a specific hornblende-biotite-augite dacitoïd mineralogy that does not occur on either Methana or Aegina. Davis (1957) also points out the large amounts of biotite in all Poros lavas, a macroscopic pinkish colour of quartz crystals (interpreted as xenocrysts) and two different types of enclave mineralogy. The presence of primary allanite was first reported by Mitropoulos (1987), who also noticed that despite the presence of this accessory mineral, its host rock shows a geochemical composition and chondrite-normalised REE pattern very similar to the allanite-free lavas.

The occasional presence of allanite, a mineral known to precipitate late in the crystallising assemblage, and common occurrence of quartz, zircon and holocrystalline aggregates of plagioclase + amphibole + biotite in all Poros host rocks (Fig. 6.18) suggest that the crystal cargo of these porphyritic lavas is (at least partially) inherited from an almost completely solidified crystal mush or sub volcanic intrusive body. Published geochemical data on the composition of amphibole crystals from volcanic deposits on Poros (Pe, 1973; Mitro-polous & Tarney, 1992; Dorais and Shriner, 2002) have been used to estimate of the P-T conditions during their crystallisation with the geothermobarometer of Ridolfi et al (2010) (Fig. 6.32). The pressure-temperature ranges calculated from these three independent literature sources define the same two crustal levels of amphibole fractionation: most amphiboles were formed at temperatures of ca. 875 - 935°C and a depth of ca. 8.5 to 12.5, but two analyses reflect crystallisation at significantly higher temperature and pressure (985°C at 19-20 km depth) (Fig. 6.32). One of these high P-T amphiboles originates from a mafic enclave, whereas a host rock

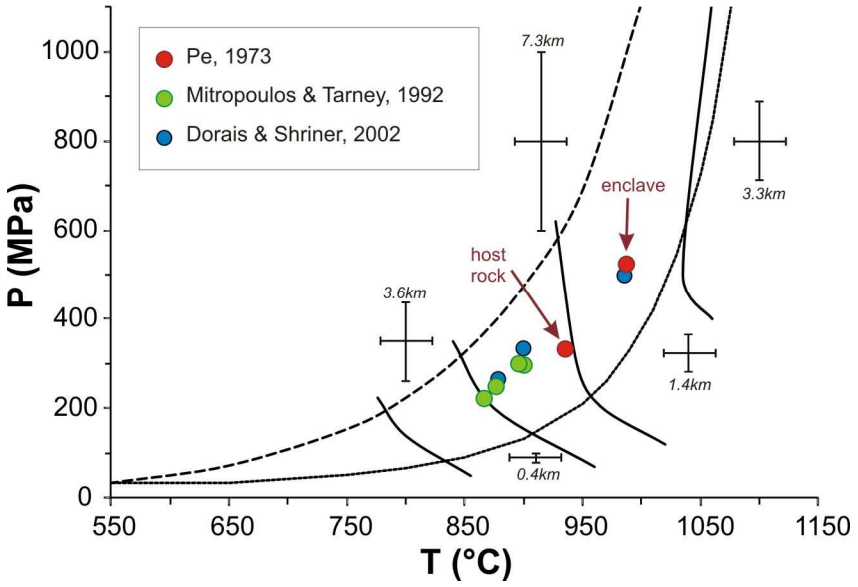

Figure 6.32. *P-T diagram for volcanic amphiboles from Poros, Aegina and Methana,* calculated according to the geothermorbarometer of Ridolfi et al. (2010). For more details or the references for the Aegina and Methana data, see Fig. 6.25 and Fig. 5.30, respectively.

amphibole from the same study (Pe, 1973) reflects formation at the shallower crustal level (Fig. 6.32). The amphibole crystallisation level at ca. 19-20 km depth is therefore proposed to reflect the level at which the basaltic andesitic magma crystallised before it came into contact with a crystal-rich magma at ca. 8.5-12.5 km depth. This gap in amphibole geochemistry between crystals from the Poros host rocks and their more mafic enclaves adds to their distinctly different whole rock compositions (Fig. 6.20-6.27). The relatively narrow compositional ranges of both enclaves and host rocks, and the large geochemical gap in between, furthermore suggests limited chemical mixing between the dacitic andesite magmas and their basaltic andesitic enclaves. Physical mingling of these two geochemically distinct magmas, however, did occur as shown by 1) the presence of the rounded, more mafic enclaves (Fig. 6.7D-E), 2) occasional olivine antecrysts in the lavas which are thought to originate from the enclave magma (Fig. 6.18K), and 3) the presence of holocrystalline plagioclase-amphibole-biotite aggregates, or individual amphibole, plagioclase, biotite or quartz antecrysts in the enclaves which are probably derived from the host rock magma (Fig. 6.19).

The whole rock geochemistry of the Poros volcanic deposits is usually intermediate to the compositional ranges displayed by the volcanic centre of Aegina. Poros magmas, however, are characterised by the higher amounts of Li, elevated Sc, Cr, V and Cs concentrations, lower Fe_2O_3, TiO_2, MnO and Y contents and a high $^{208}Pb/^{204}Pb$ composition (Fig. 6.21, 6.23, 6.24 & 6.27). Comparison of the primitive mantle- and chondrite-normalised trace element abundance patterns of the Poros host rocks to volcanic deposits of similar differentiation from Aegina shows that they mostly resemble the Kakoperato rhyodacites (Fig. 6.24A-6.25A). The petrogenesis of the Kakoperato lavas has been shown to involve remobilisation of an older felsic crystal mush by a mafic replenishment with a slightly different genetic origin (Kakoperato enclaves have the geochemical characteristics of Aegina's phase 2 magmas whereas the Kakoperato rhyodacite has an Aegina phase 1 composition). The primitive mantle- and chondrite-normalised trace element abundance patterns of the Poros enclaves, on the other hand, show most similarities with the Aegina phase 2 volcanic deposits (Fig. 6.24B & 6.25B) - exactly those basaltic andesites that are interpreted as the mafic replenishments initiating the second phase of volcanism.

Both on Aegina and Methana, renewal of volcanic activity is thought to result from the onset of a new tectonic regime which involved crosscutting of different fault systems (Pe-Piper & Piper, 2013). The structural development of Poros also includes a Pliocene phase during which NW-SE and WNW-ESE normal faults are formed and intersect one another (Schwandner, 1998). Figure 6.6 shows that such an intersection of normal faults is located directly below the' peninsula of Sferia which itself consists of fissure erupted lavas with a NW-SE and WNW-ESE orientation. It is therefore likely that the volcanic deposits of Poros represent a single volcanic eruption which coincided with a change in the Saronic Gulf's tectonic regime similar to the ones that triggered renewal of volcanic activity on Aegina and Methana. At such tectonically active times, extensional faults created new magma pathways below intersecting faults which allowed upwelling of significant volumes of hot and hydrous arc magmas to rise towards the surface. During their rise to the surface, mafic magmas became trapped beneath a nearly solidified crystal mush or sub-volcanic intrusion ca. 8.5-12.5 km below Poros. Interaction between the underplating hot mafic magma and the overlying cooler crystal mush led to partial melting of the latter.

Despite wide-spread petrographic and geochemical evidence for remobilisation of largely solidified shallow intrusions by (multiple) mafic injections as an important eruption trigger, this process requires substantial amounts of enthalpy and mafic intrusions comparable in size to the stalled crystal mushes (Murphy et al., 2000; Snyder, 2000; Allen, 2001; Couch et al., 2001; Bachmann et al., 2002; Bachmannn et al., 2007, Huber et al., 2010). Recent studies based on numerical modelling and experimental petrology, however, show that mafic replenishments are not only responsible for heating up a crystal mush but can also add upwards migrating volatiles and increase its internal pressure. Mafic underplating can thus induce small amounts of melting (10-20%) and enhance volatile oversaturation in an overlying crystal mush. The increased pressure from gas bubbles and melt

fractions results in mechanical deformations of the stalled magma which greatly reduce its viscosity, accelerate its self-assimilation and eventually trigger its eruption without requiring intense chemical mixing between mafic injection and rejuvenated mush (Bachmann & Bergantz, 2003; Bachmann & Bergantz, 2006; Huber et al., 2011; Pistone et al., 2013).

Given petrographic and geochemical characteristics of the Poros dacitic andesites and their basaltic andesitic enclaves, and the growing scientific recognition of mafic underplating-induced transitions from rheologically locked-up crystal mushes to sluggishly convecting magma bodies as an important eruption mechanism, this process is proposed as petrogenesis for the one-off effusive volcanic eruption in the southern part of Poros island. The eruption of biotite-amphibole-zircon-allanite-bearing silicic ignimbrites in the Pannonian Basin during Miocene flare-up of volcanic activity is similarly interpreted as triggered by mingling between evolved crystal mushes and mafic replenishments (Czuppon et al., 2012).

6.8 Petrogenesis of the volcanic rocks of Aegina and Poros

The volcanic rocks studied on **Aegina** represent lava flows and solidified plugs at effusive vents and (both massive lavas and autoclastic breccia) erupted during two separate periods of volcanic activity. The first volcanic phase is thought to have lasted at least 2 Ma and covered two thirds of the island with mainly enclave-bearing andesites. A more detailed study of the Kokkinovrahos biotite-hornblende andesites, which are geographically isolated in the NE, shows that whereas host rocks have a homogeneous mineralogy and geochemistry, the enclaves display a lot more compositional variation. A distinct geochemical gap separates the Kokkinovrahos biotite-hornblende andesites enclaves from their host rocks. All other volcanic deposits from the first phase of activity also display a geochemical gap between their host rocks and enclaves. Phase 1 biotite-hornblende andesite host rocks all show a similar mineralogical composition (plagioclase + amphibole + clinopyroxene + biotite + Fe-Ti-oxides + apatite ± orthopyroxene ± quartz ± zircon) and geochemistry. The Palaiochora dacitic andesites and Skotini andesites, however, have more distinct mineralogies and geochemical compositions. The Palaiochora dacitic andesites represent the most felsic deposits of the first volcanic phase and are located atop the sedimentary basement in the north. They combine the absence of enclaves with distinctly brown-green to bluish-green pleochroic amphibole crystals and a significantly different geochemical composition. The Skotini andesites represent the oldest and most mafic lavas of the first volcanic phase. They are scattered in the central-western parts of Aegina and contain yellow olivine crystals and quartz-rich xenoliths.

The first volcanic phase was followed by a prolonged period of volcanic quiescence (up to 1 Ma) during which the volcanic deposits of the first phase were largely weathered, eroded and re-deposited as a volcaniclastic apron that covers most of the southern part of Aegina. The renewal of volcanic activity is represented by the westerly located Kakoperato lava flow which contains numerous more mafic enclaves in a phenocryst-poor, glassy host rock with plagioclase + amphibole + biotite + clinopyroxene + Fe-Ti-oxides + apatite + quartz ± zircon. This second period of volcanism is however markedly shorter than the first one and mainly comprises deposition of basaltic andesites in the central Oros and Lazarides area. In comparison with the deposits of the first phase, the second phase volcanics contain markedly fewer enclaves and nearly no hydrous minerals free of disequilibrium features. Both quartz mantled by pyroxene and olivine are occasionally present in the Oros-Lazarides basaltic andesites of which the mineralogy mainly comprises plagioclase + clinopyroxene + hydrous mineral pseudmorphs + Fe-Ti-oxides + apatite ± amphibole ± orthopyroxene. Only the (inferred) youngest lavas of the enclave-bearing Oros hornblende andesite have significant amounts of fresh, euhedral amphibole and a geochemical composition similar to the more mafic lavas of the first volcanic phase.

Despite their mineralogical-geochemical differences, all of Aegina's volcanic deposits can be derived from the composition of this study's most mafic basaltic enclave – as shown by major element

and Sr-Nd isotopic models of fractional crystallisation, assimilation and magma mixing. The petrogenesis of the first and second phase volcanic deposits is however inferred to be distinctly different. The amphibole-bearing intermediate magmas of the first phase underwent different fractional crystallisation steps at varying crustal depths before their eruption was triggered by a mafic injection. The different crystal populations of the phenocryst-rich host rocks and large scatter in the enclaves' geochemistry reflects the presence of antecrysts from earlier differentiation steps in both rock types. Geochemistry and petrography of the first phase volcanic rocks also indicate that interaction between replenishing enclave magma and more felsic crystal mush was limited to physical mingling and only minor involvement of chemical mixing.

The geochemical composition and petrographic characteristics of all second phase Oros-Lazarides magmas, however, can be most easily explained by intense magma mixing and hybridisation between Aegina's primitive magma and the Kakoperato rhyodacitic host rock. Erupted at the hinge between deposition of the main volumes of volcanic rocks from the first and second phase, the Kakoperato unit displays a dual geochemistry in which the host rocks have all the characteristics of first phase lavas but the enclaves reflect an origin from the second period of volcanic activity. This apparent discrepancy is explained by a petrogenesis in which the Kakoperato rhyodacitic host rock represents a batch of crystal-rich phase 1 magma trapped in the crust where it continued to differentiate throughout the pause of volcanism but which was eventually remobilised by injection of a large volume of more mafic phase 2 magma. This hypothesis is supported by major element modelling which suggests crystal fractionation of evolved, felsic mineral phases from the host lavas and by the latter's rounded, resorbed phenocrysts and large volumes of glassy groundmass that indicate partial melting.

The small volcanic peninsula of **Poros** island is thought to represent andesitic-dacitic lavas deposited in a single eruption event. Both enclaves and host rocks define a relatively small compositionally range on either side of the distinct geochemical between them – suggesting that there was only limited mixing between the host rock and enclave magmas. The enclaves display a mineralogical and geochemical composition similar to Aegina's phase 2 enclaves (Fig. 6.21-6.22-6.23-6.26) which suggests that they had a petrogenesis similar to these mafic replenishment magmas from Aegina. The host rocks, however, show a distinctly different mineralogical and geochemical composition that is unique amongst the Saronic Gulf lavas (significantly more biotite and occasionally allanite, high Sr, Cs, Pb and Li and low Y and Ba – Fig. 7.3). Amphibole major element compositions confirm that the felsic crystal mush (or sub volcanic intrusion) from which the Poros host lavas are derived underwent crystal fractionation at a crustal differentiation level that is not reflected in the amphibole geochemistry on either Aegina or Methana. The volcanic deposits of Poros are therefore interpreted as a 'one-off' volcanic event during which mafic replenishment triggered the eruption of arc-magmas that reside and differentiate below Poros.

Chapter 7: Magma genesis below Aegina, Methana & Poros: comparison and influence of local tectonics

Chapters 5 and 6 present the petrogeneses of the volcanic deposits of Aegina, Methana and Poros, inferred from detailed descriptions of their petrography, thorough study of their geochemical composition and integration of this new information with literature data. In order to investigate the spatial-temporal evolution of volcanic activity throughout the Saronic Gulf, Chapter 7 compares the results from these previous chapters and discusses the link between extensional tectonics and volcanism in the western part of the South Aegean arc. The geochemical characteristics of the three magmatic centres are first compared to one another to facilitate subsequent identification of the different sources that played a role in the petrogenesis of the Saronic Gulf volcanic rocks. All petrogenetic sources and processes identified in the volcanic deposits of Aegina, Methana and Poros are then discussed within the framework of the local geodynamic system and subduction zones in general. This chapter finishes with a summary of the main conclusions that emerged from this study petrographic-geochemical study of volcanism in the Saronic Gulf.

7.1 Comparing the geochemistry of volcanic rocks on Aegina, Methana and Poros

All major and trace element concentrations and Sr-Nd-Hf-Pb isotopic compositions obtained in this study for the volcanic deposits of the Saronic Gulf are presented in Appendices B, C, D and E, respectively. The geochemical composition of sedimentary xenolith and basement samples collected from Aegina and Methana are documented in Appendix F. To avoid cluttering of diagrams, all literature data are omitted except for the few published major element concentrations of the Poros volcanics.

In the following diagrams, host rocks are often open symbols whereas enclaves are usually filled symbols. All samples of Methana's volcanic depostis are presented in green apart from the petrogenetically different Loutses South host rocks which are orange-yellow (see Fig. 7.1). The samples from Aegina are subdivided into those from the first phase of volcanic activity (blue symbols) and those from the second (purple symbols) (see Fig. 7.1). The Kakoperato rhyodacite, representing renewal of volcanic activity on Aegina, has a blue symbol for its very evolved host rocks that are derived from a phase 1 magma, but a purple symbol for its enclave that has the geochemical characteristics of the magmas from the second phase (see Fig. 7.1). Volcanic samples from Poros are indicated in red and the two igneous xenoliths found on Methana and interpreted as chilled margins of a magma chamber are represented by grey crosses (see Fig 7.1).

7.1.1 Major element compositions

Figure 7.1B shows that all volcanic deposits of the Saronic Gulf broadly define a single trend in which most host rocks group together in the andesitic compositional field and the majority of enclaves have a basaltic andesitic composition. A few basaltic enclaves and rhyodacitic host rocks are also found on Aegina and Methana (Fig.7.1B). When the distinct geochemical composition of Aegina's Kakoperato host rocks are not taken into account, these diagrams furthermore show that the volcanic

centre of Methana represents the overall largest geochemical variation. This large geochemical range is thereby continuous as it lacks the geochemical gap between host rocks and enclaves that is distinctly present in the geochemistry of the Aegina and Poros volcanics (Fig. 7.1). Despite their overall geochemistry, the different volcanic suites show subtle variations in their potassium contents: whereas all Methana samples are medium-K volcanics and the majority of the Aegina phase 1 rocks plot in the high-K series, the volcanic deposits of Poros and of Aegina's second phase of volcanic activity plot in the middle and straddle the boundary between medium-K and high-K compositions (Fig. 7.1A).

Other major and minor element variation diagrams confirm that the Methana volcanic deposits often usually define the overall largest spread in geochemical composition and lack the geochemical gap present between all host rocks and enclaves from Aegina and Poros (Fig. 7.2). Calcium and iron are the only elements for which all three volcanic centres show a single trend with little to no scatter, from most mafic basalts DPM36 and IA72 to most felsic host rock DPM42 and the Kakoperato rhyodacites (Fig. 7.2A & C). Only the two igneous xenoliths have significantly higher Ca contents (Fig. 7.2A). In contrast to these well-defined CaO and Fe_2O_3* trends, the MgO variation diagram shows significant scatter for the mafic compositions of the Saronic Gulf samples and three sub-trends for the more felsic rocks (end-members of which are DPM26, DPM42 and IA61) (Fig. 7.2B). Titanium, manganese and aluminium concentrations show a similar variation with increasing silica contents, starting from one geochemical field (with some scatter) for the enclaves and ending in multiple trends

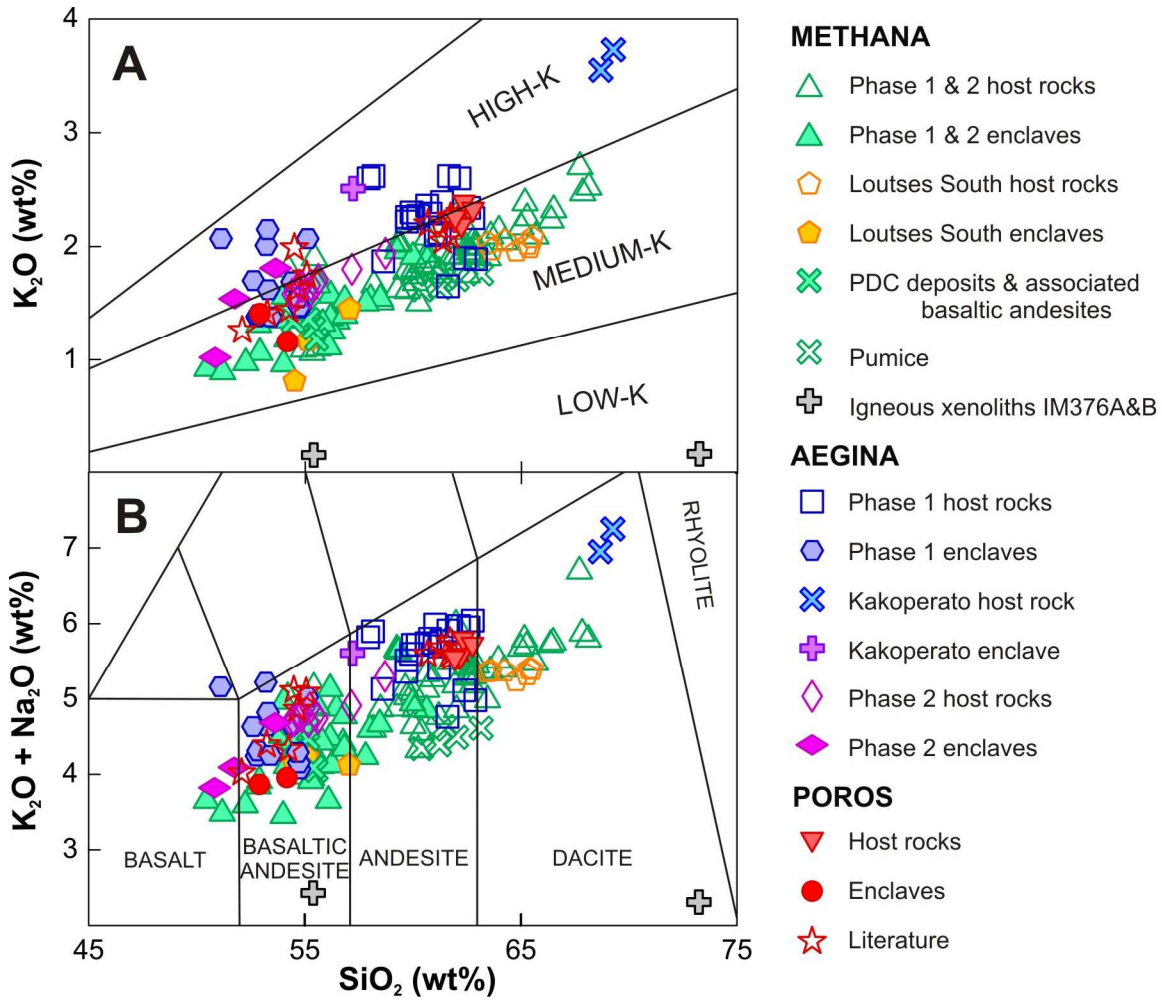

Figure 7.1. *Geochemical classification of the volcanic rocks from the Saronic Gulf*. (A) K_2O-SiO_2 classification diagram according to Gill (1981). (B) Total Alkali versus Silica diagram after Le Maitre et al. (2002).

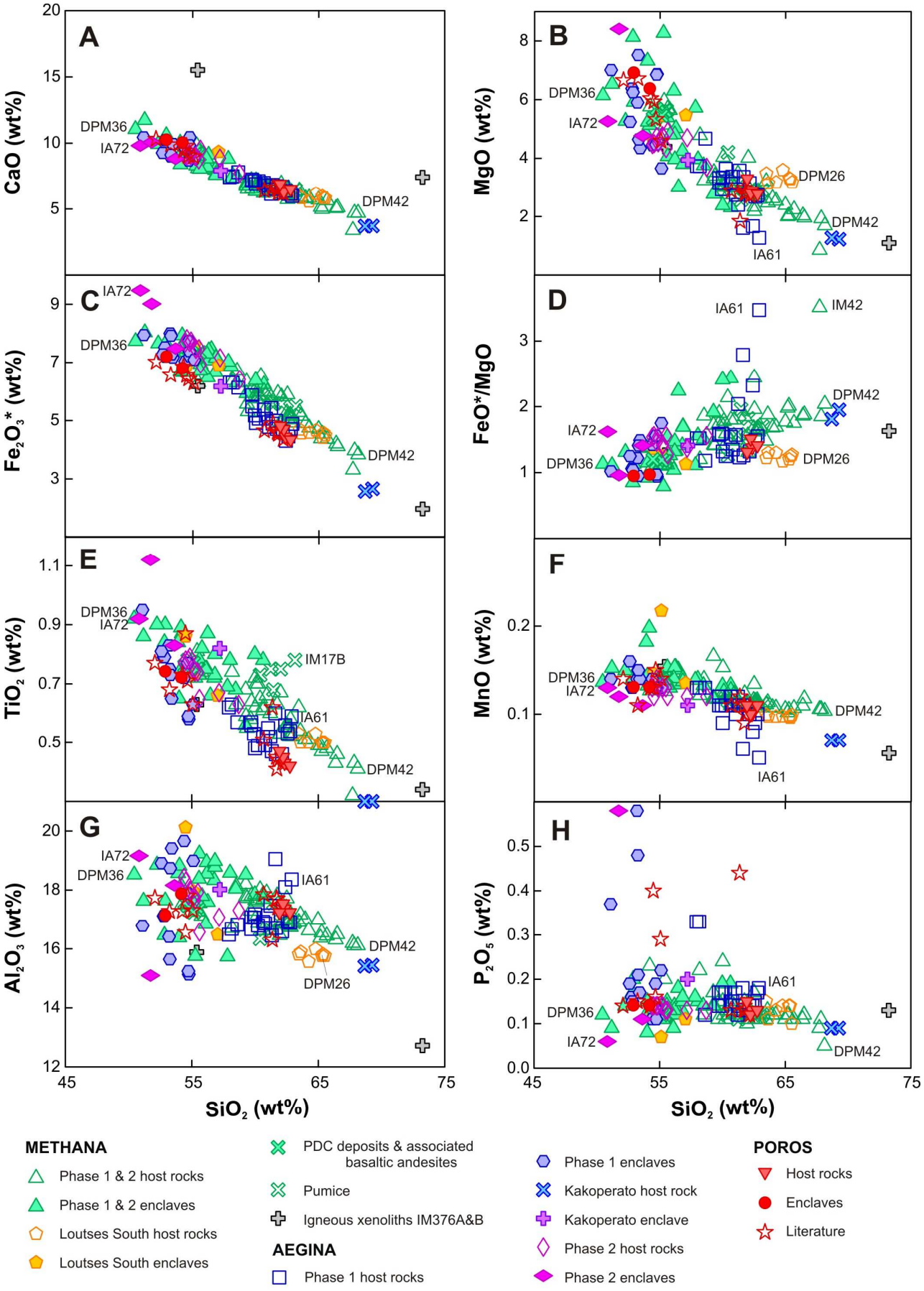

Figure 7.2. *Harker variation diagrams of the whole rock major and minor element contents of all Aegina, Methana and Poros volcanic deposits*.

for the host rocks towards the compositions of IA61, DPM26 and DPM42 (Fig. 7.2E-G). Most Saronic Gulf volcanic rocks have phosphor contents that range from 0.05 to 0.25 wt%, but a few samples from Aegina and literature values for Poros plot at significantly higher P_2O_5 concentrations of up to 0.60 wt% (Fig. 7.2H). The major element geochemistry of the Methana volcanic suite usually overlaps with the Aegina phase 1 compositions so that together they define a large compositional range in the middle of which the Poros and Aegina phase 2 samples often plot (Fig. 7.2). The Poros' samples however plot at slightly lower Fe_2O_3* values (Fig. 7.2C), consistent with their somewhat lower FeO*/MgO, TiO_2 and MnO concentrations for a given silica content (Fig. 7.2D-F).

7.1.2 Trace element geochemistry

The trace element variation diagrams of the volcanic deposits of the Saronic Gulf show broadly the same characteristics as their major element composition. Aegina and Methana have similar Sc concentrations which also overlap with the Poros host rocks at higher Sc contents but which don't include the Poros enclaves which contain the overall highest amounts of scandium (Fig. 7.3A). All Poros samples have Cr concentrations higher than the main Aegina-Methana trend but still within the Saronic Gulf compositional range which shows a lot of scatter, especially for the enclaves which seem to define two different trends (Fig. 7.3B – Ni and Co geochemistry is similar). Vanadium (and Cu) show a negative correlation with increasing silica contents which defines one main series for Aegina, Methana and Poros (Fig. 7.3C). The Poros enclaves thereby plot at the highest V concentrations together with the Aegina phase 2 volcanic rocks which define an individual trend above the Aegina phase 1 and Methana samples (Fig. 7.3C). The yttrium (and zinc) contents of the Poros enclaves also coincide with the Aegina phase 2 samples, but this time plot well below most Aegina phase 1 and Methana enclaves (Fig. 7.3D). Poros host rocks also have low Y concentrations and coincide with the most Y-poor Aegina phase 1 lavas (the Kokkinovrahos host rocks - Fig. 7.3D). Whereas the geochemical ranges of Aegina and Methana largely overlap one another for the above discussed compatible elements, their Sr concentrations are distinctly different: most Methana volcanic deposits have low Sr contents (200-450 ppm) whereas all Aegina lavas and the Methana Loutses South deposits contain significantly more Sr (450-900 ppm) – Poros enclaves and host rocks have intermediate Sr levels (400-450 ppm) (Fig. 7.3E). With regard to the incompatible LILE Ba, the Aegina phase 1 lavas have distinctly higher concentrations (400 – 1100 ppm) than the other volcanic deposits of the Saronic Gulf (ca. 200-400 ppm) (Fig. 7.3F). Aegina and Methana have varying Cs contents that largely overlap one another, with Poros enclaves and Aegina phase 2 samples plotting at higher Cs contents and the Poros host rocks containing the overall highest amounts of Cs (Fig. 7.3G). Rubidium and Be show Harker variation diagrams similar to that of Cs, but the Li concentrations of both enclaves and host rocks from Poros plot well above Aegina and Methana samples (Fig. 7.3H). The lead contents (and U and Th) of the three volcanic centres seem to define two different trends: most Methana samples show a slight positive correlation with increasing silica contents towards DPM42 whereas most Aegina host rocks represent a steeper upward trend with increasing differentiation, towards IM42 (Fig. 7.3I). The Kokkinovrahos enclaves and host rocks plot at even higher lead concentrations towards the Kakoperato rhyodacites, and the Poros samples define a series at the boundary of the Methana and Aegina compositional ranges (Fig. 7.3I). Despite scatter, incompatible HFSE Nb (and Ta, Zr) shows a trend of positive correlation with increasing differentiation in which the large compositional ranges of Methana and Aegina phase 1 overlap, the Aegina phase 2 rock define a narrower range at the lowest Nb concentrations and the Poros samples contain intermediate Nb amounts (Fig. 7.3J).

The major, minor and trace element variation diagrams discussed above suggest that the Saronic Gulf deposits can be roughly divided into two groups: 1) the more differentiated Aegina Phase 1 host rocks, the Poros host rocks and Methana pumice and host rocks (including Loutses South host rocks), and 2) the more mafic Aegina Phase 1 enclaves, the Aegina Phase 2 host rocks and enclaves, the Poros enclaves and the Methana enclaves and PDC deposits with associated basaltic andesites.

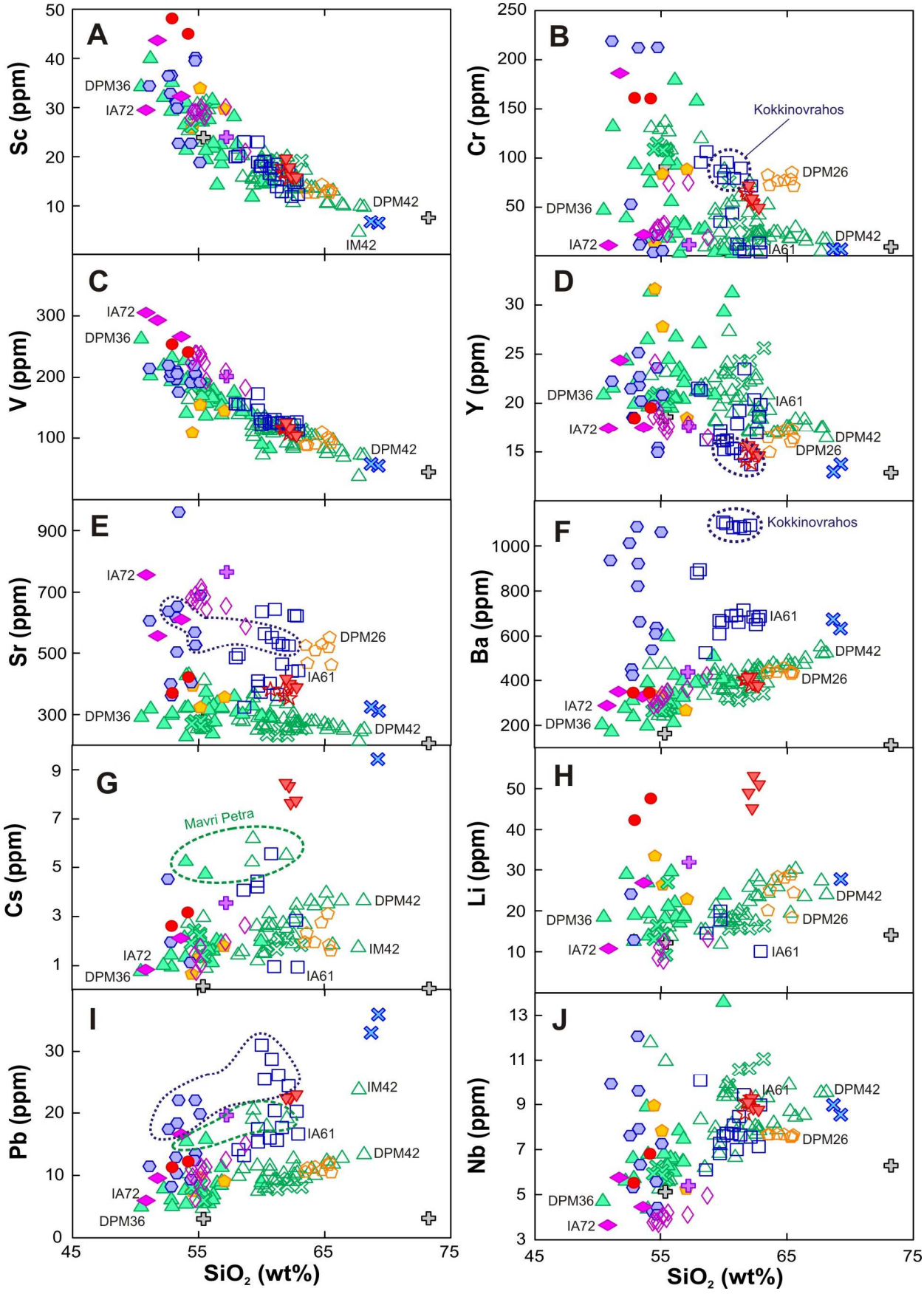

Figure 7.3. *Whole rock trace element Harker variation diagrams for all volcanic rocks of Aegina, Methana and Poros* sampled in this study. Symbols as in Fig. 7.2.

Figure 7.4 shows the primitive mantle-normalised trace element abundance patterns of the first, more silica-rich group. The Poros host rocks all have a similar trace element composition which defines a relative steep pattern with higher amounts of LILE and lower HREE contents than any Methana sample (Fig. 7.4A). Their pattern most resembles that of the Loutses South host rocks but they contain slightly higher Cs, Rb, U and Pb contents (Fig. 7.4A). The Poros host rocks also have slightly higher LILE and lower LREE concentrations than the Aegina phase 1 host rocks and their primitive mantle-normalised trace element abundance patterns most resemble the (even somewhat steeper) patterns of the Kakoperato rhyodacites (Fig. 7.4B). Comparison between Methana and Aegina also reveals some distinct differences: Aegina phase 1 host rocks have a positive Ba anomaly and higher amounts of Th, U, K, Pb, Sr and P than the Methana host rocks which contain a negative Ba anomaly (Fig. 7.4C). The more mafic, less evolved volcanic rocks sampled on Poros, Aegina and Methana are shown in Figure 7.5. The primitive mantle-normalised trace element abundance patterns of the Poros enclaves plot within the range of patterns of the Methana enclaves, and they are very similar to the trace element patterns of Methana's basaltic andesitic lavas (Fig. 7.5A). As already indicated by the major, minor and trace element variation diagrams, the Kakoperato enclave, Aegina phase 2 host rocks and enclaves and Poros enclaves all have similar trace element patterns which are distinctly different from the Aegina phase 1 enclaves which have a positive Ba anomaly, similar to lower amounts of Th and U but higher Nb, Ta, Sr and P concentrations (Fig. 7.5B). Comparison between Methana's more mafic samples and Aegina's basaltic andesites shows that primitive mantle normalised trace element abundance patterns of the former are somewhat more horizontal, with lower LILE and higher HREE contents, than the latter (Fig. 7.5C). Aegina phase 2 host rocks and enclaves have trace element patterns intermediate to the Methana enclaves and the Aegina phase 1 enclaves but which overall resemble more those of the Methana basaltic andesites, with distinctly negative Ba and P anomalies (Fig. 7.5C). The phase 1 enclaves have only slightly negative to no P anomalies – as does phase 2 enclave IA78 which has a geochemistry that is overall distinct from the other Aegina phase 2 samples (Fig. 7.5C).

Figure 7.6 presents the chondrite-normalised REE patterns of volcanic rocks from Aegina, Methana and Poros divided into the same more felsic (Fig. 7.6A-C) and more mafic (Fig.7.6D-F) compositional groups as discussed above. The Methana host rocks contain overall higher REE concentrations than the Aegina phase 1 host rocks, and show a relatively straight slope from the MREE to the HREE in comparison to the slightly downwards dipping pattern of the Aegina phase 1 samples (Fig. 7.6A-C). The Kakoperato rhyodacitic host rocks represent the most distinct spoon-shape pattern of all the Saronic Gulf's more felsic samples, similar to the Loutses South host rocks of which the pattern, however, lacks the slightly higher amounts of HREE than MREE (Fig. 7.6A-C). The four Poros host rock samples have very similar chondrite-normalised REE patterns that are intermediate to those of the Kakoperato rhyodacites and the Loutses South host rocks (Fig. 7.6A-B). Chondrite-normalised REE patterns of the more mafic samples are overall less steep (lower LREE and higher HREE contents) than those of the more felsic rocks (Fig. 7.6). The Methana enclaves and basaltic andesitic lavas show the flattest patterns, with a stronger downward slope from LREE to MREE, and a more sub-horizontal slope from the MREE to the HREE (Fig. 7.6D-F). In contrast, Aegina's more mafic samples have a steeper pattern that starts at higher LREE and ends at lower HREE in a nearly continuous slope – especially so for phase 2 enclave IA78 (Fig. 7.6D-F). None of the Methana or Aegina more mafic enclaves show a spoon-shaped pattern - only the Poros enclaves have a chondrite-normalised REE pattern that is somewhat reminiscent of a spoon-shape (Fig. 7.6D-E). All Poros, Aegina and Methana volcanic deposits furthermore display a (small) negative Eu anomaly (Fig. 7.6).

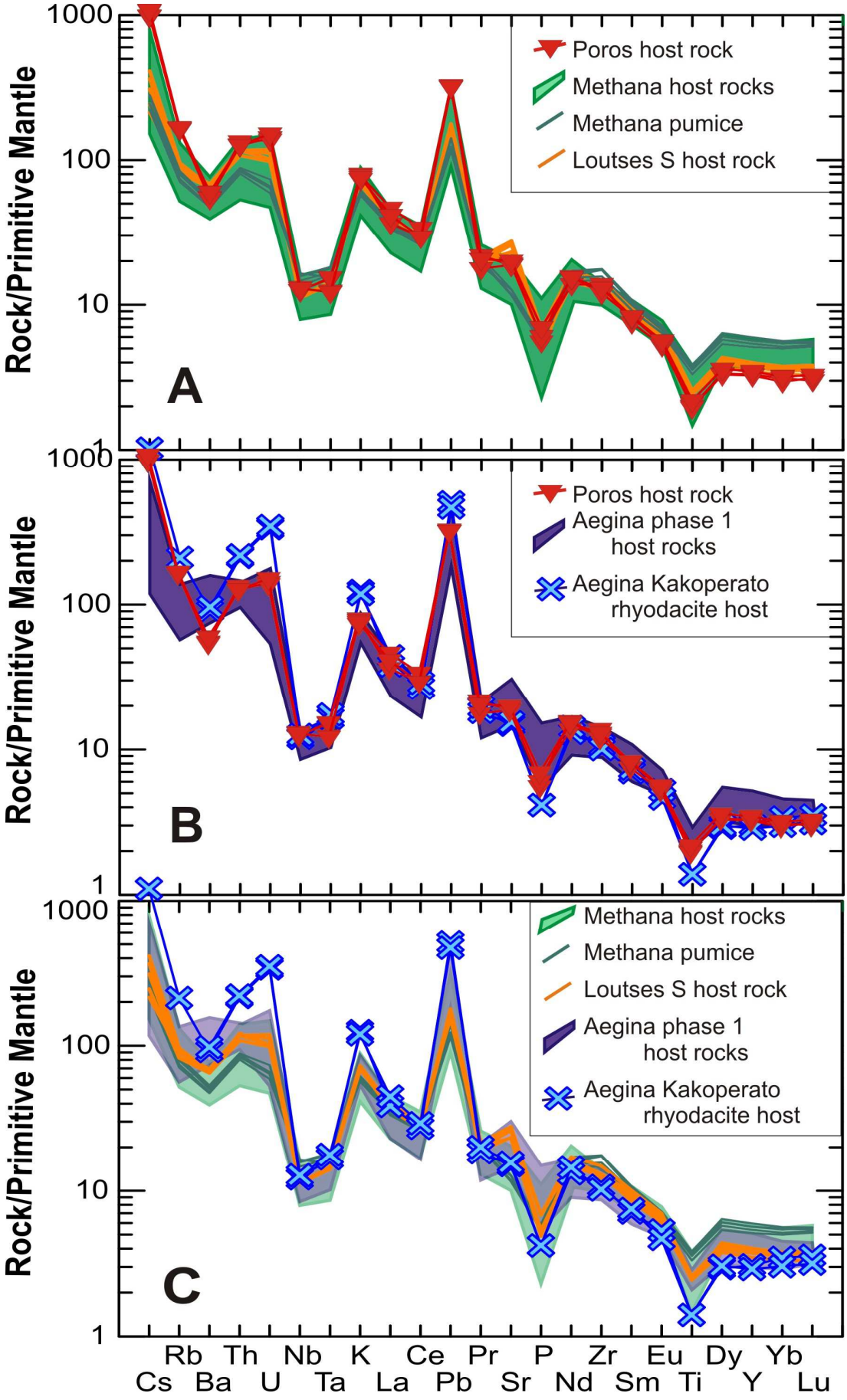

Figure 7.4. *Primitive mantle normalised trace element abundance patterns for the further evolved, more silica-rich lavas of Poros, Methana and Aegina.* Normalisation factors from Sun & McDonough (1989).

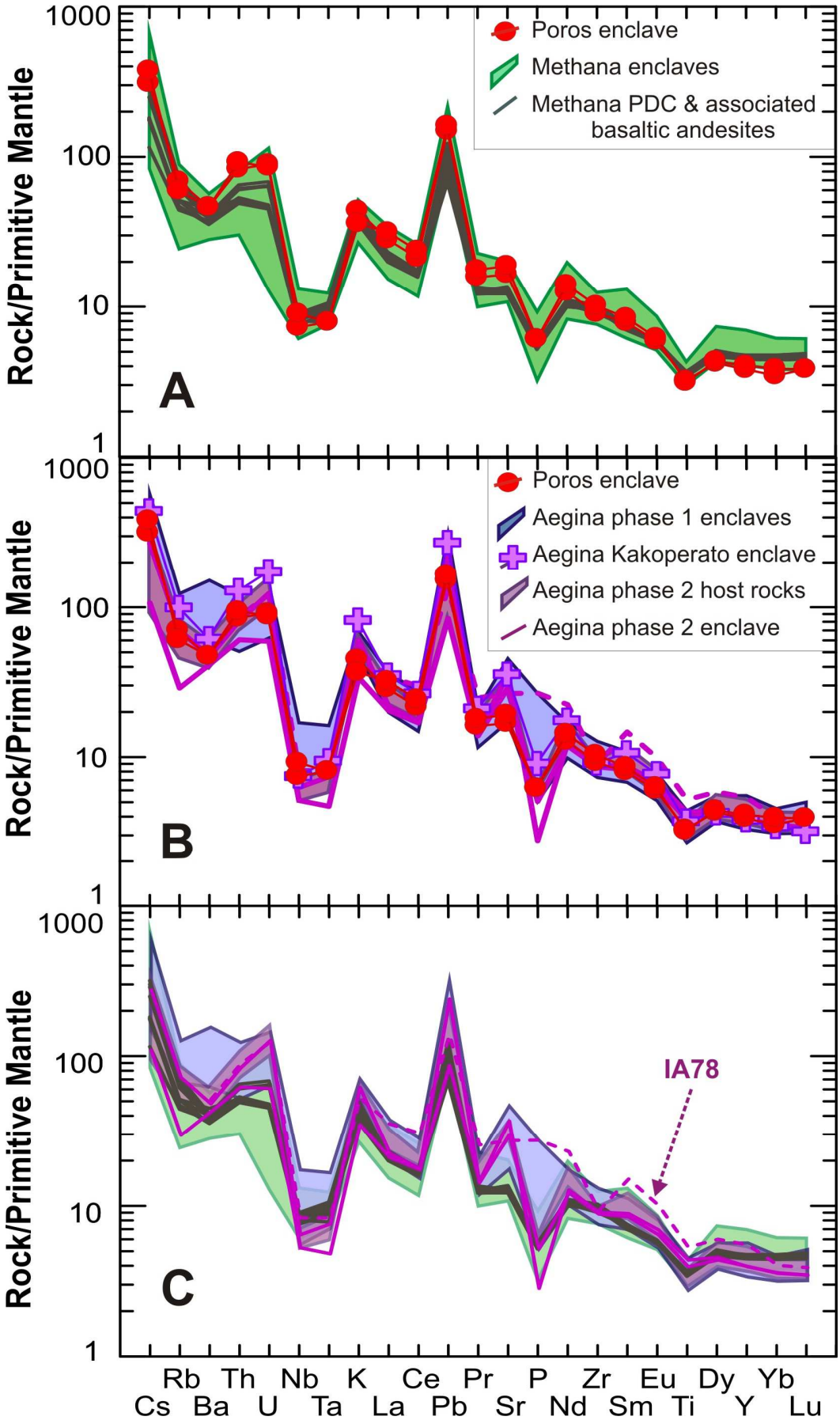

Figure 7.5. *Primitive mantle normalised trace element abundance patterns for the more primitive, less silica-rich magmas of Poros, Methana and Aegina.* Normalisation factors from Sun & McDonough (1989).

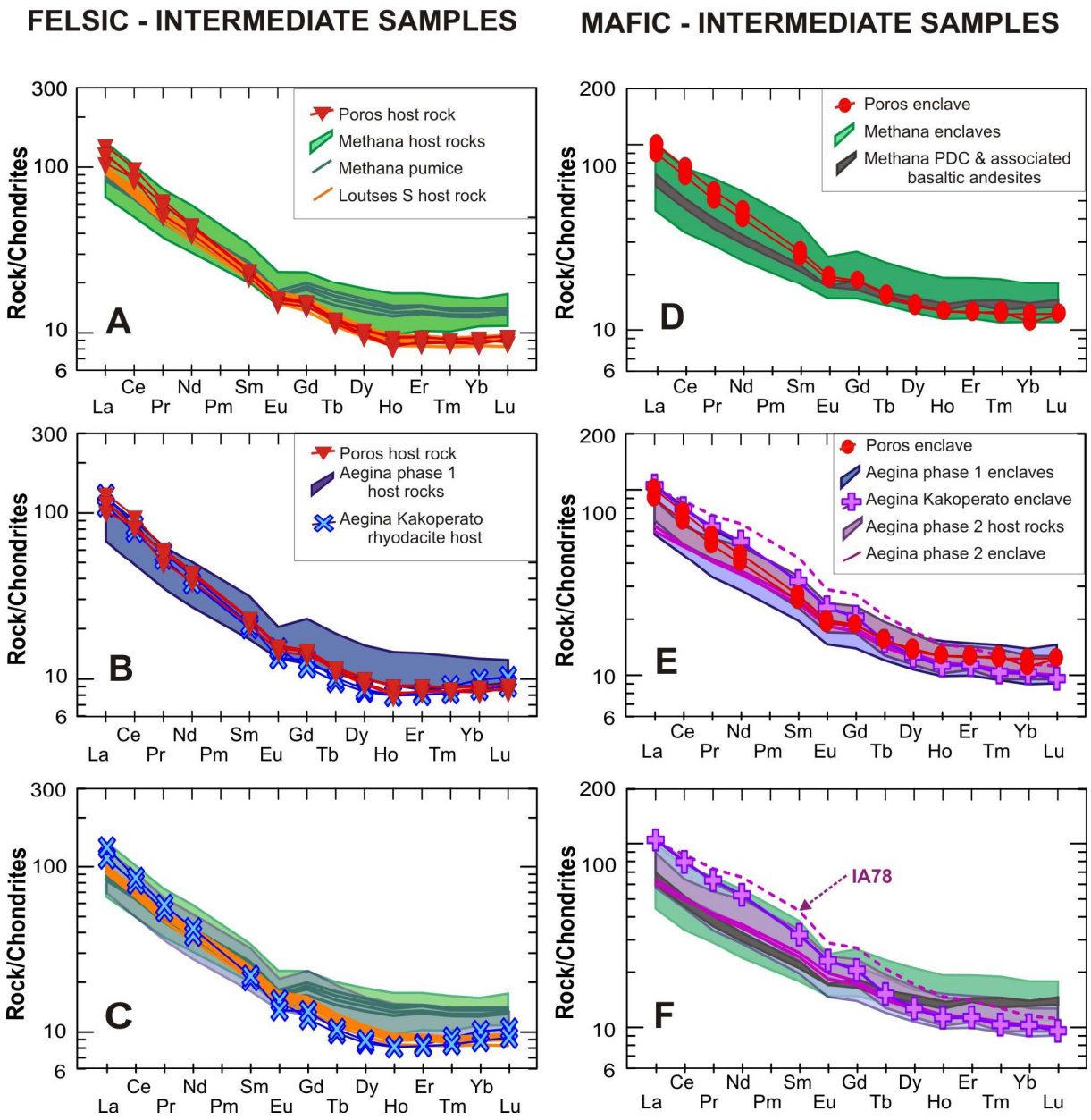

Figure 7.6. *Chondrite-normalised rare earth element diagrams for all volcanic rocks of Aegina, Methana and Poros.* Normalisation factors from Sun & McDonough (1989)

7.1.3 Sr-Nd-Hf-Pb isotope geochemistry

Figure 7.7 shows the variation of the Sr, Nd, Hf and Pb isotopic composition of the Saronic Gulf volcanic deposits with increasing differentiation. Strontium isotopic ratios show a positive correlation with increasing differentiation for all three centres, which represent two distinct series (Fig. 7.7A). At lower $^{87}Sr/^{86}Sr$ values, Aegina's phase 2 samples and the Loutses South host rocks represent a linear trend (from IA72 to DPM26) which is parallel to the Aegina phase 1 – Methana – Poros series that is defined by most mafic Methana enclave DPM36 at lower silica contents, but which has two different end members at the silica rich end of the diagram (dacite DPM43 and pumice IM383) (Fig. 7.7A). There is an overall negative correlation between the $^{143}Nd/^{144}Nd$ values of the Saronic Gulf volcanic deposits and their silica contents (Fig. 7.7B). The two trends that could be observed in the Sr isotopic compositions are however not reflected in the Nd isotope ratios (Fig. 7.7B). Within the $^{143}Nd/^{144}Nd$

isotopic composition, IA72 and DPM36 define the more primitive composition, whereas there seem to be up to three end-members at the more silica-rich end of the series (DPM26, DPM42, IM383) (Fig. 7.7B). A small number of enclaves with silica contents ranging from 50 to 55 wt%, including the Poros enclaves and IA78, define a distinct linear trend at slightly lower $^{143}Nd/^{144}Nd$ values than the more mafic end of the main series (Fig. 7.7B). Despite a similar negative correlation between $^{176}Hf/^{177}Hf$ and SiO_2 contents, there are no sub-trends that are clearly distinct from the main trend (Fig. 7.7C). The $^{207}Pb/^{204}Pb$ ratios of all Saronic Gulf samples (apart from IP46) form a well-defined positive correlation with increasing silica contents (Fig.7.7E). Their $^{206}Pb/^{204}Pb$ and $^{208}Pb/^{204}Pb$ compositions also reflect this positive correlation but no aberrant isotope composition for IP46 (Fig. 7.7D-F). Besides the aberrantly low $^{207}Pb/^{204}Pb$ ratio of allanite-bearing host rock IP46, the Poros volcanic deposits contain (amongst the) most radiogenic $^{208}Pb/^{204}Pb$ of all three volcanic centres (Fig. 7.7F).

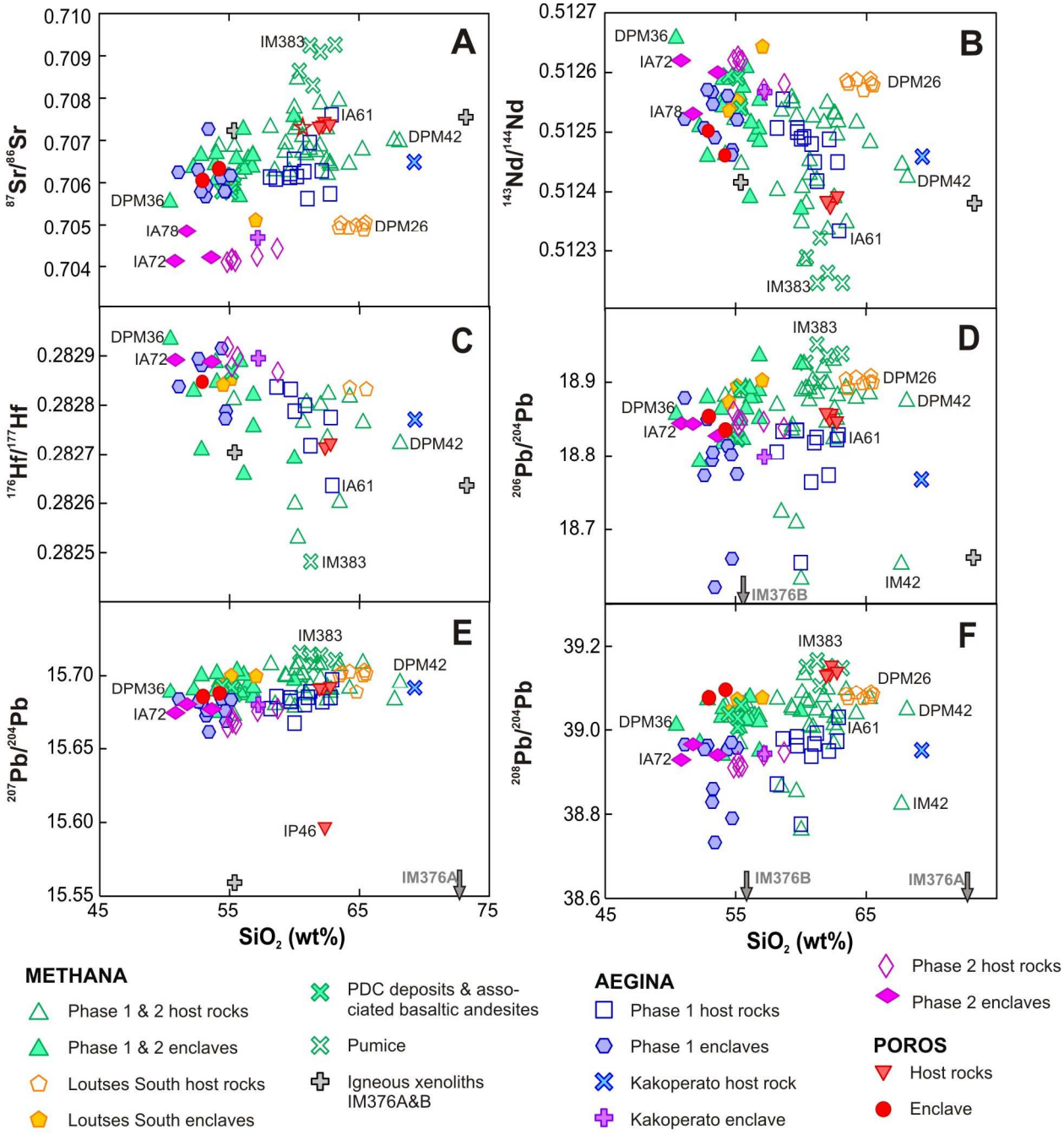

Figure 7.7. *Variation of the Sr, Nd, Hf and Pb isotopic compositions of the volcanic rocks from Aegina, Methana and Poros with increasing silica contents.* Symbols as in 7.2.

7.2 Sources reflected in the isotope geochemistry of the Saronic Gulf lavas

The positive correlation of 87Sr/86Sr, 206Pb/204Pb, 207Pb/204Pb and 208Pb/204Pb in combination with the negative correlation of 143Nd/144Nd and 176Hf/177Hf with increasing amounts of silica indicates that the Saronic Gulf magmas underwent crustal contamination during differentiation (Fig. 7.7). Closer observation of the trends shown by the different petrogenetic groups, however, suggests that there could be decoupling between these 6 radiogenic isotope ratios (Fig. 7.7) and that the final **Sr-Nd-Hf-Pb isotopic fingerprint** of the volcanic rocks may **reflect** the predominance of a **different source for each isotope system**. The lead isotope ratios of Methana's volcanic deposits, for example, mainly reflect the Pb isotopic composition of the (hydrothermally altered) country rock of their final crustal magma chamber (see section 5.5.3). Their 87Sr/86Sr and 143Nd/144Nd ratios, however, seem to be large derived from simple binary mixing between most mafic Methana enclave DPM36 and pumice IM383 (Fig. 5.17A). Only the the Loutses South host rocks and Mavri Petra lavas plot outside this simple mixing trend and are thought to reflect slightly different petrogenetic processes of early garnet differentiation and addition of a subducted sediment melt, respectively (see sections 5.7.4 - 5.7.5 and Fig. 5.35). Petrogenesis of the volcanic deposits on Aegina has been shown to involve significantly less magma mixing, resulting in the preservation of the 87Sr/86Sr fingerprints characteristic to the first and second phase magmas. The Nd isotopic composition of the Aegina phase 1 and phase 2 lavas is however not distinctly different, leading to decoupling between the Sr and Nd isotope ratios and three main 87Sr/86Sr-143Nd/144Nd end members for the Aegina magmas: phase 1 enclave IA72, phase 2 enclave IA102 and most evolved host rock IA61 (see Fig. 6.31). The Pb isotopic composition of the Aegina samples also reflects three main end-members of which only most evolved host rock IA61 represents an end-member for all three isotope systems but where the two mafic end-members for Pb differ from those defining the Sr-Nd compositional range (IA80 and IA345, see Fig. 6.27).

Sedimentary xenoliths and basement from Aegina and Methana were tested as potential crustal contaminants, but none were suitable to explain the **Sr-Nd isotopic composition** of the host rock with the most crust-like signature (IA383 for Methana, and IA61 for Aegina – see Fig. 5.22-5.23, and Fig. 6.31, respectively). The less evolved $^{87}Sr/^{86}Sr$-$^{143}Nd/^{144}Nd$ compositions are however successfully reproduced by fractional crystallisation of the most mafic enclave and concurrent assimilation of a local sedimentary sample (Methana: DPM36 and either the volcaniclastic or calc-silicate xenolith, Fig. 5.22-5.23; Aegina: IA72 and limestone IA62, Fig. 6.31). However, this good agreement between the observed and calculated Sr-Nd isotope ratios of Aegina's and Methana's intermediate volcanic rocks does not necessarily mean that the more mafic enclaves were contaminated by exactly those shallow sedimentary lithologies. Especially the Aegina lavas are unlikely to have assimilated significant amounts of limestone similar to IA62 as this process would also lead to higher amounts of CaO and no such calcium increase is present (Fig. 7.2). Successful modelling of the $^{87}Sr/^{86}Sr$-$^{143}Nd/^{144}Nd$ ratios is therefore interpreted to reflect crystal fractionation in crustal levels with a Sr-Nd geochemistry similar to the volcaniclastic and calc-silicate xenoltihs (Methana) or limestone basement (Aegina).

None of the analysed sedimentary samples contained enough **Pb** to characterise its **isotopic composition**, ruling them out as an important source for the Pb isotopic signature of the volcanics.

Additional complications are introduced by **contamination by antecrysts, and/or xenolithic material**, reflected in (1) the $^{87}Sr/^{86}Sr$ composition of the Loutses South enclaves which seems contaminated by antecrysts from their characteristically unradiogenic host magma (Fig. 5.22); (2) the aberrant Pb isotopic composition of IM379, the host lava sampled nearby the two unradiogenic igneous xenoliths (Fig. 5.26); (4) the $^{87}Sr/^{86}Sr$ composition of the phase 2 Kakoperato enclave which likely reflects contamination of (plagioclase) antecrysts from its Kakoperato host rock – supported by field observations (Fig. 6.5A & Fig. 6.31A); (5) the Sr-Nd-Pb isotopic composition of phase 2 enclave IA78 which systematically plots between the phase 1 and phase 2 samples and reflects the large amount of phase 1 cumulate crystals in this enclave (confirmed by its petrographic texture and aberrant major, minor and trace element geochemistry, Fig. 6.17C-E and Fig. 6.23-6.25, respectively);

and (6) Poros host rock IP46 which is both the only sample from this study that contains a large allanite crystal *and* the volcanic rock with the by far lowest $^{207}Pb/^{204}Pb$ composition (Fig. 7.7E). Other petrological and geochemical studies of magmatic rocks also showed that incorporation of crystals from a different origin or petrogenetic stage (cumulate crystals from a different, preceding magma; crustal xenocrysts from sedimentary, plutonic or metamorphic country rock; phenocrysts from an earlier differentiation stage, crystal cargo of a different magma, …) can have a significant influence on the whole rock major and trace element and isotope geochemistry of the resulting magma (see for example Holden et al., 1991; Beard, 2008; Francalanci et al., 2012; Larrea et al., 2013).

Despite this variety in compositional end-members identified on Aegina, Methana and Poros, and the fact that the geochemical behaviour of Sr, Nd, Hf and Pb is dominated by different mechanisms, the Sr-Nd-Hf-Pb isotopic composition of the Saronic Gulf volcanic rocks can still be used to broadly identify the main sources involved in the genesis of these arc magmas. In the following paragraphs and figures the radiogenic isotope geochemistry of the Aegina, Methana and Poros lavas are compared to a number of global reservoirs (Depleted Mantle (DM) – Rehkamper & Hoffman, 1997; Average Oceanic arc Primitive Basalt (AOPB) and Average Continental arc Primitive Basalt (ACPB) - Kelemen et al., 2003; Salters & Stracke, 2004; Bulk Silicate Earth (BSE) Workman and Hart, 2005; and GLObal Subducting Sediment (GLOSS) - Plank & Langmuir, 1998). The isotope geochemistry of regional rock samples was also tested as potential representatives of (1) subducted sediments (marine tephra from the Ionian Sea, derived from borehole 964A which is located on the subducting plate directly opposite from the Saronic Gulf – Clift & Busztajn, 1999; Weldeab et al., 2002), (2) lower crustal country rocks (lower crustal xenoliths (LC2 & LC3) from the western Pannonian Basin, north of the Aegean micro-plate – Kempton et al., 1997), and (3) upper crustal country rocks (Palaeozoic gneisses which form the basement of the central part of the Aegean arc (Ios1, 2 & 3) – Buettner et al., 2005; and a biotite granodiorite from the Laurion area, 50 km east of Aegina – Juteau et al., 1986). The compositional fields of Atlantic MORB and of Ocean Island Basalts (OIB) that define the mantle end-members HIMU, DMM, EM1 and EM2 are taken from Hoffman (2003); the Northern Hemisphere Reference Line (NHRL) is from Hart (1984); the geochron is based on the Pb isotopic composition of the Canyon Diablo meteorite (Chen & Wasserburg, 1983) and present-day lead (Stacey & Kramers, 1975); the εNd-εHf Terrestrial Array (TA) is from Vervoort et al. (2011).

Figure 7.8 presents the geochemical modelling calculations for the **Sr-Nd geochemistry** of the volcanic rocks from Aegina, Methana and Poros. The Nd-Sr isotopic composition of the above mentioned different reservoirs and potential end members are presented together with the Saronic Gulf samples in the overview diagram of Fig. 7.8A. A close-up of this diagram shows that the most primitive samples from the Saronic Gulf, basaltic enclaves IA72 and DPM36, have Sr-Nd signatures that plot within the field of ocean island basalts derived from more enriched mantle sources (Fig. 7.8B – mustard yellow field with DMM, HIMU, EM1 and EM2 as end-members). The most primitive magmas of the Saronic Gulf are, however, significantly more enriched (higher $^{87}Sr/^{86}Sr$ and lower $^{143}Nd/^{144}Nd$ ratios) than the average $^{87}Sr/^{86}Sr$-$^{143}Nd/^{144}Nd$ isotopic composition of primitive oceanic and continental arc magmas (Fig. 7.8A&B - black and red star outline star, respectively. If this enriched Sr-Nd isotopic signature of most mafic enclaves DPM36 and IA72 is representative of the enriched character of the metasomatised mantle wedge from which partial melting produced the primitive Saronic Gulf magmas, their $^{87}Sr/^{86}Sr$-$^{143}Nd/^{144}Nd$ isotopic composition can be modelled as addition of a subduction component to the depleted mantle. Simple mixing calculations between the depleted mantle (DM - dark grey '**X**') and either globally subducted sediments (GLOSS - yellow cross) or Ionian tephra which are likely subducted below the Saronic Gulf (full black star) however fails to reproduce the more mafic enclaves from the Saronic Gulf (Fig. 7.8B). All mafic volcanic rocks from Aegina, Methana and Poros however do plot in between the DM-GLOSS and DM-tephra mixing lines, suggesting that addition to the depleted mante of a subduction component with similar Sr-Nd geochemistry might explain their $^{87}Sr/^{86}Sr$ $^{143}Nd/^{144}Nd$ isotope ratios (Fig. 7.8B). Figure 7.8B shows that addition of about 2-3% of a

GLOSS-tephra mixture with a Sr-Nd geochemical composition intermediate to those of GLOSS and the Ionian tephra (see Table 7.1) can indeed reproduce the $^{87}Sr/^{86}Sr$ $^{143}Nd/^{144}Nd$ signature of the most mafic enclaves of Aegina and Methana. The only difference between the GLOSS-tephra mixture used to model the Sr-Nd isotopic composition of DPM36 and the mixture used for modelling IA72, is that the

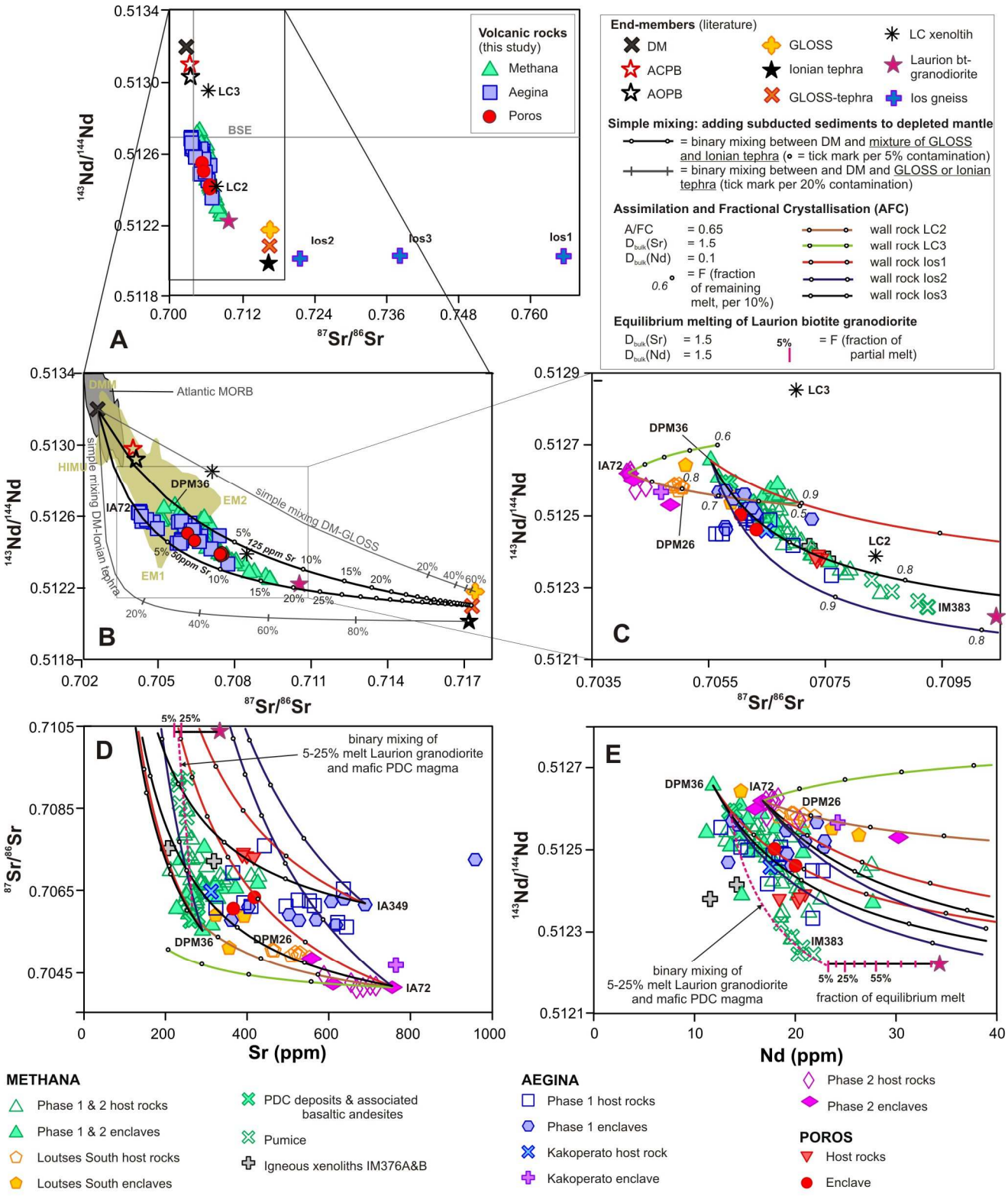

Figure 7.8. *Geochemical modelling of the Sr-Nd contents and isotopic composition of the Saronic Gulf volcanic deposits involving both end-members from the greater Aegean Sea are and from subduction zones around the world.* Symbols in diagrams (A) and (B) see inset in diagram (A), symbols in diagrams (C) to (E) see legend at the bottom of the figure.

former requires a higher Sr concentration (125ppm) than the latter (50ppm) (Table 7.1 and Fig. 7.8B). Alternatively, if IA72 would represent the primitive magma that is formed below all three Saronic Gulf volcanic centres, Methana's most primitive sample DPM36 can also be modelled by 40% FC of this primitive basalt IA72 with simultaneous assimilation of lower crustal xenolith LC3 (Fig. 7.8C). The diagrams of Sr and Nd concentrations versus the isotope ratios, however, do not support this petrogenesis (Fig. 7.8D-E). I therefore propose that the 'subduction component' that is added to the sub-Saronic Gulf mantle wedge might have maintained the same Sr-Nd isotopic signature throughout the area's ca. 4Ma volcanic history, but that the amount of Sr added to the mantle wedge was significantly less in case of the primitive magmas of Aegina's second period of volcanic activity.

	End member 1	**End member 2**			
	Depleted Mantle[1]	*Globally Subducted Sediments*[2]	*Ionian tephra*[3]	*GLOSS – tephra*	
				mix 1	*mix 2*
Sr concentration	11.3	327	6.5	50	125
$^{87}Sr/^{86}Sr$ ratio	0.702500	0.717300	0.717057	0.717175	
Nd composition	1.12	45	45	45	
$^{143}Nd/^{144}Nd$	0.513200	0.512180	0.512015	0.512100	
Addition of 2-3% of this 2nd end member to the depleted mantle reproduces…		/	/	**IA72**	**DPM36**
[1] Rehkamper & Hofmann, 1997; [2] Plank & Langmuir, 1998; [3] Clift & Busztajn, 1999 a Weldeab et al., 2002					

Table 7.1. *Sr-Nd contents and isotopic composition of the different sources involved in the primitive magma genesis of the Saronic Gulf volcanic deposits.*

Further unravelling of the different $^{87}Sr/^{86}Sr$-$^{143}Nd/^{144}Nd$ trends of the Saronic Gulf magmas requires two different petrogenetic models: one for the Aegina phase 2 lavas and Loutses South host rocks, and a second one for all other Aegina, Methana and Poros volcanic deposits (Fig. 7.8C). The first trend can be reproduced by fractional crystallisation of a basaltic IA72 magma whilst assimilating a lower crustal country rock similar to the Panonian Basin derived xenolith LC2 (Fig. 7.8C). The $^{87}Sr/^{86}Sr$-$^{143}Nd/^{144}Nd$ AFC model calculations suggest that after 20% of fractional crystallisation the remaining melt is similar to Loutses South host rock DPM26 – and this geochemical model is also supported by the individual Sr (Fig. 7.8D) and Nd (Fig. 7.8E) isotopic systems, using the same AFC parameters. The Sr-Nd geochemistry of Poros and the remaining Aegina and Methana volcanic deposits can be reproduced by crystal fractionation of a DPM36 magma whilst assimilating a country rock with a $^{87}Sr/^{86}Sr$-$^{43}Nd/^{144}Nd$ composition similar to any of the three Ios basement gneisses (Fig. 7.8C). These AFC model calculations between DPM36 and basement gneisses Ios1, 2 and 3 do not only reproduce the entire range of intermediate to felsic Aegina-Methana-Poros magmas – they could even reflect the petrogenesis of the Laurion biotite granodiorite (Fig. 7.8C). Further testing of this hypothesis within the individual Sr and Nd geochemical systems, however, reveals that AFC of IA72 in an Ios 1 country rock and AFC of DPM36 in an Ios 2 country rock can explain the Nd geochemistry of all Saronic Gulf samples – except the Methana pumice (Fig. 7.8E). The same AFC calculations for the Sr compositions can only reproduce the Aegina phase 2, Methana and Poros lavas – but not the very Sr-rich Aegina phase 1 deposits or Methana pumice (Fig. 7.8D). The Sr geochemical end-member within the Aegina phase 1 volcanic rocks, besides outlier enclave IA346, is enclave IA349. None of the geochemical modelling attempts succeeded in reproducing this enclave's specific Sr geochemistry, but AFC model calculations starting from a melt similar to IA349 in contact with an Ios 3 wall rock are successful in reproducing the Sr geochemistry of the Sr-enriched Aegina phase 1 samples (Fig. 7.8D). The basement rocks exposed on Ios thus seem to be representative of the country rocks assimilated

by the more primitive Saronic Gulf magmas during their main AFC differentiation steps towards all Aegina, Methana and Poros lavas as well as the Methana PDC deposits and associated basaltic andesites. Only the Nd geochemistry of Methana's phase C pumice fallout deposits can not be adequately explained by the above simple mixing and AFC models (Fig. 7.8E). Petrographic observations and major element modelling of these pumice samples suggest partial melting of a more evolved crystal mush or sub volcanic intrusive body as the final petrogenetic step prior to eruption (see Chapter 5). Equilibrium melting of a crystal rich mush or sub volcanic intrusion similar to the Laurion biotite granodiorite can render a partial melt (5-25% of the initial rock) with a Sr-Nd isotopic composition similar to that of most crustally enriched pumice IM383 (Fig. 7.8D-E). The bulk distribution coefficient chosen for Nd in this partial melting process (1.5) is thereby chosen on the basis of mineral/melt Nd distribution coefficients for relevant minerals in dacitic, rhyolitic and granitic melts (0.14-0.29 in plagioclase, 1.03-5.19 in amphibole, 0.01-2.7 in biotite, 1.3-5.2 in clinopyroxene, 0.15-1.36 in magnetite-ilmenite, 21.0-57.1 in apatite, 0.3-6.5 in zircon, GERM distribution coefficient database). A study into the REE distribution among minerals in a granodiorite furthermore showed that accessory phases sphene and allanite largely control the behaviour of REE in granitic magmas (Gromet & Silver, 1983). Neither of these minerals was observed in the very crystal-poor pumice lapilli, but the presence of allanite in Poros host rock IP46 has been interpreted to reflect a further-evolved, allanite-bearing crystal mush or sub volcanic intrusion which formed the Poros host rock magmas through partial melting. It is therefore not unlikely that the felsic crystal mush or sub volcanic intrusive body which was partially molten and subsequently erupted as the phase C pumice also contained allanite (Nd distribution coefficient of 1400-1840 in high-silica rhyolitic magmas, GERM). A Nd bulk distribution coefficient of 1.5 during partial melting of a crystal-rich intrusive body geochemically similar to the Laurion granodiorite is therefore realistic. Applying equilibrium melting of the Laurion granodiorite and subsequent mixing of such a 5-25% partial melt with the mafic PDC magma that is inferred to have replenished the magma chamber of the pumice magma can also successfully reproduce the Sr geochemistry of all Methana pumice samples (Fig. 7.8D). I therefore propose that the Laurion biotite granodiorite is representative of the felsic crystal mush and/or sub volcanic intrusive body which was stalled below Methana before undergoing 5-25% of partial melting due to a significant mafic replenishment with which it partially mixed before erupting as the Methana Phase C pumice.

The same geochemical modelling approach is used to narrow down the identity of the potential end-members reflected in the Pb isotopic trends of the Aegina, Methana and Poros volcanic rocks. As mentioned above, **the Pb geochemistry** is decoupled from the Sr-Nd system and there are even indications for the predominance of different sources for the individual $^{206}Pb/^{204}Pb$, $^{207}Pb/^{204}Pb$ and $^{208}Pb/^{204}Pb$ fingerprints of some volcanic deposits. These discrepancies are also present in the more successful modelling calculations of the Pb geochemistry of the Saronic Gulf volcanics (Fig. 7.9). A first discrepancy is that whereas the $^{87}Sr/^{86}Sr$-$^{143}Nd/^{144}Nd$ isotopic composition of the more mafic volcanic rocks plot within the ocean island basalt field, their $^{206}Pb/^{204}Pb$ and $^{207}Pb/^{204}Pb$ ratios plot outside this field at more radiogenic compositions (see mustard yellow fields in Fig. 7.8B and 7.9A). The $^{208}Pb/^{204}Pb$ ratios of the Saronic Gulf lavas are however similarly to less radiogenic that enriched ocean island end-members EM1 and EM2 – reflecting the different behaviour of the $^{208}Pb/^{204}Pb$ isotopic composition relative to the $^{206}Pb/^{204}Pb$ and $^{207}Pb/^{204}Pb$ ratios. Another discrepancy is the fact that whereas the Sr-Nd isotopic composition of GLOSS is significantly more crustally enriched than that of the Saronic Gulf volcanic suite, the GLOSS Pb isotope ratios are similar to those of most mafic enclaves IA80 and IA345. The aberrantly low Pb isotope ratios of igneous xenoliths IM376A&B and allanite-bearing Poros host rock IP46 furthermore plot within the field of Atlantic MORB, close to the NHRL (Fig. 7.9A&C), whilst their $^{87}Sr/^{86}Sr$-$^{143}Nd/^{144}Nd$ isotope ratios plot within the Saronic Gulf volcanic suite. The exact petrogenesis of these unradiogenic Pb samples is unclear, but the igneous xenoliths are interpreted to reflect the initial Pb isotopic composition of primitive Saronic Gulf magmas. The most primitive Sr-Nd isotopic composition from Aegina and Methana can be explained by a mixture of 2.5% subducted sediment and tephra to a depleted mantle wedge. In case of the Pb

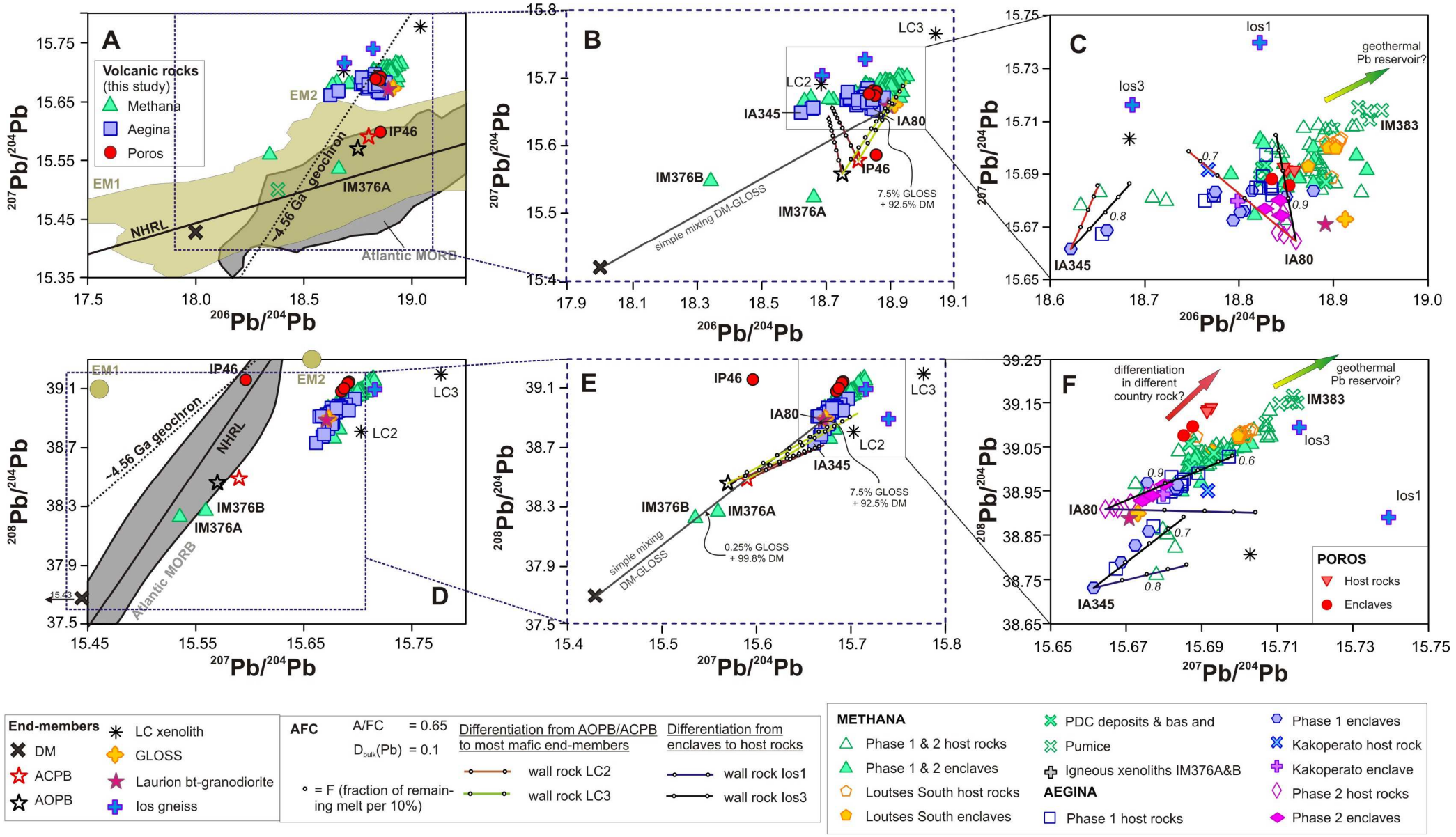

Figure 7.9. *Geochemical modelling of the Pb isotopic composition of the Saronic Gulf volcanic deposits involving both end-members from the greater Aegean Sea are and from subduction zones around the world.* Symbols in diagrams (A), (B), (D) and (E) see inset in diagram (A), symbols in diagrams (C) to (F) see legend at the bottom of the figure.

isotopic composition, however, only the Pb isotopic composition of most mafic enclave IA80 can be reproduced by adding 7-8% of GLOSS to DM (Fig. 7.9B&E), as well as the $^{207}Pb/^{204}Pb$ and $^{208}Pb/^{204}Pb$ systematics of most unradiogenic samples IM376A&B by adding 0.2-0.3% GLOSS to DM (Fig. 7.9E). The Pb isotopic composition of IA345 can not be explained by this process of mantle wedge metasomatism (Fig. 7.9B&E). Another geochemical modelling approach involved using the average Pb isotopic composition of primitive arc basalts (AOPB & ACPB) as primitive Saronic Gulf magmas which underwent AFC in a crustal level similar to lower crustal xenoliths LC2 or LC3 (Fig. 7.9B&E). This model of lower crustal contamination of can partially reproduce the Pb isotopic composition of mafic end-members IA345 and IA80 (Fig. 7.9B&E). So in comparison to the Sr-Nd isotopic system where enclaves IA72 and DPM36 represent the most primitive Saronci Gulf magmas, the Pb isotopic system indicates enclaves IA80 and IA345 as most primitive end-members (Fig. 7.9C&F), but their Pb isotope ratios can not, as was the case for the Sr-Nd isotope ratios of IA72 and DPM36, be (solely) explained by addition of a subduction component to the depleted mantle. Instead, the Pb isotopic system seems to reflect a(n extra) role for lower crustal assimilation in the petrogenesis of the Saronic Gulf's most unradiogenic lead containing enclaves. Starting from mafic magmas with the Pb isotopic composition of IA80 and IA345, a second stage of fractional crystallisation involving assimilation of crustal material similar to the Ios 1 and 3 basement gneisses reproduces the $^{206}Pb/^{204}Pb$, $^{207}Pb/^{204}Pb$ and $^{208}Pb/^{204}Pb$ ratios of most Saronic Gulf volcanic rocks (Fig. 7.14C & F). Applying the same A/FC ratio and lower (LC2 & 3) and upper (Ios 1 and 3) crustal wall rock compositions as the ones used in the Sr-Nd geochemical models can thus also explain the Pb isotopic composition of most volcanic deposits. Only the Pb isotopic composition of the more radiogenic Loutses South lavas, Phase C pumice and a few host rocks sampled from the same area can not be explained in this way. This very enriched Pb geochemistry is probably reflecting incorporation of a geothermally altered shallow basement lithology which represents a uniform Pb isotope reservoir of limited extent, as suggested by the correlation between the sampling locality and Pb geochemistry of Methana's volcanic outcrops (see section 5.5.3 and Fig. 5.25). Whereas the Sr-Nd isotopic composition of the Methana pumice lapilli could be reproduced by partial melting of a lithology similar to the Laurion granodiorite, the Pb isotope ratios of this plutonic rock are too low to explain the overall most radiogenic Pb isotopic composition of these explosive deposits (Fig. 7.9C&F). The unknown endmember responsible for the distinct $^{208}Pb/^{204}Pb$ trend reflected in the Pb geochemistry of both the Poros enclaves and host rocks is probably also the result of differentiation within a country rock with slightly different Pb isotopic composition (Fig. 7.9F). The fact that most of the Poros' amphibole analyses suggest crystallisation at a temperature-pressure range which represents a crustal level at which no Aegina or Methana hornblendes seem to have been formed (Fig. 7.10) could be supportive of this hypothesis, if lithological boundaries within the crust of the Saronic Gulf area are predominantly horizontal.

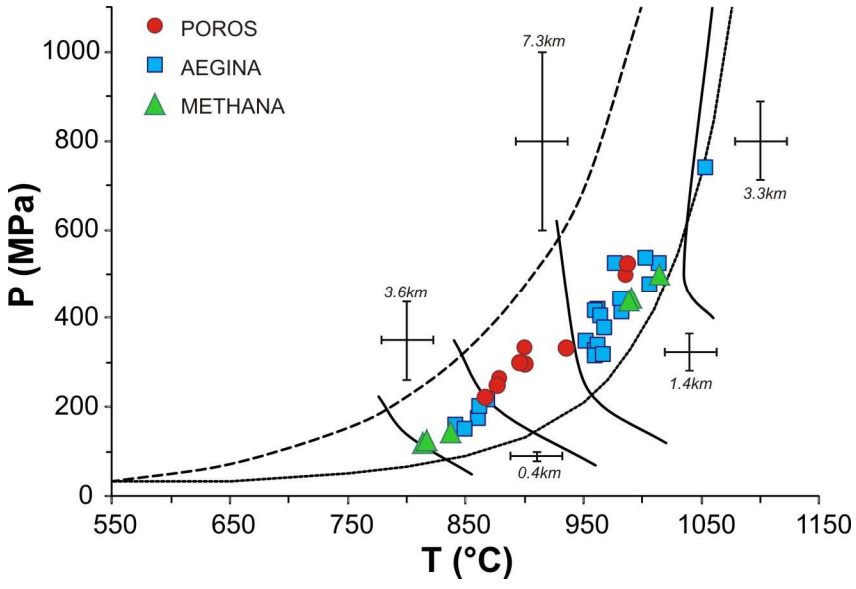

Figure 7.10. *P-T diagram for volcanic amphiboles from Poros, Aegina and Methana,* calculated according to the geothermorbarometer of Ridolfi et al. (2010). For references and details on the variety of amphibole compositions per volcanic unit on Methana, Aegina and Poros, see Fig. 5.29, Fig. 6.29 and Fig. 6.32, respectively.

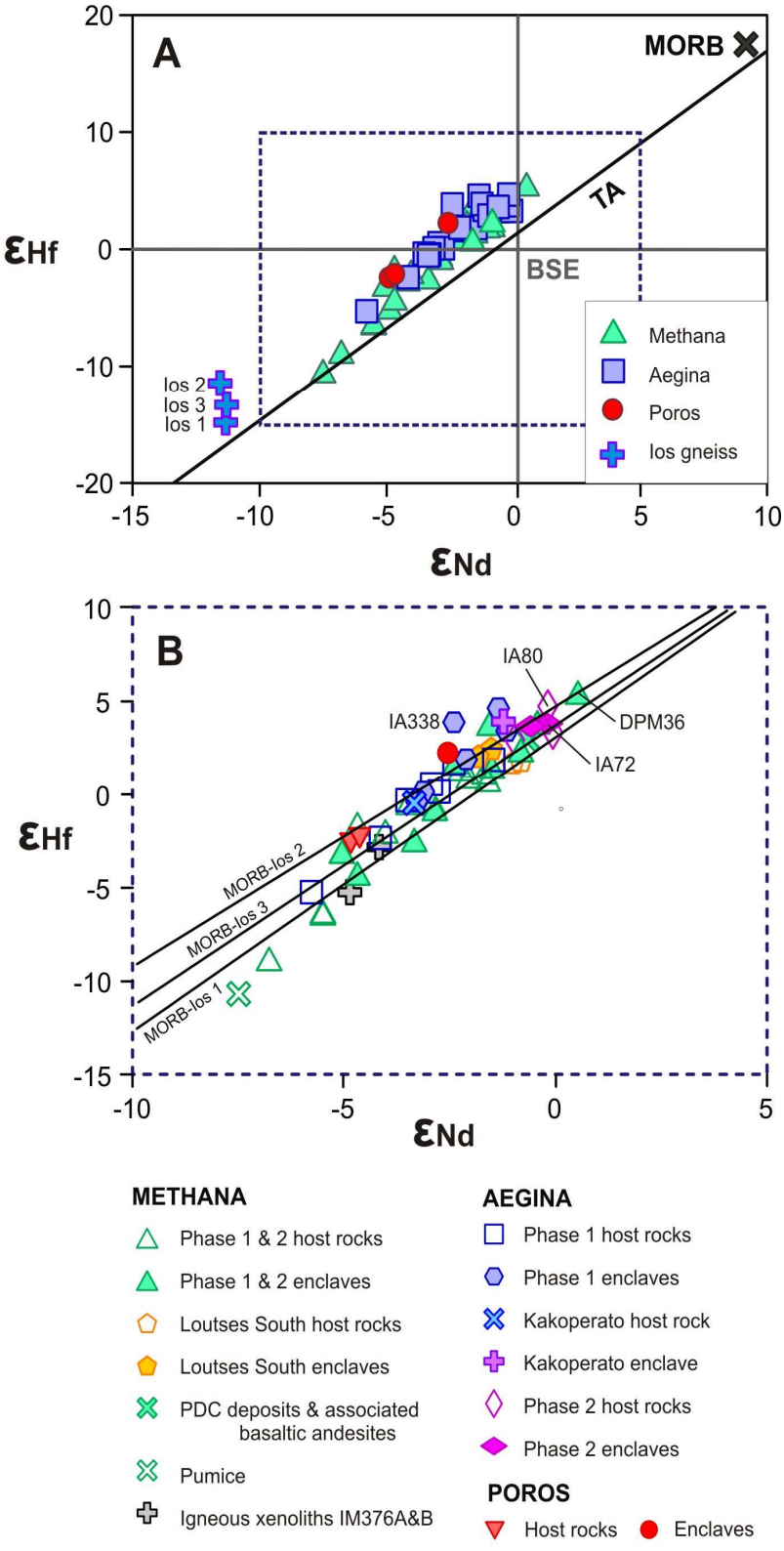

Figure 7.11. εNd-εHf *geochemical composition of the volcanic deposits of Aegina, Methana and Poros* seems to mainly reflect mixing between MORB and and upper crustal lithologies.

Figure 7.11 shows the **εNd-εHf composition** of the Saronic Gulf samples, fresh MORB and Ios gneisses relative to the terrestrial array (εNd and εHf values calculated using $^{143}Nd/^{144}Nd_{CHUR(0)}$ = 0.512630 and $^{176}Hf/^{177}Hf_{CHUR(0)}$ = 0.282785 - Bouvier et al., 2008). The volcanic samples from Aegina, Methana and Poros generally plot along the terrestrial array and define a linear trend between fresh MORB and the metamorphic basement rocks from Ios – suggesting that the Nd-Hf isotopic composition of these arc magmas can be interpreted to mainly result from mixing between a primitive magma and a crustal end-member (Fig. 7.11A). The petro-genesis inferred from the Sr-Nd and Pb systematics was tested on the Nd-Hf isotopic geochemistry, but in the absence of Hf isotopic data for the previously used lower crustal xenoliths, only the suitability of the Ios gneisses as end-members could be evaluated (Fig. 7.11B). Binary mixing between a relatively primitive magma (MORB) and these upper crustal contaminants does indeed reproduce the $^{143}Nd/^{144}Nd$-$^{176}Hf/^{177}Hf$ isotope ratios of the most mafic samples collected from the Saronic Gulf (DPM36, IA80 and IA72) (Fig. 7.11B). Further contamination of these mafic melts with the Ios gneisses can furthermore reproduce the Hf-Nd isotopic composition the $^{143}Nd/^{144}Nd$ -$^{176}Hf/^{177}Hf$ composition of the majority of the Aegina, Methana and Poros lavas (Fig. 7.11B). A few enclaves plot slightly above these mixing lines whereas the most evolved samples from the Saronic Gulf (pumice lapilli IM383 and host rock IM303) plot at lower εHf values (Fig. 7.11B). The latter, more enriched values suggest incorporation of zircons from a partially molten more evolved crystal mush or sub volcanic intrusion, whereas the former could reflect a greater influence of marine sediments.

7.3 Processes reflected in the trace element composition of the Saronic Gulf lavas

Due to the predominance of upper crustal mixing between more mafic melts and more felsic crystal mushes, the majority of Methana's host rocks and enclaves from both the first and second period of volcanic activity define a single geochemical trend (Fig. 7.3). Besides partially overprinting processes (and sources) involved in earlier steps of the petrogenesis, this homogeneous 'main trend' also allows identification of volcanic rocks with a distinctly different geochemical composition such as the of the Loutses South host rocks, the Mavri Petra lavas and the Aegina phasae 2 magmas (see section 5.6.5, section 5.6.4 and section 6.6.4, respectively). As illustrated in Figure 5.34, petrogenesis of the primitive Methana magmas often involves addition of a subducted slab-derived hydrous fluid to the mantle wedge. Subsequently, amphibole fractionation plays a dominant role in the differentiation process of these mafic magmas which rarely erupt as lavas, but either stall in the sub-arc crust and evolve to felsic crystal mushes and/or sub volcanic intrusive bodies, or intrude into such an evolved batch of stalled magma in which they are then entrained as mafic enclaves during eruption. The crystal-rich magma that was remobilised and erupted as the Loutses South host rocks, however, seems to have undergone an extra differentiation step involving fractionation of garnet in the lower crustal roots of the volcanic system – the mafic magma remobilising the Delta 2 host rock from the Kossona Vouno locality might have had a similar petrogenesis (see section 5.6.5). Both the mafic and more felsic magma that mingled prior to eruption as Methana's youngest volcanic deposits (the Mavri Petra flow), were shown to have the geochemical signature of a subducted sediment-derived hydrous melt whereas an aqueous fluid seems to suffice to explain the geochemistry of all the other Methana magmas (see section 5.6.4). The distinct geochemical gap between enclaves and their host rocks observed across all volcanic deposits on Aegina reflects a much smaller role for magma mixing in their petrogenesis and allows a detailed reconstruction of the different fractional crystallisation steps through which mafic magmas similar to the phase 2 basaltic andesites evolved to intermediate-felsic crystal mushes such as the phase 1 dacitic andesites. The subsequently crystallising mineral assemblages are thereby dominated by early and persistent precipitation of plagioclase and amphibole. The Aegina phase 1 and phase 2 host rocks and enclaves furthermore show distinct Sr-Ba contents and $^{87}Sr/^{86}Sr$ ratios, reflecting the involvement of different sources for the phase 1 and phase 2 magma genesis. The Kakoperato rhyodacite flow thereby embodies the transition between the first and second period of volcanic activity as its host rock represents a partially molten felsic crystal mush of the first phase remobilised by a mafic replenishment of the second phase (see section 6.6.4). The (spatially defined) clustering of certain Aegina host rocks and enclaves from the first period of volcanic activity remains unexplained. Petrography and geochemistry of the Poros volcanic deposits suggest that they represent a single volcanic eruption. The host rocks' whole rock composition suggests a petrogenesis different from any of the Aegina or Methana magmas, in agreement with inferred crustal levels of amphibole crystallisation at which no Aegina or Methana amphiboles seem to have formed (Fig. 7.10). The Poros enclaves represent the mafic magma that rejuvenated this biotite-rich, allanite-containing host rock proto-magma and have a geochemical composition similar to the basaltic andesitic enclaves of the other two centres. The following section will investigate whether comparison between the geochemical whole rock composition of the Aegina, Methana and Poros volcanic deposits can shed extra light on their petrogenetic differentiation paths.

From the Sr-Nd-Hf-Pb isotope geochemical modelling in the previous section it became clear that the **mantle wedge** below the Saronic Gulf area can be approximated by the depleted mantle source of MORB magmas. High field strength element (HFSE) ratios such as Ta/Nb and Zr/Nb are generally assumed to be little or not affected by subduction processes and can thus be used to investigate whether this mantle source has a homogeneous geochemical composition (Gertisser & Keller, 2003). Figure 7.12A shows that the Ta/Nb ratios of all-but-one volcanic samples from Aegina, Methana and Poros plot within the range of 0.045 to 0.085, and are not correlated with age, geographical location or Zr/Nb ratios. The densest cluster thereby represents a Ta/Nb composition of 0.07±0.015 (see black circle in Fig. 7.12A) – suggesting that all magmas from the Saronic Gulf originated from the same mantle source, regardless of the geographical location or timing of their eruption. The spread in these

Ta/Nb ratios probably reflects the influence that accessory minerals such as rutile, ilmenite, biotite and phengite can exert on Nb-Ta fractionation when present in either the crystallising mineral assemblage of the melting residue (Nehring et al., 2010; John et al., 2011; Marschall et al., 2013; Stepanov & Hermann, 2013). The minority of Saronic Gulf volcanic samples which plot at a slightly lower Ta/Nb range of 0.05 to 0.06 are mostly enclaves and could reflect incorporation of antecrystic Fe-Ti-oxides (can fractionate between Nb and Ta) and amphibole (can incorporate trace amounts of Zr) fractionated from more mafic magmas (Fig. 7.12A). Whereas the Ta/Nb composition is similar for all Aegina, Methana and Poros samples, their Zr/Nb concentration ratios define two distinct groups: samples from Methana, Poros and Aegina phase 1 have Zr/Nb ratio of 17±5 whereas the Aegina phase 2 magmas have a higher value of 27±3 (Fig. 7.12A). Whereas this distinctly different Zr/Nb ratio of the Aegina phase 2 magmas could be interpreted as the fingerprint of a different mantle source (Gertisser & Keller, 2003), this seems rather unlikely given the otherwise similar Ta/Nb value and Nd-Hf-Pb isotope ratios of the overall most primitive samples IA72 and DPM36. It therefore seems more likely that the significantly higher Zr/Nb that characterises the phase 2 magmas either reflects 1) a larger proportion of partial melt (the higher incompatibility of Nb than that of Zr will be more noticeable in smaller degrees of partial melting), or 2) varying P-T conditions of subducted sediment melting, leading to different proportions of zircon and rutile in the solid residue (Hermann & Rubatto, 2009). Figure 7.12A furthermore confirms that both the Kakoperato enclave and more evolved phase 2 lavas are derived from mixing between the phase 1 Kakoperato rhyodacite and the most primitive phase 2 magma (see black line in Fig. 7.12A) as well as the earlier suggested presence of phase 1 cumulate crystals in phase 2 enclave IA78.

Although an uncommon source of primitive melts in present-day subduction zones, **partial melting of the subducted slab** at sub-arc depths (representing the pressure-temperature range in which the oceanic crust is metamorphosed to eclogite) is shortly considered here. This process was probably more common in Archean arcs but is at present restricted to subduction zones characterised by an unusually high geothermal gradient, for example subduction of very young, and therefore still relatively hot, oceanic crust (Defant & Drummond, 1990; Defant & Kepezhinskas, 2001). The arc lavas that subsequently erupt with little to no further differentiation are known as ‘adakites’ and their petrography is characterised by an assemblage of plagioclase and amphibole with frequent occurrence of biotite, clinopyroxene and Fe-Ti-oxides (Defant & Drummond, 1990). Although this mineral assemblage is also observed in the majority of volcanic rocks in the Saronic Gulf, it is not typical of mafic arc lavas as these usually lack amphibole phenocrysts despite compelling geochemical evidence for the importance of amphibole fractionation in their petrogenesis (Davidson et al., 2007). Large degrees of partial melting of a subducted metabasalt involves the presence of garnet in the solid residue, leading to the distinct geochemical composition of ‘adakites’ which are characterised by Sr > 400 ppm, Y < 18 ppm, significant depletion of the HREE relative to the MREE, SiO_2 > 56 wt%, Al_2O_3 ≥ 15 wt%, MgO ≤ 3 wt% (rarely above 6 wt%) and $^{87}Sr/^{86}Sr$ usually < 0.7040 (Defant & Drummond, 1990; Rapp & Watson, 1995, Hermann & Green, 2001). Figures 7.12B-D show that none of the Saronic Gulf lavas comply with all of the above geochemical criteria – suggesting that there are no true adakites amongst the volcanic rocks of Aegina, Methana or Poros. The geochemistry of the more evolved high Sr – low Y Loutses South and Aegina phase 2 lavas does, however, approach the composition of adakites and has slightly less HREE than MREE, representing the least spoon-shaped chondrite-normalised REE patterns of all samples (Fig. 7.6 and Fig. 7.12B-D). This distinct geochemical composition is therefore thought to reflect the influence of garnet stability and will be discussed in more detail later on in this section.

Whereas the subducted oceanic crust is an unlikely source for (significant) contributions of partial melts to the mantle wedge, its underlying **serpentinised lithosphere** is generally considered as the main carrier of water into the sub-arc P-T range where its dehydration eventually leads to hydrous melting of the mantle wedge and arc magmatism (Ulmer & Trommsdorff, 1995; Ulmer, 2001).

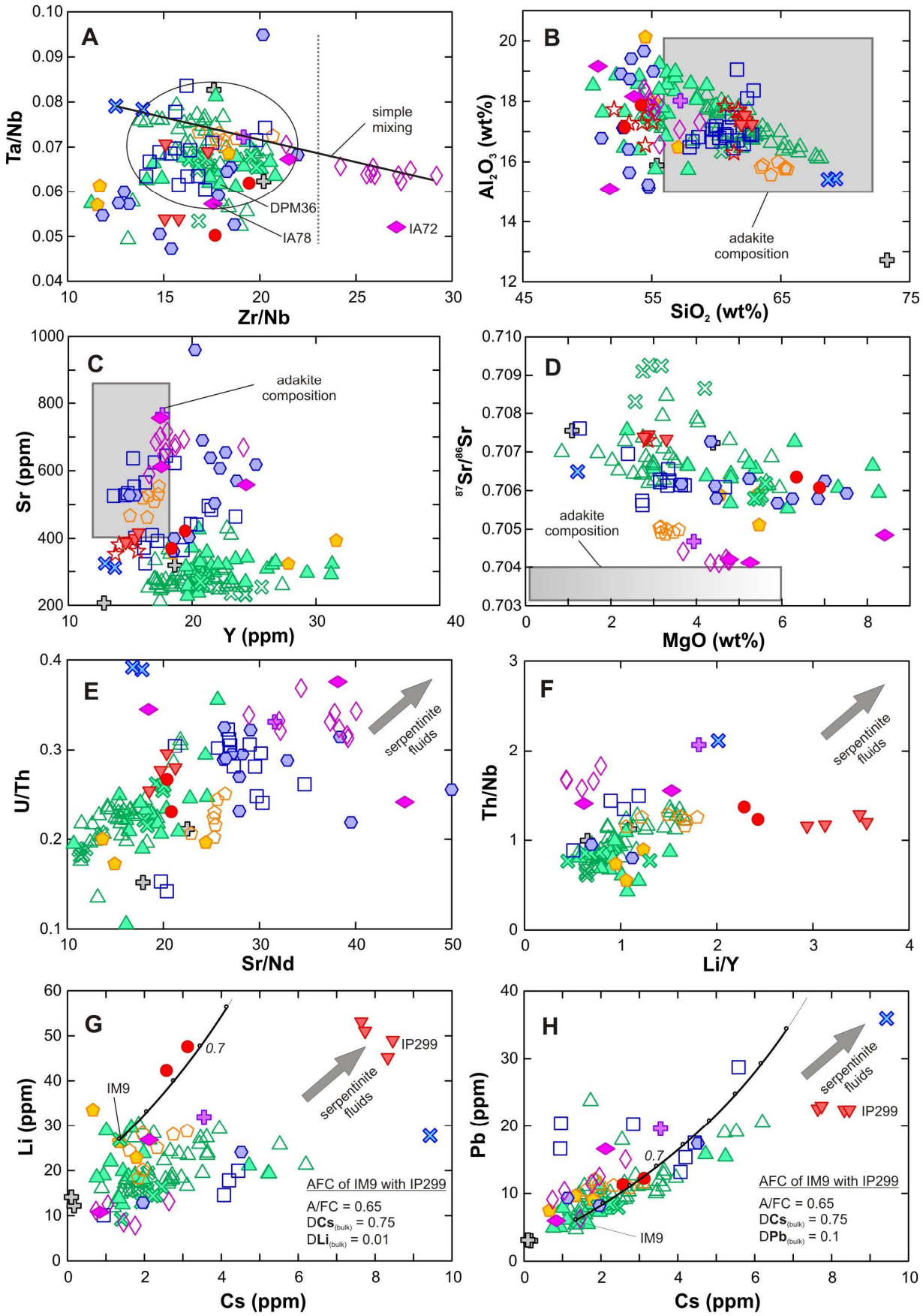

Figure 7.12. *Presentation of trace element and 87Sr/86Sr composition of all (magmatic) Saronic Gulf samples* in diagrams which, according to relevant literature, should *identify significant different mantle sources* (A), *partial melts of subducted oceanic crust* (B-D) and significant addition of *serpentinite-derived aqueous fluids* (E-H). See text for discussion, symbols as in Fig. 7.11.

Experiments showed that the trace elements signature of such serpentinite-derived aqueous fluids are characterised by high concentrations of B, Pb, As and Cs (Tenthorey & Hermann, 2004). In situ analysis of the trace element distribution of serpentinites from MORB, passive margins and fore-arcs worldwide revealed that bulk serpentinites show up to several orders of magnitude enrichments in Cl, B, Sr, U, Sb, Pb, Rb, Cs and Li relative to elements of similar compatibility during mantle melting (Kodolányi et al., 2012). Based on these data, dehydration of subducted serpentinites is suggested to release fluids with high B/Nb, B/Th, U/Th, Sb/Ce and Sr/Nd. Despite the fact that serpentinites represent the bulk lithology of globally subducted slab, their geochemical imprint on erupting arc magmas is often considerably masked by the trace element characteristics of subducted sediment fluids as these have considerably higher overall trace element contents (Kodolányi et al., 2012). Could the distinct enrichment of the Poros host rocks in both Cs and Li (Fig. 7.3G-H) nevertheless reflect preservation of a 'serpentinite signature'?

Plotting the element ratios suggested to characterise serpentinite-derived aqueous fluids shows that whereas the Poros host rocks contain the distinctly highest Li/Y ratios in the Saronic Gulf, their Sr/Nd values are similar to those of Methana's basaltic andesites (Fig. 7.12E-F). Their U/Th and Nb/Th ratios are amongst the highest of all Saronic Gulf arc magmas (Fig. 7.12E-F). Shifting the focus to those 'serpentinite signature' trace elements that are least likely influenced by fractional crystallisation and for which geochemical data are available (Li, Cs and Pb) Fig. 7.12G-H does suggest that the Poros host rocks might still reflect the addition of a serpentinite fluid to the mantle wedge. But Li and Cs are also enriched in clays and in the continental crust, so this signature could merely reflect addition of a subducted sediment source or assimilation of a crustal country rock which are specific for the Poros host rock magma, and distinctly different from subducted sediment sources and/or assimilation contaminants in all Methana and Aegina magmas. Given the possibility to explain the different $^{87}Sr/^{86}Sr$ ratios of the Aegina phase 1 and phase 2 deposits with just one subducted sediments end-member (see Table 7.1) and the fact that Poros is located very near Aegina and Methana, it seems unlikely that there is a distinctly different subducted sediment source that contaminated only the mantle wedge below Poros. Assimilation of a crustal country rock that did not play a role in the petrogenesis of the Aegina and Methana magmas, however, is in agreement with the chemical composition of Poros amphiboles which reflect fractional crystallisation at a single, relatively deep (mid-lower crustal) differentiation level where none of the Aegina and Methana amphiboles seem to have been formed (Fig. 7.10).

The relatively radiogenic Sr-Pb isotopic composition of the Poros host rocks is similar to that of the other Saronic Gulf lavas as well as to crustal compositions. The Sr isotopic composition of Mid Atlantic Ridge seafloor serpentinites defines a relatively narrow range (0.7080-0.7095) which lacks correlation with crustal age but is similar to North-Atlantic seawater and in the range of ultramafic rocks recovered from the Atlantic, leading to the interpretation that the low $^{87}Sr/^{86}Sr$ ratio of Sr-poor mantle rocks is easily re-equilibrated during seawater-rock interaction (Boschi et al., 2013). The Pb isotopic compositional range of oceanic mantle ($^{206}Pb/^{204}Pb$ = 16.5-19.5, $^{207}Pb/^{204}Pb$ = 15.1-15.8 and $^{208}Pb/^{204}Pb$ = 36-40) is larger than the global MORB range, similar to the Pb isotopic variety in orogenic and xenolith peridotites (Warren & Shirey, 2012) and slightly less radiogenic than the Pb isotope range reflected in worldwide collected ocean floor serpentenites ($^{206}Pb/^{204}Pb$ = 18.2-20.0, $^{207}Pb/^{204}Pb$ = 15.4-16.0 and $^{208}Pb/^{204}Pb$ = 37.5-39.9 – Kodolányi, 2009). The Sr-Pb isotopic composition of the Poros host rocks ($^{87}Sr/^{86}Sr$ = 0.7060-0.7074, $^{206}Pb/^{204}Pb$ = 18.84-18.86, $^{207}Pb/^{204}Pb$ = 15.6-15.7 and $^{208}Pb/^{204}Pb$ = 39.1-39.2) could therefore also reflect addition of a Sr and Pb-enriched serpentinite fluid to the mantle wedge. Although the geochemical signature of serpentinite-derived fluid addition to the mantle wedge is commonly thought to be overprinted by fluid and/or melt additions from subducted metabasalts and metapelites, it has been argued that the high oxygen fugacity, characteristic of arc-related volcanic rocks worldwide, is inherited from serpentinite-derived fluids – and not reflecting subducted basalts or sediments (Elburg & Kamenetsky, 2007). So if one of the geochemical characteristics of subduction zone magmas might actually reflect serpentinite-derived aqueous fluids, there might be other serpentinite signatures that are not (completely) overprinted

throughout the subsequent steps of magma genesis. The earlier interpretation of a different petrogenetic origin for the Poros host rocks than for their enclaves, based on their varying trace element trends, is furthermore confirmed by successful geochemical modelling of the Poros enclaves' Li, Cs and Pb contents as the result of AFC from a 'normal' Methana-Aegina basaltic andesite magma upon replenishing the Poros host rock magma chamber (Fig. 7.12G-H – PDC rock IM9 interpreted to reflect mafic replenishments around the time of Poros volcanism; assimilated crystal mush represented by Poros host rock IP299; distribution coefficient for Pb the same as used for the isotope geochemical models in Fig. 7.9; distribution coefficients for Cs and Li based on GERM values for element partitioning between an andesitic melt and a plagioclase-amphibole-biotite mineral aggregate; Poros enclaves represent 70% of remaining melt). The geochemical composition of the Poros host rocks therefore seems to reflect a petrogenetic history that is unique amongst the Saronic Gulf volcanic deposits, and which could reflect 1) preservation of a 'serpentinite signature', 2) fractional crystallisation in a geochemically distinct mid-lower crustal country rock, or 3) a combination of the previous two petrogenetic models.

Besides melt extraction from a similar mantle wedge, the geochemistry of the Saronic Gulf volcanic rocks also reflect the typical 'subduction zone signature' in their primitive mantle normalised trace element patterns: large positive anomalies for K, Pb & Sr combined with negative anomalies for Nb-Ta, P & Ti, commonly interpreted as the fingerprint of the **subducted slab-derived hydrous component** that metasomatised the sub-arc mantle wedge (Fig. 7.4 & 7.5 – Gill, 1981; Ulmer, 2001; Gertisser & Keller, 2003; Elburg, 2010). But does this signature originate from the subducted oceanic basalts or from the subducted sediments? Is it an aqueous fluid or a hydrous melt? And is it constant in space and time, or does it have a different identity below Aegina, Methana and Poros and/or change with time? These questions are not easily answered using only the whole rock geochemistry of arc volcanic rocks known to have undergone a number of differentiation steps within a continental crust of similar composition as subducted sediment. Unless the geochemical composition of the subducted oceanic crust is well-constrained and distinct from the subducted sediments and overlying crust, it is impossible to distinguish its geochemical fingerprint in the related arc magmas. In the absence of geochemical data of the oceanic crust or sediments subducted specifically below the Saronic Gulf, the trace element geochemistry of the volcanic deposits from Aegina, Methana and Poros is screened for the fingerprint of the 'subduction component' which represents the combined effect of fluid addition from (altered) oceanic basalts and the overlying meta-sediments. Combination of the recognised resemblance of specific trace element contents and ratios in subducted sediments and arc magmas, and assumptions of the relative (in)solubility of these incompatible trace elements in hydrous phases lead to the common application of certain trace element ratios to identify the character of the subduction component-derived fluid phase (for example Pb/Ce, Rb/Nb, Ba/La, Sr/Nd,… - high ratios suggest an aqueous fluid, low ratios point towards a hydrous melt) (Pearce, 1982; Othman et al., 1989; Gertisser & Keller, 2003; Elburg et al., 2013). Despite the fact that these trace element ratios can also be controlled by accessory phases involved in either partial melting or fractional crystallisation (for example fractionation of Th/La, Th/U, Ce/Pb by allanite - Hermann & Rubatto, 2009), the Saronic Gulf volcanic deposits consistently show coherent trends in these diagrams (Fig. 7.13A-D). Figure 7.13A shows that the majority of Methana's volcanic deposits and the Aegina phase 2 define one geochemical composition of lower Pb/Ce and Ba/La compositions, which could reflect a predominantly 'melt' character of the subduction component. The Aegina phase 1 lavas, on the other hand, define a single range at higher Pb/Ce and Ba/La values, which is commonly thought to suggest a predominantly hydrous subduction component (Fig. 7.13A). The Poros volcanic rocks are again characterised by a bimodal geochemistry: enclaves plot within the Methana-Aegina phase 2 field, confirming their petrogenetic similarity with these magmas, whereas the Poros host rocks define a small field together with the Mavri Petra lavas – reflecting once more the distinctly different primitive source composition inferred for both deposits (Fig. 7.13A). To test the consistency of these observed trends, the trace element ratios are individually plotted against $^{87}Sr/^{86}Sr$ – which is capable of

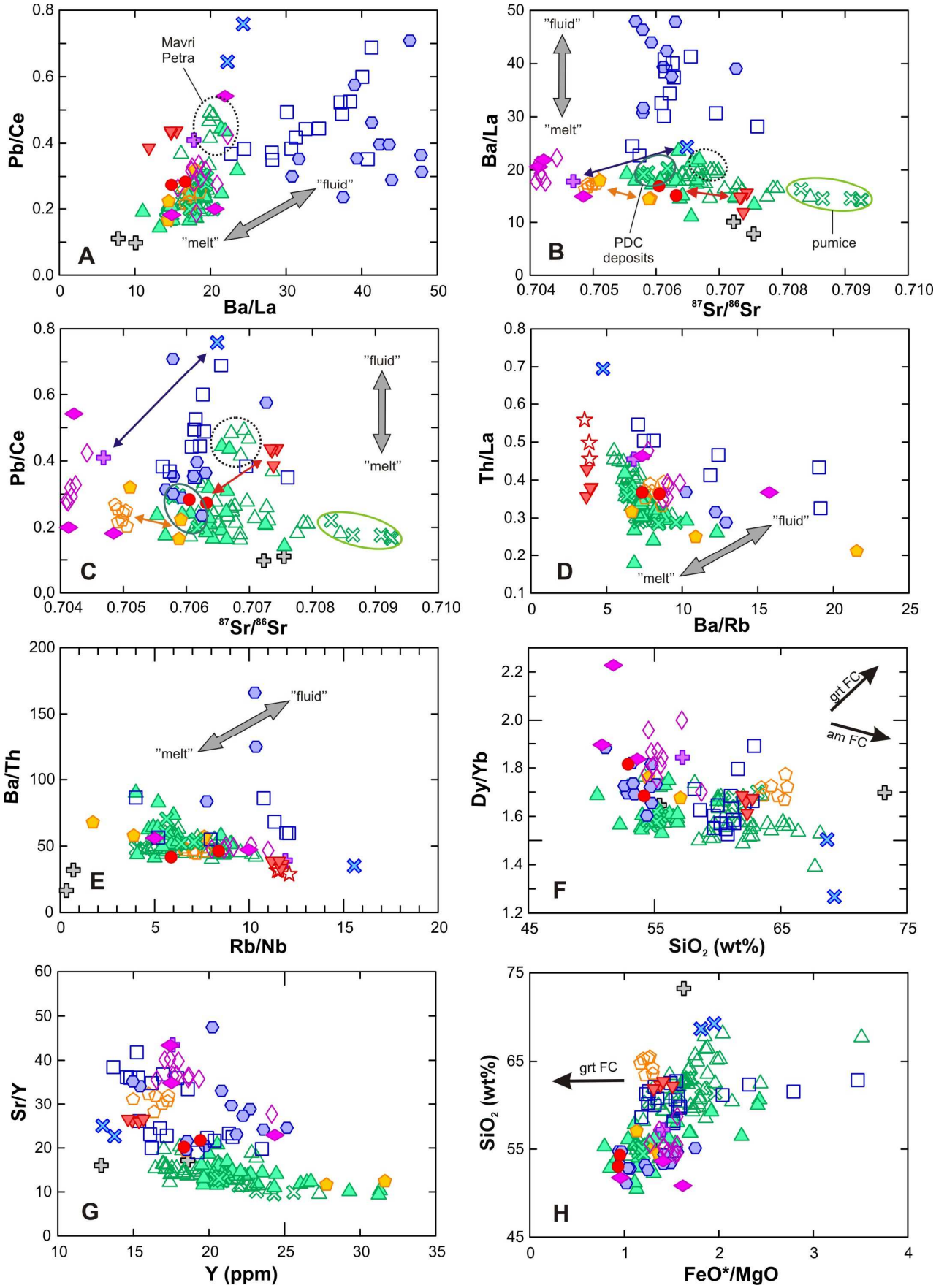

Figure 7.13. *Presentation of trace element and $^{87}Sr/^{86}Sr$ composition of all (magmatic) Saronic Gulf samples* in diagrams which are thought to *distinguish between a hydrous 'melt' or aqueous 'fluid' type of subduction component* (A-E) *and the different geochemical signatures of garnet (grt) and amphibole (am) FC (F-H).* See text for discussion, symbols as in Fig. 7.11.

identifying distinct source compositions whilst at the same time being a water soluble element itself (Fig.7.13B-C). Comparison of Fig. 7.13B to Fig. 7.13C shows that the general trends observed in Fig. 7.13A are consistent: the Aegina phase 1 lavas are characterised by a more 'fluid'-rich component with a relatively narrow intermediate Sr isotopic composition ($^{87}Sr/^{86}Sr$ = 0.7055-0.7065). All other Saronic Gulf volcanic rocks suggest a more 'melt'-like subduction component, though with distinct $^{87}Sr/^{86}Sr$ ratios for Aegina phase 2 (0.7040-0.7045), Loutses South (0.7050) and a broad Sr isotopic range for Methana (0.7055-0.7095) (Fig. 7.13-C). The Poros host rocks and Mavri Petra lavas are also defining clusters of similar composition, distinct from the main trends, in these two diagrams (see red arrow in Fig. 7.17B-C). The bimodal composition of the Poros deposits is thereby not the only enclave-host rock discontinuity: the Kakoperato and Loutses South host rocks and enclaves, for which also a different petrogenetic origin for the felsic mush and mafic injection was inferred, show similar to larger discrepancies (see blue and yellow arrow, respectively, in Fig. 7.13B-C). The same significant geochemical gap is observed between Methana's pyroclastic deposits, although here it is not so clear whether this is because they truly started out as geochemically different magmas, or whether the pumice's specific crustal petrogenesis of advanced differentiation in an (inferred) hydrothermally altered shallow crustal level and subsequent re-melting is the main cause. The fact that the deposits with the most 'crustal' $^{87}Sr/^{86}Sr$ composition and petrographic evidence for intense re-melting also plot at the most 'melt'-like signature seems to suggest that the above discussed diagrams do not only reflect the more 'fluid' or 'melt' like character of the subduction component, but also different sources and processes in later stages of the magmagenesis. This is illustrated by the diagrams in Fig.7.13D-E which, despite supposedly being similar in differentiating between 'fluid' and 'melt' predominance of the subduction component as Fig. 7.13A, show some distinctly different trends (compare the relative position of for example Poros host rocks and enclaves, Loutses South host rocks and enclaves, Kakoperato host rocks and enclave, Aegina phase 1 and phase 2 lavas). The main trends that are systematically present in all diagrams is a distinct composition for (1) the Poros host rocks, (2) all Methana magmas (including Mavri Petra) and (3) the Aegina phase 1 lavas, but a composition for the Aegina phase 2 lavas very similar to the Methana deposits (Fig. 7.13A, D-E). It is therefore proposed that these trace element variation diagrams show the total effect of mantle-to-surface petrogenesis on these lavas (both sources and process) and therefore suggest that whilst arc magmatism remained relatively the same throughout Methana's history, there was shift in sources and/or processes between the Aegina magmas erupted in the first and in the second period of volcanic activity.

Once the primitive magmas are formed and start their ascent to the surface, their further differentiation is mainly influenced by their initial geochemical composition as well as that of the crustal levels at which they stall. Varying crustal differentiation levels thereby represent a range of pressure-temperature regimes which also influence the identity of the crystallising mineral assemblage and hence the geochemical evolution of the residual melts. As suggested by Davidson et al. (2007) for arcs worldwide, the **majority** of the volcanic rocks in the Saronic Gulf have a whole rock composition which reflects important **fractionation of amphibole**. The geochemically distinct Loutses South host rocks, however, seem to have **also** undergone an early deep crustal differentiation step involving **garnet fractionation**. Comparison of the geochemistry of Aegina, Methana and Poros shows that the whole rock composition of the Poros host rocks reflects similarities with the distinct geochemistry of the Loutses South host rocks, indicating that these rocks could also be influenced by garnet fractionation. Figures 7.13F-H present diagrams which are, on the basis of the geochemistry of arc rocks worldwide and experiments relevant for the study of crystallisation of magmas in the roots of island arcs (Davidson et al.,2007, and Alonso-Perez et al., 2009, respectively), suggested for the distinction between amphibole and garnet fractionation. For those Saronic Gulf suites that represent a continuous range across different levels of differentiation (the majority of Methana host rocks and enclaves and the Aegina lavas), Fig. 7.13F & G clearly show that they follow the trend of amphibole fractionation. The two lava groups which might represent the influence of garnet crystallisation define smaller clusters which individually represent a restricted silica range. This complicates any judgement on the 'differentiation trend' they might reflect as it is not known from which more mafic magma they were derived (Fig. 7.13F-H). Judging from their position relative to the amphibole fractionation trends

represented by the Methana and Aegina magmas, however, they do seem to deviate towards a geochemistry that is defined by a different petrogenetic process.

Fractionation of garnet in the sub-arc lower crust is not a differentiation process commonly observed in present-day subduction-related volcanic rocks (Davidson et al., 2007). The petrographic and geochemical study of igneous rocks representing the base of a 40 km thick arc crust furthermore showed that amphibole fractionation alone can also lead to an 'adakitic signature' of high Sr/Y and Mg# and low Y and Al_2O_3 without involvement of garnet in a melt residue or crystallising assemblage (Dessimoz et al. 2012). For the Saronic Gulf high Sr/Y lavas, however, this petrogenesis is unlikely as this process of largely amphibole dominated fractionation 1) coincides with a delay of plagioclase saturation as reflected in the lack of Eu-anomalies in the derived magmas and 2) is shown to have occurred at emplacement pressures of ca. 1 GPa. Neither of these two circumstances apply for any of the Saronic Gulf magmas as they all show small negative anomalies (Eu* ranges from 0.75 to 1.0, with average of 0.85±0.1 compared to the Eu anomaly range of 0.64 to 3.72 with average > 1 for the samples studied by Dessimoz et al. (2012)) and undergo differentiation at significantly shallower levels (based on maximum fractionation pressures derived from amphibole analyses which are commonly 100-600 MPa, except for one analysis at 800 MPa - Fig. 7.10 - and geophysical estimates which showed the crustal thickness below the Saronic Gulf to be ca. 32km). I therefore propose that the high Sr/Y Loutses South and Poros host rocks reflect the sporadic involvement of garnet fractionation in the crustal petrogenesis of the Saronic Gulf magmas. Despite the fact that garnet fractionation is generally believed to be a rare occurrence in sub-arc magmagenesis, there are a few cases of garnet-bearing arc-related volcanic rocks. A petrographic and geochemical study of one of these describes the presence of garnet cogenetic antecrysts in (biotite)-hornblende andesites (Bach et al., 2012). Geothermobarometry on these garnets and their pyroxene and hornblende inclusions reveal that most garnets crystallised during cooling from 1000°C to 700-800°C at a constant pressure of ~ 1GPa, but analysis of one subgroup of garnets revealed crystallisation at higher crustal levels and lower temperatures (ca. 800 MPa and 600-700°C) (Bach et al., 2012).

Besides inferred fractional crystallisation of amphibole (and sometimes garnet) at greater depth, major and trace element modelling of the volcanic suites on Methana and Aegina revealed which minerals take part in the crystallising assemblage during **fractional crystallisation in the final crustal differentiation level** (see sections 4.5.1, 4.5.2 and 6.6.3). Plagioclase, amphibole, Fe-Ti-oxides, clinopyroxene and apatite were shown to be involved in the differentiation of both host rocks and enclaves. Despite their presence in the (more mafic) volcanic rocks, olivine and orthopyroxene are rarely involved in the successful crystal fractionation models, suggesting that these minerals formed during earlier differentiation steps. The presence of quartz, biotite and zircon in the (more felsic) lavas is also not matched by a role for these minerals in the crystal fractionation models and are therefore interpreted to also represent an earlier crystallisation phases. All volcanic deposits of the Saronic Gulf show, without exception, signs of varying degrees of **mingling and mixing** between the products of these earlier differentiation steps. The final petrogenetic step prior to eruption thus seems to always involve **replenishment** of more felsic crystal mush (proto-magma of the host rocks) **by a more mafic magma** (proto-magma of the enclaves). Subsequent eruptions are usually effusive in style and lead to the deposition of andesitic-dacitic lavas with basaltic-andesitic enclaves. The eruptions that marked renewal of volcanic activity on Methana and Aegina, however, involve extrusion of enclave-free basaltic andesites shortly after eruption of more felsic, enclave-bearing magmas. In both cases, petrographic characteristics of these preceding felsic rocks show clear signs of significant **partial melting**. The basaltic-andesitic lavas erupted at the start the second volcanic phase are therefore interpreted as a large mafic injection that induced this partial melting of an overlying felsic crystal mush or sub volcanic intrusion, which in turn triggered eruption of the latter and gradual tapping of the layered magma chamber. On Methana, this large mafic replenishment seems to have triggered the only Plinian eruption that occurred in the Saronic Gulf. On Aegina, the very viscous and enclave-rich Kakoperato rhyodacite was effusively deposited after which the mafic magma that resided below it found new magma pathways along NNE-SSW and ENE-WSW fissures.

7.4 Saronic Gulf volcanism: Spatial-temporal evolution and influence of local tectonics

Based on the above described identification of varying sources and processes, 6 main volcanic suites can be distinguished within the Saronic Gulf arc lavas: Poros host rocks, Methana Loutses South host rocks, Methana phase A-H volcanic rocks, Methana 'Mavri Petra' phase G lavas, Aegina phase 1 rocks and Aegina phase 2 lavas (including the Poros enclaves).

The potassium contents of these petrogenetic trends broadly reflect lower **K_2O contents** for Methana phase A-G deposits, higher amounts for Poros host rocks, the Mavri Petra flow and Aegina phase 2 lavas and the highest potassium concentrations for the magmas of Aegina's first phase of volcanic activity (Fig. 7.14A). Across-arc trends in potassium are usually reflected by K_2O-enrichment with increasing vertical distance to the subducting plate. Common interpretations of this K-depth or K-h relationship include decreasing melt percentages towards the rear of the arc and/or differences in the amount and/or the nature of the subduction component – with likely feedback between all these parameters as shallower subduction will mainly cause dehydration and the fact that a hydrous addition induces higher degrees of mantle melting than a melt-enriched addition (Gertisser & Keller, 2003; Elburg, 2010). As the dominant character ('fluid' or 'melt') of the subduction component below Aegina, Methana and Poros can not be unequivocally defined, only a link to the relative depth of the subducted slab remains to try explain the varying K contents in the Saronic Gulf.

The volcanic centres of Methana and Poros are located at a similar distance from the trench, which is ca. 20 km closer than Aegina (see Chapter 2). The majority of in-situ volcanic deposits exposed on Methana are younger than 0.9Ma (Gaitanakis & Dietrich, 1995) whereas the lavas of Poros are dated at ~ 2.5 Ma (Matsuda et al., 1999). The island of Aegina comprises volcanic deposits that span a similar period of time: the age of the phase 1 lavas largely predates the Poros volcanism whilst the magmas from the short-lived phase 2 volcanic activity erupted afterwards (ca. 4.4-3.0 Ma and 2.1 Ma, respectively – see Table 6.2 and references therein). This means that both in the Poros-Methana area and on Aegina, the potassium contents of the arc magmas decreased with time (Fig. 7.14). Could this **'reverse' K-h relationship** reflect ongoing subduction roll-back in the South Aegean arc? Over time, south-westward retreat of the downgoing slab resulted in an increase of relative vertical distance between the Saronic Gulf and the subducted African crust, which might have moved beyond the critical maximum distance for the generation of arc magmas below Aegina, explaining the cessation of volcanic activity in this rear-arc centre since ca. 2.0 Ma (Fig. 7.14). However, increasing depth of the subducted slab below the arc is thought to result in a more melt-like subduction component with higher K contents than its more hydrous equivalent as well as leading to smaller degrees of partial mantle melting than the latter. So a time-dependent increase in vertical distance to the subducted slab is expected to lead to an increase in potassium contents with time instead of the observed decrease. South-westward migration of the subduction zone does also involve 'slab roll-back mantle suction' which intensifies convection in the mantle wedge and leads to the introduction of new asthenospheric mantle below the Saronic Gulf. As new mantle is pulled below the Saronic Gulf from the north-east, this asthenospheric influx will have a different geochemical composition and is not yet contaminated by the 'subduction component', possibly explaining the lower K_2O contents in the Aegina phase 2 lavas prior to cessation of volcanism (Fig. 7.14). Below the longer lived combined magmatic system of Methana-Poros, the initial influx of new, less sediment-contaminated mantle could be reflected in the compositional difference and shift towards lower K-contents from the Poros host rocks (2.5Ma) to Methana's main volcanic phase (Phase D to G lavas). In more recent times, this 'new' mantle influx seems to have been geothermally equilibrated to a sub-arc configuration similar to that of the Aegina phase 2 magmas, as suggested by the K_2O contents of the 2200 year old phase H Mavri Petra lavas (Fig. 7.14).

Although this hypothesis involving slab roll-back and influx of new lithospheric mantle in order to explain the spatially and time-dependent geochemical variation (Fig. 7.14) might seem far-fetched, an equivalent idea has been put forward as potential explanation for the observed geochemical and petrological variation of magmatism in the Tyrrhenian Sea basin. Located in a similarly complex

geodynamic setting of subduction, back-arc spreading, collisional compression and extension, Peccerillo (2005) describes how the area's volcanic deposits show an eastwards increase in potassium contents which might be linked to the east-south-eastward slab roll back of the Ionian-Adriatic subducted plates.

The temporal change in relative vertical distance between the volcanic centres of the Saronic Gulf and the subducted slab did not only influence the magma's potassium contents. Figure 7.14B presents the 6 volcanic suites in a diagram with an x-axis reflecting possible influence of serpentinite hydrous fluids and a y-axis that discriminates between a rather melt or a rather aqueous slab-derived fluid addition to the mantle wedge. Comparing this diagram to the evolution of the subduction zone configuration in the sketches below seems to still reflect the **correlation** between **vertical distance to** the **subducted slab and** the **nature of** the **slab-derived hydrous fluids**. The main volcanic phases on Methana and both periods of volcanic activity on Aegina are inferred to have taken place when the Saronic Gulf was at an intermediate height above the subducted African slab (bottom panel Fig. 7.14). The magmas that were formed during this volcanic period represent one series with a trace element composition that points to a largely aqueous nature for the subducted slab-derived fluid that metasomatised the primitive mantle source (Fig. 7.14B). The Poros host rocks, which are inferred to represent remobilisation of an older, geochemically and mineralogically distinct felsic crystal mush, seem to reflect a serpentinite-derived hydrous fluid addition which is in agreement with the small vertical distance between Poros and the subducted slab in those days (Fig. 7.14). Deposits from the historical Mavri Petra eruption, on the other hand, point to a larger role for subducted sediment derived melts – in keeping with the present-day large vertical distance between Methana and the African slab (Fig. 7.14B). However, the Saronic Gulf volcanic rocks seem to have only rarely be able to preserve the chemical signature of their subduction component which became largely overprinted by subsuequent crustal differentiation processes. So whereas the relatively high Sr isotopic composition of the Poros host rocks might reflect equilibration between serpentinites and sea-water, the distinct Sr geochemistry of the Loutses South host rocks does not necessarily reflect a different primitive magma. It is instead proposed to reflect a relative increase in Sr concentrations during garnet fractionation at lower crustal levels so that in turn these magmas with elevated Sr contents were less sensitive to subsequent crustal contamination of their $^{87}Sr/^{86}Sr$ value (Fig. 7.14C). Despite the fact that the Aegina phase 1 and phase 2 magmas seem derived from the same primitive source (Fig. 7.14A-B) they do have a distinct gap in their $^{87}Sr/^{86}Sr$ ratios (Fig. 7.14C). This discrepancy between the Sr isotopic composition of Aegina's phase 1 and phase 2 lavas can however be derived from the same primitive magma sources but through different processes of subduction component addition to the mantle wedge. Strontium geochemical modelling calculations shows that addition of one single subducted sediment component to the depleted mantle can result in these two very different Sr compositions through either addition as an aqueous fluid in which Sr is very mobile (Sr-rich addition of 125ppm – formation of Aegina phase 1 magmas) or as a hydrous melt in which Sr will be less inclined to partition into (Sr-poor subduction compoenten of 50 ppm) and thus form primitive Aegina phase 2 magmas. Ofcourse, the change in the nature of the subduction component from a rather aqueous fluid to more of a hydrous melt can be traced back to subduction roll back which will increase over time the distance between Aegina and the subducted slab, favouring partial melting of the latter as it sinks deeper into the asthenosphere (Fig. 7.14).

The plate tectonics-scale geodynamic framework (subduction zone setting and slab roll back) is shown to be responsible for the geochemical characteristics of the Saronic Gulf magmas, and it is straightforward that rising magmas will use crustal weaknesses as pathways to the surface. But is it also possible that the extensional tectonics are in fact triggering the eruption of these arc magmas, instead of merely facilitating them? Could it be that it is the region's tectonic framework that actually determines when and where these arc magmas erupt?

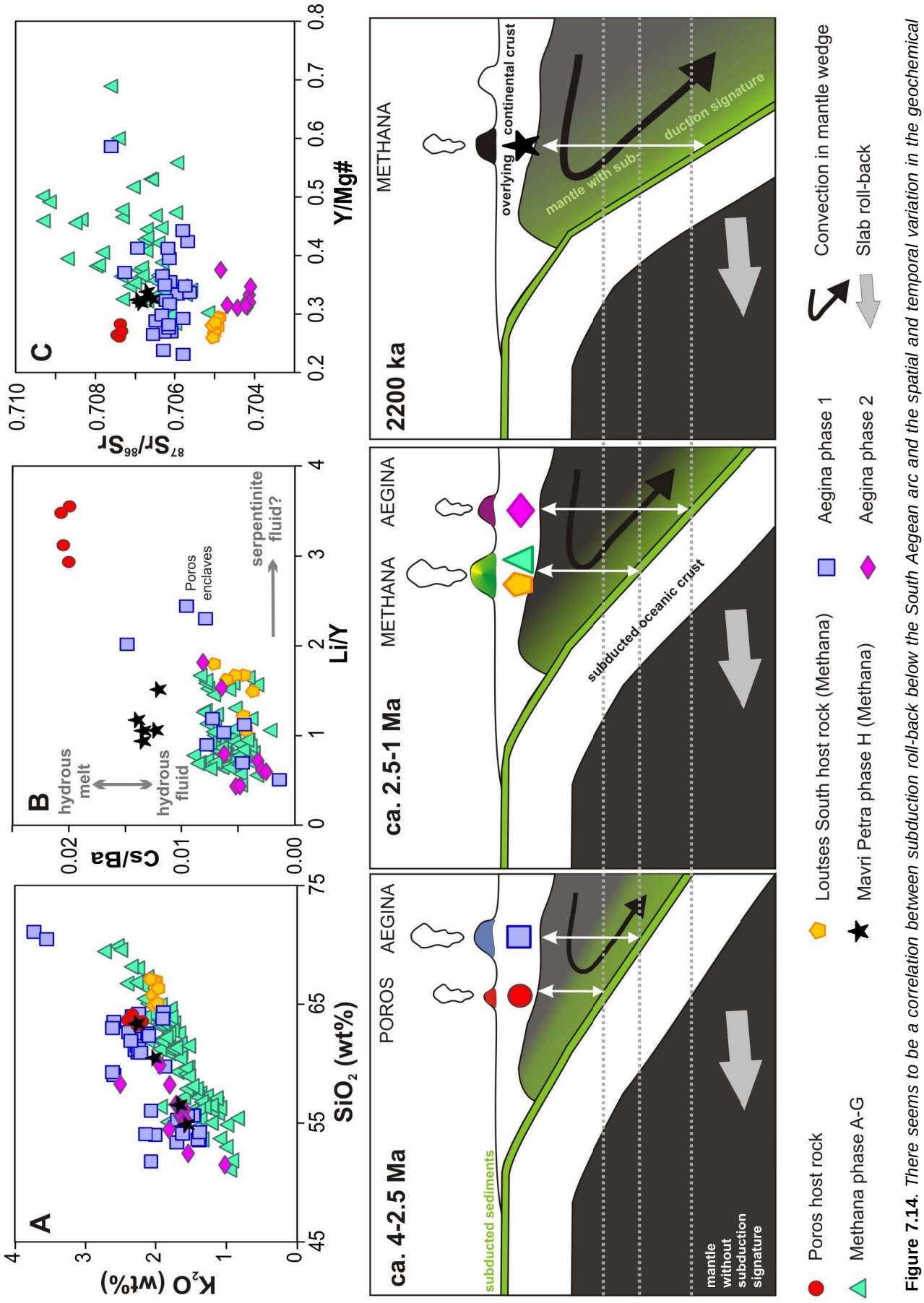

Figure 7.14. *There seems to be a correlation between subduction roll-back below the South Aegean arc and the spatial and temporal variation in the geochemical composition of the 6 main volcanic suites of the Saronic Gulf.*

Interaction between local extensional tectonics and Saronic Gulf volcanism is inferred from the geometry of eruption vents and fissures parallel to major fault sytems, the location of the submarine Pausanius volcano along the bordering normal fault of a graben and the marine record that shows the occurrence of significant basin subsidence prior to deposition of Aegina's first volcanic products (see section 2.5). The volcanic peninsula of Methana has furthermore been the scene of a case study on the effects of changing regional tectonics on arc volcanoes (Pe-Piper & Piper, 2013). It is in this study that the explosive eruption of the Phase C pyroclastic deposits was first recognised as the initiation of a second period of volcanic activity after prolonged volcanic quiescence and that his renewal of volcanism was related to the onset of crustal-scale NE-SW faulting. Volcanic rocks deposited prior to this explosive eruption are emplaced on N-S lystric faults and E-W striking faults controlled the location of eruption vents on Methana throughout the second period of activity (Pe-Piper & Piper, 2013) (Fig. 2.9).

The emplacement of Methana's PDC deposits and associated basaltic andesites near and on top of the highly fractured limestone basement also indicates an influence of the local tectonic regime on the location of eruptive vents. Methana's volcanic vents have furthermore shifted from the centre of Methana (Phase A to G) to the NW margin of the peninsula (Mavri Petra flow) to the further NW situated submarine Pausanius volcano. This relatively recent migration of Methana's volcanic activity occurs in a direction that is parallel to the subducted slab (Fig. 2.5) which is itself moving back in SW direction whilst gradually opening up NW-SE extensional faults that trigger magma ascent and eruption. Comparison of the geological map of Aegina (Fig. 6.1) with the fault systems that were subsequently active on Methana (Fig. 2.9) shows a similar correlation between the arrangement of Aegina's eruption vents and fissures and the changing direction of newly formed extensional faults. The Kakoperato flow which represents the start of the second period of volcanic activity on Aegina is furthermore thought to have a petrogenesis similar to the explosively erupted Methana pumice deposits: despite their different eruption styles, both felsic rocks show petrographic indications of significant partial melting and their eruption was followed by the only basaltic-andesitic lavas to have been deposited on either island. The change in extensional tectonics that triggered a Plinian eruption on Methana through addition of a large mafic injection into an upper crustal magma chamber thus seems to have also caused upwelling of a very large batch of mafic magma below Aegina, which in turn led to partial melting and eruption of the Kakoperato magma and subsequent tapping of the magma' chamber's mafic layer during eruption of the Aegina phase 2 lavas. The one-off volcanic eruption along Poros' southern coastline roughly coincided with the renewal of volcanic activity on Methana and Aegina. The Poros lavas are also oriented along two cross-cutting extensional fault systems and both their mineralogy and petrology suggests that the host rocks represent remobilisation (through partial melting) of a felsic crystal mush or sub volcanic intrusive body that underwent crystal fractionation at a differentiation level that is distinct from the crustal magma chamber levels inferred to below Methana or Aegina. The Poros enclaves, on the other hand, have a geochemical signature similar to the Aegina phase 2 lavas which seemed to have triggered the Kakoperato eruption.

All these observations point towards a strong link between the timing and location of volcanic activity in the Saronic Gulf, and the (changes of) the regional stress regime. The magmas themselves have an undoubtedly subduction-zone derived geochemical composition, but it seems that de tectonic structures of the Saronic Gulf create the pathways for these magmas to ascent towards the surface and perhaps erupt. So whereas subduction of the African slab beneath the Aegean micro-plate causes the formation of the Saronic Gulf arc magmas, they seem to often arrest in the 32 km thick crust. The regional, crustal scale tectonics randomly sample these stalled crystal mushes whenever a change in the local stress regime triggers (re-)activiation of extensional tectonics along which new volumes of primitive magma rise and replenish the older felsic crystal mushes.

The link between tectonic regime and exact locations of magmatic structures is also observed in the wider area around the Saronic Gulf: from the Argolic Gulf and Argolis peninsula south of Methana to the Sousaki-Crommyonia area on mainland Greece to the north, there is a entire network of large

plutonic bodies (Efstathiou et al., 2013). The fact that the shape, orientation and location of these intrusions can all be related to both crustal and sub-crustal extensional stress fields is compelling evidence that the pathways of both intrusive and volcanic magmatism in the Saronic Gulf are controlled by the local tectonic regime (Efstathiou et al., 2013).

7.5 Saronic Gulf magmatism: main conclusions

Whereas all volcanic rocks of the Saronic Gulf have a subduction-related origin, timing and location of their emplacement at the earth's surface seems governed by the local tectonic regime: during times of (re-)activation of extensional tectonics, previously differentiated magmas rise and erupt along active faults systems.

The andesitic dacitic lavas of Aegina, Methana and Poros often contain basaltic andesitic enclaves interpreted to be globules of a more mafic magma that replenished a more felsic crystal mush, leading to remobilisation and eruption of the latter. During its ascent to the surface, more mafic magmas get trapped in the magma chambers of older and colder, more felsic crystal mushes. As they pond at the bottom of this magma chamber, their heat might lead to small degrees of partial melting of the overlying crystal mush. As they themselves cool down against the felsic magma and the wall rock, they will undergo crystal fractionation. The latter process will start to form a framework of randomly organised prismatic phenocrysts when second boiling leads to vesiculation, decreasing the densitiy of the mafic magma which in turn breaks up and gets dispersed throughout the overlying felsic magma. Enclaves rising in the felsic magma and interaction between these two magmas triggers effusive eruption of the remobilised, felsic magma as enclave-bearing lavas. The fact that enclaves are present in nearly all effusive deposits suggests that this differentiation step of mafic replenishment and remobilisation is fundamental in the petrogenesis of the Saronic Gulf volcanics. The only exceptions to this are the basaltic andesitic lavas that were the secondly deposited unit upon renewal of volcanic activity and which are interpreted to represent enclave magmas.

On Aegina, these phase 2 lavas erupted along newly formed fissures in the central part of the island, following eruption of the Kakoperato rhyodacite in the western part were also many phase 1 lavas were deposited. Although this Kakoperato flow represents the first unit of the second phase of volcanic activity on Aegina, its Sr isotopic composition clearly shows affinity with the phase 1 magmas. In conjunction with a petrography that strongly points to partial melting, the Kakoperato rhyodacite is interpreted as a phase 1 felsic crystal mush that had stalled in the crust and was undergoing further crystal fractionation and solidification when a large batch of phase 2 mafic magma was injected into its magma chamber, induced its partial melting and upon (limited) magma mingling and mixing triggered the effusive eruption of the Kakoperato phase 1 rhyodacite with its phase 2 enclaves. The majority of the replenishing phase 2 magma was subsequently erupted along fissures in the Nikolaki-Oros-Lazarides area.

On Methana, the phase C pumice fallout deposits represent the initiation of the second period of volcanic activity. Their petrographic characteristics are also indicative of significant partial melting and (very limited) pre-eruptive mingling and mixing with the magmas of the PDC deposits that were subsequently erupted along the peninsula's southerly and north-westerly located, intensely fractured limestone basement. The main difference between renewal of volcanic activity on Methana and Aegina, however, is the explosive eruption style in which this event occurred on Methana. This deviation from the effusive eruption style that is typical of Saronic Gulf volcanism is thought to have been triggered by melting of hydrous mineral phases such as amphibole and biotite. Adding large volumes of partial melts of these minerals to the crystal mush's remaining melt could have induced oversaturation of volatile phases which in turn exsolved into gas bubbles, dramatically increasing the pressure within the magma body and leading to explosive volcanic activity.

This Plinian eruption left behind a large collapse-caldera in the centre of Methana peninsula, which, however, has been largely filled by the second phase lava flows and domes. The fact that there is no clear evidence of explosive activity in the westernmost part of the South Aegean arc thus mainly reflects the long period of time that since has passed, allowing both erosion of the pumice and PDC deposits and estrusion of the new lavas to both cover the explosive units and fill in the caldera. So in comparison to the only partially filled and thus still easily recognisable ca. 50 ka caldera on Nisyros, new volcanic activity virtually wiped out all traces of the ca. 2Ma Plinian eruption on Methana.

The small volcanic peninsula on Poros represents a single volcanic eruption of enclave-bearing lavas which are also deposited along major extensional faults. The andesitic dacitic host rocks have a distinct biotite-rich and allanite-bearing mineralogy that is unique amongst the Saronic Gulf volcanic deposits. The Poros enclaves, however, are both mineralogically and geochemically very similar to Aegina phase 2 lavas. This suggests a petrogenesis for the Poros lavas equivalent to the Kakoperato rhyodacite: a felsic crystal mush or subvolcanic intrusion that has since long been stalled in the crust below Poros and which was replenished and subsequently remobilised by a mafic magma of (partially) different origin. The fact that the crustal differentiation level below Poros, deduced from amphibole fractionation, is distinctly different to the amphibole crystal fractionation levels inferred to be present below Aegina and Methana, seems to support the hypothesis of a specific crustal differentiation level for the Poros magmas.

K/Ar ages obtained for the Poros lavas (ca. 2.7Ma) coincide with the age of Aegina's Kakoperato rhydoacite (3.1±0.4Ma) and both fall within the age gap defined between a single age obtained for Methana's phase A volcanic basement (3.5±0.9Ma) and the age of the oldest phase C effusive lavas (1.4±0.3Ma). This indicates that the one-off volcanic episode on Poros coincided with renewal of volcanic activity on both Aegina and Methana. Further refinement of the age of Methana's pyroclastic deposits is required, but it seems that the change in regional tectonics which caused explosive renewal of volcanism on Methana also caused the (last) volcanic episodes on Poros and Aegina.

Trace element geochemistry and Sr-Nd-Hf-Pb isotopic composition indicate that the magma genesis below the Saronic Gulf can be represented by addition of a single subduction component (intermediate in composition to globally subducted sediments and Ionian tephra likely to be subducted below the area) to a depleted mantle wedge. This subducted slab-derived component is thereby usually a hydrous fluid, but a serpentinite-derived aqueous signature might be recognised in the Poros host rocks and the youngest Mavri Petra flow on Methana seems to reflect addition of a hydrous melt to the mantle wedge. These primitive magmas subsequently undergo a range of differentiation stages in the more than 32km thick continental crust, involving fractional crystallisation and concurrent assimilation of wall rock. Deeper crustal differentiation levels can be geochemically approximated by lower crustal xenoliths from the Pannonian basin north to the Aegean microplate and are inferred to involve fractional crystallisation of olivine, plagioclase, clinopyroxene, orthopyroxene, Fe-Ti-oxides and apatite. Further differentiation in more shallow magma chambers involves fractional crystallisation of amphibole, plagioclase, clinopyroxene, orthopyroxene, Fe-Ti-oxides, apatite and biotite whilst assimilating wall rock with a composition similar to the gneisses from Ios. Though commonly observed in thin sections, Cr-spinel, quartz and zircon could not be successfully included in the crystallising mineral assemblage of the fractional crystallisation geochemical models. The Cr-spinel inclusions in olivine are thus probably formed at the very start of magma differentiation from very mafic magmas of which we could not collect a sample. Zircon and quartz crystallisation on the other hand seems to occur in stalled crystal mushes or sub volcanic intrusive bodies from which there is also no subaerial equivalent. A few volcanic units seem to have also undergone an early stage of garnet fractionation in the roots of the Saronic Gulf arc system (Loutses South host rocks, Kossona Vouno enclaves, Poros host rocks?). Magma mixing and mingling are the second most important differentiation processes besides crystal fractionation and concurrent assimilation of wall rock. They are not only reflected in the ubiquitous presence of enclaves or mineral disequilibrium features, but also expressed in the geochemical scatter of certain trace element concentrations and isotopic compositions, which results

from significant incorportation of antecrysts. Magma mixing is thereby distinctly more important in the petrogenesis below Methana – as shown by the lack in geochemical gap between enclaves and host rocks otherwise present in the volcanic rocks on Aegina and Poros. Methana is furthermore distinct due to the presence of a hydrothermal system that seems to have homogenised Pb isotopic compositions in specific portions of the upper 3 km of the crust. This geothermal system strongly affects the geochemical composition of Methana's magmas as they pass through or reside in this hydrothermally altered upper section of the crust. The phase C pumice deposits display the most evolved geochemistry of all Saronic Gulf deposits and might reflect partial melting of sub volcanic intrusive body similar to the Laurion granodiorite.

The geothermal system is also one of the reasons that Methana is regarded as a present-day active volcanic centre. Other reasons are the historic eruption (ca. 220 BC) of the youngest Mavri Petra flow and the probably even more recent submarine volcanic eruption of the Pausanius volcano. The Mavri Petra flow and Pausanius volcano thereby lie increasingly more north-westward from the centre of Methana. This could reflect progressive activation of extensional fault systems which is caused by ongoing slab roll back that pulls at the Saronic Gulf continental crust in south-westward direction.

Nederlandse samenvatting

De studie van vulkanische gesteenten heeft een grote vooruitgang geboekt sinds de algemene aanvaarding en verdere ontwikkeling van het geologische concept van de platentektoniek zo'n 50-60 jaar geleden. Eén van de relatief nieuwe inzichten daarbij is het ontstaan van vulkanische eilandbogen boven subductie zones. Dehydratatie van de subducerende oceaanplaat leidt tot migratie van waterige fluïda in de bovenliggende mantelwig die door toevoeging van dit water smeltpuntverlaging ondergaat en partieel opsmelt. De resulterende primitieve magmas stijgen daarop naar het aardoppervlak waar zij kunnen uitbarsten in subductie vulkanen.

Hoewel de grote lijnen van dergelijk subductie vulkanisme ondertussen bekend zijn, ontbreken er nog tal van details die belangrijk zijn om te begrijpen hoe magma bronnen en processen enerzijds variëren van eilandboog tot eilandboog en anderzijds de uiteindelijke mineralogie, geochemie en wijze van uitbarsten van de lavas bepalen. Verder onderzoek in de verschillende aspecten van subductie vulkanisme zijn voorts ook belangrijk omdat (1) ertsen van bepaalde zeldzame elementen en kostbare metalen gerelateerd zijn aan subductie-gerelateerde magmatische gesteenten, (2) de continentale korst waarop wij leven is opgebouwd door processen gelijkaardig aan deze die momenteel plaatsvinden in subductie zones en (3) de overgrote meerderheid van gevaarlijke historische vulkaanuitbarstingen plaatsvonden in vulkaanbogen.

Vulkanisme in de Zuid-Egeische boog is uitdrukking aan het aardoppervlak van noordwaartse subductie van de Afrikaans oceanische plaat onder het continent Eurazië, meer bepaald onder de Egeïsche microplaat. Van oost naar west bestaat deze eilandboog uit de actieve vulkanische centra van Nisros-Yali-Kos, Santorini, Milos en Aegina-Methana-Poros. De centrale en oostelijke subductievulkanen zijn daarbij veelvoudig bestudeerd gedurende de laatste decennia, maar de vulkanische centra in de westelijke Saronische Golf zijn nagenoeg onbekend. Geofysisch, vulkanologisch en petrologisch onderzoek toont nochtans aan dat er belangrijke verschillen zijn tussen Aegina-Methana-Poros wat betreft de dikte van de continentale korst waarop deze vulkanen zich bevinden, de mineralogische en geochemische samenstelling van de vulkanieten en de wijze waarop deze aan het aardoppervlak werden afgezet.

Dit doctoraatsonderzoek behandelt in detail de petrografische en geochemische kenmerken van de vulkanische afzettingen van de Saronische Golf en integreert deze nieuwe gegevens met data uit de literatuur om een zo volledig mogelijk beeld te bekomen van de magmagenese onder en de vulkanische activiteit op Aegina, Methana en Poros. Veldobservaties en een nauwkeurige microscopie studie leidden daarbij tot de selectie van relevante gesteente monsters voor geochemische analysen. De concentraties aan hoofdelementen werden bepaald via ICP-OES analyse van met flux opgesmolten gesteentepoeders. Een tweede set gesteentepoeders werd opgelost in sterke zuren en de spoorelement concentratie ervan gemeten via ICP-Q-MS. Op basis van de hoofd-en spoorelement geochemie werden daarop de meest representatieve vulkanieten van de Saronische Golf gekozen om, na oplossing in sterke zuren, bepaling van hun Sr, Nd, Hf en Pb isotopische samenstelling te ondergaan op via MC-ICP-MS.

Uit dit onderzoek blijkt dat alle vulkanieten van de Saronische Golf enerzijds de karakteristieken van subductie-gerelateerde magmas vertonen maar dat anderzijds zowel het tijdsbestek als de exacte situering van hun uitbarsting aan het aardoppervlak bepaalde worden door lokale extensie tektoniek in de Egeïsche microplaat. Migratie van de vulkanische activiteit op Methana van het centrum van het schiereiland naar de noordwestelijk rand (Mavri Petra lavas) en verder noordwestwaarts naar de

submariene Pausanius vulkaan wordt gelinkt aan progressief openen van NW-ZO georiënteerde extensionele breuken door de zuidwestwaarts beweging van de gesubduceerde Afrikaans plaat.

Vulkanische gesteenten van Aegina, Methana en Poros zijn voornamelijk andesietische tot dacietische lavas met basaltisch andesietische enclaves. De petrogenese van deze gesteenten wordt voorgesteld als een felsische, kristal-rijke magma kamer die een injectie van opstijgend, meer mafisch en dus warmer magma krijgt. Het kristalrijke magma zal daarop opwarmen en deels opsmelten terwijl het mafische magma afkoelt en een raamwerk van willekeurig georiënteerde kristallen vormt. Kristallisatie van het mafische magma kan daarbij leiden tot oververzadiging van de resterende smelt aan volatiele fasen. Ontgassing leidt vervolgens tot vesiculatie van het mafische magma dat daardoor een kleinere densiteit bekomt en kan opstijgen, opbreken en in verspreid raken in het bovenliggende, deels heropgesmolten en nu minder visceuze kristal-rijke magma. Interactie tussen dergelijke globules van mafisch magma en het felsiche magma waarin het word opgenomen kan het geheel weer in beweging zetten en uiteindelijk een uitbarsting veroorzaken van enclave-houdende gastgesteenten. Het feit dat nagenoeg alle Saronische Golf vulkanieten dergelijke meer mafische enclaves bevatten doet het vermoeden rijzen dat dit proces van remobilisering van een visceus, felsisch magma door toevoegen van een warmer mafisch magma een essentiële stap is in hun petrogenese.

De enige uitzonderingen zijn de enclave-loze basaltisch andesietische lavas die zowel op Aegina als Methana werden afgezet kort na de initiatie van een tweede fase van actief vulkanisme. Deze magmas zijn geïnterpreteerd als de mafische injecties onderaan de magma kamer van de meer felsische magmas die vlak ervoor tot uitbarsting kwamen. Deze felsische magmas zijn enerzijds de Kakoperato rhydoaciet op Aegina en anderzijds de puimsteen afzettingen op Methana. Beiden vertegenwoordigen de heropleving van vulkanische acitiveit na een langdurige periode zonder uitbarstingen, en beiden vertonen duidelijke petrografische kenmerken van significante heropsmelting. De Kakoperato rhydacietische gastgesteenten hebben daarbij duidelijk de geochemische karakteristieken van de vulkanieten van Aegina's eerste vulkaan fase, terwijl de Kakoperato enclaves erg gelijken op de vervolgens uitgevloeide mafisch-intermediaire lavas van de tweede vulkaan phase. In tegenstelling tot de effusieve eruptie van de Kakoperato magmas vertegenwoordigen de puimsteen afzettingen van Methana een explosieve uitbarsting. Deze Plinische eruptie luidde de start van de tweede fase van vulkanische activiteit op Methana in. Een significant groter volume aan inkomend mafisch magma wordt verantwoordelijk geacht voor het opsmelten van waterhoudende mineralen zoals amfibool en biotiet, waardoor de smelt van het felsische kristalrijke magma oververzadigd wordt aan volatiele fasen. Ontgassing van dit magma kan dan een plotse volumetoename veroorzaakt hebben die aanleiding gaf tot de enige explosieve uitbarsting die tot nog toe is geïdentificeerd in de Saronische Golf. Net zoals op Aegina leidt geleidelijk aftappen van de felsisch-mafisch gelaagde magma kamer tot een daaropvolgende uitbarsting van basaltisch andesietische magmas. De instortingscaldera die gevormd tijdens deze explosieve uitbarsting gevormd werd in het centrum van het schiereiland Methana is in de loop der jaren weer opgevuld met nieuwe lava domes and flows. Het nagenoeg ontbreken van pyroclastica en instrotingskraters in de Saronische Golf wil dus niet eenduiding zeggen dat er in dit deel van de Zuid-Egeïsche boog geen Plinische vulkaanuitbarstingen waren. Het duidt er alleen op dat deze een stuk langer geleden gebeurden dan deze die ongeveer 50 000 jaar geleden de instortingscaldera van Nisyros vormde: waar de krater op Nisyros reeds deels is opgevuld en overdekt met jongere effusieve vulkanieten, zijn de ongeveer 2 miljoen jaar oude Methana caldera en puimsteen afzettingen nagenoeg volledig uitgewist.

Het 1 vierkante km schiereiland ten zuiden van Poros vertegenwoordigt vulkanische afzettingen van één enkele effusieve eruptie. Net zoals op Aegina en Methana bestaan deze lavas uit dacietisch-andesietische gastgesteenten met basaltisch andesietische enclaves. De Poros enclaves vertonen daarbij sterke gelijkenissen met de mafisch-intermediaire lavas van Aegina's tweede fase vulkanische activiteit. De Poros gastgesteenten zijn daarentegen gekenmerkt door een mineralogische en geochemische samenstelling die uniek is in de Saronische Gulf. Uit literatuur gegevens over de hoofdelement samenstelling van amfibolen afkomstig van Aegina, Methana en Poros blijkt ook dat de

amfibolen van Poros uitkristalliseerden bij een temperatuur en druk die een magma-differentiatielevel in de korst vertegenwoordigen dat verder geen rol lijkt gespeeld te hebben in de petrogenese van de Aegina en Methana magmas. K/Ar ouderdommen voor de lavas op Poros (ongeveer 2.7My) and de Kakoperato rhydoaciet (3.1±0.4My) intermediair aan de 3.5±0.9My en 1.4±0.3My ouderdom van de vulkanische afzettingen op Methana die stratigrafisch respectievelijk ouder en jonger zijn dan de puimsteen afzettingen. Het lijkt er dus op dat activering van een nieuwe set extensionele breuken niet alleen een Plinische eruptie op Methana veroorzaakte, maar eveneens een laatste grote uitbarsting op Aegina en de enige fase van vulkanische activiteit op Poros. Datering van de pyroklastische afzettingen van Methana kan hier uitsluitsel over geven.

Geochemische modelleringen tonen aan dat alle primitieve magmas van de Saronische Golf gevormd kunnen worden door toevoeging van één enkele subductie component aan een verarmde mantel wig. Deze subductie component was daarbij meestal een waterige vloeistof hoofdzakelijk afkomstig van een mengsel tussen klassiek gesubduceerde sedimenten en tefra die specifiek in de Saronische Golf subduceren. Enkel de geochemische samenstelling van de Poros gastgesteenten lijkt te wijzen op een sterke invloed van voornamelijk serpentiniet-gerelateerde waterige vloeistoffen die toegevoegd werden aan de mantelwig, terwijl de jongste vulkanieten op Methana, de Mavri Petra lava, dan weer de signatuur van een waterige smelt vertoont. Deze primitieve magmas hebben vervolgens een reeks differentiatie stappen ondergaan in de continentale korst onder de Saronische Golf alvorens ze uitbarstten aan het aardoppervlak. Hoofdelement modelleringen suggereren dat in dieper gelegen magmakamers een mineraal assemblage van olivijn, plagioklaas, clinopyroxeen, orthopyroxeen, Fe-Ti-oxides en apatiet uitkristalliseert. Fractionele kristallisatie gaat daarbij gepaard met assimilatie van van een gesteente met een geochemische samenstelling gelijkaardig aan deze van onder korst xenolieten van het Panonische Bekken, ten noorden van de Egeïsche microplaat. Een tweede uitkristalliserende mineraal assemblage bevat amfibool, plagioklaas, clinopyroxeen, orthopyroxeen, Fe-Ti-oxides, apatiet en biotiet in ondieper gelegen magmakamers waarvan het omgevingsgesteente compositioneel gelijkaardig is aan de verschillende types gneiss van Ios. Het feit dat geen van de modelleringen kristallisatie van Chroomspinel toelaat terwijl dit mineraal meermaals als euhedrische inclusie aanwezig is in olvijn, doet vermoeden dat er nog een eerdere, diepergelegen fractionatie fase is waarbij meer mafische magmas zijn betrokken dan deze die in de Saronische golf bemonsterd werden. De aanwezigheid van kwarts en zirkoon in tal van meer felsische gastgesteenten kan eveneens niet verklaart voor worden via fractionele kristallisatie berekeningen op basis van de gekende gehele gesteente composities. Dit zou erop kunnen wijzen dat er een extra fase is van felsische mineralen-gedomineerde fractionele kristallisatie waarvan geen representatieve eindproducten gevonden werden op de vulkanische centra. De opvallende spoorelement samenstelling van sommige lavas lijkt ook te wijzen op een (sporadische) rol voor granaat fractionatie nabij de korst-mantel grens.

Na fractionele kristallisatie is vermenging van magmas het tweede belangrijkste differentiatieproces voor alle Saronische Golf vulkanieten. Dit proces is enerzijds sterk weerspiegelt in de aanwezigheid (1) van enclaves, (2) van een grote variëteit aan mineraal voorkomens die duiden op disequilibrium, (3) van olivijn en kwarts in éénzelfde slijpplaat en (4) van een soms erg sterke spreiding in de spoorelement en isotopische samenstelling, waarschijnlijk ten gevolge van het uitwisselen van kristallen tussen verschillende generaties van mamga. Magma vermenging is daarbij het sterkst vertegenwoordigt op Methana waar er geen een distinctief verschillende geochemische samenstelling is voor gastgesteenten en enclaves. Methana heeft verder ook een hydrothermaal systeem dat de geochemische samenstelling (vooral Pb isotopen) homogeniseert binnen bepaalde segmenten van de bovenste drie km van de korst. Transport of verdere differentiatie van de Methana magmas in deze sterk hydrothermaal gealtereerde lagen veroorzaakt een laatste grote contaminatie van hun magmas. De puimstenen vertonen de sterkst gedifferentieerde isotopische samenstelling en kunnen verklaard worden door partieel opsmelten van een sub vulkanische intrusief lichaam met een geochemische compositie gelijkaardig aan de Laurion granodioriet.

References

Albarède, F., 1995. Introduction to geochemical modelling. Cambridge University Press, Cambridge. 543 pp.

Allen, S.R., 2001. Reconstruction of a major caldera-forming eruption from pyroclastic deposit characteristics: Kos Plateau Tuff, eastern Aegean Sea. Journal of Volcanology and Geothermal Research, 105, 141-162.

Alonso-Perez, R., Müntener, O. and Ulmer, P., 2009. Igneous garnet and amphibole fractionation in the roots of island arcs: experimental constraints on andesitic liquids. Contributions to Mineralogy and Petrology, 157, 541-558.

Anastasakis, G. and Piper, D.J.W., 2005. Late Neogene evolution of the western South Aegean volcanic arc: sedimentary imprint of volcanicity around Milos. Marine Geology, 215, 135-158.

Annen, C., Blundy, J.D. and Sparks, R.S.J., 2006. The genesis of intermediate to silicic magmas in deep crustal hot zones. Journal of Petrology, 47, 3, 505-539.

Bach, P., Smith, I. E. M. and Malpas, J. G., 2012. The origin of garnets in andesitic rocks from the Northland arc, New Zealand, and their implication for sub-arc processes. Journal of Petrology, 53, 1169-1195.

Bachmann, O., Dungan, M.A. and Lipman, P.W., 2002. The Fish Canyon magma body, San Juan Volcanic Field, Colorado: rejuvenation and eruption of an upper-crustal batholith. Journal of Petrology, 43, 1469-1503.

Bachmann, O. and Bergantz, G.W., 2003. Rejuvenation of the Fish Canyon magma body: A window into the evolution of large-volume silicic magma systems. Geology, 31, 789-792.

Bachmann, O. and Bergantz, G.W., 2006. Gas percolation in upper-crustal silicic crystal mushes as a mechanism for upward heat advection and rejuvenation of near-solidus magma bodies. Journal of Volcanology and Geothermal Research, 149, 85-102.

Bachmann, O., Charlier, B.L.A. and Lowenstern, J.B., 2007. Zircon crystallisation and recycling in the magma chamber of the rhyolitic Kos Plateau Tuff (Aegean arc). Geology, 35, 73-76.

Bachmann, O., Schoene, B., Schnyder, C. and Spikings, R. A., 2010. The 40Ar/39Ar and U/Pb dating of young rhyolites in the Kos-Nisyros volcanic complex, eastern Aegean arc, Greece: Age discordance due to excess 40Ar in biotite. Geochemistry Geophysics Geosystems, 11, Q0AA08, doi: 10.1029/2010GC003073.

Bailey, J.C., Jensen, E.S., Hansen, A., Kann, A.D.J. and Kann, K., 2009. Formation of heterogeneous magmatic series beneath North Santorini, South Aegean island arc. Lithos, 110, 20-36.

Baker, J., Peate, D., Waight, T and Meyzen, C. 2004. Pb isotopic composition of standards and samples using a 207Pb-204Pb double spike and thallium to correct for mass bias with double-focussing MC-ICP-MS Chemical Geology, 211, 275-303.

Barclay, J. and Carmichael, I.S.E., 2004. A hornblende basalt from western Mexico: Water-saturated phase relations constrain a pressure-temperature window of eruptibility. Journal of Petrology, 45, 3, 485-506.

Beard, J.S., 2008. Crystal-melt separation and the development of isotopic heterogeneities in hybrid magmas. Journal of Petrology, 49, 1027-1041.

Best, M.G., 2003. Igneous and metamorphic petrology. Second edition. Blackwell Science Ltd, 729p.

Boschi, C., Bonatti, E., Ligi, M., Brunelli, D., Cipriani, A., Dallai, L., D'Orazio, M., Früh-Green, G. L., Tonarini, S., Barnes, J. D. and Bedini, R. M., 2013. Serpentinization of mantle peridotites along an uplifted lithospheric section, Mid Atlantic Ridge at 11° N. Lithos, 178, 3-23.

Bouvier, A., Vervoort, J.D. and Patchett, P.J., 2008. The Lu-Hf and Sm-Nd isotopic composition of CHUR: constraints from unequilibrated chondrites and implications for the bulk composition of terrestrial planets. Earth and Planetary Science Letters, 273, 48-57.

Braschi, E., Francalanci, L. and Vougioukalakis, G.E., 2012. Inverse differentiation pathway by multiple mafic magma refilling in the last magmatic activity of Nisyros Volcano, Greece. Bulletin of Volcanology, 74, 1083-1100.

Bryan, W.B., Finger, L.W. and Chayes, F., 1969. Estimating proportions in petrographic mixing equations by least-squares approximation. Science, 163, 926-927.

Buettner, A., Kleinhanns, I.C., Rufer, D., Hunziker, J.C. and Villa, I.M., 2005. Magma generation at the easternmost section of the Hellenic arc: Hf, Nd, Pb and Sr isotope geochemistry of Nisyros and Yali volcanoes (Greece). Lithos, 83, 29-46.

Buckley, V.J.E., Sparks,R.S.J. and Wood, B.J., 2006. Hornblende dehydration reactions during magma ascent at Soufrière Hills Volcano, Montserrat. Contributions to Mineralogy and Petrology, 151, 121-140.

Cantner; K., Carey, S. and Nomikou, P., 2014. Integrated volcanologic and petrologic analysis of the 1650AD eruption of Kolumbo submarine volcano, Greece. Journal of Volcanology and Geothermal Research, 269, 28-43.

Carpentier, M., Chauvel, C., Maury, R.C. and Mattielli, N., 2009. The 'zircon effect' as recorded by the chemical and Hf isotopic compositions of Lesser Antilles forearc sediments. Earth and Planetary Science Letters, 287, 86-99.

Chappell, B.W. and White, A.J.R., 1991. Restite enclaves and the restite model. In: Didier, J. and Barbarin, B. (Editors), Enclaves and granite petrology. Elsevier, Amsterdam, pp. 375-381.

Chappell, B.W., 1996. Magma mixing and the production of compositional variation within granite suites: evidence from granites of Southern Australia. Journal of Petrology 37, 449-470.

Charlier, B.L.A., Wilson, C.J.N., Lowenstern, J.B., Blake,S., Van Calsteren, P.W. and Davidson, J.P., 2005. Magma generation at a large, hyperactive silicic volcano (Taupo, New Zealand) revealed by U-Th and U-Pb systematics in zircons. Journal of Petrology, 46, 3-32.

Chauvel, C., Lewin, E., Carpentier, M., Arndt, N.T. and Marini, J.-C., 2007. Role of recycled oceanic basalt and sediment in generating the Hf-Nd mantle array.

Chen, J.H. and Wasserburg, G.J., 1983. The least radiogenic Pb in iron meteorites, Fourteenth Lunar and Planetary Science Conference, Abstracts, Part I, 103-104.

Chiaradia, M., Ulianov, A., Kouzmanov, K. and Beate, B., 2012. Why large porphyry Cu deposits like high Sr/Y magmas? Scientific Reports, 2, 685, doi:10.1038/srep00685.

Cioni, R., Marianelli, P., Santacroce, R. and Sbrana, A., 2000. Plinian and Subplinian eruptions. In: Siggurdsson, H., Houghton, B., McNutt, S.R., Rymer, H. and Stix, J. (eds), Encyclopedia of volcanoes. Academic Press, 477-494.

Clift, P. and Blusztajn, J., 1999. The trace-element characteristics of Aegean and Aeolian volcanic arc marine tephra. Journal of Volcanology and Geothermal Research, 92, 321-347.

Coombs, M.L., Eichelberger, J.C. and Rutherford, M.J., 2002. Experimental and textural constraints on mafic enclave formation in volcanic rocks. Journal of Volcanology and Geothermal Research 119, 125-144.

Cottrell, E., Gardner, J.E. and Rutherford, M.J., 1999. Petrologic and experimental evidence for the movement and heating of the pre-eruptive Minoan rhyodacite (Santorini, Greece). Contributions to Mineralogy and Petrology, 135, 315-331.

Couch, S., Sparks, R.S.J., and Carroll, M.R., 2001. Mineral disequilibrium in lavas explained by convective self-mixing in open magma chambers. Nature 411, 1037-1039.

Cox, K.G., Bell, J.D. and Pankhurst, R.J., 1979. The interpretation of igneous rocks. George Allen and Unwin Ltd, 450p.

Czuppon, G., Lukács, R., Harangi, S., Mason, P.R.D. and Ntaflos, T., 2012. Mixing of crystal mushes and melts in the genesis of the Bogács Ignimbrite suite, northern Hungary: An integrated geochemical investigation of mineral phases and glasses. Lithos, 148, 71-85.

D'Alessandro, W., Brusca, L., Kyriakopoulos, K., Michas, G. and Papadakis, G., 2008. Methana, the westernmost active volcanic system of the south Aegean arc (Greece): Insight from fluids geochemistry. Journal of Volcanology and Geothermal Research, 178, 818-828.

Davi, M., De Rosa, R. and Holtz, F., 2010. Mafic enclaves in the rhyolitic products of Lipari historical eruptions; relationships with the coeval Vulcano magmas (Aeolian Islands, Italy). Bulletin of Volcanology 72, 991-1008.

Davis, E.N., 1957. Die Jungvulkanischen Gesteine von Aegina, Methana und Poros, und deren Stellung im Rahmen der Kykladenprovinz, . Publikationen herausgegeben von der Stiftung "Vulkaninstitut Immanuel Friedländer", Nr. 6. Guggenbühl and Huber Schweizer-Spiegel-Verlag Zürich, 85p.

Davidson, J., Turner, S., Handley, H., Macpherson, C. and Dosseto, A., 2007. Amphibole "sponge" in arc crust? Geology, 35, 9,787-790.

de Boorder, H., Spakman, W., White, S.H and Wortel, M.J.R., 1998. Late Cenozoic mineralisation, orogenic collapse and slab detachment in the European Alpine Belt. Earth and Planetary Science Letters, 164, 569-575.

Defant, M. and Drummond, M., 1990. Derivation of some modern arc magmas by melting of young subducted lithosphere. Nature, 347, 662-665.

Defant, M. J. and Kepezhinskas, P., 2001. Evidence suggests slab melting in arc magmas. Eos Transactions AGU, 82, 65–69.

De Muynck, D., 2008. Development of separation methods and measurement protocols for Sr and Pb isotopic analysis of archaeological artefacts by means of single-collector and multi-collector ICP-mass spectrometry. Unpublished PhD thesis, Ghent University.

De Muynck, D., Huelga-Suarez, G., Van Heghe, L., Degryse, P. and Vanhaecke, F., 2009. Systematic evaluation of a strontium-specific extraction chromatographic resin for obtaining a purified Sr fraction with quantitative recovery from complex and Ca-rich matrices. Journal of Analytical Atomic Spectrometry, 24, 1498-1510.

Deniel, C. and Pin, C., 2001. Single-stage method for simultaneous isolation of lead and strontium from silicate samples for isotopic measurements. Analytica Chemica Acta, 426, 95-103.

DePaolo, D. J., 1981. Trace element and isotopic effects of combined wall rock assimilation and fractional crystallisation. Earth and Planetary Science Letters, 53, 189-202.

De Pelsmaeker, E., 2011. Petrologie en geochemie van de Pleistocene δ-2 vulkanische afzetting op Methana, Egeïsche boog, Griekenland. Unpublished MSc thesis, Ghent University, Belgium.

Dessimoz, M., Müntener, O. and Ulmer, P., 2012. A case for hornblende dominated fractionation of arc magmas: the Chelan Complex (Washington Cascades). Contributions to Mineralogy and Petrology, 163, 567-589.

Dickinson, W.R., 1970. Global Tectonics. Science, 168, 1250–1259.

Dickinson, W.R., 1971. Plate tectonic models of geosynclines. Earth and Planetary Sciene Letters, 10, 165-174.

Didier, J., 1973. Granites and their enclaves: the bearing of enclaves on the origin of granites. (English translation from the French manuscript by Renouf, J.T.) Developments in Petrology 3, Elsevier, Amsterdam, 393 p.

Didier, J. and Barbarin, B., 1991. Enclaves and granite petrology. Developments in Petrology 13, Elsevier, Amsterdam, 626 p.

Dietrich, V.J., Mercolli, I. and Oberhänsli, R. 1988. Dazite, High-Alumina-Basalte und Andesite als Produkte amphiboldominierter Differentiation (Aegina und Methana, Ägäischer Inselbogen). Schweizer Mineralogische und Petrographische Mitteilungen, 68, 21-39.

Dietrich, V.J, Gaitanakis, P., Mercolli, I. and Oberhänsli, R., 1993a. Geological map of Greece, Aegina island, 1:25000. Swiss Federal Institute of Technology, Zurich.

Dietrich, V.J, Gaitanakis, P., Mercolli, I. and Oberhänsli, R., 1993b. Geological map of Greece, Aegina island, 1:25000. Bulletin of the Geological Society of Greece, 28, 3, 555-566.

Dilek, Y. and Altunkaynak, S., 2009. Geochemical and temporal evolution of Cenozoic magmatism in western Turkey: mantle response to collision, slab break-off, and lithospheric tearing in an orogenic belt. In: van Hinsbergen, D.J.J., Edwards, M.A. and Govers, R. (eds). Collision and collapse at the Africa-Arabia-Eurasia subduction zone. The Geological Society, London, Special Publications, 311, 213-233.

Di Paola, G.M., 1974. Volcanology and petrology of Nisyros island (Dodecanese, Greece). Bulletin Volcanologique, 38, 944-987.

Dominguez, G., Wilkins, G. and Thiemens, M.H., 2011. The Soret effect and isotopic fractionation in high-temperature silicate melts. Nature 473, 70-73.

Dorais, M. J. and Shriner, C. M., 2002. A comparative electron microprobe study of 'Aeginetan' wares with potential raw material sources from Aegina, Methana and Poros, Greece. Geoarchaeology: An International Journal, 17, 555-577.

Dotsika, E., Poutoukis, D., Michelot, J.L. and Raco, B., 2009. Natural tracers for identifying the origin of the thermal fluids emerging along the Aegean volcanic arc (Greece): Evidence of arc-type magmatic water (ATMW) participation. Journal of Volcanology and Geothermal Research, 179, 19-32.

Dotsika, E., Poutoukis, D. and Raco, B., 2010. Fluid geochemistry of the Methana peninsula and Loutraki geothermal area, Greece. Journal of Volcanology and Geothermal Research, 104, 97-104.

Druitt, T.H., Edwards, L., Mellors, R.M., Pyle, D.M., Sparks, R.S.J., Lanphere, M., Davies, M. and Barriero, B., 1999. Santorini Volcano. Geological Society Memoir no. 19., 165p.

Eeckhout, S. 2012. Petrografische studie van de Kokkinovrahos daciet (Aegina, Griekenland). Stageverslag van het project ter beëindiging van de bacheloropleiding.

Efstathiou, A., Tzanis, A., Chailas, S., Lagios, E. and Stamatakis, M., 2012. Imaging of the Methana volcanic complex, Greece, with magnetotelluric and aeromagnetic data. Poster presented at the EGU General Assembly, Vienna, Austria, 22-28 April.

Efstathiou, A., Tzanis, A., Chailas, S. and Stamatakis, M., 2013. Deep structure and magmatic activity at the NW Hellenic volcanic arc with 3D aeromagnetic inversion and seismotectonic analysis. Oral presentation at the EGU General Assembly, Vienna, Austria, 7-12 April.

Eichelberger, J.C., 1995. Silicic volcanism: ascent of viscous magmas from crustal reservoirs. Annual Review of Earth and Planetary Sciences, 23, 41-63.

Eichelberger, J.C., Chertkoff, D.G., Dreher, S.T. and Nye, C.J., 2000. Magmas in collision: rethinking chemical zonation in silicic magmas. Geology, 28, 603-606.

Elburg, M., 1996. Evidence of isotopic equilibration between microgranitoid enclaves and host granodiorite, Warburton granodiorite, Lachlan fold belt, Australia. Lithos 38, 1-22.

Elburg, M., Vroon, P., van der Wagt, B. and Tchalikian, A., 2005. Sr and Pb isotopic composition of five USGS glasses (BHVO-2G, BIR-1G, BCR-2G, TB-1G, NKT-1G). Chemical Geology, 223, 169-207

Elburg, M. A. and Kamenetsky, V. S., 2007. Dehydration processes determine fO_2 of arc and intraplate magmas. Geochimica et Cosmochimica Acta, 71, A252.

Elburg, M.A., Kamenetsky, V.S, Foden, J.D and Sobolev, A., 2007. The origin of medium-K ankaramitic arc magmas from Lombok (Sunda arc, Indonesia): Mineral and melt inclusion evidence. Chemical geology, 240, 260-279.

Elburg, M., 2010. Sources and processes in arc magmatism: the crucial role of water. Geologica Belgica, 13, 3, 119-134.

Elburg, M., Smet, I. and De Pelsmaeker, E., 2013. Influence of source materials and fractionating assemblage on magmatism along the Aegean Arc, and implications for crustal growth. In: Gómez-Tuena, A., Straub, S. M. and Zellmer, G. F. (eds). Orogenic andesites and crustal growth. Geological Society, London, Special Publications, 385, doi:10.1144/SP385.1

Faccenna, C., Bellier, O., Martinod, J., Piromallo, C. and Regard, V., 2006. Slab detachment beneath eastern Anatolia: A possible cause for the formation of the North Anatolian fault. Earth and Planetary Science Letters, 242, 85-97.

Faccenna, C. and Becker, W., 2010. Shaping mobile belts by small-scale convection. Nature, 465, 602-605.

Feeley, T.C. and Dungan, M.A., 1996. Compositional and dynamic controls on mafic-silicic magma interactions at continental arc volcanoes: Evidence from Cordón El Guadal, Tatara – San Pedro complex, Chile. Journal of Petrology, 37, 1547-1577.

Feeley, T.C., Wilson, L.F. and Underwood, S.J., 2008. Distribution and compositions of magmatic inclusions in the Mount Helen dome, Lassen Volcanic Center, California: Insights into magma chamber processes. Lithos 106, 173-189.

Fisher, R. V. and Schmincke, H.-U., 1984. Pyroclastic rocks. Springer-Verlag, Berlin, Heidelberg, 472 p.

Francalanci, L., Vougioukalakis, G.E., Perini, G. and Manetti, P., 2005. A west-east traverse along the magmatism of the South Aegean volcanic arc in the light of volcanological, chemical and isotope data. In: Fytikas, M. and Vougioukalakis, G.E. (eds) The South Aegean active volcanic arc. Present knowledge and future perspectives. Elsevier B.V. Developments in volcanology, 7, 65-111.

Francalanci, L., Vougioukalakis, G.E. and Fytikas, M., 2007. Petrology and volcanology of Kimolos and Polyegos volcanoes within the context of the South Aegean arc, Greece. Geological Society of America Special Papers, 418, 33-65.

Francalanci, L., Avanzinelli, R., Nardini, I., Tiepolo, M., Davidson, J.P. and Vannucci, R., 2012. Crystal recycling in the steady-state system of the active Stromboli volcano: a 2.5-ka story inferred from in situ Sr-isotope and trace element data. Contributions to Mineralogy and Petrology, 163, 109-131.

Fytikas, M., Innocenti, F., and Mazzuoli, R. 1972. Geologic map of Greece: Methana Sheet, 1:50,000. Institute of Geology and Mineral Exploration, Athens.

Fytikas, M., Giuliani, O., Innocenti, F., Marinelli, G. and Mazzuoli, R., 1976. Geochronological data on recent magmatism of the Aegean Sea. Tectonophysics, 31, T29-T34.

Fytikas, M., Innocenti, F., Manetti, P., Mazzuoli, R., Peccerillo, A. and Villari, L., 1984. Tertiary to Quarternary evolution of volcanism in the Aegean region. Geological Society, London, Special Publications, 17, 697-699.

Fytikas, M., Innocenti, F., Kolios, N., Manetti, P., Mazzuoli, R., Poli, G., Rita, F. and Villari, L., 1986. Volcanology and petrology of volcanic products from the island of Milos and neighbouring islets. Journal of Volcanology and Geothermal Research, 28, 297-317.

Fytikas, M. Innocenti, F., Kolios, N., Manetti, P. and Mazzuoli, R., 1987. The Plio-Quarternary volcanism of Saronikos area (western part of the active Aegean volcanic arc). Annales Géologiques des Pays Helleniques, 33, 3-45.

Garçon, M., Chauvel, C., France-Lanord, C., Huyghe, P. and Lavé, J., 2013. Continental sedimentary processes decouple Nd and Hf isotopes. Geochimica et Cosmochimica Acta, 121, 177-195.

Gaitanakis, P., 1984. Geological Map of Greece – 1:50000, Megara Sheet and Piraeus Sheet. Institute of Geology and Mineral Exploration, Athens.

Gaitanakis, P. and Dietrich, V., 1995. Geological Map of Methana Peninsula 1:25000. Stiftung Vulkaninstitut Emmanuel Friedländer, ETH, Zurich.

Geological Society of America, 2012.GSA Geological Timescale 2012 [pdf] Available at: <http://www.geosociety.org/science/timescale/> [Accessed 18 April 2013].

GeoReM: http://georem.mpch-mainz.gwdg.de. Accessed in 2013.
Jochum, K. P., Nohl, U., Herwig, K., Lammel, E., Stoll, B. and Hofmann, A. W., 2006. GeoReM: A New Geochemical Database for Reference Materials and Isotopic Standards. Geostandards and geoanalytical Research, 29, 333-338.

GERM (Geochemical Earth Reference Model) distribution coefficient database: http://earthref.org/KDD/

Gertisser, R. and Keller, J. 2003. Trace element and Sr, Nd, Pb and O isotope variations in medium-K and high-K volcanic rocks from Merapi volcano, Central Java, Indonesia: Evidence for the involvement of subducted sediments in Sunda Arc magma genesis. Journal of Petrology, 44, 457-489.

Gertisser, R., Preece, K., and Keller, J., 2009. The Plinian lower pumice 2 eruption, Santorini, Greece: Magma evolution and volatile behaviour. Journal of Volcanology and Geothermal Research. 186, 387-406.

Gill, J., 1981. Orogenic andesites and plate tectonics. Springer-Verlag, Berlin-Heidelberg-New York, 390 p.

Govers, R. and Wortel, M.J.R. 2005. Lithopshere tearing at STEP faults: Response to edges of subduction zones. Earth and Planetary Science Letters, 236, 505-523.

Grasset, O. and Albarède, F., 1994. Hybridisation of mingling magmas with different densities. Earth and Planetary Science Letters 121, 327-332.

Gromet, L.P. and Silver, L.T., 1983. Rare earth element distributions among minerals in a granodiorite and their petrogenetic implications. Geochimica et Cosmochimica Acta, 47, 925-939.

Gronvold, K., Halldorsson, S.A., Oskarsson, N, Sigurdsson, G. and Sverrisdottir, G., 2007. Isotope-heterogeneity of the monogenetic Thjorsa lava eruption, Iceland - source and crustal influence. American Geophysical Union, Fall Meeting 2007, abstract #V33B-1396

Groppelli, G. and Viereck-Goette, L. (eds), 2010. Stratigraphy and geology of volcanic areas. The Geological Society of America, Inc., Special Paper 464, 291 p.

Gülen, L., 1990. Isotopic characterization of Aegean magmatism and geodynamic evolution of the Aegean subduction, in: Proceedings of International Earth Sciences Congress on Aegean Regions, Savaşçın, M.Y. and Eronat, A.H. (eds), 2, 143–166.

Hanchar, J.M. and Watson, E.B., 2003. Zircon Saturation Thermometry. In: Hanchar, J.M. and Hoskin, P.W.O. (Eds). Zircon. Reviews in Mineralogy and Geochemistry, 53, Mineralogical Society of America, Washington D.C., 89-112.

Hart, S. R., 1984. A large-scale isotopic anomaly in the Southern Hemisphere mantle. Nature, 309, 753-757.

Hermann, J. and Green, D. H., 2001. Experimental constraints on high pressure melting in subducted crust. Earth and Planetary Science Letters, 188, 149-168.

Hermann, J., Spandler, C., Hack, A. and Korsakov, A.V., 2006. Aqueous fluids and hydrous melts in high-pressure and ultra-high pressure rocks: Implications for element transfer in subduction zones. Lithos, 92, 399-417.

Hermann, J. and Rubatto, D., 2009. Accessory phase control on the trace element signature of sediment melts in subduction zones. Chemical Geology, 265, 512-526.

Hoffman, A.W., 2003. Sampling mantle heterogeneity through Oceanic Basalts: Isotopes and trace elements. In: Holland, H.D and Turekian, K.K. (eds) Treatise on Geochemistry: The mantle and core. Elsevier, Oxford, 61-101.

Holden, P., Halliday, A.N., Stephens, W.E. and Henney, P.J., 1991. Chemical and isotopic evidence for major mass transfer between mafic enclaves and felsic magma. Chemical Geology, 92, 135-152.

Holness, M.B., Martin, V.M. and Pyle, D.M., 2005. Information about open-system magma chambers derived from textures in magmatic enclaves: the Kameni islands, Santorini, Greece. Geological Magazine, 142, 637-649.

Holness, M.B. and Bunbury, J.M., 2006. Insights into continental rift-related magma chambers: Cognate nodules from the Kula Volcanic Province, Western Turkey. Journal of Volcanology and Geothermal Research, 153, 241-261.

Houghton, B.F., Wilson, C.J.N. and pyle, D.M., 2000. Pyroclastic fall deposits. In: Siggurdsson, H., Houghton, B., McNutt, S.R., Rymer, H. and Stix, J. (eds), Encyclopedia of volcanoes. Academic Press, 555-570.

Huber, C., Bachmann, O. and Dufek, J., 2010. The limitations of melting on the reactivation of silicic mushes. Journal of Volcanology and Geothermal Research, 195, 97-105.

Huber, C., Bachmann, O. and Dufek, J., 2011. Thermo-mechanical reactivation of locked crystal mushes: Melting-induced internal fracturing and assimilation processes in magmas. Earth and Planetary Science Letters, 304, 443-454.

Hübner, A., Rahders, E., Rahner, S., Halbech, P. and Varnavas, S.P., 2004. Geochemistry of hydrothermally influenced sediments off Methana (western Hellenic volcanic arc). Chemie der Erde, 64, 75-94.

Innocenti, F., Manetti, P., Peccerillo, A. and Poli, G., 1981. South Aegean volcanic arc: geochemical variations and geotectonic implications, Bulletin Volcanologique, 44, 3, 377-391.

John, T., Klemd, R., Klemme, S., Pfänder, J.A., Hoffman, J.E. and Gao, J., 2011. Nb-Ta fractionation by partial melting at the titanite-rutile transition. Contributions to Mineralogy and Petrology, 161, 35-45.

Jolivet, L. and Brun, J-P., 2010. Cenozoic geodynamic evolution of the Aegean. International Journal of Earth Sciences, 99, 109-138.Karagianni, E.E., Papazachos, C.B., Panagiotopoulos, D.G., Suhadolc, P., Vuan, A. and Panza, G.F., 2005. Shear velocity structure in the Aegean area obtained by inversion of Rayleigh waves. Geophysical Journal International, 160, 127-143.

Jerram, D.A. and Martin, V.M., 2008. Understanding crystal populations and their significance through the magma plumbing system. In: Annen, C.and Zellmer, G. F. (eds) Dynamics of crustal magma transfer, storage and differentiation. Geological Society, London, Special Publications 304, 133-148.

Juteau, M., Michard, A. and Albarède, F., 1986. Pb-Sr-Nd isotope geochemistry of some recent circum-Mediterranean granites. Contributions to Mineralogy and Petrology, 92, 331-340.

Karagianni, E.E., Papazachos, C.B., Panagiotopoulos, D.G., Suhadolc, P., Vuan, A. and Panza, G.F., 2005. Shear velocity structure in the Aegean area obtained by inversion of Rayleigh waves. Geophysical Journal International, 160, 127-143.

Kassaras, I., Makropoulos, K., Bourova, E., Pedersen, H. and Hatzfeld, D. 2005. Upper mantle structure of the Aegean derived from two-station phase velocities of fundamental mode Rayleigh waves. In: Fytikas, M. and Vougioukalakis, G. E. (eds) The South Aegean active volcanic arc. Present knowledge and future perspectives. Elsevier.

Kelemen, P.B., Hanghoi, K., and Greene, A.R., 2003. One view of the geochemistry of subduction-related magmatic arcs, with an emphasis on primitive andesite and lower crust. In: Holland, H. and Turekian, K. (eds.) Treatise on Geochemistry: The Crust. Elsevier, Oxford, 593-659.

Kempton, P.D., Downes, H. and Embey-Isztin, A., 1997. Mafic granulite xenoliths in the Neogene alkali basalts from the Western Pannonian Basin: insights into the lower crust of a collapsed orogen. Journal of Petrology, 38, 941-970.

Kersting, A. B., Arculus, R. J. and Gust, D. A., 1996. Lithospheric contributions to arc magmatism: isotope variations along strike in volcanoes of Honshu, Japan. Science, 272, 1464-1468.

Kessel, R., Schmidt, M.W., Ulmer, P. and Pettke, T., 2005. Trace element signature of subduction-zone fluids, melts and supercritical liquids at 120-180 km depth. Nature, 437, 724-727.

Kocak, K., Zedef, V. and Kansum, G., 2011. Magma mixing/mingling in the Eocene Horoz (Nigde) granitoids, Central southern Turkey: evidence from mafic microgranular enclaves. Mineralogy and Petrology 103, 149-167.

Kodolányi, J., 2009. The geochemistry of ocean floor serpentinites and their high pressure metamorphic equivalents. Unpublished PhD thesis, University of Bern.

Kodolányi, J., Pettke, T., Spandler, C., Kamber, B. and Gméling, K., 2012. Geochemistry of ocean floor and fore-arc serpentinites: Constraints on the ultramafic input to subduction zones. Journal of Petrology, 53, 235-270.

Larrea, P., França, Z., Lago, M., Widom, E., Galé, C. and Ubide, T., 2013. Magmatic processes and the role of antecrysts in the genesis of Corvo island (Azores archipelago, Portugal). Journal of Petrology, 54, 769-793.

Langmuir, C.H., Vocke, R.D., Hanson, G.N. and Hart, S.R., 1978. A general mixing equation with application to Icelandic basalts. Earth and Planetary Science Letters 37, 380-392.

Le Maitre, R. W. (Editor), Streckeisen, A., Zanettin, B., Le Bas, M. J., Bonin, B., Bateman, P., Bellieni, G., Dudek, A., Efremova, S., Keller, J., Lameyre, J., Sabine, P. A., Schmidt, R., Sørensen, H., and Wooley, A. R., 2002. Igneous rocks: A classification and glossary of terms: recommendations of the International Union of Geological Sciences, Subcommission on the systematic of igneous rocks. Cambridge University Press, Cambridge, 236 p.

Makris, J., Papoulia, J. and Drakatos, G., 2004. Tectonic deformation and micro-seismicity of the Saronikos Gulf, Greece. Bulletin of the Seismological Society of America, 94, 920-929.

Manning, C.E., 2004. The chemistry of subduction-zone fluids. Earth and Planetary Science Letters, 223, 1-16.

Marschall, H.R., Dohmen, R. and Ludwig, T., 2013. Diffusion-induced fractionation of niobium and tantalum during continental crust formation. Earth and Planetary Science Letters, 375, 361-371.

Martin, V.M., Holness, M.B. and Pyle, D.M., 2006a. Textural analysis of magmatic enclaves from the Kameni Islands, Santorini, Greece. Journal of Volcanology and Geothermal Research 154, 89-102.

Martin, V.M., Pyle, D.M. and Holness, M.B., 2006b. The role of crystal frameworks in the preservation of enclaves during magma mixing. Earth and Planetary Science Letters 248, 787-799.

Matsuda, J.-I., Senoh, K., Maruoka, T., Sato, H. and Mitropoulos, P., 1999. K-Ar ages of the Aegean volcanic rocks and their implications for the arc-trench system. Geochemical Journal, 33, 369-377.

McDonough, W.F. and Sun, S.-S., 1995. Composition of the Earth. Chemical Geology, 120, 223-253. doi: 10.1016/0009-2541(94)00140-4.

Míkóva, J. and Denkóva, P., 2007. Modified chromatographic separation scheme for Sr and Nd isotope analysis in geological samples. Journal of Geosciences, 52, 221-226.

Mitropoulos, P., 1987. Primary allanite in andesitic rocks from the Poros volcano, Greece. Mineralogical Magazine, 51, 601-604.

Mitropoulos, P., Tarney, J., Saunders, A.D. and Marsh; N.G., 1987. Petrogenesis of Cenozoic volcanic rocks from the Aegean island arc. Journal of Volcanology and Geothermal Research, 32, 177-193.

Mitropoulos, P. and Tarney, J., 1992. Significance of mineral composition variations in the Aegean island arc. Journal of Volcanology and Geothermal Research, 51, 283-303.

Moore, G. and Carmichael, I.S.E., 1998. The hydrous phase equilibria (to 3kbar) of an andesite and basaltic andesite from western Mexico: constraints on water content and conditions of phenocryst growth. Contributions to Mineralogy and Petrology, 130, 304-319.

Mortazavi, M. and Sparks, R.S.J., 2004. Origin of rhyolite and rhyodacite lavas and associated mafic inclusions of Cape Akrotiri, Santorini: the role of wet basalt in generating calcalkaline silicic magmas. Contributions to Mineralogy and Petrology, 146, 397-413.

Murphy, M.D., Sparks, R.S.J., Barclay, J., Carroll, M.R. and Brewer, T.S., 2000. Remobilisation of andesite magmas by intrusion of mafic magma at the Soufrière Hills Volcano, Montserrat, West Indies. Journal of Petrology, 41, 21-42.

Müller, P., Kreuzer, H., Lenz, H. and Harre, W., 1979. Radiometric dating of two extrusives from a Lower Pliocene marine section on Aegina Island, Greece. Newsletters on Stratigraphy, 8, 70–78.

Münker, C., Weyer, S., Scherer, E. and Mezger, K., 2001. Separation of high field strength elements (Nb, Ta, Zr, Hf) and Lu from rock samples for MC-ICPMS measurements. Geochemistry Geophysics Geosystems G³, 2, DOI:10.1029/2001GC000183.

Nebel, O., Morel, M.L.A. and Vroon, P.Z., 2009. Isotope dilution determinations of Lu, Hf, Zr, Ta and W, and Hf isotope compositions of NIST SRM 610 and 612 glass wafers. Geostandards and Geoanalytical Research, 33, 4, 487-499.

Nehring, F., Foley, S.F. and Hölttä, P., 2010. Trace element partitioning in the granulite facies. Contributions to Mineralogy and Petrology, 159, 493-519.

Nesse, W. D., 2004. Introduction to optical mineralogy. Third edition. Oxford University Press, New York, 348 p.

Neumann, H., Mead, J. and Vitaliano, C. J., 1954. Trace element variation during fractional crystallisation as calculated from the distribution law. Geochimica et Cosmochimica Acta, 6, 90-99.

Nixon, G.T., 1988. Petrology of the younger andesites and dacites of Iztaccíhuatl Volcano, Mexico: I. Disequilibrium phenocryst assemblages as indicators of magma chamber processes. Journal of Petrology, 29, 2, 213-264.

Nomikou, P., Papanikolaou, D., Alexandri, M., Sakellariou, D. and Rousakis, G., 2013. Submarine volcanoes along the Aegean volcanic arc.

Orihashi, Y., Maeda, J., Tanaka, R., Zeniya, R. and Niida, K., 1998. Sr and Nd isotopic data for seven GSJ rock reference materials; JA-1, JB-1a, JB-2, JB-3, JG-1a, JGb-1 and JR-1. Geochemical Journal, 32, 205-211.

Othman, D. B., White, W. M. and Patchett, J., 1989. The geochemistry of marine sediments, island arc magma genesis, and crust-mantle recycling. Earth and Planetary Science Letters, 94, 1-21.

Papazachos, B.C. and Panagiotopoulos, D.G., 1993. Normal faults associated with volcanic activity and deep rupture zones in the southern Aegean volcanic arc. Tectonophysics, 220, 301-308.

Papazachos, C. B., Hatzidimitriou, P. M., Panagiotopoulos, D. G. and Tsokas, G. N., 1995. Tomography of the crust and upper mantle in southeast Europe. Journal of Geophysical Research, 100, 12405-12422.

Papazachos, C. and Nolet, G., 1997. P and S deep velocity structure of the Hellenic area obtained by robust nonlinear inversion of travel times. Journal of Geophysical Research, 102, 8349-8367.

Papazachos, B.C., Karakostas, V.G., Papazachos, C.B. and Scordilis, E.M., 2000. The geometry of the Wadati-Benioff zone and the lithospheric kinematics in the Hellenic arc. Tectonophysics, 319, 275-300.

Paraskevopoulos, G. M., 1958. Geochemistry and regional relationship of Tertiary and Quaternary igneous rocks from the Aegean region and adjacent areas. Tschermaks Mineralogische und Petrographische Mitteilungen,6, 13–72.

Pavlakis, P., Lykoussis, V., Papanikolaou, D. and Chronis, G., 1990. Discovery of a new submarine volcano in the western Saronic Gulf: The Pausanias volcano. Bulletin of the geological Society of Greece, 24, 59-70.

Pearce, J. A. 1982. Trace element characteristics of lavas from destructive plate boundaries. In: Thorpe, R.S. (ed.) Orogenic andesites and related rocks. John Wiley and Sons, Chichester, England, 528-548.

Peccerillo, A., 2005. Plio-Quaternary volcanism in Italy. Petrology, geochemistry, geodynamics. Springer-Verlag, Berlin Heidelberg, 365p.

Pe, G.G., 1971. Geochemistry of some Aegean lavas. Unpublished PhD thesis, Cambridge University.

Pe, G.G., 1972. Geochemistry and chemical mineralogy of the lavas of Crommyonia. Annales Géologiques des Pays Helléniques, 24, 257-275.

Pe, G.G., 1973. Petrology and geochemistry of volcanic rocks of Aegina, Greece. Bulletin Volcanologique, 37, 491-514.

Pe, G.G., 1974. Volcanic rocks of Methana, South Aegean arc, Greece. Bulletin Volcanologique, 38, 270-290.

Pe, G.G., 1975. Strontium isotope ratios in volcanic rocks from the northwestern part of the Hellenic arc. Chemical Geology, 15, 53-60.

Pe-Piper, G., 1994. Lead isotopic compositions of Neogene volcanic rocks from the Aegean extensional area. Chemical Geology, 118, 27-41.

Pe-Piper, G., Piper, D.J.W. and Reynolds, P.H., 1983. Paleomagnetic stratigraphy and radiometric dating of the Pliocene volcanic rocks of Aegina, Greece. Bulletin Volcanologique, 46, 1-7.

Pe-Piper, G. and Hatzipanagiotou, K., 1997. The Pliocene volcanic rocks of Crommyonia, western Greece and their implications for the early evolution of the South Aegean arc. Geological Magazine, 134, 55-66.

Pe-Piper, G. and Piper, D.J.W., 2001. Late Cenozoic, post-collisional Aegean igneous rocks: Nd, Pb and Sr isotopic constraints on petrogenetic and tectonic models. Geological Magazine, 138, 653-668.

Pe-Piper, G. and Piper, D.J.W., 2002. The South Aegean arc. In: Pe-Piper, G. and Piper, D.J.W. The igneous rocks of Greece. The anatomy of an orogen. Gebrüder Borntraeger, Berlin – Sturtgart, 393-437.

Pe-Piper, G. and Piper, D.J.W., 2005. The South Aegean active volcanic arc: relationships between magmatism and tectonics. In: Fytikas M and Vougioukalakis GE (eds). The South Aegean active volcanic arc. Present knowledge and future perspectives. Elsevier B.V. Developments in volcanology, 7, 113-133.

Pe-Piper, G. and Piper, D.J.W., 2006. Unique features of the Cenozoic igneous rocks of Greece. In: Dilek, Y. and Pavlides, S., eds., Postcollisional tectonics and magmatism in the Mediterranean region and Asia: Geological Society of America Special Paper 409, 259-282.

Pe-Piper, G. and Moulton, B., 2008. Magma evolution in the Pliocene-Pleistocene succession of Kos, South Aegean arc (Greece). Lithos, 106, 110-124.

Pe-Piper, G. and Piper, D.J.W., 2013. The effect of changing regional tectonics on an arc volcano: Methana, Greece. Journal of Volcanology and Geothermal Research, 260, 146-163.

Perugini, D., Poli, G. and Mazzuoli, R., 2003. Chaotic advection, fractals and diffusion during mixing of magmas: evidence from lava flows. Journal of Volcanological and Geothermal Research 124, 255-279.

Perugini, D. and Poli, G., 2012. The mixing of magmas in plutonic and volcanic environments: Analogies and differences. Lithos, doi: 10.1016/j.lithos.2012.02.002

Pichler, H. and Schiering, H., 1977. The Thera eruption and the Late Minoan-IB destructions on Crete. Nature, 267, 819-822.

Pin, C. and Zalduegui, J. F. S., 1997. Sequential separation of light rare-earth elements, thorium and uranium by miniaturized extraction chromatography: Application to isotopic analyses of silicate rocks. Analytica Chemica Acta, 339, 79-89.

Piper, D.J.W. and Perissoratis, C., 2003. Quaternary neotectonics of the South Aegean arc. Marine Geology, 198,259-288.

Pistone, M., Caricchi, L., Ulmer, P., Reusser, E. and Ardia, P., 2013. Rheology of volatile-bearing crystal mushes: Mobilization vs. viscous death. Chemical Geology, 345, 16-39.

Plank, T. and Langmuir, C.H., 1998 The chemical composition of subducting sediment and its consequence for the crust and mantle. Chemical Geology, 145, 325-394.

Raczek, I., Jochum, K.P.and Hofmann, A. W., 2003. Neodymium and strontium isotope data for USGS reference materials BCR-1, BCR-2, BHVO-1, BHVO-2, AGV-1, AGV-2, GSP-2 and eight MPI-DING reference glasses. Geostandards Newsletter, 27, 173-179.

Rapp, R.P. and Watson, E.B., 1995. Dehydration melting of metabasalt at 8-32 kbar: implications for continental growth and crust-mantle recycling. Journal of Petrology, 36, 4, 891-931.

Rehkamper, M. and Hofmann, A.W., 1997. Recycled ocean crust and sediment in Indian Ocean MORB. Earth and Planetary Science Letters, 147, 93-106.

Reiss, W., Stübel, A. and Fritsch, Freiherr von, K.W.G., 1867. Ausflug nach den vulkanischen Gebirgen von Aegina und Methana im Jahre 1866. Heidelberg, 1867, 84p.

Ridolfi, F., Puerini, M., Renzulli, A., Menna, M. and Toulkeridis, T., 2008. The magmatic feeding system of El Reventador volcano (Sub-Andean zone, Ecuador) constrained by texture, mineralogy and thermobarometry of the 2002 erupted products. Journal of Volcanology and Geothermal Research, 176, 94-106.

Ridolfi, F., Renzulli, A. and Puerini, M., 2010. Stability and chemical equilibrium of amphibole in calc-alkaline magmas: an overview, new thermobarometric formulations and application to subduction-related volcanoes. Contributions to Mineralogy and Petrology, 160, 45-66.

Rinaldi, M. and Venuti, M.C., 2003. The submarine eruption of the Bombarda volcano, Milos island, Cyclades, Greece. Bulletin of Vulcanology, 65, 282-293.

Robert, U., Foden, J. and Varne, R., 1992. The Dodecanese Province, SE Aegean: A model for tectonic control on potassic magmatism. Lithos, 28, 241-260.

Rose, W.I., Jr., Pearson, T. and Bonis, S., 1977. Nuee ardente eruption from the foot of a dacite lava flow, Santiaguito Volcano, Guatemala. Bulletin of Volcanology, 40, 1-16.

Robertson, A.H.F., Trivic, B., Deric, N. and Bucur, I I., 2012. Tectonic development of the Vardar ocean and its margins: Evidence from the Republic of Macedonia and Greek Macedonia. Tectonophysics, http://dx.doi.org/10.1016/j.tecto.2012.07.022.

Rosman, K.J.R. and Taylor, P.D.P., 1998. Isotopic compositions of the elements 1997. IUPAC technical report. Pure and Applied Chemistry, 70, 1, 217-235.

Rudnick, R.L., 1995. Making continental crust. Nature, 378, 571-578.

Russell, W.A., Papanastassiou, D.A. and Tombrello, T.A., 1978. Ca isotope fractionation on earth and in other solar-system materials. Geochimica et Cosmochimica acta, 42, 1075-1090.

Rutherford, M.J. and Hill, P.M., 1993. Magma ascent rates from amphibole breakdown: an experimental study applied to the 1980-1986 Mount St.Helens eruptions. Journal of Geophysical Research, 98, B11, 19667-19685.

Sachpazi, M., galvé, A., Laigle, M., Hirn, A., Sokos, E., Serpetsidaki, A., Marthelot, J.-M., Pi Alperin, J.M., Zelt, B. and Taylor, B., 2007. Moho topography under central Greece and its compensation by Pn time-terms for the accurate location of hypocenters: The example of the Gulf of Corinth 1995 Aigion earthquake. Tectonophysics, 440, 53-65.

Salters, V.J.M. and Stracke, A., 2004. Composition of the depleted mantle. Geochemistry Geophysics Geosystems 5, doi: 10.1029/2003GC000597.

Schmid, R., 1981. Descriptive nomenclature and classification of pyroclastic deposits and fragments: Recommendations of the IUGS Subcommission on the Systematics of Igneous Rocks. Geology, 9, 41-43.

Schmincke, H.-U., 2006. Volcanism. Springer-Verlag, Berlin Heidelberg, 1st ed. 2004. Corr. 2nd printing, 324p.

Schwandner, F.M., 1998. Polyphase meso- to cenozoic structural development of Poros island (Greece). Bulletin of the Geological Society of Greece, 32, 129-136.

Sha, L.K., 2012. Concurrent fractional and equilibrium crystallisation. Geochimica et Cosmochimica Acta 86, 52-75.

Shaw, D., 1970. Trace element fractionation during anatexis. Geochimica et Cosmochimica Acta, 34, 237-243.

Shimizu, A., Sumino, H., Nagao, K., Notsu, K and Mitropoulos, P., 2005. Variation in noble gas isotopic composition of gas samples from the Aegean arc, Greece. Journal of Volcanology and Geothermal Research, 140, 321-339.

Siggurdsson, H., Houghton, B., McNutt, S.R., Rymer, H. and Stix, J., 2000. Encyclopedia of volcanoes. Academic Press, 1417p.

Sisson, T. W., 1994. Hornblende-melt trace-element partitioning measured by ion microprobe. Chemical Geology, 117, 331-344.

Sisson, T.W. and Bacon, C.R., 1999. Gas-driven filter pressing in magmas. Geology, 27, 613-616.

Smet, I., De Muynck, D., Vanhaecke, F. and Elburg, M., 2010. From volcanic rock powder to Sr and Pb isotope ratios: a fit-for-purpose procedure for multi-collector ICP-mass spectrometric analysis. Journal of Analytical Atomic Spectrometry, 25, 7, 1025-1032.

Smith, D.J., Petterson, M.G., Saunders, A.D., Millar, I.L., Jenkin, G.R.T., Toba, T., Naden, J. and Cook, J.M., 2009. The petrogenesis of sodic island arc magmas at Savo volcano, Solomon Islands. Contributions to Mineralogy and Petrology, 158, 785-801.

Snyder, D., 2000. Thermal effects of the intrusion of basaltic magma into a more silicic magma chamber and implications for eruption triggering. Earth and Planetary Science Letters, 175, 257-273.

Sodoudi, F., Kind, R., Hatzfeld, D., Priestley, K., Hanka, W., Wylegalla, K., Stavrakakis, G., Vafidis, A., harjes, H.-P. and Bohnhoff, M., 2006. Lithospheric structure of the Aegean obtained from P and S receiver functions. Journal of Geophysical Research, 111, B12307, doi:10.1029/2005JB003932.

Spandler, C., Martin, L.H.J. and Pettke, T., 2012. Carbonate assimilation during magma evolution at Nisyros (Greece), South Aegean Arc: Evidence from clinopyroxenite xenoliths. Lithos, 146-147, 18-33.

Spandler, C. and Pirard, C., 2013. Element recycling from subducting slabs to arc crust: A review. Lithos, 170-171, 208-223.

Sparks, R.S.J., Sigurdsson, H. and Wilson, L., 1977. Magma mixing: a mechanism for triggering acid explosive eruptions. Nature, 267, 315-318.

Sparks, R.S.J., 1985. Archaeomagnetism, Santorini volcanic eruptions and fired destruction levels on Crete. Nature, 313, 74-76

Sparks, R.S.J., 1997. Causes and consequences of pressurisation in lava dome eruptions. Earth and Planetary Science Letters, 150, 177-189.

Stacey, J.S. and Kramers, J.D., 1975. Approximation of terrestrial lead isotope evolution by a two-stage model. Earth and Planetary Science Letters, 26, 207-221.

Stepanov, A.S and Hermann, J, 2013. Fractionation of Nb and Ta by biotite and phengite: Implications for the “missing Nb paradox”. Geology, 41, 303-306.

St. Seymour, K., 1996. The Kakoperato rhyodacite flow, Aegina volcano: a window to the intricacies of a calcalkaline subvolcanic magma chamber. Neues Jahrbuch für Mineralogie – Abhandlungen (Journal of Mineralgy and Geochemistry), 171, 61-89.

Suckale, J., Rondenay, S., Sachpazi, M., Charalampakis, M., Hosa, A. and Royden, L.H., 2009. High-resolution seismic imaging of the western Hellenic subduction zone using teleseismic scattered waves. Geophysical Journal International, 178, 775-791.

Sun, S. and McDonough, W. F., 1989. Chemical and isotopic systematics of oceanic basalts: implications for mantle composition and processes. In: Saunders AD and Norry MJ (eds) Magmatism in the ocean basins. Geological Soc. Special Publ., 42, 313-345.

Tanaka, T., Togashi, S., Kamioka, H., Amakawa, H., Kagami, H., Hamamoto, T., Yuhara, M., Orihashi, Y., Yoneda, S., Shimizu, H., Kunimaru, T., Takahashi, K., Yanagi, T., Nakano, T., Fujimaki, H., Shinjo, R., Asahara, Y., Tanimizu, M. and Dragusanu, C., 2000. JNdi-1: a neodymium isotopic reference in consistency with LaJolla neodymium. Chemical Geology, 168, 279-281.

Tenthorey, E. and Hermann, J., 2004. Composition of fluids during serpentinite breakdown in subduction zones: evidence for limited boron mobility. Geology, 32, 865-868.

Tirel, C., Gueydan, F., Tiberi, C. and Brun, J-P., 2004. Aegean crustal thickness inferred from gravity inversion. Geodynamical implications. Earth and Planetary Science Letters, 228, 267-280.

Turcotte, D.L. and Schubert, G., 2002. Plate Tectonics. In: Geodynamics (2 ed.), Cambridge University Press, pp1–21.

Ubide, T., Arranz, E., Lago, M., Galé, C. and Larrea, P., 2012. The influence of crystal settling on the compositional zoning of a thin lamprophyre sill: A multi-method approach. Lithos, 132-133, 37-49.

Ulmer, P. and Trommsdorff, V., 1995. Serpentine stability to mantle depths and subduction-related magmatism. Science, 268, 858-861.

Ulmer, P., 2001. Partial melting in the mantle wedge – the role of H_2O in the genesis of mantle-derived 'arc-related' magmas. Physics of the Earth and Planetary Interiors, 127, 215-232.

Vaggelli, G., Pellegrini, M., Vougioukalakis, G.E., Innocenti, F. and Francalanci, L., 2009. Highly Sr radiogenic tholeiitic magmas in the latest inter-Plinian activity of Santorini volcano, Greece. Journal of Geophysical Research, B114, doi: 10.1029/2008JB005936.

van der Zwan, F.M., Chadwick, J.P. and Troll, V.R., 2013. Textural history of recent basaltic-andesites and plutonic inclusions from Merapi volcano. Contributions to Mineralogy and Petrology, 166, 43-63.

Van Heghe, L., 2013. The development and evaluation of analytical methods, based on multi-collector – inductively coupled plasma – mass spectrometry (MC-ICP-MS) for high-precision isotopic analyses of Cu, Fe and Zn in human blood, applicable in medical diagnosis. Unpublished PhD thesis, Ghent University.

van Hinsbergen, D.J.J., Snel, E., Garstman, S.A., Marunteanu, M., Langereis, C.G., Wortel, M.J.R. and Meulenkamp, J.E., 2004. Vertical motions in the Aegean volcanic arc: evidence for rapid subsidence preceding volcanic activity on Milos and Aegina. Marine Geology, 209, 329-345.

van Hinsbergen, D.J.J., Hafkenscheid, E., Spakman, W., Meuelenkamp, J.E. and Wortel, R., 2005. Nappe stacking resulting from subduction of oceanic and continental lithosphere below Greece. Geology, 33, no. 4, 325-328.Vernon, R.H., 2004. A practical guide to rock microstructure. Cambridge University Press, 594p.

Vernon, R. H. and Collins, W. J., 2011. Structural criteria for identifying granitic cumulates. Journal of Geology, 119, 127-142.

Vervoort, J.D., Plank, T. and Prytulak, J., 2011. The Hf-Nd isotopic composition of marine sediments. Geochimica et Cosmochimica Acta, 75, 5903-5926.

Viccaro, M., Ferlito, C., Cortesogno, L., Cristofolini, R. and Gaggero, L., 2006. Magma mixing during the 2001 event at Mount Etna (Italy): Effects on eruptive dynamics. Journal of Volcanology and Geothermal Research, 149, 139-159.

Volti, T.K., 1999. Magnetotelluric measurements on the Methana peninsula (Greece): modelling and interpretation. Tectonophysics, 301, 111-132.

von Leyden, R., 1940. Der Vulkanismus des Golfes von Ägina und seine Beziehungen zur Tektonik. Methana – Ägina – Poros. Publikationen herausgegeben von der Stiftung "Vulkaninstitut Immanuel Friedländer", Nr. 1. Guggenbühl and Huber Schweizer-Spiegel-Verlag Zürich, 150p.

Wallace, P. J. and Carmichael, I. S. E., 1999. Quaternary volcanism near the Valley of Mexico: implications for subduction zone magmatism and the effects of crustal thickness variations on primitive magma compositions. Contributions to Mineralogy and Petrology, 135, 291-314.

Walsh, F.N, 1997. Inductively coupled plasma-atomic emission spetrometry. In: Gill, R. (ed), Modern analytical geochemistry: An introduction to quantitative chemical analysis techniques for earth, environmental and material scientists. Harlow, Addison Wesley Longman, 41-66.

Walsh, F.N, Gill, R. and Thirlwall, M.F., 1997. Dissolution procedures for geological and environmental samples. In: Gill, R. (ed), Modern analytical geochemistry: An introduction to quantitative chemical analysis techniques for earth, environmental and material scientists. Harlow, Addison Wesley Longman, 29-40.

Warren, J.M and Shirey, S.B., 2012. Lead and osmium isotopic constraints on the oceanic mantle from single abyssal peridotite sulfides. Earth and Planetary Science Letters, 359-360, 279-293.

Washington, H.S., 1894. A petrographical sketch of Aegina and Methana. Part I. Introduction. The Journal of Geology, 2, 789-813.

Washington, H.S., 1895a. A petrographical sketch of Aegina and Methana. Part II. Petrographical description. The Journal of Geology, 3, 21-46.

Washington, H.S., 1895b. A petrographical sketch of Aegina and Methana. Part III. The Journal of Geology, 3, 138-168. Warren, J. M. and Shirey, S. B., 2012. Lead and osmium isotopic constraints on the oceanic mantle from single abyssal peridotite sulphides. Earth and Planetary Science Letters, 359-360, 279-293.

Weis, D., Kieffer, B., Maerschalk, C., Pretorius, W. and Barling, J., 2005. High-precision Pb-Sr-Nd-Hf isotopic characterisation of USGS BHVO-1 and BHVO-2 reference materials. Geochemistry Geophysics Geosystems, 6, 2, doi:10.1029/2004GC000852.

Weis, D., Kieffer, B., Hanano, D., Nobre Silva, I., Barling, J., Pretorius, W., Maerschalk, C. and Mattielli, N., 2007. Hf isotope compositions of U.S Geological Survey reference materials. Geochemistry Geophysics Geosystems, 8, doi:10.1029/2006GC001473.

Weldeab, S., Emeis, K.-C., Hemleben, C. and Siebel, W., 2002. Provenance of lithogenic surface sediments and pathways of riverine suspended matter in the Eastern Mediterranean Sea: evidence from $^{143}Nd/^{144}Nd$ and $^{87}Sr/^{86}Sr$ ratios. Chemical Geology, 186, 139-149.

Wilcox, R. E., 1999. The idea of magma mixing: History of a struggle for acceptance. The Journal of Geology, 107, 421-432.

Williams, H., Turner, F.J. and Gilbert, C.M., 1954. Petrography. An introduction to the study of rocks in thin sections. W.H. Freeman and Company, San Francisco. 406p.

Woodhead, J.D. and Hergt, J.M., 2000. Pb-isotope analyses of USGS reference materials. Geostandards Newsletter, 24, 33-38.

Workman, R.K. and Hart, S.R., 2005. Major and trace element composition of the depleted MORB mantle (DMM). Earth and Planetary Science Letters, 231, 53-72.

Wright, J.V., Smith, A.L. and Self, S., 1980. A working terminology of pyroclastic deposits. Journal of Volcanology and Geothermal Research, 8, 315-336.

Zellmer, G., Turner, S. and Hawkesworth, C., 2000. Timescales of destructive plate margin magmatism: new insights from Santorini, Aegean volcanic arc. Earth and Planetary Science Letters, 174, 265-281.

Zellmer, G.F. and Turner, S.P., 2007. Arc dacite genesis pathways: Evidence from mafic enclaves and their hosts in Aegean lavas. Lithos 95, 346-362.

Appendix A: Short description and GPS-coordinates of each sampled outcrop

Sampling location	***Sample***	***Rock type***	***Outcrop/sample description***	***GPS-coordinates (WGS-84)***		***Height above sea level (m)***
				N	***E***	
1	DPM4 DPM5	host rock enclave	Massive, somewhat jointed lava flow, partially red oxidised	37°35.581'	23°22.992'	267
2	DPM8 DPM9 DPM10	host rock enclave enclave	3m large lava block; within badly sorted block-and-ash flow deposit	37°35.440'	23°22.862'	216
3	DPM11 DPM12	host rock enclave	Fresh looking blocks of lava within a block-and-ash flow deposit	37°35.923'	23°22.731'	469
4	DPM16	host rock	Jointed and brecciated lava flow	37°35.738'	23°22.693'	443
5	DPM18 DPM19	host rock enclave	Brecciated lava with red-grey flow banding	37°35.580	23°22.670'	397
6	DPM20 DPM22 DPM23	host rock enclave enclave	Two very large lava blocks in badly sorted block-and-ash flow deposit	37°35.369'	23°22.820'	211
7	DPM24 DPM25	enclave host rock	Fresh lava block; in block-and-ash flow deposit	37°35.334'	23°22.720'	219
8	DPM26	host rock	Red-oxidised lava breccia	37°35.209'	23°22.507’	252
9	DPM27	host rock	Lava block in block-and-ash flow deposit	37°35.129'	23°22.342	227
10	DPM28 DPM29A DPM29B	host rock enclave enclave	More fresh-looking lava blocks in red-oxidised block-and-ash flow deposit	37°35.261'	23°22.422'	303
11	DPM30A	host rock	Massive lava; partially red-oxidised	37°35.469'	23°22.436'	343
12	DPM32	enclave	Lava blocks, not in situ, at the top	37°35.347'	23°22.210'	407
13	DPM33	host rock	Red-oxidised lava breccia, in situ	37°35.406'	23°22.193'	418
14	DPM34 DPM35A	host rock enclave	Red-oxidised lava breccia, in situ	37°36.395'	23°23.932'	304
15	DPM36	enclave	Red-oxidised lava breccia, in situ	37°36.407'	23°23.892'	315
16	DPM39 DPM41A DPM41B	host rock enclave enclave	Lava blocks, not in situ at the bottom of the Kossona Vouno lava flow, fresh grey and red-oxidised	37°36.461'	23°24.140'	184
17	DPM42	host rock	Badly weathered scoriaceous lava	37°35.811'	23°23.846'	207
18	DPM45 DPM46	host rock host rock	Lava blocks, fresh grey, from block-and-ash flow deposit	37°35.805'	23°23.785'	224
19	DPM47 DPM49	host rock enclave	Massive, jointed lava; fresh grey	37°36.022'	23°23.751'	184
20	DPM50	host rock	Fresh-looking jointed lava	37°35.314'	23°23.900'	52
21	DPM52 DPM53	host rock enclave	Brecciated lava, fresh grey	37°35.367'	23°24.035'	90
22	DPM54	host rock	Lava in black-and-ash flow deposit	37°35.391'	23°24.024'	86
23	DPM55 DPM56A DPM56B	host rock enclave enclave	Larger blocks of lava, fresh grey, in poorly sorted block-and-ash flow deposits	37°35.454'	23°24.004'	92
24	DPM57 DPM58	host rock host rock	Lava blocks, not in situ, at the bottom of the SW lava flow	37°35.014'	23°22.092'	143
25	DPM61	host rock	Massive, jointed lava	37°35.768'	23°22.220	501
26	DPM63 DPM64	host rock enclave	Large lava block in block-and-ash flow deposit	37°35.836'	23°22.272'	517
27	DPM66 DPM67	host rock enclave	Red- oxidesed brecciated lava With red-grey flow banding	37°35.977'	23°22.426'	601

Sampling location	***Sample***	***Stratigraphic Unit (Pe-Piper & Piper, 2013)***	***Rock type***	***Outcrop/sample description***	***GPS-coordinates (WGS-84)***		***Height above sea level (m)***
					N	***E***	
8-13 ,24	***DPM...***	***Phase A***	***Delta 2***	***'Loutses South' - see Chapter 4 and Appendix A1***			
28	IM317	Phase A	host rock	Badly sorted block and ash flow deposit, autoclastic	37°36.167'	23°19.887'	77
29	IM43	Phase A	host rock	1m lava block, in top of badly sorted block and ash flow deposit	37°36.315'	23°19.842'	101
30	IM42	Phase B	host rock	Badly sorted block and ash flow deposit, with layer of brecciated lava	37°36.613'	23°19.713'	171
31	IM30	Phase B	host rock	Badly sorted block and ash flow deposit	37°37.069'	23°20.198'	299
32	IM18 IM368 IM369 IM389	Phase B	host rock host rock enclave host rock	Badly sorted 'volcaniclastic apron' below phase C pumice deposit: Angular and more rounded lava blocks and scoriaceous lava in fine-grained matrix with also smaller volcanic clasts. Lava blocks are both grey and reddish, porphyritic, contain numerous enclaves	37°34.924'	23°20.877'	18
	IM382 IM283 IM388 *IM386*	Phase C 'Akri Pounda'	light pumice dark pumice banded pumice *xenolith*	Well sorted fallout deposit above volcaniclastic apron phase B: 75-85% white to light grey pumice, mostly 1-6 cm, some up to 20cm; 10% darker grey pumice ; some pumice with bands of the light and Dark colour*; 5-15% lithic clasts from phase B or sedimentary*			
33	IM290 IM291	Phase B	host rock enclave	Massive grey coloured lava flow, porphyritic, with many enclaves (sometimes red oxidised), some flow banding, jointing	37°36.723	23°23.423'	307
34	IM17B	Phase C	pumice	Well sorted, bedded, pumice and tuff fallout deposit (with lithic clasts)	37°34.894'	23°20.845'	33
35	DPM65	Phase C	pumice	Well sorted, stratified fallout deposit of pumice, tuffs and tuffites	37°35.836'	23°22.189'	514
36	IM310	Phase C	host rock	Massive, jointed lava flow with many enclaves	37°37.484'	23°21.855'	359
37	IM9 IM10	Phase C 'Akri Pounda'	host rock host rock	Block and ash flows, sometimes more massive auto (?) brecciated usually red oxidised lava, some fresher grey blocks	37°34.911'	23°21.318'	86
38	IM13 IM359 IM364 *IM362* *IM363*	Phase C 'Akri Pounda'	host rock host rock host rock *xenolith* *xenolith*	Black and red pyroclastic deposits of badly sorted block and ash and scoria and ash flows *Within the black, scoriaceous block and lapilli flow some sedimentary* *xenoliths were present*	37°34.795'	23°21.447'	17
39	IM23	Phase C	host rock	Badly weathered block and ash flow deposits	37°35.172'	23°21.381'	96
40	IM24	Phase C	host rock	Badly weathered block and ash flow deposits	37°35.213'	23°21.306'	73
41	IM372 IM373 IM379 *IM376A* *IM376B*	Phase C 'Paleo Kastro'	host rock enclave host rock *c-gr xenolith* *c-gr xenolith*	In situ massive lava flows, mostly grey, some red parts, porphyritic, contain more scoriaceous top and basal breccias as well as darker grey enclaves (4-70cm) *About 10 by 12 cm large, bit angular xenolith, coarse-grained,* *contains silica & white veins; light part = A; dark green part = B*	37°35.177' 37°35.185'	23°20.933' 23°20.951'	18 22

Sampling location	***Sample***	***Stratigraphic Unit (Pe-Piper & Piper, 2013)***	***Rock type***	***Outcrop***	***GPS-coordinates (WGS-84)***		***Height above sea level (m)***
					N	***E***	
42	IM32 IM36	Phase C 'Ag. Andreas'	host rock host rock	Weathered/overgrown pyroclastic flows as well as lava flows with scoriaceous top and basal capping breccias	37°37.311'	23°19.351'	79
43	IM393 IM394	Phase C 'Ag. Andreas'	host rock *xenolith*	Pyroclastic deposits; badly sorted, red and black block and ash and scoria and ash flow deposits ; *contains white coloured xenoliths*	37°37.203'	23°19.261'	165
44	IM395 *IM396*	Phase C 'Ag. Andreas'	host rock *xenolith*	Pyroclastic deposits; badly sorted, red and black block and ash and scoria and ash flow deposits ; *contains white coloured xenoliths*	37°37.204'	23°19.413'	184
	IM397	*Basement*		*Upper-Triassic limestone*			
1-7, 14-23, 25-27	***DPM…***	***Phase D***	***Delta 2***	***'Loutses North', 'Tsonaka' & 'Kossona Vouno' - see Chapter 4 and Appendix A1***			
45	IM318 IM319	Phase D 'NW and. flows'	enclave host rock	In situ massive lava flows, broken up along joints; porphyrytic, fresh grey with darker grey enclaves (1-5 cm)	37°35.789'	23°20.186'	26
46	IM313	Phase D	host rock	Massive, jointed lavas, grey to red, some flow banding, enclaves	37°35.275'	23°23.710'	98
47	IM308	Phase F	host rock	Autoclastic lava breccia, grey (to red), some flow banding, enclaves	37°37.391'	23°21.682'	362
48	IM315 IM316	Phase G 'C and. volcan.'	host rock enclave	In situ, somewhat weathered and auto brecciated lava flows, grey, porphyritic, with enclaves	37°35.391'	23°23.498'	183
49	IM303 IM301	Phase G 'C and. volcan.'	host rock enclave	In situ massive lava flow, intensively broken up by parallel, closely spaced fractures; grey lava with (angular) greenish enclaves	37°37.584	23°22.591'	188
50	IM21	Phase G	host rock	In situ massive lava, jointed, fresh grey, few small enclaves	37°35.390'	23°21.369'	119
51	IM294 IM295	Phase G 'EW fissure vlc.'	enclave host rock	Weathered top of in situ, jointed dome lavas and below outcrop of block and ash flow, with enclaves	37°36.515'	23°23.240'	462
52	IM296 IM297 IM298	Phase G 'EW fissure volcanoes'	host rock enclave enclave	In situ massive lava flows, broken up along joints; porphyrytic, fresh grey with darker grey enclaves (5-35 cm)	37°36.259'	23°22.630'	518
53	IM29	Phase H	host rock	In situ massive lava flow, jointed, many enclaves, scoriaceous parts	37°37.123'	23°19.978'	390
54	IM40	Phase H	enclave	In situ massive lava flow, jointed, many enclaves, scoriaceous parts	37°36.856'	23°19.787'	185
55	IM399 IM400	Phase H 'Mavri Petra'	host rock enclave	Large ex situ lava blocks, fresh, rolled downhill from the higher up massive lava flows; with many enclaves	37°36.988'	23°19.664'	207
56	IM401	Phase H	host rock	In situ massive lava flow, jointed, many enclaves, scoriaceous parts	37°36.935'	23°19.713'	205
57	*IM14*	*Basement.*		*Lower-Cretaceous limestone*	37°34.799'	23°21.512'	31
58	*IM26*	*Basement*		*Upper-Jurassic siliciclastic rock (conglomerate)*	37°34.937'	23°22.160'	151

Sampling location	***Sample***	***Stratigraphic Unit (this study)***	***Rock type***	***Outcrop/sample description***	***GPS-coordinates (WGS-84)***		***Height above sea level (m)***
					N	***E***	
FIRST PERIOD OF VOLCANIC ACTIVITY							
59	IA341	Pyroclastic rocks	tuff	Layered, yellow-beige, fine-grained ash layer (welded) dipping 35° S	37°44.376’	23°30.421’	136
60	IA102 IA101	Skotini andesite	host rock enclave	Massive lava flow with cooling joints, showing flow banding through alternation of grey and red matrix; in places crosscut by felsic dike	37°42.465'	23°27.896 '	5
61	IA329 IA331A IA331B IA332	Skotini andesite	host rock host rock enclave enclave	Massive lava flow, cooling joints, due to age spherically weathered and further fragmented, groundmass grey & fresh looking; contains some yellow ol, lots of plag, also black hbl (and px); <15 cm enclaves fine-to coarse-grained; location of only xenolith found on Aegina:	37°43.213'	23°27.930'	92
	IA328A		*xenolith*	*Mainly quartz, recrystallised, granular, crumbly, 3x4x4 cm*			
62	IA61 IA340	Palaiochora dacitic andesite	host rock host rock	Massive lava flow, jointed, fresh (in road cut); grey groundmass, white plag, black hbl and bt; small, c-gr enclaves RARE	37°44.889’	23°28.974’	203
63	IA63	Palaiochora dacitic andesite	host rock	Overgrown massive lava; bt up to 1 cm; small, c-gr enclaves RARE	37°45.142’	23°28.737’	304
64	IA55 IA56 IA336 IA338 IA348	Kokkinovrahos biotite-hornblende andesite	host rock host rock enclave enclave enclave	Roadcut of ca. 1m high massive lava with joints; light grey matrix, white plag, black hbl and bt, few green cpx(?); small c-gr enclaves, also a cluster of ca. 20 of 1-3cm c-gr enclaves; furthermore larger f-gr enclaves common. IA336 & IA348 = rare, up to 7 cm large enclaves with plag, some hbl and many green cpx (?) phenocrysts	37°45.092'	23°32.340'	140
65	IA349	Kokkinovrahos bt-hbl and	enclave	Brecciated lava in road cutting; 30-40 cm f-gr dark grey enclave	37°45.200'	23°32.781'	145
66	IA350	Kokkinovrahos bt-hbl and	host rock	Brecciated lava in road cutting; grey matrix, plag, hbl, bt	37°45.246'	23°32.475'	204
67	IA346 IA345	Kokkinovrahos bt-hbl and	host rock enclave	Road cutting in switchback, base = massive jointed lava flow with on top ‘capping breccia’; plag, bt, hbl, green cpx(?); c-gr enclaves	37°45.365'	23°32.312’	115
68	IA344 IA352 IA355B	Kokkinovrahos bt-hbl and	host rock host rock enclave	Vent area and upper part of flow; top = fresh-looking lava breccia, some large radial jointed blocks, below = lichen-covered brecciated lava; plag, hbl, bt, green cpx(?); few + small c-gr enclaves, 2 colours	37°46.099’	23°32.763’	110
69	IA59 IA60	Phase 1 bt-hbl andesite	host rock enclave	Massive lava flow, jointed; grey matrix, white plag, black hbl and bt; many enclaves, large ones too, IA60 = part of f-gr, >55 cm enclave	37°44.034’	23°32.355’	38
70	IA67 IA66	Phase 1 bt-hbl andesite	host rock enclave	Lava plug with short-spaced, subvertical fractures/foliation = from pressure flow through vent; many f-gr enclaves, with reaction rim bt	37°43.649’	23°32.035'	75
71	IA65	Phase 1 bt-hbl andesite	host rock	Grey to red-oxidised groundmass, plag, hbl, bt & rare pinkish quartz	37°44.223’	23°29.065’	327

Sampling location	***Sample***	***Stratigraphic Unit (this study)***	***Rock type***	***Outcrop/sample description***	***GPS-coordinates (WGS-84)***		***Height above sea level (m)***
					N	***E***	
72	IA103 IA104	Phase 1 bt-hbl andesite	host rock enclave	Brecciated lava to massive lava with joints; groundmass grey or red-oxidised, phenocrysts of plag, hbl & bt; f-gr up to 10 cm enclaves	37°41.131’	23°29.343’	264
73	IA94	Phase 1 bt-hbl andesite	host rock	Lava breccia at shore; f-gr grey groundmass, plag + hbl (±cpx ±qtz)	37°43.257’	23°27.410’	1
74	IA325	Phase 1 bt-hbl andesite	host rock	Brecciated lava near vent/plug, also jointed; f-gr grey groundmass,	37°43.448’	23°27.471’	106
75	IA327	Phase 1 bt-hbl andesite	host rock	plag, hbl and some green cpx; FEW & small, dark grey, f-gr enclaves	37°43.509’	23°27.495’	144
VOLCANIC QUIESCENCE							
76	IA322 IA321	Volcaniclastic apron	host rock enclave	Large boulders/blocks + small in situ outcrop of lava, weathered; grey matrix, plag, hbl, bt; many and large (up to 30 cm) dark f-gr enclaves	37°43.611’	23°26.882’	22
SECOND PERIOD OF VOLCANIC ACTIVITY							
77	IA97 IA98 IA333	Kakoperato rhyodacite	host rock enclave host rock	Lava breccia on flank of lava flow, weathered, covered with lichen; host rock = c-gr, crumbly; grey, glassy groundmass; plag + hbl + bt + qtz + cpx; many + large, f-gr & c-gr enclaves with qtz ocelli	37°42.868’	23°27.941’	24
78	IA73 IA74	Nikolaki andesite	host rock host rock	Lava breccia on flank of lava flow, weathered, covered with lichen; f-gr, very dense,grey rock; plag + cpx + hbl + qtz (ocelli), NO enclave	37°34.684’	23°29.524’	347
79	IA68	Oros-Lazarides bas and	host rock	Jointed lava, weathered; grey, plag + cpx, also few hbl	37°43.633’	23°31.656’	157
80	IA71 IA72	Oros-Lazarides basaltic andesite	host rock enclave	Jointed, massive lava flow in road cut; dark grey, f-gr groundmass; plag + cpx (?+ol?); f-gr, vesicular enclave	37°43.213’	23°31.219’	92
81	IA83	Oros-Lazarides bas and	host rock	Large lava blocks in breccia; dark grey, vesicular rock, qtz ocelli	37°42.843’	23°30.079’	299
82	IA80	Oros-Lazarides bas and	host rock	Brecciated lava to massive lava; grey; plag + cpx + qtz ocelli	37°42.860’	23°29.820’	292
83	IA85 IA88	Oros-Lazarides bas and	host rock host rock	Lava breccia, autoclastic, blocks; varying intensity of grey ground - mass & vesicularity; IA85 = most vesicles; IA88 = darkest grey	37°42.155’	23°29.303’	249
84	IA93	Oros-Lazarides bas and	host rock	Brecciated lava to massive lava; grey; plag + cpx + qtz ocelli	37°42.589’	23°29.717’	251
85	IA75 IA77 IA78	Oros hornblende andesite	host rock enclave enclave	Massive, jointed lava flow; grey groundmass; plag + cpx + (some) hbl + qtz heterogeneously distributed; small qtz xenolith? small hbl-cpx-holocrystall xenolith? Many ≠ sized enclaves, IA77 = f-gr, IA78 = c-gr	37°42.565’	23°30.103’	255
NON-VOLCANIC LITHOLOGIES							
86	*IA342* *IA343*	*Basement* *(Late Palaeozoic)*		*Limestone* *Calcarenite*	37°45.100’	23°31.086’	151
87	*IA54*	*Basement (Triassic)*		*Limestone*	37°45.247’	23°32.072’	144
88	*IA62*	*Basement (Jurassic)*		*Limestone*	37°45.142'	23°28.737’	304

Sampling location	***Sample Nr*** / ***Unit (Schwandner, 1998)***	***Rock type***	***Outcrop/sample description***	***GPS-coordinates (WGS-84)***		***Height above sea level (m)***
				N	***E***	
89	IP46 / Andesite	host rock	Fresh road cut, 4-5m high massive, jointed lava; dark grey and red patchy groundmass; many plag, large bt and some am, also few pinkish qtz; small enclaves scattered throughout	37°29.837’	23°27.773'	25
90	IP49 IP50 / Dacite	host rock enclave	Fresh, angular blocks from blasting parts of the massive lava outcrop; dark grey groundmass with red patches; many plag, large bt and ; few pinkish qtz, also am; enclaves sometimes contain qtz ocelli	37°29.808’	23°27.687'	69
91	IP53 / Dacite	enclave	Weathered, rounded bedrock of massive lava at top of hill; groundmass mainly red (only few grey patches), lots of large plag and bt phenocrysts, a few pinkish qtz crystals; large fine-gr enclave, 20 cm x 8 cm, with large plag, bt and qtz ocelli	37°29.988'	23°27.455'	56
92	IP299 / Dacite	host rock	Angular block from blasting part of the outcrop – fresher than weathered lava at the top next to clock tower; groundmass mainly dark grey (only few red patches), lots of large plag phenocrysts, also prismatic am and bt; some small, rounded enclaves	37°29.975’	23°27.135'	39
93	IP300 / Andesite	host rock	Somewhat weathered, in situ outcrop of massive lava between houses; groundmass mainly dark grey (only few red patches), lots of large plag phenocrysts, also prismatic am, bt and few pinkish qtz crystals; small, rounded enclaves scattered throughout	37°30.174'	23°27.381’	37

Appendix B: WR major element composition

and trace element contents

obtained with ICP-OES

Unit (this study)	***Loutses E flow***				***Loutses SE flow***											***Loutses NW***
Rock type	*Host rock*		*Enclave*		*Host rock*					*Enclave*						*Host rock*
sample	**DPM4**	**DPM11**	**DPM5**	**DPM12**	**DPM8**	**DPM16**	**DPM18**	**DPM20**	**DPM25**	**DPM9**	**DPM19**	**DPM10**	**DPM22**	**DPM23**	**DPM24**	**DPM61**
SiO_2 (wt%)	61.95	63.59	56.26	58.02	64.24	62.46	62.75	62.82	62.95	53.92	55.60	56.78	59.26	58.47	56.18	64.98
TiO_2 (wt%)	0.53	0.54	0.87	0.78	0.51	0.56	0.55	0.53	0.52	0.84	0.78	0.72	0.56	0.68	0.75	0.49
Al_2O_3 (wt%)	16.46	17.16	17.59	18.58	16.62	17.40	17.03	16.73	16.86	18.57	19.23	18.33	18.52	18.04	18.55	16.98
Fe_2O_3* (wt%)	4.93	5.15	7.41	6.86	4.75	5.27	5.19	5.05	4.92	7.34	6.94	6.66	5.93	6.30	6.48	4.70
MnO (wt%)	0.11	0.11	0.15	0.14	0.11	0.12	0.12	0.11	0.11	0.18	0.15	0.13	0.12	0.13	0.15	0.11
MgO (wt%)	3.06	2.47	5.02	3.96	2.53	2.84	2.83	2.72	2.60	4.81	4.06	4.24	2.77	3.75	3.96	2.39
CaO (wt%)	6.33	5.91	9.11	7.28	5.85	6.09	6.17	5.97	5.84	8.86	8.06	7.96	6.73	7.35	8.07	5.70
Na_2O (wt%)	3.26	3.28	2.87	3.05	3.35	3.43	3.25	3.35	3.44	3.16	3.18	3.01	3.70	3.12	3.56	3.50
K_2O (wt%)	1.92	2.09	1.25	1.54	2.04	1.99	1.93	2.00	2.00	1.35	1.69	1.40	1.96	1.54	1.57	2.17
P_2O_5 (wt%)	0.10	0.13	0.12	0.15	0.12	0.12	0.12	0.12	0.11	0.12	0.15	0.13	0.14	0.14	0.14	0.11
Total without LOI (wt%)	98.65	100.42	100.66	100.36	100.10	100.28	99.94	99.39	99.35	99.16	99.84	99.37	99.71	99.53	99.42	101.12
LOI (wt%)	0.08	0.57	0.22	0.66	0.17	0.38	0.10	0.21	0.54	0.68	0.68	0.41	1.16	0.33	0.81	0.31
Mg#	55.19	48.67	57.31	53.34	51.32	51.70	51.97	51.63	51.12	56.51	53.68	55.75	48.10	54.14	54.75	50.18
FeO*/MgO	1.45	1.88	1.33	1.56	1.69	1.67	1.65	1.67	1.70	1.37	1.54	1.41	1.92	1.51	1.47	1.77
Sc (ppm)	16.60	13.91	30.72	22.47	13.57	15.56	15.87	14.22	13.65	26.45	19.38	22.42	11.76	20.17	21.70	12.61
V (ppm)	116.1	108.3	159.3	157.3	104.1	86.9	108.1	108.9	102.1	227.0	157.5	163.8	138.9	144.2	178.6	82.7
Cr (ppm)	44.10	18.73	92.70	26.05	23.68	22.82	23.04	24.45	23.62	17.03	17.74	33.84	3.21	27.74	22.70	21.94
Ni (ppm)	17.12	10.70	24.79	10.73	10.47	11.41	10.24	10.92	12.07	21.54	22.93	11.80	16.56	9.58	20.18	11.52
Cu (ppm)	9.34	12.31	45.27	22.98	10.84	12.97	7.17	11.54	9.45	33.39	10.13	16.82	15.50	8.57	14.63	10.97
Zn (ppm)	48.25	49.77	67.37	66.91	50.13	55.50	52.74	51.26	50.91	70.51	73.35	64.68	64.65	64.55	63.57	48.81
Sr (ppm)	259.2	278.8	275.8	308.0	277.2	289.3	272.4	273.5	272.9	320.0	342.8	318.7	327.9	301.1	329.5	269.4
Y (ppm)	17.12	19.26	23.17	26.05	17.00	19.19	19.46	17.15	18.37	26.47	24.45	20.40	20.84	21.18	26.74	17.55
Zr (ppm)	125.5	131.8	114.1	124.1	115.5	125.5	114.7	134.3	127.4	99.9	49.9	112.8	129.6	122.5	114.0	124.3
Ba (ppm)	397.9	454.9	291.2	393.3	458.3	445.0	461.9	451.1	450.4	336.8	596.7	340.4	505.9	396.9	422.8	467.6

Unit (this study)	***Loutses NW section***				***Loutses S flow***					***Loutses SW flow***					***Kossona Vouno***	
Rock type	*Host rock*			*Enclave*	*Host rock*			*Enclave*		*Host rock*				*Enclave*	*Host rock*	
sample	**DPM63**	**DPM66**	**DPM67**	**DPM64**	**DPM26**	**DPM28**	**DPM30A**	**DPM29A**	**DPM29B**	**DPM27**	**DPM33**	**DPM57**	**DPM58**	**DPM32**	**DPM34**	**DPM39**
SiO_2 (wt%)	63.96	63.46	62.03	56.17	65.38	64.24	63.47	55.12	57.05	65.29	65.52	63.62	64.78	54.51	62.59	65.67
TiO_2 (wt%)	0.51	0.62	0.67	0.75	0.50	0.50	0.53	0.73	0.66	0.50	0.50	0.50	0.53	0.86	0.55	0.48
Al_2O_3 (wt%)	17.00	16.91	16.85	18.94	15.81	15.56	15.81	17.96	16.48	15.76	15.76	15.89	15.99	20.12	17.00	16.44
Fe_2O_3* (wt%)	4.90	5.28	5.82	7.06	4.57	4.58	4.69	7.59	6.89	4.41	4.49	4.56	4.66	6.89	5.19	4.36
MnO (wt%)	0.11	0.11	0.11	0.13	0.10	0.10	0.10	0.22	0.14	0.10	0.10	0.10	0.10	0.15	0.11	0.11
MgO (wt%)	2.62	3.21	4.01	4.81	3.28	3.17	3.47	5.45	5.47	3.31	3.17	3.14	3.59	4.55	2.88	2.24
CaO (wt%)	5.78	6.39	6.92	8.18	5.83	5.57	5.97	9.05	9.33	5.96	5.82	5.83	6.15	8.88	6.57	5.64
Na_2O (wt%)	3.37	3.08	2.99	3.11	3.41	3.32	3.33	3.06	2.67	3.30	3.31	3.40	3.28	3.33	3.36	3.39
K_2O (wt%)	2.14	1.90	1.86	1.37	1.99	2.05	2.03	1.17	1.45	2.02	2.08	1.97	1.96	0.81	1.95	2.09
P_2O_5 (wt%)	0.12	0.11	0.11	0.13	0.14	0.13	0.15	0.07	0.11	0.14	0.10	0.11	0.14	0.12	0.11	0.11
Total without LOI (wt%)	100.51	101.06	101.38	100.65	100.99	99.22	99.53	100.41	100.25	100.78	100.86	99.11	101.18	100.21	100.31	100.53
LOI (wt%)	0.47	0.62	0.43	0.42	0.18	0.21	0.14	0.23	0.32	0.17	0.29	0.40	0.53	0.73	0.37	0.62
Mg#	51.43	54.58	57.73	57.44	58.73	57.85	59.42	58.73	61.14	59.76	58.32	57.73	60.41	56.68	52.37	50.45
FeO*/MgO	1.68	1.48	1.31	1.32	1.25	1.30	1.22	1.25	1.13	1.20	1.27	1.30	1.17	1.36	1.62	1.75
Sc (ppm)	13.67	17.23	19.92	22.71	12.61	12.61	13.60	33.92	29.68	13.23	13.13	12.63	14.34	25.84	16.21	13.01
V (ppm)	104.6	102.0	122.7	167.0	97.2	90.6	89.3	154.8	145.3	101.6	92.2	88.2	110.6	109.3	122.7	95.9
Cr (ppm)	23.67	52.28	74.93	33.13	85.35	76.58	82.71	83.58	88.43	78.28	71.22	72.17	77.16	10.92	34.26	28.23
Ni (ppm)	10.71	11.75	14.91	10.87	52.42	46.59	52.30	28.59	32.57	50.07	43.73	43.94	50.19	33.43	15.82	13.15
Cu (ppm)	9.46	10.11	10.70	13.17	26.49	25.37	26.39	33.79	39.33	21.69	23.09	22.59	17.34	99.04	16.24	13.47
Zn (ppm)	50.23	53.94	57.07	68.11	49.82	49.44	51.10	76.95	60.78	47.27	50.50	50.65	48.74	57.69	49.70	48.34
Sr (ppm)	276.4	251.2	246.7	328.3	553.4	508.3	526.2	323.3	356.4	518.7	461.6	466.6	530.0	393.0	274.4	262.9
Y (ppm)	16.94	20.84	22.16	20.64	17.32	16.93	16.46	27.78	18.48	16.01	16.37	14.98	17.26	31.64	17.86	18.32
Zr (ppm)	136.7	152.4	153.4	122.8	1567.0	139.1	143.9	91.4	96.5	133.9	128.6	137.1	138.1	103.4	125.7	116.3
Ba (ppm)	473.5	388.1	362.3	337.9	428.3	436.8	432.1	332.2	266.8	436.4	434.6	443.6	456.9	334.2	426.5	471.3

Appendix B: Whole rock ICP-OES data

Unit (this study)	***Kossona Vouno***				***Tsonaka***											
Rock type	*Enclave*				*Host rock*								*Enclave*			
sample	**DPM35A**	**DPM36**	**DPM41A**	**DPM41B**	**DPM42**	**DPM45**	**DPM46**	**DPM47**	**DPM50**	**DPM52**	**DPM54**	**DPM55**	**DPM49**	**DPM53**	**DPM56A**	**DPM56 B**
SiO2 (wt%)	52.90	50.45	55.81	51.18	68.13	67.84	62.81	66.38	66.50	60.03	59.27	65.17	57.82	54.15	60.64	59.99
TiO2 (wt%)	0.90	0.92	0.82	0.86	0.41	0.43	0.58	0.43	0.46	0.62	0.68	0.49	0.69	0.89	0.78	0.80
Al2O3 (wt%)	17.64	18.52	17.79	17.63	16.11	16.11	17.19	16.31	16.49	17.66	18.20	16.37	15.73	18.15	17.69	17.85
Fe2O3* (wt%)	7.45	7.73	6.74	8.03	3.83	3.97	5.14	4.20	4.11	5.75	6.33	4.38	7.02	7.93	6.24	6.39
MnO (wt%)	0.14	0.14	0.13	0.15	0.10	0.11	0.11	0.11	0.12	0.15	0.17	0.10	0.14	0.20	0.13	0.13
MgO (wt%)	5.92	6.14	4.80	6.53	1.69	1.93	2.86	2.03	1.96	3.05	3.31	2.00	5.72	5.13	2.31	2.38
CaO (wt%)	10.58	11.05	9.15	11.73	4.69	4.70	6.05	5.05	5.11	6.43	6.83	5.15	8.80	9.33	6.21	6.35
Na2O (wt%)	2.85	2.73	3.10	2.59	3.27	3.40	3.39	3.49	3.43	3.34	3.25	3.41	2.73	2.93	2.92	3.03
K2O (wt%)	1.06	0.92	1.32	0.89	2.52	2.47	1.91	2.23	2.32	1.74	1.62	2.38	1.50	1.18	1.93	1.91
P2O5 (wt%)	0.20	0.12	0.13	0.09	0.05	0.11	0.11	0.11	0.12	0.15	0.17	0.12	0.16	0.12	0.19	0.19
Total without LOI (wt%)	99.65	98.72	99.78	99.67	100.81	101.06	100.15	100.34	100.62	98.93	99.82	99.57	100.30	100.01	99.06	99.03
LOI (wt%)	1.00	1.19	0.19	0.35	1.57	1.61	0.97	1.02	1.50	-0.07	-0.07	1.31	0.76	0.05	0.96	0.85
Mg#	61.15	61.14	58.54	61.69	46.57	49.06	52.45	48.88	48.65	51.21	50.88	47.43	61.72	56.17	42.29	42.52
FeO*/MgO	1.13	1.13	1.26	1.11	2.04	1.85	1.62	1.86	1.88	1.70	1.72	1.98	1.11	1.39	2.43	2.41
Sc (ppm)	35.08	34.23	27.51	39.93	9.68	9.90	14.95	10.22	9.95	14.41	15.68	10.46	28.09	29.71	14.54	14.82
V (ppm)	231.6	262.3	176.1	202.4	71.7	72.4	109.4	77.5	68.9	113.7	122.0	74.8	175.3	198.5	82.8	89.6
Cr (ppm)	93.45	46.93	55.64	131.89	15.96	16.51	20.56	19.33	14.69	11.16	10.38	17.49	157.9	74.81	2.15	5.18
Ni (ppm)	34.26	32.82	26.77	40.46	8.44	8.02	8.88	9.11	8.06	6.04	8.33	9.22	25.97	31.31	3.23	4.59
Cu (ppm)	34.92	23.52	34.59	49.92	7.70	5.66	10.74	10.09	9.48	10.69	9.92	11.92	23.32	41.92	9.15	10.21
Zn (ppm)	56.80	57.86	63.81	69.88	50.63	44.33	49.05	50.42	43.14	53.45	53.73	50.25	65.18	79.59	71.07	68.43
Sr (ppm)	303.7	290.8	314.4	317.8	251.92	243.8	263.0	256.0	249.1	295.5	309.6	251.0	357.7	322.6	291.4	295.7
Y (ppm)	19.90	20.85	19.50	21.54	16.45	17.45	19.15	18.30	17.54	20.45	22.60	17.53	21.20	31.31	31.23	29.29
Zr (ppm)	85.3	84.3	96.1	83.7	134.1	146.6	131.2	134.3	150.1	138.2	140.0	147.2	115.7	98.3	200.4	191.7
Ba (ppm)	238.5	202.4	295.5	171.0	522.4	517.7	435.4	470.6	497.3	427.3	422.2	484.3	388.1	349.4	393.0	407.0

Unit (Pe-Piper & Piper, 2013)	***Phase A***		***Phase B***								***Phase C***						
Rock type	*Host rock*		*Host rock*						*Enclave*		*Pumice*					*Bas and*	
sample	**IM317**	**IM43**	**IM42**	**IM30**	**IM18**	**IM368**	**IM389**	**IM290**	**IM291**	**IM369**	**IM17B**	**IM382**	**IM383**	**IM388**	**DPM65**	**IM9**	**IM10**
SiO_2 (wt%)	59.66	58.51	67.71	60.40	55.42	54.21	60.65	61.75	56.47	NA	63.16	62.03	61.24	60.41	61.46	55.53	55.39
TiO_2 (wt%)	0.58	0.63	0.32	0.65	0.81	0.87	0.61	0.63	0.66	NA	0.78	0.75	0.75	0.73	0.68	0.75	0.75
Al_2O_3 (wt%)	17.29	18.13	16.19	18.02	17.26	17.50	16.63	17.81	18.55	NA	16.91	16.92	16.63	16.34	17.56	17.34	17.42
Fe_2O_3* (wt%)	5.81	6.71	3.31	6.53	6.31	6.66	5.31	5.94	7.46	NA	5.49	5.57	5.59	5.87	5.59	7.35	7.28
MnO (wt%)	0.12	0.14	0.11	0.12	0.13	0.13	0.11	0.12	0.15	NA	0.11	0.11	0.11	0.12	0.11	0.14	0.14
MgO (wt%)	3.02	3.24	0.85	2.75	5.14	5.76	3.23	2.89	3.00	NA	2.90	2.75	3.18	4.20	2.57	5.63	5.62
CaO (wt%)	7.19	7.43	3.39	6.88	8.08	9.03	6.72	6.41	8.15	NA	6.45	6.70	6.80	6.97	6.80	9.10	9.18
Na_2O (wt%)	3.36	3.35	3.99	2.71	3.25	3.22	3.25	3.58	3.53	NA	2.85	2.78	2.75	2.72	2.90	2.87	2.81
K_2O (wt%)	1.78	1.51	2.70	1.84	1.90	1.80	2.08	1.91	1.34	NA	1.76	1.71	1.64	1.62	1.73	1.18	1.28
P_2O_5 (wt%)	0.11	0.12	0.09	0.13	0.20	0.23	0.15	0.15	0.18	NA	0.12	0.12	0.11	0.12	0.12	0.12	0.12
Total without LOI (wt%)	98.94	99.77	98.64	100.04	98.50	99.39	98.75	101.19	99.50	NA	100.54	99.43	98.80	99.09	99.52	100.0	100.0
LOI (wt%)	0.05	-0.13	0.35	1.41	0.91	0.57	1.27	0.43	0.15	NA	2.14	2.56	2.13	1.93	1.95	0.46	0.40
Mg#	50.75	48.89	33.69	45.48	61.75	63.12	54.62	49.12	44.34	/	51.13	49.47	52.94	58.66	47.65	60.27	60.45
FeO*/MgO	1.73	1.86	3.51	2.14	1.10	1.04	1.48	1.85	2.24	/	1.70	1.82	1.58	1.26	1.96	1.17	1.17
Sc (ppm)	17.1	15.8	4.7	15.4	22.9	25.9	16.1	15.1	14.2	32.2*	19.5	19.5	19.7	20.0	17.9	43.1	43.0
V (ppm)	131.7	145.6	37.5	112.9	148.7	161.2	111.9	116.9	156.3	189.4*	112.7	114.4	115.3	120.3	125.3	184.4	186.1
Cr (ppm)	21.3	8.9	2.0	8.9	110.5	131.4	54.4	4.6	3.7	235.8*	18.6	23.0	39.7	109.8	14.8	117.0	113.4
Ni (ppm)	25.8	5.9	21.7	25.7	33.9	45.5	31.7	4.2	27.7	62.1*	9.8	25.7	39.7	71.4	25.6	34.3	32.5
Cu (ppm)	16.1	5.4	3.8	11.6	12.0	14.2	9.6	NA	34.3	16.3*	6.8	7.0	9.2	9.8	10.2	NA	NA
Zn (ppm)	61.3	68.7	59.9	80.8	45.3	56.8	56.8	62.0	66.7	59.3*	49.3	65.3	59.8	63.7	61.3	NA	NA
Sr (ppm)	249.9	268.0	216.1	270.5	388.1	422.9	299.6	289.7	327.6	252.2*	247.5	248.5	244.4	248.4	260.1	262.9	266.1
Y (ppm)	19.9	22.3	18.9	28.8	22.9	23.4	19.4	21.0	24.0	19.9*	25.9	25.6	25.1	23.9	22.8	21.7	22.0
Zr (ppm)	116.2	114.0	163.3	156.9	143.9	157.7	146.7	136.2	154.8	98.7*	187.5	187.1	183.1	165.3	155.4	111.7	111.6
Ba (ppm)	NA	329.6	NA	NA	455.0	NA	NA	431.6	NA	238.6*	339.4	NA	NA	NA	NA	270.0	308.0

Unit (Pe-Piper & Piper, 2013)	***Phase C***															***Phase D***	
Rock type	*Bas and*		*PDC deposit*					*Host rock*					*Enclave*	*Igneous xenolith*		*Host rock*	
sample	**IM32**	**IM36**	**IM13**	**IM359**	**IM364**	**IM393**	**IM395**	**IM372**	**IM379**	**IM23**	**IM24**	**IM310**	**IM373**	**IM376A**	**IM376B**	**IM313**	**IM319**
SiO_2 (wt%)	54.69	55.15	55.61	54.91	55.32	55.14	54.44	58.18	60.03	61.20	55.77	59.72	52.84	73.24	55.39	65.27	60.65
TiO_2 (wt%)	0.78	0.77	0.73	0.72	0.73	0.77	0.76	0.74	0.72	0.60	0.74	0.64	0.84	0.34	0.63	0.47	0.62
Al_2O_3 (wt%)	17.47	17.24	17.55	17.26	17.43	17.65	17.58	16.70	17.02	16.61	17.12	17.80	16.46	12.72	15.88	16.55	17.85
Fe_2O_3* (wt%)	7.28	7.26	7.12	7.13	7.31	7.21	7.12	6.38	6.11	5.79	7.27	6.08	7.67	1.97	6.18	4.54	6.00
MnO (wt%)	0.14	0.14	0.13	0.14	0.14	0.14	0.14	0.12	0.12	0.11	0.14	0.12	0.14	0.06	0.15	0.10	0.13
MgO (wt%)	5.68	5.53	5.69	5.69	5.95	5.45	5.36	4.78	4.04	3.47	5.64	2.87	8.13	1.09	4.39	2.03	2.99
CaO (wt%)	9.33	9.17	9.00	9.53	9.81	9.43	9.31	7.53	7.17	6.61	9.09	6.55	9.72	7.42	15.52	4.99	6.56
Na_2O (wt%)	3.09	3.14	3.03	2.88	2.89	3.11	3.13	2.93	2.84	2.98	2.86	3.41	2.53	2.14	2.27	3.45	3.24
K_2O (wt%)	1.41	1.46	1.10	1.09	1.06	1.36	1.34	1.66	1.80	1.78	1.25	1.61	1.31	0.17	0.16	2.25	1.88
P_2O_5 (wt%)	0.12	0.12	0.11	0.11	0.11	0.12	0.12	0.22	0.24	0.12	0.12	0.15	0.17	0.13	0.14	0.12	0.14
Total without LOI (wt%)	99.99	100.00	100.06	99.46	100.75	100.37	99.29	99.24	100.08	99.27	100.00	98.96	99.80	99.26	100.72	99.76	100.08
LOI (wt%)	0.26	0.29	1.00	0.06	-0.04	0.32	0.25	0.98	1.13	1.15	0.31	-0.04	0.76	0.10	0.17	1.00	0.73
Mg#	60.73	60.16	61.26	61.24	61.69	59.95	59.84	59.72	56.69	54.30	60.61	48.38	67.73	52.24	58.44	46.96	49.69
FeO*/MgO	1.15	1.18	1.13	1.13	1.11	1.19	1.20	1.20	1.36	1.50	1.16	1.90	0.85	1.63	1.27	2.01	1.80
Sc (ppm)	41.6	40.0	31.2	31.1	32.0	27.8	27.4	22.2	20.2	19.3	43.1	15.4	30.6	8.2	24.3	10.1	14.9
V (ppm)	187.4	181.6	186.1	191.0	175.2	181.3	178.8	137.7	117.0	122.4	181.8	122.3	191.9	45.0	168.8	78.7	110.7
Cr (ppm)	119.0	112.6	134.4	127.8	136.9	107.3	107.3	132.2	97.6	63.3	115.3	9.9	293.8	6.6	88.0	12.3	24.9
Ni (ppm)	42.1	39.8	41.4	47.6	50.0	50.7	50.7	70.6	54.6	13.9	34.4	8.0	106.1	30.8	39.2	4.2	12.9
Cu (ppm)	NA	NA	22.4	24.7	31.6	40.8	34.5	24.0	12.9	7.4	NA	10.4	12.3	42.7	38.1	8.4	7.5
Zn (ppm)	NA	NA	50.6	61.7	61.6	61.3	60.8	57.5	60.4	45.5	NA	55.2	60.9	19.1	59.2	48.4	53.7
Sr (ppm)	276.5	278.1	256.9	255.1	255.2	270.6	272.3	284.3	266.7	331.9	273.2	285.4	298.4	214.5	314.1	247.1	289.8
Y (ppm)	22.2	21.7	20.0	20.0	20.4	21.1	21.0	22.6	23.8	21.27	21.5	21.4	22.7	13.3	19.2	17.3	21.4
Zr (ppm)	101.7	107.2	107.8	104.0	105.7	98.6	130.4	149.3	160.5	143.2	111.2	136.4	114.6	110.8	103.7	153.8	140.7
Ba (ppm)	281.9	281.7	256.2	NA	NA	NA	NA	NA	NA	390.1	276.3	380.3	NA	NA	NA	466.9	384.5

Unit (Pe-Piper & Piper, 2013)	***Phase D***	***Phase F***	***Phase G***										***Phase H***				
Rock type	*Enclave*	*Host*	*Host rock*					*Enclave*					*Host rock*			*Enclave*	
sample	**IM318**	**IM308**	**IM315**	**IM303**	**IM21**	**IM295**	**IM296**	**IM316**	**IM301**	**IM294**	**IM297**	**IM298**	**IM29**	**IM399**	**IM401**	**IM40**	**IM400**
SiO2 (wt%)	56.83	60.09	60.92	60.25	62.51	62.52	62.75	56.83	56.10	52.25	54.00	55.28	62.00	59.29	59.36	55.57	54.03
TiO2 (wt%)	0.73	0.70	0.66	0.70	0.56	0.55	0.52	0.80	0.75	0.90	0.65	0.72	0.53	0.59	0.55	0.73	0.74
Al2O3 (wt%)	18.78	17.60	17.91	16.87	17.71	16.97	16.78	18.98	16.84	18.85	16.38	15.75	17.48	17.78	17.72	18.38	18.82
Fe2O3* (wt%)	7.18	5.97	5.99	5.84	5.89	5.06	5.03	7.15	7.30	7.65	7.48	7.29	4.89	5.57	5.31	6.71	6.69
MnO (wt%)	0.14	0.13	0.12	0.12	0.13	0.11	0.11	0.14	0.14	0.15	0.14	0.14	0.11	0.12	0.12	0.13	0.13
MgO (wt%)	3.79	3.01	3.00	3.30	2.18	2.33	2.75	3.80	6.30	5.27	7.32	8.27	2.82	3.52	3.39	5.39	5.24
CaO (wt%)	7.65	6.88	6.47	7.01	6.06	5.73	5.99	7.57	8.82	9.92	10.02	8.29	6.04	6.97	6.52	8.05	8.39
Na2O (wt%)	2.95	3.18	3.44	2.82	3.53	3.31	3.40	3.24	2.54	2.62	2.49	2.70	3.72	3.62	3.60	3.24	3.40
K2O (wt%)	1.39	1.68	1.82	1.50	1.75	2.13	2.04	1.53	1.11	0.97	0.96	1.21	2.27	2.02	2.03	1.66	1.56
P2O5 (wt%)	0.15	0.12	0.14	0.11	0.17	0.12	0.12	0.16	0.09	0.14	0.08	0.11	0.14	0.14	0.14	0.14	0.15
Total without LOI (wt%)	99.60	99.36	100.47	98.52	100.48	98.84	99.49	100.18	99.99	98.71	99.52	99.77	100.00	99.61	98.73	100.0	99.14
LOI (wt%)	0.62	0.20	0.68	-0.20	0.66	0.76	1.03	0.53	0.25	0.78	0.56	0.73	0.61	-0.02	0.03	0.32	0.15
Mg#	51.15	49.98	49.79	52.83	42.24	47.68	52.01	51.28	63.10	57.72	65.97	69.22	53.33	55.59	55.80	61.41	60.82
FeO*/MgO	1.70	1.78	1.80	1.59	2.44	1.96	1.64	1.69	1.04	1.31	0.92	0.79	1.56	1.42	1.41	1.12	1.15
Sc (ppm)	18.6	18.9	15.9	21.0	10.7	13.4	13.5	20.1	31.5	32.0	31.5	27.0	17.5	15.6	14.0	NA	21.5
V (ppm)	138.5	69.9	122.3	128.8	88.1	79.1	99.1	156.0	181.7	212.7	190.2	166.8	91.6	106.9	97.4	NA	137.2
Cr (ppm)	31.1	33.8	13.5	52.7	4.6	21.8	44.0	10.1	200.8	38.0	349.6	442.7	22.5	49.5	41.4	NA	96.1
Ni (ppm)	16.6	7.0	9.5	NA	3.0	7.4	16.0	10.6	29.0	5.4	86.5	136.1	11.7	37.7	10.4	NA	77.6
Cu (ppm)	11.0	8.0	15.9	9.5	8.6	7.9	13.5	11.1	9.0	20.2	9.3	10.8	NA	16.6	20.3	NA	19.1
Zn (ppm)	64.2	53.1	51.3	67.3	60.3	49.1	43.5	61.8	54.5	73.5	68.0	51.1	NA	56.7	51.1	NA	63.8
Sr (ppm)	317.7	266.2	289.9	245.7	296.5	250.9	257.0	323.22	241.5	268.7	232.1	259.1	332.1	352.5	353.7	NA	417.4
Y (ppm)	22.6	23.8	20.4	24.1	22.8	22.8	19.0	22.1	22.0	24.7	19.9	19.7	17.7	18.3	17.5	NA	20.7
Zr (ppm)	143.0	149.9	135.1	163.7	152.6	150.2	128.0	134.2	123.2	103.7	83.4	109.2	134.0	130.4	144.0	111.2	127.5
Ba (ppm)	324.4	356.3	425.5	323.1	402.6	407.7	403.1	400.5	223.4	278.2	NA	271.9	470.1	NA	443.9	NA	NA

Unit (this study)	***Pyro-clastics***	***Skotini andesite***						***Palaiochora dacitic andesite***			***Kokkinovrahos biotite-hornblende andesite***						
Rock type	*Tuff*	*Host rock*			*Enclave*			*Host rock*			*Host rock*						*Enclave*
sample	**IA341**	**IA102**	**IA329**	**IA331A**	**IA101**	**IA331B**	**IA332**	**IA61**	**IA63**	**IA340**	**IA55**	**IA56**	**IA344**	**IA346**	**IA350**	**IA352**	**IA336**
SiO_2 (wt%)	53.74	58.61	57.93	58.16	54.39	53.20	53.26	62.90	62.39	61.61	62.14	60.80	60.23	60.00	61.65	61.33	54.76
TiO_2 (wt%)	0.42	0.57	0.62	0.63	0.72	0.83	0.75	0.59	0.56	0.60	0.46	0.49	0.49	0.48	0.46	0.47	0.58
Al_2O_3 (wt%)	7.59	16.82	16.48	16.68	19.66	16.41	15.64	18.36	18.10	19.05	16.59	16.86	16.79	17.18	16.71	16.45	15.13
Fe_2O_3* (wt%)	5.15	6.13	6.31	6.30	7.03	8.00	7.92	4.88	4.30	4.99	4.62	5.06	5.06	4.91	4.71	4.89	7.21
MnO (wt%)	0.07	0.13	0.13	0.13	0.14	0.14	0.15	0.05	0.08	0.06	0.10	0.11	0.11	0.09	0.11	0.11	0.13
MgO (wt%)	12.82	4.67	3.73	3.73	4.44	5.90	7.52	1.27	1.67	1.61	3.15	3.37	3.64	3.34	3.36	3.58	6.87
CaO (wt%)	18.34	7.80	7.42	7.49	9.63	9.07	8.99	5.98	6.38	6.52	6.68	6.80	7.12	6.90	6.75	6.84	10.45
Na_2O (wt%)	0.79	3.26	3.22	3.28	2.97	3.21	2.49	3.09	3.21	3.11	3.37	3.51	3.45	3.47	3.29	3.38	2.61
K_2O (wt%)	1.25	1.87	2.60	2.62	1.69	2.01	2.15	1.89	1.90	1.65	2.60	2.29	2.27	2.25	2.62	2.39	1.46
P_2O_5 (wt%)	0.18	0.12	0.33	0.33	0.11	0.58	0.48	0.18	0.14	0.18	0.14	0.15	0.17	0.14	0.13	0.14	0.13
Total without LOI (wt%)	100.36	100.00	98.78	99.35	100.78	99.36	99.36	99.18	98.72	99.37	99.84	99.42	99.32	98.77	99.80	99.58	99.33
LOI (wt%)	25.01	0.72	1.04	1.08	0.54	1.88	1.05	2.34	1.79	2.73	1.70	0.85	1.37	1.75	1.54	1.45	0.92
Mg#	83.14	60.14	53.95	54.01	55.59	59.36	65.31	33.93	43.45	38.98	57.43	56.93	58.75	57.43	58.55	59.20	65.37
FeO*/MgO	0.36	1.18	1.52	1.52	1.42	1.22	0.95	3.47	2.32	2.79	1.32	1.35	1.25	1.32	1.26	1.23	0.94
Sc (ppm)	11.55	23.07	19.95	20.13	22.70	31.24	30.98	12.31	11.90	12.87	16.96	17.63	19.10	18.1	17.1	18.5	40.2
V (ppm)	100.4	155.5	156.7	156.4	191.4	196.8	210.0	113.1	113.2	121.2	123.3	125.7	128.4	122.9	126.9	125.6	204.5
Cr (ppm)	227.0	106.3	NA	95.7	3.3	212.1	309.9	3.7	NA	4.0	71.7	79.3	95.5	79.8	NA	89.8	262.7
Ni (ppm)	186.4	46.8	NA	46.3	12.4	90.7	122.5	3.7	NA	4.2	16.8	21.0	22.3	18.3	NA	21.6	30.5
Cu (ppm)	39.7	42.3	34.2	37.2	28.2	36.2	84.5	8.6	12.2	9.1	49.5	28.9	51.7	29.1	15.1	4.5	33.5
Zn (ppm)	79.5	50.2	53.8	54.7	56.7	62.5	68.3	52.1	51.9	55.5	42.2	48.2	45.9	49.4	87.8	12.0	53.0
Sr (ppm)	334.4	323.9	484.7	495.9	403.8	618.0	503.5	442.8	440.7	464.4	525.7	553.4	565.4	636.6	527.5	533.6	527.4
Y (ppm)	17.0	16.2	21.6	21.3	19.8	25.2	21.8	19.9	20.4	23.5	13.7	15.3	16.2	15.2	14.6	14.8	15.4
Zr (ppm)	90.6	98.8	140.7	142.0	93.4	142.6	126.8	145.8	163.1	158.6	111.6	115.5	118.7	133.4	151.0	125.2	81.9
Ba (ppm)	212	524	880	894	537	1085	821	688	685	716	1091	1081	1098	1105	1077	1085	635
Pyrocl. = pyroclastic rocks																	

Unit (this study)	***Kokkinovrahos biotite-hornblende andesite***					***Phase 1 biotite-hornblende andesite***										***Volcaniclastic apron***	
Rock type	*Enclave*					*Host rock*		*Enclave*		*Host rock*		*Enclave*	*Host rock*			*Host rock*	*Enclave*
sample	**IA338**	**IA345**	**IA348**	**IA349**	**IA355B**	**IA59**	**IA67**	**IA60**	**IA66**	**IA65**	**IA103**	**IA104**	**IA94**	**IA325**	**IA327**	**IA322**	**IA321**
SiO_2 (wt%)	52.61	53.41	54.73	55.11	53.30	59.71	59.92	52.77	52.84	61.22	59.70	54.68	61.04	62.58	62.78	60.64	51.10
TiO_2 (wt%)	0.81	0.65	0.59	0.63	0.73	0.56	0.53	0.79	0.79	0.52	0.57	0.77	0.55	0.53	0.54	0.52	0.95
Al_2O_3 (wt%)	18.91	19.41	15.24	18.99	18.74	17.07	17.06	17.12	17.13	17.47	16.67	17.89	17.14	16.93	16.89	16.92	16.78
Fe_2O_3* (wt%)	7.28	7.17	7.39	7.09	7.28	5.48	5.17	7.52	7.20	5.43	5.87	7.74	4.78	4.45	4.71	5.37	7.94
MnO (wt%)	0.16	0.14	0.13	0.13	0.15	0.12	0.11	0.13	0.13	0.12	0.11	0.13	0.10	0.09	0.10	0.12	0.14
MgO (wt%)	5.24	4.34	6.85	3.65	4.64	3.15	2.93	6.38	6.25	2.40	3.32	4.47	2.74	2.68	2.73	3.13	7.01
CaO (wt%)	9.26	9.93	9.84	8.84	9.11	7.25	7.12	10.08	10.23	6.14	7.14	8.68	6.50	6.14	6.15	6.98	10.44
Na_2O (wt%)	2.93	2.87	2.68	2.95	3.20	3.25	3.30	2.86	2.91	3.29	3.14	2.74	3.89	3.61	3.79	3.38	3.09
K_2O (wt%)	1.70	1.38	1.47	2.07	1.62	2.26	2.30	1.38	1.40	2.12	2.22	1.55	2.10	2.34	2.25	2.36	2.07
P_2O_5 (wt%)	0.19	0.17	0.11	0.22	0.21	0.17	0.17	0.16	0.15	0.12	0.14	0.19	0.17	0.15	0.17	0.15	0.37
Total without LOI (wt%)	99.10	99.48	99.05	99.69	98.97	99.01	98.60	99.18	99.03	98.82	98.88	98.84	99.02	99.50	100.11	99.57	99.90
LOI (wt%)	1.28	1.22	1.91	1.08	1.58	1.14	1.18	2.30	1.09	1.55	1.02	1.56	0.61	1.27	1.00	1.06	0.45
Mg#	58.78	54.54	64.76	50.51	55.78	53.23	52.86	62.73	63.25	46.65	52.84	53.33	53.17	54.39	53.48	53.57	63.63
FeO*/MgO	1.25	1.49	0.97	1.75	1.41	1.57	1.59	1.06	1.04	2.04	1.59	1.56	1.57	1.49	1.55	1.54	1.02
Sc (ppm)	36.4	22.7	39.5	18.8	29.9	18.89	18.02	32.86	36.52	13.9	23.0	29.4	15.5	14.8	15.2	16.6	34.4
V (ppm)	219.4	175.9	206.8	191.8	205.6	146.8	132.3	201.1	208.2	126.2	173.2	219.3	131.4	122.6	127.7	125.4	214.4
Cr (ppm)	53.0	13.5	212.4	5.0	10.9	86.9	NA	NA	336.6	6.7	34.8	20.9	11.6	NA	12.8	43.4	218.9
Ni (ppm)	24.6	16.7	35.2	9.4	17.4	19.9	NA	NA	47.1	6.5	12.1	13.4	11.7	NA	10.9	17.8	68.9
Cu (ppm)	13.3	29.8	24.5	33.6	15.2	29.6	25.9	34.1	18.1	25.0	33.7	26.0	39.1	26.2	30.6	50.0	30.4
Zn (ppm)	71.3	63.3	57.7	65.1	75.1	53.8	52.8	55.0	52.9	55.4	52.0	65.6	50.1	49.8	50.1	50.7	57.0
Sr (ppm)	638.2	959.8	527.3	689.9	654.3	392.3	372.4	400.0	361.5	365.2	410.0	570.2	644.3	624.4	622.6	401.7	607.0
Y (ppm)	21.5	20.2	15.0	20.8	22.7	17.2	16.1	18.5	18.5	19.2	16.8	23.6	17.9	17.0	18.6	15.4	22.3
Zr (ppm)	117.3	81.9	82.9	129.5	117.2	124.9	123.5	103.7	99.3	132.0	107.6	102.1	141.9	144.2	141.2	120.3	125.6
Ba (ppm)	1012	663	639	1061	921	669	661	450	423	661	610	610	693	651	673	690	936

Appendix B: Whole rock ICP-OES data

Unit (this study)	***Kakoperato rhyodacite***			***Nikolaki andesite***		***Oros-Lazarides basaltic andesite***								***Oros hornblende andesite***		
Rock type	*Host rock*		*Enclave*	*Host rock*		*Host rock*				*Enclave*	*Host rock*			*Host rock*	*Enclave*	
sample	**IA97**	**IA333**	**IA98**	**IA73**	**IA74**	**IA71**	**IA83**	**IA85**	**IA88**	**IA72**	**IA80**	**IA93**	**IA68**	**IA75**	**IA77**	**IA78**
SiO_2 (wt%)	69.26	68.68	57.21	55.61	57.16	55.24	55.18	54.74	54.52	50.83	54.85	54.39	58.71	55.48	53.63	51.74
TiO_2 (wt%)	0.30	0.30	0.82	0.65	0.67	0.74	0.75	0.78	0.78	0.92	0.79	0.77	0.63	0.74	0.83	1.12
Al_2O_3 (wt%)	15.44	15.41	18.02	16.57	17.07	17.66	17.79	17.81	18.30	19.16	17.99	18.43	17.31	17.92	18.16	15.09
Fe_2O_3* (wt%)	2.66	2.57	6.17	6.94	7.16	7.45	7.49	7.69	7.82	9.47	7.74	7.67	6.41	7.48	7.48	9.01
MnO (wt%)	0.07	0.07	0.11	0.12	0.12	0.13	0.13	0.14	0.12	0.13	0.13	0.13	0.12	0.13	0.11	0.12
MgO (wt%)	1.22	1.27	3.94	4.91	4.70	4.74	4.77	4.74	4.50	5.26	4.53	4.47	3.69	4.33	4.77	8.41
CaO (wt%)	3.71	3.70	7.92	9.54	8.87	9.00	9.01	9.18	9.05	9.81	9.07	9.09	7.71	8.73	8.82	10.07
Na_2O (wt%)	3.52	3.40	3.10	3.03	3.11	3.22	3.10	3.11	3.12	2.80	3.12	3.11	3.36	3.11	2.87	2.55
K_2O (wt%)	3.73	3.55	2.51	1.71	1.80	1.66	1.59	1.66	1.59	1.02	1.65	1.58	1.94	1.67	1.81	1.54
P_2O_5 (wt%)	0.09	0.09	0.20	0.13	0.13	0.14	0.14	0.14	0.14	0.06	0.14	0.14	0.13	0.13	0.11	0.58
Total without LOI (wt%)	100.0	99.05	100.0	99.22	100.79	99.99	99.97	99.99	99.92	99.46	100.02	99.78	100.01	99.74	98.59	100.22
LOI (wt%)	1.89	1.86	1.21	0.33	0.28	0.03	0.67	0.04	0.29	0.89	0.28	0.34	0.56	0.35	0.81	0.95
Mg#	47.69	49.55	55.85	58.38	56.52	55.74	55.79	54.99	53.27	52.40	53.71	53.58	53.25	53.38	55.80	64.90
FeO*/MgO	1.95	1.81	1.41	1.27	1.37	1.42	1.41	1.46	1.56	1.62	1.54	1.54	1.56	1.56	1.41	0.96
Sc (ppm)	6.4	6.7	24.0	28.9	30.1	29.2	30.1	29.1	29.2	29.5	28.8	27.9	21.0	28.1	32.3	43.7
V (ppm)	55.1	58.0	201.4	194.5	209.7	232.1	237.9	238.8	233.5	305.2	238.5	223.3	183.1	222.6	266.3	292.9
Cr (ppm)	6.4	6.6	11.1	74.1	74.9	33.2	30.5	28.8	25.8	10.5	28.3	21.3	18.7	21.6	21.3	186.3
Ni (ppm)	5.1	5.5	12.5	24.9	24.3	18.3	18.2	16.8	16.0	14.3	15.9	15.1	13.3	15.4	16.1	37.7
Cu (ppm)	7.7	11.0	25.8	80.5	63.3	74.0	73.3	46.4	54.4	101.3	41.5	55.0	36.0	75.3	53.6	80.5
Zn (ppm)	32.8	33.5	48.0	53.0	55.7	62.8	65.5	62.8	59.0	63.9	60.9	61.7	56.4	57.3	53.9	55.7
Sr (ppm)	311.8	324.8	765.3	644.4	655.4	702.7	716.0	692.7	668.9	756.2	668.8	680.4	588.9	684.6	611.3	558.4
Y (ppm)	13.7	13.0	17.6	17.6	17.9	17.4	18.0	19.3	24.2	17.4	18.6	18.7	16.5	17.1	17.5	24.4
Zr (ppm)	119.0	112.3	103.4	108.5	99.5	104.0	106.0	98.9	105.3	98.9	103.0	110.0	106.0	106.7	96.0	101.2
Ba (ppm)	634	674	437	352	363	321	338	301	287	288	293	318	423	337	327	350

Volcanic unit (Schwandner, 1998)	***Poros andesite***		***Poros dacite***			
Rock type	*Host rock*		*Host rock*		*Enclave*	
sample	**IP46**	**IP300**	**IP49**	**IP299**	**IP50**	**IP53**
SiO_2 (wt%)	62.34	62.22	62.76	61.94	52.95	54.23
TiO_2 (wt%)	0.43	0.45	0.42	0.47	0.74	0.72
Al_2O_3 (wt%)	17.37	17.54	17.24	17.24	17.12	17.85
Fe_2O_3* (wt%)	4.44	4.70	4.34	4.81	7.18	6.78
FeO* (wt%)	3.99	4.23	3.91	4.32	6.46	6.10
MnO (wt%)	0.10	0.10	0.11	0.11	0.13	0.13
MgO (wt%)	2.88	2.80	2.77	3.30	6.90	6.36
CaO (wt%)	6.50	6.30	6.51	6.90	10.21	10.00
Na_2O (wt%)	3.41	3.39	3.40	3.29	2.45	2.79
K_2O (wt%)	2.39	2.19	2.33	2.26	1.40	1.15
P_2O_5 (wt%)	0.13	0.12	0.13	0.15	0.14	0.14
Total without LOI (wt%)	100.01	99.81	100.01	100.46	99.24	100.14
LOI (wt%)	1.15	1.29	1.31	1.24	1.07	1.04
Mg#	56.28	54.17	55.84	57.66	65.56	65.02
FeO*/MgO	1.38	1.51	1.41	1.31	0.94	0.96
Sc (ppm)	16.09	17.84	15.80	19.64	47.99	44.87
V (ppm)	107.43	117.27	103.86	126.16	252.84	240.09
Cr (ppm)	53.53	58.80	49.43	71.98	160.60	159.87
Ni (ppm)	11.63	13.21	11.36	26.25	27.56	26.39
Cu (ppm)	23.05	25.92	24.69	31.33	57.44	47.08
Zn (ppm)	55.56	53.09	53.54	52.45	55.04	53.59
Sr (ppm)	391.48	399.53	388.51	416.56	368.49	419.97
Y (ppm)	14.92	15.37	14.64	15.67	18.39	19.48
Zr (ppm)	152.94	139.74	132.37	143.58	107.12	120.25
Ba (ppm)	383.85	417.16	374.94	413.72	342.97	342.87

Appendix C: WR trace element concentrations

obtained with ICP-Q-MS

Appendix C: Whole rock ICP-Q-MS data

Unit (this study)	***Loutses SE flow***				***Loutses NW section***				***Loutses S flow***				
Rock type	*Host rock*		*Enclave*		*Host rock*			*Enclave*	*Host rock*			*Enclave*	
sample	**DPM8**	**DPM20**	**DPM9**	**DPM10**	**DPM63**	**DPM66**	**DPM67**	**DPM64**	**DPM26**	**DPM28**	**DPM30A**	**DPM29A**	**DPM29B**
Li (ppm)	25.86	27.14	26.81	19.00	27.31	24.25	22.24	18.62	18.31	28.30	20.07	26.34	22.83
Be (ppm)	1.31	1.25	1.32	0.94	1.29	1.17	1.09	0.98	1.42	1.44	1.44	1.26	0.95
Co (ppm)	11.84	12.35	21.39	18.47	11.88	12.91	15.39	18.92	14.90	14.29	15.34	21.26	25.10
Ga (ppm)	17.24	17.53	18.72	18.70	18.58	18.55	18.07	19.33	18.25	19.02	17.84	16.94	15.96
Rb (ppm)	68.68	67.60	41.61	40.53	70.70	56.74	54.49	37.85	49.45	57.90	53.99	30.48	40.03
Zr (ppm)	72.64	70.45	39.67	103.32	75.55	72.00	88.58	106.38	100.53	89.01	96.05	42.62	90.04
Nb (ppm)	7.88	7.84	8.89	6.48	8.17	9.30	9.03	6.55	7.59	7.69	7.66	7.83	5.25
Mo (ppm)	1.63	1.61	1.63	1.48	1.65	1.33	1.49	1.54	0.72	1.03	0.58	0.63	0.52
Cs (ppm)	3.43	3.46	2.13	1.76	3.62	2.67	2.51	1.59	1.84	1.95	1.96	1.34	1.79
La (ppm)	23.83	23.54	22.43	18.99	24.22	23.60	22.02	18.83	26.28	25.25	25.91	22.96	14.82
Ce (ppm)	42.09	41.72	45.80	36.97	42.79	45.12	42.67	37.07	44.96	44.58	49.04	43.21	28.38
Pr (ppm)	4.42	4.43	5.35	4.28	4.47	4.92	4.77	4.28	5.62	5.19	5.46	5.94	3.58
Nd (ppm)	16.12	16.27	20.75	16.99	16.27	18.73	18.54	16.90	21.92	19.84	20.81	23.65	14.60
Sm (ppm)	3.09	3.15	4.37	3.51	3.11	3.75	3.84	3.59	4.22	3.83	4.00	4.91	3.27
Eu (ppm)	0.86	0.87	1.26	1.06	0.86	0.98	0.99	1.06	1.11	1.02	1.06	1.40	0.98
Gd (ppm)	2.93	3.03	4.40	3.73	3.02	3.71	3.83	3.57	3.66	3.43	3.44	4.59	3.24
Tb (ppm)	0.46	0.46	0.69	0.56	0.46	0.58	0.61	0.56	0.53	0.49	0.49	0.74	0.51
Dy (ppm)	2.82	2.85	4.41	3.47	2.82	3.52	3.76	3.51	3.05	2.88	2.87	4.53	3.15
Ho (ppm)	0.59	0.59	0.93	0.73	0.58	0.72	0.78	0.72	0.60	0.58	0.58	0.95	0.65
Er (ppm)	1.75	1.75	2.78	2.16	1.76	2.13	2.29	2.16	1.74	1.70	1.65	2.83	1.91
Tm (ppm)	0.27	0.27	0.42	0.32	0.27	0.32	0.34	0.33	0.26	0.25	0.25	0.42	0.28
Yb (ppm)	1.83	1.83	2.84	2.18	1.80	2.09	2.24	2.18	1.72	1.67	1.67	2.84	1.88
Lu (ppm)	0.29	0.29	0.44	0.34	0.29	0.32	0.35	0.34	0.26	0.27	0.25	0.43	0.28
Hf (ppm)	2.08	2.04	1.49	2.69	2.19	2.18	2.52	2.72	2.84	2.56	2.67	1.60	2.49
Ta (ppm)	0.60	0.60	0.51	0.41	0.63	0.66	0.62	0.40	0.55	0.55	0.55	0.48	0.36
Pb (ppm)	10.00	10.33	7.59	8.41	11.01	9.48	9.06	6.86	12.04	11.34	10.57	9.62	9.07
Th (ppm)	10.31	9.97	5.39	5.87	10.91	8.28	7.29	5.80	8.73	8.90	9.61	5.75	4.69
U (ppm)	2.42	2.27	1.34	1.34	2.46	1.68	1.65	1.26	1.95	2.17	1.94	1.15	0.92

Unit (this study)	***Loutses SW***					***Kossona Vouno***					***Tsonaka***			
Rock type	*Host rock*				*Enclave*	*Host rock*		*Enclave*			*Host rock*			*Enclave*
sample	**DPM27**	**DPM33**	**DPM57**	**DPM58**	**DPM32**	**DPM34**	**DPM39**	**DPM35 A**	**DPM36**	**DPM41 A**	**DPM42**	**DPM47**	**DPM55**	**DPM56 B**
Li (ppm)	28.76	24.42	25.03	28.01	33.46	28.26	30.14	18.90	18.42	29.49	23.91	23.42	29.23	23.79
Be (ppm)	1.62	1.38	1.35	1.68	1.43	1.26	1.33	0.77	0.65	0.99	1.52	1.55	1.35	1.13
Co (ppm)	14.68	14.37	14.08	15.62	24.95	13.95	11.31	26.23	27.86	22.98	7.98	9.15	9.08	11.20
Ga (ppm)	19.01	17.61	17.78	19.92	17.78	17.71	17.63	17.54	17.64	18.31	18.08	18.03	17.58	20.01
Rb (ppm)	58.00	55.18	50.46	54.00	15.51	63.09	65.74	29.04	23.15	38.93	74.68	74.31	79.16	55.40
Zr (ppm)	95.97	80.69	81.77	92.93	58.30	68.81	61.20	85.74	76.05	80.77	76.41	79.17	75.28	180.98
Nb (ppm)	7.55	7.64	7.67	7.67	8.95	7.68	8.44	5.72	4.70	6.63	9.54	8.52	9.87	13.58
Mo (ppm)	1.36	0.70	0.71	1.36	0.63	1.27	1.15	1.51	0.94	1.11	1.95	1.62	1.95	1.68
Cs (ppm)	3.11	1.61	2.33	2.75	0.66	2.24	1.85	0.94	0.76	1.66	3.64	3.63	3.95	1.98
La (ppm)	25.47	25.15	23.87	26.55	23.24	23.92	25.76	12.93	10.52	16.42	26.93	24.80	26.93	30.65
Ce (ppm)	47.67	51.56	44.66	48.91	45.20	41.69	43.58	25.19	20.80	31.20	48.04	45.09	47.79	61.63
Pr (ppm)	5.22	5.35	4.90	5.51	6.28	4.53	4.64	3.22	2.75	3.64	5.01	4.88	4.93	7.08
Nd (ppm)	19.63	20.17	18.36	20.93	26.31	16.55	16.81	13.33	11.84	14.57	17.74	17.50	17.67	27.70
Sm (ppm)	3.70	3.90	3.55	4.07	5.80	3.21	3.14	3.21	2.99	3.27	3.20	3.33	3.28	5.61
Eu (ppm)	1.00	1.03	0.96	1.06	1.45	0.89	0.86	1.01	0.97	1.01	0.83	0.85	0.85	1.32
Gd (ppm)	3.26	3.34	3.04	3.62	5.47	3.16	3.07	3.38	3.29	3.39	2.97	3.11	3.16	5.36
Tb (ppm)	0.47	0.49	0.45	0.51	0.87	0.49	0.47	0.55	0.56	0.54	0.45	0.48	0.48	0.83
Dy (ppm)	2.77	2.84	2.63	2.98	5.33	3.00	2.87	3.52	3.61	3.42	2.75	3.01	2.93	5.07
Ho (ppm)	0.55	0.57	0.52	0.60	1.10	0.62	0.60	0.72	0.74	0.70	0.55	0.62	0.60	1.04
Er (ppm)	1.63	1.63	1.51	1.74	3.18	1.86	1.81	2.11	2.20	2.03	1.68	1.86	1.80	3.06
Tm (ppm)	0.24	0.25	0.23	0.26	0.47	0.28	0.27	0.31	0.32	0.30	0.26	0.29	0.27	0.45
Yb (ppm)	1.66	1.65	1.56	1.77	3.03	1.94	1.84	2.05	2.14	1.98	1.80	1.96	1.86	3.05
Lu (ppm)	0.26	0.25	0.23	0.27	0.45	0.30	0.29	0.32	0.33	0.31	0.28	0.30	0.29	0.47
Hf (ppm)	2.73	2.29	2.34	2.59	1.81	1.99	1.92	2.31	2.09	2.25	2.27	2.35	2.26	4.50
Ta (ppm)	0.54	0.56	0.56	0.54	0.51	0.58	0.64	0.36	0.29	0.44	0.72	0.63	0.75	0.85
Pb (ppm)	11.65	10.45	11.16	10.82	7.47	10.07	11.79	5.01	4.92	5.46	13.31	12.73	12.28	8.81
Th (ppm)	9.47	9.80	9.42	9.67	4.93	9.75	10.64	4.16	3.16	5.76	10.86	9.87	12.04	9.30
U (ppm)	2.37	2.02	2.03	2.22	0.85	2.27	2.17	1.02	0.78	1.20	2.53	2.30	2.84	1.81

Unit *(Pe-Piper & Piper, 2013)*	***Phase A***		***Phase B***								***Phase C***						
Rock type	*Host rock*		*Host rock*						*Enclave*		*Pumice*					*Bas-And*	
sample	**IM317**	**IM43**	**IM42**	**IM30**	**IM18**	**IM368**	**IM389**	**IM290**	**IM291**	**IM369**	**IM17B**	**IM382**	**IM383**	**IM388**	**DPM65**	**IM9**	**IM10**
Li (ppm)	17.04	15.24	27.26	18.00	18.35	17.96	16.56	18.88	17.03	19.85	16.34	15.66	15.81	15.52	19.43	26.86	9.19
Be (ppm)	1.12	1.12	1.64	1.50	1.41	1.33	1.19	1.30	1.31	0.73	1.02	0.91	0.88	0.87	0.95	0.90	0.93
Co (ppm)	14.97	15.16	4.27	15.47	21.09	22.43	13.58	14.01	18.95	28.94	11.17	11.37	11.94	15.79	11.14	23.93	23.78
Ga (ppm)	17.38	18.78	19.24	17.97	16.78	18.20	17.29	18.20	17.74	15.21	17.47	16.75	16.03	16.56	16.44	NA	NA
Rb (ppm)	56.10	45.02	86.28	57.17	62.99	57.59	64.34	58.21	39.18	31.31	47.65	48.07	42.42	44.50	50.31	31.86	31.83
Zr (ppm)	71.82	96.55	75.38	138.26	133.56	138.00	92.06	97.08	48.46	98.65	167.83	145.29	157.26	142.20	129.94	99.39	99.14
Nb (ppm)	6.83	6.20	9.51	9.36	10.95	11.78	9.69	7.46	7.83	5.58	11.05	10.63	10.57	9.87	9.06	5.73	5.65
Mo (ppm)	1.21	1.22	0.92	1.11	1.33	1.17	1.26	1.21	0.96	0.82	1.11	1.00	0.95	0.96	1.21	0.68	0.73
Cs (ppm)	2.61	1.57	1.73	2.55	2.96	2.72	3.11	2.72	2.03	1.44	1.83	2.07	1.66	1.82	2.09	1.36	1.40
La (ppm)	19.14	16.84	27.71	24.27	32.39	32.18	26.86	22.23	24.26	16.53	24.01	22.92	21.98	21.97	21.55	15.57	15.03
Ce (ppm)	36.06	33.22	50.84	48.63	62.10	62.94	50.51	41.48	45.87	33.25	49.05	47.04	45.65	45.03	43.07	30.19	29.82
Pr (ppm)	4.00	3.87	5.33	5.70	7.00	7.15	5.41	4.78	5.42	3.90	5.56	5.33	5.16	5.07	4.83	3.64	3.53
Nd (ppm)	15.08	15.29	18.62	22.53	26.91	27.58	19.99	18.23	20.76	15.62	21.81	20.72	20.30	19.67	18.58	14.59	14.47
Sm (ppm)	3.18	3.33	3.28	4.81	5.09	5.27	3.83	3.65	4.20	3.34	4.50	4.35	4.33	4.16	3.84	3.27	3.22
Eu (ppm)	0.90	0.97	0.84	1.22	1.33	1.38	1.01	0.99	1.13	0.98	1.14	1.07	1.09	1.06	1.01	0.96	0.95
Gd (ppm)	3.21	3.44	3.36	4.81	4.62	4.80	3.52	3.52	4.04	3.42	4.48	4.28	4.24	4.09	3.76	3.37	3.37
Tb (ppm)	0.51	0.56	0.47	0.75	0.69	0.70	0.53	0.55	0.63	0.55	0.72	0.68	0.68	0.64	0.60	0.56	0.55
Dy (ppm)	3.23	3.60	2.74	4.54	4.06	4.07	3.19	3.39	3.91	3.45	4.44	4.21	4.23	3.99	3.73	3.49	3.49
Ho (ppm)	0.68	0.76	0.57	0.94	0.82	0.82	0.65	0.70	0.81	0.71	0.90	0.86	0.87	0.82	0.78	0.72	0.72
Er (ppm)	2.09	2.28	1.78	2.81	2.36	2.37	1.96	2.09	2.49	2.12	2.64	2.61	2.61	2.44	2.36	2.21	2.20
Tm (ppm)	0.31	0.35	0.28	0.42	0.35	0.34	0.29	0.32	0.36	0.31	0.39	0.38	0.38	0.36	0.35	0.34	0.33
Yb (ppm)	2.14	2.40	1.97	2.73	2.36	2.31	1.98	2.15	2.45	2.11	2.61	2.55	2.52	2.39	2.32	2.18	2.20
Lu (ppm)	0.33	0.37	0.31	0.43	0.35	0.36	0.31	0.33	0.38	0.33	0.39	0.38	0.39	0.37	0.36	0.34	0.34
Hf (ppm)	2.13	0.99	2.25	3.59	1.99	3.49	2.48	2.62	1.60	2.57	2.04	3.72	4.03	3.63	3.42	2.58	2.55
Ta (ppm)	0.51	0.35	0.70	0.63	0.54	0.68	0.66	0.52	0.51	0.36	0.59	0.70	0.69	0.64	0.62	0.39	0.37
Pb (ppm)	11.51	11.07	23.69	17.88	11.07	10.25	11.48	10.26	8.75	6.93	8.14	8.29	7.77	7.96	9.49	6.05	5.94
Th (ppm)	7.74	5.91	10.64	7.82	9.73	9.47	9.87	7.67	6.50	5.20	6.97	6.95	6.45	6.71	7.11	4.43	4.33
U (ppm)	1.79	1.44	1.87	1.70	2.16	2.06	2.21	1.75	1.48	1.15	1.27	1.31	1.17	1.27	1.46	0.98	0.93

Unit *(Pe-Piper & Piper, 2013)*	***Phase C***															***Phase D***	
Rock type	*Bas-And*		*PDC deposit*					*Host rock*					*Enclave*	*Igneous xenolith*		*Host rock*	
sample	**IM32**	**IM36**	**IM13**	**IM359**	**IM364**	**IM393**	**IM395**	**IM372**	**IM379**	**IM23**	**IM24**	**IM310**	**IM373**	**IM376A**	**IM376B**	**IM313**	**IM319**
Li (ppm)	16.38	14.52	16.03	14.82	13.01	14.37	13.01	15.26	18.42	20.02	13.71	11.82	12.49	14.09	12.18	19.41	18.29
Be (ppm)	1.28	1.28	0.90	0.78	0.72	1.00	1.00	0.97	1.03	1.22	0.99	1.10	0.78	1.27	0.99	1.11	1.22
Co (ppm)	25.66	25.13	23.76	24.39	25.83	25.51	24.42	21.20	17.73	15.03	24.17	14.66	30.57	3.81	14.68	9.89	13.44
Ga (ppm)	NA	NA	17.49	15.49	16.04	16.19	15.48	17.45	16.49	17.40	NA	18.82	15.99	13.49	14.76	17.16	18.35
Rb (ppm)	44.84	43.77	27.41	31.63	29.13	41.49	38.06	50.28	49.97	49.38	33.03	44.83	34.51	2.10	3.57	72.53	52.25
Zr (ppm)	86.72	87.52	94.70	93.20	94.72	80.20	84.44	108.69	108.96	75.87	98.97	117.00	110.81	31.56	54.48	58.35	104.52
Nb (ppm)	6.25	6.07	5.58	5.25	5.24	5.87	5.93	8.32	9.36	7.96	5.65	7.17	6.61	6.29	5.13	8.69	8.12
Mo (ppm)	0.78	0.79	0.85	0.72	0.54	0.94	0.93	0.78	0.96	1.34	0.73	0.96	0.83	1.04	1.49	1.32	1.26
Cs (ppm)	2.45	2.31	0.89	1.38	1.35	2.22	1.92	1.43	2.17	2.08	1.30	1.20	1.43	0.10	0.17	3.51	2.68
La (ppm)	14.46	14.38	14.42	13.60	13.32	14.00	13.80	22.66	24.42	22.16	15.67	19.58	18.07	15.01	16.18	24.54	21.46
Ce (ppm)	29.00	28.66	28.63	27.46	27.30	27.98	27.67	44.66	46.55	43.43	30.73	38.78	36.97	28.25	30.91	44.66	41.16
Pr (ppm)	3.39	3.38	3.43	3.26	3.28	3.37	3.32	5.22	5.52	4.86	3.58	4.52	4.43	3.20	3.66	4.75	4.70
Nd (ppm)	14.07	14.02	13.85	13.12	13.22	13.58	13.42	20.45	21.34	18.69	14.37	17.71	18.06	11.54	14.19	17.14	18.17
Sm (ppm)	3.22	3.23	3.12	3.01	3.08	3.19	3.17	4.16	4.38	3.78	3.31	3.69	3.97	2.37	3.07	3.23	3.69
Eu (ppm)	0.95	0.92	0.94	0.94	0.95	0.97	0.96	1.10	1.12	1.01	0.96	1.03	1.11	0.62	0.91	0.87	1.04
Gd (ppm)	3.33	3.63	3.29	3.20	3.30	3.40	3.34	4.06	4.24	3.64	3.27	3.63	3.92	2.24	3.16	3.26	3.62
Tb (ppm)	0.57	0.55	0.54	0.52	0.54	0.55	0.55	0.64	0.66	0.57	0.56	0.57	0.62	0.37	0.51	0.48	0.57
Dy (ppm)	3.56	3.66	3.41	3.33	3.38	3.53	3.50	3.89	4.04	3.52	3.49	3.56	3.83	2.19	3.16	2.82	3.56
Ho (ppm)	0.75	0.76	0.71	0.70	0.72	0.73	0.73	0.78	0.81	0.73	0.72	0.74	0.78	0.45	0.66	0.58	0.74
Er (ppm)	2.24	2.29	2.11	2.12	2.16	2.26	2.22	2.30	2.42	2.14	2.14	2.21	2.31	1.31	1.94	1.74	2.23
Tm (ppm)	0.36	0.35	0.31	0.31	0.32	0.32	0.33	0.34	0.36	0.32	0.35	0.33	0.34	0.19	0.29	0.26	0.33
Yb (ppm)	2.28	2.26	2.12	2.12	2.15	2.24	2.21	2.24	2.41	2.16	2.22	2.27	2.23	1.29	1.92	1.81	2.29
Lu (ppm)	0.35	0.35	0.32	0.33	0.33	0.34	0.34	0.34	0.36	0.32	0.33	0.35	0.34	0.19	0.29	0.28	0.36
Hf (ppm)	2.34	2.34	0.97	2.47	2.49	2.17	2.31	2.91	2.94	1.48	2.63	1.49	2.90	1.00	1.76	1.84	1.49
Ta (ppm)	0.42	0.40	0.31	0.36	0.35	0.40	0.40	0.55	0.62	0.46	0.39	0.48	0.41	0.52	0.32	0.65	0.58
Pb (ppm)	7.92	8.48	6.96	5.49	4.69	8.50	8.03	9.83	8.46	9.25	6.44	7.45	6.08	3.12	3.02	11.78	10.62
Th (ppm)	5.39	5.12	4.40	4.16	4.06	5.01	5.08	6.95	7.60	7.61	4.52	6.07	5.32	7.05	5.11	9.95	7.50
U (ppm)	1.40	1.30	0.97	0.93	0.92	1.31	1.32	1.43	1.49	1.49	0.99	1.27	1.11	1.07	1.08	2.28	1.73

Appendix C: Whole rock ICP-Q-MS data

Unit *(Pe-Piper & Piper, 2013)*	***Phase D***	***Phase F***	***Phase G***										***Phase H***				
Rock type	*Enclave*	*Host*	*Host rock*					*Enclave*					*Host rock*			*Enclave*	
sample	**IM318**	**IM308**	**IM315**	**IM303**	**IM21**	**IM295**	**IM296**	**IM316**	**IM301**	**IM294**	**IM297**	**IM298**	**IM29**	**IM399**	**IM401**	**IM40**	**IM400**
Li (ppm)	18.14	17.98	17.55	17.12	17.34	23.71	23.39	18.60	21.94	28.88	13.82	18.06	25.71	19.29	21.23	21.05	19.29
Be (ppm)	1.14	1.15	1.10	1.00	1.26	1.44	1.36	1.18	0.75	0.74	0.65	1.00	1.99	1.79	1.96	1.78	1.98
Co (ppm)	16.94	12.66	13.46	14.09	10.57	10.36	12.60	19.02	23.05	20.18	29.15	31.92	10.97	15.52	14.52	19.17	22.06
Ga (ppm)	19.81	18.89	16.99	18.33	18.13	18.84	17.36	19.31	16.72	19.47	15.07	16.48	NA	17.77	18.03	NA	18.15
Rb (ppm)	38.52	51.31	54.27	46.07	47.98	66.24	65.41	38.70	31.12	22.41	27.13	36.75	83.57	72.91	80.76	56.57	57.78
Zr (ppm)	122.49	76.72	85.98	145.21	138.52	102.20	80.06	115.25	56.90	97.00	78.68	85.90	90.84	99.69	99.51	103.26	118.03
Nb (ppm)	7.46	9.52	6.65	9.93	8.03	9.31	7.97	6.45	6.00	5.60	4.36	6.80	8.08	7.64	7.96	6.28	6.79
Mo (ppm)	1.22	0.77	1.01	1.17	1.35	1.44	1.41	0.90	0.75	0.99	0.71	1.08	0.91	1.25	1.22	0.91	0.96
Cs (ppm)	1.97	1.52	2.63	1.49	1.89	2.90	3.13	1.74	1.12	1.01	1.34	1.97	5.52	5.22	6.20	4.72	5.24
La (ppm)	17.95	24.45	21.67	21.89	21.21	25.39	22.17	18.57	14.39	11.70	10.98	15.77	22.99	20.89	22.27	16.40	17.74
Ce (ppm)	36.43	45.94	39.44	43.71	42.25	48.62	40.56	36.40	29.23	24.63	22.39	30.50	46.03	39.32	41.61	35.56	35.41
Pr (ppm)	4.37	5.27	4.65	5.01	4.94	5.37	4.44	4.48	3.62	3.18	2.75	3.66	4.36	4.31	4.54	3.85	4.19
Nd (ppm)	17.60	20.17	17.77	19.59	19.48	20.25	16.41	18.08	14.69	13.57	11.19	14.60	15.90	16.24	16.85	15.27	16.63
Sm (ppm)	3.76	4.07	3.59	4.11	3.93	4.00	3.23	3.85	3.34	3.35	2.73	3.21	3.25	3.25	3.32	3.24	3.64
Eu (ppm)	1.11	1.08	1.01	1.07	1.10	1.00	0.88	1.13	0.95	1.04	0.86	0.95	0.90	0.95	0.96	1.05	1.10
Gd (ppm)	3.82	3.99	3.51	4.11	3.80	3.86	3.14	3.84	3.49	3.72	3.04	3.29	2.93	3.17	3.16	3.38	3.52
Tb (ppm)	0.61	0.63	0.55	0.66	0.59	0.61	0.49	0.60	0.57	0.63	0.51	0.53	0.47	0.49	0.49	0.55	0.56
Dy (ppm)	3.84	3.95	3.41	4.15	3.68	3.81	3.08	3.78	3.62	4.10	3.32	3.38	2.78	3.04	2.99	3.26	3.48
Ho (ppm)	0.80	0.82	0.71	0.86	0.77	0.78	0.64	0.78	0.75	0.87	0.71	0.70	0.58	0.62	0.63	0.67	0.72
Er (ppm)	2.39	2.42	2.11	2.51	2.29	2.34	1.92	2.32	2.16	2.61	2.14	2.08	1.82	1.92	1.89	2.08	2.15
Tm (ppm)	0.36	0.36	0.32	0.37	0.35	0.35	0.29	0.35	0.31	0.39	0.32	0.31	0.28	0.29	0.29	0.32	0.31
Yb (ppm)	2.44	2.42	2.18	2.47	2.43	2.42	2.03	2.35	2.07	2.62	2.15	2.08	1.87	1.98	1.98	2.13	2.17
Lu (ppm)	0.38	0.37	0.34	0.38	0.38	0.37	0.31	0.36	0.31	0.40	0.33	0.31	0.29	0.31	0.31	0.32	0.34
Hf (ppm)	1.00	1.51	1.49	1.52	1.52	1.49	2.00	1.51	1.00	0.49	2.17	0.98	2.55	2.67	2.67	2.77	3.06
Ta (ppm)	0.49	0.66	0.46	0.68	0.42	0.66	0.60	0.41	0.40	0.38	0.31	0.46	0.64	0.58	0.61	0.51	0.46
Pb (ppm)	11.26	9.43	9.15	7.93	9.01	12.63	11.22	8.97	6.09	7.83	5.40	7.27	19.11	18.97	20.46	15.76	15.42
Th (ppm)	5.12	8.08	7.64	6.82	6.57	9.06	8.90	5.44	2.57	3.06	3.68	5.41	10.94	9.39	10.11	6.84	6.75
U (ppm)	1.19	1.09	1.51	1.35	1.46	1.96	2.12	1.03	0.27	0.63	0.86	1.30	3.12	2.87	3.14	2.01	2.40

Unit (this study)	***Pyro-clastics***	***Skotini andesite***					***Palaiochora dacitic andesite***		***Kokkinovrahos biotite-hornblende andesite***						
Rock type	*Tuff*	*Host rock*		*Enclave*			*Host rock*		*Host rock*					*Enclave*	
sample	**IA341**	**IA102**	**IA331A**	**IA101**	**IA331B**	**IA332**	**IA61**	**IA340**	**IA55**	**IA56**	**IA344**	**IA346**	**IA352**	**IA336**	**IA338**
Li (ppm)	NA	14.54	NA	NA	NA	NA	10.08	NA	NA	NA	NA	NA	NA	NA	24.07
Be (ppm)	0.89	1.89	2.44	1.18	2.77	2.55	1.68	1.87	2.23	2.84	2.63	2.57	0.89	1.63	2.83
Co (ppm)	8.37	21.05	19.48	20.72	29.86	33.68	5.89	7.41	15.23	15.20	13.53	14.68	8.37	25.61	22.22
Ga (ppm)	9.65	NA	18.42	18.81	13.65	16.07	19.70	25.48	17.90	19.56	18.94	19.09	9.65	17.22	14.76
Rb (ppm)	NA	73.90	NA	44.01	NA	NA	35.92	NA	87.15	NA	NA	NA	NA	NA	78.45
Zr (ppm)	27.76	NA	67.37	NA	71.03	109.49	87.38	103.74	50.72	NA	57.28	56.95	61.64	59.30	36.59
Nb (ppm)	4.94	6.10	10.08	4.25	12.07	9.61	8.98	9.44	8.09	7.73	7.61	7.65	4.94	4.43	7.62
Mo (ppm)	3.30	1.33	1.29	0.82	1.21	0.51	0.72	0.35	0.53	0.31	0.38	0.75	3.30	0.45	0.52
Cs (ppm)	NA	4.07	NA	1.13	NA	NA	0.94	NA	5.58	NA	NA	NA	NA	NA	4.52
La (ppm)	11.22	16.08	21.90	13.65	22.63	18.68	24.42	25.48	26.96	28.54	26.76	29.17	11.22	15.37	21.16
Ce (ppm)	21.20	29.74	40.12	26.31	41.12	35.52	47.51	47.50	47.93	48.50	45.08	49.97	21.20	29.13	47.81
Pr (ppm)	2.60	3.32	4.66	3.45	5.25	4.52	5.61	5.87	5.07	5.07	4.96	5.09	2.60	3.39	5.78
Nd (ppm)	10.45	12.61	18.56	14.30	22.14	19.11	21.74	23.52	18.36	18.64	18.35	18.41	10.45	13.74	22.86
Sm (ppm)	2.11	2.67	3.85	3.21	4.82	4.23	4.42	4.79	3.55	3.40	3.40	3.32	2.11	3.01	4.51
Eu (ppm)	0.49	0.89	1.04	0.95	1.34	1.19	1.08	1.19	0.95	0.90	0.90	0.89	0.49	0.86	1.31
Gd (ppm)	2.05	2.68	3.67	3.25	4.57	4.04	3.99	4.71	3.08	3.07	2.99	2.97	2.05	2.87	4.31
Tb (ppm)	0.32	0.43	0.57	0.50	0.70	0.63	0.61	0.70	0.45	0.44	0.44	0.42	0.32	0.45	0.62
Dy (ppm)	1.94	2.78	3.46	3.22	4.15	3.80	3.63	4.04	2.70	2.64	2.60	2.53	1.94	2.73	3.71
Ho (ppm)	0.39	0.60	0.70	0.66	0.84	0.77	0.71	0.82	0.55	0.55	0.52	0.52	0.39	0.57	0.76
Er (ppm)	1.15	1.74	2.09	1.94	2.43	2.28	2.05	2.36	1.64	1.67	1.58	1.57	1.15	1.69	2.19
Tm (ppm)	0.17	0.27	0.31	0.29	0.36	0.35	0.30	0.35	0.25	0.26	0.25	0.24	0.17	0.25	0.32
Yb (ppm)	1.06	1.71	2.02	2.01	2.28	2.23	1.92	2.25	1.77	1.68	1.58	1.61	1.06	1.65	2.15
Lu (ppm)	0.16	0.27	0.31	0.29	0.35	0.34	0.28	0.33	0.27	0.28	0.25	0.26	0.16	0.25	0.32
Hf (ppm)	0.73		2.03	2.23	2.37	2.96	2.72	3.01	1.61	1.63	1.79	1.78	1.85	1.73	1.53
Ta (ppm)	0.34	0.51	0.64	0.29	0.66	0.55	0.57	0.60	0.54	0.53	0.54	0.53	0.34	0.29	0.36
Pb (ppm)	7.63	13.16	14.12	9.32	12.91	10.28	16.62	17.66	28.72	25.48	30.99	26.12	7.63	13.46	17.40
Th (ppm)	3.04	8.78	7.87	4.31	6.68	6.43	7.96	8.24	12.56	11.94	11.68	12.35	3.04	5.85	6.10
U (ppm)	9.25	2.65	2.54	1.27	1.80	2.09	1.13	1.26	3.72	2.87	3.05	3.78	9.25	1.84	1.41

Unit (this study)	***Kokkinovrahos biotite-hornblende andesite***				***Phase 1 biotite-hornblende andesite***							***Volcaniclastic apron***		***Kakoperato rhyodacite***	
Rock type	*Enclave*				*Host rock*	*Enclave*	*Host rock*		*Enclave*	*Host rock*		*Host rock*	*Enclave*	*Host rock*	
sample	**IA345**	**IA348**	**IA349**	**IA355B**	**IA59**	**IA66**	**IA65**	**IA103**	**IA104**	**IA94**	**IA327**	**IA322**	**IA321**	**IA97**	**IA333**
Li (ppm)	NA	NA	NA	NA	12.86	NA	NA	19.91	NA	NA	NA	NA	NA	27.71	NA
Be (ppm)	2.18	1.59	2.49	2.81	1.21	2.73	1.94	1.79	1.68	1.64	1.78	1.89	2.02	2.18	2.30
Co (ppm)	18.45	26.41	17.05	19.29	25.58	12.73	12.43	16.77	21.29	12.40	11.80	14.70	30.96	5.48	5.66
Ga (ppm)	25.93	19.13	22.87	24.42	16.18	19.00	24.22	16.57	25.68	18.44	18.43	21.48	18.84	NA	20.70
Rb (ppm)	NA	NA	NA	NA	41.27	NA	NA	81.59	NA	36.36	56.79	NA	NA	133.08	NA
Zr (ppm)	37.58	69.11	46.16	35.77	58.97	82.58	55.42	51.70	84.70	NA	NA	57.46	109.43	NA	64.71
Nb (ppm)	6.33	4.11	7.26	7.92	5.32	7.55	8.47	6.82	5.58	7.00	7.13	7.71	9.92	8.55	8.98
Mo (ppm)	0.22	0.14	0.95	0.31	0.90	0.21	1.11	1.44	0.83	0.60	1.06	1.45	1.09	0.70	0.74
Cs (ppm)	NA	NA	NA	NA	1.96	NA	NA	4.44	NA	0.96	2.84	NA	NA	9.43	NA
La (ppm)	16.99	13.77	25.04	21.12	13.74	29.17	21.55	20.25	19.26	28.31	29.65	22.04	24.93	26.06	30.31
Ce (ppm)	38.32	31.10	50.12	46.38	27.32	49.94	40.64	35.45	35.03	53.23	55.02	38.29	48.68	47.38	51.16
Pr (ppm)	4.63	3.20	5.41	5.86	3.35	4.95	4.47	4.03	4.66	5.78	6.01	3.96	5.56	5.01	5.44
Nd (ppm)	19.20	13.34	20.97	24.12	13.76	17.79	17.22	15.27	19.61	21.68	22.78	14.90	22.91	17.53	19.33
Sm (ppm)	3.98	3.01	4.05	4.80	3.13	3.15	3.48	3.09	4.37	3.91	4.14	2.94	4.79	3.09	3.27
Eu (ppm)	1.11	0.85	1.08	1.28	0.95	0.84	0.91	0.85	1.18	1.02	0.99	0.82	1.32	0.88	0.77
Gd (ppm)	3.53	2.91	3.53	4.16	3.24	2.79	3.36	2.99	4.17	3.72	3.71	2.77	4.38	2.41	2.68
Tb (ppm)	0.54	0.45	0.53	0.63	0.51	0.40	0.53	0.45	0.67	0.50	0.51	0.43	0.66	0.36	0.38
Dy (ppm)	3.28	2.76	3.17	3.80	3.22	2.39	3.25	2.82	4.06	2.93	3.01	2.63	3.84	2.13	2.21
Ho (ppm)	0.67	0.56	0.65	0.77	0.66	0.49	0.68	0.58	0.83	0.61	0.62	0.55	0.77	0.45	0.45
Er (ppm)	2.01	1.65	1.91	2.27	1.95	1.46	2.06	1.75	2.46	1.76	1.71	1.66	2.23	1.36	1.33
Tm (ppm)	0.30	0.24	0.29	0.34	0.29	0.22	0.32	0.26	0.37	0.27	0.28	0.26	0.33	0.23	0.21
Yb (ppm)	1.94	1.52	1.83	2.19	1.90	1.46	2.05	1.76	2.36	1.74	1.81	1.70	2.04	1.68	1.47
Lu (ppm)	0.30	0.23	0.28	0.33	0.29	0.23	0.33	0.27	0.37	0.26	0.27	0.27	0.31	0.26	0.23
Hf (ppm)	1.44	2.08	1.68	1.46	1.82	2.25	1.77	1.70	2.37	3.50	3.65	1.79	2.94	3.21	2.04
Ta (ppm)	0.38	0.39	0.43	0.40	0.28	0.52	0.59	0.42	0.36	0.52	0.51	0.60	0.57	0.67	0.71
Pb (ppm)	22.03	22.03	19.85	18.36	8.20	24.38	15.59	17.50	12.36	20.38	20.26	15.98	11.45	35.93	32.99
Th (ppm)	5.92	5.99	9.11	5.35	5.06	12.11	8.15	10.19	5.09	12.27	12.24	11.28	10.21	18.09	18.55
U (ppm)	1.51	1.31	2.62	1.58	1.46	3.40	2.48	3.18	1.64	3.04	3.44	3.44	2.96	7.04	7.27

Unit (this study)	***Kakoperato rhyodacite***	***Nikolaki andesite***		***Oros-Lazarides basaltic andesite***								***Oros hornblende andesite***		
Rock type	*Enclave*	*Host rock*		*Host rock*				*Enclave*	*Host rock*			*Host rock*	*Enclave*	
sample	**IA98**	**IA73**	**IA74**	**IA71**	**IA83**	**IA85**	**IA88**	**IA72**	**IA80**	**IA93**	**IA68**	**IA75**	**IA77**	**IA78**
Li (ppm)	31.91	NA	NA	12.50	7.81	8.46	NA	10.76	11.12	NA	NA	13.12	26.81	NA
Be (ppm)	1.91	1.35	1.32	1.19	1.37	1.07	1.34	1.09	1.22	1.28	1.31	1.44	1.20	1.33
Co (ppm)	17.38	23.11	22.33	24.11	24.91	23.78	22.82	33.83	23.63	22.91	22.94	17.93	24.77	34.65
Ga (ppm)	NA	26.05	18.80	NA	NA	NA	29.28	21.70	NA	29.23	28.42	NA	19.85	22.14
Rb (ppm)	64.32	NA	41.50	32.65	37.41	33.13	NA	18.28	32.42	NA	NA	54.60	44.49	NA
Zr (ppm)	NA	93.82	NA	104.10	106.01	98.91	96.25	91.85	91.91	96.70	97.80	94.56	86.18	85.91
Nb (ppm)	5.40	4.21	4.11	4.07	4.08	3.82	3.85	3.65	3.70	3.77	3.92	4.96	4.46	5.76
Mo (ppm)	0.57	0.48	0.61	0.58	0.70	0.62	0.53	0.51	0.51	0.38	0.47	0.65	0.69	0.49
Cs (ppm)	3.55	NA	1.96	1.05	1.76	1.46	NA	0.84	0.74	NA	NA	2.64	2.12	NA
La (ppm)	24.56	20.11	20.63	17.19	17.48	16.63	18.30	13.99	16.46	17.25	16.12	18.99	14.93	23.52
Ce (ppm)	47.90	35.78	38.08	35.50	35.74	33.42	37.23	29.93	32.53	32.82	32.74	35.54	30.62	52.61
Pr (ppm)	5.92	4.79	5.02	4.32	4.45	4.46	5.18	3.90	4.20	4.18	4.02	4.32	3.81	6.84
Nd (ppm)	24.21	20.02	20.45	17.92	18.30	18.54	23.14	16.76	17.68	17.77	17.09	17.15	16.02	30.24
Sm (ppm)	4.81	4.21	4.32	3.97	4.02	4.01	5.13	3.84	3.87	3.86	3.70	3.60	3.65	6.51
Eu (ppm)	1.32	1.15	1.21	1.05	1.09	1.13	1.41	1.13	1.11	1.13	1.07	0.98	1.05	1.65
Gd (ppm)	4.16	3.75	3.83	3.57	3.89	4.14	4.80	3.61	3.57	3.61	3.44	3.47	3.47	5.48
Tb (ppm)	0.56	0.56	0.55	0.53	0.54	0.57	0.72	0.54	0.56	0.55	0.52	0.48	0.52	0.77
Dy (ppm)	3.17	3.28	3.22	3.12	3.20	3.45	4.21	3.26	3.29	3.27	3.08	2.89	3.14	4.30
Ho (ppm)	0.63	0.65	0.64	0.62	0.66	0.68	0.83	0.65	0.69	0.66	0.62	0.59	0.64	0.82
Er (ppm)	1.85	1.87	1.77	1.82	1.87	2.05	2.35	1.85	1.92	1.92	1.83	1.76	1.84	2.28
Tm (ppm)	0.26	0.28	0.27	0.27	0.30	0.29	0.35	0.27	0.29	0.29	0.27	0.25	0.26	0.32
Yb (ppm)	1.72	1.78	1.61	1.67	1.82	1.85	2.15	1.72	1.82	1.84	1.70	1.70	1.71	1.93
Lu (ppm)	0.24	0.26	0.24	0.26	0.28	0.29	0.32	0.25	0.28	0.27	0.26	0.27	0.25	0.28
Hf (ppm)	2.94	2.55	2.58	2.78	2.88	2.68	2.64	2.65	2.57	2.64	2.69	2.69	2.49	2.70
Ta (ppm)	0.39	0.27	0.27	0.26	0.26	0.25	0.24	0.19	0.24	0.24	0.25	0.35	0.30	0.33
Pb (ppm)	19.61	11.33	12.48	10.38	11.41	6.25	9.82	5.97	9.09	11.06	9.05	15.05	16.58	9.57
Th (ppm)	11.17	7.26	7.19	6.74	6.85	6.37	6.17	5.14	5.83	6.05	6.53	9.06	6.92	7.36
U (ppm)	3.70	2.33	2.39	2.11	2.17	2.11	2.09	1.24	1.99	1.96	2.24	3.34	2.60	2.54

Volcanic unit (Schwandner, 1998)	***Poros andesite***		***Poros dacite***			
Rock type	*Host rock*		*Host rock*		*Enclave*	
sample	**IP46**	**IP300**	**IP49**	**IP299**	**IP50**	**IP53**
Li (ppm)	53.10	45.18	51.04	49.00	42.16	47.44
Be (ppm)	3.22	3.30	3.13	3.15	1.73	2.42
Co (ppm)	10.45	12.46	9.75	13.65	26.96	25.96
Ga (ppm)	NA	19.72	NA	18.92	NA	18.98
Rb (ppm)	104.07	103.87	102.41	105.43	46.31	40.08
Zr (ppm)	72.32	79.15	72.20	90.03	97.57	106.1
Nb (ppm)	8.84	9.28	8.77	9.10	5.50	6.79
Mo (ppm)	0.58	0.71	0.59	0.80	0.59	0.52
Cs (ppm)	7.64	8.33	7.74	8.46	2.59	3.14
La (ppm)	24.73	28.20	31.61	28.10	20.47	22.98
Ce (ppm)	51.66	51.97	59.53	51.31	39.82	44.65
Pr (ppm)	4.84	5.62	5.95	5.62	4.61	5.16
Nd (ppm)	18.42	20.26	20.96	20.46	18.01	20.09
Sm (ppm)	3.30	3.55	3.61	3.64	3.69	3.96
Eu (ppm)	0.87	0.91	0.90	0.94	1.05	1.10
Gd (ppm)	2.91	3.07	3.12	3.14	3.67	3.69
Tb (ppm)	0.44	0.44	0.42	0.45	0.56	0.55
Dy (ppm)	2.45	2.61	2.41	2.63	3.28	3.38
Ho (ppm)	0.48	0.52	0.46	0.53	0.69	0.69
Er (ppm)	1.41	1.54	1.45	1.55	1.98	2.01
Tm (ppm)	0.22	0.23	0.22	0.23	0.31	0.30
Yb (ppm)	1.52	1.57	1.44	1.56	1.81	2.01
Lu (ppm)	0.22	0.24	0.23	0.24	0.30	0.30
Hf (ppm)	3.81	2.15	3.38	2.37	2.64	2.78
Ta (ppm)	3.81	2.15	3.38	2.37	2.64	2.78
Pb (ppm)	0.61	0.50	0.62	0.49	0.34	0.34
Th (ppm)	22.57	22.40	22.96	22.41	11.21	12.12
U (ppm)	10.59	10.74	11.27	10.65	7.49	8.31

Appendix D: WR Sr, Nd and Pb isotopic compositions obtained with MC-ICP-MS

Unit (this study)	***sample***	$^{87}Sr/^{86}Sr$	**1StdDev**	$^{143}Nd/^{144}Nd$	**1StdDev**	$^{206}Pb/^{204}Pb$	**1StdDev**	$^{207}Pb/^{204}Pb$	**1StdDev**	$^{208}Pb/^{204}Pb$	**1StdDev**
Host rock Loutses-SE	***DPM8***	0.706432	0.000036	0.512515	0.000015	18.8780	0.0020	15.6909	0.0018	39.0380	0.0051
Host rock Loutses-SE	***DPM20***	0.706409	0.000038	0.512517	0.000018	18.8815	0.0028	15.6901	0.0024	39.0387	0.0069
Enclave Loutses-SE	***DPM9***	0.706421	0.000037	0.512550	0.000021	18.8630	0.0028	15.6890	0.0025	39.0293	0.0070
Enclave Loutses-SE	***DPM10***	0.706363	0.000043	0.512505	0.000016	18.8883	0.0022	15.6885	0.0020	39.0315	0.0050
Host rock Loutses-NW	***DPM66***	0.707927	0.000039	0.512348	0.000023	18.8918	0.0025	15.7067	0.0020	39.0951	0.0046
Host rock Loutses-NW	***DPM67***	0.707858	0.000046	0.512336	0.000024	18.8978	0.0027	15.7074	0.0023	39.0964	0.0054
Enclave Loutses-NW	***DPM64***	0.706313	0.000042	0.512515	0.000010	18.8787	0.0025	15.6865	0.0022	39.0207	0.0048
Host rock Loutses-S	***DPM26***	0.704870	0.000052	0.512581	0.000017	18.9080	0.0035	15.7033	0.0032	39.0903	0.0078
Host rock Loutses-S	***DPM28***	0.704913	0.000042	0.512588	0.000013	18.9060	0.0030	15.7026	0.0028	39.0883	0.0068
Host rock top Loutses-S	***DPM30A***	0.704916	0.000045	0.512586	0.000015	18.9038	0.0045	15.7002	0.0037	39.0845	0.0095
Enclave Loutses-S	***DPM29A***	0.705913	0.000048	0.512552	0.000019	18.8945	0.0038	15.6998	0.0034	39.0720	0.0079
Enclave Loutses-S	***DPM29B***	0.705105	0.000038	0.512643	0.000016	18.9024	0.0051	15.6996	0.0043	39.0760	0.0108
Host rock Loutses -SW	***DPM27***	0.704994	0.000050	0.512589	0.000014	18.8996	0.0029	15.7002	0.0027	39.0781	0.0067
Host rock Loutses -SW	***DPM33***	0.705054	0.000039	0.512578	0.000017	18.8996	0.0035	15.7014	0.0029	39.0840	0.0079
Host rock Loutses -SW	***DPM57***	0.705040	0.000036	0.512581	0.000014	18.8918	0.0031	15.7018	0.0030	39.0749	0.0064
Host rock Loutses -SW	***DPM58***	0.704983	0.000037	0.512570	0.000014	18.8984	0.0027	15.6886	0.0023	39.0751	0.0060
Enclave Loutses - SW	***DPM32***	0.705885	0.000037	0.512536	0.000015	18.8734	0.0051	15.6928	0.0047	39.0427	0.0116
Host rock Kossona Vouno	***DPM34***	0.706192	0.000045	0.512530	0.000012	18.8637	0.0025	15.6908	0.0020	39.0291	0.0051
Enclave Kossona Vouno	***DPM36***	0.705536	0.000049	0.512657	0.000021	18.8562	0.0030	15.6882	0.0026	39.0103	0.0073
Enclave Kossona Vouno	***DPM41A***	0.705667	0.000042	0.512608	0.000019	18.8636	0.0031	15.6882	0.0032	39.0228	0.0071
Host rock Tsonaka	***DPM42***	0.706964	0.000035	0.512424	0.000014	18.8739	0.0024	15.6950	0.0023	39.0470	0.0063
Enclave Tsonaka	***DPM56B***	0.707558	0.000041	0.512371	0.000017	18.9243	0.0026	15.6968	0.0021	39.0437	0.0055

Phase (Pe-Piper & Piper, 2013)	**Type**	***sample***	**$^{87}Sr/^{86}Sr$**	**1StdDev**	**$^{143}Nd/^{144}Nd$**	**1StdDev**	**$^{206}Pb/^{204}Pb$**	**1Std Dev**	**$^{207}Pb/^{204}Pb$**	**1Std Dev**	**$^{208}Pb/^{204}Pb$**	**1Std Dev**
A	Host rock	***IM317***	0.706255	0.000039	0.512526	0.000030	18.7085	0.0032	15.6809	0.0028	38.8529	0.0068
A	Host rock	***IM43***	0.706276	0.000037	0.512535	0.000012	18.7230	0.0025	15.6797	0.0022	38.8634	0.0058
B	Host rock	***IM42***	0.706990	0.000034	0.512445	0.000021	18.6526	0.0035	15.6830	0.0030	38.8230	0.0083
B	Host rock	***IM30***	0.707367	0.000045	0.512380	0.000021	18.8908	0.0035	15.6991	0.0028	39.0692	0.0079
B	Host rock	***IM18***	0.706853	0.000043	0.512446	0.000020	18.8857	0.0026	15.6939	0.0022	39.0550	0.0055
B	Host rock	***IM368***	0.706856	0.000041	0.512462	0.000023	18.8808	0.0032	15.6958	0.0026	39.0553	0.0064
B	Host rock	***IM389***	0.707087	0.000036	0.512429	0.000025	18.8748	0.0022	15.7008	0.0021	39.0649	0.0054
B	Host rock	***IM290***	0.706729	0.000044	0.512515	0.000015	18.9197	0.0038	15.7078	0.0033	39.0784	0.0084
B	Enclave	***IM291***	0.706559	0.000036	0.512493	0.000026	18.8794	0.0036	15.6951	0.0031	39.0324	0.0084
B	Enclave	***IM369***	0.706378	0.000040	0.512496	0.000028	18.8476	0.0041	15.6937	0.0034	39.0204	0.0089
C	Pumice	***IM17B***	0.709262	0.000038	0.512246	0.000016	18.9384	0.0021	15.7106	0.0017	39.1485	0.0047
C	Pumice	***IM382***	0.709093	0.000041	0.512263	0.000021	18.9355	0.0040	15.7138	0.0037	39.1528	0.0094
C	Pumice	***IM383***	0.709246	0.000030	0.512246	0.000022	18.9511	0.0037	15.7142	0.0033	39.1665	0.0074
C	Pumice	***IM388***	0.708643	0.000038	0.512289	0.000025	18.9262	0.0031	15.7153	0.0028	39.1512	0.0065
C	Pumice	***DPM65***	0.708299	0.000034	0.512322	0.000023	18.8997	0.0035	15.7070	0.0033	39.1057	0.0085
C	Ass bas and	***IM10***	0.706181	0.000053	0.512540	0.000016	18.8919	0.0036	15.6868	0.0033	39.0590	0.0076
C	Ass bas and	***IM36***	0.705873	0.000046	0.512596	0.000017	18.8225	0.0042	15.6870	0.0037	39.0055	0.0090
C	PDC	***IM359***	0.706132	0.000038	0.512521	0.000026	18.8868	0.0051	15.6839	0.0041	39.0411	0.0100
C	PDC	***IM364***	0.706062	0.000036	0.512544	0.000034	18.8492	0.0053	15.6725	0.0047	38.9666	0.0120
C	PDC	***IM393***	0.705770	0.000039	0.512590	0.000031	18.8246	0.0035	15.6920	0.0030	39.0282	0.0076
C	PDC	***IM395***	0.705796	0.000043	0.512595	0.000032	18.8287	0.0035	15.6932	0.0030	39.0374	0.0075
C	Host rock	***IM372***	0.707302	0.000043	0.512402	0.000022	18.8685	0.0035	15.7073	0.0032	39.0725	0.0078
C	Host rock	***IM379***	0.707761	0.000036	0.512348	0.000018	18.6325	0.0050	15.6780	0.0028	38.7616	0.0097
C	Host rock	***IM23***	0.706784	0.000032	0.512419	0.000015	18.8849	0.0020	15.6929	0.0019	39.0467	0.0049

Phase (Pe-Piper & Piper, 2013)	**Type**	***sample***	**$^{87}Sr/^{86}Sr$**	**1StdDev**	**$^{143}Nd/^{144}Nd$**	**1StdDev**	**$^{206}Pb/^{204}Pb$**	**1Std Dev**	**$^{207}Pb/^{204}Pb$**	**1Std Dev**	**$^{208}Pb/^{204}Pb$**	**1Std Dev**
C	Host rock	**IM24**	0.706213	0.000050	0.512524	0.000140	18.8923	0.0038	15.6879	0.0033	39.0635	0.0087
C	Enclave	**IM373**	0.706639	0.000035	0.512459	0.000020	18.8787	0.0036	15.6998	0.0032	39.0709	0.0075
C	Igneous xenolith	**IM376A**	0.707548	0.000039	0.512381	0.000025	18.6619	0.0098	15.5352	0.0084	38.2267	0.0202
C	Igneous xenolith	**IM376B**	0.707231	0.000042	0.512416	0.000027	18.3418	0.0054	15.5592	0.0045	38.2677	0.0117
D	Host rock	**IM313**	0.706769	0.000047	0.512482	0.000016	18.8840	0.0032	15.7083	0.0029	39.0742	0.0071
D	Host rock	**IM319**	0.706711	0.000038	0.512452	0.000018	18.8903	0.0028	15.6914	0.0024	39.0086	0.0063
D	Enclave	**IM318**	0.706648	0.000034	0.512484	0.000017	18.8507	0.0024	15.6847	0.0020	38.9491	0.0048
F	Host rock	**IM308**	0.707264	0.000034	0.512407	0.000014	18.8881	0.0041	15.7038	0.0038	39.0885	0.0094
G	Host rock	**IM315**	0.706655	0.000029	0.512525	0.000017	18.9021	0.0025	15.6863	0.0021	39.0054	0.0054
G	Host rock	**IM303**	0.708446	0.000036	0.512283	0.000017	18.9243	0.0028	15.7080	0.0025	39.1325	0.0066
G	Host rock	**IM21**	0.706517	0.000040	0.512531	0.000022	18.9294	0.0026	15.6829	0.0023	38.9666	0.0059
G	Host rock	**IM295**	0.707272	0.000033	0.512390	0.000023	18.8233	0.0032	15.6920	0.0030	39.0118	0.0078
G	Host rock	**IM296**	0.706461	0.000032	0.512495	0.000018	18.8496	0.0016	15.6881	0.0013	39.0013	0.0035
G	Enclave	**IM316**	0.706633	0.000031	0.512553	0.000014	18.9354	0.0021	15.6913	0.0018	39.0188	0.0045
G	Enclave	**IM301**	0.707255	0.000035	0.512390	0.000014	18.8911	0.0026	15.7002	0.0023	39.0770	0.0060
G	Enclave	**IM294**	0.706355	0.000035	0.512509	0.000018	18.7916	0.0029	15.6898	0.0026	38.9687	0.0071
G	Enclave	**IM297**	0.706065	0.000031	0.512542	0.000034	18.8167	0.0055	15.6744	0.0046	38.9394	0.0115
G	Enclave	**IM298**	0.705935	0.000042	0.512562	0.000019	18.8484	0.0023	15.6867	0.0021	39.0044	0.0055
H	Host rock	**IM29**	0.706863	0.000051	0.512548	0.000017	18.8456	0.0040	15.6978	0.0036	39.0415	0.0092
H	Host rock	**IM399**	0.706713	0.000039	0.512557	0.000029	18.8351	0.0028	15.6999	0.0025	39.0531	0.0064
H	Host rock	**IM401**	0.706916	0.000041	0.512549	0.000029	18.8407	0.0039	15.6992	0.0030	39.0479	0.0074
H	Enclave	**IM40**	0.706563	0.000070	0.512575	0.000016	18.8223	0.0042	15.7031	0.0037	39.0579	0.0052
H	Enclave	**IM400**	0.706683	0.000043	0.512588	0.000029	18.8260	0.0036	15.7013	0.0030	39.0501	0.0074

Unit (this study)	**Type**	***sample***	$^{87}Sr/^{86}Sr$	**1StdDev**	$^{143}Nd/^{144}Nd$	**1StdDev**	$^{206}Pb/^{204}Pb$	**1StdDev**	$^{207}Pb/^{204}Pb$	**1StdDev**	$^{208}Pb/^{204}Pb$	**1StdDev**
Skotini andesite	Host rock	**IA102**	0.706085	0.000060	0.512555	0.000020	18.8337	0.0042	15.6853	0.0038	38.9785	0.0103
	Host rock	**IA331A**	0.706134	0.000044	0.512507	0.000017	18.8054	0.0026	15.6772	0.0021	38.8713	0.0052
	Enclave	**IA101**	0.706115	0.000056	0.512561	0.000063	18.8139	0.0048	15.6836	0.0040	38.9538	0.0106
	Enclave	**IA331B**	0.705674	0.000037	0.512567	0.000015	18.7938	0.0021	15.6724	0.0017	38.8286	0.0044
	Enclave	**IA332**	0.705926	0.000036	0.512547	0.000016	18.8049	0.0021	15.6760	0.0019	38.8601	0.0046
Palaiochora dac.and	Host rock	**IA61**	0.707607	0.000040	0.512334	0.000015	18.8287	0.0026	15.6972	0.0024	39.0299	0.0062
Kokkinovrahos biotite-hornblende andesite	Host rock	**IA55**	0.706282	0.000047	0.512488	0.000016	18.7733	0.0021	15.6818	0.0019	38.9498	0.0046
	Host rock	**IA56**	0.706261	0.000060	0.512480	0.000038	18.7639	0.0058	15.6799	0.0048	38.9377	0.0118
	Host rock	**IA344**	0.706147	0.000034	0.512492	0.000012	/		/		/	
	Host rock	**IA346**	0.706551	0.000041	0.512489	0.000017	18.6551	0.0022	15.6673	0.0019	38.7760	0.0049
	Enclave	**IA338**	0.706307	0.000038	0.512507	0.000016	18.7730	0.0029	15.6818	0.0024	38.9539	0.0062
	Enclave	**IA345**	0.707269	0.000029	0.512491	0.000015	18.6220	0.0025	15.6614	0.0020	38.7328	0.0051
	Enclave	**IA348**	0.705786	0.000032	0.512470	0.000017	18.6603	0.0028	15.6687	0.0016	38.7902	0.0055
	Enclave	**IA349**	0.706169	0.000034	0.512521	0.000014	18.7750	0.0024	15.6832	0.0021	38.9570	0.0050
Phase 1 biotite-hornblende andesite	Host rock	**IA59**	0.706217	0.000032	0.512507	0.000020	18.8346	0.0030	15.6845	0.0026	38.9624	0.0066
	Enclave	**IA66**	0.705789	0.000036	0.512571	0.000018	18.8501	0.0024	15.6813	0.0022	38.9629	0.0054
	Host rock	**IA65**	0.706948	0.000038	0.512418	0.000015	18.8253	0.0022	15.6891	0.0020	38.9921	0.0049
	Host rock	**IA103**	0.706125	0.000035	0.512500	0.000016	18.8351	0.0026	15.6820	0.0022	38.9837	0.0053
	Enclave	**IA104**	0.705797	0.000040	0.512462	0.000015	18.8013	0.0027	15.6756	0.0021	38.9701	0.0050
	Host rock	**IA94**	0.705623	0.000061	0.512450	0.000028	18.8184	0.0053	15.6848	0.0043	38.9666	0.0109
	Host rock	**IA327**	0.705736	0.000057	0.512450	0.000036	18.8227	0.0052	15.6847	0.0045	38.9730	0.0111
Volcaniclastic apron	Enclave	**IA321**	0.706246	0.000038	0.512522	0.000034	18.8788	0.0025	15.6836	0.0020	38.9651	0.0048
Kakoperato rhyodacite	Host rock	**IA97**	0.706489	0.000063	0.512459	0.000012	18.7675	0.0049	15.6916	0.0042	38.9517	0.0128
	Enclave	**IA98**	0.704685	0.000058	0.512567	0.000027	18.7986	0.0058	15.6798	0.0050	38.9434	0.0126
Nikolaki andesite	Host rock	**IA74**	0.704243	0.000064	0.512572	0.000031	18.8466	0.0051	15.6753	0.0047	38.9392	0.0111
Oros-Lazarides basaltic andesite	Host rock	**IA71**	0.704178	0.000043	0.512619	0.000012	18.8405	0.0046	15.6678	0.0037	38.9114	0.0106
	Host rock	**IA83**	0.704158	0.000052	0.512627	0.000017	18.8497	0.0035	15.6712	0.0035	38.9245	0.0089
	Enclave	**IA72**	0.704132	0.000032	0.512620	0.000019	18.8444	0.0022	15.6743	0.0018	38.9288	0.0043
	Host rock	**IA80**	0.704098	0.000034	0.512621	0.000016	18.8603	0.0023	15.6645	0.0019	38.9100	0.0049
	Host rock	**IA68**	0.704124	0.000042	0.512620	0.000014	18.8475	0.0021	15.6667	0.0020	38.9133	0.0046
Oros hornblende andesite	Host rock	**IA75**	0.704424	0.000064	0.512581	0.000013	18.8384	0.0027	15.6771	0.0027	38.9469	0.0069
	Enclave	**IA77**	0.704216	0.000035	0.512600	0.000015	18.8273	0.0023	15.6768	0.0018	38.9405	0.0046
	Enclave	**IA78**	0.704845	0.000035	0.512531	0.000016	18.8436	0.0025	15.6801	0.0020	38.9657	0.0051

Unit (this study)	***sample***	**$^{87}Sr/^{86}Sr$**	**1StdDev**	**$^{143}Nd/^{144}Nd$**	**1StdDev**	**$^{206}Pb/^{204}Pb$**	**1StdDev**	**$^{207}Pb/^{204}Pb$**	**1StdDev**	**$^{208}Pb/^{204}Pb$**	**1StdDev**
Poros andesitic dacitic host rocks	***IP46***	0.707440	0.000050	0.512382	0.000023	18.8576	0.0033	15.5969	0.0027	39.1547	0.0072
	IP300	0.707358	0.000040	0.512376	0.000015	18.8503	0.0025	15.6916	0.0023	39.1358	0.0057
	IP49	0.707384	0.000042	0.512393	0.000017	18.8473	0.0038	15.6925	0.0034	39.1404	0.0107
	IP299	0.707329	0.000042	0.512385	0.000016	18.8586	0.0026	15.6914	0.0021	39.1320	0.0055
Poros enclaves	***IP50***	0.706057	0.000053	0.512501	0.000018	18.8537	0.0030	15.6854	0.0030	39.0760	0.0088
	IP53	0.706331	0.000031	0.512460	0.000013	18.8353	0.0016	15.6878	0.0013	39.0962	0.0034

Appendix E: WR Hf isotopic compositions

obtained with MC-ICP-MS

Unit witin volcanic stratigraphy	Rock type	Sample nr.	$^{176}Hf/^{177}Hf$	1StDev	1StError
METHANA (Pe-Piper & Piper, 2013)					
Phase B	host rock	HP DPM28	0.282835	0.000035	0.000004
Phase B	host rock	LP DPM28	0.282826	0.000042	0.000004
Phase B	enclave	DPM29A	0.282853	0.000048	0.000005
Phase B	host rock	DPM33	0.282832	0.000046	0.000005
Phase B	enclave	DPM32	0.282841	0.000050	0.000005
Phase C	pumice	IM383	0.282481	0.000051	0.000006
Phase C	PDC scoria	IM364	0.282811	0.000040	0.000004
Phase C	host rock	HP IM36	0.282868	0.000044	0.000005
Phase C	host rock	LP IM36	0.282896	0.000043	0.000005
Phase C	host rock	IM379	0.282598	0.000041	0.000004
Phase C	enclave	IM373	0.282709	0.000044	0.000005
Phase C	igneous xenolith	IM376A	0.282636	0.000054	0.000006
Phase C	igneous xenolith	IM376B	0.282704	0.000064	0.000007
Phase D	host rock	DPM8	0.282816	0.000043	0.000005
Phase D	enclave	DPM9	0.282886	0.000065	0.000007
Phase D	host rock	DPM66	0.282601	0.000047	0.000005
Phase D	host rock	HP DPM42	0.282722	0.000048	0.000005
Phase D	host rock	LP DPM42	0.282697	0.000035	0.000004
Phase D	enclave	DPM56B	0.282690	0.000046	0.000005
Phase D	host rock	DPM34	0.282822	0.000044	0.000005
Phase D	enclave	DPM36	0.282933	0.000050	0.000005
Phase D	enclave	DPM41A	0.282888	0.000039	0.000004
Phase D	host rock	HP IM313	0.282764	0.000050	0.000005
Phase D	host rock	LP IM313	0.282784	0.000043	0.000005
Phase D	host rock	IM319	0.282765	0.000043	0.000005
Phase D	enclave	IM318	0.282756	0.000044	0.000005
Phase G	host rock	IM295	0.282733	0.000045	0.000005
Phase G	enclave	IM294	0.282828	0.000050	0.000005
Phase G	host rock	IM315	0.282805	0.000046	0.000005
Phase G	enclave	IM316	0.282820	0.000043	0.000005
Phase G	host rock	IM303	0.282529	0.000051	0.000005
Phase G	enclave	IM301	0.282658	0.000045	0.000005
Phase H	host rock	HP IM29	0.282800	0.000046	0.000005
Phase H	host rock	LP IM29	0.282825	0.000043	0.000005
Phase H	enclave	IM400	0.282846	0.000045	0.000005

Unit within volcanic stratigraphy	**Rock type**	Sample nr.	**$^{176}Hf/^{177}Hf$**	**1StDev**	**1StError**
from pumice	sed xenolith	IM386	0.282635	0.000072	0.000008
from PDC deposit	sed xenolith	IM394	0.282864	0.000055	0.000006
AEGINA (this study)					
1-Skotini andesite	host rock	IA102	0.282837	0.000062	0.000007
1-Skotini andesite	enclave	IA101	0.282915	0.000064	0.000007
1-Palaiochora dac and	host rock	HP IA61	0.282636	0.000061	0.000007
1-Palaiochora dac and	host rock	LP IA61	0.282628	0.000040	0.000004
1-Kokkinovrahos bt-hbl and	host rock	HP IA56	0.282800	0.000051	0.000005
1-Kokkinovrahos bt-hbl and	host rock	LP IA56	0.282821	0.000039	0.000004
1-Kokkinovrahos bt-hbl and	enclave	HP IA338	0.282888	0.000060	0.000006
1-Kokkinovrahos bt-hbl and	enclave	LP IA338	0.282872	0.000052	0.000006
1-Kokkinovrahos bt-hbl and	host rock	IA346	0.282788	0.000061	0.000007
1-Kokkinovrahos bt-hbl and	enclave	IA348	0.282788	0.000063	0.000007
1-Phase 1 bt-hbl and	host rock	HP IA59	0.282832	0.000052	0.000006
1-Phase 1 bt-hbl and	host rock	LP IA59	0.282836	0.000047	0.000005
1-Phase 1 bt-hbl and	enclave	IA66	0.282880	0.000061	0.000007
1-Phase 1 bt-hbl and	host rock	IA65	0.282717	0.000066	0.000007
1-Phase 1 bt-hbl and	enclave	IA104	0.282773	0.000076	0.000008
1-Phase 1 bt-hbl and	host rock	IA327	0.282775	0.000062	0.000007
1-Phase 1 bt-hbl and	enclave	IA321	0.282838	0.000047	0.000005
2-Kakoperato rhyodacite	host rock	HP IA97	0.282771	0.000046	0.000005
2-Kakoperato rhyodacite	host rock	LP IA97	0.282794	0.000036	0.000004
2-Kakoperato rhyodacite	enclave	IA98	0.282895	0.000049	0.000005
2-Nikolaki andesite	host rock	IA73	0.282898	0.000069	0.000007
2-Oros-Lazarides bas and	host rock	IA80	0.282918	0.000051	0.000005
2-Oros-Lazarides bas and	host rock	IA83	0.282878	0.000052	0.000006
2-Oros-Lazarides bas and	enclave	IA72	0.282892	0.000044	0.000005
2-Oros-Lazarides bas and	host rock	IA75	0.282867	0.000058	0.000006
2-Oros-Lazarides bas and	enclave	IA77	0.282887	0.000059	0.000006
POROS (this study)					
Andesitic dacite	host rock	IP46	0.282715	0.000057	0.000006
Andesitic dacite	host rock	HP IP49	0.282718	0.000074	0.000008
Andesitic dacite	host rock	LP IP49	0.282738	0.000046	0.000005
Basaltic andesite	enclave	IP50	0.282846	0.000056	0.000006

Appendix F: WR geochemical composition of sedimentary basement and xenoliths

Appendix F: WR geochemistry of sedimentary basement & xenoliths

sample	**IM14**	**IM397**	**IM26**	**IM362**	**IM363rim**	**IM363core**	**IM386**	**IM394**	**IM396**
	Lower Cretaceous limestone	*Upper Triassic limestone*	*Upper Jurassic sandstone/ conglomerate*	*Xenolith (volcaniclastic) in PDC deposits*	*Xenolith (calcareous) in PDC deposits*	*Xenolith (calcareous) in PDC deposits*	*Xenolith (calc-silicate) in pumice*	*Xenolith (calcareous) in PDC deposits*	*Xenolith (limestone) in PDC deposits*
SiO_2 (wt%)	18.98		74.78	62.31	43.19	16.58	41.11	30.49	
TiO_2 (wt%)	0.01		0.20	0.81	0.59	0.01	0.20	0.31	
Al_2O_3 (wt%)	0.25		3.11	13.25	11.19	6.43	5.23	10.16	
Fe_2O_3*(wt%)	0.30	0.01	1.19	7.71	6.01	0.48	2.38	3.98	0.01
MnO (wt%)	0.08		0.02	0.08	0.08	0.03	0.68	0.07	
MgO (wt%)	0.98	3.37	0.40	4.43	5.51	11.30	1.92	10.27	0.77
CaO (wt%)	79.78	96.56	19.08	7.50	32.19	64.59	45.89	43.26	99.21
Na_2O (wt%)	0.01	0.00	0.73	2.01	0.16	0.03	0.94	0.71	0.00
K_2O (wt%)	0.06	0.01	0.52	2.10	0.34	0.05	0.68	0.07	0.01
P_2O_5 (wt%)	0.04	0.02	0.03	0.10	0.07	0.02	0.06	0.05	0.01
Total (wt%)	100.49	99.97	100.06	100.32	99.32	99.52	99.09	99.37	100.01
LOI (wt%)	38.72	41.94	13.44	0.30	24.90	36.36	27.92	30.00	41.62
Sc (ppm)	0.91	0.80	2.24	17.92	16.20	3.34	4.33	9.76	0.86
Zn (ppm)	4.45	5.39	9.97	89.66	25.83	18.15	40.41	26.74	3.43
Sr (ppm)	248.3	314.3	84.4	191.9	239.7	180.5	201.8	114.7	206.4
V (ppm)	9.61	8.32	19.07	117.77	89.98	26.90	34.26	44.99	8.82
Y (ppm)	2.41	0.71	4.55	18.81	10.93	10.16	12.78	17.62	2.11
Cu (ppm)	3.17	2.80	2.68	60.29	9.12	4.42	13.42	96.96	4.49
Zr (ppm)	23.2	17.2	92.1	184.4	91.9	20.4	62.4	83.8	26.1
Ba (ppm)	18.5	10.9	62.8	188.8	526.0	67.5	51.0	63.9	11.1
Li (ppm)	1.30	0.19	4.61	30.24	4.24	8.49	9.67	7.08	0.09
Be (ppm)			0.23	1.61	0.32		0.29	0.28	
Cr (ppm)	6.72	4.57	102.3	439.5	63.0	10.6	19.5	30.4	4.89
Co (ppm)	1.66	1.27	1.96	38.92	11.74	8.91	12.38	9.93	1.29
Ni (ppm)	21.86	9.12	18.03	488.1	28.12	98.46	36.99	25.99	8.59
Ga (ppm)	3.36	3.25	5.30	14.92	10.83	8.47	6.87	8.40	3.37
Rb (ppm)	1.95	0.46	13.90	81.99	6.52	1.52	22.95	3.09	0.46
Nb (ppm)	0.56	0.47	2.69	12.35	3.02	0.49	3.54	1.17	0.48
Mo (ppm)	0.32	0.33	0.31	0.46	0.74	0.41	0.35	0.41	0.27

sample	**IM14**	**IM397**	**IM26**	**IM362**	**IM363rim**	**IM363core**	**IM386**	**IM394**	**IM396**
	Lower Cretaceous limestone	*Upper Triassic limestone*	*Upper Jurassic sandstone/ conglomerate*	*Xenolith (volcaniclastic) in PDC deposits*	*Xenolith (calcareous) in PDC deposits*	*Xenolith (calcareous) in PDC deposits*	*Xenolith (calc-silicate) in pumice*	*Xenolith (calcareous) in PDC deposits*	*Xenolith (limestone) in PDC deposits*
Cs (ppm)	0.09	0.01	0.61	9.71	0.49	0.13	1.26	0.33	0.01
La (ppm)	1.45	0.71	5.98	24.64	8.48	4.08	11.50	9.43	1.36
Ce (ppm)	2.92	1.83	11.81	52.00	17.51	4.52	26.68	10.98	1.90
Pr (ppm)	0.46	0.34	1.49	5.89	1.95	1.17	3.02	2.34	0.45
Nd (ppm)	1.57	1.06	5.49	23.04	7.51	4.92	12.05	9.92	1.53
Sm (ppm)	0.31	0.21	1.07	4.67	1.66	1.15	2.44	2.21	0.30
Eu (ppm)	0.10	0.07	0.24	1.07	0.50	0.31	0.56	0.65	0.10
Gd (ppm)	0.30	0.17	0.96	4.17	1.71	1.31	2.23	2.39	0.28
Tb (ppm)	0.05	0.03	0.15	0.62	0.28	0.21	0.33	0.38	0.05
Dy (ppm)	0.27	0.13	0.83	3.54	1.71	1.30	1.84	2.39	0.25
Ho (ppm)	0.05	0.02	0.16	0.69	0.36	0.28	0.36	0.51	0.05
Er (ppm)	0.17	0.07	0.47	1.91	1.08	0.81	1.03	1.54	0.15
Tm (ppm)	0.02	0.01	0.07	0.26	0.16	0.11	0.14	0.22	0.02
Yb (ppm)	0.15	0.06	0.44	1.73	1.07	0.73	0.92	1.44	0.14
Lu (ppm)	0.02	0.01	0.06	0.25	0.16	0.11	0.14	0.23	0.02
Hf (ppm)	0.17	0.17	0.40	1.64	1.30	0.30	0.50	1.03	0.18
Ta (ppm)	0.03	0.03	0.17	0.83	0.20	0.03	0.22	0.08	0.03
Pb (ppm)	0.56	0.21	3.22	9.84	0.20	0.17	2.48	0.90	0.63
Th (ppm)	0.10	0.04	1.74	7.62	2.37	0.26	2.24	2.03	0.05
U (ppm)	0.59	0.14	0.37	1.43	0.70	0.38	0.40	0.32	0.13
$^{87}Sr/^{86}Sr$	0.707400±5	0.707789±6	0.709816±8	0.71009±80	0.708030±6	0.708129±8	0.709465±7	0.707991±7	0.707790±7
$^{143}Nd/^{144}Nd$			0.512225±5	0.512318±2	0.512511±3	0.512399±5	0.512211±2	0.512554±3	
$^{206}Pb/^{204}Pb$				18.8943±6					
$^{207}Pb/^{204}Pb$				15.6949±5					
$^{208}Pb/^{204}Pb$				39.0950±12					

sample	IA342	IA54	IA62	IA343	IA328A
	Late Palaeozoic limestone	*Triassic limestone*	*Jurassic limestone*	*Late Palaeozoic calcarenite*	*Quartz-rich xenolith Skotini and*
SiO_2 (wt%)	0.24	0.35	3.87	14.61	97.95
TiO_2 (wt%)				0.10	0.00
Al_2O_3 (wt%)	0.04	0.16	0.25	2.62	0.69
Fe_2O_3*(wt%)	0.01	0.03	0.08	0.96	0.01
MnO (wt%)	0.01	0.02	0.02	0.03	0.00
MgO (wt%)	0.82	0.52	1.23	1.16	0.01
CaO (wt%)	97.41	97.76	94.82	80.43	0.18
Na_2O (wt%)	/	/	/	0.43	0.00
K_2O (wt%)	0.01	0.03	0.06	0.37	0.06
P_2O_5 (wt%)	0.02	0.05	0.04	0.04	0.00
Total (wt%)	43.07	42.35	42.01	38.99	0.25
LOI (wt%)	98.51	98.86	100.32	100.76	98.91
Sc (ppm)	0.22	0.68	0.75	2.78	0.08
Zn (ppm)	0.38	7.71	9.40	11.68	/
Sr (ppm)	260.25	282.35	315.68	4024.33	7.80
V (ppm)	0.46	1.81	3.07	19.92	0.08
Y (ppm)	8.78	17.38	14.34	11.18	/
Cu (ppm)	2.83	14.07	13.01	21.09	3.31
Zr (ppm)	14.35	14.24	20.16	39.34	15.27
Ba (ppm)	6.75	7.96	5.62	87.09	16.95
Li (ppm)	0.14	0.25	1.77	5.60	28.56
Be (ppm)	0.02	0.04	0.04	0.28	0.07
Cr (ppm)	3.10	4.71	2.00	21.32	0.75
Co (ppm)	0.37	0.41	0.60	2.72	0.09
Ni (ppm)	5.35	6.38	5.56	20.20	0.90
Rb (ppm)	0.28	1.02	1.48	10.17	1.66
Nb (ppm)	/	0.06	0.08	1.74	0.06
Mo (ppm)	0.03	0.05	0.13	0.27	0.00
Cs (ppm)	0.01	0.06	0.14	1.73	0.04
La (ppm)	1.36	4.10	6.92	6.41	0.33
Ce (ppm)	1.33	2.19	2.88	11.97	0.64
Pr (ppm)	0.31	0.79	1.27	1.48	0.08
Nd (ppm)	1.11	3.25	5.42	5.78	0.15
Sm (ppm)	0.21	0.64	1.04	1.17	0.02
Eu (ppm)	0.05	0.16	0.24	0.26	0.01
Gd (ppm)	0.35	0.84	1.13	1.19	0.05
Tb (ppm)	0.04	0.12	0.16	0.17	0.00
Dy (ppm)	0.32	0.79	0.92	1.01	0.02
Ho (ppm)	0.08	0.19	0.19	0.20	0.00
Er (ppm)	0.25	0.57	0.52	0.57	0.01
Tm (ppm)	0.04	0.08	0.07	0.08	0.00
Yb (ppm)	0.25	0.49	0.40	0.47	0.02
Lu (ppm)	0.04	0.08	0.06	0.07	0.00
Hf (ppm)	0.03	0.04	0.05	0.25	0.04
Ta (ppm)	0.01	0.07	0.01	0.09	0.01
Pb (ppm)	0.42	0.72	0.89	3.47	0.35
Th (ppm)	0.07	0.11	0.14	1.53	0.20
U (ppm)	1.00	0.79	1.34	1.51	0.08
$^{87}Sr/^{86}Sr$	0.707385±41	0.707792±42	0.707793±49	0.708948±72	/
$^{143}Nd/^{144}Nd$	0.512266±54	0.512271±34	0.512230±31	0.512277±27	/
$^{206}Pb/^{204}Pb$	/	/	/	18.9400±29	/
$^{207}Pb/^{204}Pb$	/	/	/	15.6875±22	/
$^{208}Pb/^{204}Pb$	/	/	/	39.0007±57	/